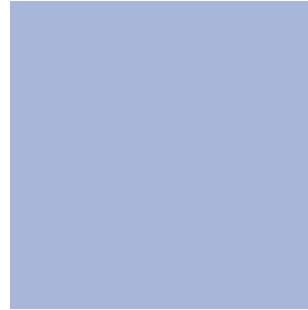


2008
nrl review



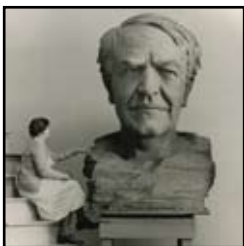
the navy's corporate laboratory

NAVAL RESEARCH LABORATORY
Washington, DC 20375

Report Documentation Page				Form Approved OMB No. 0704-0188	
Public reporting burden for the collection of information is estimated to average 1 hour per response, including the time for reviewing instructions, searching existing data sources, gathering and maintaining the data needed, and completing and reviewing the collection of information. Send comments regarding this burden estimate or any other aspect of this collection of information, including suggestions for reducing this burden, to Washington Headquarters Services, Directorate for Information Operations and Reports, 1215 Jefferson Davis Highway, Suite 1204, Arlington VA 22202-4302. Respondents should be aware that notwithstanding any other provision of law, no person shall be subject to a penalty for failing to comply with a collection of information if it does not display a currently valid OMB control number.					
1. REPORT DATE 2008		2. REPORT TYPE		3. DATES COVERED 00-00-2008 to 00-00-2008	
4. TITLE AND SUBTITLE 2008 NRL review. the navy's corporate laboratory				5a. CONTRACT NUMBER	
				5b. GRANT NUMBER	
				5c. PROGRAM ELEMENT NUMBER	
6. AUTHOR(S)				5d. PROJECT NUMBER	
				5e. TASK NUMBER	
				5f. WORK UNIT NUMBER	
7. PERFORMING ORGANIZATION NAME(S) AND ADDRESS(ES) Naval Research Laboratory, 4555 Overlook Avenue SW, Washington, DC, 20375				8. PERFORMING ORGANIZATION REPORT NUMBER	
9. SPONSORING/MONITORING AGENCY NAME(S) AND ADDRESS(ES)				10. SPONSOR/MONITOR'S ACRONYM(S)	
				11. SPONSOR/MONITOR'S REPORT NUMBER(S)	
12. DISTRIBUTION/AVAILABILITY STATEMENT Approved for public release; distribution unlimited					
13. SUPPLEMENTARY NOTES					
14. ABSTRACT					
15. SUBJECT TERMS					
16. SECURITY CLASSIFICATION OF:			17. LIMITATION OF ABSTRACT Same as Report (SAR)	18. NUMBER OF PAGES 250	19a. NAME OF RESPONSIBLE PERSON
a. REPORT unclassified	b. ABSTRACT unclassified	c. THIS PAGE unclassified			

General information on the research described in this *NRL Review* can be obtained from the Public Affairs Office, Code 1030, (202) 767-2541. Information concerning Technology Transfer is available from the Technology Transfer Office, Code 1004, (202) 767-7230. Sources of information on the various educational programs at NRL are listed in the *NRL Review* chapter entitled "Programs for Professional Development."

For additional information about NRL, the *NRL Fact Book* lists the organizations and key personnel for each division. It contains information about Laboratory funding, programs, and field sites. The *Fact Book* can be obtained from the Technical Information Services Branch, Code 3430, (202) 404-4963. The web-based *NRL Major Facilities* publication, which describes each NRL facility in detail, can be accessed at <http://www.nrl.navy.mil>.



ON THE COVER

This bust of Thomas Edison, which graces NRL's front gate area, was sculpted by Evelyn Beatrice Longman and presented to NRL by the Thomas Alva Edison Foundation, Inc. It was unveiled on December 3, 1953. Ms. Longman was an accomplished sculptor whose work can also be seen on the Lincoln Memorial in Washington, D.C. She donated her time and skill to the wreaths, ornaments, and lettering so that the original design of the monument could be completed for its allotted cost.

Approved for public release; distribution is unlimited.

NRL REVIEW STAFF

SENIOR SCIENCE EDITOR

John D. Bultman

COORDINATOR

Jonna Atkinson

CONSULTANT

Kathy Parrish

DESIGN, LAYOUT, AND GRAPHIC SUPPORT

Jonna Atkinson, Donna Gloystein, and Peggy Newman

EDITORIAL ASSISTANCE

Saul Oresky, Kathy Parrish, and Claire Peachey

PHOTOGRAPHIC PRODUCTION

Jamie Baker, Gayle Fullerton, and James Marshall



COMMANDING OFFICER

CAPT Paul C. Stewart, USN



DIRECTOR OF RESEARCH

Dr. John A. Montgomery

REVIEWED AND APPROVED

NRL/PU/3430--09-504

RN: 09-1226-0782

April 2009

Paul C. Stewart, Captain, USN
Commanding Officer

A bronze bust of a man, likely a historical figure, is mounted on a tall, light-colored stone or concrete pedestal. The bust is shown in profile, facing left. In the background, there is a modern building with large windows and a sky with some clouds. To the right, there are lush green trees and some pink flowering branches. In the foreground, there are out-of-focus red flowers.

NRL's MISSION

To conduct a broadly based multidisciplinary program of scientific and advanced technological development directed toward maritime applications of new and improved materials, techniques, equipment, systems, and ocean, atmospheric, and space sciences and related technologies.

The Naval Research Laboratory provides primary in-house research for the physical, engineering, space, and environmental sciences; broadly based applied research and advanced technology development programs in response to identified and anticipated Navy and Marine Corps needs; broad multidisciplinary support to the Naval Warfare Centers; and space and space systems technology, development, and support.

contents

2008 NRL REVIEW

FEATURES

3

OUR PEOPLE ARE
MAKING A DIFFERENCE

8

NRL INVENTIONS THAT
HAVE CHANGED THE
WORLD

17

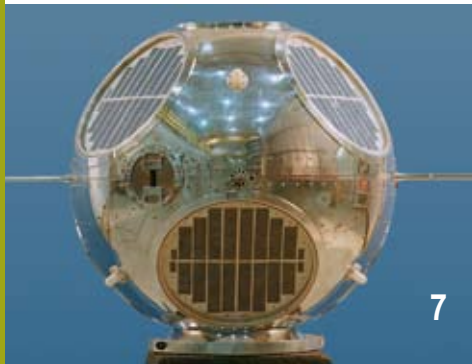
RUTH H. HOOKER
RESEARCH LIBRARY –
THE FIRST 80 YEARS

23

NRL's VANGUARD I
CELEBRATES 50 YEARS
IN SPACE

28

NANOSCIENCE AND
NANOTECHNOLOGY
AT NRL



THE NAVAL RESEARCH LABORATORY

- 35 NRL – Our Heritage
- 36 Highlights of NRL Research in 2007
- 41 NRL Today

FEATURED RESEARCH

- 71 Polymorphism in Energetic Materials
- 79 First-Principles Simulations of Violent Space-Weather Events
- 89 High-Power Fiber Lasers for Directed-Energy Applications
- 101 Plant Proanthocyanidins Bind To and Neutralize Bacterial Lipopolysaccharides
- 109 Exploring Solar Flares with Gamma Rays and Neutrons

RESEARCH ARTICLES

acoustics

- 123 Underwater Acoustic Communications for Bottom-Mounted Sensor Networks
- 125 Environmental Acoustic Variability Characterization for Adaptive Sampling

atmospheric science and technology

- 131 Environmental Mission Impact Assessment
- 134 On Tropical Cyclone Formation
- 136 SHIMMER: Innovative Technology Enabling Unprecedented Science

chemical/biochemical research

- 141 Aerobic Miniature Microbial Fuel Cells
- 143 Innovative Ionic Liquids: Electrolytes for Ion Power Sources

electronics and electromagnetics

- 149 Generalized FFT Beamsteering
- 151 Graded Bandgap Type-II Superlattice Photodiodes
- 153 Dynamics of Forward Voltage Drift in 4H-SiC PiN Diodes

information technology and communications

- 159** Mitigating Motion Sickness in Ground Vehicles
- 160** Unmanned Vehicle Mission Planning Using 4D Forecasts
- 163** Measurement and Analysis of Clutter in Electronic Displays
- 166** NRL Global Vessel Tracking Project (VTP)

materials science and technology

- 171** Carbon Surface Modification for Enhanced Corrosion Resistance
- 173** Lifetime Limiting Defects in 4H-SiC
- 174** Mobility Enhancement in Strained Antimonide Quantum Wells
- 177** Creating Spin Currents in Silicon

nanoscience technology

- 183** Multifunctional Electrode Nanoarchitectures for Electrochemical Capacitors
- 185** Enhancement of Electrical Properties by Tailoring Nanoparticles in Holmium-doped $\text{YBa}_2\text{Cu}_3\text{O}_{7-\delta}$ Superconductors
- 187** Molecular Memory Circuits Using a Virus as a Template
- 189** Single Crystal Diamond Nanomechanical Dome Resonator

ocean science and technology

- 195** Improving Underwater Imaging with Ocean Optics Research
- 197** Large-Amplitude Internal Waves in the South China Sea
- 200** Probabilistic Prediction for Improved Scientific Understanding and Improved Decision Making

optical sciences

- 205** High-Fidelity Analog Fiber Optics and Photonics for Military Applications
- 207** Tactical DIRCM Jamming Pod – Early Operational Assessment
- 210** Fiber-Optic Strain Monitoring on a Navy Cruiser
- 213** Infrared Ship Signature Model Validation from Measurements at CBD

remote sensing

- 219** Vantage™ Unmanned Air Vehicle
- 220** The Scintillation and Tomography Receiver in Space (CITRIS) Instrument for Ionospheric Research
- 222** Carbon Fiber Reinforced Polymer (CFRP) Telescope Program at the Naval Research Laboratory

- 224** Monitoring Global Surface Soil Moisture with the WindSat Polarimetric Microwave Radiometer

simulation, computing, and modeling

- 229** CREW Modeling of Effectiveness and Compatibility for Operational Test and Evaluation
- 231** Dynamics of Coronal Mass Ejections (CMEs)
- 234** Enabling Coordination During Security, Stabilization, Transition, and Reconstruction Operations

space research and satellite technology

- 239** FREND: Pushing the Envelope of Space Robotics
- 241** Wide Field of View Imaging with a VHF Phased Array
- 243** The Target Indicator Experiment on TacSat-2
- 245** Development of a Bearingless Ammonia Pump for Spacecraft Thermal Control

SPECIAL AWARDS AND RECOGNITION

- 251** Special Awards & Recognition
- 264** Alan Berman Research Publication and NRL Edison (Patent) Awards

PROGRAMS FOR PROFESSIONAL DEVELOPMENT

- 271** Programs for NRL Employees — Graduate Programs, Continuing Education, Professional Development, Equal Employment Opportunity (EEO) Programs, and Other Activities
- 273** Programs for Non-NRL Employees — Recent Ph.D., Faculty Member, and College Graduate Programs, Professional Appointments, and College and High School Student Programs

GENERAL INFORMATION

- 277** Technical Output
- 278** Key Personnel
- 279** Contributions by Divisions, Laboratories, and Departments
- 282** Subject Index
- 286** Author Index
- 287** Employment Opportunities

nrl's involved!

3

Our People Are Making a Difference

8

NRL Inventions That Have Changed the World

17

Ruth H. Hooker Research Library – The First 80 Years

23

NRL's Vanguard I Celebrates 50 Years in Space

28

Nanoscience and Nanotechnology at NRL

NRL Inventions That Have Changed **THE WORLD**

From when it first opened its doors in 1923, the Naval Research Laboratory has been a powerful force for innovation on behalf of the U.S. Navy and the Nation. The inventions that the Laboratory has produced have improved our lives and sometimes changed the world, from the earliest work in gamma-ray radiography and radio propagation to the latest developments in space technology and environmental threat detection.

The claim that our inventions and innovations have sometimes changed the world should not be made lightly. Imagine, then, how different, in fact poorer, the world would be without many of the unique contributions that the Laboratory has made to defense, health, safety, and atmospheric and environmental monitoring applications as well as to expanding the frontiers of science and technology.

Why, then, is the Laboratory's role as an inventions dynamo not more widely known? Part of the reason is due to the requirements of national security. Some of NRL's activities, such as the GRAB satellite program, are initially classified (and some remain so for long afterward as well), for obvious reasons. Others are parts of ongoing scientific research programs that involve many participants in the Department of Defense, other governmental agencies, academia, and industry, not all of whom want their involvement publicized or detailed. Yet another reason is the nature of the Laboratory's work in basic scientific research and as an innovator of technology but not the developer of the widely recognized final product. The GPS program is just one, but perhaps the best known, example of that phenomenon.

This article and the descriptions, photographs and other graphics found in this book describe some of the accomplishments that collectively demonstrate the global impact of the Laboratory's scientific achievements.



NRL – a powerful force for innovation on behalf of the U.S. Navy and the Nation.

NRL's iconic radar dish on top of Building 43 used in the historical moon relay experiment of 1951.



NRL invented and developed the first modern radar. Researchers A.H. Taylor and L.C. Young in 1922 made seminal observations of “phase distortion” in radio waves reflected from a steamer on the Potomac River. By using radio waves to detect a moving ship, they discovered the radar principle. In 1930, the NRL research team first noted that aircraft could also be detected via reflected radio waves. Based on these early observations, Dr. Young proposed a pulsed radar technique to be used for detection. Four years later, his colleague, Dr. R. Page, demonstrated the world’s first pulsed radar. A crucial component of Dr. Page’s radar was the “duplexer,” his invention that permitted use of the same antenna for transmitting and receiving. NRL installed the first operational radar aboard the battleship USS *New York* in 1939, and then quickly transferred the technology to industry for development. The technological edge afforded by radar’s ability to detect ships and aircraft from afar in all weather contributed to the U.S. victories of the Coral Sea, Midway, and Guadalcanal in World War II.



NRL invented and developed the first modern radar.

Ever since, NRL has continued to contribute to radar’s development. NRL researchers invented the plan-position indicator (PPI), the ubiquitous, familiar radar monitor with its sweeping hand that displays the ranges and bearings of all targets “visible” to the radar. (The PPI was simultaneously being invented in England, though neither country knew of the other’s work.)

The first American airborne radar, the Model ASB, was also a product of NRL’s ingenuity. Developed in 1941, Model ASB was known as the radar that fought the war from the air in the Pacific. Used for bombing, detection of ships and surfaced submarines, and airborne intercept, Model ASB was the first radar to be used in carrier-based aircraft and widened the area that could be covered by patrol planes. Experience with this radar led to the development of UHF E2 Airborne Early Warning radar, microwave intercept radar, and antisubmarine warfare periscope detection radars.

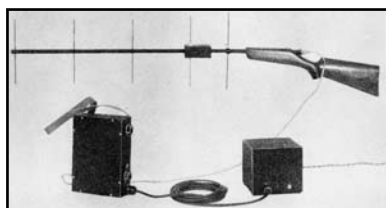


Prior to World War II, NRL developed the Model ASB radar.

The Laboratory also pioneered monopulse radar in 1943 and high frequency over-the-horizon (HF OTH) radar in 1957, later extending its use to the study of the ionosphere. The serendipitous discovery that HF OTH radar signal clutter analysis could also be used to observe sea state and winds over the ocean led to its use in weather forecasting and studying ocean dynamics for military

operations and civilian use. Radar's application to navigation, surveillance, weapon targeting, and threat detection/tracking have been invaluable to the military. The civilian uses of radar in drug interdiction, transportation, weather forecasting, astronomy, and automation have also highlighted its worth.

NRL developed and built the Model XAE in 1937, the first radio recognition identification friend-or-foe (IFF) system, to begin to solve the problem of identifying targets on the ground, sea, or in the air, particularly in overcast weather or at night. The follow-on radar system, developed in 1939, displayed the echo pulse of an identified radar target



NRL developed and built the Model XAE in 1937, the first radio recognition identification friend-or-foe (IFF) system.

on the scope and featured NRL researcher Dr. R.M. Page's pulse transponder, which is basic to pulse IFF systems and pulse beacon systems. The Mark X IFF, a later NRL-built radar beacon system, was crucial in reducing fratricide when using beyond-visual-range weapons. The Mark X was the basis of the Federal Aviation Administration's (FAA) Air Traffic Control Radar Beacon System (ATCRBS), which was later adopted by the International Civil Air Organization, making it the basis of the world's air traffic control system.

Radar's many contributions to furthering our understanding of the environment, the upper atmosphere, the oceans, and space have proven invaluable. For instance, Doppler radar is famous for its use by meteorologists to locate storms and measure wind speed and direction and by astronomers to find and measure the distances to stars as well as determine their ages. Its use by police departments to catch and prosecute speeders is also well known!

In addition, the ability of bistatic radar (that is, radar that comprises transmitting and receiving antennas separated by a considerable difference) to track objects in space contributed to NRL's Minitrack system, which could detect and track satellites. This capability led to development of the Naval Space Surveillance System (NAVSPASUR), which is part of the North American Aerospace Defense Command (NORAD). All of those developments led in turn to what became the Global Positioning System.

NRL's researchers have continued to explore the seemingly limitless capabilities of this technology, installing it aboard satellites to provide worldwide coverage and aboard aircraft to afford early-warning detection. Radar is a key sensor in the electronic countermeasure/electronic counter-countermeasure (ECM/ECCM) arena, and the Laboratory has long been active in signal intelligence, digital signal processing, decoy development, and the invention of



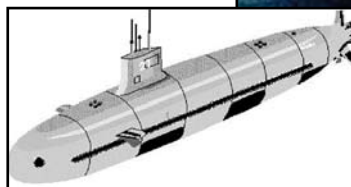
NRL pioneered monopulse radar in 1943 and high frequency over-the-horizon (HF OTH) radar in 1957.

radar-absorbing materials. The Lab's super rapid-blooming off-board chaff (Super RBOC) was the first widely used decoy system applied to all major Navy surface combatants.

Another classic example of how the NRL Radar Division's long-term R&D program has yielded fielded military systems is the AN/SPQ-9B radar, which was invented in response to the USS *Stark* cruise-missile incident and the need to detect low radar-cross-section air and surface targets in the Navy's increasing deployment in dangerous littoral environments. In 1987, the Radar Division was directed by the Naval Sea Systems Command (NAVSEA) to assess current Navy shipboard radars as candidates to incorporate a low-cost, high-quality, sea-skimmer missile detection capability for ship self defense. After completing technical feasibility and cost studies, NRL determined that the AN/SPQ-9A radar was the best candidate for incorporating an advanced air-channel capability, while maintaining its primary missions of MK 86 gun fire support and surface search. Under the auspices of the Operational Navy (OPNAV) Command in 1991, NRL developed the proof-of-concept radar, designated the AN/SPQ-9B Advanced Development Model (ADM), primarily from commercial-off-the-shelf and non-developmental-item technologies. By 1993, NRL completed integration and testing of the ADM radar and demonstrated additional detection-track and clutter-rejection performance capabilities for air targets. As a result of these successful demonstrations, Northrop Grumman Norden Systems (NGNS) was awarded a contract in 1994 to build two



Specific Emitter Identification (SEI) has been a crucial tool for the Coast Guard, Naval warships, and aircraft to support drug interdiction, enforce treaties, and monitor the movement of materials used in weapons of mass destruction.



Preproduction Kits (PPKs). After successful test and evaluation over the next ten years by NRL and NGNS, OPNAV approved full-rate production and installation on the CVN, LPD 17, CG 47, LHD 1, LHA 6, and WMSL 750 (Coast Guard blue water) class ships in 2004. As a result of the success of the AN/SPQ-9B Radar program, an important asset in protecting our armed forces, NRL's

Radar Division has received national recognition and major awards for their technical contributions.

Through the use of an ever-expanding array of hardware and techniques, including pushing the envelope of antenna design and development, radar's flexibility and applicability have grown. NRL personnel discovered how to identify specific radar transmitters uniquely by their particular signal fingerprint, catalog those emitters, and then hand off these emitters for tracking by other systems. This technology, called Specific Emitter Identification (SEI), saw action in Kosovo and Operation Iraqi Freedom, and has been a crucial tool for the Coast Guard, Naval warships, and aircraft to support drug interdiction, enforce treaties, and monitor the movement of materials used in weapons of mass destruction.

NRL invented inverse synthetic aperture radar (ISAR), a coherent imaging technique that enables classification of ships at sea by using their irregular motions to provide aspect-angle changes. The technique is also used to target long-standoff-range missiles.

Much of the emphasis that was placed on signal post processing and analysis has been moved to real-time applications to provide warfighters with up-to-the-second information and military

as well as civilian weather researchers with crucial, often lifesaving, forecasts and nowcasts.

Research at NRL continues on the development of new radar transmitters and antennas to meet the growing needs of an evermore increasingly technologically advanced Fleet and to counter the advances of opposing



The Advanced Multifunction Radar Concept (AMRFC) integrates radar, communications, and EW capabilities, thereby reducing the number of topside antennas.

forces. Three recent NRL technologies, the Microwave Microscope (MWM), the Advanced Multifunction Radio Frequency Concept (AMRFC), and the W-band Advanced Radar for Low Observable Control (WARLOC), exemplify that work.

The MWM is a state-of-the-art, low-power, ultrawideband, short-pulse, ultra-high-resolution experimental radar. Various versions are used to characterize sea scatter, detect and possibly identify anti-personnel mines, derive impulse responses of different scattering objects, and investigate through-the-wall target identification. The MWM provides a more direct physical interpretation of man-made objects and naturally occurring environments by using temporally short pulses and time-domain processing to distinguish the different features of an object or environment. The very fine range resolution provides an additional capability beyond that of typical radars. For example, the MWM's 1.8-cm resolution over 6.5 to 11.5 GHz well exceeds the 50-m or more resolution of typical 10-GHz radar systems.

AMRFC integrates radar, communications, and EW capabilities, thereby significantly reducing the number of antennas on

ships. The AMRFC testbed, located at NRL's Chesapeake Bay Detachment, can simultaneously transmit and receive multiple beams from common transmit and receive antennas under the control of common resource allocation manager software over a real-time control network.

WARLOC is a 94-GHz, high-power, coherent millimeter-wave radar that uses a gyro-klystron power amplifier, developed by NRL's Electronics Science & Technology

Division in collaboration with industrial partners Litton and CPI. Operating in the high end of the electromagnetic spectrum enables it to provide precision tracking and high resolution in range, angle, and Doppler for target identification in such diverse applications as ISAR and radar signal modulation (RSM) classification. WARLOC provides a substantial advantage over systems operating at infrared or visible frequencies in cloud, fog, and smoke conditions. While WARLOC is an excellent candidate for ship self-defense systems, it also has been applied to remote sensing applications. One such application is the detection of lower reflectivity clouds at longer ranges and, for the first time, rapid, high-resolution, two- and three-dimensional imaging of clouds.

Radar owes its continued success to the fact that it is the only reliable all-weather macroscopic sensor.

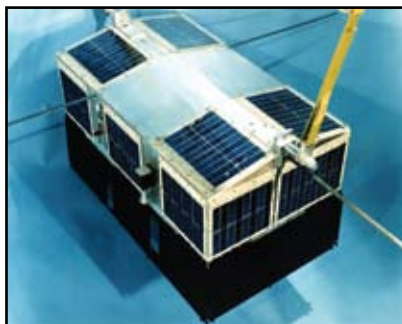


The W-band Advanced Radar for Low Observable Control (WARLOC) is a 94-GHz, high-power, coherent mmW radar.

TIMATION/GPS

After the successes that have resulted from NRL's presence in space since 1946, including pioneering space-based astronomy, it was perhaps inevitable that the Laboratory's Vanguard rockets, Minitrack (Minimum Trackable Satellite) tracking system, and the Navy Space Surveillance System (NAVSPASUR) would lead to still greater developments. NAVSPASUR was created to detect and determine the orbits of unannounced satellites passing over the U.S. and the Navy Fleet following the launch of Sputnik.

NRL's TIMATION (Time Navigation) program, begun in 1964, was the progenitor of the NAVSTAR Global Positioning System (GPS), which uses a constellation of satellites in middle-altitude, circular orbits that provides precise time and navigation data to military and civilian users. NRL's Roger Easton created this visionary, and patented, satellite navigation method for passively measuring range from the time of flight of transmit-



NRL's TIMATION (Time Navigation) program was the progenitor of the NAVSTAR Global Positioning System (GPS).

ted timing signals. More than 40 years ago, Easton and a team of NRL scientists demonstrated his concept to Navy and Department of Defense (DoD) sponsors using a single pass of the TIMATION I satellite on October 25, 1967. Time navigation, now used by GPS, requires synchronism between the onboard satellite clock and a clock at the receiver. For this historic NRL navigation demonstration, a graphical range-intercept chart was used to determine the receiver's (navigator's) position and satellite clock offset, using three or more measurements. Position accuracy of the TIMATION I demonstrations, later made with moving boats, vehicles, and airplanes, was on the order of 1/3 nautical mile, demonstrating the initial proof-of-concept for a revolutionary navigation system that would provide all-weather, real-time, 24-hour, three-dimensional (longitude, latitude, and altitude) navigation and precise time coverage throughout the world.



TIMATION I (rectangular object in center of photo) was successfully tested in a "piggyback" launch aboard an Air Force Thor-Agena D.

In 1969, the NRL TIMATION II satellite was launched in a 2-hour, circular orbit. Positioning accuracy was improved to 33 meters by transmitting the timing signal simultaneously at two frequencies, making possible correction for ionosphere delay, and the orbital position of the satellite was determined to 10 meters. Transatlantic satellite time transfer accuracy – better than one microsecond – was achieved between the U.S. Naval Observatory and the Royal Greenwich Observatory in England.

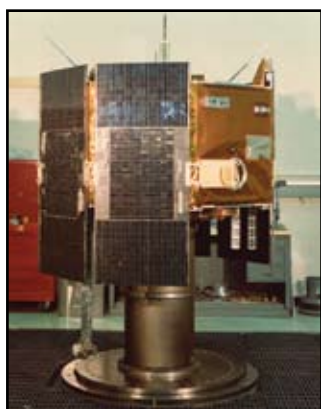
In 1973, after an intense competition between the Air Force/Aerospace 621B concept, the NRL TIMATION Program, and other proposals for the Defense Navigation Satellite System (DNSS), a DoD Joint Program Office was formed and the name changed to the Global Positioning System. All critical features, as documented in the NRL TIMATION Development Plan (published on March 2, 1971, and supported by other NRL reports, patents, and published papers) provided the initial architecture for the Global Positioning System.



Mr. Roger Easton (center), manager of the NRL NAVSTAR GPS program, and his satellite builder, Bill Huston look on.

On June 14, 1974, the NRL TIMATION III, renamed as Navigation Technology Satellite-1 (NTS-1) to reflect the joint nature of GPS, was launched in an 8-hour, circular orbit. This third NRL satellite carried a quartz clock and two digitally tuned rubidium atomic clocks – the first atomic clocks in space. World-wide time transfer was demonstrated.

On July 23, 1977, the NRL TIMATION IV, renamed Navigation Technology Satellite-2 (NTS-2) was launched into a 12-hour, circular orbit, as the first of a four-satellite constellation configured to demonstrate instantaneous navigation positioning. NTS-2 was the first satellite completely designed and built by NRL under GPS Joint Program funding. The effect of relativity on the onboard cesium atomic clocks was measured and corrected so that a GPS receiver on Earth could observe that the rate of GPS was the same rate as UTC (Universal Time Coordinated). The clock frequency stability specification of $2 \text{ pp}10^{13}$ (that is, frequency would agree within 2 parts in 10 trillion one day later) was met. NTS-2 was the first operational NAVSTAR GPS satellite.



Navigation Technology Satellite-2 (NTS-2) was the first operational NAVSTAR GPS satellite.

Since the transition of TIMATION into the joint program, NRL has continued to contribute to the growth in and integration of GPS technology in many significant ways in addition to the NTS-1 and NTS-2 work. First, it has provided substantial improvements to the on-board quartz clocks. Secondly, it has continued to analyze and publish results of frequency stability of the on-orbit quartz and rubidium clocks for the NAVSTAR satellites, analyzed the Interim Control Station at Vandenberg AFB, California, and later the frequency stability of the five GPS monitor station clocks, later expanding the analysis to include the DMA operating station. The analysis responsibility eventually included 45 clocks in a worldwide network of monitor stations and a constellation of orbiting space chronometers. The Lab expanded test and evaluation of atomic clocks with a dedicated facility at Building 53, and went on to test military GPS receivers. NRL has been instrumental in aiding GPS integration into the Fleet, working on time dissemination onboard various Navy platforms. Thirdly, NRL has continued to develop atomic clocks, such as the hydrogen maser and miniature atomic clocks. In May 1997, Boeing announced that the next generation of its NAVSTAR GPS satellites would feature an NRL-developed upgrade to convert their cesium atomic clocks, which are the essential component of the system, from analog to digital.

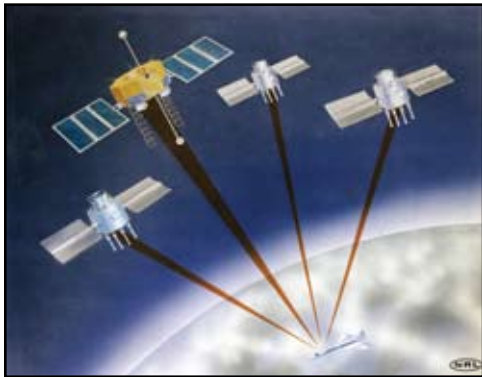


President Bush awards Mr. Roger Easton, TIMATION inventor, the National Medal of Technology for his extensive pioneering achievements in spacecraft tracking, navigation, and timing technology that led to the development of the NAVSTAR Global Positioning System (GPS).

In 1993, the National Aeronautics Association honored the GPS team (NRL, USAF, the Aerospace Corporation, Rockwell International Corporations, and IBM Federal Systems Company) for “the most significant development for safe and efficient navigation and surveillance of air and spacecraft since the introduction of radio navigation 50 years ago.” In 2005, TIMATION inventor Roger L. Easton was awarded the National Medal of Technology by President Bush.

GPS is not only a global navigation aid; it also provides precision time and time transfer throughout the world, with wide ranging and influential impact on communications and commerce, revolutionizing such diverse areas as mapping, search-and-rescue, resource management, emergency services, and traffic management.

For instance, GPS provides the 911 emergency location function in cell phones. In 2003, searchers used GPS to locate nine trapped miners in Pennsylvania. The rescuers were able to drill a six-inch air hole to their precise location, which kept them alive until a larger 22-inch shaft could be drilled and a rescue capsule lowered.

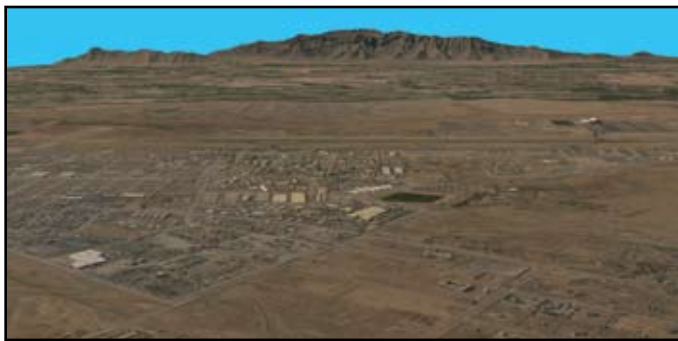


GPS provides major benefits to civil air transportation and commercial applications.

benefits to civil air transportation and commercial applications too numerous to enumerate. One sign of its acceptance is its prolifera-

GPS aided in the location and rescue of downed pilot CAPT Scott O'Grady, who was shot down over Bosnia in June 1995 and rescued six days later by U.S. Marines.

It has transformed warfare while also providing major



GPS is a crucial component of many of NRL's most important remote sensing projects such as the airborne geophysical and remote sensing survey of Afghanistan which was completed in August 2006.

tion in handheld computers used in a multitude of applications. Some GPS devices can also store attribute information and have proven invaluable to road crews. GPS has accounted for more than 800 related inventions patented by the U.S. Patent and Trademark Office in 2006. It has also become an economic powerhouse and a major contributor to growth of the tech sector; the GPS market is expected to grow to over \$22 billion this year.

Another perk NRL has received from having contributed the formational concept is that GPS has become a crucial component of many of the Lab's most important remote sensing projects, such as the airborne geophysical and remote

sensing survey of Afghanistan which was completed in August 2006. The Dragon Eye unmanned air vehicle (UAV) system, which was designed, fabricated, tested with the warfighter, and transitioned to industry by the Laboratory's Tactical Electronic Warfare Division (TEWD) in collaboration with the U.S. Marine Corps Warfighting Laboratory (MCWL), and recently displayed at the Smithsonian's National Air and Space Museum, is yet another example of the incorporation of GPS into military platforms. In addition, NRL researchers have incorporated commercial off-the-shelf GPS devices into amphibious combat vehicles to provide U.S. warfighters with an up-to-the-minute technological edge.



Dragon Eye unmanned air vehicle (UAV) system was designed, fabricated, tested with the warfighter, and transitioned to industry, and is another example of incorporating GPS into military platforms.

SOLRAD/GRAB

GRAB, America's first operational spy satellite, was another brainchild of NRL science and technology. Conceived, developed, launched, and operated in an era of evolving nuclear tensions, where knowledge of the opposing force's capabilities was crucial, GRAB is often credited with helping to keep the Cold War cold.

NRL scientists, by late 1957, were already envisioning the future of the American space program beyond Vanguard. Reid D. Mayo, at the time at NRL's Countermeasures Branch, had developed a crystal diode detector to help submarines spot enemy S-band air defense radars, essentially putting an ear above the surface in addition to the eye provided by periscopes. Not knowing about Lorenzen's and Gephard's earlier work, he wondered about the possibility of raising a sensor to orbital altitude to try to meet the Navy's expressed need for reconnaissance and surveillance. Stuck with his family at a Howard Johnson's restaurant in Pennsylvania during a snowstorm in March 1958, Mayo, while his family dozed, began thinking about the detector's possibilities and scribbled some quick

calculations on the back of the paper placemat. Could an in-orbit detector intercept Soviet air defense radar signals? At heights up to 600 miles, he figured, it was possible for his detector's theoretical sensitivity to pick up S-band (around 3000 MHz) radar pulses, such as those emitted from Soviet Gage and Token radars, and other bands as well, with modifications.

Upon his return to the Lab, Mayo sold the S-band collection idea to his branch head, Howard Lorenzen, who, unknown to Mayo, had previously co-authored with Radio Division Superintendent Louis Gebhard a proposal for G-band (around 200 MHz) electronic intelligence (ELINT) collection of Soviet early-warning radar signals from space. Lorenzen championed the idea, acquiring funding, arranging multiagency participation, and directing development. Work soon began on adapting the S-band detectors for orbital duty, where they could map Soviet air defense radars and send the intercepted signals back to Earth stations.

Following the Soviet's provocative launch of Sputnik in 1957, President Eisenhower, who had been caught by surprise by the launch, decided to more fully explore space-based reconnaissance, having already approved full-scale development of projects sponsored by the U.S. Air Force and the Central Intelligence Agency (CIA). Working on Mayo's concept of March 1958, the NRL Satellite Techniques Branch, under Martin Votaw, formerly of NRL's Vanguard team, designed the GRAB satellite bus by November of the same year. The Solar Radiation (SOLRAD) cover experiment



The Galactic Radiation and Background (GRAB) satellite was America's first operational intelligence satellite.

concept was proposed in July 1959, and Eisenhower approved of the full development of GRAB with the SOLRAD cover in August 1959. The May 1, 1960, Soviet downing of a U.S. CIA U-2 spy plane made the mission more pressing. Four days later, Pres. Eisenhower approved GRAB's launch.

GRAB 1, the Galactic Radiation and Background satellite, on June 22, 1960, soared into space piggy-backed with the Navy's third Transit navigation satellite (Transit IIA) atop an Air Force Thor Able Star rocket. Designed to intercept Soviet air



The Solar Radiation (SOLRAD) cover experiment was proposed in July 1959, and President Eisenhower approved of the full development of GRAB with the SOLRAD cover in August 1959.



GRAB was launched in June 1960, only 52 days after a U-2 was lost on a mission over Soviet territory.

defense radar energy beams that traveled into space and send them back to a network of Earth-based ground sites, GRAB 1 and the subsequent GRAB 2 operated from July 1960 until August 1962, launching ELINT into the Space Age. GRAB's circular orbit 500 miles above the Earth kept it safe from surface-to-air missiles while enabling it to pass through Soviet air defense radar. It served as proof-of-concept that an outer space-based platform could collect as much ELINT as all other sea-, air-, and land-based reconnaissance platforms operating within the satellite's field of view with no risk to personnel and at a fraction of the cost.

Code-named Project Tattletale, and later Canes (after its tight security control system, to which fewer than 200 officials in Washington, DC, had access), GRAB relayed the collected signals to overseas ground collection huts in its field of view, where they were collected, tape-recorded, and couriered

to NRL for evaluation. The National Security Agency (NSA) and the Strategic Air Command were able to exploit the data in support of definition and location of air defenses. The information that they derived from new and unusual signals led them to discover that the Soviets were already operating a radar that could support anti-ballistic missile weapons.

Of the four subsequent launches of the GRAB/SOLRAD program attempted, one was successful, on June 29, 1961.



GRAB relayed the electronic intelligence (ELINT) signals to overseas ground collection huts and they were couriered to NRL for evaluation.

Martin Votaw coordinated launch planning with the Air Force and led the NRL launch support teams at all five GRAB launches, the first four at Cape Canaveral and the final effort at Point Arguello, California. By 1962, the new National Reconnaissance Office had taken control of ELINT satellite projects, and renamed the GRAB program Poppy.

Vandenberg Air Force Base launched NRL's first Poppy mission in 1962, and NRO sponsored six more Poppy missions through the 1960s and on into the 1970s.

The GRAB program was kept secret until its declassification was announced at NRL's 75th anniversary celebration in 1998, while SOLRAD I's success in determining that radio fade-outs



Declassification of the GRAB program was announced at NRL's 75th anniversary celebration in 1998.

however, didn't know about the spy satellite that would accompany their project, fulfilling a very different but more crucial national security mission.

GRAB's success marked the rebirth of NRL's space program which had stalled after its initial rocket teams were transferred to become the heart of the newly formed NASA. Had the GRAB project failed, there is little doubt that the work that resulted in such successes as the Clementine spacecraft and the Global Positioning System would ever have been accomplished at NRL.



When GRAB began sending space-intercepted electronic intelligence signals back to Earth, it proved that a spacecraft could collect as much information as all sea, air, and land-based reconnaissance platforms within the satellite's field-of-view.

were caused by solar X-ray emissions was widely reported. SOLRAD's data verified a theory of NRL's Dr. Herbert Friedman and further explained the relationship between sunspots, solar X-ray emission, and radio wave propagation, all critical to Naval communication and the space program. Many SOLRAD scientists and engineers,



NRL'S

RUTH H. HOOKER RESEARCH LIBRARY

the first

80
years

As a “partner in research,” the NRL Research Library continues to be the most advanced research library in the Department of Defense, serving as a productivity multiplier and a transformational force that has changed the way science is done at NRL — making the NRL Research Library a sought-after resource around the world.

A “partner in research” for over 80 years...

The Library's Beginnings

Early in the Naval Research Laboratory's history, access to scientific literature was obtained and managed individually. In 1926, Mr. R. M. Langer, an NRL scientist with leanings towards literature, was asked to survey the Laboratory's information needs, particularly in regards to periodicals. The “library” at the time consisted of two bookcases and Miss Alice Olney, secretary of the Heat and Light Division, who charged out books on a part-time basis. It was determined that in order to extract maximum benefit from the literature, someone should be assigned to the library on a full-time basis. Captain E. G. Oberlin, Director of NRL, chose to employ a junior physicist, Miss Ruth Hutchison, for this task, believing that someone with an understanding of science was more important to NRL than someone with formal library training. The assignment given to Miss Hutchison was to “*keep in touch with all research in progress and see that none of the scientists should miss related information in the literature.*” Miss Hutchison started working as what was originally called a “bibliochretic” (user of books) in December 1927, personally reviewing journal articles and hand carrying them to researchers. She graduated in 1930 from George Washington University with a Library Science degree and was mar-



Mrs. Ruth Hutchison Hooker

ried in 1931, becoming Ruth Hutchison Hooker. In 1932, the library moved from Building 1 into larger, dedicated spaces on the second floor of Building 12 (then known as the Annex).

After years of compiling information on the scientific literature for NRL researchers, Mrs. Hooker published an article in *Review of Scientific Instruments* titled “A Study of Scientific Periodicals” (Vol. 6, pp. 333-338, 1935) in which she examined periodical references to identify those periodicals that were most cited in the fields of physics and radio. This seminal work of bibliometrics was similar to what Eugene Garfield (who



In 1932, the Library moved from Building 1 into larger, dedicated spaces in Building 12.

cited her work) and the Science Citation Index would do 30 years later.

In 1935 Mrs. Hooker attended her first Special Libraries Association (SLA) convention and came back with a new idea — instead of individually advising the scientists of articles they should read, she would publish a bulletin. This bulletin would announce all new publications and periodical articles, giving everyone a chance to see all the new literature, instead of Mrs. Hooker directly notifying only those to whom particular publications might be of greatest interest. This bulletin was typed on stencil and reproduced weekly, eventually becoming known as *New Research Literature*. The library's small staff and a small Naval Research Laboratory survived the Great Depression, working four-day work

weeks and cutting everything down to the essentials, but not cutting the journal subscriptions.

The NRL Library During World War II

World War II brought tremendous growth to the Naval Research Laboratory, with employment jumping from 396 in 1941 to over 4,000 in 1946. Expenditures grew from \$1.7 million to nearly \$14 million, the number of buildings grew from 23 to 67, and the number of funded projects grew from 200 to around 900 during those five years. The NRL Research

Library also grew during this time — the staff from two to eight, and the space from a single room to over 9,000 square feet of space holding 12,000 bound periodicals and 200 journal subscriptions.

In addition to the physical growth, services greatly expanded: Library staff started to index journal articles and other holdings, translated periodical and technical reports from German and Japanese, and assumed control over the laboratory's growing col-

lection of technical reports (including the receipt of several collections from disestablished laboratories). During the war, Mrs. Hooker also managed remote branch libraries in Minneapolis, Minnesota; Philadelphia, Pennsylvania; Orlando, Florida; New London, Connecticut; and at the Chesapeake Bay Detachment. She also planned for the relocation of the library to a larger facility, the basement of Building 43.

The Library After the War

After World War II, NRL and the Library were left with the task of reorganizing a hastily expanded research program and moving it back to a mix of basic and applied research projects. In 1946, the U.S. Navy had created the Office of Naval Research (ONR) as a liaison with and

supporter of basic and applied scientific research, and had also encouraged NRL to broaden its scope and become, in effect, its corporate research laboratory. By 1948, the NRL Library had assumed control of the new ONR Library as a remote branch library.

The NRL Research Library continued to grow and expand, with Mrs. Hooker becoming very involved in the Special Libraries Association, serving as president of the DC Chapter from 1945 to 1948 and president of the National SLA from 1949 to 1950. In 1950 the NRL library moved the collection of 75,000 technical reports to the third floor of Building 43, expanded to 21,000 circulating books, held over 400 journal subscriptions, and had a staff of 20.

In 1951, the Library Directors of Harvard University, MIT, and the Boston Athenaeum recommended to the Secretary of the Navy that a Coordinator of Naval Libraries position be established, and further recommended that Mrs. Hooker fill the position. She relocated to the Navy Department Library (then in the Main Navy Building on 18th and B Streets NW), and coordinated the efforts of the naval libraries across the country,



Ms. Mildred Benton

running what would become the Consortium of Naval Libraries until 1954, when she was offered a chance to return to NRL. During this period, Ms. Mildred Benton was the Chief Librarian at NRL; she moved to the role of bibliographer in 1954. Also in 1954, Ruth Hooker was named to the *Who's Who in America* publication.

Computers Arrive at the Library

In 1960, the Navy's Inspector General recommended that NRL conduct an experiment in "machine storage and retrieval of its scientific information" based upon the library's depth of indexing — over 3 million items back to 1928. The study that followed, as detailed in the March 1962 issue of *Navy Management Review*, determined that the library staff were far more efficient at information retrieval than state-of-the-art machines (four minutes average time compared with four hours). In 1964, Doris Baster, then Head of the Documents Section, attended the "Computer Programs for Library Operations" workshop at the University of Illinois, where she found that mechanization had advanced to the point of making NRL's *Operation Shoestring* possible. This project converted the journal holdings list, journal subscription lists, and circulation records of books and reports to mechanized punch cards. By 1964, the library had a staff of more than 40 and had assumed control over most of the basement and third floor of Building 43 — over 25,000 square feet. The technical reports were moved back down to the basement and the main part of the library expanded to occupy the entire third floor. Microfilm was also introduced and deployed widely throughout the library to reduce the space taken up by the continually growing collection.

In 1965, after a 38-year career, Ruth H. Hooker retired from NRL. This same year, she was elected to the Special Libraries Association Hall of Fame.

LaVera Morgan took over as Chief Librarian from 1965 to 1970. In 1967, the library spanned 20,000 square feet, had a staff of 40, held 113,000 book and bound periodical volumes, held 350,000 technical reports, and subscribed to 1,800 journal titles. Manual indexing of journal articles was replaced with a commercial system called *PANDEX Current Index to Scientific and Technical Literature* in 1969. Library staff were also making plans to move to a new library building to be constructed at NRL with over 65,000 square feet of space, with expected completion in the early 1970s. Unfortunately, circumstances prevented the construction of the building, so the move never occurred.

structured at NRL with over 65,000 square feet of space, with expected completion in the early 1970s. Unfortunately, circumstances prevented the construction of the building, so the move never occurred.

The Library Moves into the Online Age

During the 1970s the library switched from the Dewey Decimal Classification system to the Library of Congress Classification system. Doris Baster served as Chief Librarian from 1970 to 1978 and used her previous experiences with mechanization to move the library into the online world. This included staff access to ORBIT and DIALOG online search and retrieval services, the intro-



Led by Ms. Doris Baster, *Operation Shoestring* converted the journal holding list, journal subscription lists, and circulation records of books and reports to punch cards.

duction of OCLC for shared cataloging data and later for online interlibrary loans, and in 1973, direct access to the online catalog system of the Defense Documentation Center (now the Defense Technical Information Center). On October 14, 1975, Captain John Geary dedicated the library, naming it in honor of Mrs. Hooker. It thus became the first and only DoD library to be named for a living person: the *Ruth H. Hooker Technical Library* (now the Ruth H. Hooker Research Library).

Peter Imhof served as Chief Librarian from 1978 to 1986 and was instrumental in obtaining the library's first integrated library system in 1981. In 1983, the Library became one of the first libraries in the nation to offer both dial-in and network access to its library catalog. Mr. Imhof was promoted to head of the Technical Information Division and Laurie Stackpole became the Chief Librarian in 1986. In late 1987 the Research Reports Section acquired a new integrated library

system designed for the special needs of technical reports, known as Cuadra STAR. In 1988, in response to a recommendation by the Laboratory's Computer Policy Panel, the Library began lending microcomputer software to assist researchers and administrators in identifying, selecting, and using microcomputer applications. The Research Reports Section also began the conversion of its unclassified reports collection to optical storage with the development of a prototype imaging system. Subsequently, the system was modified to provide a seamless interface with Cuadra STAR, enabling researchers and staff to display full documents as part of a catalog search. This digitization effort ultimately converted 180,000 technical reports, representing over 10 million pages of content, to digital format, making it one of the first and largest digital libraries in the Federal arena. In 1989 the Microcomputer Software Support Center opened its doors, providing a software and hardware evaluation lab, a self-service CD-ROM



In 1988, the Library started digitizing 180,000 unclassified technical reports (over 10M pages). This was one of the first and largest digital libraries in the Federal arena.

search station, a scientific microcomputer software database, a laptop computer lending service, and field support of common hardware and software problems (disk recovery, virus detection/cleaning, file conversion, and software installation).

In response to a user needs assessment and the Laboratory's network improvement plan, which called for desktop access to information stored locally and remotely, the Library pioneered a

telnet-based, menu-driven system known as the InfoNet. The InfoNet provided access to the online library catalog, library databases in various formats, Laboratory information, Gopher and Telnet sites, and internal resources. It was made available to NRL employees, on-site contractors, off-site NRL locations, and the Office of Naval Research in August 1992. In September 1992 the Library upgraded its book and journal catalog, implementing Sirsi's Scientific and Technical Information Library Automation System (STILAS). This system allowed users to perform sophisticated searches and request materials online.

The Web Era

Building upon the previous digitization experiences of the 1980s and the desktop delivery expertise with InfoNet, the Library entered into a cooperative project with the American Physical Society (APS) and Los Alamos National Laboratory in 1994 to experiment with dissemination of electronic journal information.

This project enabled NRL researchers to be the first in the world to access *Physical Review E* and *Physical Review Letters* from their desktops, clearly demonstrating the viability of electronic journals. This project also set the stage for the development of the commercial product of APS, Physical Review On-Line Archive (PROLA), and creation of the NRL Research Library's TORPEDO (The Optical Retrieval Project: Electronic Documents Online).

The library also began experimenting with Mosaic browsers and created its first library Web site, InfoWeb, in late 1994. By 1994, the Office of Naval Research had disbanded their local library in favor of physical and digital access to the NRL Research Library, and NRL management had directed that the library provide desktop access for all NRL sites — primarily at Stennis, Mississippi, and Monterey, California. In 1995 TORPEDO was released, providing authorized users with the ability to search the full text of the APS journal articles,

technical reports, and other types of documents that the Library had stored as digital images. The retrieved documents could be viewed as TIFF images online and printed locally. Access to TORPEDO was made available from end-user workstations in the Library and to end-users at their desktops through the Laboratory network.

Following these early accomplishments, the NRL Library in 1995 com-



TORPEDO Ultra was released to NRL and 20 Federal agencies in 2001.

menced InfoVision/2000, a broad-based evaluation of the NRL Library to determine the library of the future. This library study team was composed of representatives from academia, government, and the scholarly publishing community. With the InfoVision/2000 study, the NRL Library received clear direction and support from Laboratory management to shift to an environment offering Web-based and digital journals whenever possible. As a 1996 response to this directive, the Library introduced a Web-based, emailed, table of contents alerting service called "Contents-to-Go" and became the first Sirsi Library Catalog site to deploy WebCat (the Web interface to the Sirsi Library Catalog) and one of the first to deploy a SQL-standard compliant library system. One year later, the NRL Library released a local installation of the Institute for Scientific Information's (ISI) Web of Science and completed its migration to a Web-based service model. Finally, in 2001, the NRL Library released TORPEDO Ultra, moving the digital content repository from TIFF (tagged image file format) to PDF (portable document format) and from Excalibur EFS (encrypting file system) to Excalibur's new concept search engine called RetrievalWare. TORPEDO Ultra was later opened up for

use by over 20 government organizations including NASA, the National Science Foundation, the Naval Postgraduate School, the National Institute of Standards and Technology, and the U.S. Naval Academy. This earned the NRL Library the *DCI Portal Excellence Award* and the *Delphi Best Practices Award* in 2002. Laurie Stackpole retired as Chief Librarian in 2002 and was succeeded by James King who served as Chief Librarian until 2007. Suzanne Ryder became Chief Librarian in 2007.

The NRL Library Today

Today, NRL's Ruth H. Hooker Research Library continues to enhance and support NRL and ONR scientists in accomplishing their research objectives through the comprehensive availability of all relevant scholarly information sources; a strategic effort to capture the NRL research portfolio; and the deployment, customization, and creation of cutting-edge information resources and services as part of the NRL Digital Library.

Traditional library services include an extensive technical report, book, and journal collection dating back to the 1800s housed within a physical facility configured for study and research, staffed with subject specialists and information professionals. The collections include 46,000 books, 80,000 bound historical journal volumes, 3,000 current journal subscriptions, and nearly 2 million technical reports in paper, microfiche, or digital format (classified and unclassified). The professional library staff members provide advanced information consulting; literature searches against all major scholarly online databases including classified databases, to produce on-demand subject bibliographies; circulation of materials from the collection including classified literature up to the SECRET level; retrieval of nearly any article, report, proceeding, or document from almost any source around the world; and

training/orientation to help researchers improve productivity through effective use of the library's resources and services.

To enhance traditional services, the NRL Research Library has developed and is continuing to expand the NRL Digital Library. The Digital Library currently provides desktop access to thousands of journals, books, and reference sources at NRL-DC; NRL-Stennis; NRL-Monterey; and the Office of Naval Research.

To provide immediate access to scholarly information, all relevant current journals and conference proceedings in the NRL Research Library's collection are now fully searchable at the researcher's desktop (nearly 3,000 titles), and over 60% of the print journal volumes are also available online. The breadth and depth of content available through *TORPEDO Ultra*, NRL's locally-loaded digital archive (<http://torpedo.nrl.navy.mil>), continues to grow and is realizing its potential as a single point of access for scholarly information by providing full text search against journals, books, conference proceedings and technical reports from 20 publishers (8+ million items, 66M pages in 2007).

The NRL Research Library has also created the innovative NRL Publications Database, which is ensuring that the entire research portfolio of written knowledge from all NRL scientists and engineers since the 1920s will be captured, retained, measured, and shared with current and future generations. It is serving as a model for other commands across the Navy and the Federal Government.

As a "partner in research," the NRL Research Library continues to be the most advanced research library in the Department of Defense, serving as a productivity multiplier and a transformational force that has changed the way science is done at NRL — making the NRL Research Library a sought-after resource around the world.

The NRL Research Library continues to be the most advanced research library in the Department of Defense...

To view the Ruth H. Hooker Research Library's timeline, visit
<http://library.nrl.navy.mil/timeline/nrl-timeline.htm>



80th Anniversary Celebration and Open House

October 10, 2007



NRL's Vanguard I celebrates 50 years in space

PROJECT VANGUARD

NRL's tiny
satellite
launches a long
legacy in space
research



50 YEARS and Counting . . .

The *Vanguard I* satellite celebrated its 50th birthday this year. Its launch on March 17, 1958, from Cape Canaveral, Florida, culminated the efforts of America's first official space satellite program begun in September 1955. The first solar-powered satellite, *Vanguard I* has the distinction of being the oldest artificial satellite orbiting the earth. Its predecessors, *Sputnik I* and *II* and *Explorer I*, have since fallen out of orbit.

Vanguard I was launched as part of the United States' participation in the International Geophysical Year (July 1957 to December 1958) in a tri-service project with the U.S. Army operating the tracking stations and the U.S. Air Force providing the launching site. As part of the scientific program for the International Geophysical Year, the Naval

the launch vehicles; developed and installed the satellite tracking system; and designed, constructed, and tested the satellites in a program headed by Dr. John Hagen. NRL's



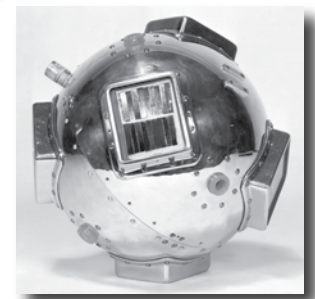
Vanguard I launch on March 17, 1958, from Cape Canaveral, FL.

Research Laboratory (NRL) was officially delegated the responsibility of placing an artificial satellite with a scientific experiment into orbit around the earth. NRL developed

proposal to conduct Project Vanguard was based on experience gained from extensive use of German V-2 and Viking rockets to probe the earth's upper atmosphere.

Vanguard I is 6 inches in diameter and weighs about 3 pounds. Its small size, compared to the Soviets' 200-pound *Sputnik I*, caused then-Soviet Premier Nikita Khrushchev to dub it "the grapefruit satellite."

In the 50 years following *Vanguard's* launch, the 3-pound satellite made more than 196,990 revolutions of the Earth and travelled 5.7 billion nautical miles, the distance from Earth to beyond the planet Pluto and half way back. In that time it has provided a wealth of information on the size and shape of the Earth, and set a number of space records as well.



The successes of *Vanguard I* set the pattern for a multitude of other space ventures in this country and abroad. *Vanguard* also served as a springboard for NRL scientists

to launch several series of space probes to study various aspects of radiation phenomena.

Vanguard I introduced much of the technology that has been applied in other U.S. satellite programs. For example, it proved that solar cells could be used for several years to power radio transmitters. *Vanguard's* solar cells operated for about seven years, while conventional batteries used to power another onboard transmitter lasted only 20 days. Now the oldest man-made satellite in orbit, *Vanguard I* has been 100 percent successful in meeting its scientific objectives. It accomplished the following:

- First orbiting package to be powered by solar energy.
- Returned a wealth of information on air density, temperature ranges, and micrometeorite impact.
- Maintained an orbit so stable that cartographers were able to more accurately redraw maps of islands in the Pacific Ocean.
- Revealed that the Earth is slightly pear-shaped rather than round.

Although *Vanguard's* solar-powered “voice” became silent in 1964, it continues to serve the scientific community. Ground-based tracking of the satellite provides data concerning the effects of the Sun, moon, and atmosphere on satellite orbits. For example:

- Fifteen years after its launch, *Vanguard* was in an orbit with an apogee height of 2,121 nautical miles above the Earth's surface, and a perigee of about 353.6 nautical miles. The orbit period was approximately 133.8 minutes.
- By 2000, *Vanguard* was in an orbit with an apogee height of 2,073 nautical miles above the Earth's surface, a perigee of 352 nautical miles, and an orbit period of 132.8 minutes.

In conjunction with the *Vanguard* launch, NRL scientists laid out a worldwide tracking system called Minitrack. Laboratory scientists later used many of the principles embodied in this system to develop a space surveillance system that can detect unannounced, radio-silent satellites passing over the United States. This became known as the Naval Space Surveillance System.

When *Vanguard I* was launched 50 years ago, it was estimated that the satellite's life expectancy would be about



A Minitrack site at Blossom Point, MD
(Top: 1956; Bottom: 2000).

200 years. Since then, scientists have extended this estimate to 2000 years. Accordingly, *Vanguard I* should be celebrating many more birthdays in space.

A CELEBRATION

at the Naval Research Laboratory



Vanguard Pioneer Panelists



Mr. Roger L. Easton



Dr. John W. Townsend



Mr. Alton E. Jones



Mr. Martin J. Votaw

March 17, 1958

VANGUARD I

50 Years in Space

March 17, 2008



Vanguard Pioneers

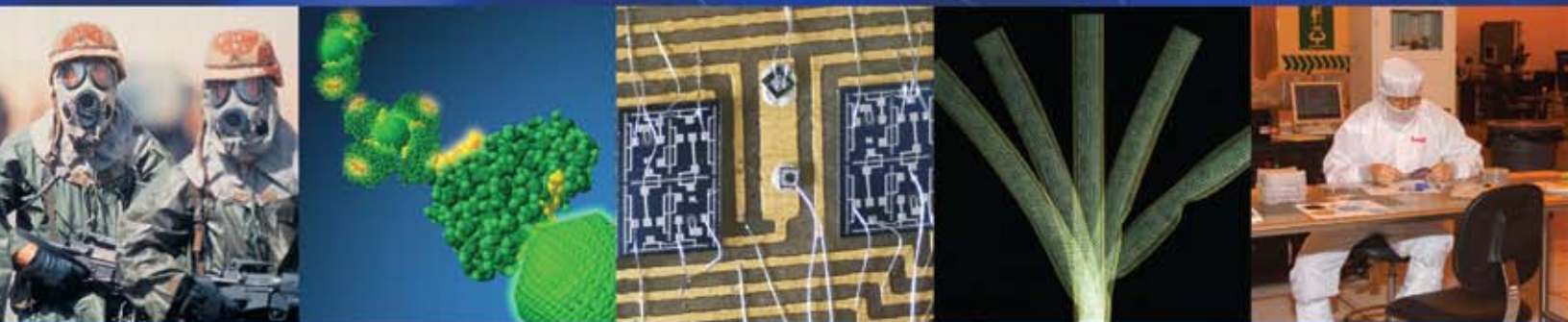


NAVAL RESEARCH LABORATORY
<http://www.nrl.navy.mil/>

NANOscience and NANOTEchnology

at the Naval Research Laboratory

The mission of the NRL Institute for Nanoscience is to conduct highly innovative, interdisciplinary research at the intersections of the fields of materials, electronics, and biology in the nanometer size domain. The Institute exploits the broad multidisciplinary character of NRL to bring together scientists and engineers with disparate training and backgrounds to tackle common goals at the intersection of their respective fields at this length scale. The Institute's science and technology (S&T) programs provide the Navy and DoD with scientific leadership in this complex, emerging area and help to identify opportunities for advances in future defense technology.



Institute for Nanoscience, Naval Research Laboratory, Washington, DC

In 1957, Sputnik started a space race that launched the greatest engineering team effort in American history. Along the way, the U.S. space program developed new technologies in the areas of energy, communications, materials, structures, and computers—all the systems that made space travel successful. In the process, these technologies spawned more than 60,000 products that shaped the global economy with direct impact on the general public.

In 2001, the events of 9/11 shocked the world and launched a campaign against world terrorism. New programs and industries focusing on homeland security and defense have appeared, and these too must ultimately incorporate advanced technologies to be successful against this daunting, 21st-century challenge. One of these advanced technologies is nanotechnology.

In 2001, President Clinton signed the National Nanotechnology Initiative (NNI), which nearly doubled the country's investment in the emerging fields of nanoscience, nanotechnology, and nanoengineering. Nanotechnology is defined by this initiative as research and technology development at the atomic, molecular, or macromolecular levels, in the length scale range of approximately 1 to 100 nanometers, resulting in (1) the creation and use of structures, devices, and systems that have novel properties and functions because of their small and/or intermediate size, or (2) the ability to control or manipulate on the atomic scale. The growth of nanotechnology interests worldwide is based on the realization that nanotechnology is much more than a decreasing length scale following the micro/miniaturization industrial revolution. There is a shared vision that nanotechnology will dramatically change the performance and function of materials and devices by capitalizing on changes that occur in the structure-property-function of materials when made at the nanometer length scale.

For example, nanotechnology is having a profound impact in shaping the semiconductor industry roadmap and future technologies for memory and information storage. Today's logic chips and mass storage technologies already incorporate nanotechnology. The logic chips in production have 45-nm nodes (and 32-nm logic technology has been demonstrated, with production scheduled in 2009), and giant magnetoresistance technology has revolutionized the hard drive industry. All of these advancements were preceded by the development of instruments and tools capable of nanoscale imaging, characterization, fabrication, and manipulation. There are of course many other nanotechnology opportunities beyond the topic of nanoelectronics. Important applications and unique opportunities will be created based on new nanomaterials and nanosensor/device discoveries. The public acceptance of nanotechnology will be won through breakthroughs in nanomedicine.

The nanotechnology initiative grew from years of basic research that developed new nanoscale imaging and manipulation tools that explored the fundamental properties of nanoscale materials and devices. Nanoscience programs at the Office of Naval Research (ONR) and NRL can be traced back to the early 1980s. The success of these early programs led the

DoD, in the mid-1990s, to identify nanoscience as a Strategic Research Area for long-term basic research funding with an aim of impacting future warfighting capabilities in chemical and biological warfare defense, weight reduction of warfighting equipment, high-performance materials for platforms and weapons, energy and energetic materials, and uninhabited vehicles and miniature satellites. NRL formally established its Institute for Nanoscience in 2001, with a foundation of DoD basic (6.1) research funds to support collaborative, interdisciplinary research projects between NRL divisions, and a new MILCON project that built high-quality nanofabrication and measurement labs that opened in October 2003.

The mission of the NRL Institute for Nanoscience is to conduct highly innovative, interdisciplinary research at the intersections of the fields of materials, electronics, and biology in the nanometer size domain. The Institute exploits the broad multidisciplinary character of NRL to bring together scientists and engineers with disparate training and backgrounds to tackle common goals at the intersection of their respective fields at this length scale. The Institute's science and technology (S&T) programs provide the Navy and DoD with scientific leadership in this complex, emerging area and help to identify opportunities for advances in future defense technology.

Past and current performers funded through the Institute are members of the following NRL divisions: Radar, Optical Sciences, Chemistry, Materials Science and Technology, Electronics Science and Technology, Center for Bio/Molecular Science and Engineering, Acoustics, Oceanography, and Marine Geosciences.

MILITARY RELEVANCE

The DoD S&T investment supports national security by maintaining a technically superior military capability or by lowering the cost and time required for providing that capability. Currently, the military faces new challenges in response to changing missions associated with irregular warfare and homeland defense including the Global War on Terrorism (GWOT) and weapons of mass destruction (WMD) (as described by the 2007 Naval S&T Strategic Plan). Our platforms and forces must become more expeditionary and versatile in order to meet these challenges. The prospect for nanoscience and nanotechnology to provide a dramatic change in the performance of materials and devices was the rationale for identifying this emerging field as one of the DoD strategic research areas for basic research funding on a long-term basis. While DoD research funded by the Services and DARPA can be broadly defined as nanomaterials, nanoelectronics, and nanosensors/devices, each agency/activity has identified special areas of focus within these categories. At NRL our interdisciplinary program focuses on these areas:

- Growing and characterizing novel nanoparticles and nanowires for use in new nanocomposites/coatings systems, nanoelectronics/nanophotonics devices, and ultra-sensitive sensor systems;
- Inventing and developing materials and systems for highly efficient energy/power storage, generation, and conversion;

- Conducting exploratory research on different nanoelectronics approaches (from spintronics to quantum dot devices) to develop a fundamental understanding of the electronic properties of these new nanoscale materials and devices; and
- Pushing the sensitivity of sensors/nanodevices to the ultimate limit of single particles or molecules.

NRL's nanoscience research programs and accomplishments described below directly impact the following Naval S&T focus areas:

- Power and Energy
- Operational Environments
- Maritime Domain Awareness
- Asymmetric and Irregular Warfare
- Information, Analysis and Communications
- Assure Access
- Distributed Operations
- Naval Warrior Performance and Protection
- Survivability and Self-Defense
- Affordability, Maintainability and Reliability

S&T CHALLENGES

Working at the nanoscale produces unique and interesting challenges that can only be resolved with appropriate instrumentation and facilities such as those available at NRL. Specific S&T challenges unique to nanomaterials for energy storage and generation include stabilizing the interface and metastable phase of the materials, preventing corrosion and breakdown, minimizing cross-talk between nanoscale components, and understanding, controlling, and optimizing disordered materials. S&T challenges associated with nanoelectronics such as quantum dots, nanoLEDs, and nanophotonics include the need for strong theoretical support to explain new quantum effects, the inability to dope nanocrystals/particles/rods, and the lack of known processing conditions to grow or etch new materials. Working with quantum dot materials also presents interesting challenges such as controlling the growth and location of the dots, developing methods to measure or individually address each dot, and raising the operating temperature of novel devices above cryogenic temperatures. Work on nanoscale chemical and biological sensors has also uncovered several unique challenges, namely, sensitivity limited by $1/f$ noise and sampling issues.

FUTURE DIRECTIONS

While the current balance between the broad research areas of the Institute programs in nanomaterials : nanoelectronics : nanosensors/devices (25%:35%:40%) appears ideal and is not anticipated to change significantly, some change in the areas of focus will occur. For example, in addition to continued interests in nanomaterials for energy storage and

generation, nanomaterials for tagging/tracking/locating applications are needed to support GWOT applications. Future nanoelectronics projects will capitalize on our pioneering work with coupled quantum dots for quantum information technology, and spintronics and graphene-based devices for future high speed and/or low power electronics. The emerging field of plasmonics also provides unique opportunities for sub-wavelength optical applications and advanced materials. In addition to a fundamental study of sensor noise issues, a new field of nanophononics (that utilizes 2D or 3D arrays of nanomechanical resonators) will emerge and create new high frequency devices for signal processing and sensing applications.

FACILITIES

The NRL Institute for Nanoscience operates a new nanoscience research building containing nanofabrication facilities and environmentally controlled measurement laboratories. The central core of the building, a 5000 sq. ft., Class 100 cleanroom, has been outfitted with the newest tools to permit lithographic fabrication, measurement, and testing of devices. The equipment includes deposition systems for metals and insulators, optical mask aligners, and etching systems. The lithography effort is supported by chemical stations and fume hoods for spinning on photo resists, baking, and developing the patterns that ultimately result in small devices and circuits. Additional new equipment acquired under our Capital Purchase Program includes an electron beam writer



for fabricating features down to 20 nanometers; a focused ion beam workstation for 10-nanometer-scale machining of materials; a scanning electron microscope for inspection of these small-scale devices; an optical pattern generator for making masks for optical lithography; and several reactive ion etchers and metal deposition systems. In addition to the cleanroom facility, the new building also contains 5000 sq. ft. of controlled-environment laboratory space, which is available to NRL researchers whose experiments are sufficiently demanding to require this space. There are 12 of these laboratories within the new building. All of them provide shielding from electromagnetic interference and very low floor vibration and acoustic levels. In addition, eight laboratories control the temperature to within ± 0.5 °C and four to within ± 0.1 °C.

INSTRUMENTATION

The following instrumentation can be found in the nanofabrication facility:

- atomic force microscope (AFM)
- benchtop transmission electron microscope
- cascade probe station
- critical point dryer
- dual-beam focused ion beam (FIB)
- e-beam writer system
- e-beam evaporator
- ellipsometer
- inductively coupled plasma-reactive ion etching systems (chlorine and fluorine)
- ion beam assisted deposition system
- ion mill
- laser micromachining tool
- laser pattern generator
- low pressure chemical vapor deposition (LPCVD) system
- optical mask aligners (0.2, 1, and 2 micron)
- optical and fluorescence microscopes
- plasma cleaner/etcher/asher
- plasma enhanced chemical vapor deposition (PECVD)
- reactive ion etching systems (chlorine and fluorine)
- scanning electron microscope (SEM)
- sputter deposition system
- surface profilometer
- thermal evaporator
- wire bonder

The following instrumentation can be found in the quiet and ultra-quiet measurement laboratories:

- atomic force microscope
- laser vibrometer
- low temperature transport measurement systems
- low temperature magnetic measurement systems
- scanning tunneling microscope
- nanoindentation tools
- nanomanipulation tools
- nanomechanical resonators
- near-field optical microscope
- physical vapor deposition
- scanning Auger microscope
- surface analysis tools
- transmission electron microscope



◀ Electron Beam Lithography



Ion Beam Deposition ▶



◀ Metrology



Transmission Electron Microscope ▶



◀ Scanning Electron Microscope

Select examples of research accomplishments in nanomaterials:

- Synthesized nanostructured ceria with improved porosity, electrical, and thermal properties for solid oxide fuel cell applications.
- Determined that the doping mechanism for semiconductor nanocrystals such as ZnSe is based on adsorption kinetics; and the optical properties of semiconductor CdSe nanorods is determined by the interaction of the one-dimensional exciton (electron-hole pair) with the surrounding medium.
- Developed a procedure for the directed self-catalyzed growth of gallium nitride nanowires.
- Invented new graphitic-like sensor materials and carbon nanotube-coated steel mesh for vapor collection.
- Synthesized new ligand-stabilized metal nanoparticle catalysts for proton exchange membrane fuel cell applications.
- Grew and characterized quantum dot molecules.
- Designed, synthesized, and characterized a new peptide structure—a cyclic beta-hairpin beta-helix—by typing together two appropriate peptide strands into a cyclic structure with beta-hairpin ends.

Select examples of research accomplishments in nanoelectronics:

- Optimized the InAs heterostructure system to achieve a desirable balance of high electron mobility, low electron density, and electron gatability.
- Demonstrated guided resonant modes in gallium nitride/sapphire photonic crystals grown for the first time as an asymmetric, supported structure directly on a surface, eliminating the need for an air gap beneath the photonic waveguide.
- Developed a method to directly write metallic nanowires on a substrate in air or vacuum using a newly developed thermal dip pen nanolithography technique.
- Demonstrated the coupling of two InAs quantum dots (that individually behave as pseudo atoms) to form a quantum dot “molecule” with an abundance of optically accessible ground and excited states.
- Demonstrated electrical injection of spin polarized electrons at zero applied magnetic field using edge-emitting, light-emitting diodes and laser structures.
- Demonstrated electrical spin injection from Fe into GaAs/InAs quantum well structures.

Select examples of research accomplishments in nanosensors and nanodevices:

- Achieved the highest open-circuit voltage (close to theoretical limit) in an organic tandem photovoltaic cell.
- Achieved record high (100× higher) emission current density from carbon nanotube field emitter arrays.
- Made the world's smallest individual organic light-emitting diode by filling a 60-nanometer hole in a 100-nanometer-thick film with a light-emitting polymer that is made to electroluminesce.
- Developed a magnetic nanorod-based platform for dynamic force spectroscopy studies of biomolecules, which included the growth of highly textured cobalt nanorods for magnetic actuation and development of gold FePt Hall sensors for detection of actuation.
- Determined that the sensitivity of two chemical sensors—one based on gold nanoparticles and another based on carbon nanotubes—is limited by 1/f noise.
- Developed a novel photoelectronic nanodevice based on oriented self-assembly of helical supramolecules encapsulating specifically designed and synthesized chromophores with helical amylose.
- Achieved a new world record reporting the highest Q in micro/nanomechanical resonators made from nanocrystalline diamond.
- Fabricated devices—single quantum dot as small as 150 nm and double quantum dot of 250 nm—toward the development of a single photon detector.
- Fabricated nanometer apertures on tapered silicon structures to be used as synthetic nanopores for stochastic sensing of ions, small molecules, and macromolecules.
- Advanced the understanding of photoinduced electron transfer between the reaction center of photosynthetic proteins and electrodes towards the construction of a novel, highly efficient photovoltaic devices.

the naval research laboratory

35

NRL – Our Heritage

36

Highlights of NRL Research in 2007

41

NRL Today

NRL — OUR HERITAGE

The Naval Research Laboratory celebrates its 85th anniversary in 2008. The world is quite different today than it was 85 years ago, but NRL's early 20th century founders knew, as we do today, the importance of science and technology in maintaining naval power and preserving national security. NRL began operations in 1923 as the United States Navy's first modern research institution.

Thomas Edison's Vision: The first step came in May 1915, a time when Americans were deeply worried about the great European war. Thomas Edison, when asked by a *New York Times* correspondent to comment on the conflict, argued that the Nation should look to science. "The Government," he proposed in a published interview, "should maintain a great research laboratory....In this could be developed...all the technique of military and naval progression without any vast expense." Secretary of the Navy Josephus Daniels seized the opportunity created by Edison's public comments to enlist Edison's support. He agreed to serve as the head of a new body of civilian experts—the Naval Consulting Board—to advise the Navy on science and technology. The Board's most ambitious plan was the creation of a modern research facility for the Navy. Congress allocated \$1.5 million for the institution in 1916, but wartime delays and disagreements within the Naval Consulting Board postponed construction until 1920.

The Laboratory's two original divisions—Radio and Sound—pioneered in the fields of high-frequency radio and underwater sound propagation. They produced communications equipment, direction-finding devices, sonar sets, and perhaps most significant of all, the first practical radar equipment built in this country. They also performed basic research, participating, for example, in the discovery and early exploration of the ionosphere. Moreover, the Laboratory was able to work gradually toward its goal of becoming a broadly based research facility. By the beginning of World War II, five new divisions had been added: Physical Optics, Chemistry, Metallurgy, Mechanics and Electricity, and Internal Communications.

World War II Years and Growth: Total employment at the Laboratory jumped from 396 in 1941 to 4400 in 1946, expenditures from \$1.7 million to \$13.7 million, the number of buildings from 23 to 67, and the number of projects from 200 to about 900.

During WWII, scientific activities necessarily were concentrated almost entirely on applied research. New electronics equipment—radio, radar, sonar—was developed. Countermeasures were devised. New lubricants were produced, as were antifouling paints, luminous identification tapes, and a sea marker to help save survivors of disasters at sea. A thermal diffusion process was conceived and used to supply some of the ^{235}U isotope needed for one of the first atomic bombs. Also, many new devices that developed from booming wartime industry were type tested and then certified as reliable for the Fleet.

Post-WWII Reorganization: The United States emerged into the postwar era determined to consolidate its significant wartime gains in science and technology and to preserve the working relationship between its armed forces and the scientific community. While the Navy was establishing its Office of Naval Research (ONR) as a liaison with and supporter of basic and applied scientific research, it was also encouraging NRL to broaden its scope and become, in effect, its corporate research laboratory. There was a transfer of NRL to the administrative oversight of ONR and a parallel shift of the Laboratory's research emphasis to one of long-range basic and applied investigation in a broad range of the physical sciences.

However, rapid expansion during WWII had left NRL improperly structured to address long-term Navy requirements. One major task—neither easily nor rapidly accomplished—was that of reshaping and coordinating research. This was achieved by transforming a group of largely autonomous scientific divisions into a unified institution with a clear mission and a fully coordinated research program. The first attempt at reorganization vested power in an executive committee composed of all the division superintendents. This committee was impractically large, so in 1949, a civilian director of research was named and given full authority over the program. Positions for associate directors were added in 1954, and the laboratory's 13 divisions were grouped into three directorates: Electronics, Materials, and Nucleonics.

The Breadth of NRL: During the years since World War II, the Laboratory has conducted basic and applied research pertaining to the Navy's environments of Earth, sea, sky, space, and cyberspace. Investigations have ranged widely—from monitoring the Sun's

behavior, to analyzing marine atmospheric conditions, to measuring parameters of the deep oceans. Detection and communication capabilities have benefitted by research that has exploited new portions of the electromagnetic spectrum, extended ranges to outer space, and provided a means of transferring information reliably and securely, even through massive jamming. Submarine habitability, lubricants, shipbuilding materials, firefighting, and the study of sound in the sea have remained steadfast concerns, to which have been added recent explorations within the fields of virtual reality, superconductivity, biomolecular science and engineering, and nanotechnology.

The Laboratory has pioneered naval research into space—from atmospheric probes with captured V-2 rockets, through direction of the Vanguard project (America’s first satellite program), to inventing and developing the first satellite prototypes of the Global Positioning System (GPS). Today, NRL is the Navy’s lead laboratory in space systems research, as well as in fire research, tactical electronic warfare, microelectronic devices, and artificial intelligence.

The consolidation of NRL and the Naval Oceanographic and Atmospheric Research Laboratory, with centers at Bay St. Louis, Mississippi, and Monterey,

California, added critical new strengths to the Laboratory. NRL now is additionally the lead Navy center for research in ocean and atmospheric sciences, with special strengths in physical oceanography, marine geosciences, ocean acoustics, marine meteorology, and remote oceanic and atmospheric sensing.

The Twenty-First Century: The Laboratory is focusing its research efforts on new Navy strategic interests in the 21st century, a period marked by global terrorism, shifting power balances, and irregular and asymmetric warfare. NRL scientists and engineers are working to give the Navy the special knowledge, capabilities, and flexibility to succeed in this dynamic environment. While continuing its programs of basic research that help the Navy anticipate and meet future needs, NRL also moves technology rapidly from concept to operational use when high-priority, short-term needs arise—for pathogen detection, lightweight body armor, contaminant transport modeling, and communications interoperability, for example. The interdisciplinary and wide-ranging nature of NRL’s work keeps this “great research laboratory” at the forefront of discovery and innovation, solving naval challenges and benefiting the nation as a whole.

HIGHLIGHTS OF NRL RESEARCH IN 2007

The scientific community at NRL conducts innovative research across a wide spectrum of technical areas, much of it detailed in the *NRL Review* chapters ahead. The following brief vignettes present a selection of the many additional projects pursued during 2007.

Dual Band Radar Program: The Dual Band Radar (DBR) Engineering Development Model is being developed under the guidance of the NAVSEA Program Executive Office, Integrated Warfare Systems (PEOIS) 2.0. It is a single integrated radar system combining the functionality of the SPY-3 Multi-Function Radar at X-band and a Volume Search Radar (VSR) at S-band. The SPY-3 portion performs horizon search, track-while-scan, surface search and navigation periscope detection, missile communications and target illumination, kill assessment, counterfire, and passive search. The VSR portion performs full volume search, aircraft marshalling, precision track, passive search, and counterfire. A common signal and data processor provides capability to optimize performance and load share between the two radar frequency bands. The system will provide an advanced multifunction radar capability resulting in air dominance on the DDG 1000 and CVN 21 ship classes.

Large Data (LD) Joint Capability Technology Demonstration (JCTD): The LD JCTD is responding to an urgent need created by the exponential growth of sensor data from sensors and processing systems that are currently overwhelming the warfighters’ ability to derive actionable information. An improvement in defense information capabilities is needed to enable net-centric warfighting. NRL has demonstrated a multi-node, fully encrypted, cross-country, high-speed, low-latency data sharing environment operating at speeds and bandwidth previously unexploited. This environment is processing large, near-real-time, classified data and is delivering product into operational sites. The LD JCTD is allowing warfighters in a theater of operation to pull the larger imagery files they need to make more thorough analysis products.

Early Operational Assessment of Pod-Mounted Directional Infrared Countermeasures System: Currently, tactical strike aircraft avoid the airspace below 20,000 feet due to the threat from infrared-guided surface-to-air missiles (SAMs). The development of a tactical infrared missile warning system and jamming pod allows this airspace to be used operationally, particularly for close air support and forward air controller

missions. An operational prototype missile warning and jamming pod to detect and defeat hostile surface-to-air and air-to-air infrared-guided missiles that are targeting the host aircraft was designed, fabricated, and tested. The missile system is based on two-color, mid-wave infrared imaging sensors developed by NRL and DRS Technologies. The sensor is capable of detecting threats at their maximum engagement ranges and cueing the directed infrared countermeasures (DIRCM) jamming system.

Coherent Stand-In Jammer: The Airborne Electronic Attack Analysis of Alternatives study identified the need for a stand-in jamming component to airborne electronic attack to augment dedicated support-jamming such as from the EA-6B or EA-18G aircraft. A stand-in jammer is needed to effectively counter radars with agilities and advanced processing capabilities designed to reduce or eliminate the effects of clutter and electronic attack; these radars are associated with modern mobile surface-to-air missile systems that may be difficult to find and engage. The Coherent Stand-In Jammer (CSIJ) effort has developed an advanced wideband electronic warfare device and demonstrated advanced airborne electronic attack from an unmanned air vehicle (UAV). The CSIJ device flying in a UAV was cued from a ground command-and-control station that received and processed radar pulse information downlinked from other UAVs outfitted with electronic support receivers. The CSIJ device is about the size of a college textbook and weighs less than 10 pounds; it generates obscuration and deception jamming techniques that generate multiple false targets and even total white-out in victim radars, preventing them from tracking targets of interest.

Miniature Microbial Fuel Cells: Microbial fuel cells (MFCs) have been used to generate electricity from natural nutrient sources for the past several decades. However, MFCs traditionally are large and bulky, require strict environmental control of the microbial environment, and operate with anaerobic conditions in the anode chamber. NRL initiated a program to apply MFCs in aerobic environments and to greatly reduce the physical size. A radically new design uses anode and cathode chambers with working volumes of approximately 1 ml. Oxygen-tolerant bacteria (*Shewanella oneidensis* species) and high surface area graphite felt electrodes enable surface area-to-chamber volume ratios of $>500 \text{ cm}^{-1}$. The result of this work has been the development of the first high power density mini-MFC, with a 2.0 cm^2 cross section and a 1.2 cm^3 volume, making the unit orders of magnitude smaller than traditional MFCs. Additionally, the mini-MFC is designed to maximize current collection and proton diffusion to the cathode, two properties that

enable unprecedented power densities of 3 W/m^2 and 500 W/m^3 . These results are an indication that further size reduction may increase power density and enable microbial energy scavengers to power microelectromechanical system (MEMS) sensor networks.

Efficient Electrical Spin Injection into Silicon from a Ferromagnetic Metal Contact: The electronics industry has relied largely on the control of charge flow through size scaling to increase performance of existing electronics. This trend has been remarkably successful. However, size scaling cannot continue indefinitely as atomic length scales are reached, so new approaches must be developed. Research has shown that spin angular momentum, another fundamental property of the electron along with charge, can be used to store and process information in metal- and semiconductor-based devices. This approach is known as semiconductor spintronics. Efficient injection and transport of spin-polarized carriers is prerequisite for developing such an approach. While significant progress has been realized in GaAs semiconductors, little has been made in silicon. Now NRL has successfully injected a current of spin-polarized electrons from an iron film through an Al_2O_3 tunnel barrier into Si(001). The circular polarization of the electroluminescence resulting from radiative recombination in Si and GaAs tracks the iron magnetization, confirming that these spin-polarized electrons originate from the iron contact. The polarization reflects Fe majority spin. This demonstration by NRL is a key enabling step for developing devices that rely on electron spin rather than electron charge, and that are expected to provide higher performance with lower power consumption and heat dissipation.

Development of Helmet-Mounted Environmental Sensors: The conditions occurring in an improvised explosive device (IED) blast that cause mild traumatic brain injury (TBI) are not understood by medical personnel. Sensing the conditions during a blast and relating those conditions to the outcome of recovery of the victims could reveal the cause(s) of TBI. To gather this information, NRL designed and prototyped an environmental sensor that mounts to the rear of a Marine helmet. The sensor measures head acceleration, direction of the blast, blast overpressure, and temperature. It records up to 400 events and has a battery life of six months. The information gathered by these devices will be used to design equipment capable of reducing the incidence and severity of TBI. The Army and Marines will be deploying these devices in Iraq in the near future.

Incoherent Combining of High-Power Fiber Lasers for Long-Range Directed Energy Applications: Recent advances in fiber lasers have made

them a leading candidate for directed energy (DE) applications. Advantages of high-power fiber lasers for such applications include high wall plug efficiency, high CW power, single-mode operation, good beam quality, compactness, favorable wavelength, low cooling requirements, low maintenance, long life, and low operating cost. To achieve the power levels needed for DE applications, it is necessary to combine a large number of fiber lasers, either coherently or incoherently, for efficient propagation over many kilometers. Coherent beam combining requires precise phase locking of the fiber lasers, polarization matching, and narrow linewidths; these requirements are difficult to achieve, and limit the individual fiber laser power. Incoherent beam combining does not have these stringent requirements and thus allows for the use of recently developed high CW power fiber lasers. The NRL high-energy fiber laser program is developing a robust, compact, highly efficient, long-range laser weapons system based on incoherently combining high-power fiber lasers. The system is suitable for near-term Navy applications and for operation on an all-electric ship.

Laboratory Investigations in Support of Nuclear-Enhanced Radiation Belt Remediation: “Killer electrons” are relativistic particles generated in high-altitude nuclear detonations that form long-lived artificial radiation belts and threaten the destruction of low Earth orbiting satellites. Such destruction would cripple military operational capabilities. In naturally occurring radiation belts, the trapped relativistic electron lifetime is controlled by plasma wave scattering. NRL researchers have shown that the lifetime of trapped energetic particles can be controlled by man-made electromagnetic waves, and have proposed two techniques for depleting artificially enhanced radiation belts by injecting the necessary wave energy to scatter electrons from their stable orbits. One technique is the direct transmission of relatively low power whistler waves over a period of ~3 to 7 days using in situ satellite-based antennas, and the other is a novel alternate method using a high-speed satellite chemical release to accomplish the remediation within an hour by injection of massive amounts of plasma wave power. Both methods ultimately rely on whistler-wave-induced particle scattering, but differ in the wave generation mechanisms and the time required to inject the requisite wave power. Laboratory experimental studies are currently under way to address the key basic physics issues associated with each remedial concept.

Development of Single-Domain Antibodies for Biothreat Detection: Conventional multi-domain antibodies are complex protein chains with a short shelf life and limited environmental stability; this places constraints on their use in antibody-based biosensors.

Single-domain antibodies (sdAbs) are less complex in structure, and so are sturdy and simple, with a small binding site. Single-domain antibodies represent a new generation of durable detection reagents that can be integrated into any antibody-based biosensor. NRL scientists built a large library of semi-synthetic sdAbs based on llama antibodies, and from it, were able to rapidly select binders specific to an array of biothreat targets (cholera, ricin, and others). The selected sdAbs possess high specificity and enhanced thermal stability in comparison to conventional antibodies. They are able to bind antigen after incubation at 95 °C while conventional antibody reagents lose activity after identical treatment. SdAbs will benefit the DoD and homeland security by permitting biosensors to function at elevated environmental temperatures over extended periods of time.

Transition of Acoustic Adaptive Sampling Capabilities: Environmental variability significantly impacts Fleet acoustic asset performance. This variability can be represented using oceanographic and acoustic modeling capabilities. To provide guidance for efficiently obtaining environmental intelligence in areas of highest uncertainty, an adaptive planning system was developed, tested, and demonstrated by NRL oceanography and acoustics groups, and is currently being transitioned to the Naval Oceanographic Office. The Ensemble Transform Kalman Filtering technique used in atmospheric modeling was applied to oceanographic modeling to generate oceanographic ensembles. Given these realizations of the environment, acoustic performance predictions were generated. The variability of the acoustic coverage over the ensemble is used to provide sampling guidance for oceanographic sensor placement. The computationally intensive system is implemented on the Major Shared Resource Center computers and runs automatically once a day in order to provide an estimate of the variability of the acoustic performance due to the variability of the oceanography. The planning tool represents a new capability in environmental analysis and mission planning.

First Light with the Long Wavelength Demonstrator Array: The Earth’s ionosphere has long precluded exploration of the HF/VHF sky at high resolution and sensitivity, leaving it one of the most poorly explored regions of the electromagnetic spectrum. NRL has pioneered HF/VHF adaptive optic techniques that permit modeling of ionospheric effects, paving the way for an emerging generation of powerful and large HF/VHF arrays, including the Long Wavelength Array (LWA). The LWA is designed to be the next-generation, large (~400 km), long-wavelength (20–80 MHz) HF/VHF synthesis imaging array that will improve sensitivities and resolutions an order of magnitude over current

systems. The leap in sensitivity and resolution of the LWA will push technology and software far beyond requirements for current systems. A technology testbed to develop new software and hardware for implementation in the LWA is being provided by the Long Wavelength Demonstrator Array (LWDA), which saw first light in 2006. First images from the LWDA showed details of the long-wavelength radio sky including the brightest sources Cassiopeia A and Cygnus A, the bright diffuse inner Galactic plane, the quiescent Sun, and other astronomic features. The 16-element LWDA will continue to operate until the first full LWA station is designed and built.

Current Dynamics at the Shelf Break: NRL deployed acoustic Doppler current profilers on the continental shelf and slope for one year in the north-eastern Gulf of Mexico as part of its Slope to Shelf Energetics and Exchange Dynamics project. The goal was to understand current dynamics at the shelf break, which is a difficult region for modeling. Empirical orthogonal function (EOF) analysis showed that two modes described most of the current variability. Wind-forced variability of the along-shelf flow was the main contributor in Mode 1, while eddies contributed much of the variability in Mode 2. Wind stress controlled currents on the shelf and slope at time scales of about a week. On longer time scales, variations in the currents on both the outer shelf and slope appeared to be related to seasonal variations in the time-cumulated wind stress curl. Winds were dominant in driving the along-shelf transports, particularly along the slope. The effective wind stress component was found to be aligned with the west Florida shelf direction rather than the local shelf direction. The measurements collected form a unique data set that is being used to understand ocean processes at the shelf break.

A Real-Time Eddy-Resolving ($1/12^\circ$) Global Ocean Prediction System with High Vertical Resolution: The world's first eddy-resolving global ocean prediction system with both high horizontal and vertical resolution began running daily in the operational queues at the Naval Oceanographic Office. The ocean model component is based on a $1/12^\circ$ global version of the Hybrid Coordinate Ocean Model (HYCOM) with ~ 7 km mid-latitude resolution. It uses the Navy Coupled Ocean Data Assimilation system which is a multivariate optimal interpolation scheme to assimilate satellite and in situ surface observation plus vertical profiles of temperature and salinity. By using data assimilation in combination with the dynamical interpolation skill of the model, the 3-dimensional ocean environment can be accurately nowcast and forecast. Each day, the system performs a 5-day hindcast up to the present time (the nowcast), and then produces

a 5-day forecast. It produces a high horizontal and vertical resolution depiction of the three-dimensional ocean environment, e.g., temperature, salinity, and currents.

Successful Through-the-Sensor Sediment Data Collection Onboard SSN688 During Operational Deployment: Knowledge of seafloor environmental properties is critical to optimal tactics for use of anti-submarine warfare (ASW) and mine countermeasures (MCM) sonar systems. The underwater sound used by these systems interacts with the seafloor differently for differing types of seafloor and sub-seafloor sediments. If the properties of these sediments are known, tactics can be developed to optimize performance of these systems. A vigorous survey and data basing program is in place to collect this sediment data, but data in forward operating areas is usually still sparse and expensive to collect with dedicated survey assets. NRL has developed a capability to collect information on seafloor sediment properties using existing sonars installed on SSN688 submarines. Collecting the data using existing sonars aboard Navy combatants reduces the need for costly dedicated environmental survey operations and provides relevant and timely information to the warfighter. This system has been used successfully to collect data at sea onboard a SSN688 submarine during an operational deployment to the western Pacific.

New Global Operational 4D-Variational Data Assimilation System: A new four-dimensional variational (4DVAR) data assimilation system, NAVDAS-AR, has been developed at NRL and applied to the Navy Operational Global Atmospheric Prediction System (NOGAPS). The new data assimilation system uses NOGAPS to dynamically constrain the four-dimensional analysis and to properly assimilate asynoptic observations. The current operational data assimilation system, NAVDAS, is based on a three-dimensional variational (3DVAR) algorithm. This algorithm is widely used in intermittent cycling data assimilation for the analysis of synoptic scales around the world. However, not all observation systems are well accommodated within an intermittent 3DVAR framework, and this framework can only produce a "snapshot" of the atmosphere at the center of the typical 6-hour observation time window. With a 4DVAR system, a continuous picture of the atmosphere over the observation time window is produced. The computational efficiency of NAVDAS-AR is superior to NAVDAS for handling the monumental increase in the volume of satellite data expected over the next decade, thereby allowing for a more timely delivery of products to the end user. NAVDAS-AR will lead to superior weather forecasts and improved forcing fields for other environ-

mental products. The system has been transitioned for operational testing at the Fleet Numerical Meteorology and Oceanography Center.

First Satellite Measurements Using Spatial Heterodyne Spectroscopy: Spatial heterodyne spectroscopy (SHS) is an innovative optical technique that allows the design of small, high-sensitivity, high-resolution spectrometers suitable for deployment on small satellites. NRL has developed several concepts that use this new technique, ranging from warfighter protection to middle atmospheric research to planetary exploration. The first high-resolution ultraviolet spectrometer using the novel SHS technique was launched into a low Earth orbit from Cape Canaveral in 2007. Called the Spatial Heterodyne Imager for Mesospheric Radicals (SHIMMER), it is the primary payload of small satellite STPSat-1; its main objectives are to demonstrate SHS for long-duration space flight and measure the hydroxyl radical (OH) in the middle atmosphere. SHIMMER has already returned several hundred thousand atmospheric measurements. In addition to the OH solar resonance fluorescence, SHIMMER detected polar mesospheric clouds (PMCs) throughout the 2007 summer season covering the equatorward edge of the PMC region at all local times.

Early Results from the SECCHI Experiment on STEREO: The Sun Earth Connection Coronal and Heliospheric Investigation (SECCHI) experiment on the NASA Solar Terrestrial Relations Observatory (STEREO) mission is providing the first three-dimensional views of solar activity. SECCHI's panoramic field of view extends from the surface of the Sun all the way through the inner heliosphere to the Earth and beyond. SECCHI consists of two identical suites of five telescopes launched on two STEREO spacecraft (Ahead and Behind) that drift away from the Earth and from each other over time, with the Ahead-Sun-Behind angle increasing by 45° per year on average. SECCHI combines images taken simultaneously from the two perspectives of the STEREO spacecraft. As the spacecraft separate over time, the stereoscopic angle is optimized for viewing features at different spatial scales in three dimensions at different times. Image pairs can be viewed through specially colored or polarized glasses

to give a three-dimensional effect. SECCHI observations are helping scientists to understand the three-dimensional structure of the solar atmosphere and coronal mass ejections. This understanding is necessary to improve our ability to predict magnetic explosions that lead to coronal mass ejections, and to follow their evolution in detail through the heliosphere.

Comprehensive Maritime Awareness (CMA) Joint Capability Technology Demonstration: The CMA JCTD is addressing serious gaps in the ability to identify and prioritize global maritime threats posed by combinations of vessels, people, and cargo. Effective maritime security and homeland defense must be balanced with efficient flow of goods. U.S. and international information resources are available to help focus attention to the most probable threats, but most of this information is not readily shared. NRL is demonstrating solutions to close the maritime security gaps: automated tracking of maritime movements; automated alerts to draw attention to potential threats; and most importantly, the development of partnerships with other nations/agencies that will facilitate improved awareness.

Front End Robotics Enabling Near-term Demonstration (FRIEND) Autonomous Robotic Grapple of Simulated Spacecraft: Many commercial and military spacecraft could benefit from an orbital repositioning service. Having such service available could allow otherwise functional satellites that are left stranded in an inoperable orbit to accomplish their missions. It could allow satellites to operate longer before needing to expend their own fuel to retire themselves, and it could allow satellites to be repositioned into new mission orbits without needing to expend their own fuel. However, the ability to safely rendezvous and dock with satellites not predesigned to accommodate this is beyond the current state of the art. DARPA and NRL are currently engaged in a multi-year effort to advance the state of the art in autonomous space-based robotics servicing. This effort has successfully accomplished autonomous full-scale hardware simulation of rendezvous and docking with mock spacecraft under simulated orbital conditions with flight-traceable autonomy algorithms, processors, and research-grade robotics.

NRL TODAY

ORGANIZATION AND ADMINISTRATION

The Naval Research Laboratory is a field command under the Chief of Naval Research, who reports to the Secretary of the Navy via the Assistant Secretary of the Navy for Research, Development and Acquisition.

Heading the Laboratory with joint responsibilities are CAPT Daniel R. Gahagan, USN, Commanding Officer, and Dr. John A. Montgomery, Director of Research. Line authority passes from the Commanding Officer and the Director of Research to three Associate Directors of Research, the Director of the Naval Center for Space Technology, and the Associate Director for Business Operations. Research divisions are organized under the following functional directorates:

- Systems
- Materials Science and Component Technology
- Ocean and Atmospheric Science and Technology
- Naval Center for Space Technology.

The *NRL Fact Book*, published every two years, contains information on the structure and functions of the directorates and divisions.

NRL operates as a Navy Working Capital Fund (NWCF) Activity. All costs, including overhead, are charged to various research projects. Funding in FY06 came from the Chief of Naval Research, the Naval Systems Commands, and other Navy sources; government agencies, such as the U.S. Air Force, the Defense Advanced Research Projects Agency, the Department of Energy, and the National Aeronautics and Space Administration; and several nongovernment activities.

PERSONNEL DEVELOPMENT

At the end of FY07, NRL employed 2597 persons—37 officers, 80 enlisted, and 2480 civilians. In the research staff, there are 790 employees with doctorate degrees, 307 with master's degrees, and 428 with bachelor's degrees. The support staff assists the research staff by providing administrative support, computer-aided design, machining, fabrication, electronic construction, publication and imaging, personnel development, information retrieval, large mainframe computer support, and contracting and supply management services.

Opportunities for higher education and other professional training for NRL employees are available through several programs offered by the Employee Relations Branch. These programs provide for graduate

work leading to advanced degrees, advanced training, college course work, short courses, continuing education, and career counseling. Graduate students, in certain cases, may use their NRL research for thesis material.

For non-NRL employees, several postdoctoral research programs exist. There are also agreements with several universities for student opportunities under the Student Career Experience Program (formerly known as Cooperative Education), as well as summer and part-time employment programs. Summer and interchange programs for college faculty members, professional consultants, and employees of other government agencies are also available. These programs are described in the *NRL Review* chapter "Programs for Professional Development."

NRL has active chapters of Women in Science and Engineering (WISE), Sigma Xi, Toastmasters International, and the Federal Executive and Professional Association. An amateur radio club, a drama group, and several sports clubs are also active. NRL has a Recreation Club that provides sports leagues and swim, whirlpool bath, gymnasium, and weight-room facilities. NRL also has an award-winning Community Outreach Program. See "Programs for Professional Development" for details on all these programs and activities.

NRL has its very own credit union. NRL Federal Credit Union (NRLFCU) was established in 1946 and serves about 20,000 NRL employees, contractors, select employee groups, and their families. Focusing on its mission of *Trusted Partners for Life*, NRLFCU provides many free and low-cost products and services including free bill payer, great rates on deposits, credit cards, auto loans, mortgages, and more. With direct deposit, Online Access, three local branches (one of them located in Bldg. 222), and nationwide access via the National Shared Branching Network, we're sure to be convenient. NRLFCU also offers full-service investment and brokerage services. For more information, contact us at 301-849-8400 or log onto www.nrlfcu.org today.

Public transportation to NRL is provided by Metrobus. Metrorail service is three miles away.

SITES AND FACILITIES

NRL's main campus in Washington, DC, consists of 87 main buildings on about 130 acres. NRL also maintains 11 other research sites, including a vessel for fire research and a Flight Support Detachment. The many diverse scientific and technological research and support facilities are described here.

RESEARCH FACILITIES

Institute for Nanoscience

The revolutionary opportunities available in nanoscience/nanotechnology have led to a National Nanotechnology Initiative. NRL has been a major contributor to the science of nanostructures and is making a commitment to expand that effort. The NRL Institute for Nanoscience was established in 2001 with a \$10 million annual budget in core research funds. The mission of the Institute for Nanoscience is to conduct highly innovative, interdisciplinary research at the intersections of the fields of materials, electronics, and biology in the nanometer size domain. The Institute exploits the broad multidisciplinary character of the Naval Research Laboratory to bring together scientists with disparate training and backgrounds to pursue common goals at the intersection of their respective fields in systems at this length scale. The objectives of the Institute's programs are to provide the Navy and DoD with scientific leadership in this complex, emerging area and to identify opportunities for advances in future defense technology. Its current research program emphasizes multidisciplinary, cross-division efforts in nanomaterials, nanoelectronics, and nanosensors/devices.

The Institute for Nanoscience building opened in January 2004. It has 5000 ft² of Class 100 clean room space for device fabrication, 4000 ft² of "quiet" space with temperature controlled to 0.5 °C, acoustic isolation at the NC35 standard (35 dB at 1 kHz), floor vibration isolation to <150 µm/s rms at 10 to 100 Hz and <0.3 mOe magnetic noise at 60 Hz. There are also 1000 ft² of "ultra-quiet" space with temperature controlled to 0.1 °C and acoustic isolation at the NC25 standard (25 dB at 1 kHz).

Radar

NRL has gained worldwide renown as the "birthplace of radar," and for more than half a century has maintained its reputation as a leading center for radar-related research and development. A number of facilities managed by NRL's Radar Division continue to contribute to this reputation.

A widely used major facility is the Compact Antenna Range (operated jointly with the Space Systems Development Department) for antenna design and development and radar cross section measurements. The range is capable of simulating far-field conditions from 1 to 110 GHz, with a quiet zone approximately 7 ft in diameter and 8 ft in length. Instrumentation covers from 1 to 95 GHz. Another strong division capability is in the Computational Electromagnetics (CEM) Facility, which has capabilities

for complex electromagnetic modeling, including radar target and antenna structures. The Radar Signature Calculation Facility within this group produces detailed computations of radar cross sections of various targets, primarily ships. The CEM facility includes multiple-CPU supercomputers that are also used to design phased array radar antennas. The tremendous synergism between the CEM group and the Compact Antenna Range Facility provides the ability to design in the CEM environment, to test in the compact range, and to have immediate feedback between the theoretical and experimental aspects to shorten the development cycle for new designs.

In connection with airborne radar, the division operates a supercomputer-based Radar Imaging Facility and an inverse synthetic aperture radar (ISAR) deployed either in the air, on the ground, or aboard ship for radar imaging data collection. A P-3 aircraft equipped with the AN/APS-145 radar and cooperative engagement capability is also available for mounting experiments.

In connection with ship-based radar, the division operates the Radar Testbed Facility at the Chesapeake Bay Detachment (CBD), Randle Cliffs, Maryland. The site has radars for long-range air search and surface search functions and features the newly developed W-band Advanced Radar for Low Observable Control (WARLOC), a fully operational high-power coherent millimeter-wave radar operating at 94 GHz. The WARLOC transmitter is capable of producing 10 kW average power with a variety of waveforms suitable for precision tracking and imaging of targets at long range. Waveforms with a bandwidth of 600 MHz can be transmitted at full power. A 6-ft Cassegrain antenna is mounted on a precision pedestal and achieves 62 dB of gain.

The Advanced Multifunction Radio Frequency Concept (AMRFC) testbed is a new installation at CBD, operated by the Radar Division, with joint participation of several other NRL divisions as well. The goal of the AMRFC program is to demonstrate the integration of many sorts of shipboard RF functions, including radar, electronic warfare (EW), and communications, by utilizing a common set of broadband array antennas, signal and data processing, and signal generation and display hardware. The testbed consists of separate active transmit and receive arrays that operate over the 6 to 18 GHz band (nominally). Current functionality of the testbed includes a multimode navigation/surface surveillance Doppler radar, multiple communication links (line-of-sight and satellite), and passive and active EW capabilities. Testbed electronics are housed in seven converted 20-ft shipping containers and trailers. The arrays are mounted on a 15° tilt-back in the ends of two of the trailers overlooking the Chesapeake Bay, simulating a possible shipboard installation.



The AMRFC testbed, located at NRL's CBD, was developed as a proof-of-principle demonstration system that is capable of simultaneously transmitting and receiving multiple beams from common transmit and receive array antennas for radar, electronic warfare, and communications. These RF functions are controlled by common resource allocation manager (RAM) software over a real-time control network. New RF functionality may be readily added to the testbed as required for further demonstrations.

The division also has access to other radar systems: the Microwave Microscope (MWM); the Navy's relocatable over-the-horizon radar (AN/TPS-71); and an experimental Cooperative Aircraft Identification system. The internally developed MWM has a high-resolution (2 cm) ultrawideband capability that is used to investigate backscatter from surface and volumetric clutter, has through-wall detection capability, and characterizes the impulse responses of scattering objects. With respect to the AN/TPS-71, the division provides direct technical support and has direct access to data. The Cooperative Aircraft Identification system is used to explore system concepts and engineering developments in connection with target identification.

Information Technology

NRL's Information Technology Division (ITD) conducts basic research, exploratory development, and advanced technology demonstrations in the collection, transmission, and processing of information to provide a basis for improving the conduct of military operations. Funded by a variety of customers and sponsors within DoD, the U.S. government, and industry, ITD's research program spans the areas of artificial intelligence, high assurance systems, modeling and simulation, virtual reality, human/computer interaction, computer and communication networks, communication systems, transmission technology, and high performance computing.

ITD research networks connect internal NRL networks via high-speed links to OC48c on the Defense Research and Engineering Network (DREN) to a range of DoD sites; and to OC192c and all-optical wavelengths across ATDnet and BoSSNET to form the DoD's Global Information Grid Evaluation Facility (GIG-EF). GIG-EF provides a coalition of early adopters the key test validation infrastructure for transforming the DoD to network-centric IPv6/MPLS convergence for future use by the services, NASA, the

intelligence community, and coalition partners. ATDnet and BoSSNET also provide the core of an extended all-optical network that supports advanced signaling and transparent wavelength routing and switching. Optical research includes introduction of emergent technology to facilitate tunable 40G and 100G all-optical operation across single wavelengths and testing of new network protocols that emphasize low latency transport across the wide area, greatly increased network capacity for both aggregate and single flows, and the evolution of all-optical networks with direct switching and tuning at the optical layer.

ITD maintains several test labs containing a wide variety of networking equipment and test gear such as network traffic generators and analyzers, signal generators, and spectrum analyzers, which allow real-time injection and monitoring of wired and wireless traffic flows from simulated and "real world" data sources. The Integrated Communications Technology (ICT) Test Lab provides testing and evaluation of advanced networking technologies in support of multiple DoD programs such as Joint Tactical Radio System, Fleet Battle Experiments, Joint Forces Command Modeling & Simulation, Joint Experimentation, JTF WARNET, and Dragon Warrior. ICT Lab computers running NRL-developed software test programs can assess the performance of military and commercial off-the-shelf (COTS) equipment such as network radios, routers, and communications security devices.

The Mobile and Dynamic Network Laboratory supports development and evaluation of next-generation communication technologies for mobile and dynamic data networks. This laboratory provides for large-scale network simulation, real-time network emulation, and live field tests of wireless, mobile networks. The General Electronics Environmental Test Facility includes automated electronic test equipment and instrumentation, a phase noise measurement system, a noise figure measurement system, precision spectrum analyzers, wide-band signal generators, a 40 ft³ environmental chamber,

and an EMI test chamber located off-site. This facility provides resources for testing the performance of electronic and fiber-optic equipment under conditions that represent deployment to and installation in a Naval ship or Marine Corps tactical environment.

ITD also hosts a number of secure labs that support research in the areas of high assurance computing and networks. The Naval Cryptographic Technology Laboratory conducts research and prototype development of programmable cryptographic technologies for Navy and DoD applications. This laboratory also allows for development of certifiable Communications Security (COMSEC)/Information Security (INFOSEC) products, including programmable cryptographic devices, cryptographic applications, and high assurance cross-domain solutions. The Naval Key Management Laboratory investigates electronic key management and networked key distribution technologies for the Navy and DoD and serves as a testbed for developing new key management components and key delivery protocols developed for the Electronic Key Management System (EKMS) and the modernized Key Management Infrastructure (KMI).

The Cyber Defense Development Lab provides unique facilities for NRL research into Navy and DoD information and network security. This lab provides direct support in the areas of computer network defense and visualization, cross-domain solutions, and reverse code analysis and support. From architectural design, review, and prototyping, to component evaluation and integration, the Cyber Defense Development Lab ensures secure capability and availability of DoD and Navy network-centric information operations. It also serves as the research and development facility for the Navy Cyber Defense Operations Command (NCDOC). It not only supports and maintains NCDOC's Prometheus Critical Network Defense (CND) suite, but also serves as the mission critical facility for Naval reverse code and malware analysis in support of both NCDOC and Naval Criminal Investigative Service operations.

ITD's Center for Computational Science (CCS) provides early access to next-generation computing and imaging technologies to NRL researchers. Assets at the CCS include a combination of clustered architecture and large uniform memory supercomputers. The most recent HPC to be commissioned in early FY08 was a Silicon Graphics 8200 series computer with 1536 processors and 6 terabytes of memory. Other leading-edge HPC resources include two Silicon Graphics 3700's and one 4700 series, each with 128 or more processors and a terabyte or more of memory. CCS also operates a unique Cray XD1 supercluster that integrates 864 AMD Opteron processor cores with 150 closely coupled FPGAs capable of providing one to two orders of magnitude processing gain.

CCS also operates a laboratory for Large Data research. NRL and the CCS Large Data lab provide the programmatic lead for several distributed facilities that extend across CONUS and overseas. The CCS lab and the others in the network provide a base OC192c (10 Gbps) environment for experimentation and proof of concept in the use and sharing of extremely large data sets of petabytes and larger. Current efforts include introduction of InfiniBand transport, new protocols such as the Session Initiation Protocol (SIP), and the use of leading-edge, high-speed cryptographic devices.

ITD has a variety of facilities dedicated to simulation and visualization of complex datasets. The Motion Imagery Laboratory provides a flexible, immersive visualization baseline for experiments in the convergence of progressive motion imagery; peer-to-peer agent driven high performance distributed computing; distributed, federated access to petabyte datasets; and a dynamic SIP control plane for direct wavelength switching.

ITD's Navy Center for Applied Research in Artificial Intelligence comprises several laboratories. The Robotics and Autonomous Systems Laboratory provides the ability to develop and evaluate intelligent software and interfaces for autonomous vehicles. Software can be evaluated in simulation, or in the real world using individual or teams of mobile robots. An 82-node computational cluster is also available for simulation, allowing faster-than-real-time evaluation of the performance of software agents, and is particularly suited to fast convergence of solutions using evolutionary computation methods.

The Immersive Simulation Laboratory utilizes a collection of COTS and specially developed components to support R&D in interfaces to virtual simulators, ranging from fully immersive to desktop simulations. This includes three optical motion capture systems for full-body tracking of multiple users and specially designed centering harnesses for dismounted infantry simulation. The lab also includes a variety of head-mounted displays, large screen displays, input control devices, graphics and audio rendering computers, and simulation software to support a wide range of research in the field of human-computer interaction.

The Warfighter Human-Systems Integration Laboratory (WHSIL) maintains a range of virtual environment interface technologies including desktop, single projection screen, and head-mounted display immersive systems. Tracking technologies associated with these systems range from simple joystick control to partial body optical tracking. In parallel, WHSIL is developing wearable, wi-fi physiological monitors and associated real-time processing algorithms for use in adaptive operational and training support technologies.

The Audio Laboratory has facilities for rendering and analyzing complex sound for military applications. The rendering systems include a 28-speaker array



The Navy Center for Applied Research in Artificial Intelligence is investigating learning and adaptation within teams of autonomous robots. Recent work has focused on a team of robots performing force protection.

arranged in five rings within a space that is deadened by 16 RPG Diffuser VariScreens, which produce realistic audio environments using pre-recorded or synthesized sound.

The 3D Virtual and Mixed Environments Laboratory explores methods by which 3D computer graphics assists in the collection, interpretation, and dissemination of information for both operational and training purposes. Augmented reality equipment includes wearable computers, optical and video see-through head-worn displays, vision-based and non-vision-based tracking components, global positioning system antennas including differential and real-time kinematic correction, and inertial tracking systems.

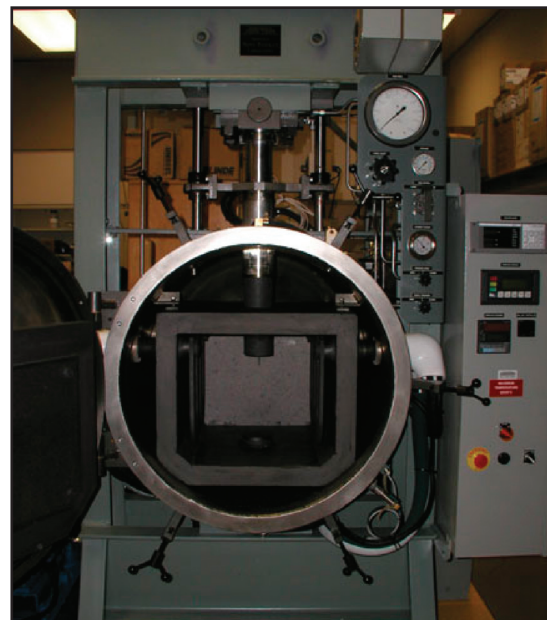
The Intent/Deception (ID) Laboratory tests various sensor suites, algorithms, and processes associated with behavioral indicators of deception. Sensors include computer vision cameras, pupil trackers, thermographic IR cameras, and high-end audio collection equipment. The ID Lab serves as an integration facility for the various sensors and an evaluation center for the algorithms needed to automate the process of determining deception.

ITD is also a partner in the Laser Communications Test Facility located at NRL's Chesapeake Bay Detachment (CBD). Three divisions (Space Systems Development Department, Optical Sciences Division, and Information Technology Division) have collaborated on a joint capability to develop and test components, subsystems, and algorithms that support freespace laser communications. The facility offers a 16 km range over water from CBD to Tilghman Island, which is ideal for studying issues of specific interest to laser communications as it pertains to Navy problems. Additionally, ITD maintains a Freespace Laser Communications Laboratory on the main campus, used to design and prototype technical solutions before testing them in the field at CBD.

ITD's Transmission Technology Branch is developing transportable high-frequency digital receivers and antenna arrays to be used at various field sites of interest. These utilize COTS high-speed digitizing PCI boards with desktop/and or laptop computers. The data collected is expected to provide new insights into ionospheric wave interactions caused by high-power radio transmitters such as the High Frequency Active Auroral Research Program (HAARP).

Optical Sciences

The Optical Sciences Division has a broad program of basic and applied research in optics and electro-



The Optical Sciences Division's 50-ton hot press for sintering transparent rare-earth-doped ceramic laser materials and ceramic spinel for transparent armor applications.

optics. Areas of concentration include fiber optics, materials and sensors in the visible and infrared, integrated optical devices, signal processing, optical information processing, panchromatic and hyperspectral imaging for surveillance and reconnaissance, and laser development.

The division occupies some of the most modern optical facilities in the country. The newest facility in Optical Sciences is a 50-ton hot press for sintering optical quality ceramic materials. Other facilities include several fiber-optic facilities including preform fabrication, draw towers, optical fiber coaters, fiber splicers, and fiber-optic sensor testing stations such as an acoustic test cell and a three-axis magnetic sensor test cell. There is also an Ultralow-loss Infrared (IR) Fiber-Optic Waveguide Facility using high-temperature IR glass technology. The Focal Plane Array Evaluation Facility allows measurement of the optical and electrical characteristics of infrared focal plane arrays being developed for advanced Navy sensors. The IR Missile-Seeker Evaluation Facility performs open-loop measurements of the susceptibilities of IR tracking sensors to optical countermeasures. A UHV multi-chamber deposition apparatus for fabrication of electro-optical devices is interfaced to a surface analysis chamber equipped with ultraviolet photoelectron spectroscopy, X-ray photoelectron spectroscopy, atomic force microscopy, and scanning tunneling microscopy. Other scanning probe facilities are equipped with atomic force and magnetic force microscopes. Another material growth facility is a molecular beam epitaxial growth system dedicated to quantum confined GaSb/InAs/AlSb structures. An extensive set of laboratories exists to develop and test new laser and nonlinear frequency conversion concepts and to evaluate nondestructive test and evaluation techniques.

Electronic Warfare

The Tactical Electronic Warfare (TEW) Division's program for electronic warfare (EW) research and development covers the entire electromagnetic spectrum. The program includes basic technology research and advanced developments and their applicability to producing EW products. The range of ongoing activities includes components, techniques, and subsystems development as well as system conceptualization, design, and effectiveness evaluation. The focus of the research activities extends across the entire breadth of the battlespace. These activities emphasize providing the methods and means to counter enemy hostile actions—from the beginning, when enemy forces are being mobilized for an attack, through to the final stages of the engagement. In conducting this program, the TEW Division has an extensive array of special



AN/ALQ-228(V)1 communications jamming pod.

research and development laboratories, anechoic chambers, and modern computer systems for modeling and simulation work. Dedicated field sites and an NP-3D EW flying laboratory allow for the conduct of field experiments and operational trials. This assemblage of scientists, engineers, and specialized facilities also supports the innovative use of all Fleet defensive and offensive EW resources now available to operational forces.

Laboratory for Structure of Matter

This laboratory investigates the atomic arrangements in materials to improve them or facilitate the development of new substances. Various diffraction methodologies are used to make these investigations. Subjects of interest include the structural and functional aspects of energy conversion, ion transport, device materials, and physiologically active substances such as drugs, antibiotics, and antiviral agents. Theoretical chemistry calculations are used to complement the structural research. A real-time graphics system aids in modeling and molecular dynamics studies. The facilities include two state-of-the-art X-ray diffraction units.

Chemistry

NRL has been a major center for chemical research in support of naval operational requirements since the late 1920s. The Chemistry Division continues this tradition. It is pursuing a broad spectrum of basic and applied research programs focusing on controlled energy release (fuels, fire, combustion, countermeasure decoys, explosives), surface chemistry (corrosion, adhesion, tribology, adsorbents, film growth/etch), advanced materials (high-strength/low-weight structures, drag reduction, damping, polymers, thin films,



Moored in Mobile Bay, Alabama, the ex-USS *Shadwell* is regularly set ablaze in a controlled environment to further the safety of operational Navy and civilian firefighting measures.

nanostructures), and advanced detection techniques (environment, chemical/biological, surveillance). The division has several research facilities.

Chemical analysis facilities include a wide range of modern photonic/electronic-, magnetic-, and ionic-based spectroscopic/microscope techniques for bulk and surface analysis. The Synchrotron Radiation Facility has intense, monochromatic X-ray photon beams tunable from 10 eV to 12 KeV available from four beam lines developed by NRL at the National Synchrotron Light Source at the Brookhaven National Laboratory. Environmental target chambers span a pressure range from 10^{-12} to 10^5 atm and temperatures from 10 to 1500 K. The Nanometer Characterization/Manipulation Facility includes fabrication and characterization capability based on scanning tunneling microscopy/spectroscopy, atomic force microscopy, and related techniques. A Materials Synthesis/Property Measurement Facility has special emphasis on polymers, surface-film processing, and directed self-assembly. Fire research facilities include a 10,000 ft³ fire-research chamber (Fire I) and the 475-ft ex-USS *Shadwell* (LSD 15) advanced fire research ship. Commensurate support has been devoted to survivability of the new classes of ships, DDX, LUN 21, LPD 17, and LHA(R).

The Marine Corrosion Test Facility located on Fleming Key at Key West, Florida, offers an ocean-air environment and clean, unpolluted, flowing seawater for studies of environmental effects on materials. Equipment is available for experiments involving weathering, general corrosion, fouling, and electrochemical phenomena, as well as coatings, cathodic protection devices, and other means to combat environmental degradation.

The Chemistry Division has focused on force protection/homeland defense (FP/HD) since September 11, 2001, especially on the development of improved

detection techniques for chemical, biological, and explosive threats. As part of a multidivisional program to develop new technology systems, the Chemistry Division is a major contributor to the NRL Institute for Nanoscience. Nanoscience complements FP/HD in that nanoscience is expected to provide dramatic improvements to chemical/biological detection, protection, and neutralization. Chemistry will approach the nanoscale from the bottom-up—building smaller atoms and molecules into nanostructures with new properties and developing the directed assembly of nanostructures into hierarchical systems. The NRL Nanoscience building is linked directly into the Chemistry building to provide both controlled access and auxiliary space for work not requiring a “low noise” environment.

Materials Science and Technology

The Materials Science and Technology Division at NRL conducts materials research using seven major division facilities.

The Magnetoelectronics Fabrication Facility consists of a Class 1000 clean room equipped with tools for lithographic construction of magnetoelectronic and spintronic devices. It provides pattern definition, metallization, dielectric layer deposition, and both reactive and Ar⁺ ion etching of wafers and small pieces.

The Electrical, Magnetic, and Optical Measurement Facility contains several complementary instruments that allow for the magnetic, electrical, optical, and heat capacity characterization of materials and devices. SQUID (superconducting quantum interference device) magnetometry and vibrating sample magnetometry are used to determine important properties of superconducting, paramagnetic, diamagnetic, and ferromagnetic materials. The transport properties of materials, namely the temperature- and magnetic-field-



The Magnetoelectronics Fabrication Facility consists of a Class 1000 clean room equipped with tools for lithographic construction of magnetoelectronic and spintronic devices.

dependent resistivity combined with heat-capacity measurements, allow for a fundamental physical understanding of electronic properties.

The Materials Processing Facility includes apparatuses for powder production by fluid atomization, thermal evaporation, and arc erosion, and a physical vapor deposition system designed to produce and coat submicron powders in situ. Facilities to process powder into bulk specimens by hot and cold isostatic pressing permit a variety of consolidation possibilities. The isothermal heat treatment facility and quenching dilatometer permit alloy synthesis and single crystal growth. Bulk alloys can be prepared by induction melting, while rapid solidified metals of thin cross section can be made by splat quenching and melt spinning. Ceramic and ceramic-matrix composites processing facilities include a wide variety of conventional, controlled atmospheric furnaces, hot presses, a ball milling apparatus, particle size determination capability, and sol-gel and organometallic coating processing capabilities.

The Mechanical Characterization Facility consists of various testing systems, many with automated computer control and data acquisition, for determining the mechanical response of materials under controlled loading/deformation and environmental conditions. Basic capabilities include quasistatic tensile and fracture testing, dynamic storage and loss moduli as a function of frequency and temperature, cyclic fatigue crack growth and corrosion fatigue testing, and stress-corrosion cracking testing.

The Thin-Film Materials Synthesis and Processing Facility provides users a wide variety of techniques for growth and processing of thin films (thickness 1 μm or less). Sputter deposition offers a versatile method of

depositing metallic and dielectric films and is a primary tool of this facility. Thermal evaporation of metals is implemented in both high-vacuum and ultrahigh-vacuum systems. Pulsed laser deposition (PLD) with variable stage temperature and controlled atmosphere allows growth of oxides. Electrolytic deposition offers efficient growth of gold and silver films. Laser direct-write ablation and deposition processes provide unique methods for imposing CAD-defined features via ablation of a substrate film and ablative mass transfer to a substrate.

The 3-MV Tandem Pelletron Accelerator Facility uses two “pelletron” charging chains to produce a terminal voltage up to 3 MV in the accelerator. Negative ions are injected at 10 to 70 keV, accelerated up to the terminal where they undergo collisions with a stripper gas or a carbon stripper foil and lose electrons, then are accelerated as positive ions back to ground potential. Protons can be accelerated up to 6 MeV, He up to 9 MeV, and highly stripped Au (+12) up to 39 MeV. The lower limit of beam energy is about 400 keV. On the analysis beam line, the sample of interest is located at the end of the beam line, and a signal generated by scattering of incident high-energy ions indicates the composition of the sample. Incident high-energy ions can also be used to damage the surface of a sample of interest, or to introduce a dopant.

The Micro/Nanostructure Characterization Facility is capable of performing transmission electron microscopy (TEM), scanning transmission electron microscopy (STEM), atomic resolution transmission electron microscopy (ARTEM), electron energy loss spectroscopy (EELS), Z-contrast imaging, and spectral imaging through the use of a JEOL 2010F transmission electron



The Micro/Nanostructure Characterization Facility is capable of performing TEM, STEM, ARTEM, EELS, Z-contrast imaging, and spectral imaging.

microscope, a Phillips CM30 transmission electron microscope, and a Leo scanning electron microscope. Other standard microstructure characterization instruments are also available.

Laboratory for Computational Physics and Fluid Dynamics

The Laboratory for Computational Physics and Fluid Dynamics maintains a highly powerful collection of computer systems applied to a broad collection of work. There are currently 120 parallel SGI processors, 512 clustered x86 processors, and several other support systems. In addition, there are more than 50 Macintoshes in the group, most of which are capable of large calculations both independently and in parallel ad hoc clusters.

The SGI computer systems comprise an SGI Altix with 64 Itanium-2 processors, an SGI Altix with 12 Itanium-2 processors, a 28-R12K-processor Origin 3800, an 8-R14K-processor Origin, and an 8-R12K-processor Origin 2000. There are two 256 x86 processor clusters well coupled with Myrinet high-speed switched interconnect.

Each system has on the order of 200 gigabytes of disk space for storage during a simulation, and at least 512 megabytes of memory per processor. All unclassified systems share a common disk space for home directories as well as almost 250 gigabytes of AFS space, which can be used from any AFS-capable system throughout the allowed Internet. The AFS capability also allows access to other storage systems including NRL's multiresident AFS (MRAFS) system, which automatically handles archiving to a multi-terabyte tape archival system.

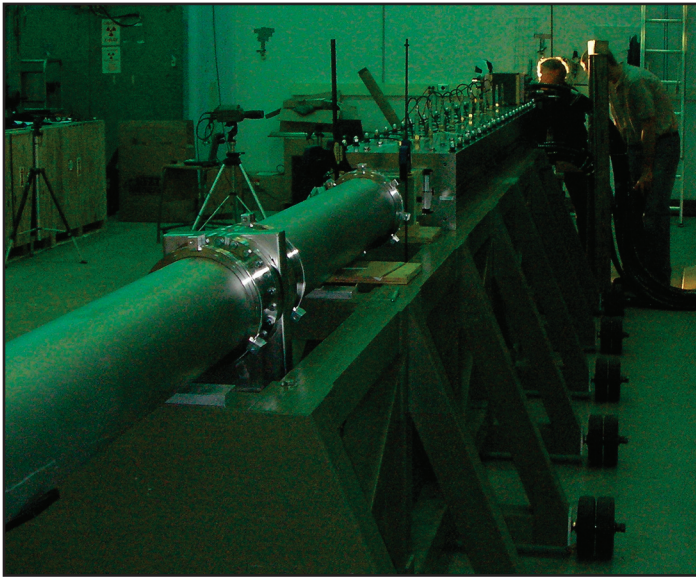
Plasma Physics

The Plasma Physics Division is the major center for in-house Navy and DoD plasma physics research. The division conducts a broad experimental and theoretic

cal program in basic and applied research in plasma physics, which includes laboratory and space plasmas, pulsed-power sources, plasma discharges, intense electron and ion beams and photon sources, atomic physics, laser physics, advanced spectral diagnostics, plasma processing, nonlinear dynamics and chaos, and numerical simulations.

The facilities include an extremely high power laser, Pharos III, for the laboratory simulation of space plasmas and nuclear weapons effects studies, and two short-pulse high-intensity lasers—the Table-Top Terawatt (T^3) laser and the Ti:Sapphire Femtosecond Laser (TFL)—to study intense laser-plasma, laser–electron beam, and laser-matter interactions. The division also has an 11 m³ space chamber capable of reproducing the near-Earth space plasma environment and a Large Area Plasma Processing System (LAPPS) facility to study material modification such as surface polymerization or ion implantation. The division has developed a variety of pulsed power sources to generate intense electron and ion beams, powerful discharges, and various types of radiation. The two largest of these pulsers, Gamble II and Mercury, are used to study the production of terawatt electron and ion beams and to produce very hot, high-density plasmas. Other generators are used to produce particle beams that are injected into magnetic fields and/or cavities to generate intense microwave pulses. A large array of high-frequency microwave sources (2.45, 35, and 83 GHz) are available to conduct research on microwave processing of advanced ceramic materials. In particular, the division added a 20-kW, continuous-wave, 83-GHz gyrotron to its facility for research on high-frequency microwave processing of materials.

The Nike 3-kJ KrF laser facility is made up of 56 laser beams and is single-pulsed (4-ns pulse). This facility provides intense radiation for studying inertial confinement fusion (ICF) target heating at short wavelengths (0.25 μm) and high-pressure physics. A second major inertial fusion system, Electra, is used to develop high-energy, high-repetition-rate KrF technology. The



NRL's Materials Testing Facility railgun. 6-m-long railgun capable of launching 0.5-kG projectiles at 2.5 km/s using an 11 MJ capacitive energy store. This system is designed to perform experiments on bore materials under high-power launch conditions.

amplifier is capable of a 5-Hz repetition rate and has produced up to 700 J of laser light in extended operation.

The Plasma Physics Division has established a new Electromagnetic Gun Laboratory to study barrel materials science issues associated with an electric gun for a future all-electric warship. The laboratory will house a 6-m-long railgun, an 11 MJ capacitive energy storage bank, and solid-state switching hardware capable of driving up to 2 MA current in a barrel. The interface between the sliding projectile and the rails will be studied by a multidivision research team in an effort to design a high-performance and long-lived electric gun barrel.

The Plasma Physics Division also operates the new High Energy Laser Laboratory, which will study laser propagation in the atmosphere, laser-aerosol interactions, laser-target interactions, and beam combining techniques. The facility currently houses two high-power continuous-wave lasers, a 700-watt, 1.064-micron-wavelength Nd:YAG laser, and four 1.075-micron-wavelength Yb: fiber lasers. These lasers will be used to demonstrate a new incoherent beam combining technique that could be the key enabling technology for a new generation of compact laser directed energy weapons.

The division's Space Physics Simulation Chamber (SPSC) simulates the near-Earth space environment, and is used to study ionospheric, magnetospheric, and solar wind plasma phenomena, to test/calibrate space-qualified instruments, and for other studies requiring a low-pressure environment. The vacuum and magnetic field subsystems of the SPSC were upgraded in FY06 to facilitate the long-duration experimental operation required for full 3D spatio-temporal volumetric data acquisition of large-volume plasmas. Five new water-

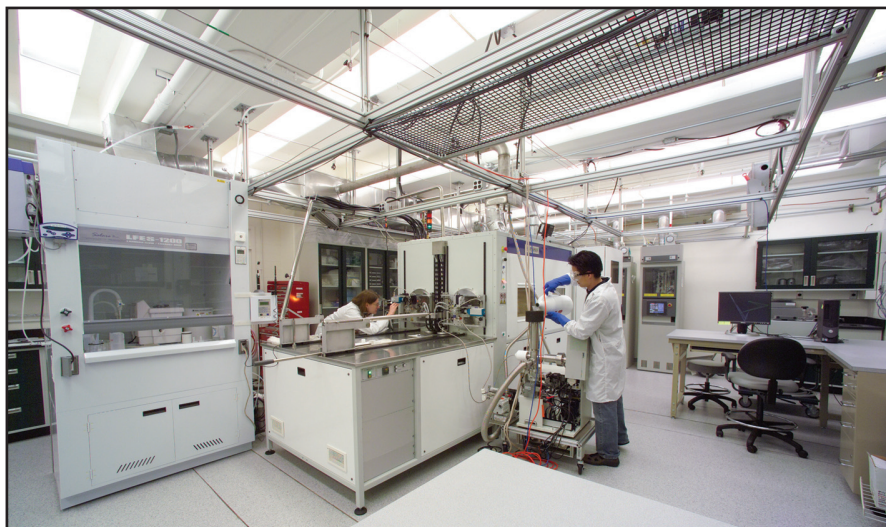
cooled electromagnets replaced the existing non-cooled magnets, allowing for higher magnetic field strengths and long-duration operation. Two new cryogenic vacuum pumps were added, allowing for lower base pressures and faster chamber cycling time.

Electronics Science and Technology

The Electronics Science and Technology Division conducts a multidisciplinary basic and applied research program to exploit the creation/discovery/invention of new enabling materials, components, and techniques in electronics. In-house efforts include research and development in solid-state electronics; electronic materials including growth, theory, and characterization of semiconductors, heterostructures, and superconductors; surface and interface science; microwave and millimeter-wave components and techniques; microelectronic device research and fabrication; nanoelectronics science and technologies; vacuum electronics; power electronics; device and process modeling and simulation; and cryoelectronics.

The division operates the Compound Semiconductor Processing Facility (CSPF), the Laboratory for Advanced Materials Synthesis (LAMS), the Epicenter, the Ultrafast Laser Facility (ULF), the Advanced Silicon Carbide Epitaxial Research Laboratory (ASCERL), the Silicon Carbide Processing Facility (SCPF), the Wafer Bonding Facility (WBF), the Power Device Characterization Facility, the Space Solar Cell Characterization Facility (SSCCF), and the Millimeter-Wave Vacuum Electronics Synthesis Facility (MWVESF).

The CSPF processes compound semiconductor devices and circuits, provides micro- and nanofabrication processing support, and selectively serves the hands-on fabrication needs of NRL scientists. The



The Electronics Science and Technology Division's Advanced Silicon Carbide Epitaxial Research Laboratory (ASCERL).

LAMS uses metallorganic chemical vapor deposition to synthesize a wide range of thin films, particularly wide bandgap semiconductors such as GaN and related alloys. The Epicenter (a joint activity of the Electronics Science and Technology, Materials Science and Technology, Optical Sciences, and Chemistry divisions) is dedicated to the growth of multilayer nanostructures by molecular beam epitaxy (MBE). Current research involves the growth and etching of conventional III-V semiconductors, ferromagnetic semiconductor materials, 6.1 Å III-V semiconductors, magnetic materials, and II-VI semiconductors. The structures grown in this facility are analyzed via in situ scanning tunneling microscopy and angle-resolved electron spectroscopy. The ULF is optimized for the characterization of photophysical and photochemical processes in materials on a timescale of tens of femtoseconds. It includes a synchronously pumped dye laser system for simulating the effects of charge deposited in semiconductors characteristic of space radiation.

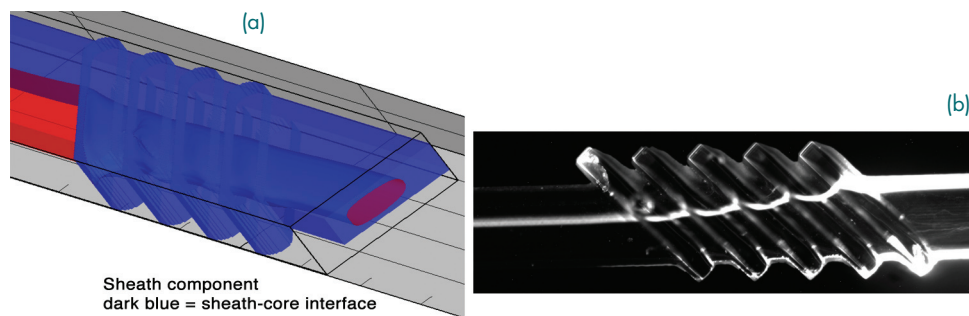
The ASCERL was dedicated in 2006 as the centerpiece of NRL efforts to develop the materials needed for the realization of high-voltage, high-power electronic components needed in future Naval systems. It employs an EPIGRESS reactor capable of growing thick, low-defect, ultra-purity, homo-epitaxial silicon carbide layers. The SCPF encompasses processing tools and equipment to support fabrication of silicon carbide (SiC) electronic power devices and emerging novel devices based on SiC and related heterojunctions. The WBF is a Class 100 clean room facility for conducting research on the fabrication of high-voltage wafer-bonded power devices and the development of novel high-performance wafer-bonded substrates for epitaxial growth of both narrow bandgap and wide bandgap

material layers. The Power Device Characterization Facility characterizes the performance and reliability of silicon and SiC power devices. The SSCCF studies the effect of particle irradiation on new and emerging solar cell technologies for space applications. The MWVESF contains a computer numerically controlled (CNC) milling machine and a CNC precision lathe capable of fabricating intricate millimeter-wave vacuum electronic components to 2.5 micron accuracy. Components include amplifiers, filters, circuits, multiple-beam amplifier cavities, gyro-TWT interaction structures, and electron gun/waveguide structures.

The Millimeter-Wave Vacuum Electronics Synthesis Facility (MWVESF) is being augmented by the installation of a wire electric discharge machining (EDM) tool in 2008. This EDM tool will allow for the realization of millimeter-wave to submillimeter-wave vacuum electronic amplifier and filter components that cannot be fabricated by conventional rotary cutting tools. EDM offers a non-contact process for both hard and soft metals as well as silicon carbide and doped silicon.

Bio/Molecular Science and Engineering

The Center for Bio/Molecular Science and Engineering conducts research and development using biotechnological approaches to support the Navy, DoD, and the nation at large. Studies are currently under way to investigate biomaterial development for electronic and structural applications, environmental quality (including pollution cleanup and control), and chemical/biological warfare defense. Other program areas of interest include optical biosensors, nanoscale manipulations, genomics and proteomics, controlled sustained release, bio/molecular and cellular arrays,



Microfabrication of sensor components at the Center for Bio/Molecular Science and Engineering. NRL microfabrication facilities were used to design, build and demonstrate microfluidic devices for sensors. Shown above is a schematic (a) and demonstration (b) of how precisely milled grooves wrap sheath solution around a sample stream in a microchannel. The demonstration was performed in a 250 μm channel. Optical fibers were used to illuminate the stream and collect the scattered signal. In this image, the sample stream was labeled with a fluorescent dye for visibility.

surface modification and patterning, energy harvesting, viral particles as scaffolds, advanced materials from self-assembly, and liquid-crystal-based electro-optic materials.

The staff of the Center is an interdisciplinary team with expertise in biochemistry and surface chemistry, biophysics, genetic engineering, cell biology, advanced organic synthesis, solid-state and theoretical physics, and electronics and materials engineering. In addition, the Center has collaborations throughout NRL, with other government laboratories, at universities, and in industry.

The Center's modern facilities include general laboratories for research in chemistry, biochemistry, molecular biology, and physics. Specialized areas include a 600 ft² Class 1000 clean room, an advanced electron microscope facility, and a scanning probe microscope laboratory. Instrument rooms provide access to a variety of spectrophotometers and other equipment used in biochemical or physical analyses of biomaterials. Additional laboratories accommodate an X-ray diffraction instrument, a liquid crystal fabrication facility, and equipment for advanced electronics, microarrays, and biosensor programs. The Center has added a plastic microfabrication facility, which enables fabrication of microfluidic and micro-optical systems in polymers, and a state-of-the-art liquid chromatograph-mass spectrometer for molecular characterization.

The Center's facilities were recently used to demonstrate the capabilities of a microarray system developed at NRL for analyzing thousands of samples in a high-throughput production process. The system accurately detected some two dozen infectious and bioterrorism agents in spiked and collected samples. This successful demonstration used the Center's laboratory facilities with NRL staff, Air Force medical personnel, and contractors. At the completion of that program, a smaller-scale version of the microarray system remained at the

Center to continue research in the area of multiplex genomics-based molecular diagnostic arrays.

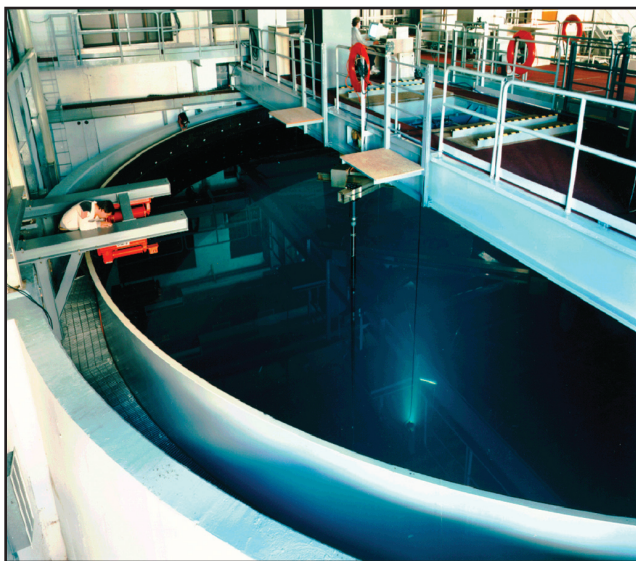
Acoustics

The Acoustics Division conducts a broad program of laboratory and at-sea research in underwater acoustic phenomena.

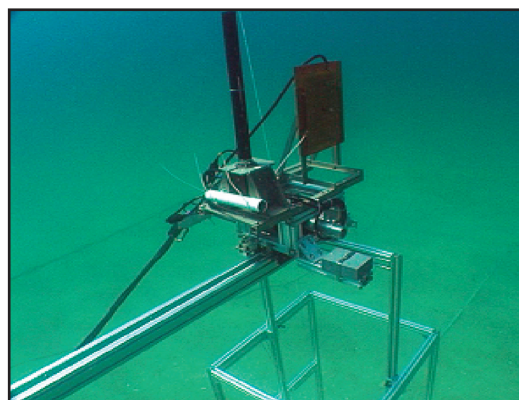
The division has three integrated structural acoustics facilities—two pools (one with a sandy bottom) and a large, in-air, semi-anechoic laboratory. These facilities support research in a number of important areas including mine detection and identification, anti-submarine warfare, and improvised explosive devices (IEDs). These facilities have a number of state-of-the-art measurement capabilities including compact range scattering, nearfield acoustic holography, and scanning laser Doppler vibrometry (LDV). The Laboratory for Structural Acoustics consists of an indoor cylindrical tank (17 m dia. x 15 m deep) filled with approximately 1 million gallons of deionized water. The key features include 1) vibration and temperature isolation through specially designed mounts which suspend the tank above its foundation, 2) feedback-controlled heating elements and adiabatic materials on the walls to reduce temperature variability, and 3) anechoic materials on the interior walls to reduce reverberation. This configuration provides a very homogenous acoustic medium with a temperature variability of less than 0.01 °C over time periods of up to several days.

A 100-meter horizontal rail-based robotic scanner is used to collect synthetic aperture acoustic scattering data from proud and buried targets at sea. The rail system is used in conjunction with impulsive broadband projectors and sensors.

The division operates state-of-the-art laboratories equipped to study the structural dynamics and performance of high-Q oscillators and other micro-mechanical systems. A number of laser Doppler vibrometers,

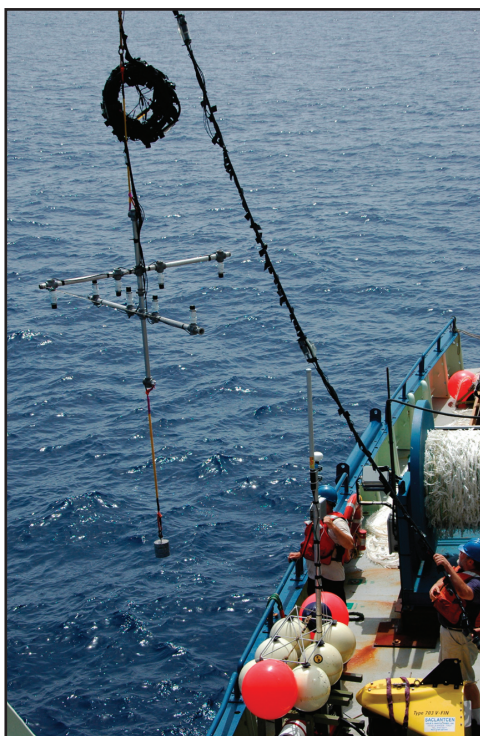


Laboratory for Structural Acoustics.



Acoustics Division rail-based robotic scanner.

The Acoustics Division operates a drifting echo-repeater buoy with a 16-element volumetric array and a moored 16-element vertical line array for multi-static active sonar applications at frequencies from 400 Hz to 10 kHz.



including a super-resolution nearfield scanning optical microscope (NSOM), permit spatial mapping of the complex vibratory motion down to resolutions of 100 nm. The laboratories include the ability to measure the mechanical and electrical properties of the micro-oscillators, and of thin films applied to them, down to 370 mK.

The Salt Water Tank Facility provides a controlled environment for studying a variety of complex ocean processes under saline conditions, especially the study of the acoustics of bubbly media. Instrumentation includes acoustic sources, amplifiers, hydrophones, environmental sensors, a digital holographic imaging system, high-speed digital cameras, and a LabVIEW-based data acquisition system.

The Geoacoustic Model Fabrication Laboratory allows researchers to fabricate rough topographical surfaces in various materials (usually plastics) for acoustic scattering and propagation measurements in water-tank facilities. The facility consists of a three-axis computer-controlled milling machine equipped with vacuum holddown and capable of cutting with 100- μ m accuracy over a 1.37×1.27 m region.

The division's SONoMAGnetic LABoratory (SOMALAB) is used to study the magnetic field produced by acoustic motions in electrically conducting media, such as sea water. This facility is shielded by two nested skins of 3/16-in. HY-80 steel plate. Inside is a 3 ft \times 6 ft \times 3 ft (W \times L \times H) plexiglass experimental water tank that is set on a vibration-insulating optical table, and is equipped with three sets of mutually perpendicular Helmholtz coils. The tank is currently instrumented with a single three-axis magnetometer with a 1 nT noise floor at 1 kHz, which is capable of measuring fields up to ± 100 μ T. Acoustic signals are generated from an external transducer.

The division operates several sound sources for the generation and reception of sound in at-sea experiments. Sound sources include three XF-4 transducers, one ITC-2077 source that can be operated while being

towed by a ship, two battery-operated organ-pipe sources that can project single tones from offboard moorings, and a towable, directional source array for active sonar studies consisting of ten individually controllable elements, at frequencies 2.5 to 5 kHz. In addition, the division has several battery-operated, rubidium-clock-controlled, programmable sound source moorings that can transmit sounds having arbitrary waveforms.

The division has a 64-channel broadband source-receiver array with time-reversal mirror functionality. Projects involving scanning focused acoustic fields and phase conjugation for multistatic sonar utilize this array to test and study time reversal methods. The transducers for the array are 6-in. spheres that operate from 500 to 3500 Hz.

The division also has several radio-controlled buoy systems with underwater receive arrays to collect acoustic and oceanic data, unattended, for periods of up to one month. One system contains a high-speed line-of-sight data link utilizing a GPS-linked directional antenna. A low-speed command and control link is available to remotely control buoy functions and array settings. A second system is deployed in the Chesapeake Bay between the NRL facility at Randle Cliffs (CBD) and Tilghman Island. The buoy is controlled from CBD by a wireless Ethernet bridge, and both processed and raw data may be recovered from the buoy as desired.

The Acoustics Division performs research to relate acoustic array gain variability to fluid dynamic variability and bottom heterogeneity in the littorals. The measurements are made with an autonomous acoustic data acquisition suite. Three independent autonomous 32-channel vertical arrays receive and store 24-bit data at a 4 kHz sample rate for 22 days. Two autonomous acoustic sources operate at 300 and 500 Hz center band with $\pm 10\%$ bandwidth and generate programmable waveforms at 50% duty cycle for 22 days. As presently configured, the systems will operate to water depths of 500 m. The division also has unique, self-recording



Fabrication of rough surfaces for acoustic analysis.

digital acquisition buoy systems (DABS) that are used to obtain multichannel (up to 128) acoustic data in the 10 Hz to 5 kHz regime. These systems provide up to 250 gigabytes of data storage.

The division conducts research addressing the channel capacity of multinode underwater acoustic communications networks. The research is conducted in the 2 to 5 kHz, 6 to 14 kHz, and 10 to 24 kHz frequency bands using two 8-channel acoustic communications data acquisition systems or modems, which can be moored or towed. The 8-element vertical arrays are configured in a 2-m or 20-m aperture and remotely controlled using a wireless LAN.

Narrowbeam 200 and 350 kHz acoustic backscattering (flow visualization) systems are used to study fine structure, internal wave, and larger scale fluid dynamic perturbation of the density and sound speed field in the ocean. A deck-mounted towing assembly consists of transducers, power amplifiers, and a real-time display and digital data acquisition system. A 25 kW radar system is used in conjunction with the flow visualization system to record the surface expression of internal waves.

The division operates high-frequency (up to 600 kHz) acoustic measurement systems to obtain scattering, target strength, and propagation data using bottom-moored instrumentation towers and a remotely operated vehicle. These data are used to simulate the performance of weapons and mine countermeasure sonars.

Remote Sensing

The Remote Sensing Division conducts a program of basic research, science, and applications to develop new concepts for sensors and imaging systems for objects and targets on Earth, in the near-Earth environment, and in deep space. The developmental effort includes active and passive sensor systems used to study and analyze the physical characteristics of phenomena that evolve from naturally occurring background radiation, such as that caused by the Earth's atmosphere and oceans, and man-made or induced phenomena, such as ship/submarine hydrodynamic effects. The research includes theory, laboratory, and field experiments leading to ground-based, airborne, or space systems for use in remote sensing, astrometry, astrophysics, surveillance, nonacoustic antisubmarine warfare, meteorological/oceanographic support systems, and environmental/global climate change initiatives. Special emphasis is given to developing space-based platforms and exploiting existing space systems.

Maritime Hyperspectral Imaging: The Remote Sensing Division conducts airborne hyperspectral data collections for characterization of the environment. Hyperspectral data are series of pictures, taken simul-

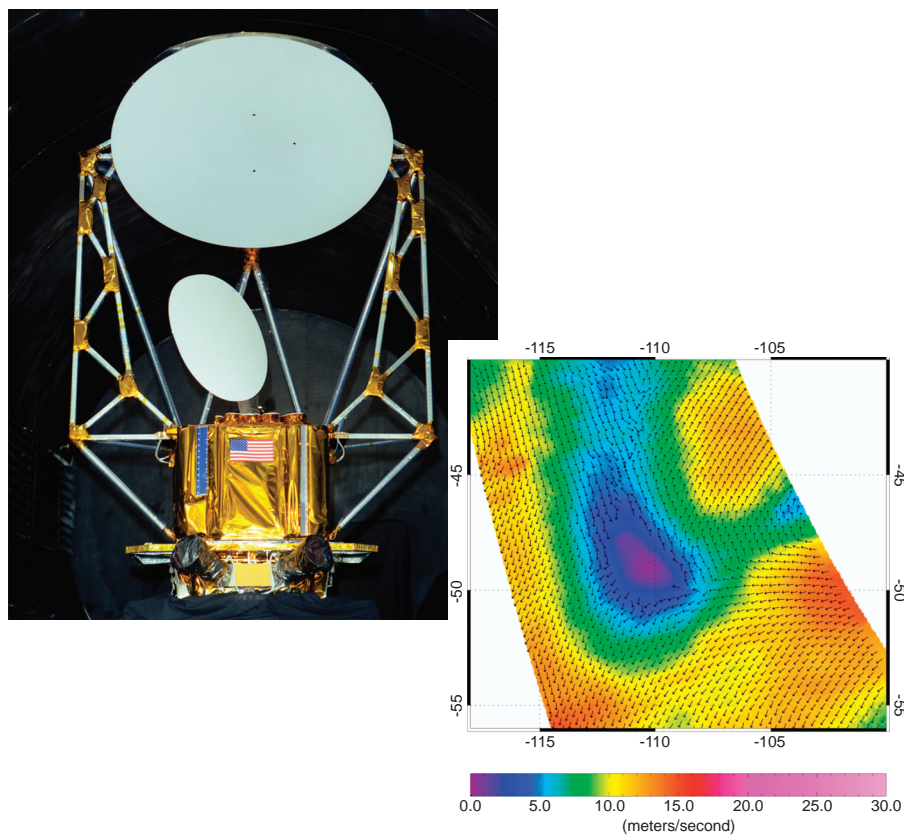
taneously, of a scene at many different wavelengths (colors). The sensors are built and calibrated in-house, although they rely heavily on COTS elements. Our current operational sensor is the airborne Portable Hyperspectral Imager for Low-Light Spectroscopy (PHILLS) system, specifically designed for use over maritime areas. It covers the 400 to 1000 nm wavelength range with 128 different wavelengths (channels). PHILLS consists of a standard video camera lens, a grating spectrograph, and a 1024×1024 -pixel charge-coupled device (CCD). The system is designed for maximum sensitivity in the blue end of the spectrum in order to optimize water-penetrating measurements. This allows retrieval of in-water geophysical parameters such as ocean bottom type (coral, sea grass, sand, rock, etc.) to water depths of 20 m (in clear water), and identification of material in the water column (phytoplankton, sediments, colored dissolved organic matter, etc.). PHILLS is very compact and can be flown at heights of 8000 to 10,000 ft. The division has also acquired a commercial Compact Airborne Spectrographic Imager (CASI-1500) hyperspectral imager with similar capabilities to the NRL-built PHILLS.

Proper interpretation of the hyperspectral data requires both radiometric and spectral calibration of the sensor. The Remote Sensing Division operates an Optical Calibration Facility to perform these calibrations, which includes a NIST-traceable integrating sphere and a set of gas emission standards for wavelength calibration. The complete process of data collection through data analysis can be handled in-house.

To validate the results of airborne hyperspectral sensing, and to support interpretation of the physical processes they reveal, the division has developed a Profiling Optics Package. This system measures the inherent optical properties of water (absorption, attenuation, and scattering) in the 400 to 700 nm range, and collects water samples for various laboratory measurements. The package has a maximum depth rating of 300 m, although it is usually operated in coastal waters of less than 50 m.

The Remote Sensing Division is beginning a two-phase, rapid-development program for maritime hyperspectral imaging from space. The first phase, now under way, is to develop a PHILLS airborne imager for use in space. This sensor, Hyperspectral Imager for the Coastal Ocean (HICO), is manifested for a July 2009 launch and will be deployed aboard the International Space Station. The second phase will be to build and launch the fully space-qualified Coastal Ocean Imaging Spectrometer (COIS) with significantly improved performance and the capability to image 20 coastal regions per day.

Hydrodynamics: The Remote Sensing Division conducts a wide range of numerical and analytical research dealing with the physics of the ocean's free



The NRL WindSat polarimetric radiometer prior to spacecraft integration, and a retrieved wind vector field obtained on September 12, 2003, in the South Pacific.



The Navy Prototype Optical Interferometer (NPOI) is used for operational astrometry and for development of distributed aperture imaging techniques.

surface. Direct numerical simulations of turbulence are made in which the free surface is treated as either flat, or as a fully nonlinear, deformable surface with waves. To test and validate the numerical results and analytical theories, experiments are conducted in the Free-Surface Hydrodynamics Laboratory to study interactions of turbulence with the free surface; wave-generation phenomena; jet flows; vorticity dynamics; and free-surface/surfactant interactions. Emphasis is placed on those processes that determine the fluxes of heat, mass, and momentum across the air-sea interface. State-of-the-art diagnostic tools are available, such as a Langmuir film balance to measure the properties of surface films, hot-wire and laser-Doppler anemometry, and the new quantitative flow techniques of laser speckle, particle tracking, and particle image velocimetry. The laboratory is also equipped with an IR camera with a 0.02 K resolution. These experimental diagnostic techniques use high-powered lasers, high-tolerance optical lenses, and extensive ultra-high-resolution video imaging hardware and PC-based computerized systems. Further computational assets consist of powerful graphical computer work stations, the NRL Connection Machine, and other off-site Cray supercomputer systems. The newest addition to the laboratory is a high-precision, computer-controlled wave generator capable of generating breaking waves 0.2 to 1.2 m in length.

Astronomy: The Navy Prototype Optical Interferometer (NPOI), a major facility of the Remote Sensing Division, is actually two collocated instruments for making high-angular-resolution optical measurements of stars. Light from widely separated individual siderostats is combined simultaneously to synthesize the angular resolution of a telescope tens to hundreds of meters in diameter. Four siderostats are placed in an array with extremely accurate metrology to enable very high precision measurements of stellar positions (wide-angle astrometry). These measurements are used by the U.S. Naval Observatory to refine the celestial reference frame, determine Earth rotation parameters, and thus satisfy Navy requirements for precise time and navigation data. They also provide determinations of basic astrophysical parameters, such as stellar masses and diameters. Additional relocatable siderostats can be placed out to distances of up to (when complete) 250 m from the array center, and used to construct very high resolution images of stars. These images provide fundamental astrophysical information on stellar structure and activity. When complete, the NPOI will be the most advanced high-resolution imaging optical interferometer in the world.

The Remote Sensing Division also has a strong program in radio astronomy, with emphasis on low-frequency (< 100 MHz) observations. The division has developed and installed 74-MHz receivers on the National Radio Astronomy Observatory's (NRAO)

Very Large Array (VLA), thereby producing the world's highest-angular-resolution and most sensitive astronomical interferometric array operating below 150 MHz. The VLA's maximum baseline is 35 km; all previous astronomical interferometers operating below 150 MHz had baselines of less than 5 km because ionospheric structure had been thought to impose phase variations that would corrupt the interferometric imaging. Work in the Remote Sensing Division has shown that radio astronomical techniques can now remove the ionospheric phase variations and extend interferometer baselines to arbitrary lengths. The success of the NRL/NRAO 74-MHz system indicates that it is possible to open a new, high-resolution, high-sensitivity astronomical window by going to an even larger, more sensitive system. Several such large interferometric systems are now in various stages of planning and development. This includes the Long Wavelength Array (LWA), a joint collaboration between the University of New Mexico, University of Texas, Los Alamos National Laboratory, and NRL Remote Sensing Division.

The LWA will provide high spatial and temporal sampling of the ionosphere for characterizing ionospheric phenomenology, and probing ionospheric microstructure and physics. It is also the ideal receiver for proposed solar radar systems which can be used to image Earthward-bound coronal mass ejections for geomagnetic storm prediction. The Long Wavelength Demonstrator Array (LWDA), a 16-element phased array deployed as a technology and scientific testbed station for the LWA, has been completed and is now in operation near Socorro, New Mexico.

Remote Sensing of the Atmosphere and Ocean Surface: The NRL Polar Ozone and Aerosol Measurement (POAM) instrument was a space-based 9-channel UV-vis solar photometer for measuring ozone and other important constituents of the stratosphere using the solar occultation technique. POAM II (1993 to 1996) and POAM III (1998 to 2005) have contributed data on a major policy issue: global ozone depletion. For most of its mission life, POAM was the only instrument making high-vertical-resolution (1 km) measurements of ozone in the polar regions of both hemispheres on a continuous basis, including unprecedented space-based coverage of the Antarctic ozone hole. POAM's orbit was ideal for monitoring the effect of chlorofluorocarbon (CFC) restrictions, and the effect of replacement chemicals, because ozone depletions are most severe in the polar regions during the late winter/early spring season in each hemisphere.

WindSat, developed and built by NRL and launched in January 2003, is the first spaceborne polarimetric microwave radiometer. Its primary mission is to demonstrate the capability to remotely sense the ocean surface wind speed and direction (wind

vector) with a passive system. WindSat, the primary payload on the DoD Space Test Program Coriolis mission, provides major risk reduction for development of the National Polar-orbiting Operational Environmental Satellite System (NPOESS) Conical-scanning Microwave Imager/Sounder (CMIS). Although WindSat wind vector retrieval algorithm development is still an important R&D effort in the Remote Sensing Division, the current algorithm is run operationally at the Navy Fleet Numerical Meteorology and Oceanography Center (FNMOC). Wind vectors are available in real time, and are included in the NRL-Monterey satellite cyclone Web site. In addition, the Remote Sensing Division is exploiting WindSat's unique data set to develop retrievals for other environmental parameters such as sea surface temperature, soil moisture, and sea ice concentration.

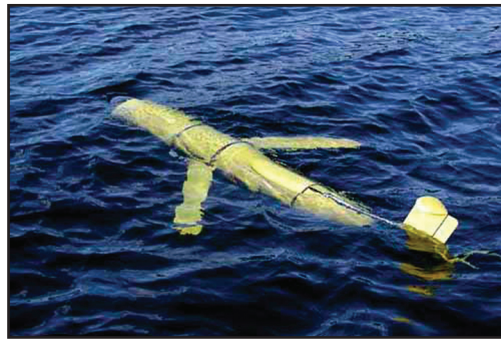
The Airborne Polarimetric Microwave Imaging Radiometer (APMIR) is a state-of-the-art multichannel microwave radiometer system designed and built by the Remote Sensing Division. APMIR was built primarily to provide extensive airborne calibration and validation of spaceborne remote sensing assets: the NRL WindSat mission, the Defense Meteorology Space Program Special Sensor Microwave Imager/Sounder (SSMIS) mission, and the future CMIS to fly on the converged NPOESS. APMIR covers five frequency bands from 5 to 37 GHz, and the 10.7, 18.7, and 37 GHz measurement bands are fully polarimetric. Frequency agility allows for frequency matching to each of the spaceborne

systems of interest. In addition to validation, APMIR provides measurements of the ocean surface wind vector, sea surface temperature, atmospheric water vapor and cloud parameters below the airplane, soil moisture, and ice/snow properties. The APMIR system is deployed on the NRL P-3 aircraft and flown at altitudes ranging from 500 to 25,000 ft over the ocean.

The Remote Sensing Division has developed a unique eye-safe volume-imaging lidar system to remotely characterize aerosol backscatter variations in coastal boundary layers, and to map those variations over hundreds of meters. Deuterium cells are used to produce a Raman wavelength shift that converts near-infrared laser pulses to 1.5 microns (an eye-safe wavelength). The deuterium cells were developed at NRL and do the conversion in a single pass—substantially simpler and more reliable than the multi-pass methane cells that are currently used by other lidar systems. The lidar uses a dual-mirror scanning system to map aerosol structures and detect their movement. Unlike Doppler lidar systems that can measure only radial wind speeds, the NRL lidar uses correlation methods and measures the wind vector (speed and direction) and turbulence.

Oceanography

The Oceanography Division is the major center for in-house Navy research and development in oceanography. It is known nationally and internationally for its



The NRL Oceanography Division's new capabilities for sensing the littoral environment include a Vertical Microstructure Profiler (VMP) (top left), a Scanfish (top right), and four Slocum Gliders (bottom). They will be used to measure the variability of temperature, salinity, currents, and optical properties both horizontally and vertically, on scales ranging from micro- to mesoscale.

unique combination of theoretical, numerical, experimental, and remotely sensed approaches to oceanographic problems. The division's modeling focus is on a truly integrated global-to-coastal modeling strategy, from deep water up to the coast including straits, harbors, bays, and inlets. This requires emphasis on both ocean circulation and wave/surf prediction, with additional emphasis on coupling the ocean models to biological, optical, and sediment models. This modeling is conducted on the Navy's and DoD's most powerful vector and parallel processing machines. The division has an in-house Ocean Dynamics and Prediction Computational Network Facility that provides computer services to scientists for program development, graphics, data processing, storage, and backup. To study the results of this intense modeling effort, the division operates a number of highly sophisticated graphic systems to visualize ocean and coastal dynamic processes.

The seagoing experimental programs of the division range worldwide. Unique measurement systems include a wave measurement system to acquire in situ spatial properties of water waves; a salinity mapper that acquires images of spatial and temporal sea surface salinity variabilities in littoral regions; an integrated absorption cavity, optical profiler system, and towed optical hyperspectral array for studying ocean optical characteristics; self-contained bottom-mounted upward-looking acoustic Doppler current profilers (ADCPs) for measuring ocean variability; and an in situ volume scattering function measurement system to support remote sensing and in-water optical programs. NRL is working jointly with the NATO Undersea Research Center (NURC) for development and deployment of the SEPTR instrument, a trawl-resistant, bottom-mounted ADCP system that includes a pop-up profiling float for real-time observation and reporting.

The Oceanography Division has acquired new capabilities for sensing the littoral environment. These include a Vertical Microstructure Profiler (VMP),

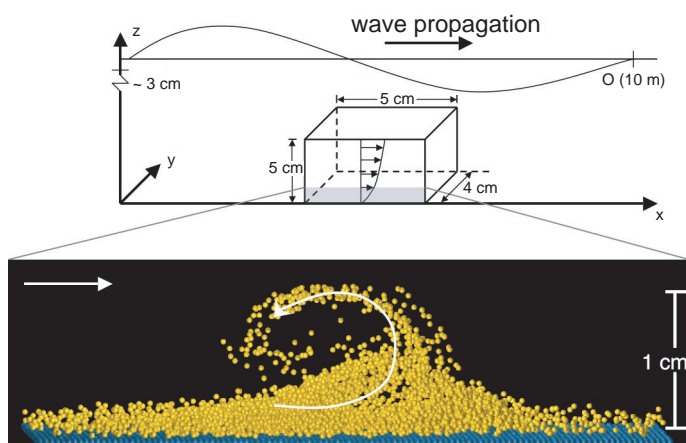
a Scanfish, and four Slocum Gliders. The turbulent dissipation rate can be quickly obtained with very high accuracy from measurements collected by the VMP. The Scanfish allows efficient and rapid three-dimensional mapping of mesoscale oceanic features. The Gliders rely on a low-powered battery-induced change of buoyancy to glide autonomously through the coastal ocean collecting both physical and optical data that are uplinked to satellite and then relayed to the laboratory or ship in near real time.

In the laboratory, the division operates an environmental scanning electron microscope for detailed studies of biocorrosion in naval materials. The division's remote sensing capabilities include the ability to analyze and process multi/hyperspectral, infrared, synthetic aperture radar, and other satellite data sources. The Ocean Optics section has added the capability to download Moderate Resolution Imaging Spectroradiometer (MODIS) data directly using the new X-band receiving system. The division is a national leader in the development and analysis of MODIS ocean color data for oceanographic processes and naval applications in littoral areas.

Marine Geosciences

The Marine Geosciences Division is the major Navy in-house center for research and development in marine geology, geophysics, geodesy, geoacoustics, geotechnology, and geospatial information and systems. The division has unique suites of instrumentation and facilities to support laboratory and field experimental programs.

The instrumentation used in the field is deployable from ships, submarines, remotely operated and unmanned vehicles, undersea platforms, airborne platforms, and by divers. Instrumentation includes an integrated airborne geophysical sensor suite with gravity, magnetic, and sea/ice/land topographic profiling sensors, all based on cm-level KGPS aircraft



In the Marine Geosciences Division, a detailed two-phase flow model for the wave bottom boundary layer is being developed to study fluid-sediment turbulent interactions at the seafloor. The upper image is a schematic of a horizontally periodic domain under a progressive gravity wave. The lower image is a snapshot of particles simulated using the discrete element method that are coupled to a three-dimensional direct numerical simulation of the turbulent fluid flow. Here the particles (yellow) are near neutrally buoyant ($S = 1.03$), and are interacting with the fluid, with each other, and with the rough bottom (blue). The image is taken right after the fourth flow reversal of a sinusoidal wave and the formation of a turbulent eddy about 1 cm in diameter is evident.

positioning. Seafloor and subseafloor measurements use the Deep-Towed Acoustics/Geophysics System, DTAGS (220 to 1000 Hz); a chirp sub-bottom profiler; high-resolution sidescan sonars (100 and 500 kHz); the Acoustic Seafloor Characterization System, ASCS (15, 30, and 50 kHz); an optically pumped marine magnetometer; several gravimeters; the In Situ Sediment Acoustic Measurement System (ISSAMS); heat flowprobe system; underwater stereo photography; and nearshore video imaging systems. ISSAMS has specialized probes that measure acoustic compressional and shearwave velocities and attenuation, sediment shear strength, and electrical conductivity in surficial marine sediments.

Five instrumented, 8-ft-long, 2220-lb, minelike cylinders are used to gather impact burial data (one system) and scour and sand wave burial data (four systems) for validation of mine burial prediction models.

Laboratory facilities include the Sediment Physical and Geotechnical Properties Laboratory and Sediment Core Laboratory. The Transmission Electron Microscopy Facility is the focal point for research in microscale biological, chemical, and geological processes. The key instrumentation includes a 300 kVa transmission electron microscope with environmental cell. The environmental cell allows real-time observations of hydrated and gaseous experiments. A high-resolution industrial CT scanner is a recent addition to the laboratory. It is used for investigating volumetric heterogeneity of sediments.

In the Geochemistry Laboratory, a photon correlation spectrometer and laser Doppler velocimeter analyze size and electrostatic properties of submicrometer-size sediment particles.

The Moving Map Composer Facility is used to design and write mission-specific map coverages for F/A-18 and AV-8B tactical aircraft onto militarized optical disks. The Geospatial Information Data Base (GIDB) capability provides Internet access to the Digital Nautical Chart data, mapping data, imagery, and other data types such as video and pictures. This development tool can be used for planning, training, and operations.

Marine Meteorology

The Marine Meteorology Division is located in Monterey, California. NRL-Monterey (NRL-MRY) serves the Navy's need for basic and applied research in atmospheric sciences and develops meteorological analysis and prediction systems and other products to support warfighting customers at the theater, operational, and tactical levels.

NRL-MRY is collocated with Fleet Numerical Meteorology and Oceanography Center (FNMOC),



NRL's Marine Meteorology Division has a direct downlink capability for real-time geostationary data from NOAA's GOES-E and GOES-W satellites.

the Navy's operational production center for numerical weather prediction (NWP) and satellite data. NRL-MRY's Atmospheric Prediction System Development Laboratory has direct connectivity to FNMOC's classified and unclassified world-class computer resources and databases, which enables the division to efficiently develop and transition analysis and prediction systems to operational use. Links to the Defense Research and Engineering Network (DREN) provide access to supercomputing resources around the country with gigabit/second speed. The in-house Supercomputer Resource Center, which currently includes an SGI Origin 2000 128-processor supercomputer and two LINUX clusters (176 and 44 processors) along with a 64-terabyte Storage Area Network, enables the division to support research in atmospheric processes such as air-sea interaction, terrain-induced flows, atmospheric predictability, and cloud/aerosol processes, and to develop and improve numerical prediction systems critical to Fleet operators around the globe.

A state-of-the-art Satellite Data Processing Laboratory allows direct downlink of real-time NOAA geostationary data (imagery and sounder data from GOES-E and GOES-W) and data relays from three other geostationary satellites. It also receives data from numerous polar orbiting platforms (NOAA satellites, Defense Meteorological Satellite Program satellites, and NASA satellites Tera, Aqua, TRMM, SEAWifs, and QuikSCAT). NRL-MRY processes near-real-time satellite data from 28 sensors and uses the data to conduct research and develop multi-sensor, multi-platform applications to support a variety of DoD operations. These research activities range from monitoring and analyzing tropical cyclone intensity in support of the Joint Typhoon Warning Center to providing dust enhancement imagery in support of combat operations in Southwest Asia. These products are transitioned to FNMOC as they reach maturity. The Satellite Data

Processing Laboratory is supported by the 24-terabyte Bergen Data Center, which has a hierarchical storage management capability to provide archival and easy retrieval of research data sets. The Bergen Data Center also provides support for the data that is archived as part of the Master Environmental Library.

NRL-MRY's Classified Satellite/Radar Data Processing Facility hosts classified computer systems to receive, process, and store classified and unclassified satellite, radar, and observational data; and develop applications for their operational use. This facility has a 22-processor LINUX cluster for high performance computing along with SIPRNET connectivity in a shielded workspace. It provides a real-time testbed for the integration of classified high-resolution data and fusion with "through-the-sensor" information collected from shipboard radars and direct broadcast meteorological satellite sensors to generate on-scene NOWCAST products used to support operational and tactical decision makers.

To support the division's expanding program in aerosol research and aerosol prediction system development, NRL-MRY designed and built the Mobile Atmospheric Aerosol and Radiation Characterization Observatory (MAARCO). MAARCO is a climate-controlled, modified, 20-ft standard container with an integrated suite of meteorological, aerosol, gas, and radiation instruments, with space available for additional sensors, that can be rapidly deployed to operate in austere locations. MAARCO enables research of atmospheric aerosols, gases, and solar radiation in strategic areas, including remote regions, overseas locales, and onboard ships at sea. Data collected during the United Arab Emirates United Aerosol Experiment (UAE²) in 2004 is being used to investigate boundary layer meteorology, aerosol microphysics, and electro-optical propagation. A second MAARCO delivered in September 2006 will be fully instrumented in early 2008.

Space Science

The Space Science Division conducts and supports a number of space experiments in the areas of upper/middle atmospheric, solar, and astronomical research aboard NASA, DoD, and other government agency space platforms. Division scientists are involved in major research thrusts that include remote sensing of the upper and middle atmospheres, studies of solar activity and effects on the Earth's ionosphere, studies of astronomical radiation ranging from the ultraviolet through gamma rays and high-energy particles, and laboratory astrophysics. In support of this work, the division maintains facilities to design, construct, assemble, and calibrate space experiments.

The division's Vacuum Ultraviolet Space Instrument Test Facility is an ultraclean solar instrument test facility designed to satisfy the rigorous contamination requirements of state-of-the-art solar spaceflight instruments. The facility has a 400 ft² Class 10 clean room and a large Solar Coronagraph Optical Test Chamber (SCOTCH). This completely dry-pumped, 550 ft³ vacuum chamber is maintained at synchrotron levels of cleanliness. Solar instrumentation up to 1 m in diameter and 5 m in length can be accommodated in the chamber. The instrument's optical performance is probed and calibrated with a variety of visible and XUV sources mounted on the chamber's 11-m beamline. The facility has a small thermal bake/vacuum test chamber used for vacuum conditioning and thermal testing of spaceflight components and subassemblies. The facility was originally developed to support the optical testing and characterization of the Large Angle Spectrometric Coronagraph (LASCO) instrument for the European Space Agency's Solar and Heliospheric Observatory (SOHO) spacecraft. More recently, components of the NRL Sun Earth Connection Coronal and Heliospheric Investigation (SECCHI) experiment,



The SECCHI Payload Operations Center at NRL showing the command and telemetry stations for the two spacecraft instrument suites, SECCHI-A (left) and SECCHI-B (right).



Left photo: Upper Stage spacecraft attached to Star48 3rd stage of Delta II 7925 booster.
Right photo: MiTex/Upper Stage launch, 21 June 2006, 2215Z. (Courtesy USAF)

developed for the NASA Solar Terrestrial Relations Observatory (STEREO), were tested in the facility. The two SECCHI visible light coronagraphs were calibrated for instrumental efficiency, and their stray light level was characterized. The SECCHI extreme ultraviolet telescope was also characterized in visible wavelengths and in the EUV. The twin STEREO spacecraft were launched on October 26, 2006, from Cape Canaveral Air Force Station (CCAFS). In the near future, the Helium Resonance Scatter in the Corona and Heliosphere (HERSCHEL) experiment will enter the NRL test facility for its calibration program.

The division has many new space instruments under development or recently completed, including SECCHI; EIS, the Extreme Ultraviolet Imaging Spectrometer for Japan's HINODE mission launched September 22, 2006, from Uchinoura Space Center, Japan; Gamma Ray Large Area Space Telescope (GLAST), a high-energy gamma-ray detector for NASA, launched June 11, 2008, from CCAFS; Spatial Heterodyne Imager for Mesospheric Radicals (SHIMMER), a spatial heterodyne spectrometer for middle atmospheric research for a DoD mission; and Tether Physics and Survivability Experiment (TiPS), ultraviolet spectrometers for upper atmospheric research for Taiwan's COSMIC program.

A network of computers, workstations, image-processing hardware, and special processors is used to analyze and interpret space data. The division's space science data acquisition and analysis effort currently includes observations and analysis of the evolution and structure of the solar corona from the disk to 0.14 AU using data from LASCO and the Extreme Ultraviolet Imaging Telescope (EIT) on the SOHO spacecraft. More recently, data is being acquired from the newly launched EIS instrument on HINODE and the twin

SECCHI instruments on the STEREO mission. NRL maintains a complete database of spacecraft observations and control over acquisition of data from new observations. These data are available to qualified investigators at DoD and civilian agencies. In addition, the division has a sounding rocket program that affords the possibility of obtaining specific data of high interest and of testing new instrument concepts. These include the general area of high-resolution solar and stellar spectroscopy, extreme ultraviolet imagery of the Sun, and high-resolution ultraviolet spectral imaging of the Sun.

The SECCHI Payload Operations Center (POC) supports ten telescopes aboard the two STEREO spacecraft orbiting the Sun. The SECCHI POC (see figure) provides observational planning and image scheduling tools, data reduction and analysis, and data archiving. Daily responsibilities include monitoring SECCHI experiment health and status, and uplink of commands, data, and observing schedules. When either STEREO spacecraft is in communication with the Deep Space Network, the SECCHI POC provides real-time commanding and obtains telemetry, including the latest solar images from all telescopes. The SECCHI POC was started before STEREO launch and supported the development, testing, and integration of the SECCHI instruments with the STEREO spacecraft.

Division scientists have developed and maintain physical models in support of their research, including Mass Spectrometer and Incoherent Scatter Radar (MSIS), the standard model for the density of the upper atmosphere; Ground-to-Space (G2S), a hybrid empirical/analysis model of the atmosphere, used for modeling infrasound propagation; Navy Operational Global Atmospheric Prediction System—Advanced Level Physics High Altitude (NOGAPS-ALPHA), a model to

extend weather modeling into the upper atmosphere; Cosmic Ray Effects on Micro Electronics (CRÈME 96), the standard model of the effect of energetic solar particles and cosmic rays on satellite electronics, solar panels, and instruments; and Global Assimilation of Ionospheric Measurement (GAIM), a physics-based model of the ionosphere that is gaining acceptance as the standard ionospheric model.

An FY07 grant to the Space Science Division funded purchase of new laboratory equipment used to perform the precise optical alignments required by space flight instrumentation developed within the Solar Physics Branch for a wide range of sponsors (NASA, NOAA, and DoD). The new equipment replaces aging equipment purchased three decades ago that required frequent costly repairs and calibrations.

Space Technology

In its role as a center of excellence for space systems research, the Naval Center for Space Technology (NCST) designs, builds, analyzes, tests, and operates spacecraft and identifies and conducts promising research to improve spacecraft and their support systems. NCST facilities that support this work include large and small anechoic radio frequency chambers, clean rooms, shock and vibration facilities, an acoustic reverberation chamber, large and small thermal/vacuum test chambers, a heat pipe integration and test facility, a spacecraft robotics engineering and control system interaction laboratory, satellite command and control ground stations, a fuels test facility, and modal analysis test facilities. Also, the Center maintains and operates a number of electrical and electronic development laboratories and fabrication facilities for space and airborne payloads, radio frequency equipment, spacecraft power systems, telemetry, and command and control systems, and includes an electromagnetic interference–electromagnetic compatibility test chamber. NCST has a facility for long-term testing of satellite clock time/frequency standards under thermal/vacuum conditions linked to the Naval Observatory; a 5-m optical bench laser laboratory; and an electro-optical communication research laboratory to conduct research in support of the development of space systems.

RESEARCH SUPPORT FACILITIES

Office of Technology Transfer

The NRL Technology Transfer Office (TTO) is responsible for NRL's implementation of the Federal Technology Transfer Act. It facilitates the transfer of NRL's innovative technologies for public benefit by negotiating patent licensing agreements and

Cooperative Research and Development Agreements (CRADAs). A license grants a company the right to make, use, and sell NRL technologies commercially in exchange for equitable licensing fees and royalties. Revenue is distributed among the inventors and NRL's general fund. Once a license is executed, TTO monitors the licensed company for its diligence in developing and commercializing the licensed invention.

TTO also negotiates Government Purpose Licenses to transition NRL technologies for manufacture and sale solely for Navy and other Government purposes.

CRADAs provide a vehicle for NRL scientists and engineers to collaborate with their counterparts in industry, academia, and state and local governments to develop NRL technologies for commercial applications. Under a CRADA, a company supports collaborative work between it and NRL and is granted an exclusive option to license technologies developed under that CRADA's funding.

TTO's responsibilities include the NRL Exhibits Program which liaisons between NRL scientists and the Technical Information Services Branch to produce full-sized and portable displays, posters, and videos for technical conferences and symposia, Capitol Hill and Department of Defense briefings, presentations to sponsors, Laboratory special events, recruitment events, and other public events. They provide writing, layout and design support, and photo/video archival searches. They also design and develop static displays for NRL buildings, such as wall arrangements, division research highlights, and award panels and cases such as those in Buildings 72, 43, 226, 28, 222, and Quarters A.

The Exhibits Program staffs the NRL booth at trade shows and scientific conferences throughout the country, providing a platform for NRL to enhance its visibility in the scientific community and in the commercial world. Together with other members of the TTO staff, the Exhibit Specialist writes summaries of NRL's emerging technologies and produces fact sheets for public dissemination.

Technical Information Services

The Technical Information Services (TIS) Branch combines publication, graphics, photographic, multimedia, and video services into an integrated organization. Publication services include writing, editing, composition, publications consultation and production, and printing management. Quick turnaround digital black-and-white and color copying/printing services are provided. TIS uses digital publishing technology to produce scientific and technical reports that can be used for either print or Web. Graphics support includes technical and scientific illustrations, computer graphics, design services, photographic composites, display posters, and framing. The HP Designjet 5500ps

wide format printer offers exceptional color print quality up to 600 dpi and produces indoor posters and signs with 56 inches being the limitation on one side. Lamination and mounting are available. Photographic services include digital still camera coverage for data documentation, both at NRL and in the field. Photographic images are captured with state-of-the-art digital cameras and can be output to a variety of media. Photofinishing services provide custom printing and quick service color prints from digital files. Video services include producing video reports and presentations of scientific and technical programs. TIS digital video editing equipment allows in-studio and on-location editing. The video production, "A Tour of NRL," won four international awards: the Crystal, the Gold Aurora, and two Bronze Tellys.

Administrative Services

The Administrative Services Branch is responsible for collecting and preserving the documents that comprise NRL's corporate memory. Archival documents include personal papers and correspondence, laboratory notebooks, and work project files—documents that are appraised for their historical or informational value and considered to be permanently valuable. The Branch provides records management services, training, and support for the maintenance of active records, including electronic records, as an important information resource. The Branch is responsible for processing NRL's incoming and outgoing correspondence and provides training and support on correct correspondence formats and practices. The Branch is responsible for NRL's Forms and Reports Management Programs (including designing electronic forms and maintaining a Web site for Lab-wide use of electronic forms), compiles and publishes the NRL Code Directory and Organizational Index, and is responsible for providing NRL postal mail services for first class and accountable mail and for mail pickup and delivery throughout NRL. The Branch also provides NRL Locator Service.



Working with a customer at the Information and Correspondence Management Section counter.



Librarians working in the NRL Research Library.

Ruth H. Hooker Research Library

The NRL Ruth H. Hooker Research Library exists to enhance and support NRL and ONR scientists in accomplishing their research objectives through the comprehensive availability of all relevant scholarly information sources; a strategic effort to capture the NRL research portfolio; and the deployment, customization, and creation of cutting edge information resources and services as part of the NRL Digital Library.

Traditional library services include an extensive technical report, book, and journal collection dating back to the 1800s housed within a physical facility configured for study and research, staffed with subject specialists and information professionals. The collections include 46,000 books, 80,000 bound historical journal volumes, 3,000 current journal subscriptions, and nearly 2 million technical reports in paper, microfiche, or digital format (classified and unclassified). Services include advanced information consulting; professional literature searches against all major scholarly online databases including classified databases, to produce on-demand subject bibliographies; circulation of materials from the collection including classified literature up to the SECRET level; retrieval of nearly any article, report, proceeding, or document from almost any source around the world; and training/orientation to help researchers improve productivity through effective use of the library's resources and services.

To enhance traditional services, the NRL Research Library has developed and is continuing to expand the NRL Digital Library. The Digital Library currently provides desktop access to thousands of journals, books, and reference sources at NRL-DC; NRL-Stennis, MS; NRL-Monterey, CA; and the Office of Naval Research.

To provide immediate access to scholarly information, all relevant current journals and conference proceedings in the NRL Research Library's collection are now fully searchable at the researcher's desktop (nearly 3,000 titles) and over 60% of the print journal volumes are also available online. The breadth and

depth of content available through TORPEDO Ultra, NRL's locally-loaded digital archive (<http://torpedo.nrl.navy.mil>), continues to grow and is realizing its potential as a single point of access for scholarly information by providing full text search against journals, books, conference proceedings and technical reports from 20 publishers (8+ million items, 66+ million pages in 2007).

The NRL Research Library has also created the innovative NRL Online Bibliography service, which is ensuring that the entire research portfolio of written knowledge from all NRL scientists and engineers since the 1920s will be captured, retained, measured, and shared with current and future generations. It is serving as a model for other commands across the Navy and Federal Government.

As a "partner in research," the NRL Research Library continues to be the most advanced research library in the Department of Defense, serving as a productivity multiplier and a transformational force that has changed the way science is done at NRL—making the NRL Research Library a sought-after resource around the world.

FIELD STATIONS

NRL has acquired or made arrangements over the years to use a number of major sites and facilities for research. The largest facility is located at the Stennis Space Center (NRL-SSC) in Bay St. Louis, Mississippi. Others include a facility at the Naval Postgraduate School in Monterey, California (NRL-MRY), and the Chesapeake Bay Detachment (CBD) and Scientific Development Squadron One (VXS-1) in Maryland. Additional sites are located in Virginia, Alabama, and Florida.

Stennis Space Center (NRL-SSC)

The NRL Detachment at Stennis Space Center, Mississippi (NRL-SSC), consists of NRL's Oceanography Division and portions of the Acoustics and Marine Geosciences divisions. NRL-SSC, a tenant activity at NASA's John C. Stennis Space Center (SSC), is located in the southwest corner of Mississippi, about 50 miles northeast of New Orleans, Louisiana, and 20 miles from the Mississippi Gulf Coast. Other Navy tenants at SSC include the Naval Meteorology and Oceanography Command, the Naval Oceanographic Office, the Navy Small Craft Instruction and Training Center, the Special Boat Team-Twenty-two, and the Human Resources Service Center Southeast. Other Federal and State agencies at SSC involved in marine-related science and technology are the National Coastal Data Development Center, the National Data Buoy Center, the U.S. Geological Survey, the Environmental Protection

Agency's Gulf of Mexico Program and Environmental Chemistry Laboratory, the Center for Higher Learning, University of Southern Mississippi, and Mississippi State University.

The Naval Meteorology and Oceanography Command and the Naval Oceanographic Office are major operational users of the oceanographic, acoustic, and geosciences technology developed by NRL researchers. The Naval Oceanographic Office operates the Major Shared Resource Center (MSRC), one of the nation's High Performance Computing Centers, which provides operational support to the warfighter and access to NRL for ocean and atmospheric science and technology.

The Acoustics, Marine Geosciences, and Oceanography divisions occupy more than 175,000 ft² of research, computation, laboratory, administrative, and warehouse space. Facilities include the sediment core laboratory, transmission electron microscope, moving-map composer facility, underwater navigation control laboratory, computed tomography scanning laboratory, visualization laboratory, ocean color data receipt and processing facility, environmental microscopy facility, maintenance and calibration systems, environmental modeling and simulation high-speed network, and numerous laboratories for acoustic, geosciences, and oceanographic computation, instrumentation, analysis, and testing. Special areas are available for constructing, staging, refurbishing, and storing seagoing equipment.

Monterey (NRL-MRY)

NRL's Marine Meteorology Division (NRL-MRY) is located in Monterey, California about 1 mile from the Naval Postgraduate School (NPS) campus on the grounds of the Navy Region Southwest Support Detachment (NSD) Annex. The NRL facility is collocated with the Navy's Fleet Numerical Meteorology and Oceanography Center (FNMOC) and a NOAA National Weather Service Forecast Office (NWSFO). The five-acre NSD Annex campus comprises four primary buildings—one occupied by NOAA, one shared by NRL and FNMOC supercomputer/operating facilities, and two large buildings dedicated to NRL-MRY and FNMOC office spaces, computer laboratories, and conference facilities. The site also provides two modular office buildings and warehouse space. NRL-MRY occupies 30,000 ft² of office and meeting space, a small library, the Supercomputing Resource Center, the Bergen Data Center, the Satellite/Radar Processing Facility, and spaces to support the Coupled Ocean/Atmosphere Mesoscale Prediction System—On Scene (COAMPS-OS®) and the Master Environmental Library.

NRL-MRY is dedicated to advancing fundamental scientific understanding of the atmosphere, including

the air-sea interface, and to applying those scientific discoveries to develop innovative objective weather prediction systems. FNMOC and the Navy's operating forces are the primary customers for the numerical weather prediction and satellite product systems developed by NRL-MRY. FNMOC is the Navy's central facility for the production and distribution of numerical weather prediction and satellite products in support of Navy operations around the globe, as well as to other defense-related activities. The collocation of the scientific developer and the operational customer results in a "Team Monterey" effort offering unique advantages to successfully implement new systems and system upgrades, and to rapidly integrate new research results into operating systems. NRL-MRY has direct access to FNMOC's large classified supercomputers, allowing advanced development to take place using the real-time on-site global atmospheric and oceanographic databases. Collocation benefits FNMOC and NRL-MRY scientists as they transition and implement mature systems. NRL-MRY scientists remain readily available to offer assistance should problems arise during system operation.

NRL-MRY benefits from its proximity to the Naval Postgraduate School, conducting collaborative research with the NPS Meteorology and Oceanography departments. NPS in turn leverages the expertise of NRL scientists as guest lecturers and thesis committee members. NRL-MRY also maintains collaborative relationships with a number of the 25 local organizations that make up the Monterey Bay Crescent Ocean Research Consortium, which coordinates and promotes research, education, and outreach activities using the Monterey Bay as a natural laboratory.

Chesapeake Bay Detachment (CBD)

NRL's Chesapeake Bay Detachment (CBD) occupies a 168-acre site at Randle Cliffs, Maryland, and provides facilities and support services for research in radar, electronic warfare, optical devices, materials, communications, and fire research. A ship-motion simulator (SMS) is used to test and evaluate radar, satellite communications, and line-of-sight RF communications systems under dynamic conditions (various sea states). The SMS can handle up to 12,000 lb of electronic systems. A roll motion of up to 30° (15° to port and 15° to starboard) can be applied to this axis. The pitch axis has a fixed motion of 10° (5° to stern and 5° to bow). Periods along both axes, pitch and roll, are variable—from a slow 32-s to a brisk 4-s rate. Variable azimuth motion can also be added to the pitch and roll action. Synchronized positioning information ($\times 1$ and $\times 36$) is available for each of the three axes of the SMS.

Because of its location high above the western shore of the Chesapeake Bay, unique experiments

can be performed in conjunction with the Tilghman Island site, 16 km across the bay from CBD. Some of these experiments include low-clutter and generally low-background radar measurements. By using CBD's support vessels, experiments are performed that involve dispensing chaff over water and characterizing aircraft and ship radar targets. Basic research is also conducted in radar antenna properties, testing of radar remote sensing concepts, use of radar to sense ocean waves, and laser propagation. CBD also hosts facilities of the Navy Technology Center for Safety and Survivability, which conducts fire research on simulated carrier, surface, and submarine platforms.

Scientific Development Squadron One (VXS-1)

Scientific Development Squadron One (VXS-1), located at Naval Air Station Patuxent River, Maryland, is manned by approximately 14 officers, 80 enlisted, and 8 civilians. VXS-1 is currently responsible for the maintenance, operations, and security of three uniquely configured NP-3D Orion aircraft and two RC-12 Beech King Air research aircraft. The squadron conducts numerous worldwide detachments in support of a wide range of scientific research projects.

In FY07, VXS-1 provided flight support for diverse research programs: Combat Surface Ship Qualifications Trials (CSSQT), combined testing of NATO surface ship EW countermeasure capability; Airborne Polarimetric Microwave Imaging Radiometer (APMIR), primary airborne collection of intercomparison data for orbiting passive microwave sensors; APY-6, testing ship identification systems using synthetic aperture radar; aerial support for Missile Defense Agency testing including Theatre High Altitude Area Defense and Aegis Missile Defense; COBALT, proof of concept for ASW detection methods; participation in Empire Challenge 07, an intelligence, surveillance, and reconnaissance (ISR) integration demonstration led by the National Geospatial-Intelligence Agency (NGA) with operational support from U.S. Joint Forces Command; Cooperative Engagement Capability (CEC) airborne hardware testing; and WESTPAC Airborne Geophysical Sensor Suite (WAGSS) oceanographic data collection and maritime survey. VXS-1's flight safety record spans 45 years and includes more than 65,000 mishap-free flight hours.

Midway Research Center

The Midway Research Center (MRC) is located on a 162-acre site in Stafford County, Virginia. Located adjacent to the Quantico Marine Corps' Combat Development Command, the MRC has 16,000 ft² of operations and administration area. Instruments include three precision 18.5-m-diameter parabolic

antennas housed in 100-ft radomes, a fast-tracking 1-m telescope currently used for satellite laser ranging, and a transportable 16-inch telescope capable of passive optical tracking and laser communications. The MRC, under the auspices of the Space Systems Development Department, provides NRL with state-of-the-art facilities dedicated solely to space-related applications in naval communications, navigation, and basic research.

Research Platforms

Mobile research platforms contribute greatly to NRL's research. These include six P-3 Orion turbo-prop aircraft and one ship, the ex-USS *Shadwell* (LSD 15), berthed in Mobile Bay, Alabama. The ex-USS *Shadwell* is used for research on aboard-ship fire-suppression techniques.

Marine Corrosion Test Facility

The Chemistry Division's Marine Corrosion Test Facility, described above in the Chemistry section, is located in Key West, Florida.

THE CORPORATE FACILITIES INVESTMENT PLAN (CFIP)

To conduct preeminent research for tomorrow's Navy, NRL must maintain and upgrade its scientific and technological equipment and provide modern research facilities. The physical plant to house this equipment must also be state of the art. NRL has embarked on a Corporate Facilities Investment Plan (CFIP) to accomplish these goals.

The CFIP is a capital investment plan that uses both Congressionally approved military construction (MILCON) funds and Laboratory overhead funds to provide modern, up-to-date laboratory facilities for NRL. Planning for future MILCON projects includes an **Autonomous Systems Research Lab** in the FY09 time frame, a **Space Systems Technology Lab** (FY10), an **Electronics Research Lab** (FY11), and the **Marine Meteorology Center** (FY11).

To complement these efforts, overhead funds are being used to renovate and upgrade laboratory and support areas in several existing buildings.



Radio Propagation and the “Skip-Distance” Effect (1925-1926)

In NRL’s earliest days, researchers A.H. Taylor and E.O. Hulburt investigated the reappearance of radio signals at considerable distances from their transmission source, a phenomenon of great importance in Naval communications. In noting the dependence of this effect on frequency, time of day, and season, they discovered the principles behind the “skip-distance effect” in agreement with experimental data up to 16,000 km. They modified Sir Joseph Larmor’s theory on the reflection of 100 kHz to 20 MHz radio signals by the ionosphere to explain HF propagation through the ionosphere and thus established the basis for modern HF wave propagation theory. Their principles led directly to NRL’s later invention of over-the-horizon radar. Using Taylor and Hulburt’s work, NRL researchers became the first to determine the frequency above which radio waves could escape the ionosphere and reach into space, thus enabling space communication.

71

Polymorphism in Energetic Materials

J.R. Deschamps, D.A. Parrish, and R.J. Butcher

79

First-Principles Simulations of Violent Space-Weather Events

C.R. DeVore and S.K. Antiochos

89

High-Power Fiber Lasers for Directed-Energy Applications

P. Sprangle, A. Ting, J. Peñano, R. Fischer, and B. Hafizi

101

Plant Proanthocyanidins Bind To and Neutralize Bacterial Lipopolysaccharides

J.B. Delehanty, B.J. Johnson, T.E. Hickey, T. Pons, and F.S. Ligler

109

Exploring Solar Flares with Gamma Rays and Neutrons

R. Murphy



Polymorphism in Energetic Materials

J.R. Deschamps,¹ D.A. Parrish,¹ and R.J. Butcher²

¹Laboratory for Structure of Matter

²Department of Chemistry, Howard University

Polymorphism often occurs in energetic materials. Differences in the forms range from conformational changes in the molecule from one system to another, to conformational equivalents packing in different manners. These differences, whether drastic or subtle, can lead to substantial alterations in stability and performance. The authors recently reported on the crystal structures of five polymorphs of picryl bromide (a common energetic precursor): the previously identified α and β forms, and three new forms, the γ , δ , and ϵ forms. A new type of interaction has been identified between the nitro groups and π -electrons of neighboring phenyl rings. Accurate estimation of the properties of new energetic materials can substantially reduce the development cost of new materials by focusing expensive scale-up and testing on only the most promising candidates. The characterization of this new force involved in crystal packing should greatly improve calculations of packing energy and thus improve predictions of explosive yield.

INTRODUCTION

Polymorphism is defined as the ability to exist in two or more chemically identical, but crystallographically distinct forms. Since the properties of a solid substance are determined by its composition and structure, polymorphs, although chemically identical, can have different properties.¹ This is important in many fields including pharmaceuticals, agrochemicals, pigments, dyestuffs, foods, and explosives. The differences that distinguish polymorphs can lead to substantial alterations in stability and performance. Regardless of the field of application, it is essential to be able to produce materials with consistent properties.

Perhaps the most studied examples of polymorphism occur in the development of pharmaceuticals, as dissolution and absorption rates depend on the exact crystal form of a polymorph. Drugs often receive regulatory approval for only a single crystalline polymorph. Because a single polymorph is described in the patent, competitors may be able to patent and market other polymorphs. In some cases the new preparations are not true polymorphs, as they exist as different hydrates with varying water content or different salts of the parent drug.

It is important to note that not all polymorphs are stable. Although the common drug aspirin (acetylsalicylic acid) was first prepared by Charles Frederic Gerhardt in 1853, a second polymorph of this drug was not discovered until 2005. Studies have shown that this new form is stable only at 100 K and reverts back to the original form at ambient temperature. This may seem like a trivial matter, but there have been cases of

individual laboratories producing one crystal form and later producing a different crystal form. As noted previously, FDA approval may exist for only a single polymorph, thus the new unanticipated polymorph can be disastrous for a drug company.

ENERGETIC MATERIALS

In the production of energetic materials, stability and density are critical properties, and these can vary widely among the polymorphs. Three of the classic cases of polymorphism at ambient conditions in the energetic field are TNT, HMX, and CL20 (Fig. 1). TNT [2,4,6-trinitrotoluene] is known to have two forms with densities of approximately 1.65 Mg/cm³. HMX [1,3,5,7-tetranitro-1,3,5,7-tetraazacyclooctane] is known to have four forms with densities ranging from 1.76 to 1.903 Mg/cm³; this is a large variation in density, and understanding how to produce the higher density polymorphs allows production of higher energy explosives. CL20 [2,4,6,8,10,12-Hexanitro-2,4,6,8,10,12-hexa-azatetracyclo(5.5.0.0^{5,9}.0^{3,11})dodecane] is known to have five forms with densities ranging from 1.915 to 2.044 Mg/cm³. Differences in the various polymorphs range from conformational changes in the molecule from one system to another, to conformational equivalents packing in different manners.

Picryl bromide (2,4,6-trinitrobromobenzene) also exhibits polymorphism. Picryl bromide is a useful chemical precursor to other energetic materials. The original determinations of picryl bromide date back to the very early days of crystallography and energetic materials research. Two picryl bromide polymorphs

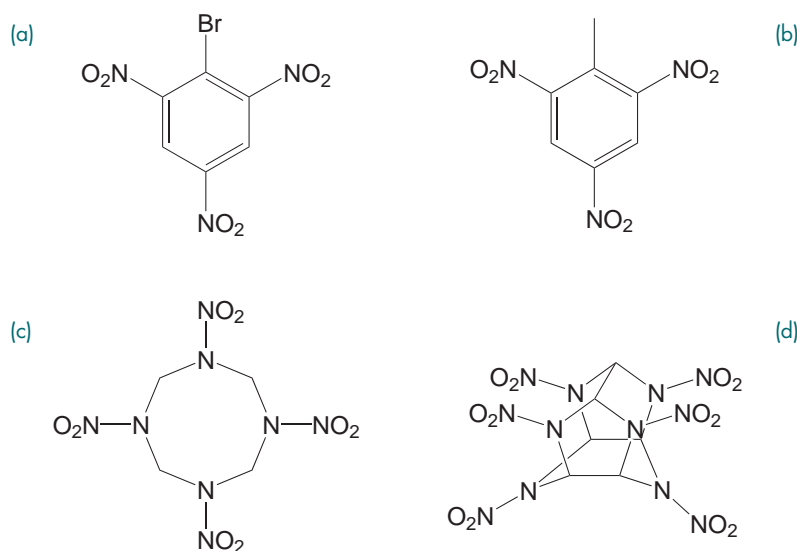


FIGURE 1
Chemical structures of picryl bromide (a), TNT (b), HMX (c), and CL20 (d).

were reported in 1933; however, no X-ray crystal structures were reported at that time. The first structural information was published in 1975 by Herbstein and Kaftory,² who reported on a series of seven co-crystals of picryl bromide with large aromatic ring compounds. Here we discuss the crystal structures of five polymorphs of picryl bromide: the previously identified α and β forms from 1933, and the newly identified γ , δ , and ϵ forms.³

PICRYL BROMIDE ANALYSIS

A vial of picryl bromide was provided to the Naval Research Laboratory by the Naval Surface Warfare Center. The sample was the result of a single synthetic batch. Upon visual examination, the crystals appeared to be consistent in nature. In preparation for data collection, a single crystal was selected for analysis and mounted on a glass fiber, and X-ray diffraction data was collected. First attempts at a structure solution were unsuccessful; the asymmetric unit seemed too large for a molecule as simple as picryl bromide and it was thought that the crystal was twinned. In an attempt to find a non-twinned crystal with the true unit cell, many other crystals were examined. In every case, the experimentally determined unit cells were larger than expected. Once it was accepted that the crystals were not twinned, the various polymorphs were carefully determined and refined. Compounds **1** α and **1** δ were collected on a Bruker three-circle platform diffractometer equipped with a SMART 1000 CCD detector using MoK α radiation ($\lambda = 0.71073$ Å), while compounds **1** β , **1** γ , and **1** ϵ were collected on a Bruker three-circle platform diffractometer equipped with a SMART 6000

CCD detector using CuK α radiation ($\lambda = 1.54178$ Å). In all cases, data collection was performed and the unit cell was initially refined using the SMART [v5.625] program. Data reduction was performed using SAINT [v6.36A] and XPREP [v6.12] programs. Corrections were applied for Lorentz and polarization effects. The structure was solved and refined with the aid of the programs in the SHELXTL-Plus [v6.10] system of programs. The full-matrix least-squares refinement on F^2 included atomic coordinates and anisotropic thermal parameters for all non-H atoms. The H atoms were included using a riding model.

THE FIVE POLYMORPHS OF PICRYL BROMIDE

The vial of picryl bromide yielded five polymorphs ($\alpha - \epsilon$ in Table 1), the two reported in 1933 plus three new forms. The consistent appearance of the crystal morphologies observed on visual inspection was not indicative of the rich variety of polymorphs eventually discovered in this single sample. This is somewhat unusual, as crystalline polymorphs generally display different crystal morphologies which are obvious upon inspection. A good example of this is the right- and left-hand forms of quartz, in which chains of silicon dioxide can have either a right- or left-hand twist and yield crystal forms that can be distinguished by visual inspection of the crystal faces.

In describing crystal structures, researchers use the symbols Z and Z' to denote the number of molecules in the unit cell and the number of molecules in the asymmetric unit, respectively. Note that for the polymorphs of picryl bromide described in Table 1, Z values range from 12 to 36 while Z' values range from 3 to 18. The

TABLE 1 — Crystallographic Parameters for the Five Polymorphs of Picryl Bromide

Form	α	β	γ	δ	ϵ
Temp. (K)	93(2)	294(2)	294(2)	93(2)	293(2)
γ (Å)	0.71073	1.54178	1.54178	0.71073	1.54178
System	Triclinic	Hexagonal	Triclinic	Trigonal	Triclinic
Space Group	P -1	P 6 ₅	P -1	P 3 ₁	P 1
a (Å)	14.8480(17)	14.8812(1)	14.9166(2)	14.8610(7)	14.9086(1)
b (Å)	14.8614(17)	14.8812(1)	14.9424(2)	14.8610(7)	14.9083(1)
c (Å)	15.3318(17)	22.5449(4)	30.3888(3)	44.007(3)	22.6784(2)
α (°)	72.762(2)	90	94.729(1)	90	95.245(1)
β (°)	80.350(2)	90	93.754(1)	90	90.116(1)
γ (°)	60.225(2)	120	119.925(1)	120	119.896(1)
V (Å ³)	2803.8(6)	4323.69(9)	5805.61(12)	8416.9(8)	4344.89(6)
Z	12	18	24	36	18
Z'	6	3	12	12	18
ρ calc. (Mg/m ³)	2.075	2.019	2.005	2.074	2.009

value of Z is related to Z' and the number of symmetry operations that relate molecules within the unit cell to each other, and is a function of the space group of the crystal. Z' is a function of how molecules pack within the asymmetric unit. Z' values of less than one are quite common. In the most recent release of the Cambridge Structural Database (CSD),⁴ out of 423,756 entries there are 110,194 entries with Z' less than 1; of these, 89,939 have a Z' of 0.5. Only 37,138 entries, fewer than 10%, have a Z' greater than 1. Z' values of 3 or greater are quite uncommon. Fewer than 1% of the structures in the database have a Z' ≥ 3 and aside from the picryl bromide polymorphs, only nine other structures have Z' of 12 and one other has a Z' of 18. Thus the crystal polymorphs of picryl bromide are among a very small group of high Z' structures. A search of the CSD for systems with greater than four polymorphs (using parameters previously defined)⁵ was conducted to determine the rarity of pentamorphic systems. Only two pentamorphic structures were found, along with one heptamorphic structure.

Several attempts were made to re-grow crystals of the various systems reported here, while searching for a simpler system (Z' = 1) as well as more potential polymorphs. Since the crystallization conditions post-synthesis were not recorded, reproducing the conditions resulting in the analyzed sample was not possible. All recrystallization attempts, using slow evaporation techniques while employing a large number of solvents and combinations of solvents, resulted exclusively in the α form.

Despite the variation in Z' and the fact that four space groups and three crystal systems are repre-

sented, there are remarkable consistencies among the five structures. All five polymorphs share a common packing arrangement within layers. There are two types of interactions that stabilize molecules within layers, C-H...O hydrogen bonds, and N-O...Br dipole-induced interactions. These interactions result in the molecules organizing themselves into two different “triad” motifs differing in their intermolecular interactions (Fig. 2). One triad (represented by the red triangle in Fig. 2) is held together by hydrogen bonds involving a C-H moiety from one molecule with a *para* nitro group of an adjacent molecule. C-H...O distances among the various polymorphs range from 3.231(5) to 3.392(5) Å, which is well within the range of expected distances for this type of hydrogen bond.

The second triad (represented by the blue triangle in Fig. 2) is formed through dipole-induced interactions between the Br of one molecule and an *ortho* nitro group from an adjoining molecule. The maximum Br...O distance observed in the five studies, 3.219(6) Å, is well within the combined van der Waals

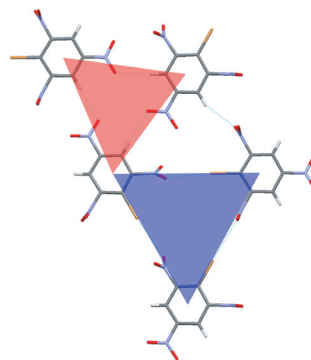


FIGURE 2
Representation of the two triad motifs in picryl bromide. The red triangle represents the hydrogen-bonded triad, the blue triangle represents the induced dipole triad.

radii (3.37 Å), indicating that these are significant stabilizing interactions. Such interactions are known to rival hydrogen bonds in strength.

Within each sheet the triads are arranged such that each dipole-induced triad is surrounded by six hydrogen-bonded triads (Fig. 3). These sheets are found in all five polymorphs. The inter-sheet spacings are also similar and are typically about 4.0 Å. The similar intra-sheet packing (Fig. 3) and spacing between the sheets is reflected in the uniformity in the observed densities of the polymorphs which range from 2.005 to 2.075 Mg/m³.

DISTINGUISHING THE POLYMORPHS

The consistent packing within sheets and spacing between sheets leaves only the relationship between the sheets to produce the subtle differences that result in the formation of the five polymorphs observed. The differences in how the sheets relate to each other is responsible for the differences in crystallographic symmetry that distinguish the polymorphs. Simplifying this somewhat, the five polymorphs can be distinguished by their layer structure. In Fig. 4 the crystallographically equivalent layers are displayed in the same color. Note that in the α form the layers are arranged ABBA where A and B are crystallographically distinct layers and the repeats are crystallographically identical. The β form is even simpler, consisting of only A layers. The γ and δ forms each have four layers; in the δ form the layers are arranged ABCD while in the γ form the layers are arranged ABCDDCBA. Note the “mirror” present in the sequence of both the α and γ forms. The ϵ form has six layers arranged ABCDEF. In addition to different

crystallographically distinct layers in each polymorph, the relationship (molecule to molecule) between layers differs from one polymorph to another. In some cases these differences are distinct and related to crystallographic symmetry, in others the differences are more subtle. In either case these differences are beyond the scope of this review.

A NEW INTERACTION

The interactions within the layers are well known and have been described previously by others. The two unique triads share indices, creating the highly consistent two-dimensional sheets observed in each polymorph. The layers depicted in Fig. 4 are held together by interactions between an *ortho* nitro group from one layer and a phenyl ring in an adjacent layer (Fig. 5). All of the *ortho* nitro groups are twisted out of the phenyl plane due to steric interactions with the Br, while the *para* nitro groups are unaffected and remain in the plane of the aromatic ring. The nitro-O...ring centroid (Cg) distances were calculated and they ranged from 2.899 to 3.215 Å. These distances are within the combined van der Waals radii (3.37 Å) of an oxygen and a carbon. Despite the fact these are O...Cg distances, it is highly likely that there are reasonably strong nitro- π associations present. A survey of the CSD yielded more than 300 structures in which a nitro oxygen is within 3.2 Å of an aromatic ring centroid. Thus there is a general tendency for molecules involving nitro groups to be stabilized in the solid state by such interactions. Despite the occurrence of this interaction in many other structures, this interaction does not appear to have been discussed in the papers reporting their struc-

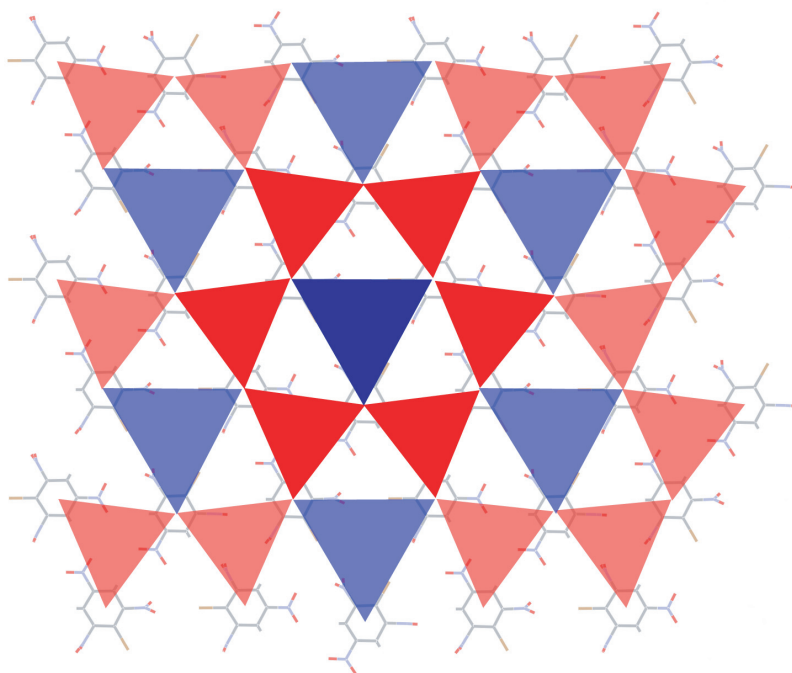
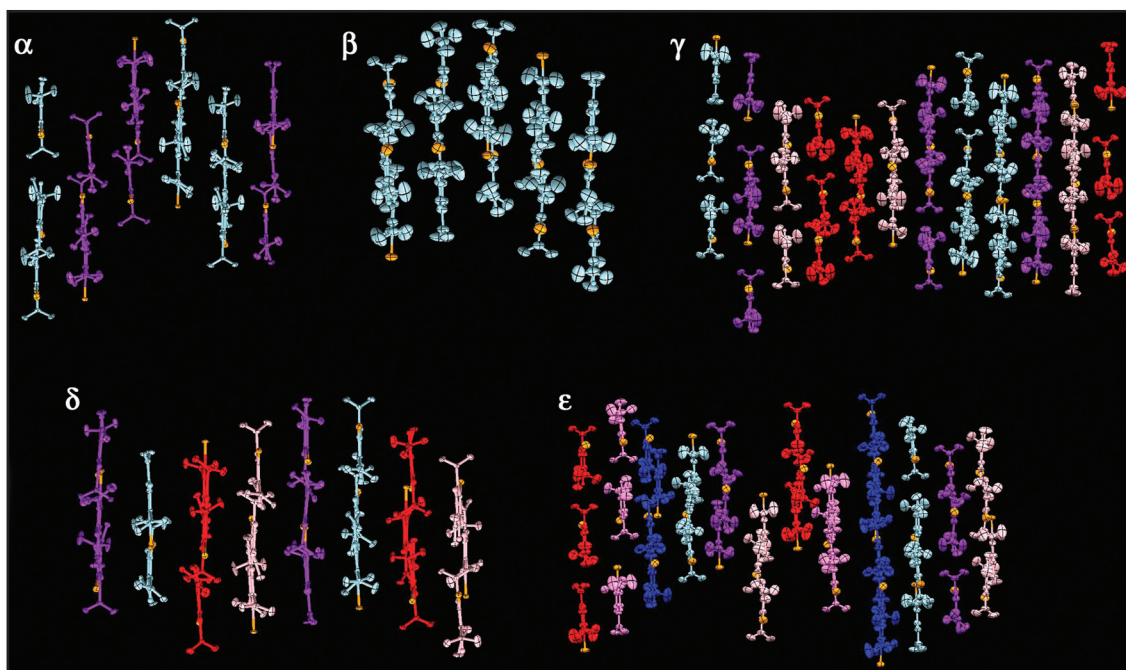
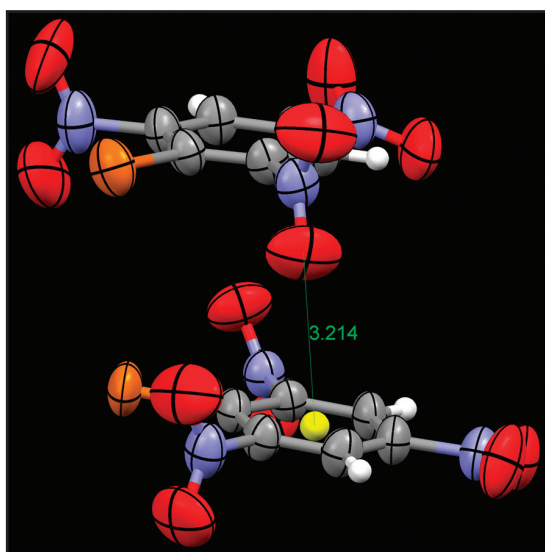


FIGURE 3
Representation of the two-dimensional sheets found in picryl bromide. Note the arrangement of hydrogen-bonded (red) triads surrounding induced dipole triads (blue).

**FIGURE 4**

Relationship between the layers in polymorphs of picryl bromide. In each image, crystallographically unique layers are depicted in a different color. Bromine atoms are shown in orange to help orient the individual molecules.

**FIGURE 5**

Geometry of the nitro- π interactions between adjacent sheets. The center of gravity (Cg) of the aromatic ring in the lower molecule is shown as a yellow sphere; the dotted line represents the O...Cg interaction. Note that the interacting nitro group in the upper molecule is twisted out of the plane of the aromatic ring to an angle of approximately 90° .

tures; however, mention has been made of the potential for π - π interactions between the aromatic ring and the π system of the nitro group. The energies of the nitro- π interactions are currently being studied and may make a significant contribution to packing energies in crystals of picryl bromide.

CONCLUSION

The X-ray structures of five polymorphs of picryl bromide were determined, with Z' values ranging from 3 to 18. Only three other compounds in the current release of the CSD have as many as five polymorphs. The large numbers of crystallographically unique molecules in these polymorphs also makes these structures noteworthy. Three distinct intermolecular interactions are responsible for stabilizing the crystal structures: C-H \cdots O hydrogen bonds, N-O \cdots Br dipole-induced interactions, and finally the N-O $\cdots\pi$ interactions. Although the N-O $\cdots\pi$ interactions are present in many other crystal structures, we were the first to note their importance in stabilizing the crystal structure. In all polymorphs the molecules pack into two-dimensional sheets, consisting of two different triad motifs. The relationship between the sheets and packing of equivalent sheets distinguish the polymorphs. Despite the differing orientations, the inter-sheet N-O $\cdots\pi$ associations are remarkably consistent. This leads to the uniform densities observed and implies that the thermodynamic energy differences from one polymorph to another

are negligible. The knowledge gained in studying these polymorphs can be applied in modeling to aid in the design of new energetic materials with greater stability and increased explosive yields.

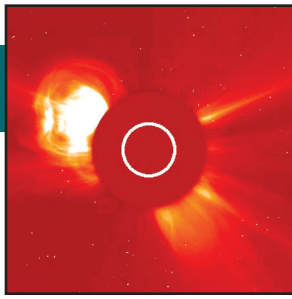
ACKNOWLEDGMENTS

The authors thank Horst Adolph of the Naval Surface Warfare Center for providing the sample of picryl bromide.

[Sponsored by ONR]

References

- ¹ J. Bernstein, *Polymorphism in Molecular Crystals*, International Union of Crystallography Monographs on Crystallography No. 14 (Oxford University Press, New York, 2002).
- ² F.H. Herbstein and M. Kaftory, "Molecular Compounds and Complexes. V. Crystallography of Equimolar Aromatic Hydrocarbon:1-X-2,4,6-trinitrobenzene Molecular Compounds. Crystal Structure of Fluoranthene: Picryl Bromide, Polymorph I," *Acta Cryst.* **B31**, 60-67 (1975); F.H. Herbstein and M. Kaftory, "Molecular Compounds and Complexes. VI. The Crystal Structure of 3/2 pyrene:picryl bromide," *Acta Cryst.* **B31**, 68-75 (1975).
- ³ D.A. Parrish, J.R. Deschamps, R.D. Gilardi, and R.J. Butcher, "Polymorphs of Picryl Bromide," *Cryst. Growth Design* **8**(1), 57-62 (2008).
- ⁴ F.H. Allen, "The Cambridge Structural Database: A Quarter of a Million Crystal Structures and Rising," *Acta Cryst.* **B58**, 380-388 (2002).
- ⁵ J. van de Streek, "Searching the Cambridge Structural Database for the 'Best' Representative of Each Unique Polymorph," *Acta Cryst.* **B62**, 567-579 (2006). ★



First-Principles Simulations of Violent Space-Weather Events

C.R. DeVore¹ and S.K. Antiochos²

¹Laboratory for Computational Physics and Fluid Dynamics

²Space Weather Laboratory, NASA Goddard Space Flight Center

We have developed a first-principles model for simulating the initiation and propagation of magnetic eruptions originating in the Sun's atmosphere. The ejecta from these violent events adversely affect military and civilian facilities and operations on Earth. Energetic particles and radiation also pose prompt, direct hazards to technological systems and humans in space. Recently we have demonstrated that slow, coherent motions across the solar surface can energize susceptible magnetic field configurations and power subsequent catastrophic eruptions. The velocities and energies of our simulated events compare favorably with those observed, as do their morphological magnetic-field and plasma signatures. Our results also exhibit homology (repeated similar events originating from a single source), prompt reformation of the source region in the low solar atmosphere, and a magnetic-bottle configuration of the ejected field in the interplanetary medium. A fundamental understanding of these phenomena is a prerequisite for future physics-based forecasting of space weather.

INTRODUCTION

The U.S. Navy relies heavily, as does our society at large, on technological systems whose operations are susceptible to disturbances in the physical environment at Earth's surface, in the atmosphere, and in space. Certainly the most familiar of these, to both sailors and the general public, are unfavorable conditions in terrestrial weather: high or low temperatures, strong winds, heavy rain or snow, and high seas, for example. Less obvious but also important are the unavoidable and in some cases unpredictable changes in Earth's electromagnetic field and in the properties of the electrically charged gases (plasmas) that comprise its ionosphere and magnetosphere. These changes are driven, for the most part, by fluctuations in the flow of magnetic field and plasma from the Sun—the solar wind. The effects of these changes can include direct damage by energetic particles to orbiting satellites, astronauts, and pilots and crew in high-altitude aircraft; disruptions of ground-to-space-to-ground and ground-to-ground wireless communications; power blackouts due to voltage spikes in terrestrial power grids; and the occasionally spectacular, and always far more benign, auroral displays. The study of these changes, their origin at the Sun, and their consequences at Earth—both natural and technological—constitutes the emerging science of space weather.

The source of the most unpredictable and detrimental space weather is also the most violent: giant explosions of magnetic field and plasma from just above the visible surface of the Sun, which then propa-

gate out into interplanetary space at high speed and strike the Earth if it happens to lie in the path of the storm. One way to characterize the typical magnitude of these events is “a billion tons of matter moving at a million miles per hour,” or 1×10^{15} g at 500 km s^{-1} . The corresponding energy content is over 1×10^{30} ergs, equivalent to the yield of about a million 30-megaton nuclear weapons. Fortunately, that energy is spread over an enormous area by the time it reaches the Earth, so that only about one millionth of it actually enters the magnetosphere. This small fraction is, however, still more than sufficient to wreak significant havoc.

As is the case with devastating terrestrial-weather phenomena such as hurricanes, tornadoes, and blizzards, it would be highly advantageous to the military and to civilian society to be able to forecast the occurrence of these most damaging space-weather events. Satellites could be put into safe mode to protect their electronics; astronauts, pilots, and crew could be sheltered from adverse particle and radiation fluxes; alternative means of communications could be employed or operations could be accelerated or delayed; operators of power plants could adopt a defensive posture against electrical surges. At this time, however, we are limited to empirically based warnings of event onset at the Sun, and to several hours to perhaps two days notice of the arrival of the streaming ejecta at Earth. Both types of forecasts suffer from substantial uncertainties due to a relative paucity of data and an incomplete understanding of the physics of space weather. We are at a disadvantage relative to terrestrial-weather forecasters due to the impracticality of placing weather stations

within the Sun's forbiddingly harsh atmosphere. This forces us to infer many important clues using remotely sensed solar data from ground- and space-based telescopes and interplanetary data from satellites sampling ejecta that are already well on their way to the Earth. Nevertheless, as we describe below, progress toward the necessary physical understanding is being made, laying the foundation for future physics-based forecasting. Our first-principles computational model can simulate the approach to, onset, and aftermath of the violent magnetic explosions at the heart of the most extreme space weather.

A VIOLENT SPACE-WEATHER EVENT

A well-observed example of such a solar storm is shown in Figures 1 and 2. It occurred on 30 July 2005, during the most magnetically active epoch of the current sunspot cycle. Figure 1 shows the source region of the storm as seen in ultraviolet light by the Transition Region And Coronal Explorer (TRACE) satellite. Light and dark regions in the image correspond to hotter and cooler plasmas, respectively, residing in the corona, the tenuous outer layer of the Sun's atmosphere. Clearly visible over much of the field of view are arching threads of plasma, some very bright and others rather dim, which are understood to delineate magnetic loops from strong sunspot and weaker background fields at the solar surface. Less obvious but also visible are very dark threads, associated with cool plasma distributed along other, very low-lying magnetic field lines. These filamentary fragments can be seen in the first two panels of Fig. 1, below the long bright thread marked by the arrow in the second panel (top middle) and in the near left of the emitting region in the first panel (top left); the latter subsequently is replaced by the short canopy of bright loops in the foreground. A time-lapse movie of these images shows that the dark filament material is ejected upward and to the right, which is the solar north direction, during this sequence beginning at about 0620 UT. A small, bright kernel of hotter plasma, marked by the arrows (white) in four successive panels, is ejected along with and accompanies the filament. The overall rapid brightening of the plasma, observed in higher energy X-rays as well as the ultraviolet, is due to heating by the magnetic field. At the end of the ejective phase (bottom right), a very bright canopy of loops overlies the whole sinuous inverse-S shaped channel previously occupied by the dark filament. The impulsive phase of this eruptive flare has concluded, and thereafter the emission from the hot flare loops fades gradually as the plasma cools in place.

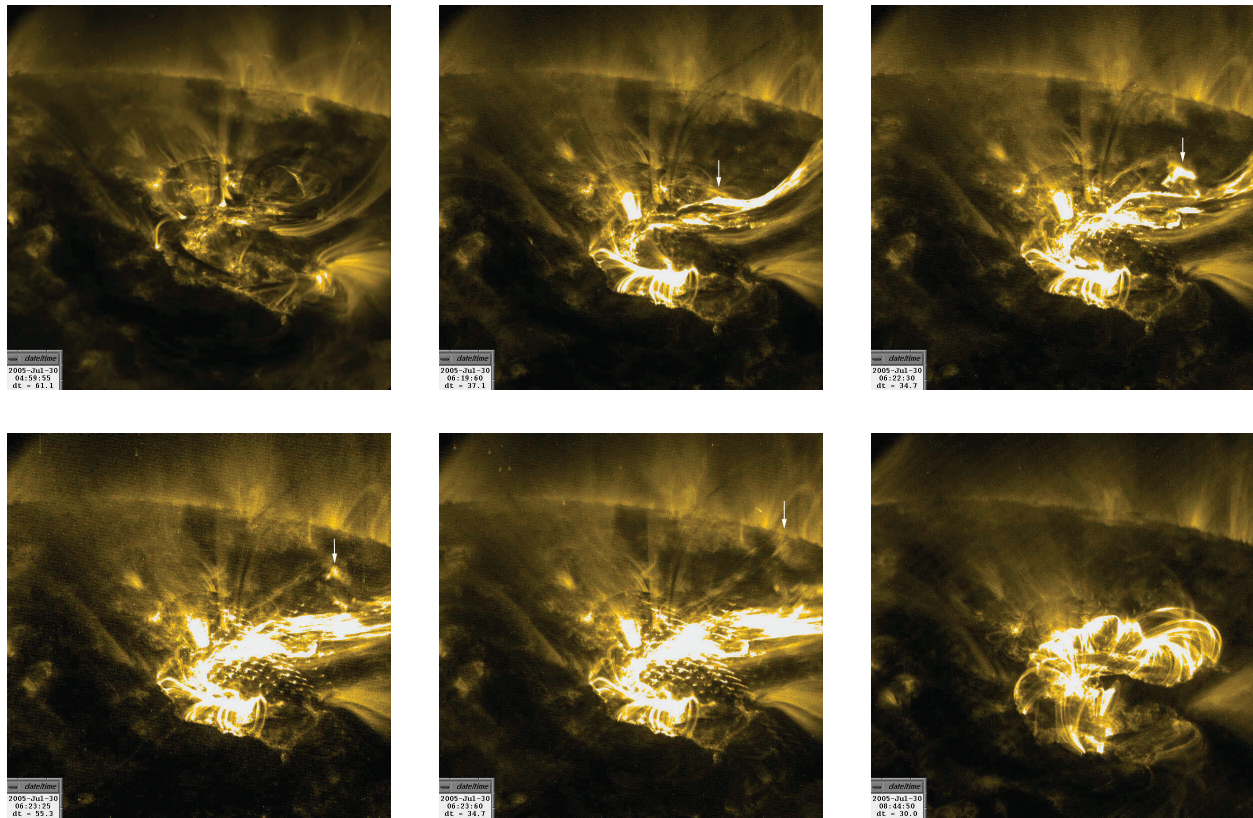
The initial development of the interplanetary consequences of this event are shown in Fig. 2, as observed

in scattered white light by the Large Angle Spectrometric CORonagraph (LASCO) instrument—whose design and development were led by NRL—on the SOLar and Heliospheric Observatory (SOHO) spacecraft. As is typical during that epoch, the background outer corona comprised several bright streamers of relatively dense plasma separated by expanses of tenuous plasma that scatters little light and so is quite dim. This sequence of panels shows two distinct explosions off of the limb of the Sun at about the 10 o'clock position. The first reaches its maximum brightness at about 0650 UT (top middle), a half hour after onset of the TRACE filament eruption, and its extent at this time suggests a speed of at least 500 km s^{-1} measured against the plane of the sky. Clearly, this coronal mass ejection (CME) expelled a large amount of plasma from the Sun into interplanetary space. About two hours later (top right), a very elongated, slightly twisted, bright thread is visible in the wake of the explosion. Thereafter, the corona relaxed (bottom left) back to essentially its configuration prior to the eruptive flare and CME (top left). A second CME, originating in the same source region, followed the first after an 11-hour delay and can be seen in the last two panels (bottom middle and right) of Fig. 2. Such multiple eruptions from a single source are certainly not unheard of, although a longer delay of up to a few days between successive occurrences is more common. Although these two CMEs departed the Sun too near the limb to have any large terrestrial impact, this is merely an accident of timing: three days later, their source region was much closer to disk center, and Earth likely would have been in the path of the storm as it has been on so many other occasions.

The eruptive flare and its associated coronal mass ejection described here are fairly typical solar events. Their signatures are common to essentially all large-scale disturbances of space weather, although the absolute and relative magnitudes of the flare and CME vary significantly across the spectrum of eruptions. The objective of our research is to understand these signatures, qualitatively and quantitatively, and to reproduce them as completely as we can in first-principles numerical simulations based on a compelling and robust physical model.

FIRST-PRINCIPLES SIMULATIONS

To advance understanding of the physics of eruptive flares and coronal mass ejections, we have developed and use two principal tools: the Adaptively Refined Magnetohydrodynamics Solver (ARMS), which performs detailed computer simulations of magnetized plasmas based on fluid-dynamical equations; and HelioSpace, which visualizes the numerical data from ARMS for interpretation and analysis. There are

**FIGURE 1**

Transition Region And Coronal Explorer (TRACE) images in 171 nm ultraviolet light of an eruptive flare that occurred on 30 July 2005. Solar north is to the right, and the limb is visible in the background. The quiescent pre-eruption state is shown at about 0500 UT (top left); the stable post-eruption state with glowing hot flare loops is shown at about 0845 (bottom right). In the intervening closely-spaced panels beginning at about 0620, a sinuous filament is ejected rapidly outward and in the northerly direction. A bright kernel of plasma in the ejecta, marked by the white arrows, cools and dims as it departs toward the upper right. The regular striations clearly visible in the last two of these panels are due to diffraction effects. A movie of the flare can be viewed at http://trace.lmsal.com/POD/movies/T171_20050730_03X.mov.

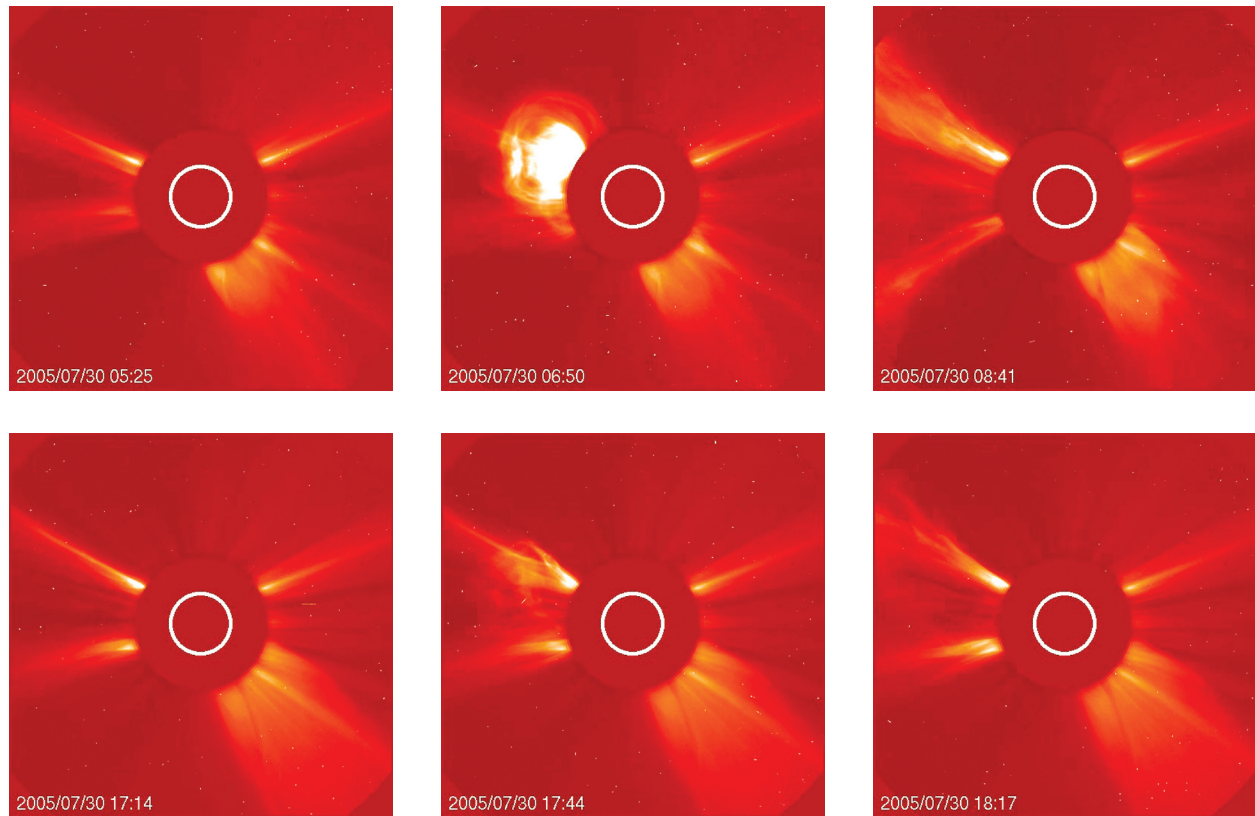


FIGURE 2

Large Angle Spectrometric CORonagraph (LASCO) images in scattered visible light of two coronal mass ejections (CMEs) that occurred on 30 July 2005. Solar north is at the top. The bright ring (white) at each image center represents the solar limb, while the larger dark circle is the occulting disk of the LASCO telescope. The quiescent pre-eruption states are shown at 0525 UT (top left) and 1714 UT (bottom left); the remaining two panels in each row show the ejected material moving outward from about the 10 o'clock position on the disk. This is the location of the TRACE filament eruption (Fig. 1), which closely precedes, and clearly is responsible for, the first CME shown here (top row). The second CME eleven hours later originated in the same source region, but TRACE unfortunately did not capture the associated flare. A movie of the CMEs is available at http://lasco-www.nrl.navy.mil/daily_mpg/2005_07/050730_c2.mpg.

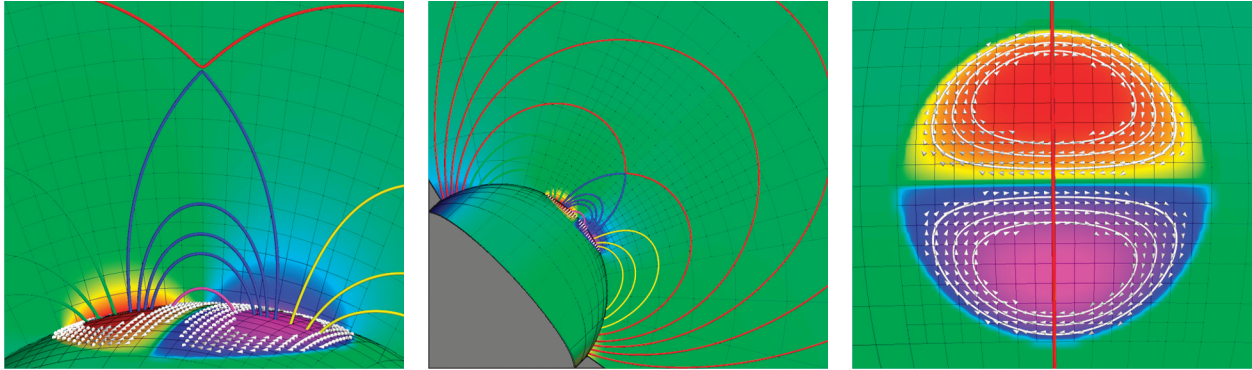
certain analogies between ARMS and sophisticated numerical models for global terrestrial weather: both solve for the large-scale, long-time behavior of their constituents using fluid equations that represent all three spatial dimensions and time, subject to the inertia of the medium and to pressure and gravitational forces. ARMS does not include the topographical and thermodynamic complexities that are so critically important to Earth's weather, but it does have to treat the critically important solar magnetic field and its associated forces on the plasma, which add their own numerical challenges. The resulting magnetohydrodynamics equations are solved using an extension of NRL's venerable Flux-Corrected Transport techniques for computational fluid dynamics. ARMS also employs adaptive mesh refinement, in which the numerical grid can be tailored to the problem being solved in order to use computational resources most efficiently, and it has been implemented on massively parallel computers, so as to harness the power of hundreds or even thousands of processors working together in synchrony to solve these complex problems. We must be able to visualize the resulting torrent of numbers effectively and in many different ways in order to interpret and understand them. HelioSpace accomplishes this with an intuitive user interface that offers several different rendering modules. It runs under all currently popular operating systems for desktop workstations and portable laptop computers.

A recent ARMS simulation of an eruptive flare and coronal mass ejection, visualized by HelioSpace, is initialized as shown in Fig. 3. The configuration is a large pair of semicircular sunspots, one on either side of the equator, embedded in the Sun's global background magnetic field, which is concentrated toward polar latitudes. The spherical solar surface, color-shaded according to the strength and sign (negative: red to yellow; positive: blue to magenta) of the radial component of the magnetic field, is seen at the bottom in the close-up view (left), from the side in the limb view (middle), and from above in the overhead view (right). A plane cutting radially through the central meridian is similarly color-shaded in the first two views. On both surfaces, we also draw lines (black) showing the boundaries of the $8 \times 8 \times 8$ blocks that make up the computational grid. These lines are most concentrated in the inner volume of the close-up view and become increasingly sparse farther away, since we have adapted the grid to resolve well only the anticipated region of principal activity. Also shown on the spherical surface are arrows and streamlines (white) of a flow that we impose there in our simulation; its purpose is discussed below. Finally, each thin cylindrical tube threading through space represents a selected individual magnetic field line. Its color is determined by the surface patches

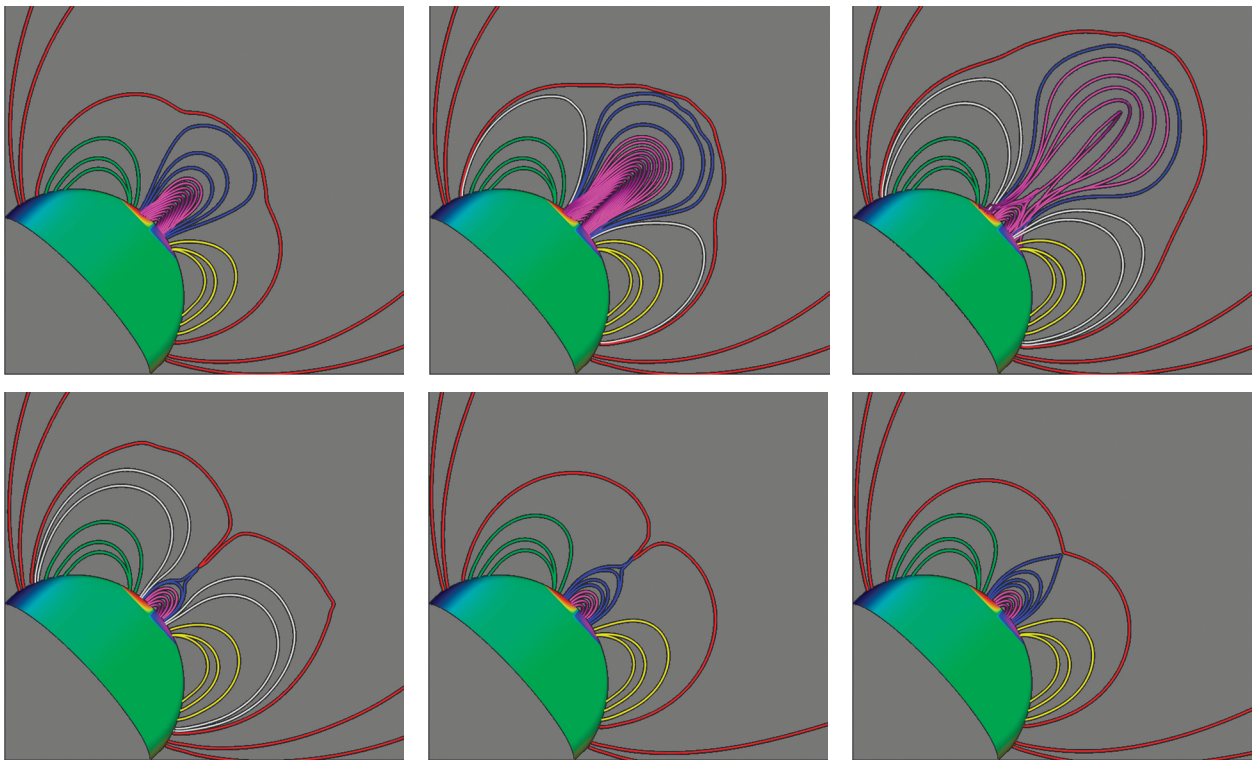
of positive and negative radial magnetic polarity at the two endpoints that are linked by that field line. We then can distinguish readily between lines that close locally across the equator and link the two sunspots (blue) from those that close remotely across the equator and link the two polar caps (red), as well as those that close within each hemisphere and link each polar cap to the nearer sunspot (north: green; south: yellow). We further distinguish the innermost equatorial field lines (magenta) whose endpoints reside within the zone of imposed surface motions from those farther out (blue) whose endpoints reside beyond that zone.

This initial field contains the minimum magnetic energy that is consistent with the prescribed distribution of sunspot and polar-cap magnetic flux at the surface. Field lines linking the two sunspots near the boundary between them—such as the one (magenta) shown in Fig. 3, and others like it at both higher and lower latitudes and at longitudes all along the extended boundary—cross over at a 90° angle and so are relatively short. In contrast, the source regions that spawn eruptive flares and coronal mass ejections invariably contain field lines that cross over their boundaries at a quite shallow angle and are very extended along those boundaries. The dark filaments pointed out in the TRACE image (Fig. 1) are comprised of such strongly sheared field lines. It is well known that sunspot rotation is an important contributing factor to the development of such lines of magnetic force, in at least some solar source regions. Thus, in our simulation model we impose clockwise rotational motions near the perimeters of the sunspots, as shown in Fig. 3. These motions gradually stretch the affected field lines (magenta) near the boundary between the sunspots, performing mechanical work that adds energy to the magnetic field. Indeed, it is this excess magnetic energy—above the minimum contained in the initial field configuration—that ultimately powers the eruption. The key issue is whether that excess energy can be converted to lift the plasma against gravity and accelerate it to high speed in the CME, and to heat the plasma on the bright loops left behind in the eruptive flare.

As the magnetic field adjacent to the boundary between the sunspots is stretched and its energy increases due to the rotational motions, the volume occupied by it expands, especially radially outward where the surrounding field is weakest. This is illustrated in the first panel (top left) of Fig. 4. The outward expansion of the increasingly sheared innermost field lines (magenta) stretches out the overlying unsheared field lines (blue) so that the downward tension force exerted by the latter remains in balance with the upward pressure force exerted by the former. In addition, the expansion compresses and reshapes the region between the field lines that link the two sunspots

**FIGURE 3**

Initial configuration for the Adaptively Refined Magnetohydrodynamics Solver (ARMS) numerical simulation, in close-up (left), limb (middle), and overhead (right) views. Grid lines (black), flow lines and directional arrows (white), and radial magnetic field strength and sign (red to blue shading) are rendered on the model solar surface and on the central-meridian plane. The cylindrical tubes are magnetic field lines colored according to whether they link the two sunspots (blue), the two polar caps (red), or a sunspot to the polar cap in its own hemisphere (north: green; south: yellow), or reside deep within the sunspot pair (magenta) and are subjected to the energizing surface flows.

**FIGURE 4**

Magnetic-breakout eruption from the ARMS numerical simulation, whose initial field configuration is shown in Fig. 3. The first three panels (top row) illustrate the accelerated eruption of the originally low-lying magnetic field lines (magenta) and plasma; the last three panels (bottom row) show the subsequent formation of the flare loops and the reestablishment of the original overlying equatorial (blue) and polar (red) field-line populations. Field lines with new connections (white) are created during the eruption and then destroyed during the flare. The time cadences are 20 minutes between the first four panels, then one hour to the fifth panel, and finally two hours to the sixth panel.

(blue) and those that link the two polar caps (red): the X-shaped intersection of the initial configuration (Fig. 3) evolves into a flattened plane interface that is very extended latitudinally in the strongly energized configuration (Fig. 4, top left). Note that the field lines in these two populations are antiparallel, since those linking the sunspots point northward, exiting the Sun from the southern sunspot and reentering the Sun in the northern sunspot; meanwhile, those linking the polar caps point southward, exiting from the north pole and reentering in the south pole. This antiparallel alignment permits pairs of these field lines to break and establish new connections with each other, exchanging endpoints in the process. These newly formed field lines (white) link each sunspot to the polar cap in its own hemisphere, as seen in the second and third panels (top middle and right).

The breaking and reconnecting of the overlying field is critically important to the eruption, because the tension force exerted by the original pairs of field lines upon the stressed field rising from below has been eliminated. The newly formed field lines do not overlie the rising energized field, and so can be pushed aside quite easily. Moreover, this process runs away catastrophically due to a positive feedback: reducing the tension force overlying the energized field allows it to rise faster and farther, which drives even faster reconnection of the residual field above it, which in turn reduces the tension force still more rapidly. As can be seen by comparing the heights of the energized field lines (magenta) across the top row of panels in Fig. 4, the result is a strongly accelerated outward expansion of the originally low-lying magnetic field and plasma. This is precisely the outcome predicted by our “magnetic breakout” model for eruptive flares and coronal mass ejections.¹

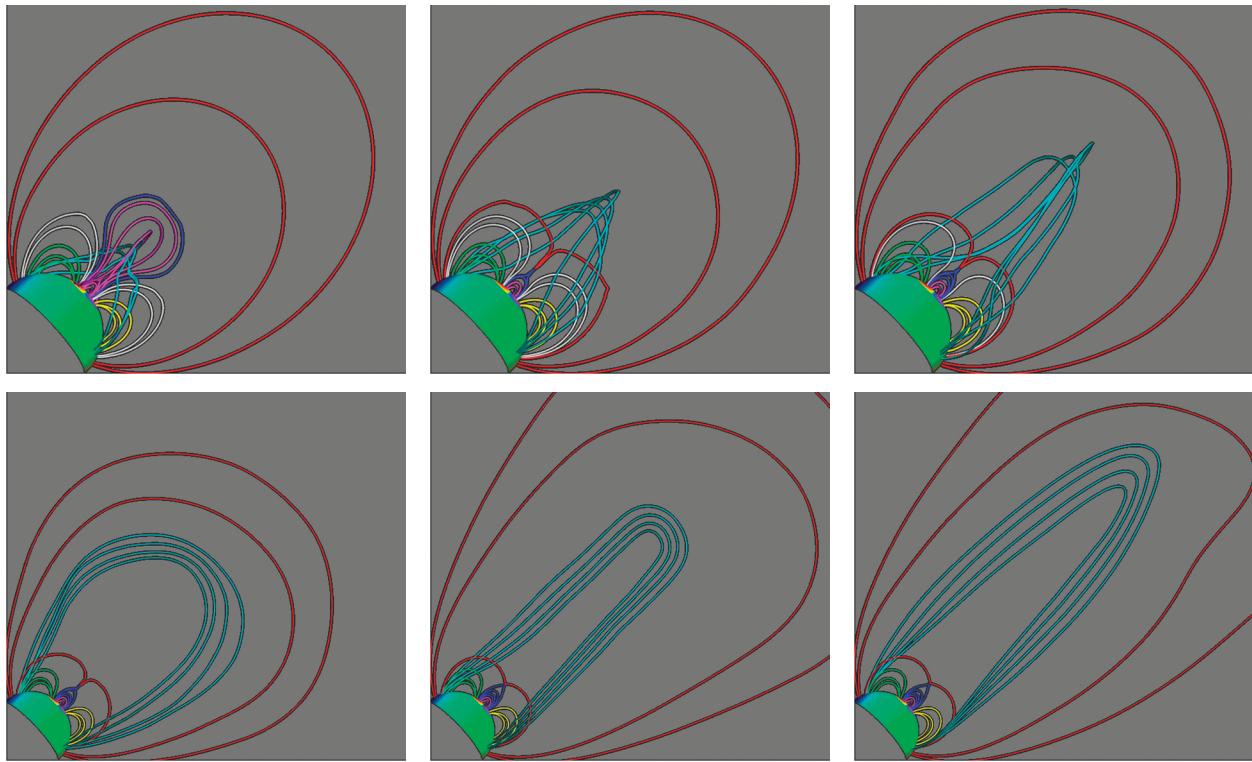
In the immediate aftermath of the eruption, field lines on both sides of the boundary between the sunspots are extremely elongated radially. Because these two populations of field lines also are antiparallel—pointing upward on the south side and downward on the north—they similarly suffer breaking and reconnecting. As they rebound back toward one another, following the impulsive outward escape of the energized field (magenta) from below, their original sunspot-linking (blue) and polar-cap-linking (red) connections get restored. This process is illustrated across the bottom row of panels in Fig. 4. The newly reformed, sunspot-linking field lines (blue) host plasma that has been heated during the breaking and reconnecting process, so that they constitute the hot loops which accompany eruptive flares (Fig. 1). The final, fully relaxed configuration at low heights in our simulation (Fig. 4, bottom right) rather closely resembles the minimum-energy configuration with which we

started (Fig. 3). This, too, is typical of solar eruptions: the considerable excess magnetic energy contained in the pre-event field is mostly absent from the post-event field, having been converted to energy of the plasma by the eruption.

The larger-scale, interplanetary consequences of the simulated eruption are shown in Fig. 5, which examines the magnetic field from more remote vantage points. In the first panel (top left), newly formed field lines (cyan) link the north and south polar regions, threading through the heart of the strongly energized field lines (magenta) that are in their rapid rise phase. Yet a third breaking and reconnecting process is responsible for their generation.² These new field lines comprise a giant, mildly twisted, transequatorial loop. As can be seen in the rest of the panels, this loop thereafter escapes the Sun into interplanetary space. Because the number of turns in the loop is fixed, as it lengthens, the twist per unit length drops and the loop becomes increasingly straight in appearance. Such mildly twisted CMEs are routinely measured in the solar wind by spacecraft and have been called “magnetic bottles,” to contrast them with the equally plentiful “flux rope” interplanetary CMEs that are much more strongly twisted and so resemble loosely wound springs. In the last panel of Fig. 5 (bottom right), the leading edge of the ejected magnetic bottle is slowing and losing some energy as it increasingly stretches the overlying polar-cap magnetic field lines (red) ahead of it. Nevertheless, the CME is still outbound at this time and more than eight solar radii from the Sun, a mere four hours after onset of the magnetic-breakout eruption.

CONCLUSIONS

The results of this first-principles numerical simulation are encouragingly consistent with the essential qualitative features of eruptive solar flares and coronal mass ejections. Also, although we stress that it is far too simple and abstracted to serve as a quantitative model for any real space weather event, it is nevertheless true that it yields approximately “a billion tons of matter moving at a million miles per hour.” These qualitative and quantitative successes give us confidence that our line of attack is a fruitful one and that our intuitive physical understanding of the genesis of the most violent space weather is sound. Many other, closely related simulations have been done, are under way, or are planned for the near future. Their aims are to advance us toward more realistic, complex, and challenging simulations of individual events, and to provide a comprehensive, quantitative grasp of how the characteristics of the source region determine the properties of the resultant disturbance. We also are examining our results to discern additional details of the observational

**FIGURE 5**

Magnetic-breakout eruption from the ARMS numerical simulation, viewed from more remote vantage points than in Fig. 4. The first panel (top left) shows the long transequatorial loop field lines (cyan) newly formed during the rapid rise phase of the eruption; these field lines and their entrained plasma subsequently escape the Sun as the coronal mass ejection. Note the scale change between the first and second rows of images. The last panel (bottom right) is at the same time as the last panel in Fig. 4, that is, four hours after eruption onset.

signatures predicted by the model, which have potential application to forecasting as well as a vital role in validating our approach. Given the required foundation of physical understanding, space-weather forecasting—like that of terrestrial weather before it—could be poised to make the transition from a basic research enterprise to a valued economic, national security, and military asset.

ACKNOWLEDGMENTS

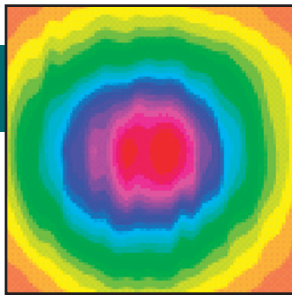
The research underlying these results has received sustained support over a number of years from the Office of Naval Research through NRL's 6.1 Core program and from the National Aeronautics and Space Administration through its numerous programs in heliophysics. The DoD High Performance Computing Modernization Program similarly has provided extensive computer resources at several sites for our computations, and its Common High-Performance-Computing Software Support Initiative funded the development of our state-of-the-art numerical tools.

We are grateful to Peter J. MacNeice and Kevin M. Olson for their vital contributions to the ARMS simulation model, Timothy J. Hall for his expert work on the HelioSpace visualizer, Jean E. Osburn and Portia K. Shingler for their able administration of our computer allocations, and James A. Klimchuk and Benjamin J. Lynch for many stimulating discussions on the physics of CMEs. We also acknowledge use of images from TRACE, a NASA Small Explorer mission run by the Stanford-Lockheed Institute for Space Research, and the LASCO telescope aboard SOHO, which is a joint mission of the European Space Agency and NASA.

[Sponsored by NASA and ONR]

References

- ¹S.K. Antiochos, "The Magnetic Topology of Solar Eruptions," *Astrophysical Journal* **502**, L181 (1998); S.K. Antiochos, C.R. DeVore, and J.A. Klimchuk, "A Model for Solar Coronal Mass Ejections," *Astrophysical Journal* **510**, 485 (1999).
- ²C.R. DeVore and S.K. Antiochos, "Homologous Confined Filament Eruptions via Magnetic Breakout," *Astrophysical Journal* **680**, 740 (2008). ★



High-Power Fiber Lasers for Directed-Energy Applications

P. Sprangle,¹ A. Ting,¹ J. Peñano,¹ R. Fischer,¹ and B. Hafizi²

¹*Plasma Physics Division*

²*Icarus Research, Inc.*

High-power fiber lasers can be incoherently combined to form the basis of a high-energy laser system for directed-energy applications. These applications include tactical directed energy and power beaming. Incoherent combining of fiber lasers has a number of advantages over other laser beam combining methods. The incoherently combined laser system is relatively simple, highly efficient, compact, robust, low-maintenance, and reliable. In this article, we characterize the atmospheric propagation of incoherently combined, high optical quality laser beams and compare them with other types of laser beams and combining methods. For tactical directed-energy applications, we find that the propagation efficiency of incoherently combined high optical quality beams is near the theoretical upper limit for any laser system with the same beam director and total power. We present results of the first atmospheric propagation experiments using incoherently combined, kilowatt-class, single-mode fiber lasers. These NRL field experiments combined four fiber lasers using a beam director consisting of individually controlled steering mirrors. The transmitted continuous-wave power was 3 kW at a range of 1.2 km with a demonstrated propagation efficiency of ~90% in moderate atmospheric turbulence. The experimental results are found to be in good agreement with simulations and theory.

INTRODUCTION

The successful development of laser weapons promises to have a profound impact on military missions throughout the services. A directed-energy (DE) laser system must be capable of delivering hundreds of kilowatts of average power to a target at multi-kilometer ranges through adverse atmospheric conditions. In addition, the laser system must be efficient, compact, robust, and reliable. While a great deal of progress has been made toward this objective, the goal will soon receive a significant boost due to advances in high-power fiber laser technology. High-power fiber lasers can also have applications in the area of power beaming, e.g., to UAVs and low-orbit satellites.

To achieve the total laser power needed for tactical DE and power beaming applications it is necessary to combine a large number of fiber lasers. Lasers can be combined coherently, spectrally, or incoherently. This article focuses on incoherent combining of high-power, high optical quality fiber lasers. This laser beam combining approach has a number of advantages over coherent or spectral combining.

In this article we discuss the characteristics of high-power fiber lasers and the progress made in increasing the output power of these devices while maintaining high optical quality. In addition, we discuss and compare the propagation efficiency of incoherently combined fiber laser arrays and coherently combined arrays in realistic atmospheric conditions for multi-kilometer propagation ranges. We conclude by present-

ing results from the first field propagation experiments which demonstrate high-power, kilometer-range incoherent combining. In these NRL experiments, four single-mode fiber lasers capable of transmitting a combined continuous-wave (CW) power of 6.2 kW were incoherently combined on a target at a range of 1.2 km. The total volume occupied by the four fiber lasers, including power supply, diode pump lasers, and fibers, is less than 2 m³. In the experiments, a total of 3 kW was transmitted over a 1.2 km range to a 10 cm radius target with the lasers at half power. Propagation efficiencies of ~90% were demonstrated in a moderately turbulent environment.

HIGH-POWER FIBER LASERS

Although a number of companies manufacture high-power fiber lasers, IPG Photonics Corp. (MA) currently has the most powerful, with over 3 kW per fiber of single-mode optical radiation.¹ Nufern (CT) now has a 1 kW, single-mode fiber laser available.² The term “single-mode” laser beam is synonymous with a diffraction-limited ideal Gaussian beam. The optical quality of a laser beam is measured in terms of the parameter M^2 , which characterizes the laser beam spreading angle. An ideal Gaussian beam, i.e., single-mode beam, is characterized by an M^2 of unity and has the smallest spreading angle of any beam profile with the same spot size (radius). Multi-mode beams have an M^2 greater than unity. The diffraction (spreading) angle of multi-mode beams is M^2 times greater than

that of a single-mode (ideal Gaussian) beam. For long-range propagation, single-mode beams are necessary.

Figure 1 illustrates the progress made in recent years in increasing the power in single-mode fiber lasers. It is anticipated that the power output of single-mode fiber lasers will reach a plateau of ~ 5 kW/fiber in approximately one year. Multi-kilowatt, single-mode fiber lasers are robust, compact, and have high wall-plug efficiency, random polarization, and large bandwidth ($\sim 0.1\%$). A 1 kW, single-mode IPG fiber laser module, operating at wavelength $\lambda = 1.075 \mu\text{m}$, excluding power supply, measures $w \times h \times d \sim 60 \text{ cm} \times 33 \text{ cm} \times 5 \text{ cm}$, weighs approximately 20 lbs, has a wall-plug efficiency of $>30\%$, and has an operating lifetime in excess of 10,000 hrs. Figure 2 shows a 1.2 kW fiber laser module manufactured by IPG. The total weight of a 2 kW IPG fiber laser, including power supply, is ~ 330 lbs. Because of the high operating efficiency, only a moderate degree of water cooling is required, i.e., ~ 2 gallons/minute/kW. To operate in a single mode, the optical core radius of the fiber must be sufficiently small. For example, the IPG single-mode 1 kW fiber lasers have an optical core radius of $\sim 15 \mu\text{m}$. Multi-mode IPG fibers, on the other hand, operating at 10 kW (20 kW) per fiber have an optical core radius of $\sim 100 \mu\text{m}$ ($\sim 200 \mu\text{m}$) and $M^2 \sim 13$ ($M^2 \sim 38$). These higher-power fiber lasers with larger values of M^2 have a more limited propagation range.

FIBER LASER COMBINING

To achieve the power levels needed for DE applications it is necessary to combine a large number of fiber lasers either coherently, spectrally, or incoherently. Coherent and spectral combining of laser beams can, in principle, result in a smaller size beam director. Coherent combining seeks to construct a phase-locked optical wavefront from many individual lasers, thus increasing the effective laser spot size and extending the propagation range. However, this approach requires extremely narrow laser linewidths and precise control

of the polarization and phase of the individual lasers. Fiber lasers with the narrow line widths required for coherent combining are currently limited in power to less than a few hundred watts per fiber due to inherent nonlinearities which broaden the linewidth. Spectral combining uses gratings to combine a large number of beams with slightly different wavelengths. This approach is also limited by the fiber laser bandwidth and the requirement that the lasers have a well-defined polarization. To date, the highest total power achieved through coherent or spectral combining is less than 1 kW. Using currently available fiber lasers, a coherently or spectrally combined DE system would be complex and require an extremely large number of lasers.

Incoherent combining has a number of advantages over coherent and spectral combining. This approach does not require narrow linewidths or phase/polarization locking of the individual lasers. Hence, it allows for the use of higher-power, multi-kilowatt fiber lasers and is much easier to implement. Incoherent combining of laser beams is achieved by overlapping the individual laser beams on a target with a beam director consisting of independently controlled steering mirrors and beam expanders³ as shown in Fig. 3. To limit diffractive spreading over the propagation range, the spot size of the beams must be large enough at the source and the beams must have good optical quality. In the absence of turbulence, the effective range of an incoherently combined array of single-mode lasers is determined by the Rayleigh range (Z_R) of an individual beam, which is given by $Z_R = \pi R_o^2 / \lambda$, where R_o is the initial beam spot size and λ is the laser wavelength. To achieve efficient propagation, the distance to the target (target range), L , should be less than $\sim 2Z_R$. For example, a single-mode fiber laser with initial spot size $R_o = 4$ cm and wavelength $\lambda = 1 \mu\text{m}$ has a Rayleigh range of ~ 5 km, so the target range should be less than ~ 10 km to avoid significant diffractive spreading. Usually, however, the spreading of the beam is dominated by atmospheric turbulence and not diffraction. This situation is discussed in the next section.

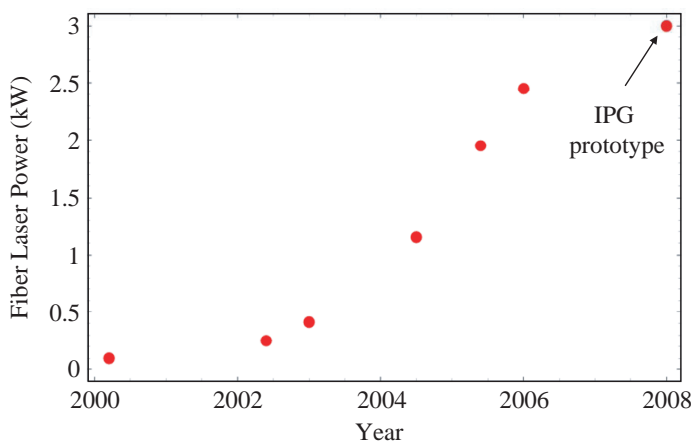
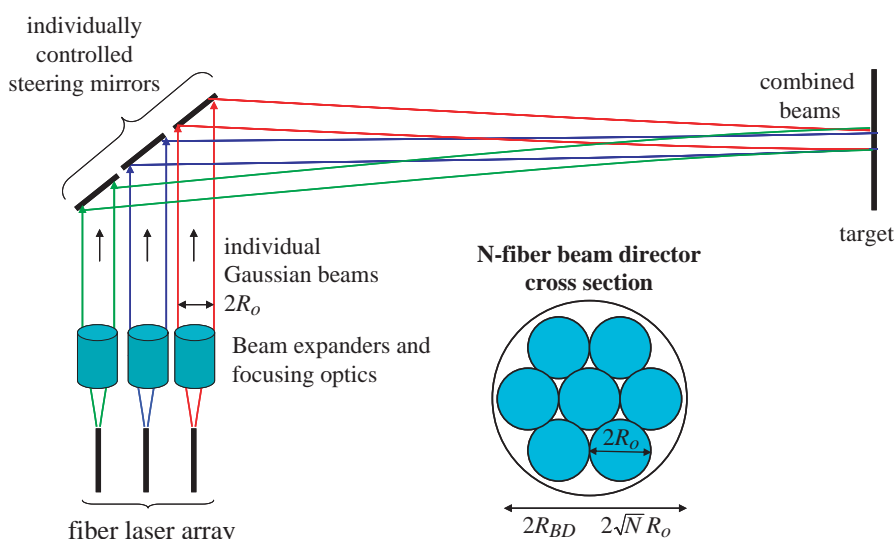
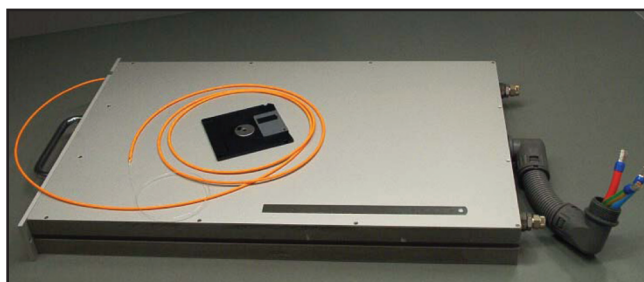


FIGURE 1
Progress made in increasing the power per fiber in single-mode fiber lasers.

FIGURE 2

IPG Photonics 1.2 kW fiber laser module. Module has dimensions $60 \times 33 \times 5$ cm, weight ~ 20 lbs, and wall-plug efficiency $\sim 30\%$.

**FIGURE 3**

Schematic diagram of incoherently combined fiber laser beams directed to a target.

Because incoherent combining allows for a higher power per fiber, the laser system is compact and readily scalable to power levels needed for DE applications. For N incoherently combined fiber lasers, the total transmitted power is N times the power in the individual fiber, and the beam director radius is $R_{BD} \approx \sqrt{N}R_o$. A 500 kW laser system would consist of 100 fiber lasers (5 kW/fiber), have a beam director radius of ~ 40 cm, and, excluding power supply, the fibers and pump diodes would occupy a volume of ~ 8 m³.

ATMOSPHERIC PROPAGATION OF LASER BEAMS

The physical processes affecting the propagation of high-power laser beams in the atmosphere are complex and interrelated. These processes include diffraction, molecular/aerosol scattering and absorption, turbulence produced by air density fluctuations, thermal blooming, and others. While it is beyond the scope of this article to consider these physical processes in detail, for the purpose of estimating and comparing the propagation efficiency of combined single-mode and multi-mode fiber lasers we consider some of the more important processes in a simplified manner. We also

discuss the use of tip-tilt compensation in the beam director to correct for the wander of the laser beam centroid due to turbulence, and quantify its limitations.

The minimum laser beam spot size, or radius, is obtained by adjusting the focal length of the transmitted beam so it equals the distance to the target, or range L . The laser beam spot size on target is then given by $R = \Theta_{\text{spread}} L$ where the spreading angle Θ_{spread} is the sum of contributions from diffraction, Θ_{diff} , atmospheric turbulence, Θ_{turb} , mechanical jitter, Θ_{jitter} , and thermal blooming, Θ_{bloom} . Thermal blooming, i.e., the self-defocusing of the laser due to absorption and the subsequent heating of the air, can be partially mitigated by propagating in an atmospheric transmission window where the absorption is low. Fortunately the fiber laser wavelength, $\lambda = 1.075$ μm , is near a narrow water vapor transmission window centered at $\lambda = 1.045$ μm . In the presence of water-based aerosols the actual transmission window is broadened⁴ and easily includes the fiber laser wavelength. For total laser power levels less than ~ 100 kW, and depending on the transverse air flow and atmospheric absorption, thermal blooming effects can usually be neglected.³ Thermal blooming near the beam director can be eliminated by introduc-

ing a transverse air flow.⁵ For the purposes of this discussion we will also neglect the small mechanical jitter contribution and concentrate on the dominant effects of turbulence and diffraction.

Atmospheric turbulence strength is described by the parameter C_n^2 , which characterizes the amplitude of density fluctuations in the air. C_n^2 normally ranges from $10^{-15} \text{ m}^{-2/3}$ (weak turbulence) to $10^{-13} \text{ m}^{-2/3}$ (very strong turbulence). The effect of turbulence on laser beam propagation is characterized by the Fried parameter (transverse coherence length), r_o , which is a function of C_n^2 and propagation range. The Fried parameter varies from tens of centimeters for weak turbulence conditions to fractions of a centimeter for strong turbulence. The spreading angle of a laser beam due to atmospheric turbulence is $\Theta_{\text{turb}} = 1.6 \lambda / \pi r_o$.^{6,7}

Comparison of Single- and Multi-Mode Propagation

The diffractive spreading angle of an individual laser beam is $\Theta_{\text{diff}} = M^2 \lambda / (\pi R_o)$. The goal of coherent combining is to reduce the diffractive spreading angle by phase locking and polarization locking N individual single-mode lasers, thus increasing the effective spot size by a factor of \sqrt{N} . For single-mode fiber lasers propagating over long distances, turbulence spreading dominates diffractive spreading, i.e., $\Theta_{\text{turb}} \gg \Theta_{\text{diff}}$, since the Fried parameter is usually less than the initial laser spot size, $r_o \ll R_o$. On the other hand, for highly multi-mode fibers ($M^2 \gg 1$), the diffractive spreading angle can be large, i.e., $\Theta_{\text{diff}} > \Theta_{\text{turb}}$. These differences between single-mode and multi-mode fibers have important consequences for their propagation efficiency and the use of adaptive optics to reduce the effects of turbulence. For single-mode fibers, the use of adaptive optics can substantially improve the propagation efficiency. However, for multi-mode fibers, adaptive optics will have little effect on the propagation efficiency because the main contribution to the spreading angle is from diffraction due to poor beam quality, i.e., high value of M^2 .

To determine the merits of incoherently combining single-mode or multi-mode fiber lasers for DE applications, it is useful to compare their propagation efficiencies. Here, we define propagation efficiency as the ratio of power on target to total transmitted laser power. In making this comparison, the fiber laser systems are assumed to have the same size beam director and the same total power. Table 1 lists the parameters of four systems that are designed to deliver a total power of 100 kW. The systems are based on currently available fiber lasers. For example, for the 3 kW per fiber and $M^2 = 1$ case, 33 fiber lasers (N_{fiber}) are required to achieve 100 kW. The corresponding M^2 values reflect the fact

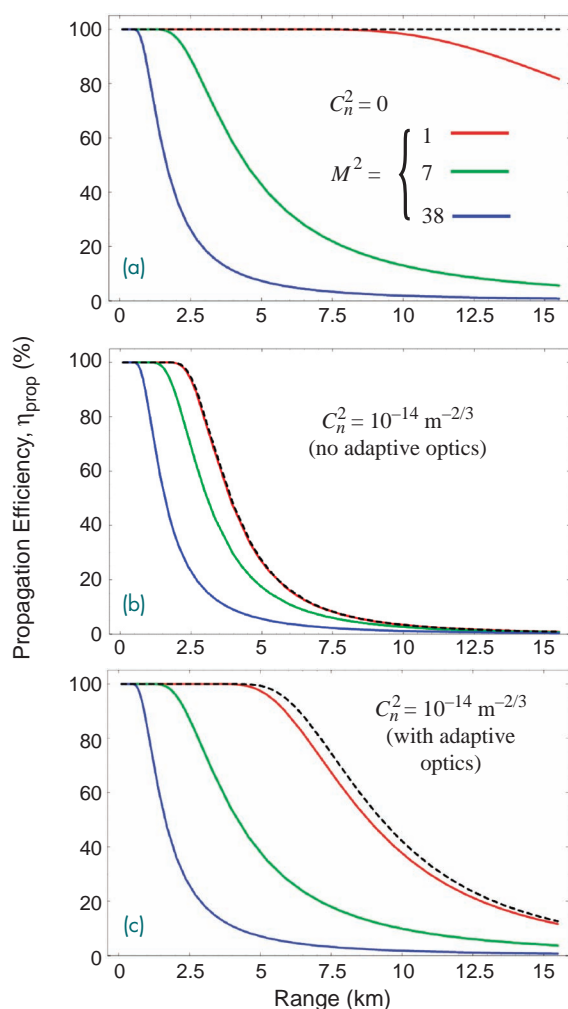
TABLE 1 — Four configurations of a 100 kW system using single-mode and multi-mode fiber lasers. Systems are labeled by color to match propagation efficiency plotted in Fig. 4. The black, dashed curve in Fig. 4 denotes an ideal Gaussian beam having a 50 cm spot size.

	Power/fiber (kW)	M^2	N_{fiber}	R_o (cm)
Red	3	1	33	8.7
Green	5	7	20	11.2
Blue	20	38	5	22.4
Black	100	1	1	50

that for multi-mode lasers the beam quality decreases (M^2 increases) as the power per fiber increases. Table 1 also gives the radius of the collimating lens for the individual fiber lasers (R_o). In all cases, the radius of the beam director is 50 cm and the target is assumed to be a circular disc with a surface area of 100 cm^2 . Figure 4 plots the propagation efficiency for $M^2 = 1, 7$, and 38 , in vacuum (Fig. 4(a)), and in a turbulent environment with $C_n^2 = 10^{-14} \text{ m}^{-2/3}$ (Figs. 4(b) and (c)). In all cases, the beams are focused onto the target. For propagation through turbulence, Fig. 4 shows the efficiency without adaptive optics (b) and with adaptive optics (c). The adaptive optics was modeled, in the results shown in Fig. 4(c), by increasing the Fried parameter by a factor of four. The dashed curves denote the case of a single ideal Gaussian beam with initial spot size equal to the radius of the beam director, i.e., the theoretical upper limit for perfectly coherently combined beams. For ranges $< 10 \text{ km}$ in vacuum (Fig. 4(a)), and for conditions in which turbulence dominates (Fig. 4(b)), the single-mode incoherently combined example (red curve) has a propagation efficiency virtually identical to that of the coherently combined beam (dashed curve), while the propagation efficiency of the various multi-mode fibers is far less. Figure 4 also shows that the use of adaptive optics can greatly improve the propagation efficiency of combined single-mode fibers but has little effect on the combined multi-mode fiber lasers.

Comparison of Incoherent and Coherent Combining

It is often stated that the advantage of coherent beam combining is that, for a given size beam director and total power level, coherent combining results in a smaller beam spreading angle compared with incoherently combined beams. For propagation in vacuum, the brightness (intensity/solid angle) of the coherently combined fiber array is N times larger than for an incoherently combined array, where N is the number


FIGURE 4

Propagation efficiency versus range for incoherently combined fiber laser beams with beam quality parameters $M^2 = 1, 7$, and 38 : (a) in vacuum, (b) in a turbulent atmosphere with $C_n^2 = 10^{-14} \text{ m}^{-2/3}$ (no adaptive optics), and (c) in a turbulent atmosphere with adaptive optics. Laser parameters are listed in Table 1. The dashed curve represents the theoretical upper limit for coherent and incoherent combining.

of fibers. While this is true for vacuum propagation, it is not relevant when the effects of atmospheric turbulence are taken into account. Beam brightness at the source is of limited importance when considering realistic DE propagation scenarios in turbulent atmospheres.

When the turbulence strength is large enough so that the Fried parameter, r_o , is less than the beam director radius, R_{BD} , coherent and incoherent combining give comparable values for spreading angle and spot size on target. This condition is usually satisfied for DE applications. For example, in moderate turbulence and a propagation distance of $L = 2 \text{ km}$, the Fried parameter is $r_o = 3 \text{ cm}$, which is typically much smaller than the beam director radius. As shown in Fig. 4(b), the power on target for an incoherently combined array of single-mode lasers with $N = 33$ (red curve) is virtually identical to that of a coherently combined array (dashed curve).

Compared to a coherently combined array, incoherently combined fiber lasers can deliver similar power levels to a remote target. This is seen by comparing the dashed (coherent array) and red (incoherent array)

curves in Fig. 4(a). For typical propagation scenarios and realistic atmospheric conditions, there is little if any advantage to coherently combining laser beams as compared to incoherently combining them.

Beam Wander and Tip-Tilt Compensation

Introducing tip-tilt correction into the individual steering mirrors can reduce the overall laser spot size on target. Tip-tilt correction redirects the centroids of the individual laser beams to cancel the effects of wander due to turbulence. This is accomplished by monitoring the intensity on target and redirecting the steering mirrors to minimize the spot size. Laser beam wander is a function of the scale size of the turbulence fluctuations. Turbulent eddies that are large compared to the laser beam diameter cause the laser beam centroid to be deflected and to wander in time due to transverse air flow. Eddies that are much smaller than the beam diameter cause spreading about the beam centroid and cannot be reduced by the use of tip-tilt compensation. The observed long time averaged laser spot size is a combination of beam wander and spread-

ing about the centroid. In weak turbulence, the beam centroid wander represents a significant contribution to the laser beam radius. As the turbulence level increases, or for long propagation ranges, the beam wander contribution to the laser spot size becomes less important. In very strong turbulence, the laser beam breaks up into multiple beams making tip-tilt compensation ineffective.

If the individual laser beams are separated by less than r_0 at the source, the wander of the centroids on the target will be correlated. In this case, it would be possible for beams to share a common tip-tilt correcting aperture, thus reducing the size and complexity of the system.

NRL FIBER LASER EXPERIMENTS

The NRL incoherent combining field propagation experiments use four IPG single-mode fiber lasers having a total output power of 6.2 kW (1 kW, 1.6 kW, 1.6 kW, and 2 kW). These initial experiments were performed at the Naval Surface Warfare Center (NSWC) in Dahlgren, VA, over a propagation range of 1.2 km. An aerial view of the propagation range is shown in Fig. 5. The laser beams propagated 4 to 10 ft above a blacktop road.

The beam director consists of four fiber output couplers and individually controlled steering mirrors which direct the four single-mode fiber laser beams onto a target. Each beam has a spot size of ~ 2.5 cm as it exits the beam director and the target is a 10-cm-radius, water-cooled power meter.

Figure 6 shows a schematic of the fiber laser output coupler and the beam expander (concave-convex lens combination) which is used to adjust the focal length. In these initial experiments the fiber lasers were operated at nearly half power because of thermal blooming in the beam director and in the atmosphere just beyond the laser source. These issues can be readily corrected in the next series of experiments by using lower-absorption optics and inducing air flow near the laser output. Thermal effects caused an axial shift of the focus with time as the total laser power was increased to ~ 3 kW. The change in the focal length was compensated for by changing the separation between the lenses in the beam expander. Figure 7 shows the beam director, output couplers, and steering mirrors used in the experiments.

The power on target as a function of time is shown in Fig. 8. After the output coupler reached thermal equilibrium (> 200 sec), the measured power was 2.8 kW, corresponding to a propagation efficiency of $\sim 90\%$. The typical errors associated with the measured transmitted power and power on target was $\pm 5\%$.

Atmospheric turbulence causes the laser beams on target to wander and change shape. Since the laser beam separation is initially much greater than r_0 , the

individual beams are uncorrelated and their centroids randomly wander with respect to each other. At times, the four beams completely overlap forming a single spot, while at other times the four individual beams are separated by typically a few centimeters. The characteristic time scale associated with beam wander is ~ 20 msec. Since the mechanical jitter angle was measured to be less than ~ 2 μ rad, the beam centroid wander is caused mainly by atmospheric turbulence.

Figure 9 displays two frames from a CCD camera, the first at ~ 180 sec and the second at ~ 300 sec, showing 2.8 kW of combined laser power on the power meter. The two frames were chosen to illustrate cases where the four beam centroids are fully overlapped and where they have maximum displacement from each other. Precise measurements of beam wander and spreading at the target are difficult and were not available for these preliminary experiments because of pixel saturation in the camera and a limited number of frame samples. However, one can estimate the beam wander and spot size from the CCD images. The lower panel of Fig. 9 indicates that the average centroid wander was ~ 4 cm and that the individual instantaneous laser spot size was ~ 2.5 cm. Hence, the long time average spot size is estimated to be $R \sim 4.7$ cm.

To compare the experimental observations with simulations and theory, the atmospheric turbulence level, C_n^2 , was measured using a scintillometer. The average value of C_n^2 during the experiments was $\sim 5 \times 10^{-14} \text{ m}^{-2/3}$ and the average transverse wind velocity was estimated to be ~ 2.5 m/sec.

Comparison of Experiments with Simulations and Theory

The Navy's High-Energy Laser Code for Atmospheric Propagation (HELCAP)^{3,4,5} was used to model the propagation experiments. The HELCAP code is



FIGURE 5
Aerial view of the laser propagation range in Dahlgren, VA.

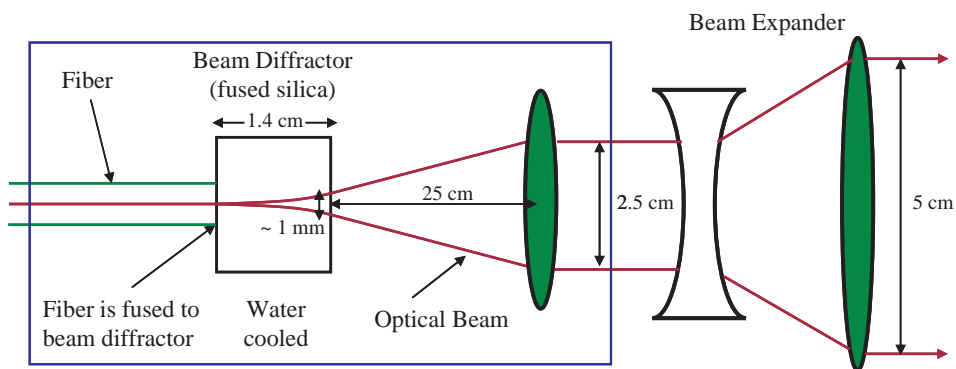


FIGURE 6
Schematic diagram of fiber output coupler and beam expander.

FIGURE 7
Beam director used for incoherent combining. Three of four fiber output couplers are shown in the foreground. Four individually controlled steering mirrors are shown in the background.

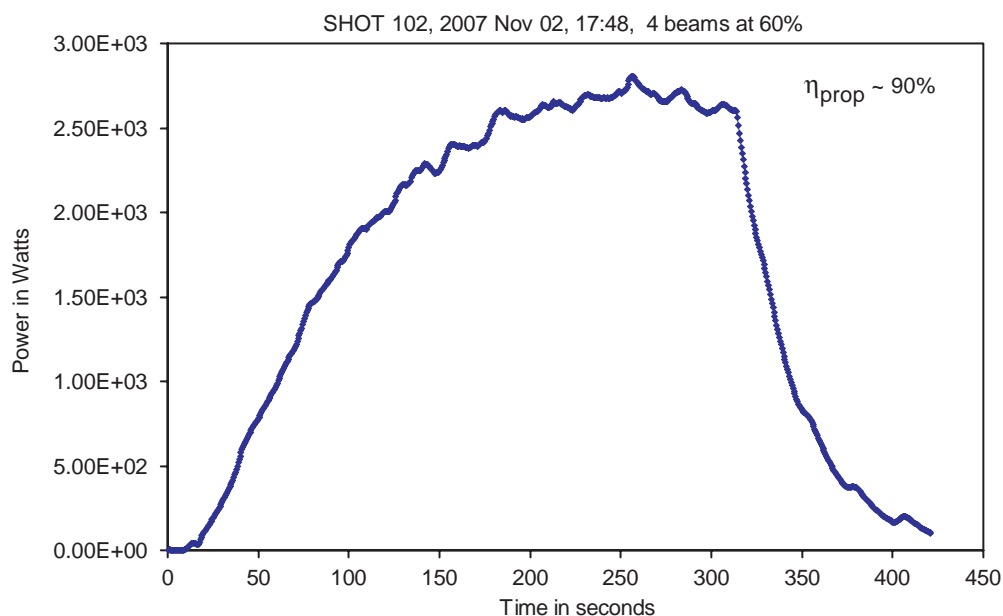
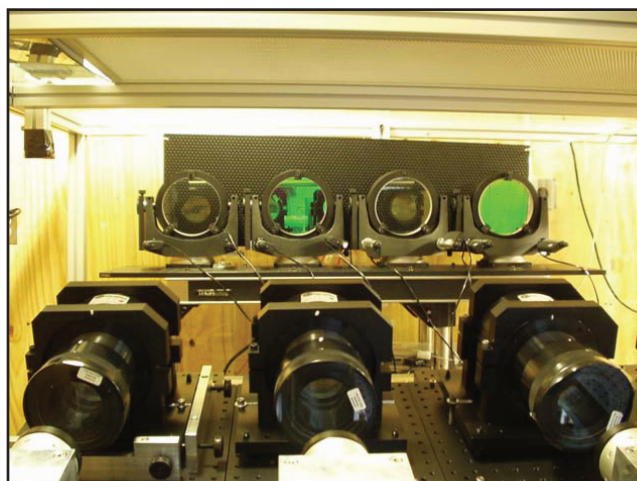
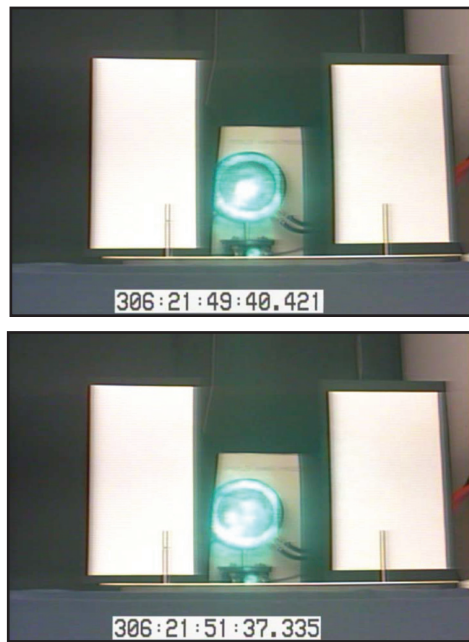


FIGURE 8
Experimentally measured power at target versus time. Target was a power meter with 45 sec response time and 10 cm radius. Average wind speed was ~ 2.5 m/sec, and measured turbulence strength $C_n^2 = 5 \times 10^{-14} \text{ m}^{-2/3}$. The maximum propagation efficiency is $\sim 90\%$. Thermal equilibrium in the power meter is reached at ~ 200 sec and the laser beams are turned off at ~ 320 sec.

**FIGURE 9**

Two CCD camera images of four beams incoherently combined on target (10 cm radius power meter) at a range of 1.2 km. The first panel shows the combined beams at ~180 sec and the second image is at ~300 sec. The later image shows the four individual beam centroids randomly displaced by ~4 cm due to atmospheric turbulence.

fully three-dimensional, time-dependent, and includes molecular/aerosol scattering/absorption, turbulence, and thermal blooming effects. The simulations assume an aerosol scattering coefficient of 0.05 km^{-1} and $1 \text{ } \mu\text{rad}$ of mechanical jitter.³

Figure 10 shows the results of HELCAP simulations in which four laser beams, with a total power of 3 kW and at a range of 1.2 km, were incoherently combined. Panel (a) shows the intensity contours of the four beams at the fiber laser output coupler. The focal length of each beam was adjusted to minimize the spot size on target. Panel (b) shows time-averaged (over a few seconds) intensity contours of the combined laser beam on the target plane. The long time average spot size on target from the simulations was ~4.6 cm compared with the experimental estimate of 4.7 cm. The intensity profile as a function of time indicates that the rms wander displacement from the simulations was ~2.5 cm compared with the experimental estimate of 4 cm. The instantaneous spot size of the individual beams from the simulations was ~3.1 cm compared with the experimental estimate of 2.7 cm.

Using atmospheric turbulence theory^{3,6,7} we calculated the laser beam wander displacement and long time averaged spot size. The calculated beam wander and long time average spot size was 2.8 cm and 4.2 cm, respectively. These calculated values are in good agreement with experimental observations and HELCAP simulations.

DISCUSSION

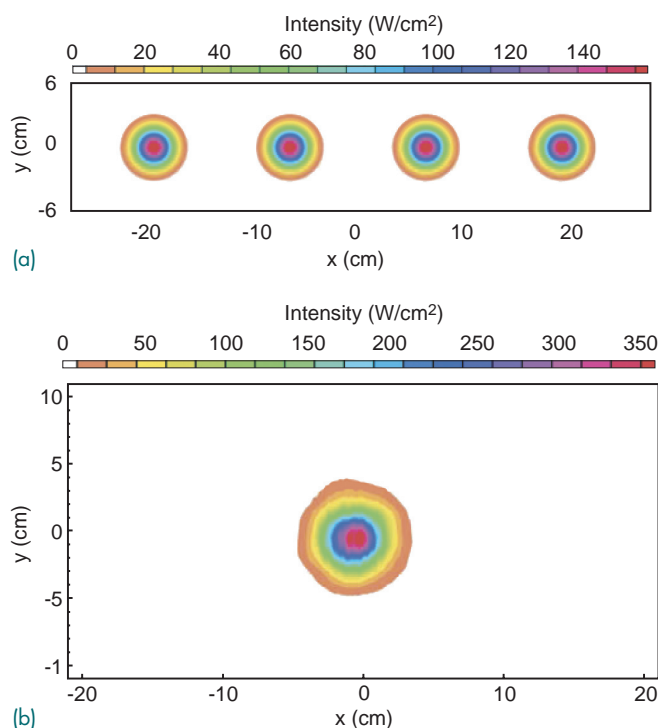
In 2008, the NRL fiber lasers will be moved to the Starfire Optical Range in Albuquerque, NM, and

propagation experiments over a 3.2 km range will take place at full power. The objectives of these experiments are to demonstrate the incoherent beam combining concept at longer range, quantify thermal blooming effects, more precisely characterize the beam wander and spreading, and validate the propagation model (HELCAP). Planned experiments will incorporate target-in-the-loop tip-tilt compensation into one of the fiber laser beams to correct for wandering of the beam centroid. Controlled thermal blooming experiments can also be carried out using a stagnation tube to eliminate the cooling effects of transverse air flow. This arrangement permits thermal blooming effects to be observed under controlled conditions and at relatively low power levels. The temporal change in the laser spot size and intensity and measurements of the air properties inside the stagnation tube will provide the necessary data to study atmospheric thermal blooming under realistic conditions.

In addition to the NRL program, other fiber laser-based DE efforts are underway. A NAVSEA lethality/propagation program being carried out at NSWC Dahlgren utilizes six multi-mode fiber lasers, each having a CW power of 5 kW and optical quality of $M^2 \sim 6$. A joint Pennsylvania State University/NSWC Crane lethality and propagation program is also under way using two multi-mode fiber lasers, 10 kW ($M^2 \sim 13$) and 5 kW ($M^2 \sim 6$).

SUMMARY

Incoherent combining of high-power fiber lasers can result in highly efficient, compact, robust, low-maintenance, and long-lifetime high-energy laser

**FIGURE 10**

HELCAp simulation showing a time-averaged transverse intensity profile of laser beams at (a) the source and (b) incoherently combined on target at a range of 1.2 km. The atmospheric turbulence level used in the simulation is the same as those measured in the experiment.

systems for directed-energy applications. In this article, we discussed the propagation of incoherently combined single-mode and multi-mode fiber laser beams through atmospheric turbulence. We compared the propagation efficiency of coherent and incoherent combining and found that under typical atmospheric conditions and propagation ranges, the propagation efficiency of incoherently combined single-mode fiber lasers is nearly identical to the theoretical upper limit for coherent combining. Hence, there is no inherent advantage to coherently combining beams for tactical directed-energy scenarios.

We presented results from the first field demonstration experiments of long-range incoherent combining. The experiments combined four fiber lasers using a beam director consisting of individually controlled steering mirrors. Propagation efficiencies of ~90%, at a range of 1.2 km, with transmitted CW power levels of 3 kW were demonstrated in moderate turbulence. Numerical simulations and theoretical results were in good agreement with experimental observation.

The NRL propagation experiments have provided important information concerning the issues associated with incoherently combining high-power, single-mode fiber lasers. These field experiments will lay the groundwork for developing a tactical DE laser system in the near term.

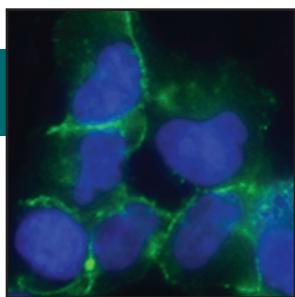
ACKNOWLEDGMENTS

We acknowledge C. Rollins, G. Dicomio, Z. Wilkes, and J. Caron for their assistance in the field experiments.

[Sponsored by NRL, ONR, and HEL-JTO]

References

- ¹ V. Gapontsev et al., "2 kW CW Ytterbium Fiber Laser with Record Diffraction-Limited Brightness," in *2005 Conference on Lasers and Electro-Optics Europe (CLEO Europe)*, p. 508 (2005).
- ² J. Edgcombe, "Kilowatt Level, Monolithic Fiber Amplifiers for Beam Combining Applications at 1 μ m," *Proceedings of the 20th Solid State and Diode Laser Technology Review* (2007).
- ³ P. Sprangle, J. Peñano, B. Hafizi, and A. Ting, "Incoherent Combining of High-Power Fiber Lasers for Long-Range Directed Energy Applications," *Journal of Directed Energy* **2**, 273-284 (2007); also NRL Memorandum Report, NRL/MR/6790--06-8963, June 2006.
- ⁴ P. Sprangle, J. Peñano, and B. Hafizi, "Optimum Wavelength and Power for Efficient Laser Propagation in Various Atmospheric Environments," *Journal of Directed Energy* **2**, 71-95 (2006).
- ⁵ J.R. Peñano, P. Sprangle, and B. Hafizi, "Propagation of High Energy Laser Beams Through Atmospheric Stagnation Zones," *Journal of Directed Energy* **2**, 107 (2006).
- ⁶ L.C. Andrews and R.L. Phillips, *Laser Beam Propagation through Random Media*, 2nd ed. (SPIE Press, Bellingham, WA, 2005).
- ⁷ R.L. Fante, "Electromagnetic Beam Propagation in Turbulent Media," *Proc. IEEE* **63**, 1669-1692 (1975). ★



Plant Proanthocyanidins Bind to and Neutralize Bacterial Lipopolysaccharides

J.B. Delehanty,¹ B.J. Johnson,¹ T.E. Hickey,¹ T. Pons,² and F.S. Ligler¹

¹Center for Bio/Molecular Science and Engineering

²Optical Sciences Division

Proanthocyanidins (PACs) are naturally occurring polymers derived from higher plants and they have recently been associated with several potential positive health benefits such as antibacterial, chemotherapeutic, and anti-atherosclerotic activities. Here we report on the binding of PACs from cranberries, tea, and grapes to lipopolysaccharide (LPS), a major component of the outer membrane of Gram-negative bacteria. LPS is the cause of several human illnesses, including sepsis and toxic shock syndrome. We show that in the case of cranberries, the majority of the LPS-binding activity is contained within a PAC fraction composed of polymers with an average degree of polymerization of 21. This PAC fraction modestly inhibits the binding of LPS to the surface of mammalian cells expressing the full complement of LPS receptors while it significantly abrogates the cellular internalization of LPS. Our results demonstrate PACs to be a new class of LPS-binding compound with potential utility in the removal of LPS from potable water sources and pharmaceutical preparations.

INTRODUCTION

During infection, bacteria cause damage to the human body in two ways: 1) they release toxins that harm and kill cells and 2) they perturb the immune system, leading to inflammation, which can be harmful in itself. In the case of Gram-negative bacteria (e.g., *Escherichia coli*), the primary trigger of the immune response is a molecule known as lipopolysaccharide (LPS), the major component of the bacterial outer cell membrane. LPS is the primary cause of sepsis, an inflammatory condition characterized by an overwhelming systemic response to bacterial infection. Sepsis has become the most common cause of death in intensive care units in the United States, causing 120,000 deaths annually and amassing \$16.7 billion in associated healthcare costs.¹ Commonly referred to as bacterial “endotoxin,” LPS is composed of three domains: 1) a bacterial membrane-proximal lipid A moiety and 2) a core oligosaccharide region which gives rise to 3) the O-antigen, a branched polysaccharide that extends from the core oligosaccharide.² When released from bacteria, LPS circulates in the blood where it interacts with receptors (TLR4 and CD14) on the surface of our immune cells (dendritic cells and macrophages), eliciting the body’s immune response. While this LPS-induced immune response is necessary for the body to effectively combat bacterial infection, if it is left unchecked, the immune response can evolve into life-threatening sepsis.

To date, a range of LPS-binding compounds has been developed in an effort to prevent LPS-induced

sepsis by inhibiting the interaction of LPS with its target receptors. These materials include peptides such as polymyxin B, hydrazones, and polyamines. Due to their toxicity and lack of specificity, however, these materials have demonstrated limited success in therapeutic settings; their use has largely been limited to *in vitro* applications where the removal of LPS from solutions is required. The need for the identification of novel LPS-binding compounds still remains.

This report describes our recent discovery that proanthocyanidins (PACs), naturally occurring polyphenolic compounds derived from higher plants, efficiently bind to and prevent the interaction of LPS with receptors on the surface of mammalian immune cells.³ This novel finding has identified PACs as a new class of LPS-binding compound with potential uses in applications requiring LPS purification and removal or the *in vivo* treatment of sepsis.

PROANTHOCYANIDINS: A NEW CLASS OF LPS-BINDING COMPOUND

Liquids containing PACs such as tea, red wine, and cranberry juice have recently been associated with several potential positive health benefits. Among the more notable of these benefits is the ability of cranberry juice to mitigate urinary tract infections by preventing the attachment of pathogenic bacteria to uroepithelial cells. This effect has been attributed to the ability of PACs to induce conformational changes in the cell surface proteins that bacteria use to attach themselves to epithelial cells.⁴

PACs are composed chiefly of the monomeric flavan subunits (+)-catechin and (–)-epicatechin and their derivatives (Fig. 1(a)). The subunits are most commonly linked together via a single intermolecular bond as is the case in PACs from tea and grapes (known as B-type PACs). In some instances, the subunits are linked together by two intermolecular bonds (A-type PACs) as is observed in cranberries. Since the potential interactions of PACs with bacterial cell surface proteins did not seem adequate to explain all of the reported activities of cranberry juice, we hypothesized that PACs might interact with other molecules on the bacterial cell surface, particularly LPS.

In this study, we assessed the LPS-binding activity of PACs from cranberries, tea, and grapes. Figure 1(b) shows the relative abilities of PACs from these various sources to inhibit the binding of *E. coli* LPS to an immobilized receptor (polymyxin B) as a function of PAC concentration. Cranberry concentrate that had been enriched through dialysis to contain molecules greater than 6,000 molecular weight (MW) showed the

lowest degree of LPS-binding with an inhibitory concentration (50%) (IC_{50}) of 10.5 μ M. PACs from grapes and tea showed intermediate degrees of LPS-binding activity, with IC_{50} values of 3.0 and 1.1 μ M, respectively. However, PACs from fresh cranberries (enriched for PACs greater than 6,000 MW) showed the greatest ability to bind to LPS, with an IC_{50} of 0.7 μ M. A further comparison of the activities of cranberry PACs as a function of size showed that the polymers greater than 6,000 MW had the highest degree of LPS binding relative to smaller PACs (Fig. 1(c)).

An analysis of the degree of polymerization within each of the different sized “pools” of cranberry PACs verified enrichment for increased polymer length within each size fraction. The fraction with the greatest LPS-binding activity corresponded to polymers with an average degree of polymerization of 21 (Table 1). All subsequent experiments were performed using this fraction (referred to henceforth as cranberry PACs).

We also found that cranberry PACs bound not only to LPS from *E. coli* but also to a number of other

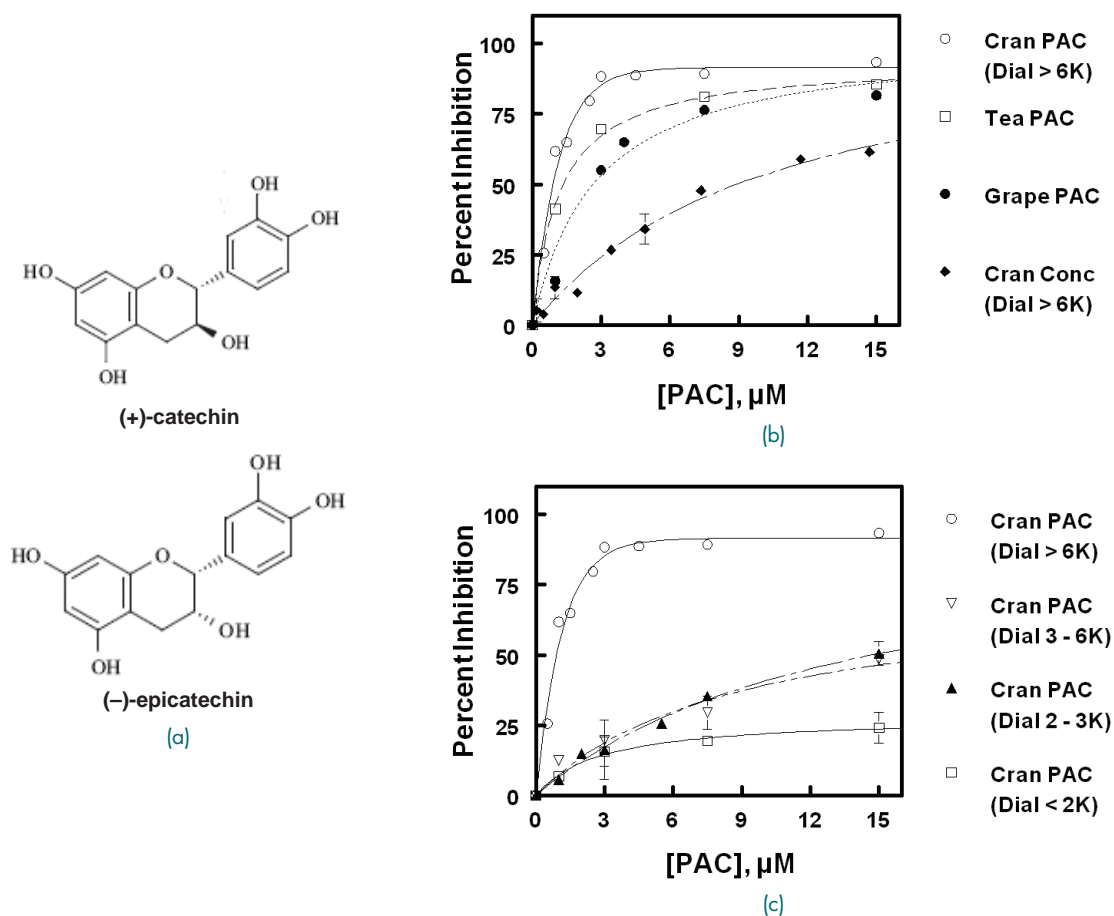


FIGURE 1

PACs interact with LPS to inhibit binding to a potent LPS-binding molecule, polymyxin B. (a) PACs are polymers commonly composed of (+)-catechin and (–)-epicatechin flavanoid subunits. (b) The LPS-binding activity of PACs from cranberry, tea, and grapes is concentration-dependent. Cranberry PACs greater than 6,000 MW show the greatest LPS-binding activity. (c) For cranberry PACs, the majority of the LPS-binding activity is contained within the fraction composed of polymers >6,000 MW (average degree of polymerization of 21).

TABLE 1 — Average Degree of Polymerization of Size-Fractionated PACs from Cranberry

PAC Fraction	Average Degree of Polymerization
Non size-fractionated	12.6
<2000	3.2
2000 – 3000	5.4
3000 – 6000	12.9
>6000	21.4

Gram-negative bacterial species (Table 2). Further, cranberry PACs bound very tightly to lipid A, the putative cell-binding domain on LPS, indicating that PACs predominantly bind to the lipid A region of the LPS molecule.

PACS INHIBIT LPS INTERACTION WITH MAMMALIAN CELLS

Based on cranberry PACs' LPS-binding ability and its large degree of interaction with the cell-binding lipid A moiety, it followed that PACs could efficiently block the interaction of LPS with mammalian cells expressing cognate LPS receptors. Using a model system in which human epithelial cells were induced to express the LPS receptors CD14 and TLR4 (to emulate our native immune cells), we found that cranberry PACs caused a modest yet significant reduction (~15%) in the amount of LPS bound to these cell surface receptors (Fig. 2(a)). However, cranberry PACs substantially inhibited (~74% inhibition) the cells' ability to internalize LPS (Fig. 2(b)). This result is consistent with the

currently accepted model of LPS interaction with its cell surface receptors in which LPS binding to its receptors is required for internalization and the onset of the inflammatory response.^{5,6} This mechanism of action is depicted schematically in Fig. 3. Through this activity, PACs are able to effectively modulate the immune response and to keep the response in check.

SUMMARY

Our work has identified naturally occurring PACs as a new class of efficient LPS-binding compound. Given the limitations of some of the currently available LPS-binding substances, it is anticipated that PACs will find great utility in LPS removal and purification applications (Fig. 4). Important targets for use would include biological materials that cannot be heat- or UV-sterilized without degradation, including many pharmaceuticals and baby juices. PACs might also prove useful in therapeutic applications such as dialysis or the *in vivo* neutralization of LPS-induced inflammation.

[Sponsored by ONR and NRL]

TABLE 2 — Binding of Cranberry LH20 PAC^a to LPS and Lipid A

Bacterial Species	Apparent IC ₅₀ (μM) ^b
LPS	
<i>Escherichia coli</i>	0.7 ± 0.2
<i>Salmonella minn.</i>	1.2 ± 0.3
<i>Shigella flexneri</i>	1.6 ± 0.3
<i>Escherichia coli</i> EH 100 (Ra mutant)	2.1 ± 0.7
<i>Salmonella minn.</i> (Rc mutant)	2.1 ± 0.5
<i>Pseudomonas aeruginosa</i>	3.4 ± 1.0
Lipid A ^c	
<i>Escherichia coli</i>	0.3 ± 0.1

^aCorresponds to PACs of greater than 6,000 molecular weight.

^bApparent IC₅₀s are shown with their corresponding 90% confidence intervals. The IC₅₀ is the concentration at which the PAC blocked 50% of the binding of LPS to the immobilized LPS-binding molecule, polymyxin B.

^cDiphosphoryl form of lipid A.

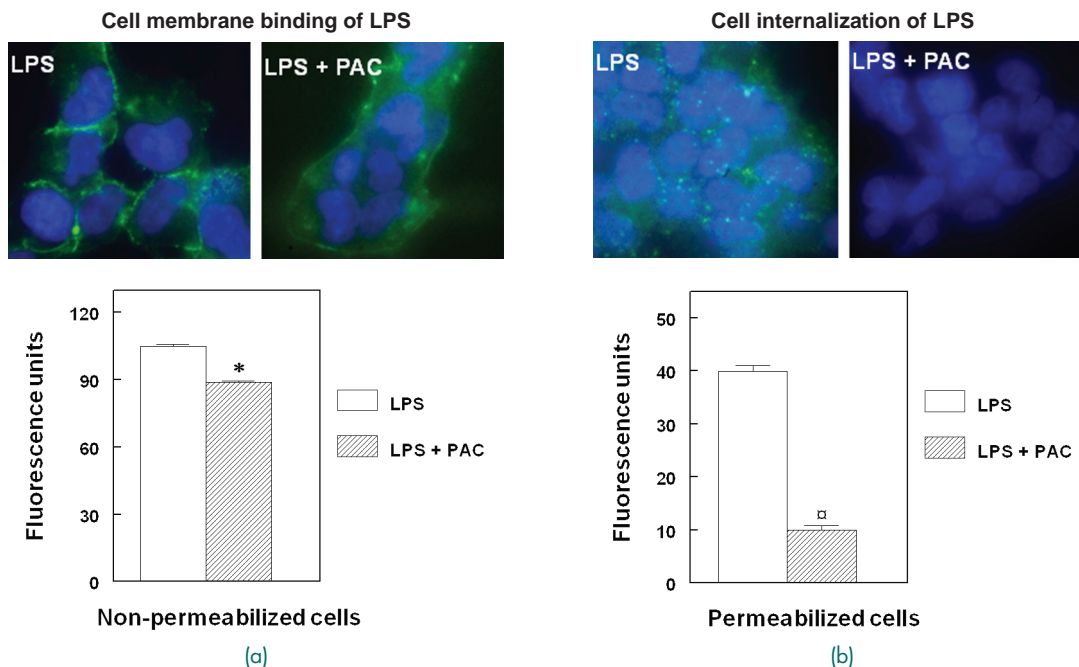


FIGURE 2

PACs slightly inhibit LPS binding to cell membranes and substantially inhibit cellular internalization of LPS. Cells expressing LPS receptors were incubated with LPS alone or with LPS plus cranberry PACs. LPS bound to the cell membrane (a) or internalized (b) was visualized using a fluorescein-conjugated antibody that binds to LPS (green). Cell nuclei are stained blue. (a) PACs slightly inhibit LPS binding to cells expressing LPS receptors on their surface. (b) PACs inhibit cell internalization of LPS. Symbols correspond to levels of significance relative to control (determined by Student's t-test): (*) $p < 0.1$ and (□) $p < 0.001$.

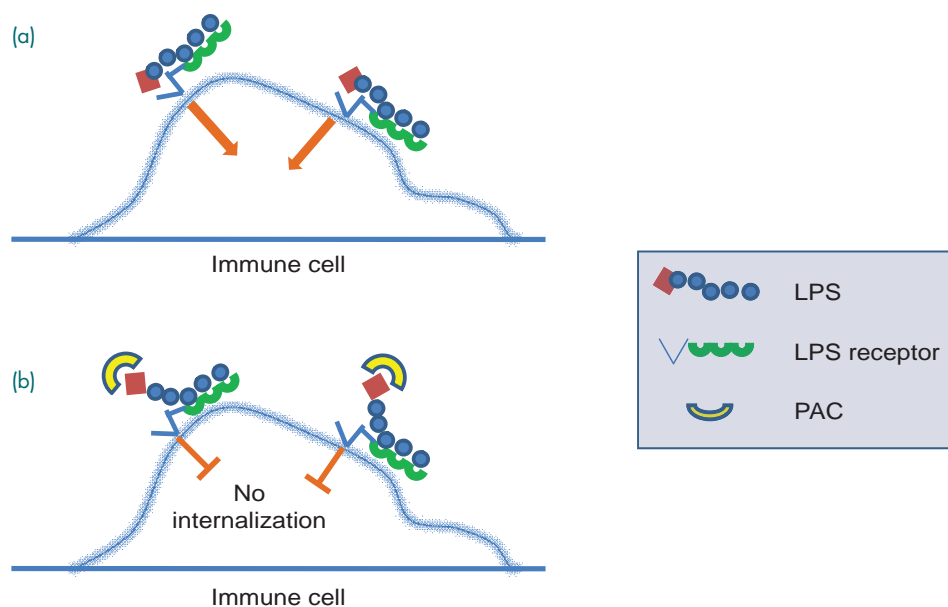
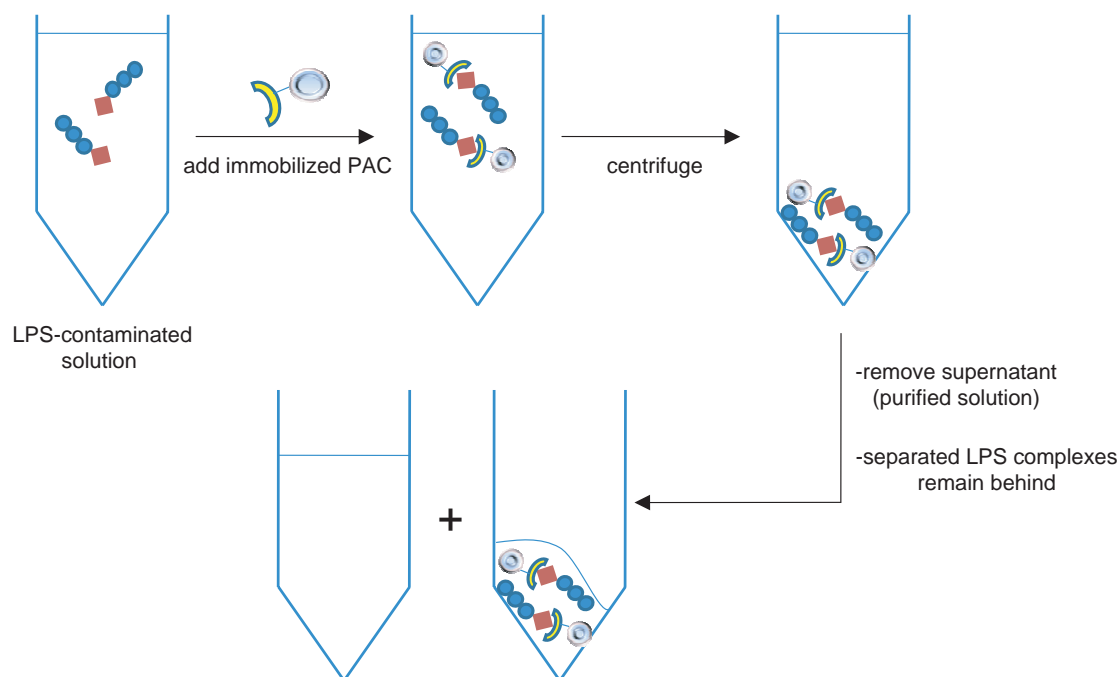


FIGURE 3

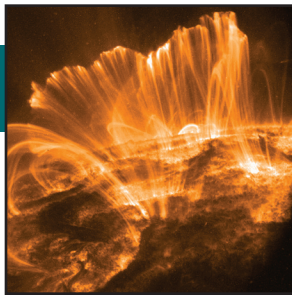
Mechanism of PACs' inhibition of LPS interaction with immune cells. (a) In the absence of PACs, LPS binds to its receptor and is efficiently internalized, where it promotes the inflammatory response. (b) In the presence of PACs, binding of LPS to its receptor is partially blocked. In this instance, LPS internalization is greatly inhibited, thereby inhibiting the inflammatory response.

**FIGURE 4**

Use of immobilized PACs for LPS removal and purification. PACs immobilized to solid supports are added to an LPS-containing solution. After complex formation, the LPS-PAC complexes are sedimented via centrifugation, leaving the purified solution in the supernatant. The purified solution is removed leaving behind the separated LPS-PAC complexes. PACs' LPS-binding activity can be used to purify LPS-contaminated solutions (e.g., potable water supplies, pharmaceutical preparations).

References

- ¹ S.D. Carrigan, G. Scott, and M. Tabrizian, "Toward Resolving the Challenges of Sepsis Diagnosis," *Clin. Chem.* **50**(8), 1301-1314 (2004).
- ² M. Caroff and D. Karibian, "Structure of Bacterial Lipopolysaccharides," *Carbohydr. Res.* **338**, 2431-2447 (2003).
- ³ J.B. Delehanty, B.J. Johnson, T.E. Hickey, T. Pons, and F.S. Ligler, "Binding and Neutralization of Lipopolysaccharides by Plant Proanthocyanidins," *J. Nat. Prod.* **70**(11), 1718-1724 (2007).
- ⁴ Y. Liu, M.A. Black, L. Caron, and T.A. Camesano, "Role of Cranberry Juice on Molecular-scale Surface Characteristics and Adhesion of *Escherichia coli*," *Biotechnol. Bioeng.* **93**, 297-305 (2006).
- ⁵ T. Shuto, K. Kato, Y. Mori, S. Viriyakosol, M. Oba, T. Furuta, T. Okiyonedo, H. Arima, M.A. Suico, and H. Kai, "Membrane-anchored CD14 is Required for LPS-induced TLR4 Endocytosis in TLR4/MD-2/CD14 Overexpressing CHO Cells," *Biochem. Biophys. Res. Commun.* **338**(3), 1402-1409 (2005).
- ⁶ H. Husebye, O. Halaas, H. Stenmark, G. Tunheim, O. Sandanger, B. Bogen, A. Brech, E. Latz, and T. Espevik, "Endocytic Pathways Regulate Toll-like Receptor 4 Signaling and Link Innate and Adaptive Immunity," *EMBO J.* **25**, 683-692 (2006). ★



Exploring Solar Flares with Gamma Rays and Neutrons

R. Murphy
Space Science Division

Gamma-ray and neutron emissions from solar flares carry information about the flaring process and conditions within the flaring magnetic loop. Extraction of this information from solar flare measurements requires an ion-acceleration, transport, and interaction model with parameters directly related to those physical processes. In this paper we describe such a magnetic-loop model. Each of the gamma-ray and neutron measurable quantities depends to varying degree on the parameters of the model. We describe these dependences and construct a self-consistent approach to the analysis of high-energy flare data that provides an optimum set of parameters. To illustrate this approach, we summarize the analysis of gamma-ray and neutron data obtained from the 1991 June 4 solar flare with the Oriented Scintillation Spectrometer Experiment (OSSE), a satellite-based instrument developed at NRL.

WHAT ARE SOLAR FLARES AND HOW DO WE LEARN ABOUT THEM?

Solar flares are explosions that occur in the atmosphere of the Sun leading to the emission of radiation covering the full range of the electromagnetic spectrum: radio, visible, UV, X-rays, and gamma rays. The energy released in a solar flare can be greater than 10^{32} ergs, enough to meet the energy demand of the United States for 100,000 years. This enormous amount of energy is dumped into the solar atmosphere in only a few tens of seconds. Flares are often associated with the escape of energetic particles (electrons, neutrons, protons, and heavier nuclei), mass ejections, and shock waves. As the shock waves move through interplanetary space, they also accelerate particles. At Earth, these various phenomena can disrupt radio communication, damage satellites and destabilize their orbits, cause failures in long-distance power lines, change the terrestrial magnetic field, and even endanger astronauts. The potential impact of such solar activity on DoD assets and enterprises is clear.

A solar flare is a stunning, violent, awe-inspiring event occurring on our nearest star, the Sun, an equally awe-inspiring object. What exactly *is* a flare? What is the mechanism that accelerates the energetic particles? How is the energy residing in the Sun's magnetic fields made available for this acceleration? What are the physical conditions at the flaring site and how do they change with time as the flare progresses? What is the connection between the energetic particles directly associated with the flare and the energetic particles seen in interplanetary space? Answering such questions would be reward enough, but with these answers we

may be able to predict the occurrence of a flare and its associated disruptions sufficiently early to allow measures to be taken to protect those DoD assets and enterprises.

The frequency of solar flares (along with other aspects of the Sun such as the number of sunspots) varies in an 11-year activity cycle related to the 22-year cycle of the reversal of the Sun's overall magnetic field. As of this writing (early 2008), we are at an activity minimum. This can be seen in Fig. 1, which shows the number of sunspots during the decay after the last activity maximum and predictions for the onset of the next. Surprisingly, some of the largest flares of previous cycles have occurred during the rising portions of the curves, before the maxima had been reached.

Because placing detectors in the hot flaring plasma at the Sun is impossible, solar flares can only be studied remotely via the various emissions they produce. The most easily observed component of flare emission is thermal radiation emitted by the hot plasma. But once the flare energy has been thermalized, most of the information about its initial release and about the subsequent physical processes associated with it are lost. Such information can be better obtained by studying the higher-energy X-ray and gamma-ray emissions produced when the electrons and ions directly accelerated by the energy release subsequently interact with the solar atmosphere. Flares can accelerate electrons to greater than 10 MeV and ions to greater than 1 GeV, corresponding to velocities very near the speed of light. By using such measurements, we seek to learn what specific acceleration process (or processes) is at work and what the physical conditions of the plasma are at the flare site.

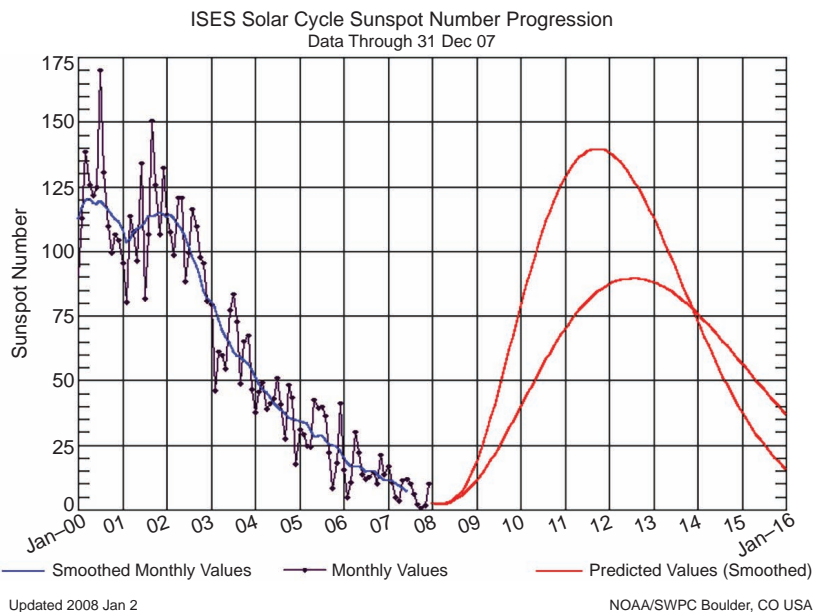


FIGURE 1
Recent sunspot numbers (2000–2007)
and predictions for the next activity
cycle (2008–2016).

Because X-ray and gamma-ray emissions are easily absorbed by the Earth's atmosphere, their detection requires flying instruments on high-altitude balloons or on satellites, such as the Oriented Scintillation Spectrometer Experiment (OSSE), the Solar Maximum Mission (SMM), the Reuven Ramaty High Energy Solar Spectroscopic Imager (RHESSI), and the Gamma Ray Large Area Space Telescope (GLAST). Such instruments allow the detailed study of flare photon spectra, bringing the power of spectroscopic analysis, a well-known, powerful tool at other wavelengths, to the study of gamma-ray emission from solar flares.

OSSE was designed and built at NRL and launched on NASA's Compton Gamma Ray Observatory (CGRO) in April 1991. Figure 2 shows CGRO being deployed into orbit by the space shuttle *Atlantis*. While its primary scientific goal was celestial, OSSE accomplished excellent observations of a number of solar flares. OSSE provided photon energy spectra from 50 keV to 10 MeV, and detection of gamma rays and neutrons above 10 MeV extended its ability to study solar flares. CGRO was de-orbited in June 2000. The SMM Gamma-Ray Spectrometer was designed and developed as a collaborative effort between the University of New Hampshire, the Max Planck Institute in Garching, Germany, and NRL. The instrument was designed to observe solar X-rays and gamma rays from 10 keV to 100 MeV; it maintained excellent performance throughout its mission from 1980 to 1989. SMM made significant contributions to both solar and celestial astronomy. RHESSI was designed and is operated by the Space Sciences Laboratory at the University of California at Berkeley. Launched in February 2002, RHESSI provides high-resolution spectroscopy and imaging of solar flares from about 3 keV to about 20

MeV. RHESSI is expected to operate throughout the onset of the next activity cycle. GLAST, launched in June 2008, is the next-generation high-energy gamma-ray observatory covering the photon energy range from 10 keV to more than 100 GeV. NRL was responsible for the design and development of the GLAST calorimeter. Intended for making observations of celestial gamma-ray sources, GLAST will also have excellent solar-flare capabilities.

HOW DOES THE ENERGY-RELEASE PROCESS REVEAL ITSELF?

The energy source for particle acceleration in solar flares is undoubtedly related to reconnection of magnetic fields in the corona, the low-density upper atmosphere of the Sun. The Sun's atmosphere is usually divided into three layers. The deepest and most dense layer is the 300-km-thick photosphere, which forms the visible "surface" of the Sun. The temperature of the photosphere decreases from about 6000 degrees Kelvin (K) at its bottom to a minimum of about 4000 K at its top. Above the photosphere is the chromosphere, with a thickness of about 10,000 km. The chromosphere is hotter than the photosphere, extending from the minimum of 4000 K to about 20,000 K where there is an abrupt change to the very hot corona (the region of this abrupt change is called the transition region). The corona extends millions of kilometers into space with temperatures exceeding a million degrees Kelvin.

Magnetic fields dominate the physical processes in the corona, and the field loop structures can be revealed by the bright, hot plasma trapped within them. This is shown by the Transition Region and Coronal Explorer (TRACE) image in Fig. 3(a) obtained at 171 Å, a wave-

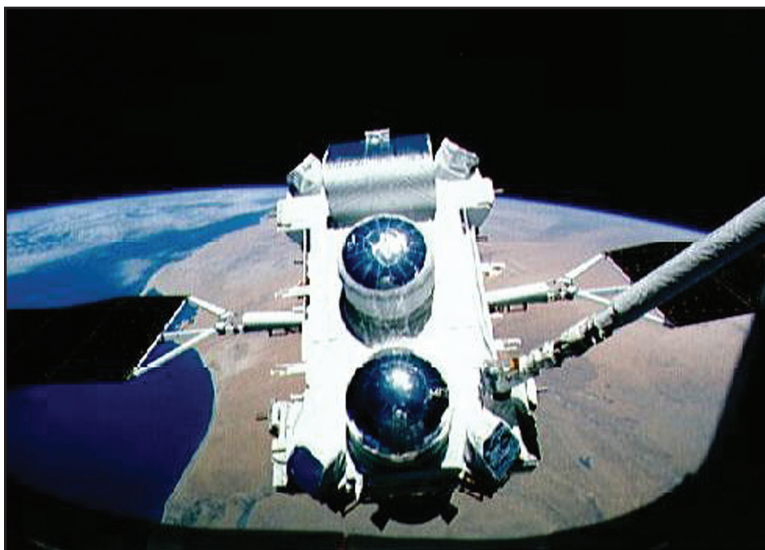


FIGURE 2
Deployment of the Compton Gamma Ray Observatory.

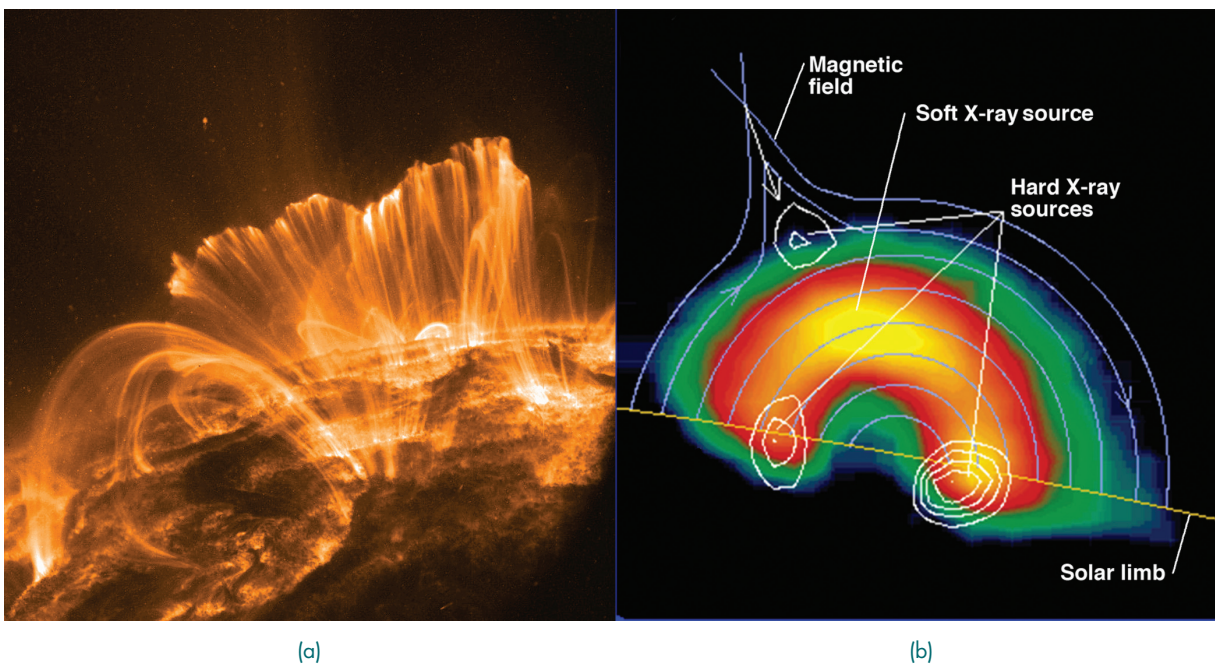


FIGURE 3
(a) TRACE image (171 \AA) of magnetic loops. (b) Yohkoh image of soft X-ray loop and hard X-ray footpoint and looptop emission.

length of light corresponding to a plasma temperature of about a million degrees Kelvin. Images of solar-flare X-ray emission show that such higher-energy emission is concentrated at the footpoints of magnetic loops (see Fig. 3(b)), implying that once the energetic particles are accelerated they are essentially trapped within a loop and interact at the higher densities associated with the footpoints. Acceleration probably occurs near the top of the loop where the density and the associated energy losses are lower, allowing for efficient acceleration. X-ray images of some flares (see Fig. 3(b)) show a third source of emission near the top of loops which may be associated with the acceleration process.

When flare-accelerated electrons interact with the solar atmosphere, they directly produce X- and gamma-ray continuum emission via bremsstrahlung, radiation that occurs when electrically charged electrons are deflected as they pass near electrically charged ambient nuclei. On the other hand, flare-accelerated ions undergo nuclear interactions with the ambient nuclei to produce excited and radioactive nuclei, neutrons, and pions (unstable elementary particles). Some of the neutrons can escape the Sun, but the other products remain trapped in the solar atmosphere and reveal themselves by subsequently producing observable gamma-ray emission via secondary processes. Except for the positron annihilation line (discussed below), gamma-ray emission from accelerated ions arises from nuclear interactions and so does not depend on the temperature or density of the ambient medium, freeing its interpretation from many of the uncertainties associated with atomic-line spectroscopy.

The measurable quantities associated with these various emissions (discussed in the following sections) allow us to learn about the flare process. They convey information about the accelerated ions responsible for their production and also about the physical conditions of the magnetic flare loop in which the particles transport from the acceleration site to the interaction region. Analyses of high-energy solar-flare emissions therefore offer the potential to learn about the structure and evolution of the flare environment in addition to particle acceleration.

Nuclear Deexcitation

An accelerated-ion interaction (for example, an accelerated proton interacting with ambient carbon) can produce a nucleus in one of its excited states which then promptly deexcites (for most nuclei, the lifetimes of excited states are less than 10^{-10} s). The transition produces a photon with energy equal to the energy difference between the two states. As this process is repeated during the course of a flare, gamma-ray lines at specific energies become visible in the spectrum.¹ Most deexcitation-line energies are from 1 to 8 MeV;

an example is the 4.439 MeV line that results when a carbon nucleus returns from its first excited state back to its ground state. Motivated by the early detection of solar-flare gamma-ray lines, the cross sections for production of the strongest deexcitation lines from solar flares were measured in the laboratory. Because these cross sections typically peak at a few tens of MeV, deexcitation lines are mostly produced when protons with energies from a few to about 20 MeV interact with ambient solar material.

Because the lifetimes of the excited states are so short, the recoiling nuclei do not lose appreciable energy before they deexcite, and so retain information about the energy and direction of the ion before interaction. This “memory” is then reflected by the precise energy of the emitted photon because it is Doppler-shifted from its rest energy. Studies of the line shapes that result from these Doppler shifts can therefore determine the angular distribution of the accelerated ions when they interacted to produce the excited nuclei. Lines resulting from interactions of the accelerated low-mass protons and alpha (α) particles with ambient nuclei heavier than He are “narrow” (with fractional widths of about 2% of the line energy) because the relatively low recoil velocity of the heavy nucleus results in minimal Doppler shifting of the photons. Heavy accelerated ions interacting with ambient H and He produce “broad” lines (with fractional widths of about 20%) because the heavy nucleus retains much of its initial velocity resulting in significant Doppler shifting.

The measurable quantities associated with deexcitation lines are (1) the time history of the emission, (2) the detailed shape and Doppler shift of the line, and (3) the relative yields of the various lines compared with other emissions. An example of a solar-flare gamma-ray count spectrum is shown in Fig. 4, the 1991 June 4 flare observed with OSSE. The nuclei responsible for the strongest deexcitation lines are noted. There are several lines from the most abundant elements in the solar atmosphere that potentially can be used in flare analyses. Also shown are the various components as determined by fitting the observed spectrum with spectra calculated with a numerical model: the narrow (red) and broad (green) deexcitation lines, and the electron bremsstrahlung (blue). Also shown are the neutron-capture line (dotted) and the positron (e^+) annihilation line (orange), discussed below.

Radioactive Nuclei and the Positron-Annihilation Line

Accelerated-ion interactions also create radioactive nuclei which decay into “daughter” nuclei according to their half-lives, which vary from fractions of a second to days. The decay product can be created in an excited state which again decays promptly, but the

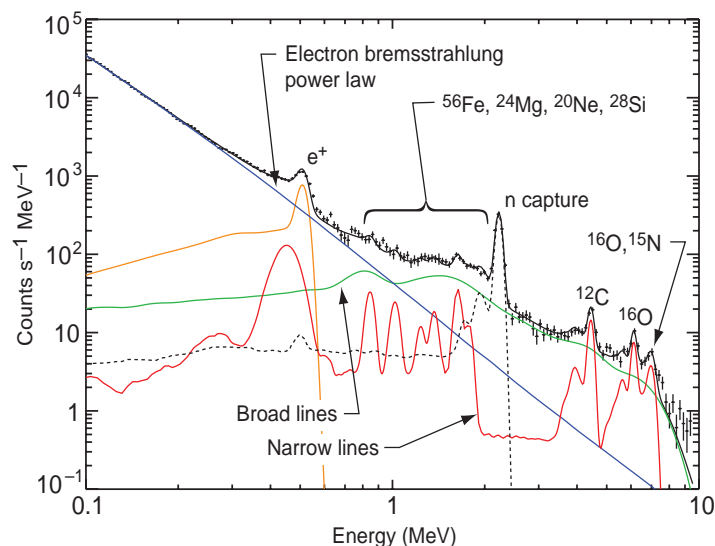


FIGURE 4
Solar-flare gamma-ray count spectrum of the 1991 June 4 solar flare observed with CGRO/OSSE.

appearance of the photon is still delayed relative to the initial nuclear reaction due to the radioactive half-life. Because they are delayed, the detectability of these lines may be enhanced since they appear after the bulk of the prompt emission has decayed away. They are also unique in that they are generally emitted after the recoil radioactive nucleus has had time to slow to thermal speeds, resulting in minimal Doppler shifting and a very narrow line. Because radioactive nuclei usually result from spallation reactions that break the target nuclei apart, their production cross sections generally have thresholds higher than those for deexcitation lines. The accelerated-ion energies are therefore somewhat higher. The measurable quantities associated with line production from radioactive nuclei are (1) the time history of the emission and (2) the yields of the various lines compared with the other emissions.

Many radioactive nuclei decay with the emission of a positron. The initial energies of the positrons are typically several hundred keV, much higher than the thermal energies of the ambient particles. The positrons then lose energy and eventually annihilate with electrons (both free electrons and bound electrons if any partially ionized atoms are present), either directly or through the formation of positronium (Ps), a bound electron-positron “atom.” Direct annihilation of a positron-electron pair at rest yields two photons, each of energy 511 keV (the rest mass of an electron or positron), producing a spectral line at 511 keV (see Fig. 4). If positronium is formed, the annihilation depends on the total spin wave function of the Ps and can result in either two 511 keV photons, producing a spectral line at 511 keV, or three photons with energies less than 511 keV, producing a continuum spectrum.

The annihilation process is complex, with the details depending strongly on the temperature, density, and ionization state of the ambient medium. These details determine the shape of the resulting annihilation line and the line/continuum ratio. The positron-annihilation line can therefore be used to probe the ambient conditions at the Sun where the positrons are annihilating. The annihilation line is unique in this, differing from deexcitation lines which, because they result directly from nuclear interactions, are independent of such ambient conditions. At 511 keV, the line energy is significantly lower than most of the deexcitation lines and is more easily scattered as the photons escape through the solar atmosphere, attenuating the line. The measurable quantities associated with the annihilation line are (1) the time history of the emission, (2) the detailed shape of the line, (3) the ratio of the line and Ps continuum yields, and (4) the yield of the line compared with the other emissions.

Neutrons

Ion interactions also produce neutrons which can be observed both directly and indirectly. Because neutrons are uncharged, those initially moving up can escape from the Sun and, if they survive the transit to Earth (neutrons free of the nucleus have a half-life of about 10 minutes), can be directly detected with instruments in orbit. Events with high-energy neutrons >200 MeV can even be detected by monitors on the Earth’s surface.

Neutrons initially moving down into the Sun may be indirectly detected because they can be captured on ambient hydrogen to produce deuterium with its

binding energy appearing as a strong gamma-ray line at 2.223 MeV (see Fig. 4). The captures occur deep in the photosphere where the density is high enough so that the time required to be captured is significantly less than the neutron lifetime. Since the probability for elastic scattering is much larger than the probability for capture, most of the neutrons thermalize first, producing a very narrow line and causing a delay in the formation of the capture photon relative to neutron formation. The ambient $^3\text{He}/\text{H}$ ratio has a strong effect on both the neutron-capture line yield and its delay because non-radiative reactions with ^3He compete with the line-producing captures on H.

The yields of the neutron-capture line and the escaping neutrons depend strongly on the angular distribution of the neutrons which in turn depends on the angular distribution of the interacting ions. Neutron production involves interacting-ion energies somewhat higher than those producing excited or radioactive nuclei, extending to 100 MeV. Escaping neutrons surviving to Earth are produced by even higher-energy ions, more than several hundred MeV. The measurable quantities associated with neutron production are (1) the time history of the neutron-capture line, (2) the time-dependent energy spectra of the neutrons arriving at the Earth, and (3) the neutron and neutron-capture line yields compared to the other emissions.

Pions

Neutral and charged pions are mesons produced in interactions of the highest-energy ions (at hundreds of MeV). Neutral pions decay (mean lifetime of 2.6×10^{-8} s) directly into two 67.5 MeV gamma rays. Charged pions decay (mean lifetime of 0.84×10^{-16} s) via muons into positrons and electrons which produce bremsstrahlung gamma rays. Positrons from positively charged pions also produce annihilation radiation, both continuum when the decay positrons annihilate in flight and 511 keV line emission when they annihilate near rest. Because the high-energy ions that produce pions can penetrate deep into the solar atmosphere, the low-energy annihilation photons will be scattered escaping the Sun, attenuating the line. The measurable quantities associated with pion-decay emission are (1) the time history of the emission, (2) the spectral shape of the radiation, and (3) its yield compared to the other emissions.

HOW IS INFORMATION EXTRACTED FROM SOLAR FLARE MEASUREMENTS?

A model is typically required to understand a complex physical system and to make predictions of its behavior, with the model described by a set of parameters representing the properties of the system.

A solar flare is a very complex system and to extract information about the flare process from high-energy flare measurements, we have developed a flare-loop transport and interaction model. The model incorporates those aspects of transport and interaction of flare-accelerated ions in a loop that are most important for gamma-ray and neutron production. It reflects the evolution of our understanding of the flare process over several decades since the foundations of high-energy flare interactions were established in a series of papers by R. Ramaty, R. Lingenfelter, and B. Kozlovsky. The energy- and angle-dependent cross sections for the most important nuclear reactions in solar flares have been measured in the laboratory. Information about the remaining reactions has been obtained with theoretical nuclear-reaction computer codes such as TALYS.

The magnetic-loop model is represented by a group of computer codes and is described by a set of parameters (discussed below) related directly to the physical processes and conditions at the flare site. For a given set of choices for these parameters, the model provides expected values for the measurable quantities associated with gamma rays and neutrons, which can be compared with observations. The parameter values may then be adjusted to give the best agreement of prediction with measurement among all the measurable quantities. But because many of the measurable quantities depend on the same parameters, deriving well-constrained values for those parameters is challenging. Early analyses often did not take these complicated inter-dependences into account in a systematic way, addressing only a limited number of parameters.

With the flare-loop model, all of these inter-dependences can be systematically addressed by identifying all relevant parameters, showing how the nature of the nuclear interactions depend on them and how the various measurable quantities are subsequently affected. With this understanding, we have constructed a comprehensive, self-consistent approach to the analysis of flare data. Success of the approach, however, does require that the available flare measurements cover a sufficiently broad range of the measurable quantities.

The Flare-Loop Transport and Interaction Model

Figure 5(a) shows a schematic diagram of a flaring loop, directly reflecting the flare-loop geometry as observed (compare with Fig. 3(b)). Figure 5(b) shows the corresponding flare loop model. The model consists of a semicircular coronal portion of length L and two straight portions extending vertically from the transition region through the chromosphere into the photosphere. Below the transition region, the magnetic field strength B is assumed proportional to a power δ of the pressure. Such a converging magnetic field can result in mirroring of accelerated particles. Turbulence in

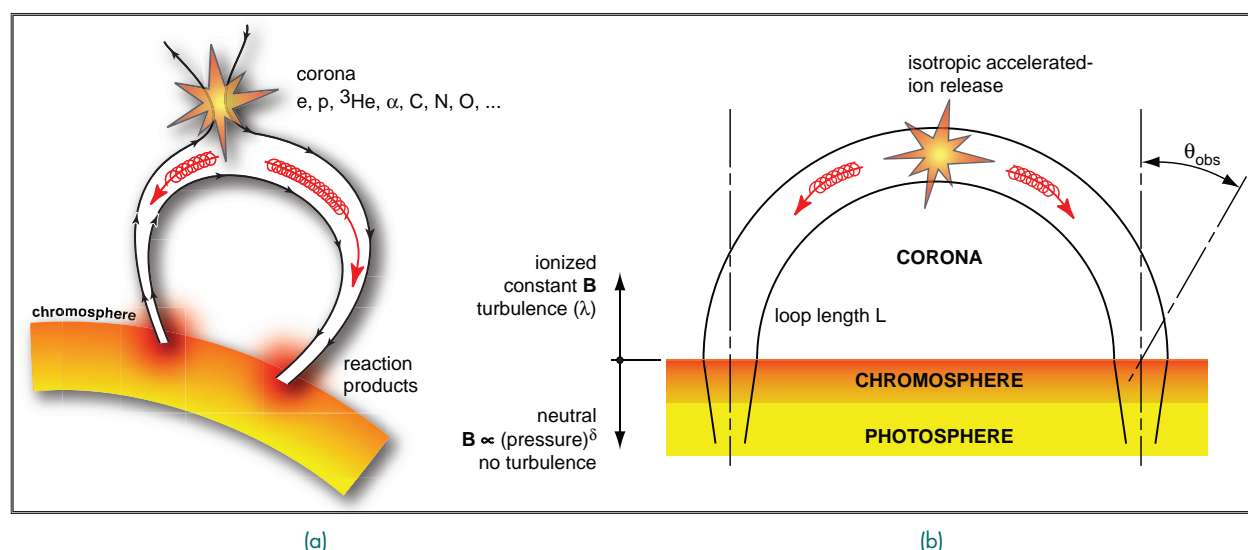


FIGURE 5
(a) flare loop schematic; (b) loop model.

the loop can cause pitch-angle scattering (PAS) which is characterized by λ , the mean free path required for an arbitrary initial angular distribution to relax to an isotropic distribution. We assume a particular density height profile $n(h)$ and ambient elemental composition for the solar atmosphere. Accelerated ions are released isotropically at the top of the loop with an assumed elemental composition and kinetic-energy spectrum (typically, a power law in energy with index s). The heliocentric angle of the flare site on the solar disc, θ_{obs} , is the angle between the normal to the solar surface at the flare and the direction to the Earth.

Using this model we have explored the dependence of the measurable quantities on the parameters. The properties of an interacting accelerated ion that most significantly affect the properties of the subsequent gamma-ray and neutron emissions are (1) the time of the interaction after release from the acceleration region, (2) the ion direction of motion at interaction, and (3) the ion kinetic energy at interaction.

Interaction Time Scale

In the absence of magnetic convergence ($\delta = 0$), ions do not mirror and the nuclear interaction time history depends only on the transit time down the loop (which depends on the loop length L) and the energy loss rate in the atmosphere (which depends on the density n). In the presence of magnetic convergence ($\delta \neq 0$), ions with initial pitch angles lying close to the loop axis also do not mirror (they are within the “loss cone”) and behave similarly. Ions outside the loss cone mirror and lose energy much more slowly as they repeatedly traverse the low-density corona. Interactions of these ions thus occur on longer time scales, with the

time scale increasing with increasing convergence δ . Turbulence in the loop causes particles to be scattered into the loss cone, continuously repopulating it. As a result, with more scattering (smaller λ) the nuclear interaction rate increases at early times and correspondingly decreases at later times.

Interacting-Ion Angular Distribution

In the absence of magnetic convergence ($\delta = 0$), there is no mirroring and the angular distribution of the interacting ions will be downward isotropic regardless of the level of PAS. In the presence of magnetic convergence ($\delta \neq 0$) but no PAS, most ions mirror and the interactions occur mostly at the ion mirror points where the density is greatest. Thus, most ions are moving parallel to the solar surface when they interact, in a “fan beam” angular distribution. Any downward contribution from those ions that do not mirror becomes even less important as δ increases. By continuously repopulating the loss cone, the effect of PAS is to produce more interactions involving downward-directed ions. This can be seen in Fig. 6, showing angular distributions for a moderate amount of magnetic convergence ($\delta = 0.2$) and three levels of PAS. Here, $\mu = \cos(\theta)$ where θ is the angle between the normal to the solar surface and the direction of the ion. With no PAS, the distribution is peaked at $\theta = 90^\circ$ ($\mu = 0$), a fan-beam distribution, with some downward-directed interactions ($\mu < 0$) from ions originally in the loss cone. As PAS increases (λ decreases), the distribution becomes more downward directed. A consequence of the angular distribution is that when it is more downward-directed, the interactions occur deeper in the solar atmosphere.

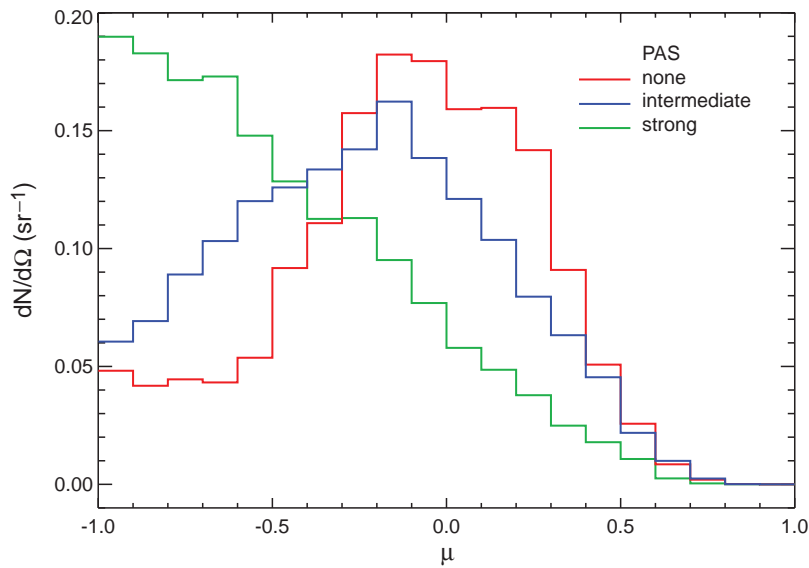


FIGURE 6
Angular distribution (reactions per steradian) of the interacting ions for $\delta = 0.2$ and several values of pitch angle scattering (PAS).

Ion Energy at Interaction

The energies of the accelerated ions at interaction are mostly determined by the combination of the accelerated-ion spectral steepness (steeply falling spectra are referred to as “soft” and less steeply falling spectra as “hard”) and the ion-energy dependence of the specific production cross section. On average, harder accelerated-ion spectra result in higher interacting-ion energies. However, cross sections involving energetic α particles typically have lower threshold energies, so increasing the ratio of the number of accelerated α particles to protons (α/p) shifts the interacting-ion energies lower.

The Dependence of the Measurable Quantities on the Loop Model Parameters

Table 1 summarizes the measurable quantities and indicates those loop parameters that affect each. In the following we discuss some of the most important of these parameter dependences. We distinguish two types of parameters: (1) acceleration parameters describing aspects of the accelerated ions and (2) physical parameters describing aspects of transport within the loop.

Narrow deexcitation-line yields and ratios depend on (1) the steepness of the accelerated-ion spectrum (here assumed a power law with index s) because of the different ion-energy dependences of their line-production cross sections, (2) the ratio of the number of accelerated α particles to protons (α/p) since both species contribute to narrow lines, and, most directly, (3) the relative abundances of the target elements in the solar atmosphere. The shape and Doppler shift of the lines depend on (1) the α/p ratio since the heavier α particles produce higher recoil velocities for the excited nucleus, (2) the ion spectrum since a harder

spectrum has more high-energy ions producing higher recoil velocities, and (3) the interacting-ion angular distribution, most directly determined by magnetic convergence (δ) and PAS (λ). Since the interacting-ion angular distribution is typically not isotropic, the location of the flare on the Sun (θ_{obs}) will also affect the observed line shape. The time history will depend on the loop length L and on the amount of mirroring (through δ and λ).

The neutron-capture line yield depends on (1) the accelerated-ion spectral index s , (2) the α/p ratio, (3) the interacting-ion angular distribution (through δ and λ) since neutrons must be moving downward to be efficiently captured, and (4) the photospheric abundance of ^3He . Because the captures occur deep in the photosphere, the capture photons can be strongly scattered, resulting in attenuation of the line, especially for flares near the solar limb where the path-length through the solar atmosphere is large. The flare location θ_{obs} is thus an important parameter. The time history depends on (1) the interacting-ion angular distribution (through δ and λ), (2) the photospheric abundance of ^3He , and (3) the flare location θ_{obs} .

Similar to the neutron-capture line, the time- and energy-dependent energy spectra of the neutrons escaping the Sun and arriving at Earth depend on (1) the accelerated-ion spectral index s , (2) the α/p ratio, (3) the interacting-ion angular distribution (through δ and λ), (4) the loop length L , and (5) the flare location θ_{obs} .

The yield of the annihilation line (which follows from positron production), depends on (1) the accelerated-ion spectral index s , (2) the α/p ratio, and, since the line can be more easily scattered than the deexcitation lines, on (3) the depth of the positron production (through δ and λ). Because of this scattering, the yield also depends on (4) the flare location θ_{obs} . The detailed

TABLE 1 — Measurable Quantities of High-Energy Flare Emissions and the Loop Model Parameters that Affect Them

Measurable Quantity	Acceleration Parameter	Physical Parameter
narrow deexcitation line fluences and ratios	$\alpha/p, s$	ambient abundances
narrow deexcitation line shift and shape	$\alpha/p, s$	$\delta, \lambda, \theta_{\text{obs}}, n(h)$
narrow deexcitation line time history	$a_{\text{ion}}(t)$	$\delta, \lambda, L, n(h)$
neutron-capture line fluence	$\alpha/p, s$	$\delta, \lambda, \theta_{\text{obs}}, n(h)$ ambient ${}^3\text{He}/\text{H}$
neutron-capture line time history	$a_{\text{ion}}(t), \alpha/p, s$	$\delta, \lambda, \theta_{\text{obs}}, L, n(h)$ ambient ${}^3\text{He}/\text{H}$
neutron fluence at Earth	$\alpha/p, s$	$\delta, \lambda, \theta_{\text{obs}}, n(h)$
neutron arrival time history at Earth	$a_{\text{ion}}(t), \alpha/p, s$	$\delta, \lambda, \theta_{\text{obs}}, L, n(h)$
511 keV line fluence	$\alpha/p, s, {}^3\text{He}/{}^4\text{He}$ acc. abundances	$\delta, \lambda, \theta_{\text{obs}}, n(h), T, X$ ambient abundances
511 keV line shape and continuum	$\alpha/p, {}^3\text{He}/{}^4\text{He}, s$	$\delta, \lambda, \theta_{\text{obs}}, n(h), T, X$
511 keV line time history	$a_{\text{ion}}(t), \alpha/p, s$ acc. abundances	$\delta, \lambda, \theta_{\text{obs}}, L, n(h), X$
pion-decay radiation yield	$\alpha/p, s$	ambient abundances
pion-decay radiation spectral shape	$\alpha/p, s$	$\delta, \lambda, \theta_{\text{obs}}, n(h)$
pion-decay radiation time history	$a_{\text{ion}}(t)$	$\delta, \lambda, L, n(h)$
images	—	L, θ_{obs}

shape of the line depends on the annihilation process which, in turn, depends on the density (n), temperature (T), and ionization state (X) of the ambient medium.

The yield and spectral shape of pion-decay radiation depends on (1) the accelerated-ion spectral index s , (2) the α/p ratio, and (3) the interacting-ion angular distribution (through δ and λ).

Analysis Algorithm for Solar-Flare Gamma-Ray and Neutron Data

From Table 1 and the above discussion we see that while there are a large number of quantities that can be measured, there are also a large number of parameters to be determined. In addition, each of the measurable quantities can depend on several parameters. Restricting an analysis to one or a small subset of the measurable quantities can result in parameter estimates that may be inconsistent with estimates derived from analysis of other measurable quantities. And if the effect of all of the relevant parameters are not properly taken into account, the uncertainties can be underestimated. A reliable analysis must utilize as many measurable quantities as possible to determine as many parameters as possible. But because of the many inter-dependences, this can be quite challenging, and additional assumptions may still be required to make progress in constraining the parameters.

We have developed a data-analysis algorithm that provides the approach and analysis steps necessary for a comprehensive analysis of solar-flare gamma-ray line and neutron data.^{1,2,3} The guiding principle of the algorithm is to first consider those measurable quantities that depend on only one or two parameters and then, using those parameter estimates, proceed to other measurables that have more complicated dependences. To illustrate the procedure, we summarize some of the results from our recent analysis of the high-energy flare data available for the 1991 June 4 flare observed with OSSE (among other instruments). The June 4 flare remains unique for its breadth of available high-energy emission measurements. In that analysis, we established well-constrained values for the parameters and showed that the loop model can account for the wide variety of measurements available for this flare with reasonable values for the parameters.

In June 1991, an active region rotated onto the solar disk and produced some of the largest flares ever recorded. The active region first appeared at the east limb on June 1 and produced an intense flare. The peak of this flare was missed by the CGRO instruments due to a routine shut-down. As there was a high probability for subsequent intense flares, a solar Target of Opportunity was declared and OSSE stopped observing its current celestial target and re-oriented to the Sun. On

June 4, a second intense flare occurred while OSSE was viewing the Sun. The flare was one of the most powerful nuclear gamma-ray line flares observed to date; most instruments, from the soft X-ray to the gamma-ray bands, saturated at its peak. Energetic particles from the flare were observed in interplanetary space by the Ulysses EPAC experiment, GOES, and IMP-8 platforms. In the visible light of $H\alpha$, the flare was located at N30E70, corresponding to a heliocentric angle θ_{obs} of about 74° .

We began the analysis with the parameter that is most directly established, the size of the flare loop determined from white-light images of the flare. (Ideally, images of gamma-ray emission loop footpoints, such as obtained with RHESSI for more recent flares, would be used.) We assume the white-light patches in the images to be footpoints where the ions interact, implying loop lengths from 11,500 km to 65,000 km, depending on which pair of patches is assumed to be associated with the loop producing the gamma rays.

The next parameter to be determined was the accelerated α/p ratio. The most direct measure of α/p is the measured fluence ratio of the 0.45 MeV deexcitation-line complex (produced exclusively by accelerated α particles) and a narrow line such as the 4.439 MeV line of C. However, this ratio also depends on the accelerated-ion spectral index s . The spectral index can be determined from the measured fluence ratio of the 6.129 MeV O and 1.634 MeV Ne lines, but this ratio also depends on α/p . We therefore simultaneously determined α/p and s by calculating values of the two fluence ratios for a range of assumed values for α/p and s and comparing them with measured fluence ratios. This provided a confidence region for the two parameters: the accelerated α/p ratio was at least 0.4 (considerably larger than the value of 0.03 found in the corona) and the spectral index s was 3.9 ± 0.2 (similar to the average value of ~ 4.2 found from analyses of SMM flares).

With α/p and s now determined, we next constrained δ and λ using the measured Doppler shift of the 4.439 MeV C line. Unfortunately, Doppler shifts from flares such as this located nearer the limb than disk center are minimal, and the resulting constraint was not useful. However, combining it with the δ - λ constraint obtained from the time history of deexcitation lines (using our already-determined value for the loop length L), we obtained a well-constrained confidence region for the two parameters. We found that convergence of the magnetic field was required and that turbulence was present in the loop.

Finally, using all of the parameter values determined so far, we calculated neutron spectra arriving at Earth and compared them with neutron count rates

obtained with OSSE. We found that the number of neutrons arriving at Earth was over-predicted, especially at early times. This can be seen in Fig. 7 comparing the measured (data points) and predicted (green curve) neutron count rates. Neutrons arriving early are higher-energy neutrons produced by high-energy accelerated ions. Reducing the number of high-energy neutrons relative to low-energy neutrons can be achieved if the accelerated-particle spectrum steepens with energy, as long as this does not affect the other measurable quantities previously analyzed. This is possible since those emissions are produced by accelerated ions with lower energies than the ions producing the neutrons escaping into space and surviving to Earth. We also show in Fig. 7 (red curve) the predicted neutron arrival time history calculated with a cutoff ion energy $E_c = 125$ MeV. We confirmed that such a cutoff did not affect the other calculated quantities.

DISCUSSION

This article presents our model for gamma-ray and neutron production by flare-accelerated ions in a magnetic loop, with model parameters directly related to the physical processes and conditions at the flare site. With this model, all of the measurable quantities associated with high-energy flare emission can be calculated, and comparison of model predictions with measurements provides constraints on the parameters. But the dependences of the measurable quantities on the parameters is complex and obtaining

parameter constraints can be difficult. We developed a flare-analysis algorithm that allows, for the first time, a comprehensive analysis of all measurable quantities. The algorithm considers first those measurable quantities that depend on only one or two parameters and then, with those parameter estimates, proceeds to other observables that have more complicated dependences. Reliable determination of all of the parameters requires that the observations cover a sufficiently wide range of the measurable quantities. To illustrate the procedure, we summarized our analysis of the 1991 June 4 flare, remarkable for its range of high-energy emission measurements.

The analysis procedure can be applied to other flares having a similarly wide range of measurable quantities, and we look forward to applying it to flare data obtained with GLAST as the new activity cycle develops. With the extended photon-energy range of GLAST, we will be able to expand our studies to the highest accelerated-ion energies. As our understanding of solar flares improves, we will be nearer the goal of predicting solar activity and preventing disruptions in our increasingly technology-dependent lives and endeavors.

ACKNOWLEDGMENTS

This work is built on many years of research by many investigators, including R. Ramaty, B. Kozlovsky, R. Lingenfelter, G.H. Share, and X.-M. Hua.

[Sponsored by NASA and ONR]

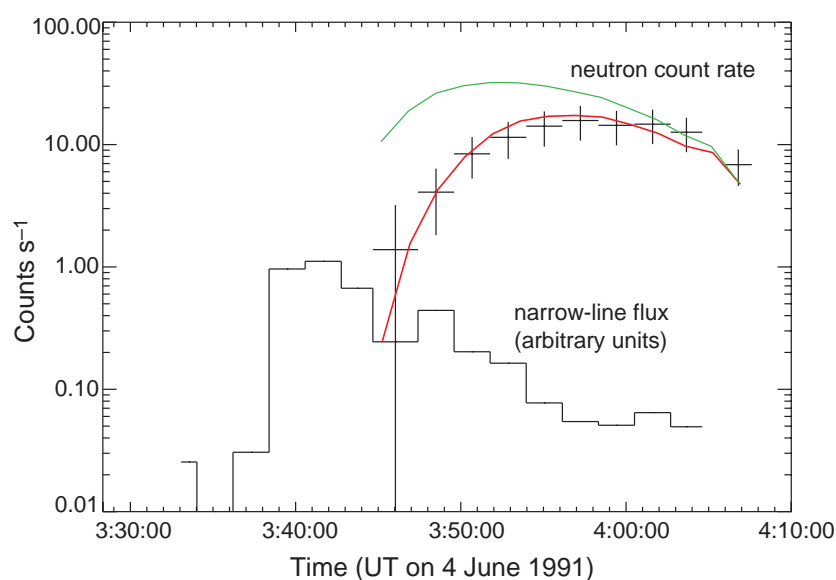
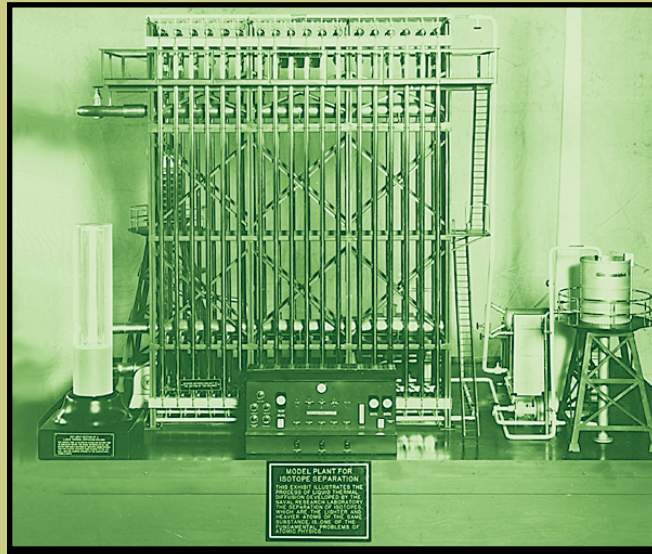


FIGURE 7

Comparison of the neutron count rate time history measured with OSSE from the June 4 flare with calculated count rate time histories. The green curve is for an unbroken power-law accelerated-ion spectrum and the red curve is for a spectrum cut off at $E_c = 125$ MeV. Also shown is the time history of the narrow deexcitation line flux (histogram).

References

- ¹ R. Ramaty, B. Kozlovsky, and R.E. Lingenfelter, "Nuclear Gamma-Rays from Energetic Particle Interactions," *Astrophysical Journal Supplement Series* **40**, 487-526 (1979).
- ² B. Kozlovsky, R.J. Murphy, and R. Ramaty, "Nuclear Deexcitation Gamma-Ray Lines from Accelerated Particle Interactions," *Astrophysical Journal Supplement Series* **141**, 523-541 (2002).
- ³ R.J. Murphy, B. Kozlovsky, G.H. Share, X.-M. Hua, and R.E. Lingenfelter, "Using Gamma-Ray and Neutron Emission to Determine Solar Flare Accelerated Particle Spectra and Composition and the Conditions within the Flare Magnetic Loop," *Astrophysical Journal Supplement Series* **168**, 167-194 (2007). ★



Liquid Thermal Diffusion Process (1939-1944)

A crucial step in the development of the atomic bomb was the separation of uranium isotopes. This was first accomplished in any appreciable quantities by using the liquid thermal diffusion process invented by Philip Abelson, who had transferred to NRL from the Carnegie Institution in order to develop the process. This became one of the Manhattan Project's four methods of obtaining enriched uranium. The Project's S-50 uranium enrichment plant in Oak Ridge, Tennessee, was built in 1944 to model NRL's plant.

123

Underwater Acoustic Communications for Bottom-Mounted Sensor Networks

P.J. Gendron

125

Environmental Acoustic Variability Characterization for Adaptive Sampling

J.P. Fabre, C. Rowley, G. Jacobs, E. Coelho, C. Bishop, X. Hong, and J. Cummings

Underwater Acoustic Communications for Bottom-Mounted Sensor Networks

P.J. Gendron
Acoustics Division

Introduction: The U.S. Navy's SEA POWER 21 FORCEnet vision demands the development of undersea sensing systems that can provide the warfighter with accurate and rapid awareness of the battlespace environment. To this end, undersea sensor networks in shallow water environments will be required to act as defensive fields and barriers in the protection of American shores, Navy assets, and sea bases.¹ The Deployable Autonomous Distributed System (DADS) is such a network, tailored for the purpose of antisubmarine warfare (ASW). Equipped with acoustic and electromagnetic sensors coupled to robust data fusion schemes, DADS automates the reduction of sensor data to useful information, thereby greatly assisting decision-making personnel to ensure that enemy submarines are kept at a distance from friendly forces.²

In support of underwater sensor networks, the Naval Research Laboratory is developing accurate communication receiver algorithms for the high-frequency, shallow-water acoustic channel. These algorithms support phase coherent communications and are suitable for long-endurance battery-powered systems. Reported here is a channel estimation based decision directed (CE-DD) algorithm for the demodulation of acoustic transmissions between bottom-mounted sensors. This algorithm has been tested on high-frequency experimental data collected recently in St. Margaret's Bay, Nova Scotia, during the 2006 Underwater Networking (Unet06) experiment and in the Gulf of Mexico, Florida, during AUVFest/Unet07 demonstrations. These tests were conducted in collaboration with Defense Research Development Canada (DRDC) as part of The Technical Cooperation Program (TTCP) Maritime Systems Group Technical Panel 9 (MAR

TP-9) sanctioned efforts. The results demonstrate that allowable rates are fundamentally linked to environmental conditions such as surface conditions, water depth, sound speed profile, and seabed properties.

Reduced Computation Channel Estimation Based Receiver Algorithm: The NRL-developed algorithm is based on a block coherent approximation of the acoustic response function and achieves computational reductions by approximating matrix inversions with conjugate gradient iterations.³ This approach offers computationally scalable processing, providing a more judicious focus of computational resources.⁴ Figure 1 is a simplified block diagram of the CE-DD algorithm for bottom-mounted, limited-aperture applications. The algorithm's adaptive filtering computations maximally exploit FFT computational methods to solve the block Toeplitz system associated with approximating a time-varying channel as coherent over short finite duration blocks.

Performance of the CE-DD Algorithm: The algorithm has been tested on ocean acoustic data sets at 44 kHz center frequency in signaling experiments associated with TTCP-MAR TP-9 sanctioned undersea networking demonstrations. The Unet06 experiment took place in St. Margaret's Bay in June 2006 in 70 m of water. The sound speed profile was downward refracting and the sediment bottom was soft and silty. The Unet07 experiment took place in June 2007 at Panama City, Florida, in the Gulf of Mexico in 20 m of water exhibiting very close to isovelocity sound speed; the bottom was sandy. In both experiments the sea surface was quite dynamic with significant wave height greater than 1 m. Figure 2 gives a representative picture of the performance of the algorithm at approximately 600 m range with 6-phone reception in St. Margaret's Bay and at 400 m range with 8-phone reception in the Gulf of Mexico. In both cases SNR was over 15 dB. The significant impact of water depth, sound speed, and sea floor

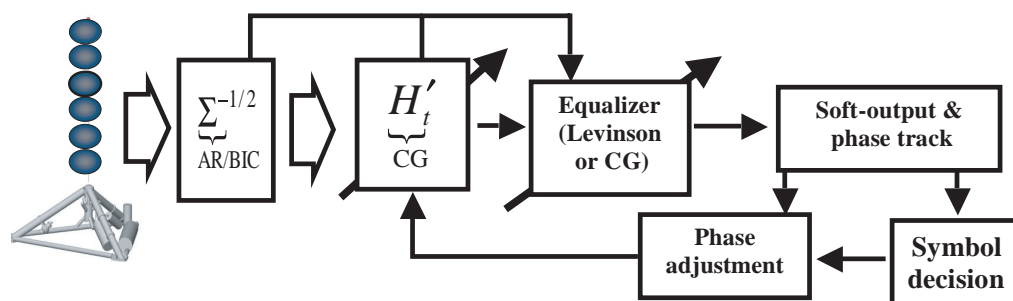
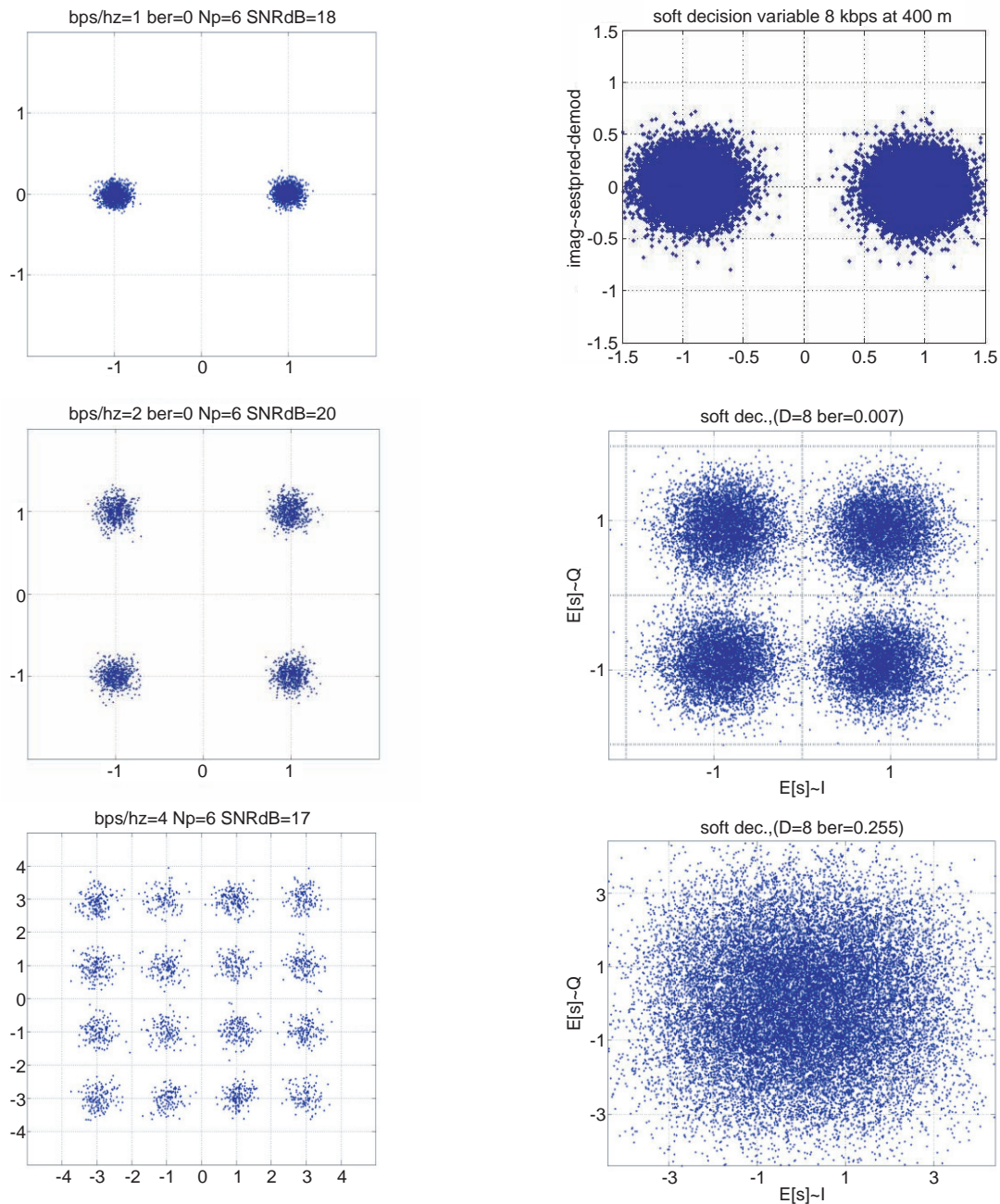


FIGURE 1
CE-DD algorithm. An equalizer on the single channel is constructed from the noise statistics and the estimated channel response functions across the array. The equalized stream is then used to make symbol and motion induced phase correction estimates.

**FIGURE 2**

Performance of the CE-DD algorithm in terms of estimated output constellation scatter plots. To the left, St. Margaret's Bay environment at 44 kHz and approximately 600 m range. To the right, Gulf of Mexico environment at approximately 400 m range. Bit densities range from 1 bps/Hz (bpsk) to 4 bps/Hz. The algorithm can support 4 bps/Hz in the downward refracting sound speed with the soft bottom of St. Margaret's Bay. Surface conditions at the two sites were similar.

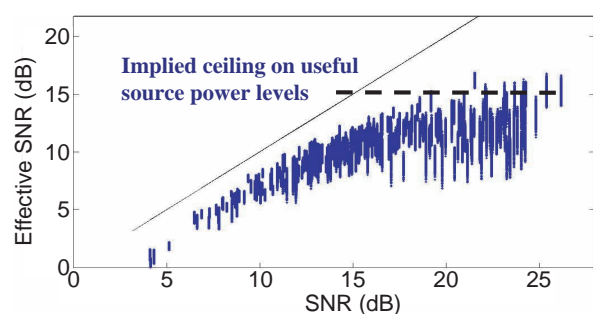


FIGURE 3

Effective SNR, incorporating the self-noise associated with channel estimation variance, as a function of SNR aggregated over all 8 (1.8 m aperture) hydrophones for the 44 kHz St. Margaret's Bay acoustic communications experiment. It is noticed that there is a ceiling on useful power levels of approximately 17 dB.

properties presents a stark contrast between these two environments when surface conditions are similar. It is demonstrated that 1.8 meters of aperture can support 4 bps/Hz signaling quite well in the more benign St. Margaret's Bay where acoustic paths are naturally refracted away from the dynamic surface. Such rates are unsupportable in the harder bottom isovelocity channel of the Gulf of Mexico. The 2 bps/Hz transmission represents a 16 kbps communication rate and at 600 m corresponds to over 8 kbps-km. Likewise the 4 bps/Hz represent a 16 kbps-km throughput.

Effects of Limited Channel Temporal Coherence:

Figure 3 summarizes the impact of channel estimation errors for St. Margaret's Bay in terms of an effective signal-to-noise ratio. The effective signal-to-noise ratio combines the ambient whitened acoustic noise power with a self-noise that scales with both channel estimation variance and acoustic power for the source signal itself.⁵ This statistic helps quantify the impact of environmental factors on receiver performance. The effective signal-to-noise ratio provides a measure of the maximum useful source levels for a given environment. In this case it is clear that signaling with received levels above 17 dB leads to no net improvement in performance and should be avoided.

Summary: The Naval Research Laboratory has developed adaptive filtering methods in support of high-rate high-frequency underwater acoustic communications for bottom-mounted sensors. These methods are accurate and are amenable to scaleable computational schemes.⁴ These algorithms have been tested in at-sea conditions from bottom-mounted configurations supporting data rates up to 4 bps/Hz at ranges of up to 1 km at received SNRs of 17 dB in suitable environments.⁵ These methods are being advanced for use in bottom-mounted sensor networks that must

operate on a limited power budget in diverse shallow water environments that exhibit a range of multipath spread and path-dependent temporal coherence.⁴

Acknowledgments: Thanks to Garry Heard of DRDC for indispensable experimental collaborations during TTCP-MAR TP9 sanctioned Unet06 and AUVFest07/Unet07 demonstrations.

[Sponsored by ONR]

References

- ¹J.A. Rice, "Enabling Undersea ForceNet with Seaweb Acoustic Networks," *SSC San Diego Biennial Review 2003, Vol. 3, Intelligence, Surveillance, and Reconnaissance*, TD3155, Space and Naval Warfare Systems Center, San Diego, CA, 2003, p. 174-180. <http://www.spawar.navy.mil/sti/publications/pubs/td/3155/td3155.html>
- ²T.N. Roy, "Deployable Autonomous Distributed System: Future Naval Capability in Undersea Warfare," *SSC San Diego Biennial Review 2003, Vol. 3, Intelligence, Surveillance, and Reconnaissance*, TD3155, Space and Naval Warfare Systems Center, San Diego, CA, 2003, p. 181-185. <http://www.spawar.navy.mil/sti/publications/pubs/td/3155/td3155.html>
- ³P. J. Gendron, "High Frequency Acoustic Communications for Networked Autonomous Littoral Surveillance," *Proceedings of Oceans07*, Aberdeen, UK, June 2007.
- ⁴P.J. Gendron, "An Empirical Bayes Estimator for In-scale Adaptive Filtering," *IEEE Transactions on Signal Processing* **53**(5), 1670-1683 (2005).
- ⁵P.J. Gendron and G.J. Heard, "High Frequency Broadband Acoustic Channel Estimation Error Analysis for St. Margaret's Bay during the Unet06 Demonstrations," *Canadian Acoustics* **34**, 40-44 (2006). ★

Environmental Acoustic Variability Characterization for Adaptive Sampling

J.P. Fabre,¹ C. Rowley,² G. Jacobs,² E. Coelho,² C. Bishop,³ X. Hong,³ and J. Cummings²

¹Acoustics Division

²Oceanography Division

³Marine Meteorology Division

Introduction: During shallow water antisubmarine warfare missions, environmental uncertainty significantly impacts Fleet asset performance. Oceanographic sensor availability, acoustic sensor coverage, and operational time limitations put constraints on efforts to observe large ocean areas. To address these challenges, NRL researchers have advanced and incorporated applied research technologies developed under several disciplines, to implement an adaptive sensor placement capability that, under certain assumptions, minimizes the uncertainty in forecasted information. The technologies incorporated include ocean data quality control, rapidly nested oceanographic modeling, data assimilation, ensemble representation of uncertainty, acoustic

performance modeling, and Ensemble Transform Kalman Filter (ETKF) adaptive sampling.

Techniques: The relocatable Navy Coastal Ocean Model (NCOM) is currently being implemented and tested at the Naval Oceanographic Office (NAVOCEANO) to provide high-resolution local mesoscale ocean forecasts to support Fleet oceanographic and acoustic operations. Observations from local sensors including gliders and Fleet measurements are assimilated into NCOM using the NRL Coupled Ocean Data Assimilation (NCODA) system. Surface forcing is provided by the Coupled Ocean/Atmosphere Mesoscale Prediction System (COAMPS®) or the Navy's Operational Global Atmospheric Prediction System (NOGAPS), and the boundary conditions are provided by a global run of NCOM available at the NAVOCEANO. Multiple sources of error in the modeling process need to be considered, including errors associated with the initialization and boundary conditions of models, numerical approximations, modeling strategies, atmospheric forcing, impact of under-sampling in the assimilation process, and unresolved scales. There are multiple approaches to address these problems. This work focused on the application of Monte Carlo methods to producing ensemble based error estimates along with the predicted state variables. Monte Carlo methods have the advantage of simplicity in their formulation and have been used extensively by the meteorological community. The atmospheric Ensemble Transform (ET) approach¹ was adapted for ocean mesoscale applications and provides a self-calibrated ensemble generation technique, such that at each initialization time, the magnitudes of the ensemble spread are re-set to match the best estimate available of the analysis error variance field. Uncertainty in the atmospheric forcing of the ocean is accounted for by forcing each ocean ensemble member with atmospheric forecasts that are smoothly but randomly shifted in time.

The sample covariance of the ensemble of forecasts provides a 4-dimensional estimate of how the covariance of the error of the ensemble mean would evolve through time if no additional observations were taken. To predict how targeted observations would reduce the forecast error variance, the Ensemble Transform Kalman Filter^{2,3} was applied to the ET ensemble. The ETKF rapidly evaluates the reduction in forecast error variance due to very large numbers of future feasible sensor deployments. The particular sensor deployment that, according to the ETKF, reduces forecast error variance more than any other proposed sensor deployment is deemed "optimal."

The acoustic properties of the ocean state are the most critical to Fleet operations. To create measures of forecast error directly related to these acoustic proper-

ties, each ensemble member is processed using the Navy Standard Parabolic Equation (NSPE) acoustic propagation model for multiple bearings at each grid point to compute transmission loss. Integrated acoustic coverage^{4,5} is then computed to provide a wide area assessment of the uncertainty (due to the ocean model variability) of the acoustic performance over the area. Methods are then used to predict optimal sensor sampling to reduce uncertainty in areas where it is high. This guidance is provided to the sensor operators in a variety of formats, including waypoints for existing sensors, or sensor placement plans for each sensor to be deployed. Once the data is collected, it is fed back into the adaptive sampling system and the process is continued.

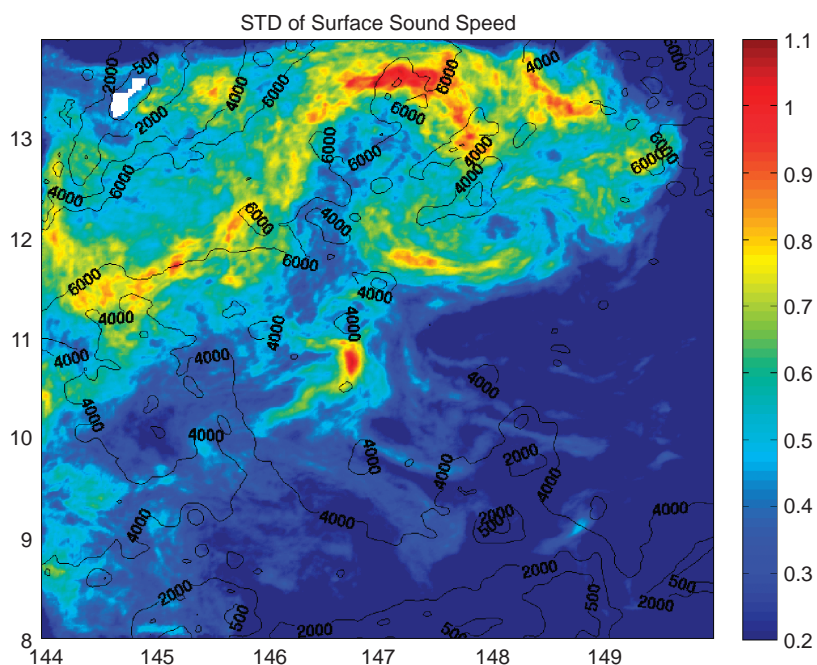
Demonstration: The adaptive sampling techniques described above were demonstrated during the Valiant Shield 07 (VS07) Fleet exercise in the eastern Pacific Ocean around Guam in the summer of 2007. Ensembles of oceanography (temperature, salinity, and sound speed) and acoustic coverage were provided daily for analysis. Variance of forecast temperature and acoustic performance over the ensemble were used as cost functions (Figs. 4 and 5) to drive the sensor placement algorithms for optimization of measurements for the purposes of reducing the error in the ocean predictions given all candidate sensor paths (Fig. 6).

This planning tool, currently being transitioned to NAVOCEANO, enables the Navy to employ assets in a way that reduces uncertainty in acoustic predictions, allowing the operational planner to maximize the desired effect. This exciting effort has many applications beyond adaptive sampling, in that it provides estimates of the environmental uncertainty. This work also resulted in improvements to various capabilities, including the NSPE, which impacts many Navy applications.

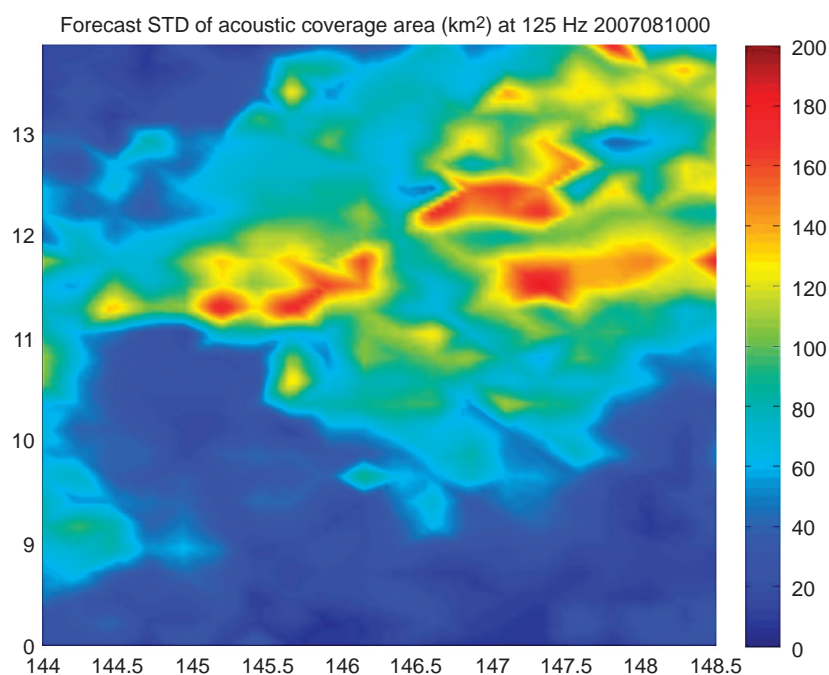
[Sponsored by ONR and SPAWAR Rapid Transition Program]

References

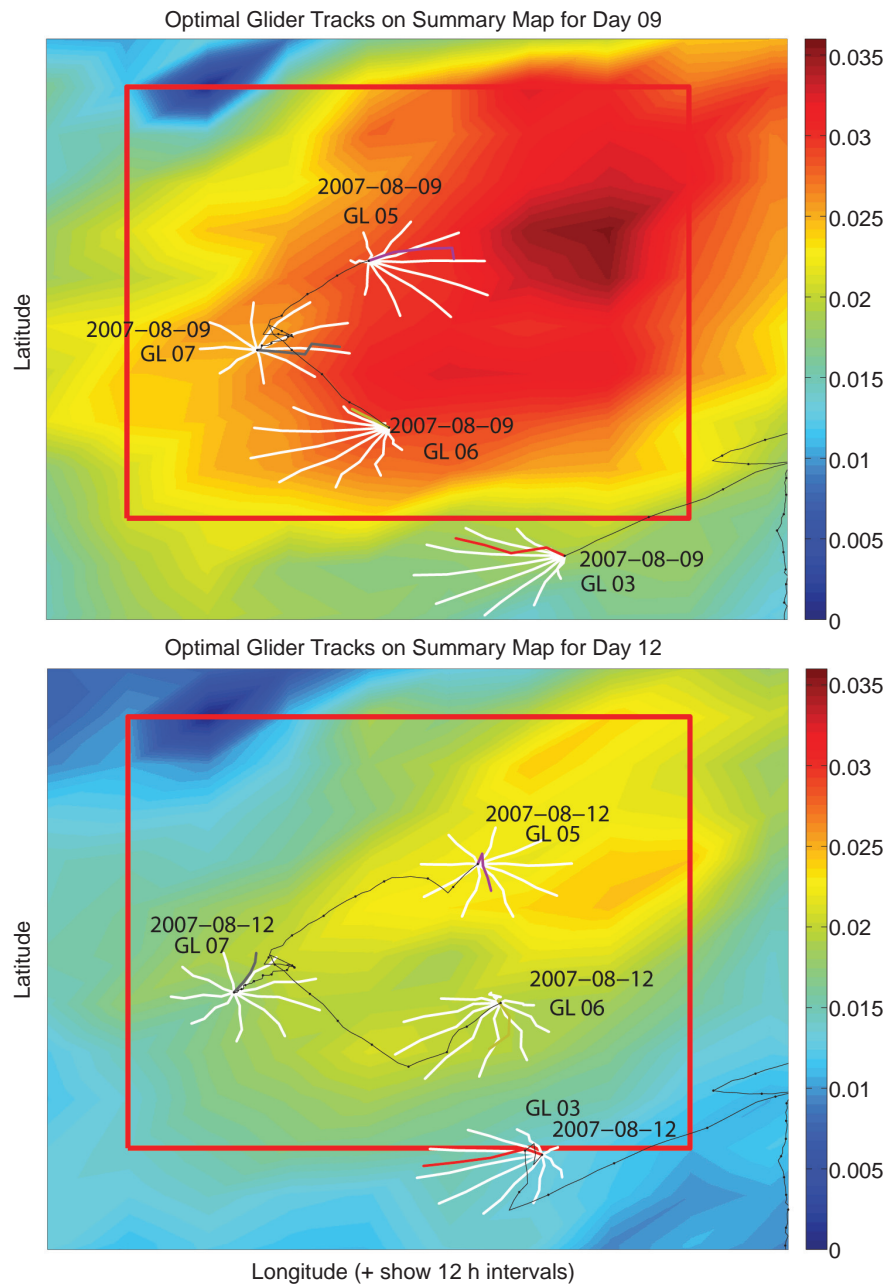
- ¹ C.H. Bishop and Z. Toth, "Ensemble Transformation and Adaptive Observations," *J. Atmos. Sci.* **56**, 1748-1765 (1999).
- ² C.H. Bishop, B.J. Etherton, and S.J. Majumdar, "Adaptive Sampling with the Ensemble Transform Kalman Filter Part I: Theoretical Aspects," *Mon. Wea. Rev.* **129**, 420-435 (2001).
- ³ G. Evensen, "The Ensemble Kalman Filter: Theoretical Formulation and Practical Implementation," *Ocean Dynamics* **53**, 343-367 (2003).
- ⁴ S.M. Dennis and J.P. Fabre, "Characterization of the Range Dependence of an Ocean Environment to Reduce Acoustic Estimation Time," *IEEE Proceedings of Oceans 2007, Vancouver*, 2007. doi:10.1109/oceans.2007.4449371.
- ⁵ J.P. Fabre, "Integrated Signal Excess as a Metric for Environmental Acoustic Assessment," *J. Acoust. Soc. Am.* **122**(5), 2942 (2007). ★

**FIGURE 4**

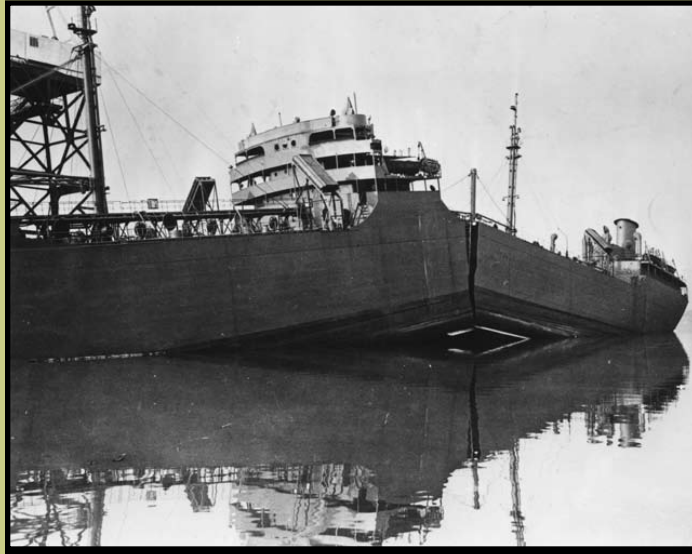
Example of variance of sound velocity at the surface over the ensemble with bathymetry contours for the exercise area. Areas of greatest model uncertainty are shown in red.

**FIGURE 5**

Example of acoustic coverage variance at a receiver depth of 100 m, over the ensemble for the exercise area, showing the areas of greatest acoustic performance uncertainty (red).

**FIGURE 6**

Example of a scenario used to reduce model error in an area of high model uncertainty (red box). The colors in the figure show the relative impact of observations in reducing the predicted error at August 9 and 12, 2007. Between these two days, gliders were steered toward locations with high predicted impact in reducing the model error. Data was assimilated into the model and the impact of observations became smaller as the model forecast became more accurate in the area of interest.



The Principles of Fracture Mechanics (1947)

NRL's George R. Irwin pioneered modern fracture mechanics. He studied the relationships between applied stresses and cracks or other defects in metallic materials and enabled the first calculations of the strength of structures containing defects. NRL used those principles to solve commercial jet aircraft and Polaris missile fracture problems. Fracture mechanics is used worldwide to design such critical structures as nuclear reactor pressure vessels, aircraft, submarines, and toxic material storage tanks and to discover why other critical structures break apart.

131

Environmental Mission Impact Assessment

J. Ballas, J. Cook, and D. Jones

134

On Tropical Cyclone Formation

M.S. Peng, B. Fu, and T. Li

136

SHIMMER: Innovative Technology Enabling Unprecedented Science

C.R. Englert, M.H. Stevens, D.E. Siskind, S.D. Eckermann, J.M. Harlander, K. Nielsen, and F.L. Roesler

Environmental Mission Impact Assessment

J. Ballas,¹ J. Cook,² and D. Jones³

¹Information Technology Division

²Marine Meteorology Division

³Applied Physics Laboratory, University of Washington

Overview: The Environmental Visualization (EVIS) system for producing environmental mission impact assessment products was accepted as a transition in 2007 by the Fleet Numerical Meteorology and Oceanography Center (FNMOC) in Monterey, CA, after passing operational testing and accreditation. EVIS is a service-oriented architecture (SOA) system¹ developed by NRL and the Applied Physics Laboratory, University of Washington, to address human factors and automation issues associated with the stress of the operational tempo. Through a series of experiments, workflow and visualization shortfalls were identified in the battlespace environmental forecasting process. Experimental analysis resulted in the development of new applications, workflows, and visualization products that together constitute the EVIS system. Formal testing demonstrated a 40% reduction in the completion time for tactical air strike forecasts.²

System Description: EVIS can be used to generate and deliver data and products providing the expected

environmental effects on operations and is particularly suited to support the generation of products for new and evolving missions, such as maritime intercept and vessel boarding. Through a suite of web services, EVIS can generate summaries of environmental impacts and related images that are available and advertised through an enterprise. The EVIS capability enables a qualified meteorology and oceanography (METOC) domain expert to access high-resolution METOC information from a remote server, create tailored products for mission planning, and do this faster than is possible with the current tools available. Mission impacts are based on threshold rules that have been gathered from METOC handbooks and other authoritative sources, which define the allowable ranges for particular environmental parameters that impact military operations. The EVIS product provides a color-coded spreadsheet or matrix, listing the mission parameters and the environmental impacts for each forecast time. Each cell in the matrix is hyperlinked to a graphic product that represents the same time period and threshold environmental parameter (see Fig. 1). The geographic product is a shaded contour plot that shows a yellow shaded area where the selected environmental parameter is expected to cause a marginal impact on military operations, and a red shaded area where the impact is expected to be severe. Products are hosted and saved on the EVIS server and can be accessed securely across the

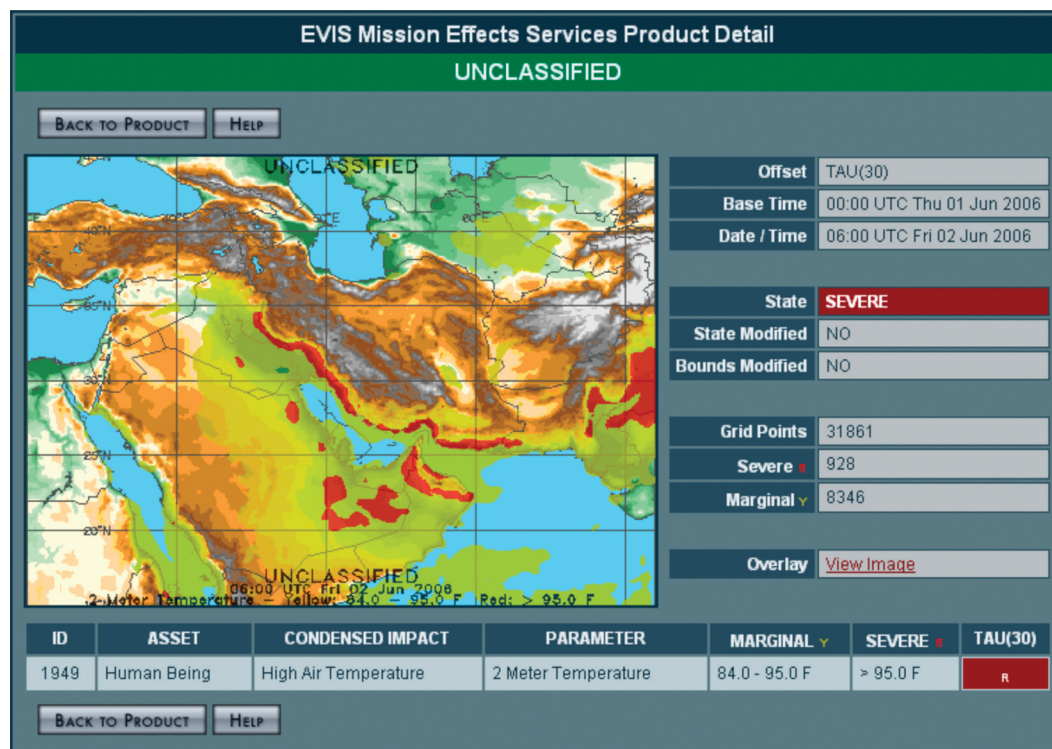


FIGURE 1

Graphical product generated in June 2006 showing the expected effect of high surface air temperature on personnel in the Middle East.

network via the Defense Information System Agency's (DISA) Federated Search service. The mission impacts can be generated for a general rectangular area, or generated for routes, route segments, and waypoints, and the thresholds for each rule can be modified by the user to meet their specific mission objectives.

Capabilities: With a service-oriented architecture design, EVIS capabilities can be orchestrated into workflows for different types of users and systems. While several orchestrations were developed and tested (both by the EVIS team and by others who had access to the EVIS service endpoints), the orchestration for FNMOC’s operational capability supports two types of users—the expert forecaster who needs to produce and post environmental effects products quickly, and the operational user who needs to understand the forecasted effect on their planned or executing missions. The services that are available (see Fig. 2) include

- delivering metadata on the environmental data that is available for analysis;

- delivering analysis (including stoplight summaries, overlay map images, and data) of the expected effects on missions;
- searching through posted products for specific effects, using search parameters for the specific time, area, mission, and impacts;
- controlling access to services and data using attributes such as citizenship and clearance; and
- establishing secure connections to servers, services, applications, and clients.

The EVIS system includes the following data-oriented capabilities:

- XML metadata describing the availability of METOC data in a specified geographic region for specified forecast times;
- raw space/time METOC product data;
- METOC mission effects in XML format produced by analyzing the raw data using threshold rules;
- search services that respond to queries (formatted according to DISA's Federated Search speci-

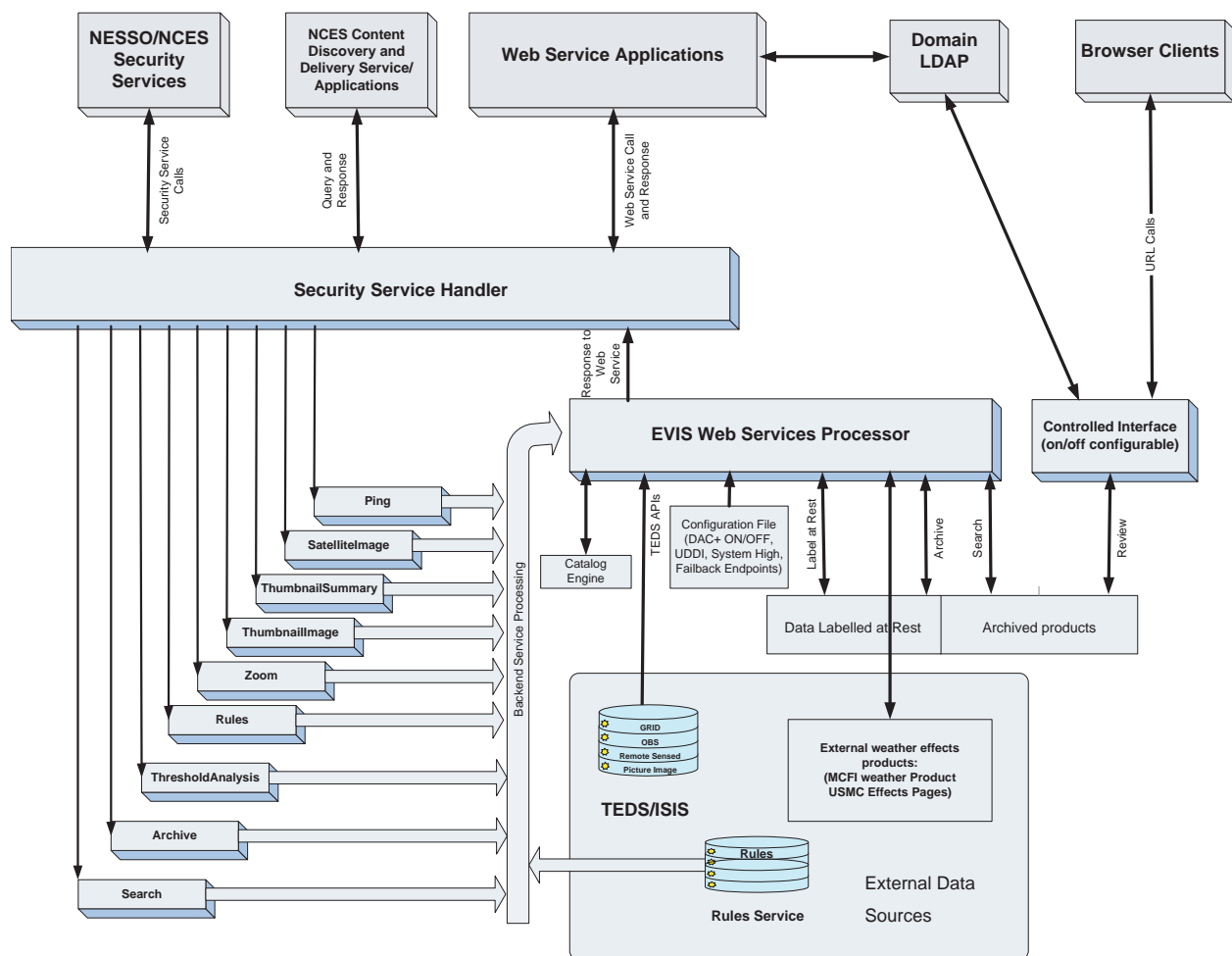


FIGURE 2
EVIS service-oriented architecture design, illustrating the interfaces to DISA's Net-Centric Enterprise Services (NCES) Security Services and Content Discovery and Delivery Service.

cation) by searching metadata files and returning results to the search engine; and

- staging of metadata about operational effects products including those produced by users of EVIS as well as products generated using other processes.

The user-oriented capability includes a portlet application available from FNMOC that orchestrates the EVIS services for authenticated users through a workflow process to define, request, and edit mission effects

analyses (see Fig. 3). This capability takes tactical forecasting from a process involving meteorological and oceanographic cognition into one that includes aspects of tactical decision making. Although mission impacts can be produced through the formal application of threshold rules to environmental data, go/no-go decisions have much in common with statistical decisions because the underlying phenomena to which the thresholds are applied have statistical variability. Therefore, in practice, the forecaster has to have flexibility in

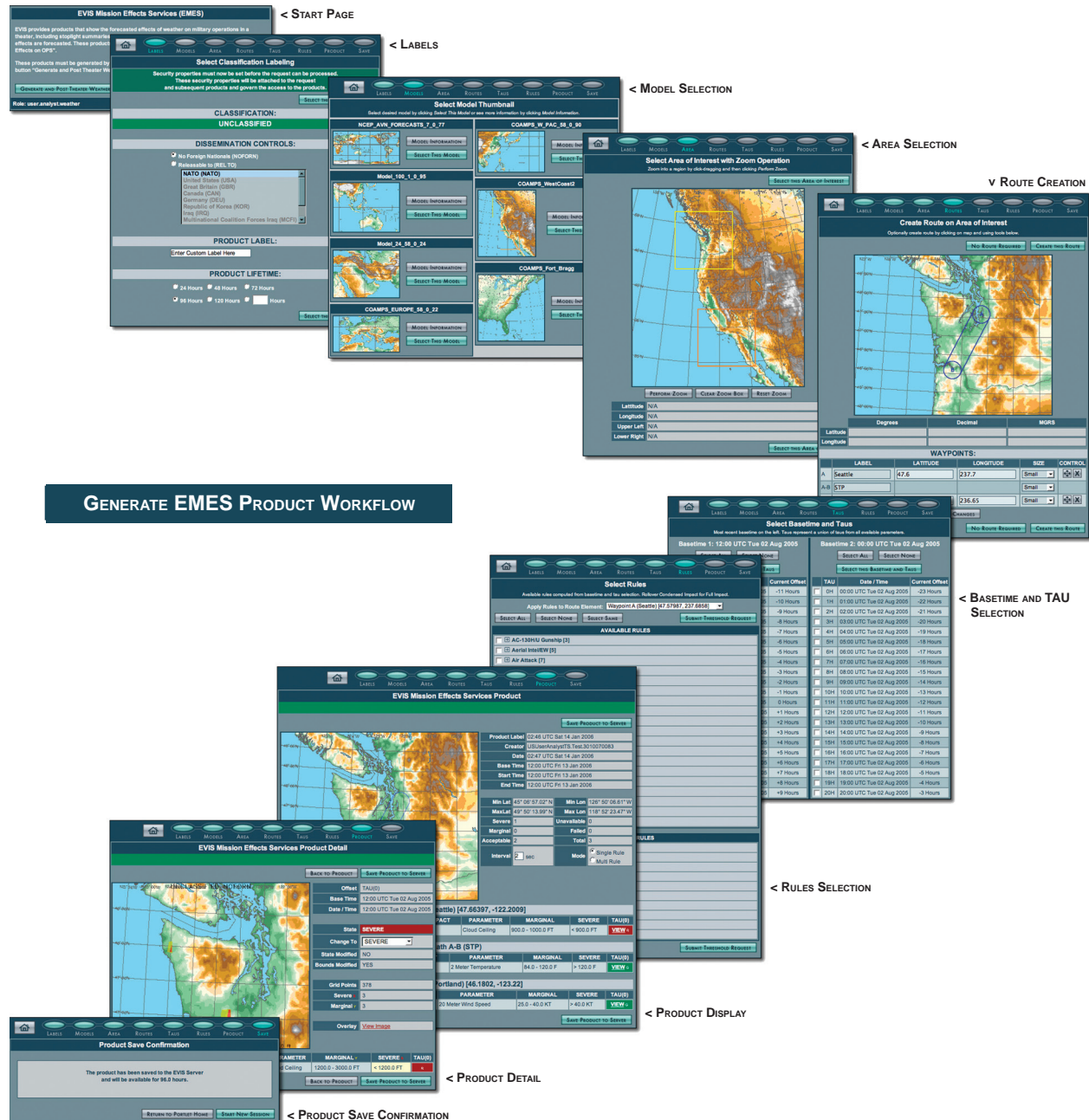


FIGURE 3

EVIS workflow showing views that a forecaster goes through to produce a product. The forecaster selects the classification of the product, model data to be used, area and route to be analyzed, the forecast times to be analyzed, and the rules to apply. The last three views illustrate reviewing the result and its details, and posting the product for dissemination and search.

applying the rules and be able to use knowledge about the details of the mission and the systems/personnel executing the mission. The EVIS portlet workflow supports the flexible tactical decision-making aspects of environmental mission analysis by providing

- forecaster control in selecting the METOC data source, the mission(s), the area of interest (AOI), routes and waypoints, forecast times, and analysis rules;
- a flexible method of generating new rules and editing these rules and setting the mission-relevant thresholds as needed;
- a graphical summary of the environmental data that falls above the threshold limits as well as hyperlinks to the raw data anywhere in the AOI; and
- a method of easily editing the computer-generated product before it is posted.

Summary: FNMOC is currently applying EVIS in support of DoD operations and exercises and making products and related data available and advertised for discovery by users on the Global Information Grid (GIG). FNMOC is now developing extensions to EVIS that incorporate environmental effects rules from a multi-service database and interfaces to additional environmental data sources.

[Sponsored by ONR and OSD]

References

- ¹D.W. Jones et al., "Environmental Visualization and Horizontal Fusion," in *Proceedings of the Battlespace Atmospheric and Cloud Impacts on Military Operations (BACIMO) Conference*, October 12–14, Monterey, CA (2005).
- ²J.A. Ballas et al., "Improved Workflow, Environmental Effects Analysis and User Control for Tactical Weather Forecasting," in *Proceedings of the Human Factors and Ergonomics Society 48th Annual Meeting*, September 20–24, 2004, New Orleans, LA (2004). ★

On Tropical Cyclone Formation

M.S. Peng,¹ B. Fu,² and T. Li²

¹Marine Meteorology Division

²Department of Meteorology, University of Hawaii

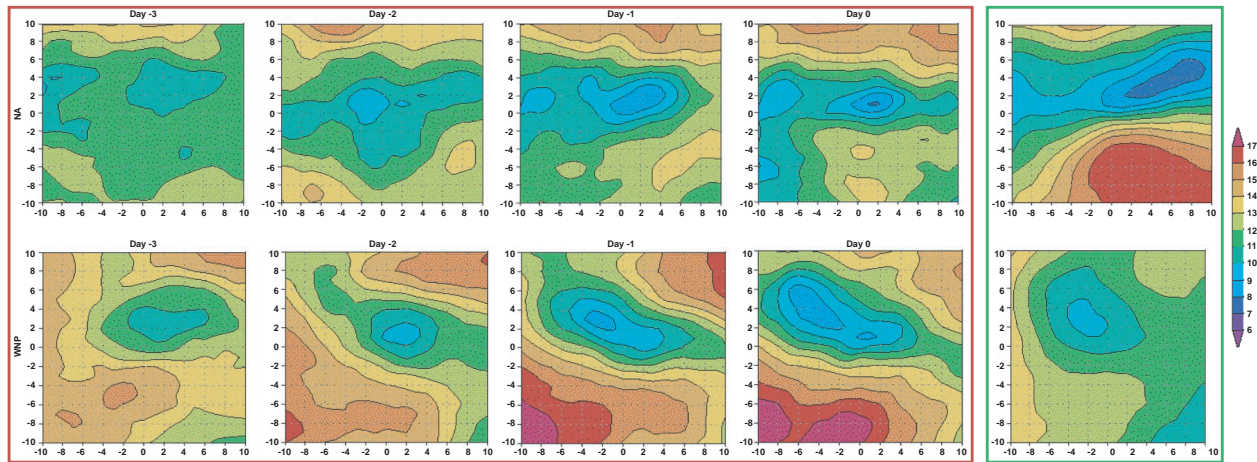
Introduction: The formation (genesis) of tropical cyclones (TCs) is a complicated process that involves interactions among multi-scale circulations. While tropical disturbances exist all the time, only a few of them may develop into TCs. In this study, the daily global analysis from the Navy Operational Global Atmospheric Prediction System (NOGAPS) is examined to understand why some disturbances develop into TCs while others do not. Significantly different characteristics of atmospheric variables associated with

developing and nondeveloping disturbances are found. The most important parameter controlling TC formation is vertical wind shear in the North Atlantic (NA) and low-level, large-scale convergence in the western North Pacific (WNP). The result suggests that different cyclogenesis mechanisms may operate for TC formation in the two oceanic basins.

Problem: While there has been a steady improvement in TC track forecasts, little progress has been made in TC genesis forecast in past decades, mainly due to the lack of accurate observations over the ocean and the complicated processes involved in TC genesis. Earlier work¹ suggested six favorable environmental conditions for TC formation. Although there are many tropical disturbances each year in different ocean basins, only a few develop into tropical cyclones. In this study, we trace tropical disturbances that formed TCs eventually and those that did not, to gain more insight into TC formation. The data set we use is NOGAPS daily analysis data with a one-degree resolution. Scenarios for the North Atlantic and the western North Pacific are investigated separately to identify possible different characteristics of the developing and nondeveloping disturbances for TC formation in these two basins.

Data and Method: Recent improvement of NOGAPS and its data assimilation system make its analysis a good proxy of real atmosphere. A time-filtering technique is applied to NOGAPS analysis for the 2003 to 2005 period to extract 3- to 8-day period synoptic-scale waves/perturbations and low-frequency (20 days or longer) background fields. A composite map is made in a 20° by 20° domain centered at the maximum low-level (850 mb) vorticity disturbance. For the developing cases, synoptic-scale disturbances are traced back three days before the genesis and composites are made for the genesis day (day 0) and the previous three days (day -1, day -2, and day -3). Disturbances with clear close-circle cyclonic circulation are considered as non-developing cases, and only one composite is made for all of them.

Results and Discussion: Figure 4 shows the composite maps of the vertical shear (200–850 mb) in terms of speed for the developing and nondeveloping cases in the North Atlantic (top) and the western North Pacific (bottom). For the developing disturbances in both the NA and the WNP, there is a gradual buildup of a low shear zone near and north of the perturbation center from day -3 to the genesis day. The composite of the nondeveloping disturbances in the NA shows a very large shear gradient across the center, with a significantly large vertical shear appearing to its south. This is consistent with recent climatology studies² that

**FIGURE 4**

Composites of the speed of the vertical shear (200–850 mb) for developing (in red frame) and nondeveloping (in green frame) disturbances in the NA (top) and WNP (bottom). The horizontal domain is a 20° by 20° region centered at the maximum low-level vorticity. Day 0 is the day when the TCs formed, Day -1 is the prior day, and so forth.

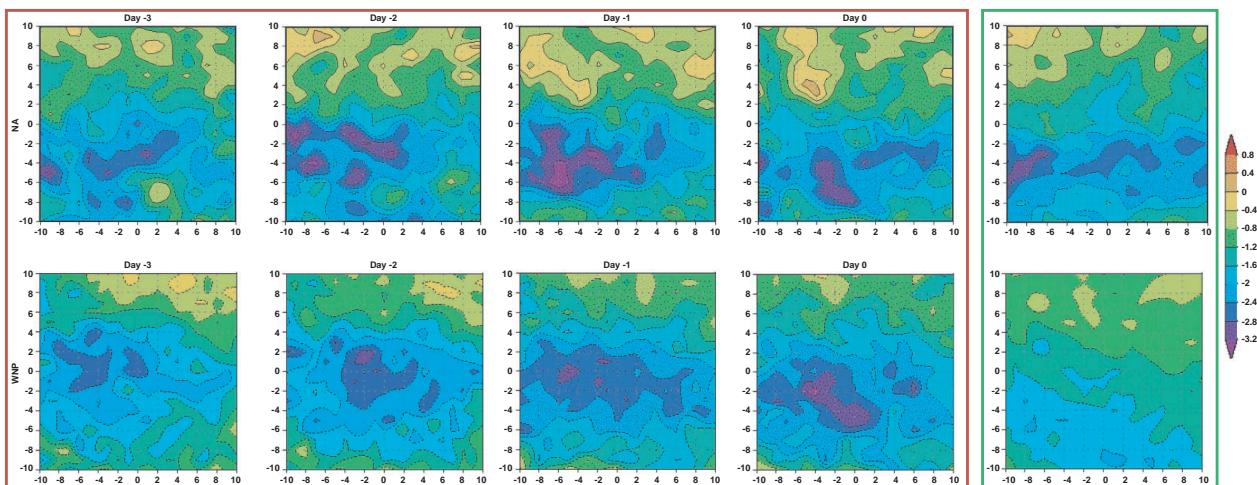
point out that the low vertical shear months of August and September correspond to the most active tropical cyclogenesis in the NA.

Contrasting to those in the NA, the vertical shear in the WNP shows a very different feature. In the WNP, the nondeveloping composite shows a smaller vertical shear than the developing cases. This indicates that the larger vertical shear does not preclude a tropical disturbance from becoming a TC in the WNP. It has been well understood that, in general, larger shear is not favorable for TC formation. The distinction between the characteristics in the NA and the WNP suggests that vertical shear plays a more important role in the NA than in the WNP in the formation of TCs.

Figure 5 illustrates the composite maps for 20-day low-pass filtered 850 mb divergence fields. In the NA, the difference between the developing and nondevel-

oping cases is small, while there is a distinct larger convergence for the developing cases in the WNP. This suggests that large-scale environmental convergence is important for TC formation in the WNP, while it is less so in the NA.

Composites of other variables show that more moisture at the lower and middle troposphere and larger low-level relative vorticity are common features for both NA and WNP developing disturbances compared to the non-developing cases. We also found that the averaged moving speed is slower in the developing cases than that in the nondeveloping cases in both the NA and the WNP. Another unique feature in the NA is that the developing disturbances are correlated well with the weakening of the upstream 500 mb easterly wind so that less dry air from the Sahara desert is brought into the eastern part of the NA where TCs

**FIGURE 5**

Same as Fig. 4, but for 20-day low-pass filtered 850 mb divergence fields.

usually form. A cyclogenesis prediction index based on this study is under development that has the potential to provide useful guidance in the operational forecast of tropical cyclone genesis.

[Sponsored by NRL]

References

- ¹W.M. Gray, "A Global View of the Origin of Tropical Disturbances and Storms," *Mon. Wea. Rev.* **96**, 669-700 (1968).
- ²A.R. Aiyer and C. Thorncroft, "Climatology of Vertical Wind Shear over the Tropical Atlantic," *J. Climate* **19**, 2969-2983 (2006). ★

SHIMMER: Innovative Technology Enabling Unprecedented Science

C.R. Englert,¹ M.H. Stevens,¹ D.E. Siskind,¹ S.D. Eckermann,¹ J.M. Harlander,² K. Nielsen,³ and F.L. Roesler⁴

¹Space Science Division

²St. Cloud State University

³Computational Physics Inc.

⁴University of Wisconsin–Madison

Introduction: On March 9, 2007, the first ultraviolet spectrometer using the innovative optical technique known as spatial heterodyne spectroscopy was launched into low Earth orbit from Cape Canaveral, FL. The Spatial Heterodyne Imager for Mesospheric Radicals (SHIMMER) is a deskjet printer-sized rugged spectrometer designed to measure solar resonance fluorescence of hydroxyl (OH) in the Earth's middle atmosphere between 30 and 100 km altitude. It is optimized for high spectral resolution, low mass, low power, low volume, and high sensitivity with no moving parts. SHIMMER is performing as expected and has already returned several hundred thousand atmospheric OH measurements. SHIMMER also detects mesospheric clouds (MCs) at their equatorward edge region, around 55° latitude, where they are believed to be most sensitive to mesospheric change. SHIMMER's unprecedented local time coverage allows the investigation of how atmospheric dynamics influence MCs and their environment and thus potentially bias the interpretation of multi-decadal cloud frequency and brightness trends. To date, SHIMMER data have already led to three significant science results, discussed briefly here.

Mesospheric Clouds Show a Systematic Daily Variation: Historically, satellite measurements of MCs were conducted almost entirely from sun-synchronous orbits at fixed local times. The SHIMMER orbit precession of about 30 minutes per day allows us to investigate the local time dependence of MCs for the first time from a satellite. Figure 6 shows the variation

of the seasonally adjusted MC frequency throughout the day, revealing a strong semi-diurnal signature.¹ The dynamic range of this signature is unexpectedly large and will help to reconcile existing satellite data sets that consist of observations at discrete local times.

Discrepancies in the Expected Diurnal Variation

of OH: Unlike with mesospheric clouds, we already knew that OH has a diurnal variation. This is because it is produced by the photodissociation of water molecules, and the photodissociation varies with the rising and setting of the sun. The surprise has been the large discrepancy with standard model results. Figure 7 shows the diurnal variation of OH as measured by SHIMMER, compared to model calculations. At 74 km, the agreement is excellent. However, at 80 km, the model underpredicts the observations in the a.m. hours and overpredicts in the p.m. hours. Good agreement is obtained at 1300 local time (LT), which is when we normalize our model to coincident H₂O observations from the NASA/AURA satellite. This discrepancy may therefore suggest a hitherto unknown diurnal variation in H₂O at 80 km. However, the required H₂O variation would have to be very large—possibly implausibly so. Much more work is required to document this discrepancy on a global and seasonal basis before we can begin to solve this puzzle.

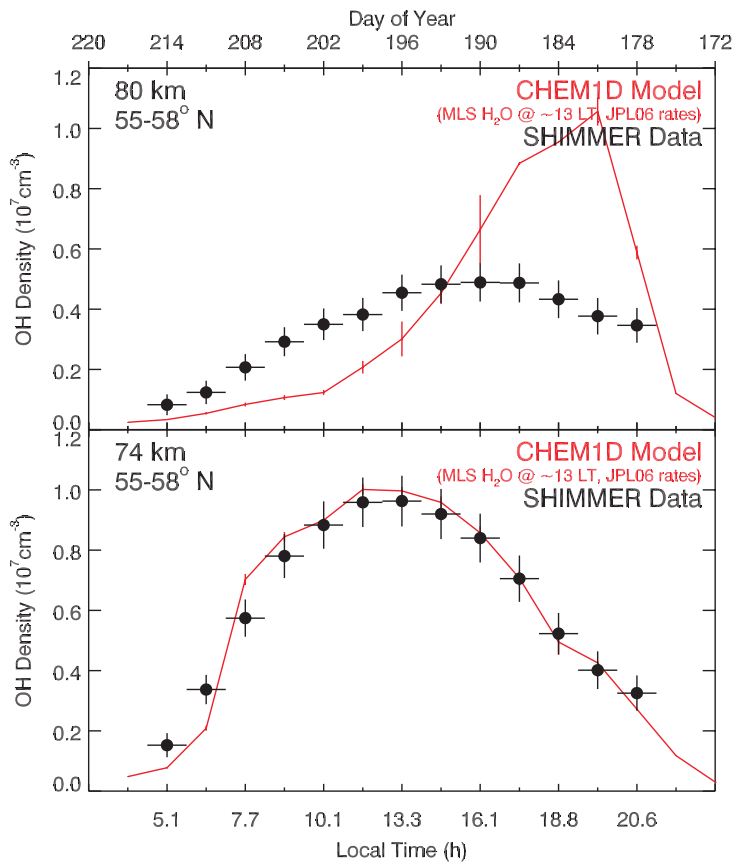
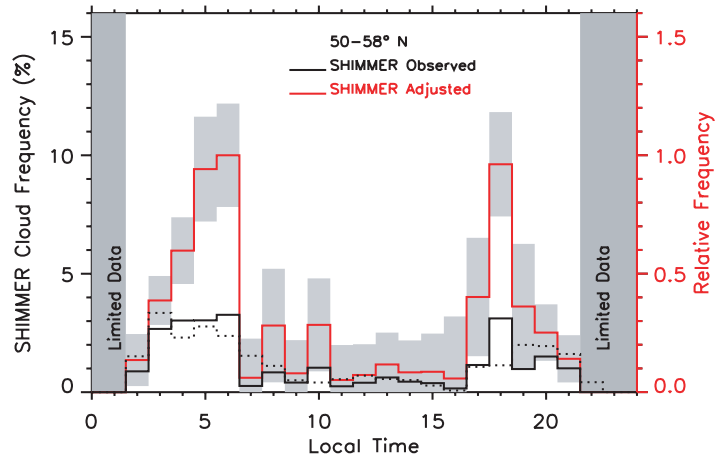
Unusual SHIMMER Cloud Observation Consistent with Navy Weather Model:

Figure 8 shows a hindcast of the water vapor saturation for June 13, 2007, from a new version of the Navy Operational Global Atmospheric Prediction System (NOGAPS). This version is called ALPHA (Advanced Level Physics High Altitude) and it is a research model that is specifically configured to provide meteorological analyses up to 100 km. The map shows an area of super-saturation ($S > 1$) protruding below 50° N where MCs are rarely seen. Within this super-saturated region the formation, growth, and presence of MC particles is possible. Since MCs are seen only sporadically at mid-latitudes, they attract much attention because this region is much more populated than the polar region and the MCs can be viewed with the unaided eye just after sunset or before sunrise. That the SHIMMER MC sightings on this day show a striking correlation with NOGAPS-ALPHA suggests that we can finally place the occurrence of these previously mysterious events on a firm meteorological footing, perhaps even to forecast them much as tropospheric clouds are forecast.²

Acknowledgments: The success of the SHIMMER mission was made possible in part by the dedicated efforts of R. Feldman, J.F. Moser, W.L. Marlin, A. Straatveit, Andrew Kochenash, and the teams at the DoD Space Test Program and AeroAstro Inc.

FIGURE 6

The observed (black) and seasonally adjusted (red) diurnal variation of mesospheric clouds as determined from SHIMMER data in the northern summer of 2007. A strong quasi diurnal signature is evident.

**FIGURE 7**

The diurnal variation of OH as observed by SHIMMER compared with photochemical model predictions. At 74 km the agreement is excellent; however, the large difference at 80 km indicates an additional, not yet identified, mechanism that is not included in the model.

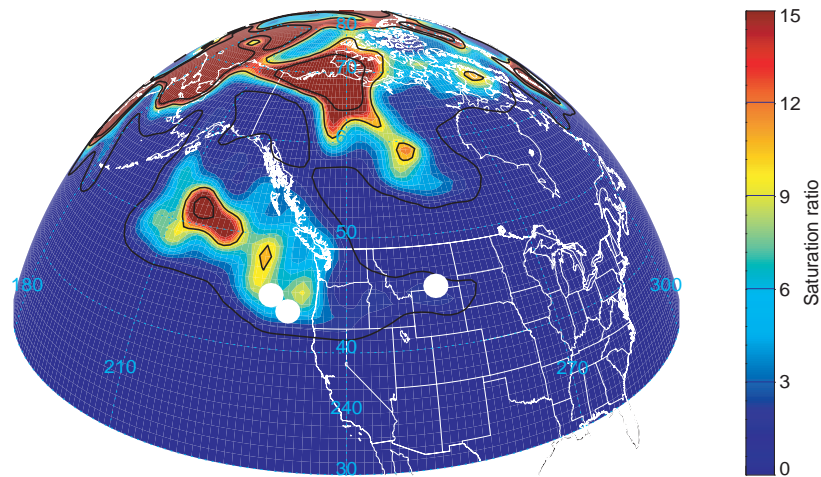


FIGURE 8

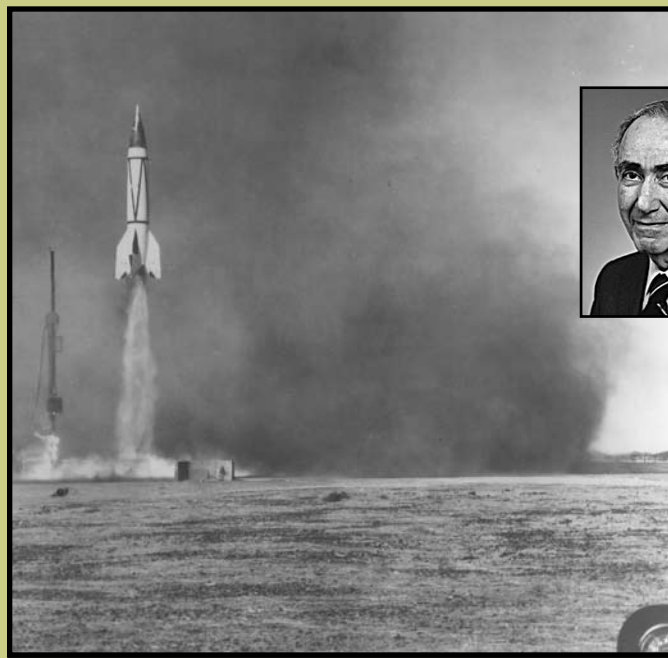
This false-color map shows the water vapor saturation hindcast using NOGAPS-ALPHA for 6 p.m. (GMT) on June 13, 2007. The map indicates a supersaturated ($S > 1$) region protruding to lower latitudes ($< 50^\circ \text{N}$) where mesospheric clouds are rarely seen. The white filled circles mark the mid-latitude cloud detections of SHIMMER for the same day, which show a striking correlation with the NOGAPS-ALPHA result.

[Sponsored by ONR, the DoD Space Test Program, and NASA]

References

¹ M.H. Stevens, C.R. Englert, S.V. Petelina, W. Singer, and K. Nielsen, "The Diurnal Variation of Noctilucent Cloud Frequency Near 55°N Observed by SHIMMER," submitted to *J. Atmospheric and Solar-Terrestrial Physics*, 2008.

² C.R. Englert, M.H. Stevens, D.E. Siskind, J.M. Harlander, F.L. Roesler, H.M. Pickett, C. vonSavigny, and A. Kochenash, "First Results from the Spatial Heterodyne Imager for Mesospheric Radicals (SHIMMER): The Diurnal Variation of Mesospheric Hydroxyl," submitted to *Geophysical Research Letters*, 2008. ★



H. Friedman

First Detection of X Rays from the Sun (1949)

In a dramatic swords-into-plowshares scientific triumph, in 1949 NRL's Herbert Friedman directed the effort to use captured German V-2 rockets in the first detection of solar X rays. These observations confirmed the Sun's role in ionization in the E region of the ionosphere, thus greatly improving understanding of the Sun's role in HF radio communications. Friedman received the National Medal of Science and the Wolf Foundation Prize in recognition of his contributions to X-ray astronomy.

141

Aerobic Miniature Microbial Fuel Cells

B.R. Ringeisen, J.C. Biffinger, J. Pietron, R. Ray, and B. Little

143

Innovative Ionic Liquids: Electrolytes for Ion Power Sources

T.E. Sutto, H.-S. Kim, and A. Piqué

Aerobic Miniature Microbial Fuel Cells

B.R. Ringeisen,¹ J.C. Biffinger,² J. Pietron,¹
R. Ray,³ and B. Little³

¹Chemistry Division

²NRL/NRC Postdoctoral Research Associate

³Oceanography Division

Introduction: Distributed autonomous sensor (DAS) networks will require sustainable energy-scavenging power sources for persistent surveillance applications. Ideally, these power sources will scale with the sensor size (micro/nanoelectromechanical) to enable covert deployment and a small power budget. Based on their ability to sustain power production for years while scavenging energy from a variety of environments and nutrients, microbial fuel cells (MFCs) are a viable solution to power water-borne DAS networks. However, to date, nearly all MFCs are large and bulky (100 cm^3 to m^3), making them significantly larger than many sensors and communication packages. Researchers in the NRL Chemistry and Oceanography Divisions have recently developed the first high power density miniature MFC (mini-MFC). The mini-MFC has a 2.0 cm^2 cross-section and a 1.2 cm^3 volume, making it orders of magnitude smaller than traditional MFCs. Additionally, the mini-MFC is designed to maximize current collection and proton diffusion to the cathode, enabling unprecedented power per area (3 W/m^2) and volume (500 W/m^3) when using graphite felt electrodes and *Shewanella oneidensis* cultured under micro-aerophilic conditions. These power densities are sustained when *S. oneidensis* biofilms on the anode are used with acellular media. Previous to this work, mixed consortia of bacteria with the ability to utilize electron donors efficiently needed to be used to produce current densities above 50 W/m^3 . The mini-MFC design and size create a unique device that enhances power production per volume when compared to any other MFC design in the literature. These results are an indication that further size reductions may further increase power density and enable microbial energy scavengers to

power DAS networks for Navy-relevant applications in the littoral water column.

Design of the Mini-MFC: Because of the relatively small power densities achieved by traditional macroscopic MFCs ($1\text{--}100\text{ W/m}^3$), it was surprising to find, when we began our work in FY2005, that the highest surface area to chamber volume ratio for any reported MFC was only 50 cm^{-1} . Higher surface area, in the form of roughened, granular, and/or fibrous surfaces, nearly always yields increased power output for all types of fuel cells. Traditional MFCs often use blocks of graphite with actual surface area equal to the geometric (footprint) surface area. By contrast, the mini-MFC (Fig. 1) is constructed using three-dimensional porous woven graphite felt electrodes to fill the entire anode and cathode chambers of the mini-MFC, enabling almost 600 cm^2 of exposed surface area to be presented in a chamber with a 2 cm^2 cross-section and 1.2 cm^3 volume (area-to-volume = 500 cm^{-1}). Additionally, instead of separating the anode and cathode by several centimeters through a narrow tube, the mini-MFC minimizes the distance between the two electrodes by placing them in contact with a $175\text{ }\mu\text{m}$ thick Nafion membrane that separates the two chambers. By decreasing the distance between the electrodes, proton diffusion between the chambers is maximized and the internal resistance is minimized.

Mini-MFC Accomplishments: As shown in Fig. 2, the mini-MFC generates the highest power per volume when using the three most popular cathode reactions: (a) oxygen reduction catalyzed by bare graphite, (b) reduction of ferricyanide, and (c) oxygen reduction catalyzed by Pt-modified graphite. These results were all obtained by using a pure culture of *S. oneidensis*, a bacterium known for its low energy conversion efficiency. All non-NRL results displayed in Fig. 2 utilize either a more energy efficient organism (in the bare carbon example) or mixed consortia of bacteria (ferricyanide and Pt cathode examples) that can more completely oxidize electron donors and nutrients avail-

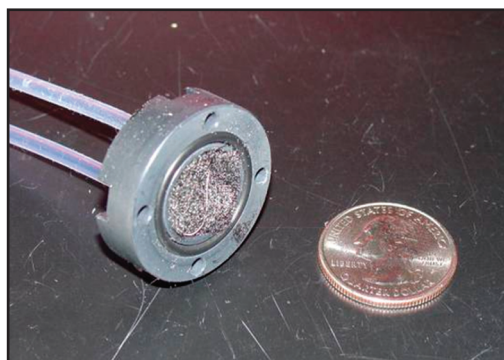
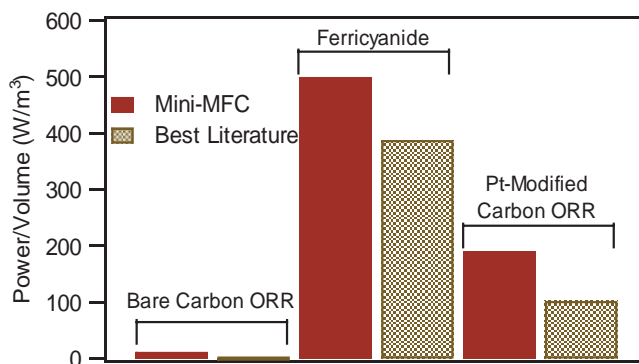


FIGURE 1
NRL's mini-MFC (anode chamber shown).

**FIGURE 2**

Power density per volume for the mini-MFC compared to best literature values for three cathode reactions. ORR = oxygen reduction reaction.

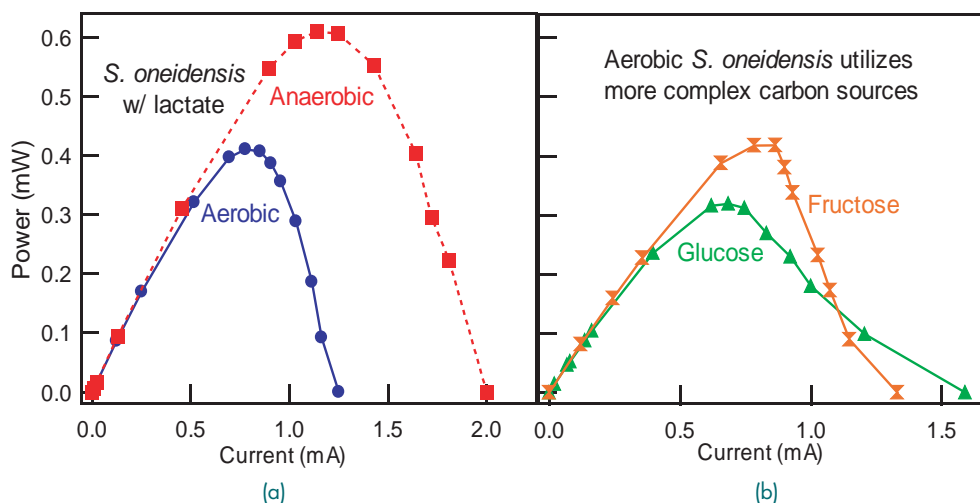
able to the microbes. Additional results have also been published that confirm the mini-MFC as a unique test reactor. We have published the first report of microbial energy production in a purely aerobic environment (Fig. 3(a)) and demonstrated the ability to generate significant power from *Shewanella spp.* using more complex and environmentally available carbon sources (Fig. 3(b)). These results have significant impact for Navy missions, as we hope to deploy these MFCs in the littoral regions of the water column where oxygen is pervasive and nutrient sources are complex (seaweed and plankton derivatives).

The Future of Water Column MFCs: We are now set to begin experiments to transition the mini-MFC from the laboratory into the littoral environment

where DAS networks could detect a range of hazards from chem/bio weapons to submarines and divers. There are many challenges to deploying such a power source, including high salt concentrations, fluctuating temperatures, and limited and intermittent nutrient supplies. We are facing these challenges by developing MFCs that use consortia of salt-tolerant microorganisms. By using a mixed culture, diverse nutrients can be utilized and more completely converted to electricity. Additionally, both cold- and heat-tolerant *Shewanella spp.* can be added to help maintain power production under stressful environmental conditions. We believe these devices could be field-tested within the next three years, enabling persistent surveillance networks to be powered through energy-harvesting microbes.

[Sponsored by NRL]

★

**FIGURE 3**

(a) Power versus current plot demonstrating for the first time that MFCs can generate power in completely aerobic environments. Power output dropped by roughly 30% due to oxygen scavenging of electrons in the anode chamber. (b) Power versus current plot demonstrating how *S. oneidensis* utilizes sugars to generate electricity under aerobic conditions.

Innovative Ionic Liquids: Electrolytes for Ion Power Sources

T.E. Sutto, H.-S. Kim, and A. Piqué
Materials Science and Technology Division

Introduction: As technologies evolve from fixed-site equipment to warfighter-portable devices, the need for safe, compact, rechargeable power sources continues to grow. In spite of the emphasis on high energy density lithium ion (Li-ion) power sources, the fire and/or explosive hazards of these severely limit their utility to the warfighter. Logistical concerns further compound these difficulties, and are reflected in numerous federal and international regulations that limit how, and how many, lithium ion batteries can be shipped together. Thus, a twofold problem exists: increasing the energy density of batteries, while at the same time improving the safety of these devices to enhance their utility to the U.S. Navy and the Joint Services.

The key component responsible for the hazards associated with lithium ion batteries is the electrolyte. Typically, these electrolytes, even in gel form, are more flammable than jet fuels. Therefore, enhancing the safety of these systems is dependent on being able to replace these common electrolytes with a safer system. An ideal replacement choice is ionic liquids (ILs).

ILs are organic-based molten salts that are liquid at ambient temperatures. In general, the composition of these ILs incorporates a thermally and electrochemically stable, positively charged ring system, and an anion, such as a perfluorinated imide. It is this thermal and electrochemical stability and the stability of the organic components that have made ILs attractive alternatives to the more common organic solvents. As salts, the ILs are highly ionically conductive, have nearly no vapor pressure, and as such are non-volatile. Thermal analysis indicates that not only are they stable to over 350 °C, but also they do not explosively ignite as most other common organic solvents do, but instead thermally degrade by charring. Additionally, their dual salt and organic nature tends to make them useful as universal solvents. All of these factors combine to make them the ideal replacement for the more common, volatile electrolytes used in today's state-of-the-art Li-ion batteries.

Technical Approach: Our research demonstrates that tri-substituted imidazolium imide-based ILs can function not only as the electrolyte in a conventional lithium ion battery, but also as a solid nanocomposite separator when combined with an electrochemically stable polymer, such as PVdF-HFP (defined below), and ceramic nanoparticles, such as TiO₂ or BaTiO₃.¹ These components combine to form different types of either solid polymer ionic liquid (SPIL) separators

when only the ionic liquid and the polymer are present, or c-SPIL separators when nanoparticulate ceramics are present. Additionally, through the use of laser direct-write (LDW) techniques, we explore the process of forming LDW lithium ion microbatteries for direct incorporation into micro-circuitry.^{2,3}

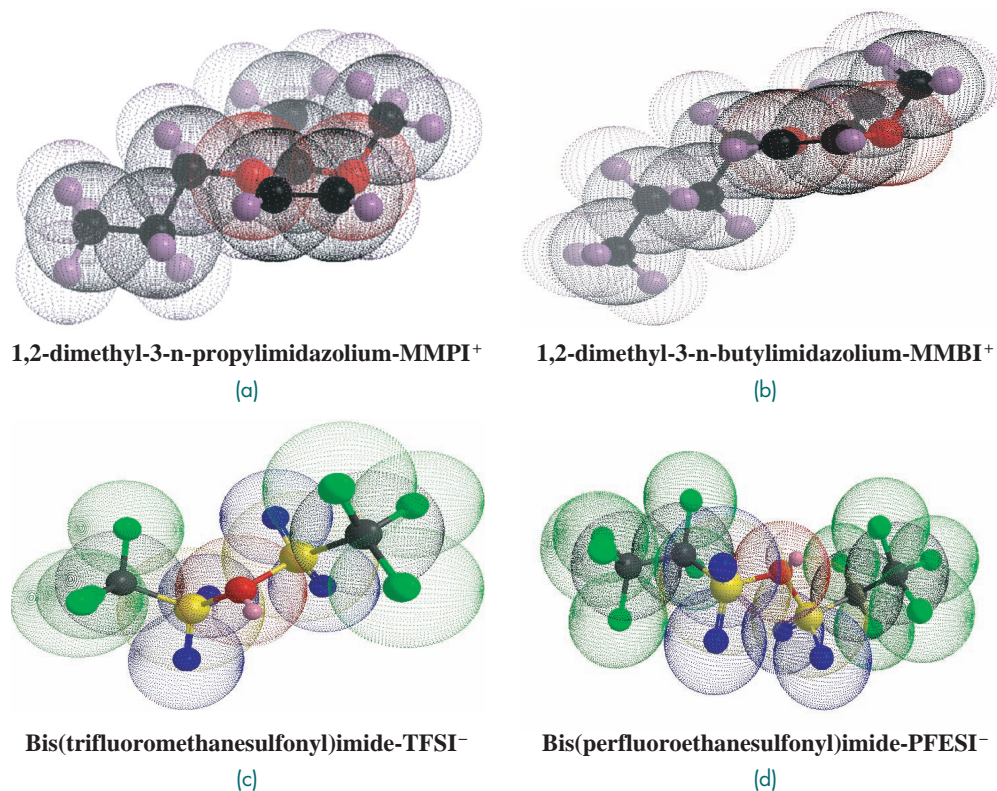
Our research focuses on the ionic liquids composed of one of the two cations shown in Figs. 4(a) and (b), and one of the two imide-based anions, shown in Figs. 4(c) and (d), for a total of four different types of ionic liquids. All of the ionic liquids used in this work are prepared and purified at NRL. Two different types of polymers are used to prepare the SPIL nanocomposite separators: poly(ethylene oxide), PEO, which is a hydrophilic type of polymer, and poly(vinylidene fluoride-co-hexafluoropropene), PVdF-HFP, a hydrophobic polymer type.⁴

Results: Figure 5(a) shows a drop-cast PVdF-HFP SPIL separator, without nanoparticles. These flexible films exhibit nearly 90 percent of the ionic conductivity of the pure ionic liquid. Figure 5(b) is a high-resolution SEM image of the nanocomposite SPIL separator used for Li-ion microbatteries, deposited by the LDW process. As shown, these c-SPIL separators can be laser transferred as solid continuous membranes into a variety of configurations, forming a solid, electrolytic separator. Thus, these SPIL separators can not only be used as separators for batteries, but also as micro-electrochemical cells for a variety of sensing and/or energy harvesting technologies.

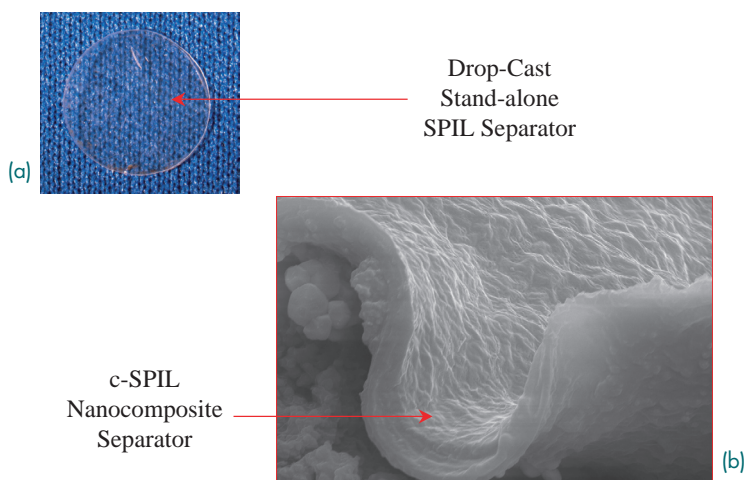
Our results also show that SPIL separators prepared using the hydrophilic polymer PEO exhibit much poorer mechanical and electrochemical characteristics when compared to SPIL separators prepared using the hydrophobic polymer PVdF-HFP. Experimental evidence indicates that in the PVdF-HFP gel the mobility of the Li ion is not limited by secondary interactions with the polymer backbone, which occur in the hydrophilic PEO-based SPIL separators. Analysis indicates that the hydrophobic tail of the imidazolium ring is strongly associated with the non-polar backbone of the PVdF-HFP, while the anion and the lithium salt are located in nanochannels within the mesoporous SPIL separator. Thus, the PVdF-HFP gels exhibit ionic conductivity comparable to the pure ionic liquid.

Figure 6 shows the charge-discharge behavior of the micro lithium ion battery created entirely by the LDW process (inset figure shows a sealed Li-ion micro-battery). The capacity, charge-discharge performance, and lifetime are all comparable to typical lithium ion batteries.

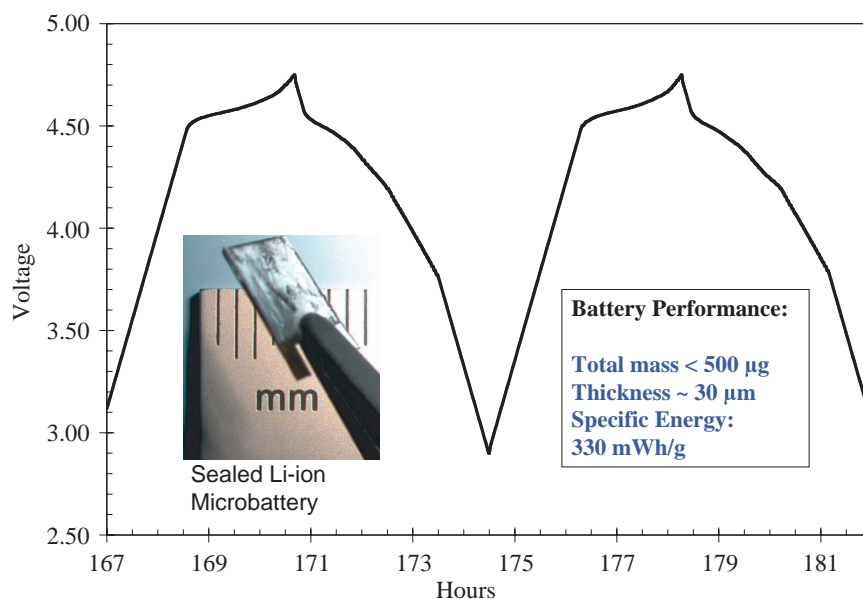
Conclusions: Our research has shown that these ionic liquids are not only suitable to replace the more flammable and dangerous types of electrolytes in

**FIGURE 4**

Molecular structure of cations (a,b) and anions (c,d) of the ionic liquids. Black spheres=carbon; red spheres=nitrogen; blue spheres=oxygen; yellow spheres=sulfur; green spheres=fluorine; purple spheres=hydrogen; small pink spheres=lone pair of electrons on the nitrogen of the imide. These four ions combine to form the following four ionic liquids: MMPI⁺TFSI⁻, MMPI⁺PFESI⁻, MMBI⁺TFSI⁻, and MMBI⁺PFESI⁻.

**FIGURE 5**

(a) Stand-alone SPIL separator composed of 80% MMPITFSI and 20% PVdF-HFP.
(b) High-resolution SEM of a LDW-written c-SPIL separator. The LDW process creates a solid, continuous, flexible separator.

**FIGURE 6**

Charge-discharge behavior of the IL-based lithium ion microbattery. Inset on the left shows a sealed lithium ion microbattery. Inset on the right lists the battery performance.

lithium ion power sources, but that they can also be directly incorporated into micro-devices. As such, the enhanced safety should significantly increase the types of applications for these ionic liquids, and the ability to field safe, high energy density systems for the war-fighter.

[Sponsored by the Army Research Office]

References

¹ T.E. Sutto, "The Electrochemical Behavior of Trialkylimidazolium Imide Based Ionic Liquids and Their Polymer Gel Electrolytes," *J. Electrochem. Soc.* **154**(11), P130-P135 (2007).

² M. Ollinger, H.S. Kim, T. Sutto, and A. Piqué, "Laser Printing of Nanocomposite Solid-state Electrolyte Membranes for Li Micro-batteries," *Applied Surf. Sc.* **252**(23), 8212-8216 (2006).

³ C.B. Arnold, T.E. Sutto, H.S. Kim, and A. Piqué, "Direct-write Laser Processing Creates Tiny Electrochemical Systems," *Laser Focus World* **40**(5), S9 (2004).

⁴ T.E. Sutto, "Hydrophobic and Hydrophilic Interactions of Ionic Liquids and Polymers in Solid Polymer Gel Electrolytes," *J. Electrochem. Soc.* **154**(10), P101-P107 (2007). ★



Improved Aircraft Canopy and Window Materials (1953-1961)

When acrylic combat aircraft canopies were suffering catastrophic failures after being hit by shrapnel or after a missile impact, causing fatal “blow-out” accidents in the early 1950s, NRL’s pioneering experience in fracture mechanics and fracture test technology was brought to bear. J. Kies studied the propagation of small cracks by shattering hundreds of acrylic canopies by projectile impact and reassembling them to trace the crack paths. Kies and I. Wolock, then at the National Bureau of Standards and later with NRL, collaborated with the Air Force and commercial manufacturers such as Rohm and Haas to develop hot stretching, a technique that could eliminate craze cracking and add to the toughness of the material. The resulting material was not only tougher but lighter and extended the service life of the canopies, and was adopted by the Navy, Air Force, and Department of Commerce for their aircraft canopies. Kies pointed out that the critical stress for a given track depended only on the product GcE , which could be directly computed from the applied stress and crack size for the test. Aircraft engineers now express fracture test results of stretch-toughened glazing materials in the unit K (named for Kies).

149

Generalized FFT Beamsteering

J.O. Coleman

151

Graded Bandgap Type-II Superlattice Photodiodes

E.H. Aifer, I. Vurgaftman, C.L. Canedy, E.M. Jackson, J.G. Tischler, J.H. Warner, R. Stine, J.R. Meyer, and L.J. Whitman

153

Dynamics of Forward Voltage Drift in 4H-SiC PiN Diodes

J.D. Caldwell, R.E. Stahlbush, K.D. Hobart, and O.J. Glembocki

Generalized FFT Beamsteering

J.O. Coleman
Radar Division

Introduction: A receive antenna's beam, the direction of maximum gain or sensitivity, need not be rigidly oriented to the physical antenna. An array antenna, hundreds or thousands of small antenna elements laid out along a line or, more usefully, on a 2D lattice, offers an electronically controlled, agile beam or even multiple beams associated with multiple antenna outputs, a technology that can enable a military radar to precisely track many objects in flight simultaneously. The classic approach to efficiently realizing many simultaneous beams uses fast Fourier transforms (FFTs) for computational efficiency but severely restricts choices of system parameters. Generalized FFT beamsteering as described here loosens those restrictions to give system designers a larger tradeoff space and therefore opportunities for cost savings and performance gains, particularly for large digital radar arrays.

Classic Array Basics: The simplest array has antenna elements spaced along a line at half-wave-length intervals. Referring to Eq. (1) in Fig. 1, suppose the p th element output is processed by its own receiver to create complex signal output s_p (a function of time, though that is not shown here). Array output or beam sum X of Eq. (1) can be made to strongly favor signals from array boresight directions normal to the array, by

designing weights w_p so that such signals add constructively in the sum while other signals largely cancel. Here p formally ranges from $-\infty$ to ∞ in the sum, but weight w_p is nonzero only for the finite number of p for which actual array elements exist.

Beam steering can be included in the beam-sum computation using the fact that a nonboresight signal arrives at the elements in sequence, with net propagation delays stepped element by element. For narrow-band signals, which are more or less sinusoidal, stepped phase shifts result, so we aim the beam sum by modifying it to cancel those phase shifts for some direction of interest as in Eq. (2) of Fig. 1, where phase-step parameter θ selects the favored direction. To simultaneously create beams for N different θ values spread around the circle and thereby spread beams across all directions, specialize Eq. (2) to $\theta = 2\pi k/N$ as in Eq. (3) and compute a beam sum X_k for each of $k = 0 \dots N-1$.

This computation can be restructured to practical advantage. First, write each p as $Nn' + n$ with n' an arbitrary integer but with the existence and uniqueness of the decomposition guaranteed by drawing n only from the N modulo- N integers, classically taken to be $0 \dots N-1$. Then define intermediate quantities x_n as in Eq. (4) and rewrite beam sum X_k of Eq. (3) as shown in Eq. (5).

This classic formulation expresses the N beam sums X_k as the size- N discrete Fourier transform (DFT) of the N intermediate variables x_n , which are precomputed using weighting and folding. This formulation makes the extraordinary computational efficiency of FFT algorithms available for computing the DFT. (For

$$X = \sum_p w_p s_p \quad \text{boresight beam} \quad (1)$$

$$X = \sum_p w_p s_p e^{-j\theta p} \quad \text{steered beam} \quad (2)$$

$$X_k = \sum_p w_p s_p e^{-j2\pi kp/N} \quad \text{many steered beams } k = 0 \dots N-1 \quad (3)$$

$$x_n \triangleq \sum_{n'} w_{Nn'+n} s_{Nn'+n} \quad \text{weighted and folded element-receiver outputs} \quad (4)$$

$$X_k = \sum_{n \in \left\{ \begin{smallmatrix} \text{all mod } N \\ \text{values} \end{smallmatrix} \right\}} x_n e^{-j2\pi k N^{-1} n} \quad \text{FFT or generalized FFT to compute beams of (3)} \quad (5)$$

$$R = \begin{bmatrix} r_{\text{rows}} & 0 \\ 0 & r_{\text{cols}} \end{bmatrix} \quad \text{determines fine beam grid within coarse-grid cell} \quad (6)$$

$$N = \begin{bmatrix} -1 & 1 \\ 2 & 2 \end{bmatrix} \begin{bmatrix} 8 & 0 \\ 0 & 8 \end{bmatrix} \quad \text{example factoring to fix generalized-FFT structure} \quad (7)$$

FIGURE 1

The key mathematics. Here Eq. (7) is for the Fig. 2 example. The other equations are general.

FFT basics see Ref. 1 or any other digital signal processing text.)

This FFT beamsteering approach is well known, as is its separate application in each of two dimensions to create beam rows and columns from a 2D array of element rows and columns.

NRL Generalizes to a Matrix FFT Size: Our work generalizes the latter 2D approach to add design flexibility. The subscripts on s_p , w_p , x_n , and X_k become length-two integer vectors, with k a row vector and the others columns. The original number of directions N becomes a nonsingular 2×2 integer matrix with the number of directions now just the magnitude $|N|$ of its determinant.

When N was a scalar, the set of “all mod- N values” summed over in Eq. (5) of Fig. 1 was any fixed set of N integers that ensured a unique decomposition $p = Nn' + n$ for every integer p , with $n = 0 \dots N - 1$ the customary choice. A similar unique decomposition is required now as well, but now $p = Nn' + n$ involves matrix N and vectors n , n' , and p , and n is drawn from any fixed set of $|N|$ modulo- N column vectors. Similarly, k now ranges over a set of modulo- N row vectors that gives every length-two integer row vector a unique decomposition $k'N + k$. In Eq. (5), exponent $kN^{-1}n$ is still a scalar but is now the product of a row vector, a square matrix, and a column vector.

Remarkably, if the array elements are laid out on a regular lattice, whether square, triangular, or neither, Eq. (5) of Fig. 1 with all these generalizations still

creates a family of $|N|$ distinct beams and the principles underlying the classic FFT here lead to analogous algorithms. The efficiency of classic FFTs arises through factoring common factors out of sums and systematically sharing intermediate results. That is just as true here, and the results are just as computationally powerful.

The modulo- N ideas extend cleanly to the vector-matrix case because their scalar and vector versions both derive fundamentally from the same ideas in elementary group theory. Likewise, classic FFT algorithms and the generalized FFT algorithms of this work are both special cases of fast Fourier transforms on groups, a well-developed area in the mathematics community.

More Classics—The Grating-Lobe Offset Lattice:

Beam-pointing parameter θ in Eq. (2) of Fig. 1 is a length-two vector with coordinates plotted horizontally and vertically in Fig. 2. In that θ space the globe shown has latitude and longitude lines corresponding respectively to a direction's elevation and azimuth relative to array boresight. A visible beam, one with θ inside the globe, is a signal direction of arrival favored in the corresponding beam sum. An invisible beam, one with θ outside the globe, is irrelevant to the array's physical operation.

There are always invisible beams in the mathematics, however, because beam sum X in Eq. (2) of Fig. 1 is periodic in θ . If X has a beam characterized by a particular θ , then it also has one characterized by θ plus

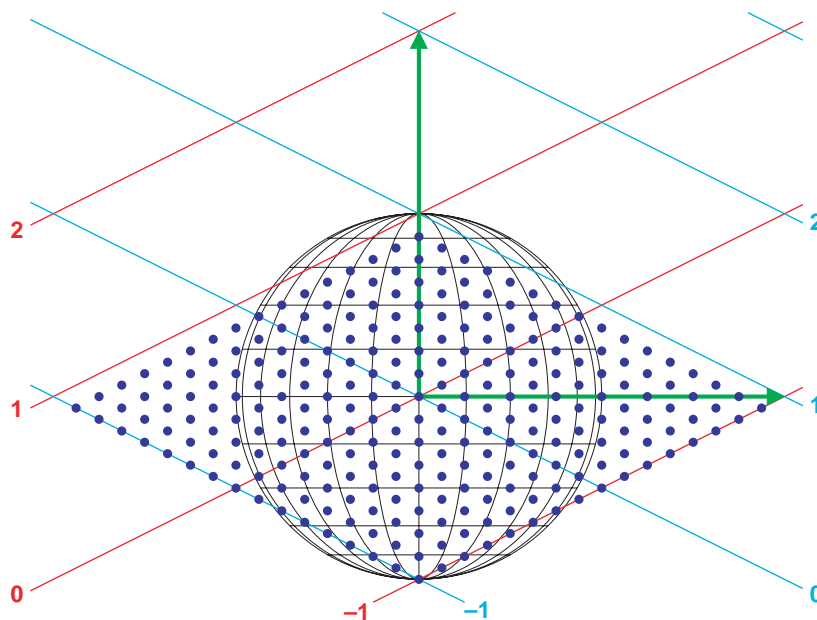


FIGURE 2

The θ plane. Dots in the direction-of-arrival coordinate globe represent beam locations computed by the generalized FFT. The beam layout and the structure of that FFT is determined by the choice of a coarse grid, which must include the basis vectors (green) of the grating-lobe lattice.

any member of a grating-lobe offset lattice comprising integer-weighted combinations of the large basis vectors shown as arrows in Fig. 2. Element spacing and placement geometry are ordinarily chosen—this is where the classic half-wavelength spacing arises—so that one period of the grating-lobe offset lattice completely contains the visible globe. Then no periodic replica of a desired beam can ever become visible and thus become a grating lobe.

The Increased Design Choice of the NRL

Approach: In the design process a coarse grid is laid out in the θ space with grid lines at arbitrary orientations and angles—in Fig. 2 they make large diamonds—but such that the grating-lobe basis vectors fall on grid points with small integer coordinates, here $[-1 \ 1]$ and $[2 \ 2]$.

A matrix L is constructed with those two vectors as its rows. This will result in some (nonunique) set of $|L|$ grid cells exactly tiling the plane. Within each of those $|L|$ grid cells are r_{rows} rows by r_{cols} columns of θ values, here shown by dots, corresponding to beam directions realized in this scheme. The Fig. 2 example has $r_{rows} = r_{cols} = 8$. By varying these two parameters and how the coarse grid is chosen, many beam-position layouts are possible.

Matrix N is then constructed as $N = LR$, where R is a diagonal matrix of the r_{rows} and r_{cols} as in Eq. (6) of Fig. 1. Matrix N for the Fig. 2 example is shown in Eq. (7).

The $N = LR$ factorization yields a generalized FFT algorithm built from $|L|$ blocks, each built in turn from r_{rows} ordinary FFTs of size r_{cols} and r_{cols} ordinary FFTs of size r_{rows} . Complex-exponential “twiddle factors” (the traditional name) that were factored out of sums in the FFT derivation are applied to the block outputs, and the final array output to realize a beam then requires only a one-term-per-block linear combination of those twiddled block outputs. The computations leading to twiddled block outputs are shared across all beams. Only the final linear combinations of $|L|$ terms are specific to beams. (In the Fig. 2 example $|L| = 4$.) Values of θ outside the globe are irrelevant, as are those inside the globe but impractically close to its edge, so not all of the linear combinations need even be computed.

For a detailed treatment of this generalized FFT beamsteering technique, see Ref. 2.

[Sponsored by NRL]

References

- ¹ A.V. Oppenheim and R.W. Shafer, *Digital Signal Processing* (Prentice Hall, Englewood Cliffs, New Jersey, 1975).
- ² J.O. Coleman, “A Generalized {FFT} for Many Simultaneous Receive Beams,” Naval Research Laboratory, NRL Memo Report 9029, June 29, 2007. ★

Graded-Bandgap Type-II Superlattice Photodiodes

E.H. Aifer,¹ I. Vurgaftman,² C.L. Canedy,²
E.M. Jackson,³ J.G. Tischler,¹ J.H. Warner,¹ R. Stine,⁴
J.R. Meyer,² and L.J. Whitman⁴

¹*Electronics Science and Technology Division*

²*Optical Sciences Division*

³*SFA, Inc.*

⁴*Chemistry Division*

Introduction: An infrared focal plane array (IRFPA) is a dense array of sensors and readout circuitry that creates the image in an infrared camera. IRFPAs are at the core of infrared detector systems for finding and tracking missiles in space, guiding missile seekers, seeing in the dark, mapping ocean temperatures, and defeating camouflage and decoys. For the past decade, continuous improvement of IRFPAs based on mercury cadmium telluride have dramatically enhanced performance and expanded capabilities in the mid-wave (3–5 μm) and long-wave (8–14 μm) infrared (MWIR and LWIR) bands. However, further improvements demanded by the next generation of detector systems are driving investigations of other material systems.

A promising material system for the next generation of IRFPAs is the type-II superlattice (T2SL) lattice-matched to GaSb. Although the T2SL detector concept was proposed over 30 years ago,¹ only in the last few years has this design begun to demonstrate its potential. NRL researchers have been at the forefront, making key innovations including the W-structured T2SL (WSL), the graded-bandgap T2SL photodiode,² and most recently, shallow-etch mesa isolation.

T2SL Photodiodes: The simplest form of T2SL, illustrated in Fig. 3(a), consists of alternating layers of GaSb and InAs. The type-II nature of the band alignment is evident in the relative position of the InAs conduction band (CB), which is lower in energy than the GaSb valence band (VB). In a short-period superlattice, however, the energy levels in each layer are shifted by quantum confinement, with the electron levels moving up and the hole levels moving down, opening up a positive energy gap as indicated by the carrier positions. There are several advantages in using the T2SL for infrared detection. First, one can conveniently adjust the energy gap over a very wide range (3–30 μm) by varying the layer thicknesses. Second, the electron effective mass is heavier than in the bulk material (and about three times larger than that of mercury cadmium telluride). The heavier mass strongly suppresses dark-current caused by tunneling between the conduction and valence bands. Finally, a gap opens in

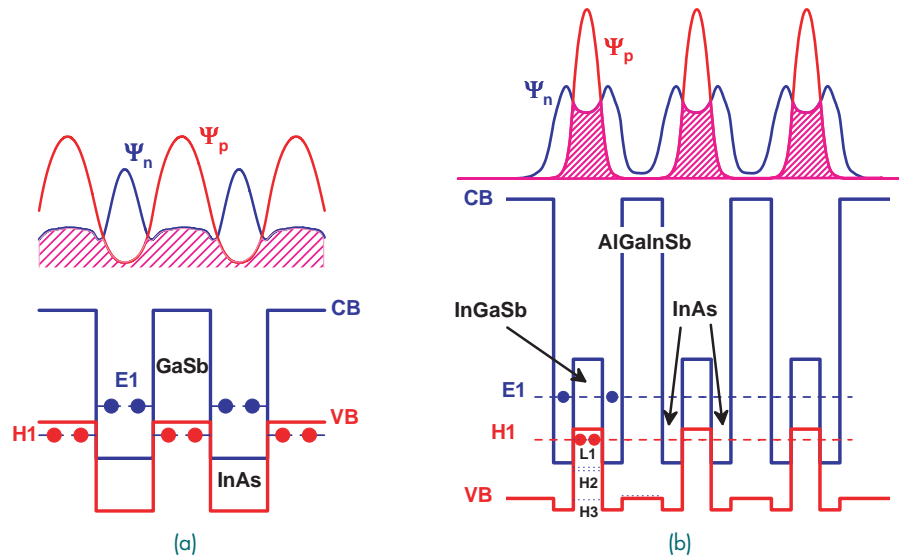


FIGURE 3
(a) Simple T2SL and (b) WSL heterostructures and wavefunctions.

the superlattice band structure between the light-hole (L1) and heavy-hole (H1) bands, and this gap can be engineered to reduce Auger processes, thereby increasing the operating temperature range of the device.

An important NRL innovation was to adapt the WSL—originally developed at NRL for MWIR laser applications—for use in photodiodes. The more complex WSL structure, shown in Fig. 3(b), includes a second InAs layer that makes the electron wavefunction symmetric about the hole states, and adds AlGaInSb barriers that more strongly confine the wavefunctions (without completely localizing them). This structure results in a four-fold increase in electron mass over the basic T2SL, and a nearly two-dimensional bandstructure that strongly enhances optical absorption near the band edge.

Graded-Bandgap WSL: Although the dark-current performance of T2SL-based photodiodes improved with the WSL design, it was still limited by defect-mediated processes such as trap-assisted tunneling and excess generation-recombination. We achieved a major breakthrough in controlling these processes with the graded-bandgap WSL, illustrated in red in Fig. 4(a). In this structure, the band edges are smoothly graded in the vicinity of the junction, increasing from the narrow-gap IR absorbing layer to the much wider-gap n^+ -doped superlattice that forms the cathode. The band profile is carefully shaped to form a very large tunneling barrier, and to suppress generation-recombination current. The key to realizing this structure is the flexibility afforded by the WSL, which allows independent control of the band edges while maintaining

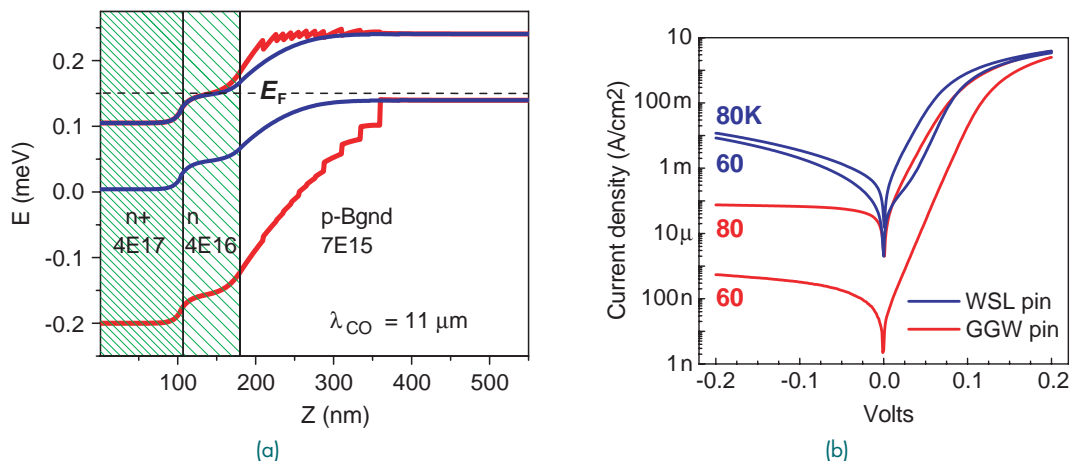
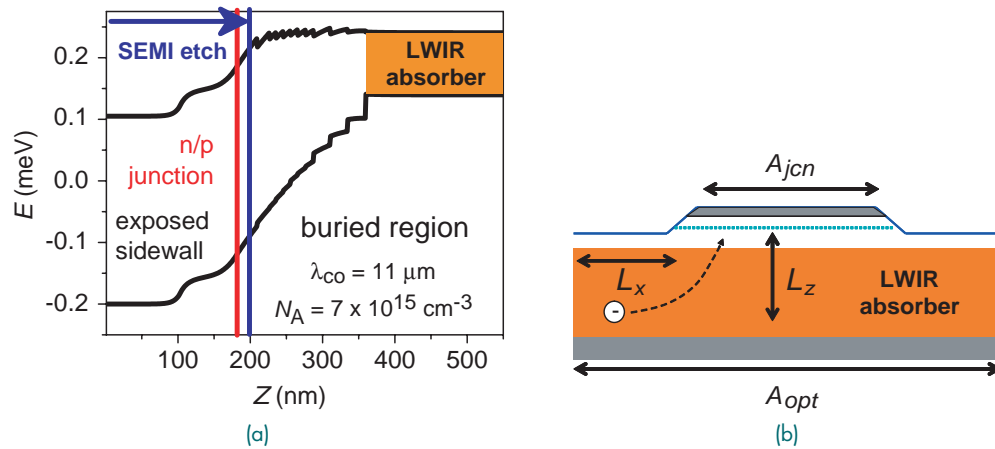


FIGURE 4
Comparison of graded-bandgap (red) and uniform WSL (blue) photodiode: (a) bandstructure; (b) current-voltage characteristics.

**FIGURE 5**

SEMI process for graded-bandgap T2SL photodiodes: (a) bandstructure; (b) schematic of photodiode cross-section. A_{jcn} = junction area; A_{opt} = optical area; L_x = lateral diffusion length; L_z = vertical diffusion length.

a good lattice match to the substrate. For comparison, the band edges of a uniform (ungraded) diode with the same bandgap are shown in Fig. 4(a) in blue. The dark-current performance of the two structures is displayed in Fig. 4(b), with the graded structure (GGW) having a dark-current >100 times lower at 60 K and >10 times lower at 80 K.

Shallow-Etch Mesa Isolation: In a LWIR focal plane array, typically made with pixels 20 to 40 μm wide isolated by deep trenches, the limiting factor in dark-current performance is often surface recombination and leakage involving defect states on mesa sidewalls. However, surface leakage is readily controlled in MWIR T2SL photodiodes, to the extent that commercially produced FPAs are presently available. In this context, bandgap grading leads to a powerful means to addressing surface leakage. The solution, illustrated in Fig. 5, is to fabricate mesa diodes on graded-bandgap structures with LWIR and very long wave infrared (VLWIR) absorbers such that only wider-gap (MWIR) layers are exposed on the surface, greatly simplifying passivation. We have thus developed the technique of shallow-etch mesa isolation (SEMI) employing two separate etch steps on graded-gap T2SL photodiodes. First a shallow etch is used to electrically isolate neighboring pixels, terminating just past the junction but well within the MWIR-gap region of the diode. A deep etch is then performed along the periphery of the array to allow contact to the backside anode. The LWIR or VLWIR layers remain undisturbed and protected by at least 100 nm of material, and the entire pixel is optically functional. Using SEMI, we have been able to achieve bulk-limited performance on pixels with mesa diameters as small as 24 μm . Furthermore, the electrical junction area can be reduced to a fraction of the pixel area without loss of quantum efficiency, provided the junction is within a lateral diffusion length of the

pixel border (10–15 μm). Using this approach, we have achieved a factor of three reduction in bulk junction current.

[Sponsored by NRL]

References

- ¹ G.A. Sai-Halasz, R. Tsu, and L. Esaki, "A New Semiconductor Superlattice," *Appl. Phys. Lett.* **30**, 651 (1977).
- ² I. Vurgaftman, E.H. Aifer, C.L. Canedy, J.G. Tischler, J.R. Meyer, J.H. Warner, E.M. Jackson, G. Hildebrandt, and G.J. Sullivan, "Graded Band Gap for Dark-Current Suppression in Long-Wave Infrared W-Structured Type-II Superlattice Photodiodes," *Appl. Phys. Lett.* **89**, 121114 (2006). ★

Dynamics of Forward Voltage Drift in 4H-SiC PiN Diodes

J.D. Caldwell, R.E. Stahlbush, K.D. Hobart, and O.J. Glembocki

Electronics Science and Technology Division

Background: 4H-silicon carbide (SiC) is desired for electronic devices designed to be operated at high temperatures or at high electric powers. However, difficulties in the growth of high-purity, low defect density substrates and epitaxial layers have limited the use of SiC in commercial and military applications. One such impediment is the nucleation and expansion of Shockley stacking faults (SSFs) during forward-bias device operation (stressing), which induces an undesirable increase in the forward voltage drop (V_f). While efforts have been made to reduce the number of SSFs within a given device, these defects continue to provide a significant technological hurdle to the commercialization of 4H-SiC electronic devices, most especially for larger-area power devices that require close to defect-free active regions.

Electrical Degradation: The expansion of SSFs in SiC induces a drift in V_f . In other words, during forward-bias operation, the voltage required to turn the device on (reach a threshold current) increases continuously. Therefore, the turn-on voltage is a moving target and renders the device useless. This degradation in the forward-bias characteristics is illustrated in Fig. 6(a), where current-voltage (IV) curves collected from a PiN diode are presented. The initial IV curve is shown in blue. A current density of 14 A/cm^2 was then injected into the diode for twelve consecutive 5-min intervals, with each interval leading to a progressive flattening of slope of the IV curves (V_f drift increase). The final curve, collected after 60 total minutes of stressing is presented in red. This degradation is due to SSFs, which are localized, planar changes in the crystal stacking order from hexagonal (4H-SiC) to cubic (3C-SiC). Since cubic SiC has a significantly reduced bandgap, this causes the SSFs to act as tilted, planar electron traps. A schematic of a PiN diode is presented in Fig. 6(b) to illustrate the orientation of the SSFs.

SSF Expansion: Presented in Fig. 7(a) is an electroluminescence (EL) image collected from a 4H-SiC PiN diode prior to device stressing. In SiC, EL images are collected by driving a constant current (here, 1.4 A/cm^2) through the device for given time (here, 5 or 10 sec). In SiC, when current carriers (electrons and holes) recombine at defects such as SSFs, they give off excess energy in the form of light, which can be imaged using a CCD camera. In this image the partial dislocations that bound the SSFs can be seen as red lines. Since the SSFs are tilted 8° from the horizontal (see Fig. 6(b)), top-view EL images of the epilayer illustrate the position of these defects at a given time. As shown in Fig. 7(b), upon electrical stressing (1.75 min at 25 A/cm^2), the SSFs expand significantly, with the red partial

dislocations now larger and clearly highlighting the periphery of the violet, triangular-shaped SSFs. The bright blue, vertical EL line indicates that one of the SSFs has terminated at the p-n junction. In Fig. 7(c), we see that following 8 min at 25 A/cm^2 , almost all of the faults that were expanding to the left have also terminated there.

SSF Contraction: Until recently, it was believed that SSFs were the energetically favorable state; therefore, if enough energy was provided, the 4H-SiC would be readily converted into 3C-SiC SSFs. Here at NRL, it was discovered that thermal annealing of heavily faulted (degraded) PiN diodes for extended periods at temperatures between 210° and 700°C led to the complete contraction of all SSFs. This is illustrated in Fig. 7(d), where the diode was annealed at 700°C for 4 hrs. Annealing also induced a complete and repeatable recovery of the V_f drift, as presented in Fig. 6(c), where IV curves collected following several subsequent annealing cycles at 505°C are displayed. These observations clearly illustrate that SSFs are not the thermodynamically favorable state.

Temperature Effects on V_f Drift: Further experimentation at NRL determined that continued device stressing led to a maximum V_f drift; however, temperature increases (or decreases in stressing current) reduced SSF expansion and therefore reduced this V_f drift maximum, as illustrated in Fig. 8(a). It was also determined that the annealing process is accelerated if an electrical current is injected during the process (current-induced recovery), which is illustrated in Fig. 8(b). In this case, the device was initially stressed at room temperature (blue circles) until the V_f drift maximum was attained. Following this, the device was heated to 242°C (red squares) and the same current

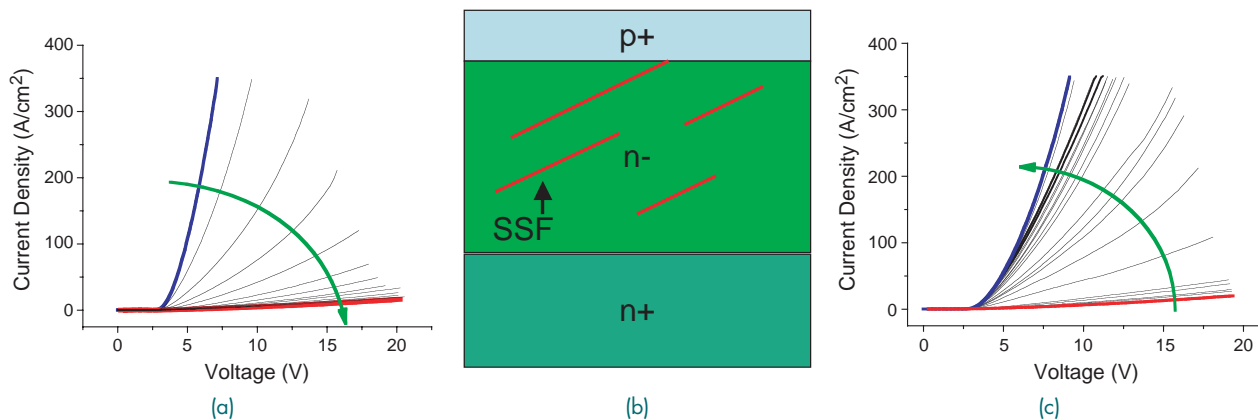
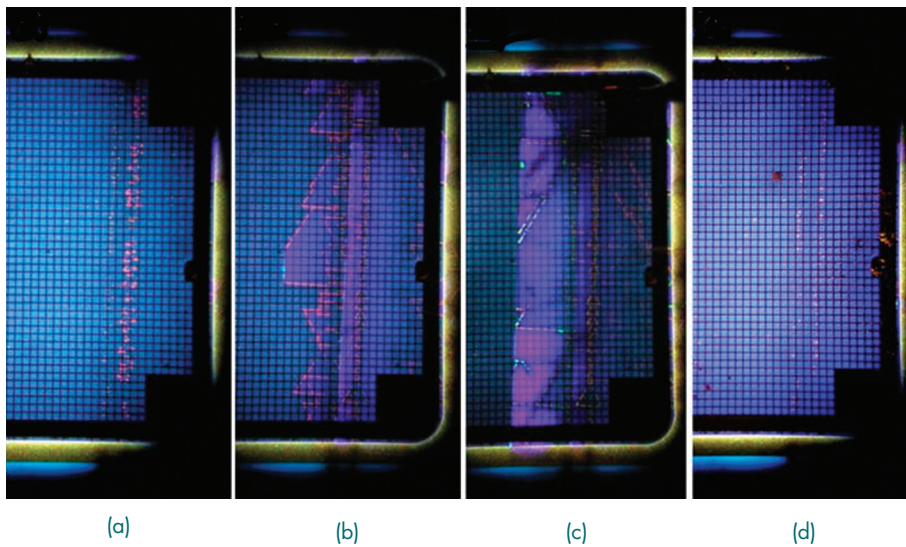
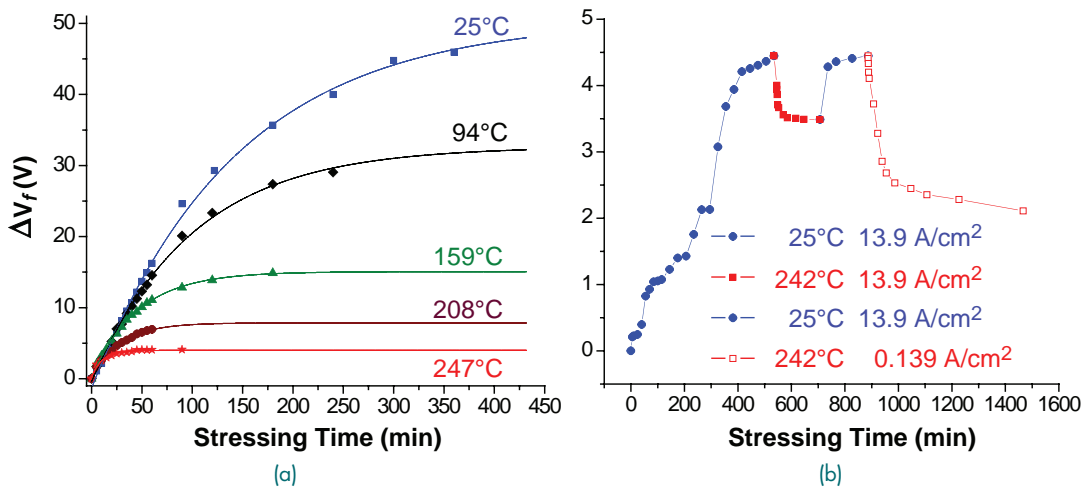


FIGURE 6 (a) Current-voltage (IV) traces collected prior to device stressing (blue curve), and following twelve consecutive 5-min periods of 14 A/cm^2 device stressing. (b) Pictorial representation of the cross-sectional view of a SiC PiN diode. The red lines represent the SSFs that are tilted 8° from the horizontal. (c) IV curves collected following subsequent periods of annealing at 505°C . In both (a) and (c), the red and blue curves denote the IV data from the diode in the heavily faulted and the unfaulted states, respectively.

**FIGURE 7**

Electroluminescence (EL) images collected (a) prior to device stressing, (b) following 1.75 min of stressing and (c) 8 min of stressing at 25 A/cm², and (d) following a 4-hour, 700 °C anneal. The black regions are where the metal contact is present.

**FIGURE 8**

(a) Plot of the change in the V_f as a function of the stressing time within the same diode at various stressing temperatures. The device was fully annealed before each series of experiments at a given temperature. (b) Similar to (a), but the stressing temperature and current were changed at different points during the experiment (see legend) to illustrate current-induced recovery of the V_f drift. While the stressing was completed at various temperatures, the IV data points were collected at 25 °C.

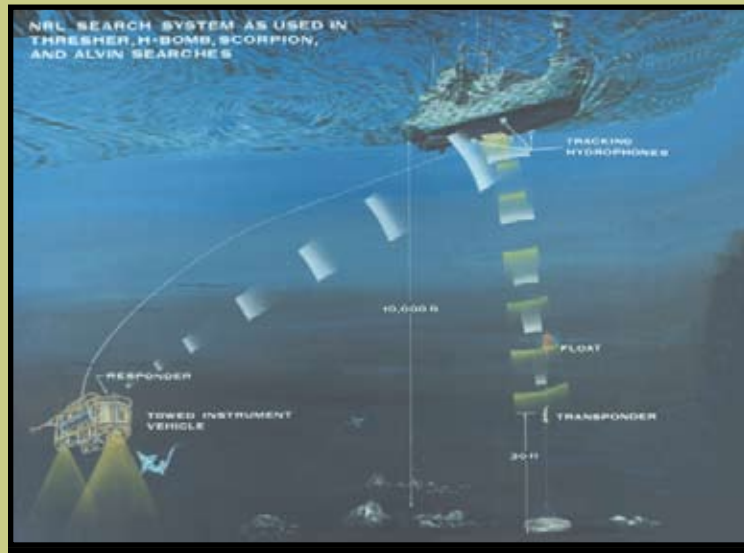
was applied, which led to the V_f drift partially recovering, eventually reaching a new, reduced maximum V_f drift. The temperature was then returned to room temperature and the process repeated; however, when the temperature was raised this second time, the current was reduced 100× (red, open squares), leading to an even larger V_f drift recovery.

Summary: These results illustrate that SSF expansion and its deleterious effects can be controlled to

some degree, thereby providing hope that functional SiC bipolar devices may be possible, even if some small, yet manageable, SSF density is present, especially at elevated operating temperatures. It also demonstrates that degraded devices may be repeatedly recovered. It should also be noted that very recently, NRL has developed a new epitaxial growth technique that has been observed to reduce the density of the SSF nucleation sites by up to 98%.

[Sponsored by ONR]





Deep Ocean Search (1963-1970)

Part of the fascination with the HMS *Titanic* springs from its second life as probably the most famous site of underwater exploration and salvage. NRL's deep-towing technology was the invention that enabled the later work on finding the *Titanic*. Originally invented years earlier for underwater acoustic research, NRL's unmanned deep-towed instrument vehicle, or "fish," was first applied to a deep-ocean seafloor search for the nuclear submarine USS *Thresher* (SSN 593), which was lost on April 10, 1963, in deep water 260 miles east of Boston, Massachusetts, with its crew of 112 and 17 civilian technicians. After having to terminate the search in September due to the onset of harsh weather, the *Thresher* wreckage was found and photographed after only 8 hours of operation when the search resumed in May 1964. By then, NRL had acquired the retired cargo ship USNS *Mizar* as the launch and tow vehicle for the "fish," which included an array of sensors including a set of three cameras, sidescan sonar, strobe lights, a magnetometer, a transponder, a sonar pinger, and a telemetry system. NRL continued to develop the technology, and its resulting Deep Ocean Search System was successfully used in more than 30 missions between 1965 and 1974, most notably locating and recovering a lost H-bomb off the coast of Spain in 1966 and locating and photographing the lost submarine USS *Scorpion* (1968), the deep submersible *Alvin* (1969), and the French submarine *Eurydice* (1970). Other Navy organizations took over the emergency search mission in 1980. The NRL-developed deep-ocean search technology was transferred to other government and private organizations.

159

Mitigating Motion Sickness in Ground Vehicles

J.T. Coyne, R. Stripling, E. Rovira, D. Hunter, J.V. Cohn, K. Brendley, G. Zwick, and G. Carter

160

Unmanned Vehicle Mission Planning Using 4D Forecasts

B.S. Bourgeois and H.A. Morris

163

Measurement and Analysis of Clutter in Electronic Displays

M.C. Lohrenz, M.R. Beck, J.G. Trafton, and M.L. Gendron

166

NRL Global Vessel Tracking Project (VTP)

D.J. Bielecki

Mitigating Motion Sickness in Ground Vehicles

J.T. Coyne,¹ R. Stripling,¹ E. Rovira,² D. Hunter,³
J.V. Cohn,¹ K. Brendley,³ G. Zwick,² and G. Carter²

¹Information Technology Division

²United States Military Academy

³Artis LLC

Introduction: Motion sickness (MS) represents a challenge to many warfighters, particularly those in command and control vehicles (C2V). Research by the U.S. Army and NASA¹ suggest that as many as 90% of operators in a C2V experience some performance decrements and MS symptoms. Common solutions to MS emphasize pharmacological interventions, such as promethazine and dimenhydrinate (Dramamine™). The challenge with these approaches is that they often lead to decrements in cognitive performance and drowsiness. The sensory conflict theory suggests that MS arises in conditions where the sensory systems, specifically the visual and vestibular systems, detect different motions. This paper provides evidence for an information technology solution to MS, called Motion Coupled Visual Environment (MOCOVE),² which attempts to resolve MS by artificially introducing couplings between visual and vestibular motion cues.

The MOCOVE device contains a set of accelerometers that detect physical motion and uses software to provide an Earth-referenced, stabilized viewing scene. For example, when MOCOVE accelerometers detect a roll movement of the vehicle, MOCOVE software rotates the computer display window in the opposite direction, at a rate proportional to the rate of physical rotation of the vehicle. Similarly, if MOCOVE accelerometers detect an upward movement of the vehicle (usually called heave), then MOCOVE software acts to move the display window downward proportionally.

Previous research demonstrated the potential for using MOCOVE to reduce MS in a ship motion simulator (SMS). Participants viewed motions with and without MOCOVE as the SMS provided pitch and roll motions. Due to technical issues with the sensors, all participants on day one did not have MOCOVE, while on day two they had MOCOVE. Initial results, which used the motion sickness assessment questionnaire (MSAQ) scores collected at 5-minute intervals during the study, suggested a reduction in MS symptoms on day two supporting MOCOVE. However, it is not clear if this difference was potentially due to adaptation to the environment. The current study was designed to determine (a) how effective MOCOVE (see Fig. 1) is in a moving ground vehicle and (b) the extent to which repeated exposure will affect MS and performance.

Methodology and Results: The experiment was conducted at the United States Military Academy

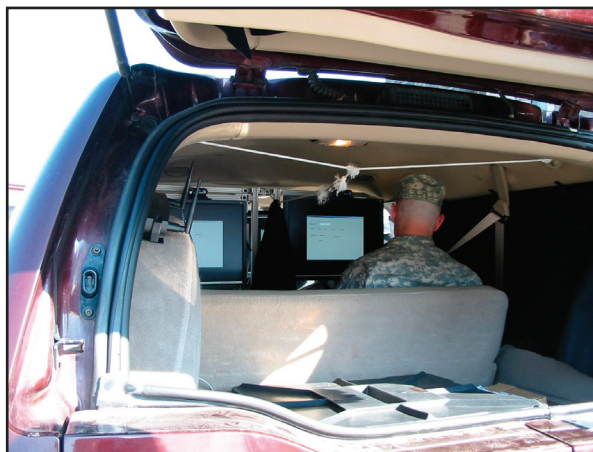


FIGURE 1
MOCOVE test vehicle.

(USMA), West Point, NY, with 21 first-year cadets participating in the study. Each participant took part in training and two driving sessions. The first driving session could be held on the same day as the training, but the final driving session had to be held on a subsequent day. The two driving sessions were identical except that half the participants had MOCOVE on the first day and the other half had the uncoupled system on the first day.

Participants received approximately 1 hour of training on a cognitive-motor battery and a simplified C2V task prior to entering the vehicle. Data were collected from the participants before the vehicle began moving, twice during each drive, and immediately after the completion of each drive (Fig. 2).

The data indicated a significant difference decrease in participants' ratings of MS on the first day compared to the second day. While there was no overall difference between MOCOVE and the uncoupled system, further analysis found that the difference between the two systems was significant on the first day.

Summary: The study provided some evidence of the effectiveness of MOCOVE in reducing motion sickness symptoms. More importantly, the current results appeared to be influenced by the more powerful effect of previous exposure (i.e., on the previous day). This pattern of results was unexpected because adaptation to MS at sea typically requires hours or days of continuous, prolonged exposure. The present study provides some initial data for adaptation to MS in ground vehicles with uncoupled motions; however, future research needs to examine this issue further.

The MOCOVE effect may have been weaker than expected because the system used in the current experiment was a modified version of the system designed for ship motions, which are characterized by movement along the rotational axis (i.e., pitch and roll) and

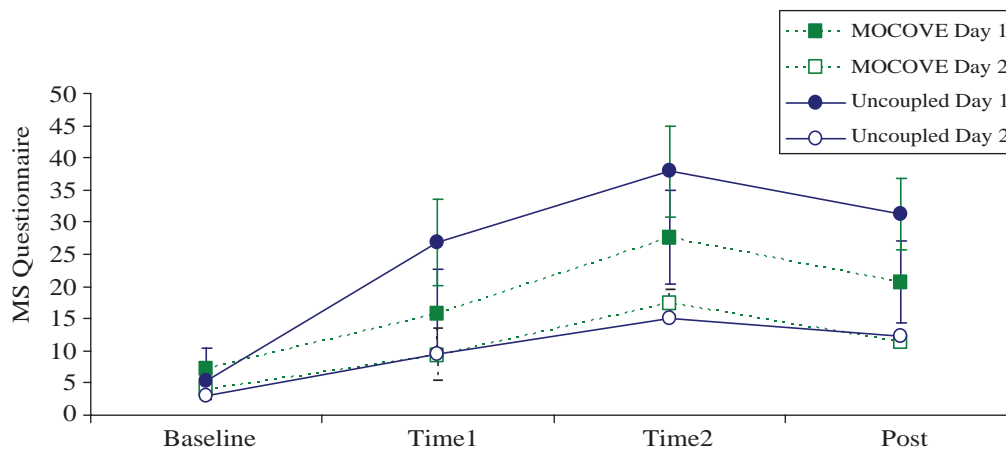


FIGURE 2
Motion sickness self-report data.

not lateral movement (i.e., accelerating and braking). There is some indication in the literature that it is these motions (braking/acceleration) that contribute most to motion sickness in land vehicles, and it is possible that the MOCOVE system being used could not adequately compensate for them. Design of a new ground vehicle-specific version of MOCOVE is already underway. This new design will feature a static window where the operators will perform their tasks while the background of the display will feature a moving terrain depiction based upon the vehicle's motion. It is hypothesized that this display may have a more pronounced reduction of MS.

[Sponsored by ONR]

References

- ¹P.S. Cowings, W.B. Toscano, C. DeRoshia, and R. Tauso, "Effects of Command and Control Vehicle (C2V) Operational Environment on Soldier Health and Performance," *J. Human Performance in Extreme Environments*, 5(2), 66-91, 2001.
- ²K.W. Brendly, J.V. Cohn, J. Marti, and P. DiZio, "Demonstration of a Motion Coupled Virtual Environment (MOCOVE) - A Device for Reducing Spatial Disorientation in Uncoupled Virtual and Motion Environments," Proceedings of the Human Factors and Ergonomics Society 46th Annual Meeting, 2002, pp. 766-70. ★

Unmanned Vehicle Mission Planning Using 4D Forecasts

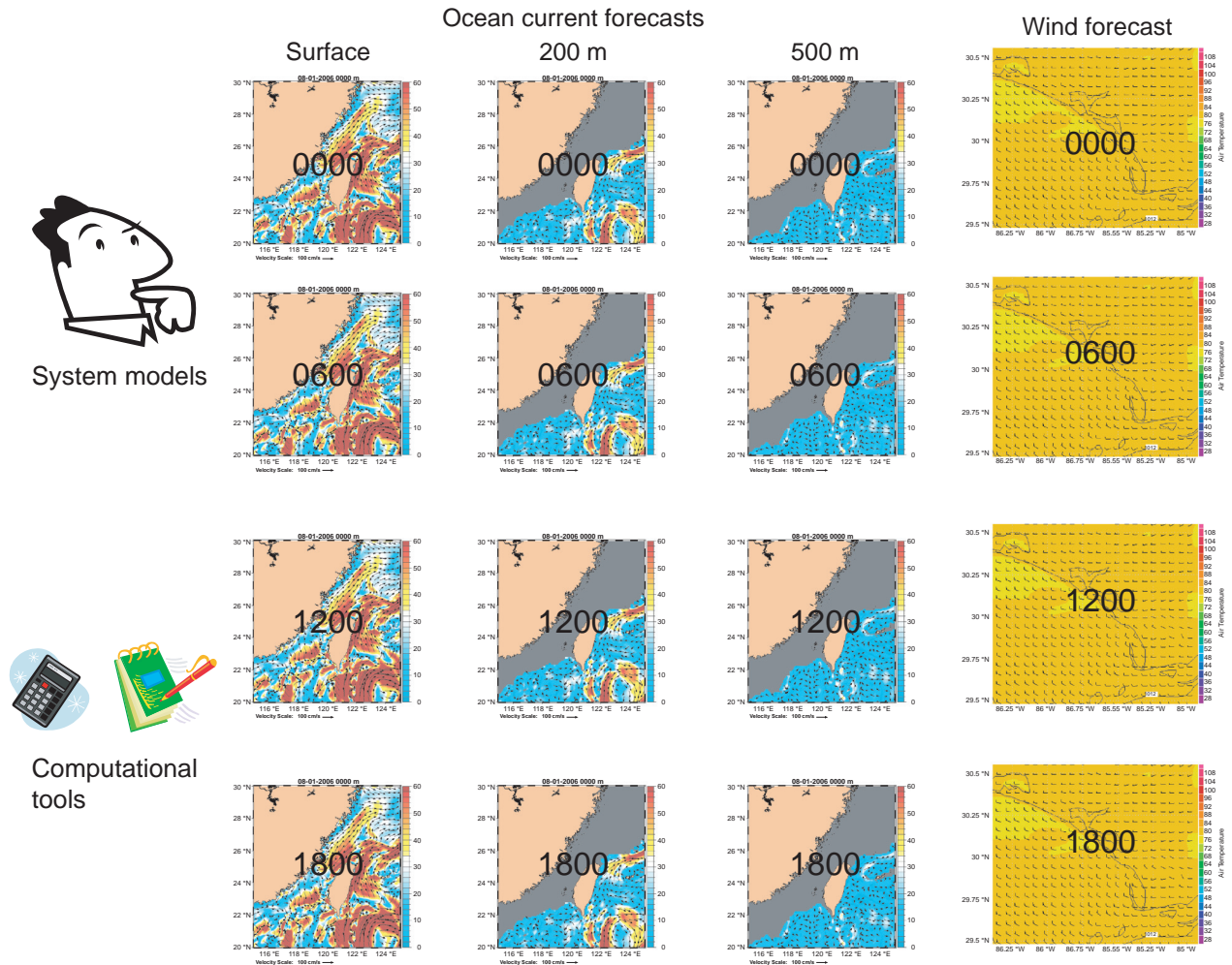
B.S. Bourgeois and H.A. Morris
Marine Geosciences Division

Introduction: We are engaged in the development of mission planning software for autonomous underwater vehicles (AUVs) supporting the Naval Oceanographic Office's underwater glider and AUV programs. Planning missions for underwater vehicles require the consideration of "static" features such as bathymetry,

territorial boundaries, and shipping lanes and also time variant features such as water density, sea state, and currents that can be estimated using model forecasts. These myriad considerations result in a $4D \times N$ geospatial-temporal constraint satisfaction problem, where N is the number of factors and D is typically represented as a value at a specific (x, y, z) location and time t . The difficulty inherent in this decision-making process is the simultaneous manipulation and visualization of these variables, which is accomplished today through human observation of multiple 2D slices of the $4D \times N$ cube as shown in Fig. 3. Another complicating factor is the large size of the forecast datasets, which can approach a gigabyte in size.

Geographic Information Systems: Geographic Information Systems (GIS) have been used extensively for $2D \times N$ geospatial decision-making and to a lesser extent for $3D \times N$ geospatial-temporal decision-making.¹ A goal of this research is to take advantage of the inherent capabilities in standard GIS systems, such as standardized data formats and graphic user interfaces (GUIs), common geospatial databases, multilayered computations, and assimilation of both raster and vector data. CJMTK (Commercial Joint Mapping Toolkit), provided by the Defense Information Systems Agency (DISA) for command and control applications, has become the de facto DoD GIS standard² and provides this functionality. However, existing GIS systems have difficulty handling very large datasets and provide little support for 4D visualization. The objective of this research is to develop approaches to the manipulation and visualization of $4D \times N$ data within CJMTK that will assist human mission planners with this complex problem.

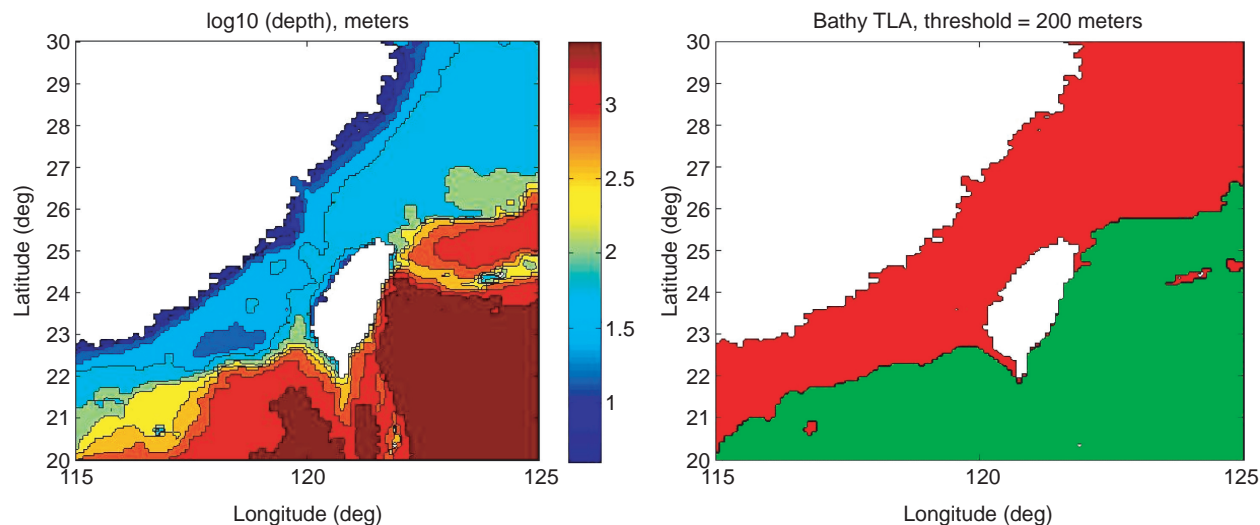
Decision-making Using Traffic Light Analysis: For the development of software that will assist with the creation of a viable vehicle mission plan that

**FIGURE 3**

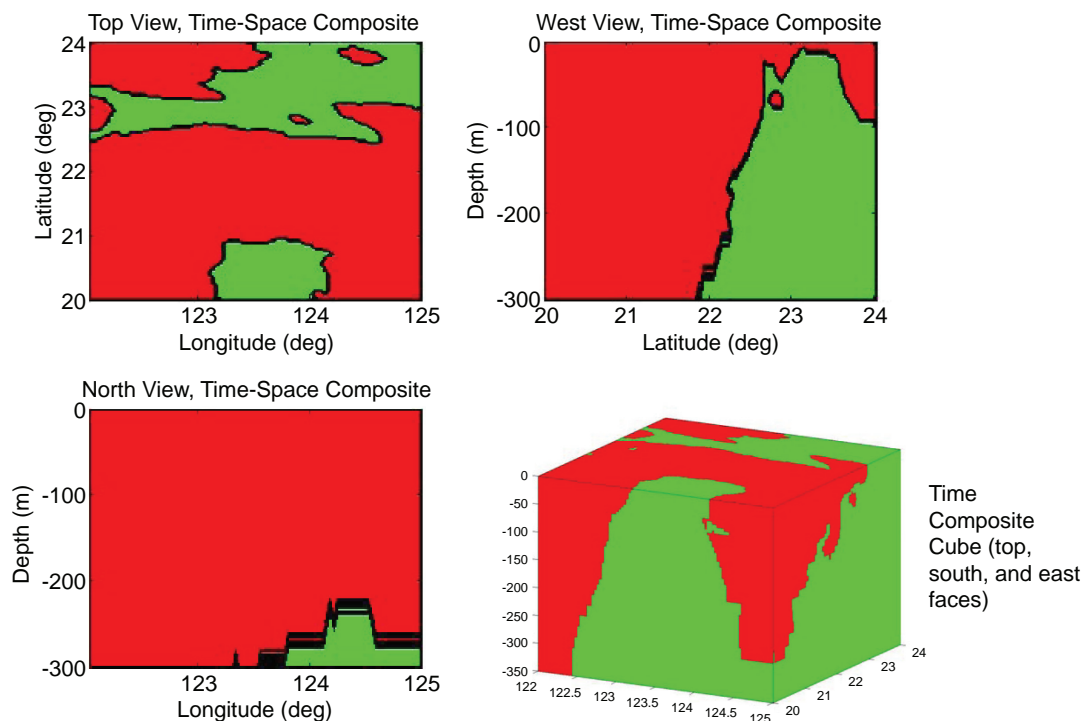
This figure depicts the standard approach of trying to visualize the impact of $4D \times N$ variables by displaying individual 2D slices of each variable over time. Ocean current would require an x, y slice at each depth of interest for each time interval of interest. 2D plots could be used to show forecast weather, but if winds at different altitudes were also a consideration, then 2D slices for each altitude of interest would be needed at each time interval. For lack of adequate geospatial software to assist with this process, the computational tools used are all too often a calculator and a note pad. Without the assistance of software that can manipulate this data, creation and optimization of mission plans that consider all of these variables is left to the mind of an experienced operator. While the human expert offers a significant ability to mentally process this information, the result typically lacks numeric and quantitative analysis of alternatives.

considers environmental influences, it is important to recognize the respective roles and limitations of data visualization and simulation. Essentially, the role of data visualization is to allow the user to create potentially viable mission plans, while the role of simulation is to provide a quantitative analysis of the proposed mission plan using the relevant environmental data. The visualization of $4D \times N$ data is inherently limited in that a human cannot readily project where and when a vehicle will be within the $4D \times N$ problem space. Consequently, the use of visualization is largely limited to drawing distinctions between regions of the $4D \times N$ space that present obvious obstacles and regions in which a mission may be viable.

Traffic Light Analysis (TLA) has been adopted as an approach to helping the human discern “no-go” regions from those in which a specified mission objective may be achievable. Time-invariant 2D fields such as bathymetry provide a straightforward example of this process, where an operator would select a range of acceptable ocean depths for a given mission and the software would visually designate geographic areas that do not meet these constraints as “red.” This is illustrated in Fig. 4, where the actual bathymetry (log scale) is shown on the left, and the TLA with a threshold of 200 m is shown on the right. This process becomes slightly more complicated for 4D data, and for this we use a “time-space composite” approach. Figure 5 shows

**FIGURE 4**

The bathymetry data (logarithmic scale) in the area of interest is shown on the left. The Traffic Light Analysis (TLA) of this data, using a specified threshold of 200 m, is shown on the right. The red indicates the geographic area, based on the user-specified threshold, in which it would be unacceptable to operate a particular vessel.

**FIGURE 5**

This figure shows the result of a “time-space composite” TLA. The time composite operation results in a 3D cube that is shown on the bottom right. This is generated by flagging as red all locations within the cube that violate a user-specified threshold at any time. The top, north, and west 2D time-space composite results shown are each generated by doing a similar logical OR operation perpendicular to the indicated plane. The red areas are different on the faces of the cube than on the 2D time-space composites since the time-space composite will show red if any location in the cube “below” each (i, j) position violates the threshold. The resulting time-space composite views will necessarily represent the most conservative application of the threshold, but if the remaining non-red regions are sufficient to accomplish mission objectives, the operator can proceed to specifying a mission plan and then simulation. Numerous time-space perspectives can be generated by using average, maximum, and other basic mathematical functions. For example, a station-keeping mission might use the average to indicate the net motion of the water mass over time.

the time-space composite of a time-varying current field, where the thresholds are applied at each location and time within the forecast current data. The final 2D results shown (top, west, and north views) are generated by using an OR operation first to collapse time and then to collapse space in each direction.

Summary: Traffic Light Analysis can be used to help an operator visually display areas within the $4D \times N$ problem space that are restrictive based on user-specified parameters. An additional benefit of this approach is a dramatic reduction (on the order of 1:1000) in the amount of data that the GIS software must handle. Even on very large 4D datasets, TLAs can be computed very quickly using fairly simple external programs. With this design, the GIS GUIs are used to identify the data source file and specify the threshold values, but the actual computations would be handled by external programs. Once computations have been completed, the result is loaded into the GIS as a viewable layer, and then GIS functionality can be used on the N variables to create a composite multilayer “no-go” region. Developing a mission plan is then a matter of translating mission objectives into a sequence of navigation goals that can be simulated.

[Sponsored by ONR]

References

- ¹ P. Jankowski, S. Robischon, D. Tuthill, T. Nyerges, and K. Ramsey, “Design Consideration and Evaluation of a Collaborative, Spatio-Temporal Decision Support System,” *Transactions in GIS*, 335-354, 2006.
- ² S. Riley “A Shared View of the Battlespace,” *C4ISR* 5(2), March 2006, www.C4ISRjournal.com. ★

Measurement and Analysis of Clutter in Electronic Displays

M.C. Lohrenz,¹ M.R. Beck,² J.G. Trafton,³ and M.L. Gendron¹

¹Marine Geosciences Division

²Louisiana State University, Baton Rouge, LA

³Information Technology Division

Introduction: Electronic geospatial displays are common—from aircraft moving-maps to handheld GPS devices. As new data sources become available, users are tempted to display everything of interest: digital charts, satellite imagery, weather data, etc. The ensuing clutter can impact a user’s ability to access, interpret, and effectively use the displayed information. This paper presents a model of display clutter comprised of global and local components, which we compared with subjective clutter ratings and target

search performance. Our results suggest strong correlations between our global clutter metric and subjective ratings, and between our local clutter metric and search performance.

Clutter Model: Rosenholz et al.¹ define clutter as the state in which excess items, or their representation or organization, lead to a degradation of performance at some task. We describe global clutter as the total amount of clutter in a display, and local clutter as the amount immediately surrounding a target of interest (e.g., an airport symbol). We theorize a combination of global and local clutter impacts visual search (finding a target of interest). We predict visual search is largely affected by local clutter: if the area surrounding a target is cluttered, the target will be harder to find. However, if people perceive the entire display as cluttered (high global clutter), not only may they be less likely to use it, but they may search more slowly and carefully than if they perceive it as uncluttered (low global clutter).

We suggest clutter is a function of “color density” and “saliency” (Fig. 6). We define color density as a measure of how tightly packed similar-colored pixels are within an image. We compute this by clustering all the image’s pixels in 3D (2D location and color), such that adjacent pixels of similar colors cluster together, and calculating the density of pixels in each cluster. Each cluster models a visually discernible “feature” on

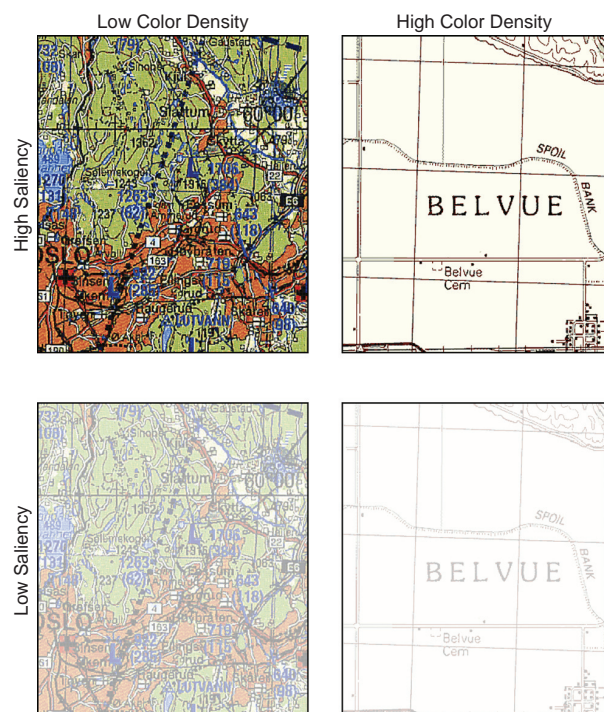


FIGURE 6
Electronic chart samples illustrating the impact of color density and saliency on clutter.

the display. We compute saliency as a weighted average of color differences among adjacent features (clusters). Greater color differences result in higher saliency; highly salient features are typically easier to detect. Lower color density suggests higher clutter, especially when saliency (between features) is high. When saliency is low, color density has less impact on clutter because features are less discernible. We propose the following clutter model:

$$\text{clutter} = 15(1 - \text{color density}) * \exp[-6.3 \exp(-\text{saliency}/10)] - 0.0002.$$

For very low saliencies, clutter remains very low, regardless of color density. When saliency is high, clutter becomes a function of color density only. For more information about this model, the reader is referred to Lohrenz and Gendron.²

Correlations with Human Perception and Performance: Participants completed two tasks (target search followed by subjective clutter ratings) to examine how well our model estimates clutter in one type of geospatial display: aeronautical charts. Fifty-five under-

graduate students were shown 54 charts, displayed as 256-color GIF images. We made two copies of each chart: one with a target (elevation symbol) in a low local-clutter area (Fig. 7), and the other with the target in a high local-clutter area. We cropped each chart to a 60 × 60 pixel “snippet” centered on the target and ran the clutter algorithm on the snippet to compute local clutter. We considered four independent variables (2 × 2 × 3 factorial): global clutter (low, medium, high); local clutter (low, high); target shape (two types); and set size (4, 8, 16 distractors).

For the target search task, we recorded percent completed trials (a trial was terminated if the participant could not find the target after 45 seconds), percent correct, and reaction time. Local and global clutter affected all three search measures (shown in Table 1, which compares the actual clutter values—not binned—against performance measures). Both types of clutter slowed search time, as expected, with the effect of local clutter increasing as global clutter increased (Fig. 8(a)). Global clutter affected percent completed trials and percent correct only for high local clutter (Figs. 8(b) and (c)). Similarly, the effect of local clutter

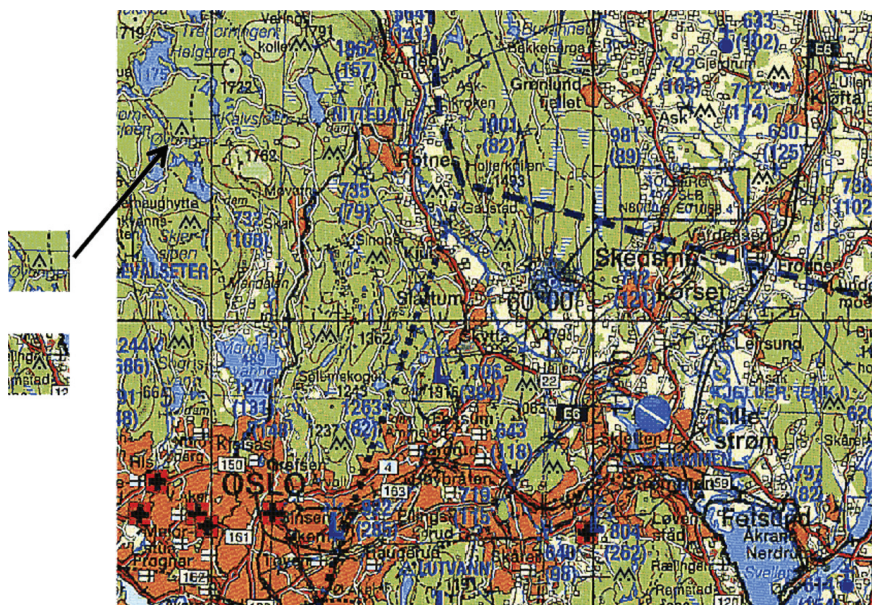
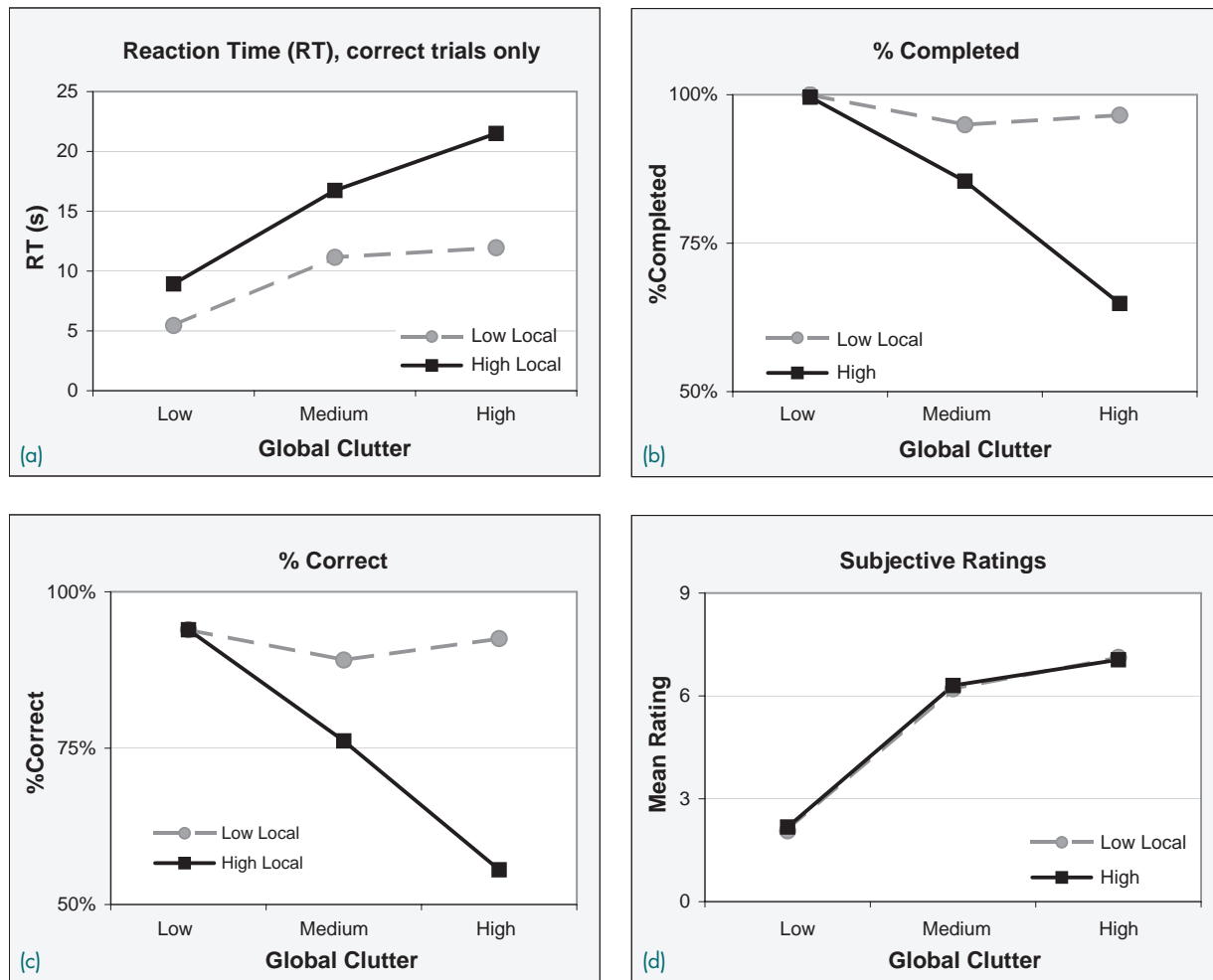


FIGURE 7
High global-clutter chart with low (top left) and high (bottom left) local-clutter targets. There were two copies of each chart, one for each local clutter condition. (The chart shown is the low local-clutter version, so only the low local-clutter target is present in this chart).

TABLE 1 — Individual Effects on Target Search Performance

Independent Variable	Mean RT		% Completed		% Correct	
	t ratio	p	t ratio	p	t ratio	p
Local clutter metric	12.38	<0.0001	-7.57	<0.0001	-7.90	<0.0001
Global clutter metric	7.85	<0.0001	-5.31	<0.0001	-5.68	<0.0001
Target type	1.48	0.14	-2.17	<0.05	-2.00	<0.05
Set size	-0.85	0.40	0.70	0.48	1.02	0.31

**FIGURE 8**

(a) Only global clutter affected subjective clutter ratings. Local clutter had no effect. (b) Both global and local clutter slowed reaction time. (c-d) Local clutter had a greater effect than global clutter on the number of trials participants were able to complete (including both correct and incorrect trials) and the number of correct trials. In both (c) and (d), global clutter only had an effect if the target was in a high local-clutter region.

was largest when global clutter was high. Finally, there was a strong correlation ($r = 0.77$) between local clutter and reaction time.

In the subjective ratings task, which always followed the target search task, participants rated each chart from 0 (no clutter) to 9 (extremely cluttered). Results for low and high local-clutter charts are identical (Fig. 8(d)) indicating only global clutter had an effect on subjective clutter ratings, as expected. There was a very strong correlation ($r = 0.86$) between the global clutter metric and mean ratings. Neither target type nor set size had any effect.

Conclusions: This paper presents a model of clutter for complex geospatial displays. Our results suggest saliency and color density are important components of clutter. Our global clutter metric correlates very well with subjective ratings of display clutter.

Both global and local clutter significantly impact target search performance, with the effect of local clutter increasing as global clutter increases.

Acknowledgments: This work was sponsored by NRL (6.2 Program Element 602435N). We thank Geary Layne and Stephanie Myrick for their assistance. We thank the Louisiana State University Psychology Department for computer resources and students to participate in the clutter experiments.

[Sponsored by NRL]

References

- ¹ R. Rosenholtz, Y. Li, J. Mansfield, and Z. Jin, "Feature Congestion: A Measure of Display Clutter," *SIGCHI 2005*, Portland, OR, pp. 761-770, April 2005.
- ² M. Lohrenz and M. Gendron, "A 3D Clustering Algorithm to Model Clutter in Electronic Geospatial Displays," *J. Management and Engineering Integration* 1(1), Summer 2008 (in press). ★

NRL Global Vessel Tracking Project (VTP)

D.J. Bielecki
Space Science Division

Introduction: In 2003, a call for Maritime Domain Awareness (MDA) architectures was issued by Honorable John Young, then Assistant Secretary of the Navy for Research, Development, and Acquisition (ASN RD&A). The Naval Research Laboratory's Space Systems Development Department (SSDD) responded with a global architecture and estimates of resource requirements. The response featured a layered defense approach, incorporating support from sensors, databases, and information feeds ranging from National Technical Means (NTM) to Open Source Intelligence (OSINT). Essential elements of the system were funded. A Modular Sensor System (MSS) provided protection for a port, harbor, or key infrastructure element. A highly automated virtual database and information extraction capability was provided at the GENSER level. At the NTM level, a fully automated vessel tracking system provided tracks and updates for the Atlantic Ocean.

Innovative Technology (IT) Development: One of the key developments in this architecture was a major subsystem designated as the Common Distributed Virtual Database with Information Extraction (CDVD/IE). NRL engineers in SSDD rose to the challenge of creating an enterprise, web-based, client-server architecture that could aggregate and fuse the many disparate databases and feeds that are needed for MDA. Among other challenges, the engineers had to conceive and implement an innovative architecture that balanced the need to access over 200 distinct and different sources of information, without massive federation of databases that could create network bottlenecks and

require massive storage resources. In solving this and other challenges, NRL engineers created a new way of employing spatial database features to fuse multiple candidate sources into integrated maritime vessel tracks; more information can be found in the *2006 NRL Review*.¹

Layered Defense Approach: Although the cost of the entire global system for vessel tracking was beyond the funding available, a meaningful project was devised that required tracking as many vessels as could be done automatically in the Gulf of Mexico and Atlantic Ocean. However, it was NRL's global vision that convinced Department of Defense (DoD) seniors to place this work at the laboratory, and follow-on Joint Concept Technology Demonstrations (JCTDs) have achieved much of the original vision such as global coverage. Figure 9 shows the vision that intrigued DoD thinkers.

Modular Sensor System: The philosophy of global situational awareness must provide solutions for key infrastructure elements such as specific local resources of high value that must be afforded even higher levels of protection. The MSS could provide such protection for a key military base, port, harbor, or other installations that are susceptible to maritime threats, combining innovative subsystems from both industry and internal NRL development sources. The MSS design provides a remotely controllable automatic collection command center for multiple sensors including a Track While Scan (TWS) radar, an advanced electronic support measure (ESM) system to provide electronic intelligence (ELINT) data, a Precision Direction Finder (PDF), a UYX-4 RF Characterization system for Specific Emitter Identification (SEI), an Automatic Identification System (AIS) receiver, and an acoustics measurement and signal processing suite. The MSS

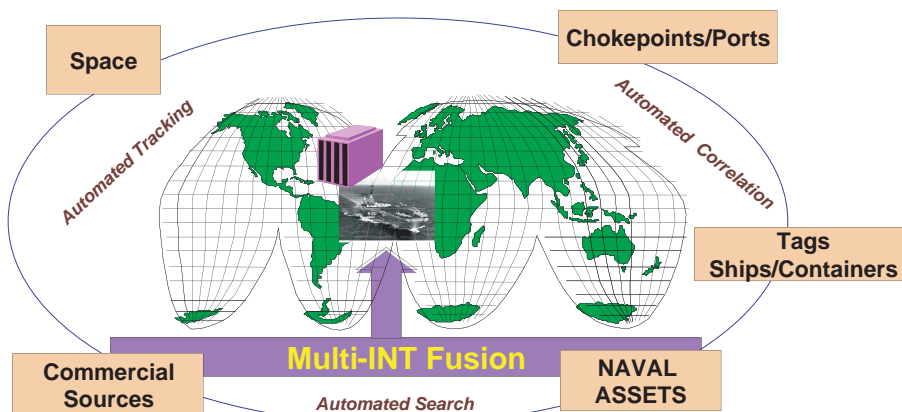


FIGURE 9
NRL's global vessel tracking architecture.

also provides an independent global positioning system (GPS) and synchronous timing system, local and wide-area communications connectivity, and a Data Distribution System that can provide data to CDVD/IE for VTP within the MSS sensor coverage area (nominal 20 nmi). Although costs dictated commercial options for most sensors, readers should note that the UYX-4 SEI algorithm techniques were originated at NRL's Tactical Electronic Warfare Division. The acoustic sensor suite was developed for VTP by NRL's Acoustic Division. The full MSS complement of capabilities is shown in the block diagram of Fig 10.

Web-Enabled Application: MSS needed to fuse a large number of sources for MDA data specific to what is termed the “point defense” of a critical location. VTP also needed to respond to the needs of the operational military to do more with less by automating as many manual processes as possible. For this reason, the entire operation of MSS is fully automated and can provide 24/7 situational awareness with no staff at all. For routine functional checks or an occasional reset of a subsystem, the entire system can be maintained via a series of simple web pages that not only provide situational awareness, but also allow the user to check on instrument and equipment status and health. These

capabilities are available over a network connection from the user's web browser, leveraging the popular Google™ Earth visualization software.

Summary: The Vessel Tracking Project was initiated after September 11, when national level priorities on Maritime Domain Awareness were increased by a presidential directive stipulating higher levels of preparedness and situational awareness. Fortunately, VTP was able to respond to these national priorities and has transitioned functional elements to both the U.S. Coast Guard (USCG) as well as the Office of Naval Intelligence (ONI) enterprise at the National Maritime Intelligence Center (NMIC) in Suitland, MD. The system has been well received at the flag level within the DoD, Navy, and USCG. Two JCTDs at NRL were subsequently awarded, building on VTP technologies to provide truly global capabilities and even more sophisticated MDA solutions, keeping NRL at the forefront of this crucial national endeavor.

[Sponsored by ONR]

Reference

- ¹ M.D. Bell, S.M. Elliott, T.Y. Yang, and P. You, “Multi-Source Maritime Vessel Tracking,” *2006 NRL Review*, pp. 144-146. ★

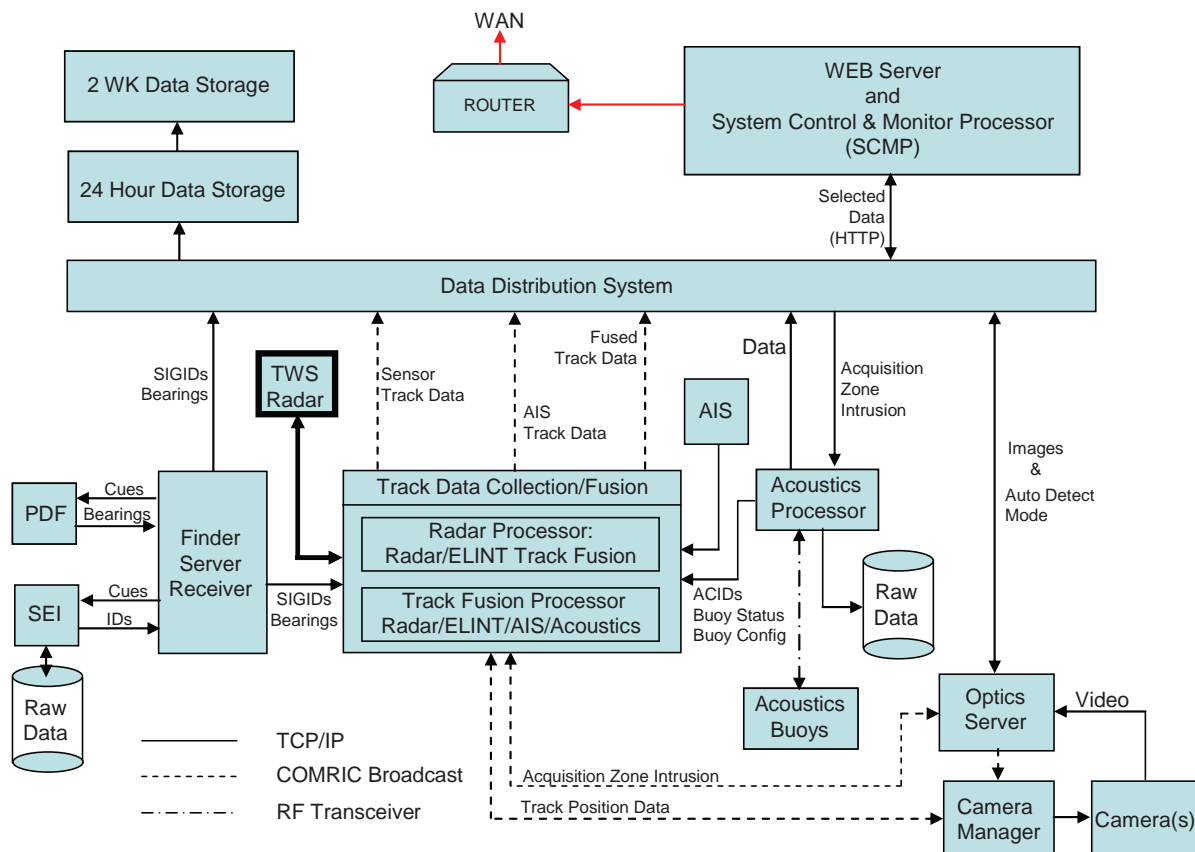


FIGURE 10
NRL's modular sensor system (MSS).



Aqueous Film-Forming Foam (AFFF) (1964-1966)

The catastrophic fires aboard the USS *Forrestal* on July 29, 1967, and aboard the USS *Enterprise* on January 14, 1969, made more effective fire suppression of paramount importance to the Navy. By this time, NRL had already begun research that eventually led to the development of aqueous film-forming foam (AFFF), one of the most far-reaching benefits to worldwide aviation safety. AFFF quickly extinguishes hydrocarbon fuel fires and forms an aqueous film on the fuel surface that prevents evaporation and, hence, reignition of the fuel fire. The foam's self-healing property rapidly reseals scars in the film layer caused by falling debris or firefighting activity. NRL's R.L. Tuve and E.J. Jablonski devised the concept and patented the first formulation, twinning it with their previous invention, Purple-K-Powder, in a dual-agent firefighting apparatus. They elicited the aid of the Minnesota Mining and Manufacturing Company (now 3M) to synthesize the fluorinated intermediates and agents for formula improvements that contributed to the success of the AFFF development. AFFF is now used aboard all Navy aircraft carriers, by all branches of the U.S. armed forces and NATO members, and is in the inventory of almost all civilian firefighting departments in the U.S. and around the world. International standards organizations recognize it for the protection of facilities where catastrophic fuel fires can occur, such as civilian airfields, refineries, and fuel-tank farms. Two foam units from the Metropolitan Washington Airports Authority that responded to the 9/11 terrorist attack on the Pentagon fought the fires with AFFF.

171

Carbon Surface Modification for Enhanced Corrosion Resistance

P.M. Natishan, F.J. Martin, E.J. Lemieux, T.M. Newbauer, R. Rayne, and R.A. Bayles

173

Lifetime Limiting Defects in 4H-SiC

P.B. Klein, B.V. Shanabrook, S.W. Huh, A.Y. Polyakov, M. Skowronski, J.J. Sumakeris, and M.J. O'Loughlin

174

Mobility Enhancement in Strained Antimonide Quantum Wells

B.R. Bennett, J.B. Boos, M.G. Ancona, N. Papanicolaou, J.G. Champlain, R. Bass, and B.V. Shanabrook

177

Creating Spin Currents in Silicon

B.T. Jonker, G. Kioseoglou, A.T. Hanbicki, C.H. Li, and P.E. Thompson

Carbon Surface Modification for Enhanced Corrosion Resistance

P.M. Natishan,¹ F.J. Martin,¹ E.J. Lemieux,¹
T.M. Newbauer,² R. Rayne,¹ and R.A. Bayles¹

¹Chemistry Division

²SAIC

Introduction: Case hardening by carburization has long been recognized to produce wear-resistant surfaces in steels. Historically, case hardening has not been applicable to chromium-containing alloys such as stainless steels (SS), due to chromium carbide formation that significantly degraded corrosion performance. As a result, the availability of case-hardened (and consequently wear-resistant) alloys for applications in corrosive environments was extremely limited. A new low-temperature (450°–500 °C) paraequilibrium carburization technique has been developed for introducing carbon into stainless steel surfaces without formation of carbides.^{1,2} This surface modification technique has been termed Low-Temperature Colossal Supersaturation (LTCSS). Paraequilibrium refers to the concept that the diffusion of substitutional solutes (metal atoms, such as Cr and Ni in the alloy) is slower than the diffusion of interstitial solutes (atoms such as carbon, that fit between metal alloy atoms). Substitutional solutes are effectively immobile under LTCSS treatment conditions, whereas carbon can diffuse considerable distances into the alloy. These interstitially hardened surfaces constitute a new branch of engineered materials, in which improved corrosion resistance is attained alongside improvements in wear and fatigue resistance.

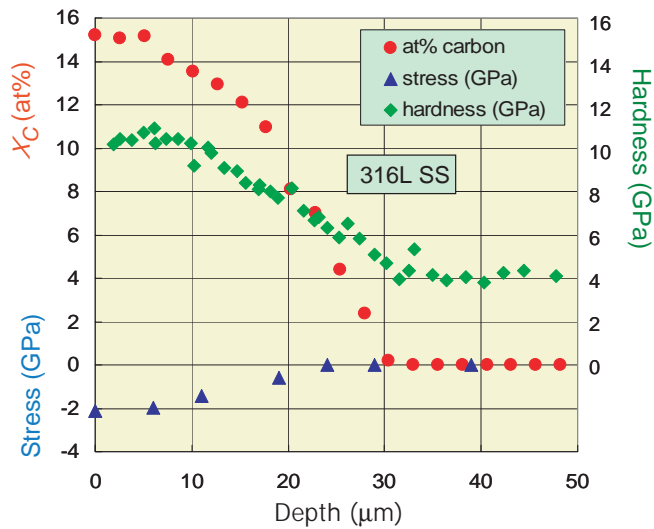
Improved Surface Hardness: The effect of LTCSS treatment on austenitic stainless steels has been shown to dramatically increase surface hardness through residual compressive surface stress (important for fatigue resistance and wear resistance). Figure 1 shows the surface carbon concentrations, residual surface stresses, and hardness resulting from LTCSS treatment. Carbon concentrations of up to 15 atomic percent can be generated in the near-surface region encasing the entire treated component. The large concentration of interstitial carbon induces a lattice expansion that results in surface compressive stresses greater than 2 GPa (300 ksi). These large residual compressive stresses significantly enhance the high cycle fatigue endurance limit,² increasing the service life of the material. Increasing the surface hardness of the material increases wear resistance. Near-surface Vickers microhardness values (HV) of 1200 HV have been obtained on LTCSS-treated 316L SS, representing a significant increase in surface hardness over the substrate material (Vickers 300 HV). To give some perspective,

environmentally unfavorable hard chrome coatings are frequently used on critical aircraft components to increase wear resistance, where surface hardnesses can reach as high as 1100 HV. Thus a LTCSS-treated 316 SS has a surface hardness that rivals the best hard chrome coating. A surprising feature of LTCSS treatment is that the inherently good ductility of the base material is retained in the treated surface.² Additional positive attributes of LTCSS include no net dimensional changes in treated components, treatment of all exposed surfaces, and the ability to batch process large numbers of components at once.

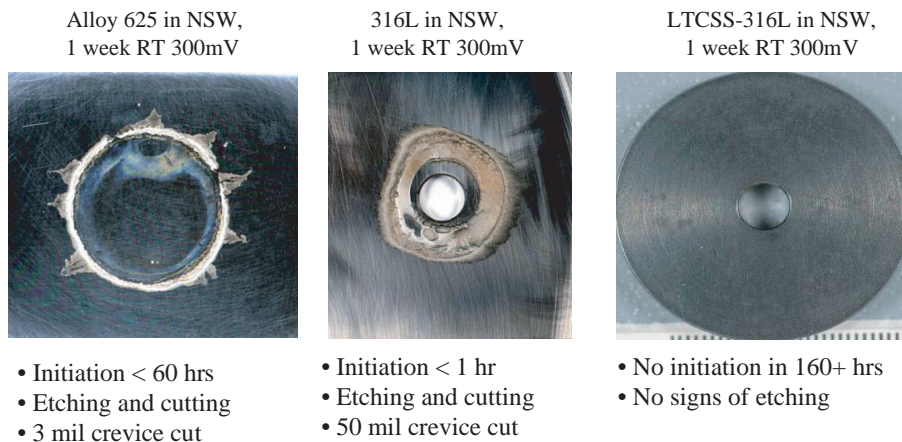
Pitting Corrosion Resistance: Electrochemical testing at NRL to determine pitting corrosion resistance³ has shown that there is dramatic increase in the pitting resistance of the LTCSS-treated 316 SS when compared to the untreated material. LTCSS treatment increased pitting potential from +320 millivolts (mV) for untreated material to +950 mV for the LTCSS-treated material.⁴ The pitting potential is an electrochemical parameter used in laboratory testing to compare the pitting resistance of materials; a high positive value is desired. This is a dramatic increase in pitting corrosion resistance such that under practical conditions experienced in natural seawater (NSW) environments, LTCSS-treated 316 SS is virtually immune to pitting corrosion.

Crevice Corrosion Resistance: Crevice corrosion resistance is another aspect of corrosion behavior of particular interest to the Navy. Comparison of crevice corrosion resistance for untreated 316L SS and LTCSS-treated 316L is presented in Fig. 2. Crevice corrosion damage on an untreated 316L coupon following one week of crevice exposure is shown in the center of the figure. LTCSS-modified 316L (far right) did not initiate crevice corrosion under these exposure conditions (+300 mV, ambient temperature seawater) during the one-week test. Figure 2 also includes results published for Alloy 625 (left photo, an exotic Ni-22Cr-9Mo superalloy) for the same test conditions and crevice cell design.³ These results indicate that the corrosion resistance of LTCSS-treated 316L was greatly increased compared to the untreated 316 and the more expensive, high-grade Ni alloy.

Summary: Low-Temperature Colossal Supersaturation is a process for introducing carbon in excess of 15 atomic percent into stainless steels without formation of carbides. The results of the NRL work show that LTCSS treatment dramatically improved the localized corrosion resistance (both pitting and crevice corrosion) of 316L austenitic SS in ambient temperature seawater. LTCSS treatment has the potential to be applied to a multitude of alloys already used by the Navy. This

**FIGURE 1**

Carbon concentration, surface hardness, and residual stress profiles for LTCSS-modified 316L stainless steel (from Ref. 2).

**FIGURE 2**

Photographs of crevice corrosion specimens after testing (RT = run time). Unmodified 316L SS (center) and LTCSS-modified 316L SS (right) after week-long ambient seawater (NSW) crevice corrosion testing at +300 mV. At left, Alloy 625 (high-grade Ni-Cr-Mo alloy) exposed to similar conditions (from Ref. 3).

in turn would increase the service life of components and increase readiness and availability of naval assets. In addition, LTCSS-treated surfaces, in most cases, have hardness values greater than hard chrome and thus present a potential alternative to this environmentally undesirable, toxic, wear-resistant and corrosion-resistant coating.

Acknowledgments: The authors gratefully acknowledge Dr. Airan Perez of the Office of Naval Research for financial support and technical direction of this work. The authors also wish to thank Mr. Peter Williams and Dr. Sunniva Collins of Swagelok Company (Solon, OH) for significant technical assistance and for performing LTCSS treatments of the stainless steel coupons employed in this work. The authors also acknowledge G.M. Michal, F. Ernst, H.

Kahn, and A.H. Heuer of Case Western University for many stimulating discussions.

[Sponsored by ONR]

References

- ¹ P.C. Williams and S.V. Marx, Swagelok Company, Low-Temperature Case-Hardening Processes, U.S. patent 6,093,303 (July 25, 2000).
- ² G.M. Michal, F. Ernst, H. Kahn, Y. Cao, F. Oba, N. Agarwal, and A.H. Heuer, "Carbon Supersaturation due to Paraequilibrium Carburation: Stainless Steels with Greatly Improved Mechanical Properties," *Acta Materialia* **54**, 1597-1606 (2006).
- ³ F.J. Martin, P.M. Natishan, K.E. Lucas, E.A. Hogan, A.M. Grolleau, and E.D. Thomas, "Crevice Corrosion of Alloy 625 in Natural Seawater," *Corrosion* **59**, 498-504 (2003).
- ⁴ E.J. Martin, E.J. Lemieux, T.M. Newbauer, R.A. Bayles, P.M. Natishan, H. Kahn, G.M. Michal, F. Ernst, and A.H. Heuer, "Carburization-Induced Passivity of 316 L Austenitic Stainless Steel," *Electrochemical and Solid-State Letters* **10**, C76 (2007). ★

Lifetime Limiting Defects in 4H-SiC

P.B. Klein,¹ B.V. Shanabrook,¹ S.W. Huh,²
A.Y. Polyakov,² M. Skowronski,² J.J. Sumakeris,³
and M.J. O'Loughlin³

¹Electronics Science and Technology Division

²Carnegie Mellon University

³Cree, Inc.

Introduction: Efforts are under way to develop electrical power systems for Naval vessels and aircraft to be controlled by small, efficient, and reliable solid-state electronic devices, such as high-power (>10 kV) switching diodes. This has provoked significant interest in advancing technology based on 4H-SiC, as this semiconductor is much more capable of withstanding the required high power densities than is Si, which has been the standard material for these applications. Development of these devices requires that the SiC material be of sufficient purity, since defects (alterations from the perfect periodic lattice of Si and C atoms) can trap mobile charge carriers (electrons or holes), thus causing degradation of important electrical properties, such as the average lifetime of the minority carriers. In order to reduce the concentration of these defects (or “traps”), it is important to determine their chemical structure, so that appropriate strategies may be applied during or after material growth to minimize their incorporation.

Experiment: In this work, the defects that limit the minority carrier lifetime (MCL) are investigated by carrying out measurements of both carrier lifetimes and defect concentrations in a carefully characterized set of samples. Defects are identified and their concentrations are determined by deep-level transient spectroscopy (DLTS), in which the measurement of the temperature-dependent rate of emission of trapped carriers from the defects determines the characteristic thermal energy necessary to free the carriers from the traps. This temperature dependence is employed to establish a fingerprint that identifies the defect. The chemical nature of the defect is generally determined by independent correlations between these DLTS signatures and other measurements that reflect the local defect structure. Carrier lifetimes are measured by time-resolved photoluminescence (TRPL), in which a short pulse of laser light creates free electrons and holes in the material, and the measured decay rate for the recombination of these excess carriers provides a measure of the average MCL.¹ Measurements are carried out on a set of 4H-SiC samples grown with varying layer thickness between 9 and 104 μm . By fitting the variation of the measured lifetimes with layer thickness to a theoretical expression, two competing contributions to the lifetime can be separated—recombination in the bulk and

recombination at the sample surface. As the inverse of the bulk lifetime is proportional to the concentration of the defect that limits the lifetime, it is the bulk lifetime that is of interest in correlating carrier lifetime with defect concentration.

Results: Figure 3 shows typical DLTS spectra for these layers, the peaks representing signatures of defects that trap electrons (a) and holes (b). These are the dominant defects that affect the electrical properties of the material. Z1/Z2 and EH6/EH7 are DLTS designations of two important electron traps. A Ti-related electron trap and two boron-related hole traps, B (boron impurity) and the “D-center,” are observed; the latter is a boron impurity bonded to a nearby defect. An as-yet unidentified hole trap at 0.85 eV and electron trap at 1.1 eV (not shown) are also observed.

The correlation between the measured defect concentrations and the measured carrier lifetimes is shown in Fig. 4(a) as a function of layer thickness. It is clear from the figure that the defect concentration and inverse carrier lifetime (blue) exhibits strong correlation only for the Z1/Z2 center (red), suggesting that this is the dominant defect that limits the lifetime. In Fig. 4(b) the measured dependence of the carrier lifetime on layer thickness (circles) is compared to the fitted value (squares). The bulk lifetimes obtained from this fit are plotted versus Z1/Z2 concentration in the inset. The resulting linear relationship confirms the identification of Z1/Z2 as the defect that controls the MCL.

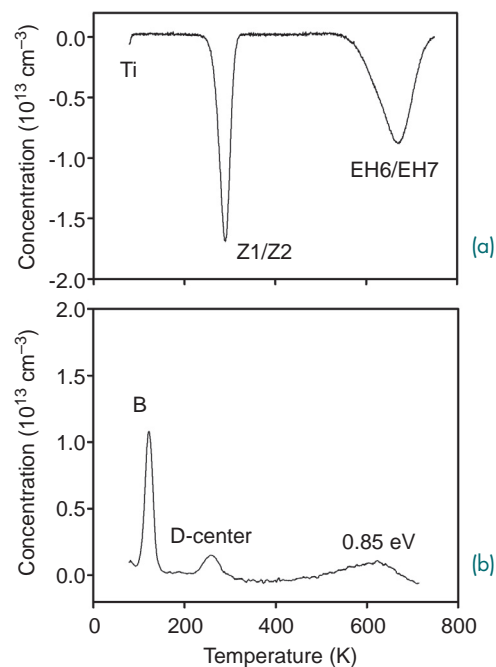
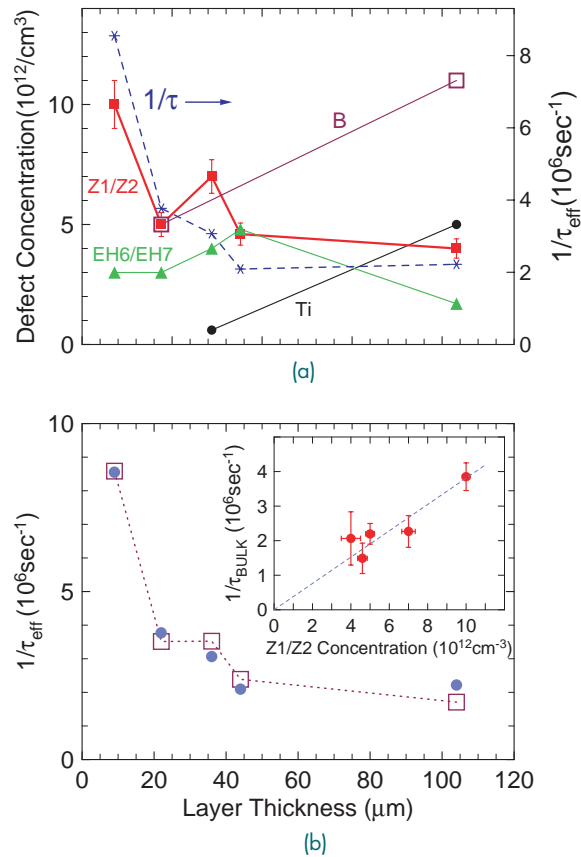


FIGURE 3
Typical DLTS spectra of the dominant electron traps
(a) and hole traps (b) in 4H-SiC.

FIGURE 4
Dependence upon 4H-SiC layer thickness of the (a) concentrations of the dominant defects and the inverse carrier lifetime (blue); and (b) comparison of the measured (circles) and fitted (squares) thickness dependence of the carrier lifetime. From this fit, the linear dependence of the inverse bulk lifetime with Z1/Z2 concentration (inset) is determined.



This conclusion is further confirmed by carrying out DLTS measurements within a device structure, where a large concentration of minority holes could be injected into the material by applying a voltage across the device. Trapping of these holes on filled (negatively charged) electron traps changes the electrical charge on the trap, so that it no longer contributes to the DLTS signal. Under these conditions, a large decrease in the Z1/Z2 DLTS signal was observed, indicating rapid minority hole capture, while there was little effect on the other electron traps. Hence, these cannot be effective traps for minority holes, so that Z1/Z2 alone must control the MCL in these materials. The Z1/Z2 defect has been identified² as containing a carbon vacancy (i.e., a missing carbon atom). Thus, with this identification of Z1/Z2 as the dominant lifetime killer, it becomes possible to increase carrier lifetimes by varying material growth parameters or by post-growth annealing at high temperatures, where vacancies are no longer stable.

Conclusions: These measurements have identified Z1/Z2—a carbon-vacancy related defect—as the dominant defect controlling the minority carrier lifetime in 4H-SiC material. With appropriate changes in material growth parameters or with high-temperature annealing, the concentration of these defects may be reduced

and the carrier lifetimes increased, thus enhancing the material properties for device applications.

[Sponsored by ONR and NRL]

References

- ¹ O. Kordina, J.P. Bergman, C. Hallin, and E. Janzén, "The Minority Carrier Lifetime of n-type 4H- and 6H-SiC Epitaxial Layers," *Appl. Phys. Lett.* **69**, 679 (1996).
- ² K. Danno and T. Kimoto, "Investigation of Deep Levels in n-type 4H-SiC Epilayers Irradiated with Low-Energy Electrons," *J. Appl. Phys.* **100**, 113728 (2006). ★

Mobility Enhancement in Strained Antimonide Quantum Wells

B.R. Bennett, J.B. Boos, M.G. Ancona, N. Papanicolaou, J.G. Champlain, R. Bass, and B.V. Shanabrook
Electronics Science and Technology Division

Background: Low-power electronics is essential for a number of military and commercial applications. Previous work at NRL has demonstrated high-performance, low-power, antimonide-based compound semiconductor transistors. In these devices, InAs is used as an electron channel with mobilities as high as 30,000 cm²/V-s at room temperature.¹ This work has

been transitioned to industry for analog applications, resulting in X-band and W-band low-noise amplifiers with record low power consumption (a factor of 3 and 10 lower than InP- and GaAs-based amplifiers, respectively). For digital and mixed-signal applications, power consumption can be minimized by designing circuits with complementary n(electron)- and p(hole)-channel transistors. These circuits consume negligible power except when being switched. Military applications for this technology are expected to include high-speed analog-to-digital conversion for high-performance radar and miniature air vehicles (MAVs), autonomous sensing, and application-specific integrated circuits (ASICs).

A major obstacle to achieving low-power complementary circuits using compound semiconductors is that hole mobilities are generally much smaller than electron mobilities. For example, the hole mobility of InAs is only $450 \text{ cm}^2/\text{V}\cdot\text{s}$. The goal of our work at NRL is to produce quantum wells with hole mobility as high as possible. To do so, we have employed band-structure engineering techniques. The valence bands of semiconductors include both heavy- and light-hole bands. Under normal conditions, these bands are degenerate, meaning that both have significant hole occupation. If a strain is applied to the material, however, the degeneracy will be lifted, and the effective mass of the occupied heavy-hole band will decrease. This should lead to an increase in hole mobility because the mobility is inversely proportional to the effective mass.

Experimental Methods: For this study, we selected two heterostructures to investigate mobility enhance-

ment by strain. To illustrate our choices, we show a plot of energy gap versus lattice constant for various semiconductors in Fig. 5. For one structure, we use the binary compound GaSb as the channel and ternary alloys of $\text{AlAs}_x\text{Sb}_{1-x}$ as the barrier. We can adjust the strain in the GaSb by changing x , the mole fraction of AlAs. The other structure uses $\text{In}_y\text{Ga}_{1-y}\text{Sb}$ as the channel and $\text{Al}_{0.70}\text{Ga}_{0.30}\text{Sb}$ as the barrier. In this case, the compressive strain in the quantum well increases as we increase y , the mole fraction of InSb. We grow the layers by molecular beam epitaxy (MBE) on GaAs substrates. In the MBE growth process, furnaces loaded with Ga, In, Al, As, and Sb are placed in a high-vacuum environment so that beams of atoms (or molecules) emitted from the furnace can impinge on a substrate target and form a single-crystal semiconductor film. Figure 6 is a photograph of the NRL Epicenter, which includes four MBE systems. The cross-section of our InGaSb-channel structure is shown in Fig. 7(a). A $1.5 \mu\text{m}$ thick layer of $\text{Al}_{0.70}\text{Ga}_{0.30}\text{Sb}$ accommodates the 8% lattice mismatch with respect to the GaAs substrate. The quantum well is only 7.5–12.5 nm thick. Holes are introduced in the channel by a 5-nm Be-doped layer of $\text{Al}_{0.70}\text{Ga}_{0.30}\text{Sb}$ located 21 nm below the channel. The growth is terminated by InAlSb and InAs cap layers. The band structure is shown in Fig. 7(b). The valence band offset between the AlGaSb and the InGaSb allows the confinement of holes in the InGaSb channel—an essential requirement for a p-channel transistor.

Results: The epitaxial layers were characterized by atomic force microscopy (AFM), high-resolution X-ray diffraction (XRD), and Hall/van der Pauw transport

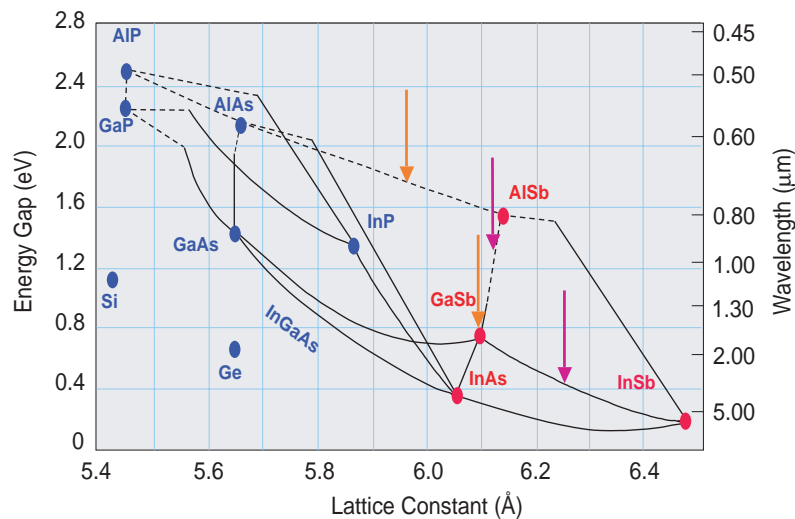


FIGURE 5

Energy gap versus lattice constant for common semiconductors. The purple arrows represent our $\text{In}_y\text{Ga}_{1-y}\text{Sb}/\text{AlGaSb}$ heterostructures; the orange arrows represent our $\text{GaSb}/\text{AlAs}_x\text{Sb}_{1-x}$ heterostructures. In both cases, the narrow-gap quantum well is in compressive strain.

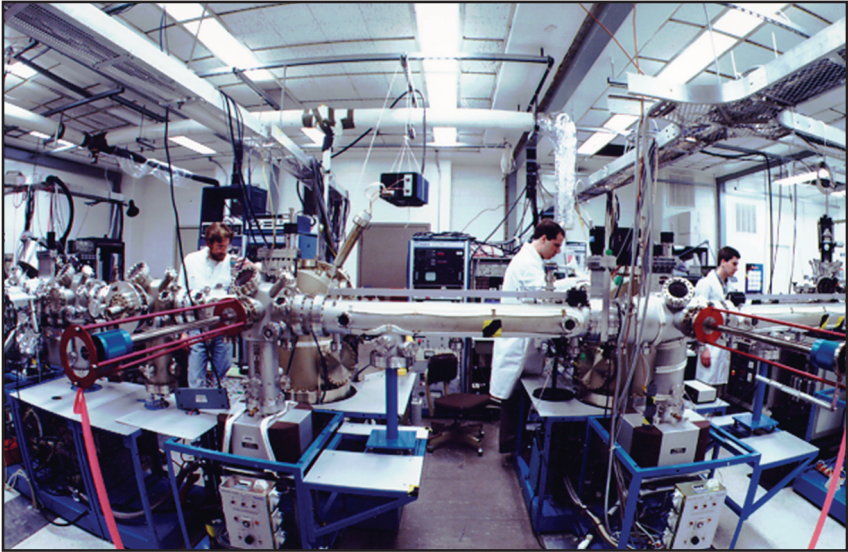


FIGURE 6
The NRL Epicenter includes four MBE systems as well as etching and analysis chambers.

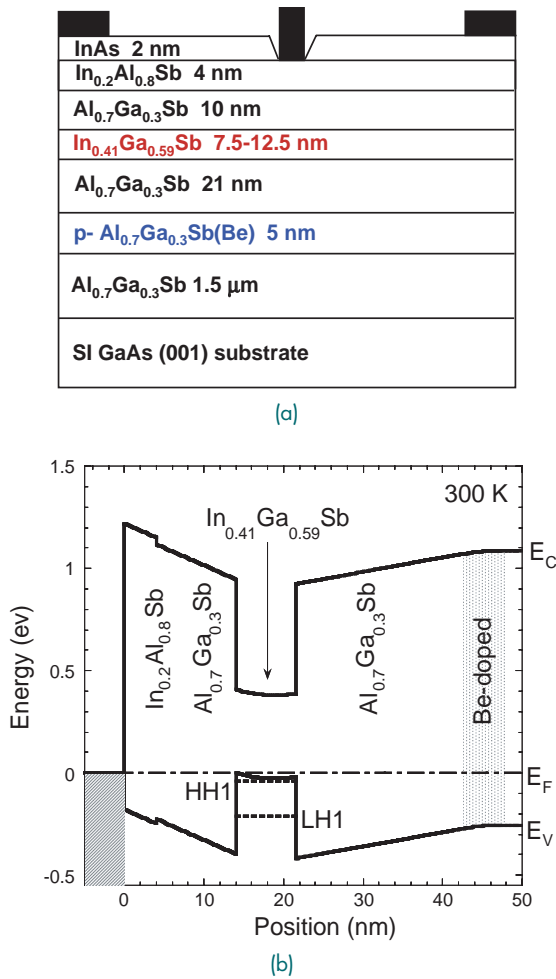


FIGURE 7
Cross section (a) and energy band diagram (b) of InGaSb-channel field-effect transistor structure.

measurements. The AFM indicates the surfaces are smooth, with rms roughness values near 1–2 nm over a $5 \times 5 \mu\text{m}$ area. The XRD measurements allow us to determine the composition of the ternary layers and hence the strain in the quantum wells. The transport measurements yield the mobility and density of holes in the quantum wells. Previously, three groups reported GaSb/AlGaSb quantum wells with room-temperature hole mobilities of 180–270 $\text{cm}^2/\text{V}\cdot\text{s}$. For our GaSb/ $\text{AlAs}_x\text{Sb}_{1-x}$ heterostructures, we obtained room-temperature mobilities of 400–1100 $\text{cm}^2/\text{V}\cdot\text{s}$, with the highest values for x near 0.23 and strains near 1.1%. For strains higher than 1.4%, the mobility decreased.

In Fig. 8, we plot the room-temperature mobility as a function of the InSb mole fraction for $\text{In}_y\text{Ga}_{1-y}\text{Sb}/\text{AlGaSb}$ heterostructures. For a quantum well thickness of 12.5 nm (pink circles), as the InSb mole fraction increases, the hole mobility increases, presumably due to enhanced strain-induced splitting of the valence bands as discussed earlier. For x values greater than 0.41, however, the mobility decreases. We also observed degradation in the structural properties measured by XRD. We attribute this to the formation of misfit dislocations in the quantum well. These dislocations form when the thickness of a mismatched layer becomes too large. We decreased the InGaSb thickness to 7.5 nm and achieved mobilities as high as 1500 $\text{cm}^2/\text{V}\cdot\text{s}$, a world record for any compound semiconductor. It is clear that band-structure engineering is enhancing hole mobility.

We have fabricated transistors on both types of heterostructures and the results are promising. For example, heterojunction field effect transistors (HFETs) with gate lengths of 0.20–0.25 μm exhibit transconductances of 100–150 mS/mm and values of f_{max} , the frequency at which the transistor power gain is unity, of 27–34 GHz. Future work will focus on achieving even

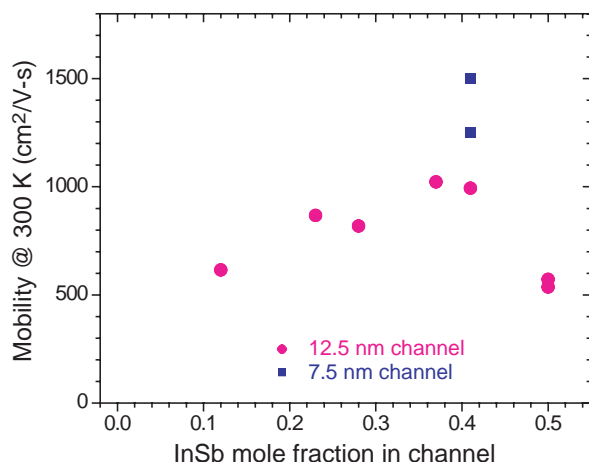


FIGURE 8 Room-temperature hole mobility as a function of InSb mole fraction for $\text{In}_y\text{Ga}_{1-y}\text{Sb}/\text{AlGaSb}$ quantum wells.

higher hole mobilities and integrating p-channel and n-channel transistors to demonstrate complementary circuits operating at extremely low powers.

[Sponsored by ONR]

References

- ¹B.R. Bennett, R. Magno, J.B. Boos, W. Kruppa, and M.G. Ancona, "Antimonide-based Compound Semiconductor Electronics: A Review," *Solid-State Electronics* **49**, 1875 (2005).
- ²B.R. Bennett, M.G. Ancona, J. Brad Boos, and B.V. Shanabrook, "Mobility Enhancement in Strained p-InGaSb Quantum Wells," *Appl. Phys. Lett.* **91**, 042104 (2007).
- ³J.B. Boos, B.R. Bennett, N.A. Papanicolaou, M.G. Ancona, J.G. Champlain, R. Bass, and B.V. Shanabrook, "High Mobility p-channel HFETs using Strained Sb-based Materials," *Electr. Lett.* **43**, 834 (2007). ★

Creating Spin Currents in Silicon

B.T. Jonker,¹ G. Kioseoglou,² A.T. Hanbicki,¹ C.H. Li,¹ and P.E. Thompson³

¹Materials Science and Technology Division

²NRC Postdoctoral Associate

³Electronics Science and Technology Division

Semiconductor Spintronics: The electronics industry to date has relied upon the control of charge flow, combined with size scaling (i.e., reducing the physical size of elements such as transistors), to continuously increase the performance of existing electronics. This trend, widely known as Moore's Law, has been remarkably successful. However, size scaling cannot continue indefinitely as atomic length scales are reached (the "Moore's Law Roadblock"), so new approaches must be developed. Basic research efforts at NRL and elsewhere have shown that spin angular momentum, another fundamental property of the electron, can be used to store and process information in solid-state devices. Subsequently, the *International Technology Roadmap for Semiconductors*¹ has identified the electron's spin as a new state variable that should be explored for processing information in the fundamentally new ways that will be required beyond the ultimate scaling limits of silicon-based complementary metal-oxide-semiconductor (CMOS) technology. This approach is known as semiconductor spintronics.

The Challenge: Electrical injection and transport of spin-polarized carriers is prerequisite for developing such an approach. Although good results have been realized in III-V semiconductors such as gallium arsenide,² little progress has been made in silicon, despite its overwhelming dominance of the industry. This is because spin-polarized carriers can be readily created and probed by powerful optical spectroscopic

techniques in direct-gap semiconductors (e.g., GaAs), but these techniques often fail or are very difficult to use in indirect-gap materials such as silicon. Thus the challenge is twofold: to develop a means to electrically inject spin-polarized carriers into silicon, and to develop a means to detect and quantify their behavior.

Spin Injection and Detection: To create spin-polarized carriers in silicon, we electrically inject them from a ferromagnetic metal contact, which naturally has more electrons with spin oriented in a particular direction determined by the magnetization (“spin-up” or “majority spin”) than in the opposite direction (“spin-down” or “minority spin”). The spin polarization in a typical ferromagnetic metal is $\sim 45\%$. A thin layer of aluminum oxide between an iron contact and the silicon serves as a tunnel barrier to facilitate spin injection by controlling the series resistance and preventing interaction between the iron and the silicon, as shown in Fig. 9. To detect the presence of the spin-polarized electrons and assess the efficiency of injection, we design sample structures that allow the electrons to radiatively recombine. By conservation of momentum, the electrons’ spin angular momentum is transferred to the photons, which we can detect, and an analysis of the polarization of the weak electroluminescence (EL) provides a direct measure of the initial electron spin polarization.

Figure 9 shows a band diagram of the contact region and the two types of samples studied.³ First, Si *n-i-p* doped heterostructures were grown by molecular beam epitaxy (MBE) on *p*-doped Si(001) wafers. Second, Si epilayers (*n*-doped, 80 nm thick) were grown on *n*-Al_{0.1}Ga_{0.9}As/GaAs/*p*-Al_{0.3}Ga_{0.7}As quantum well structures on *p*-GaAs(001) substrates. Although the crystalline quality of the Si is lower and an additional heterointerface is introduced (Si/Al_{0.1}Ga_{0.9}As), these latter samples emit strong EL from the direct-gap GaAs. This enables a quantitative determination of the spin polarization of the electrons which go through the Si and reach the GaAs via standard analysis using quantum selection rules.²

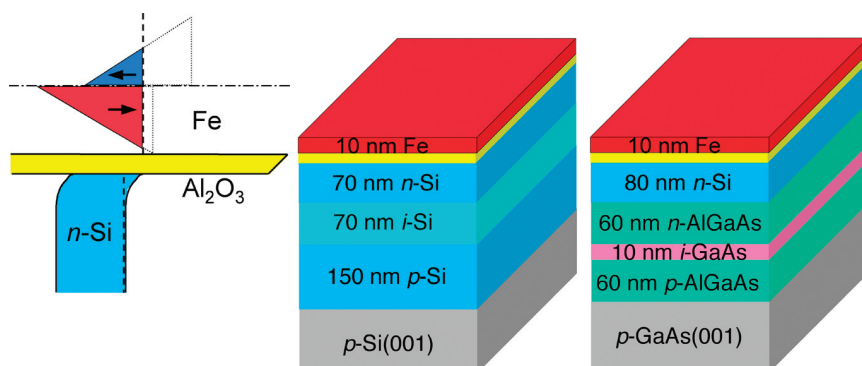
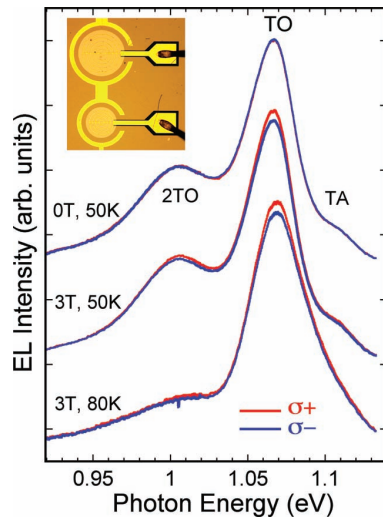


FIGURE 9
Band diagram of the Fe/Al₂O₃/Si contact and cross section of the two types of samples studied.

Surface-emitting light-emitting diode (LED) structures are fabricated from each sample type. Typical spectra from the Si *n-i-p* LEDs are shown in Fig. 10 at 50 K and 80 K (the EL is too weak at higher temperatures); electrons electrically injected from the iron radiatively recombine in the Si, with the dominant emission peak at 1.07 eV. At zero field (0 T), no circular polarization is observed because the Fe magnetization and corresponding electron spin orientation lie in-plane and orthogonal to the light propagation direction. Although spin injection may occur, it cannot be detected with this alignment. Thus, a magnetic field is applied to rotate the Fe spin orientation out-of-plane, and the spectral features then exhibit circular polarization, P_{circ} , as shown by the difference between the red ($\sigma+$) and blue ($\sigma-$) curves in the 3 T spectra.

The magnetic field dependence of P_{circ} for each feature is summarized in Fig. 11. As the Fe magnetization (and electron spin orientation) rotates out of plane with increasing field, P_{circ} increases and saturates. Note that for each feature, P_{circ} tracks the magnetization of the Fe contact, shown as a solid line scaled to the data, demonstrating that the spin orientation of the electrons that radiatively recombine in the Si originates with the spin polarization of the Fe contact. A rate equation analysis which includes the electrons’ radiative and spin lifetimes shows that the net spin polarization of the electrons in the Si is 30%. The spin injection process is therefore relatively efficient, given that the initial spin polarization of the Fe is only 45%.

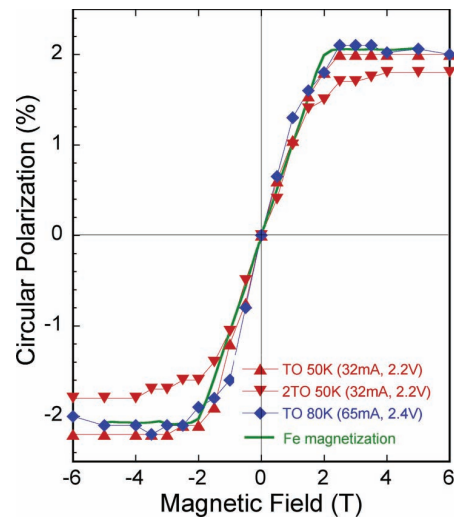
Support for this estimate is provided by data from the second type of sample which incorporates a GaAs quantum well, where the EL is much stronger and persists to 125 K. In these samples, electrons injected from the Fe into the Si drift across the Si/Al_{0.1}Ga_{0.9}As interface with applied bias and radiatively recombine in the GaAs. Standard quantum selection rule analysis of the data determine that the GaAs electron spin polarization is 10%. This value is remarkably high and attests to the robust character of spin transport, given the large lattice mismatch of Si/GaAs, the additional air-exposed interface, and the band offsets involved.

**FIGURE 10**

Electroluminescence spectra from the Si *n-i-p* structure with the Fe/Al₂O₃ contact at 50 K and 80 K, and at magnetic fields of 0 T and 3 T. The inset shows an optical photograph of the LEDs studied. Spectral peaks corresponding to transverse acoustic (TA) and transverse optical (TO) mediated recombination are identified in the figure.

FIGURE 11

Magnetic field dependence of P_{circ} for the spectral features shown in Fig. 10.

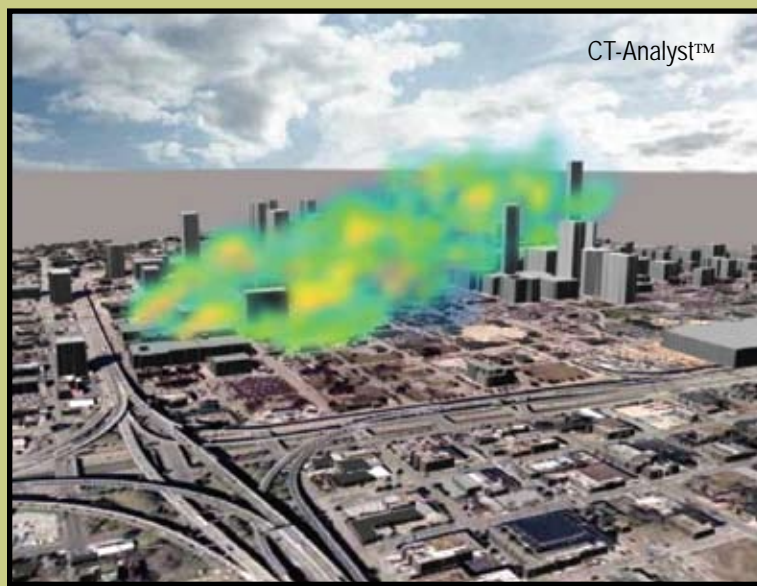


Impact and Outlook: This approach injects spin-polarized electrons near the silicon conduction band edge with near unity conversion efficiency and low bias voltages (~ 2 eV) compatible with CMOS technology. The realization of efficient electrical injection and significant spin polarization using a simple magnetic tunnel barrier compatible with “back-end” silicon processing will greatly facilitate development of silicon-based spintronic devices.

[Sponsored by NRL]

References

- ¹ *International Technology Roadmap for Semiconductors*, 2007 Edition, pp. 30-43, <http://www.itrs.net/reports.html>.
- ² B.T. Jonker and M.E. Flatté, “Electrical Spin Injection and Transport in Semiconductors,” Ch. 7 in D.L. Mills and J.A.C. Bland, eds., *Nanomagnetism: Ultrathin Films, Multilayers and Nanostructures*, 227-272 (Elsevier, Amsterdam, 2006).
- ³ B.T. Jonker, G. Kioseoglou, A.T. Hanbicki, C.H. Li, and P.E. Thompson, “Electrical Spin Injection into Silicon from a Ferromagnetic Metal/Tunnel Barrier Contact,” *Nature Physics* **3**, 542 (2007). ★



Flux-Corrected Transport (1970-1976)

NRL scientists started to conduct theoretical and computational investigations of high-altitude nuclear effects (HANE) for the Defense Nuclear Agency in the late 1960s. While performing this work in 1970 and 1971, they developed an entirely new technique for solving fluid dynamic continuity equations on a computer. This technique, flux-corrected transport (FCT), enabled precise calculations of shock and steep gradient phenomena by eliminating the oscillations, ripples, and numerical diffusion that had plagued all other techniques for decades. FCT has also been applied to missile silo design, naval oceanography, nonacoustic submarine warfare, atmospheric communications research, civil hydrodynamics and water resources research, mine safety, atmospheric pollution transport, supernova explosions, solar weather prediction, laser and ion-beam fusion, aerodynamics, and base and force protection against weapons of mass destruction (WMD). The most recent applications include the 3-D urban aerodynamics computations for CT-Analyst™ and urban defense against WMDs. Between 1973 and 1988, the original paper on FCT was NRL's most cited publication, and more than 500 computational laboratories, universities, and companies have adopted it for solving fluid flow problems that impact military operations, civil projects, and public health and safety.

183

Multifunctional Electrode Nanoarchitectures for Electrochemical Capacitors

J.W. Long and D.R. Rolison

185

Enhancement of Electrical Properties by Tailoring Nanoparticles in Holmium-doped $\text{YBa}_2\text{Cu}_3\text{O}_{7-\delta}$ Superconductors

R.L. Holtz, R. Goswami, and G. Spanos

187

Molecular Memory Circuits Using a Virus as a Template

A.S. Blum, C.M. Soto, and B.R. Ratna

189

Single Crystal Diamond Nanomechanical Dome Resonator

M.K. Zalalutdinov, J.W. Baldwin, B.B. Pate, J. Yang, J.E. Butler, and B.H. Houston

Multifunctional Electrode Nanoarchitectures for Electrochemical Capacitors

J.W. Long and D.R. Rolison
Chemistry Division

Introduction: The term electrochemical capacitor (EC) describes a diverse class of energy-storage devices that bridges the critical performance gap on the power vs energy density plane between the high power densities offered by conventional capacitors and the high energy densities of batteries.¹ Although from both practical and fundamental perspectives, ECs are closely related to batteries, electrochemical capacitors can be differentiated by charge-discharge response times that are on the order of seconds and by their exceptional cycle life (typically many tens to hundreds of thousands of cycles). The most visible technologies that will be impacted by ECs are hybrid-electric power systems, where significant increases in energy efficiency can be achieved through the recovery of energy normally wasted during braking of repetitive motion, thanks to the rapid charge-discharge response of ECs. Hybrid-electric power systems will become increasingly beneficial not only for transportation applications but also for large industrial equipment, including cranes and elevators.

Improvements in the high-power performance of electrochemical capacitors and batteries for applications ranging from mission-critical electronics and sensors to hybrid-electric power systems require a fundamental re-design of the underlying electrode architectures on the nanoscale. We recently demonstrated one such example of a multifunctional electrode nanoarchitecture in which electroactive nanoscale manganese oxide deposits cover the walls of the tortuous aperiodic structure of ultraporous carbon nanofoams

and related porous carbons.² In such a configuration (see Fig. 1), the nanostructured carbon substrate serves as a high-surface-area, massively parallel 3D current collector for the poorly conducting MnO_2 coatings, and defines the internal pore structure of the electrode, which facilitates the infiltration and rapid transport of electrolyte (i.e., solvent and ions) to the nanoscopic MnO_2 phase. The interest in manganese oxides for ECs has grown rapidly in recent years, primarily due to the low cost and low toxicity of MnO_2 compared to other metal oxides.³ By redesigning the structures of MnO_2 -containing electrodes as multifunctional nanoarchitectures, significant improvements in charge-discharge response will be achieved, while retaining the inherent advantages of MnO_2 .

New Results: To achieve the multifunctional MnO_2 -carbon nanoarchitecture illustrated in Fig. 1, we developed a simple, scalable electroless deposition process, based on the redox reaction of aqueous permanganate with pre-formed carbon nanofoam substrates. We discovered that by maintaining the permanganate precursor solution between neutral and basic pH conditions, MnO_2 deposits directly on the surface of the nanofoam in a self-limiting fashion as 10–20 nm thick coatings of MnO_2 nanofilaments (see transmission electron micrograph in Fig. 2), and these MnO_2 deposits permeate the macroscopic thickness (180 μm) of the carbon nanofoam. Nitrogen-sorption measurements and scanning electron microscopy confirm that the through-connected pore network of the nanofoam is retained in the MnO_2 -carbon nanoarchitecture, which is critical for realizing rapid charge-discharge of the resulting electrode.

In an electrochemical capacitor, the MnO_2 coating serves as a “bank” for charge storage via redox reactions involving cations from the contacting aqueous electro-

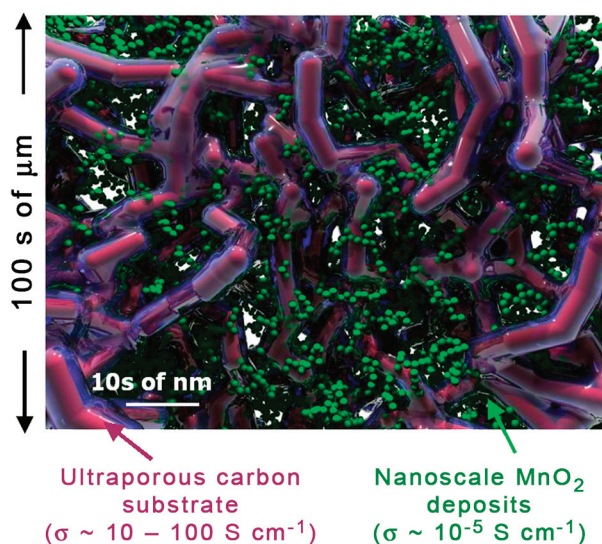
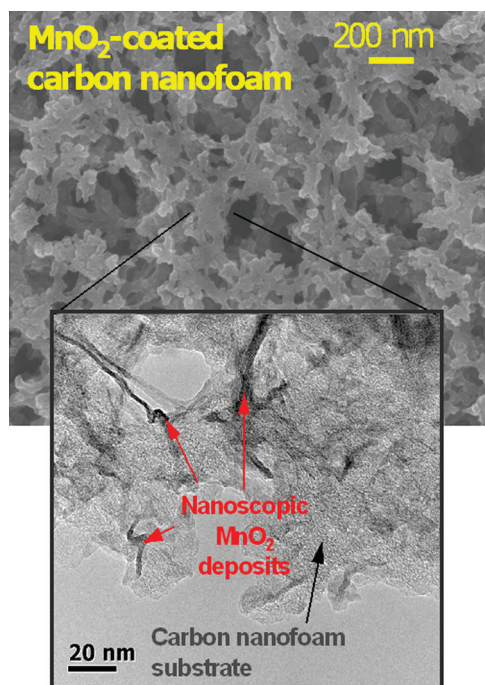


FIGURE 1

Schematic of the interior of a multifunctional nanoarchitecture comprising a carbon nanofoam or related ultraporous carbon coated with nanoscale deposits of nanoscale MnO_2 . The approximate electrical conductivities (σ) of both components are noted.

**FIGURE 2**

Scanning electron micrograph (top) and transmission electron micrograph (bottom) of a MnO₂-carbon nanofoam hybrid nanoarchitecture.

lyte and electrons from the external circuit, resulting in significant enhancements in capacitance for MnO₂-carbon nanoarchitectures with respect to what can be achieved solely by the innate double-layer capacitance (20–40 $\mu\text{F cm}^{-2}$) at the unmodified carbon nanofoam surface. For example, the mass-normalized capacitance of carbon nanofoam structures can be increased by a factor of four, even at MnO₂ weight loadings of <40%. Enhancements in charge-storage capacity are even more dramatic when normalized to either the volume or the geometric area (i.e., the “footprint” of the electrode on the current collector) of the electrode structure, which are unaltered by MnO₂ deposition. For the same conditions described above, both the volumetric and the footprint-normalized capacitance are increased by a factor of ten after MnO₂ deposition, and in terms of absolute performance, the footprint-normalized capacitances of the MnO₂-carbon nanofoams routinely exceed 3 F cm⁻². The ability to realize high capacitance per unit area, enabled in this case by the 3D multifunctional electrode design, is a critical advantage when powering microelectronics devices that have a limited areal footprint for the power source. Although these initial results are very promising, we anticipate further performance improvements by tuning such parameters as the mass loading and crystal structure of the MnO₂ mass loading, and the pore structure of the supporting carbon nanofoam.

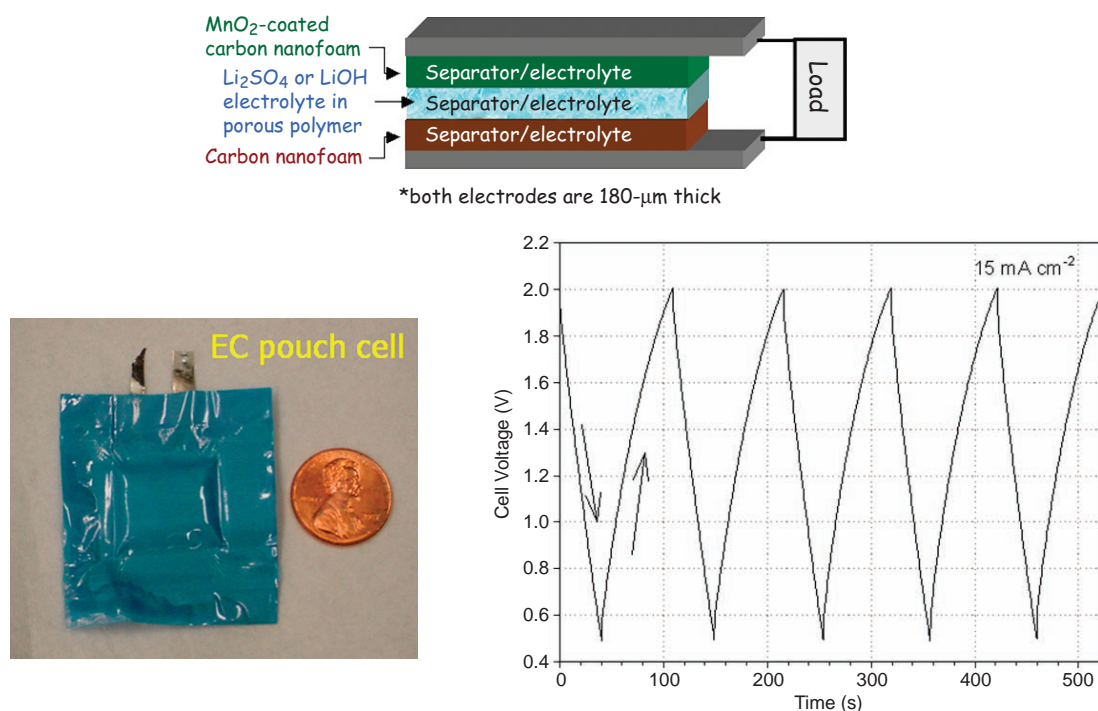
Impact: Ultimately, the materials developed in this program will be deployed in 2-V aqueous asymmetric capacitors, in which high-rate performance will be

significantly enhanced through the use of well-designed MnO₂-carbon nanoarchitecture cathodes. Prototype EC cells assembled and tested at NRL are already demonstrating such promise (see Fig. 3). With further fine-tuning of MnO₂-carbon cathodes and application of the nanoarchitecture design approach to the carbon anode, asymmetric ECs that deliver energy densities >40 Wh kg⁻¹ and exhibit charge-discharge response times of <10 s can be realized, which would represent a significant advancement over current state-of-the-art ECs, which have energy densities of <5 Wh kg⁻¹. Combining such performance metrics in an EC design that utilizes aqueous electrolytes will yield a class of safe, low-cost energy-storage devices with superior combinations of energy and power density that will enable emerging civilian and military applications. The transition of technology resulting from this program is already under way, with a patent application and corresponding licensing agreement to develop and commercialize ECs based on NRL-developed materials.

[Sponsored by ONR]

References

- ¹ B.E. Conway, *Electrochemical Supercapacitors: Scientific Fundamentals and Technological Applications* (Kluwer Academic/Plenum Publishers, New York, 1999).
- ² A.E. Fischer, K.A. Pettigrew, D.R. Rolison, R.M. Stroud, and J.W. Long, “Incorporation of Homogeneous, Nanoscale MnO₂ within Ultraporous Carbon Structures via Self-limiting Electroless Deposition: Implications for Electrochemical Capacitors,” *Nano Lett.* **7**, 281-286 (2007).
- ³ D. Bélanger, T. Brousse, and J.W. Long, “Manganese Oxides: Battery Materials Make the Leap to Electrochemical Capacitors,” *Interface* **17**, in press. ★

**FIGURE 3**

Schematic of asymmetric EC cell with NRL-developed electrodes (top); photo of prototype cell (bottom left); and electrochemical cycling of an aqueous-electrolyte EC pouch cell between 0.5 and 2 V, showing full cell charge-discharge in tens of seconds.

Enhancement of Electrical Properties by Tailoring Nanoparticles in Holmium-Doped YBa₂Cu₃O_{7-δ} Superconductors

R.L. Holtz,¹ R. Goswami,² and G. Spanos¹

¹Materials Science and Technology Division

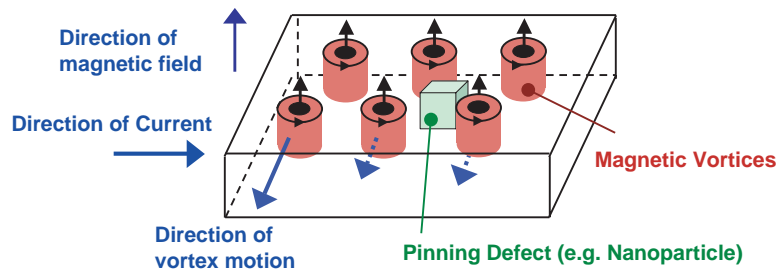
²SAIC

Background: High-temperature superconducting (HTS) tape and wire are promising for high power density shipboard motor and generator applications. There is a need, however, for improving the performance and stability of these materials in high magnetic fields in order to fully exploit this technology. The Naval Research Laboratory, with our extensive expertise and sophisticated capabilities for microstructural analysis, has been approached by and is working closely with several HTS wire processing groups, including HTS manufacturers American Superconductor Corporation and Metal Oxide Technologies Incorporated, as well as the U.S. Air Force Research Laboratory, to understand the basic relationships between microstructure and performance of HTS tapes.

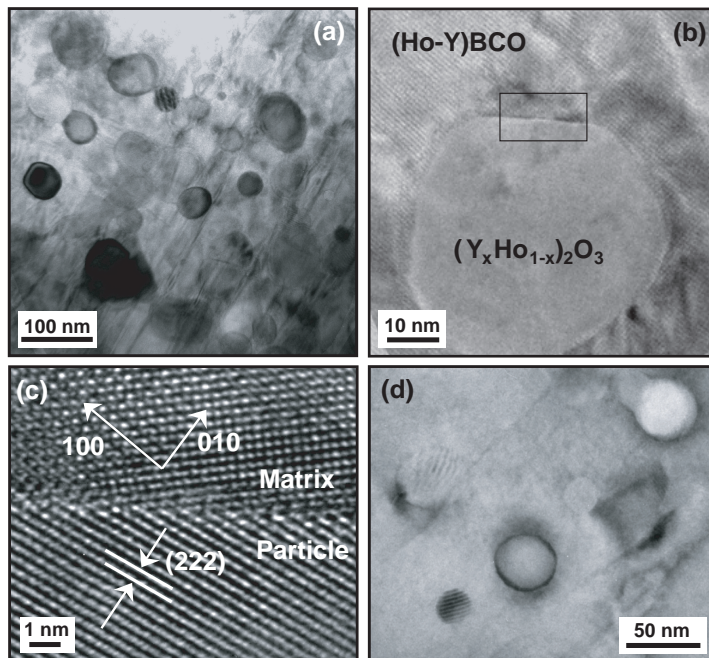
Flux Pinning in Superconductors: Magnetic flux penetrates a Type II superconductor in the form of “vortices,” which consist of circulating currents surrounding the flux. If these vortices move, an effective

resistance is created, which degrades the critical current density and the transition temperature of the superconductor. If the vortices are prevented from moving, by “pinning” them, this enhances the critical current. This mechanism is suggested in Fig. 4, which depicts a slab of superconductor under the actions of a current and a magnetic field. The presence of flux pinning centers, such as second phase particles, for example, results in a pinning force that inhibits vortex motion. Pinning centers are most effective when the size and spacing is comparable to that of the vortices, on the order of 10 to 100 nm; hence, dense dispersions of nanoparticles in that size range provide very effective flux pinning.

Nanoparticles in YBCO: Figure 5(a) shows a transmission electron microscopy (TEM) image of a distribution of nanoparticles in the size range of 10 to 100 nm in an HTS coating of composition YBa₂Cu₃O₇ (YBCO) doped with holmium (Ho:Y ratio 1:1). This particular specimen was submitted to NRL for analysis by American Superconductor Corporation. The HTS coating is formed by high-rate metal-organic deposition and subsequent heat treatment. NRL determined that two types of nanoparticles, (Y_xHo_{1-x})₂O₃ and Cu-Ba-Ho-Y (exact stoichiometry yet to be determined), are formed during the deposition process. Figure 5(b) shows one partially faceted (Y_xHo_{1-x})₂O₃ particle, and Fig. 5(c) is a high-resolution TEM image of the interface between the matrix and a nanoparticle, showing

**FIGURE 4**

A schematic diagram illustrating the concept of pinning of the vortices by nanoparticles embedded in the superconductor.

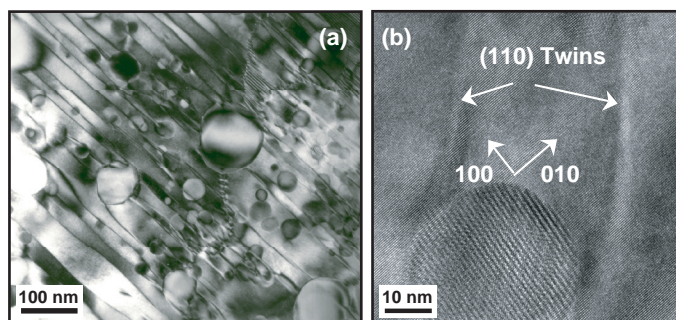
**FIGURE 5**

(a) A bright-field transmission electron microscopy (TEM) image showing the nanoparticles in the superconducting matrix in a Ho-doped YBCO sample. (b) A high-resolution TEM (HRTEM) image showing a coarse $(Y_xHo_{1-x})_2O_3$ particle. (c) A higher magnification HRTEM image showing that the particle/matrix interface of the coarse particle, obtained from the rectangular box in (b), is not fully coherent. (d) A fine particle showing the dark lobes around the particle suggesting that the particle is associated with a strain field.

that it is crystallographically not fully coherent. Figure 5(d) shows a TEM image of several nanoparticles in another Ho-doped YBCO specimen. The dark lobes around the particles are due to strain fields. The results indicate that the nanoparticles are associated with relatively large strain fields, and it is these strain fields that likely provide the pinning force for the vortices. NRL also has found that nanoparticles formed in YBCO films also can stabilize other defects such as twin boundaries, antiphase boundaries, stacking faults, intergrowth, and plane buckling, all of which result in additional contributions to vortex pinning.¹

Crystallographic Twins: Crystallographic twin boundaries, i.e., grain boundaries of relatively good atomic fit between regions of different (but symmetrical) crystallographic orientation, provide extra pinning, although they are less effective than nanoparticles. It is known that (110) twins (twins whose boundaries lie

parallel to a (110) direction in the crystals) form during transformation from the tetragonal to the orthorhombic phase, as the material is cooled from high processing temperatures. Figure 6(a) shows a Ho-doped YBCO specimen with a large number of (110) transformation twins (the linear features), in addition to a high density of nanoparticles. By correlating the density and sizes of the nanoparticles and the twins with the critical current density of the HTS specimens, and studying these features as a function of excess holmium content, the optimum composition for tailoring critical current retention in magnetic fields is found. NRL also has identified an interesting interaction between nanoparticles and twin boundaries. Figure 6(b) provides a high-resolution TEM image of twin boundaries that appear to be bent in the vicinity of a nanoparticle, presumably due to the presence of the strain field around the nanoparticle. Investigation of this observation is continuing.

**FIGURE 6**

(a) A bright-field TEM image near the [001] zone of the superconducting matrix showing nanoparticles embedded in the matrix for a Ho-doped YBCO sample (lower Ho concentration than specimen of Fig. 5). Note the (110) twins. (b) HRTEM image showing the (110) twins. Note the apparent bending of twins close to the particle. Such bending could result from the interaction of strain fields present close to the particle and the twins.

Significance: Basic understanding of the effects of different kinds of flux-pinning features in superconducting coatings, such as nanoparticles and twins, allows the tailoring of the superconductor performance of HTS wire in magnetic fields. In particular, in superconducting motor and generator coils, there are substantial magnetic fields perpendicular to the superconducting tape, which produce a very large suppression of the critical current in the YBCO. With the controlled addition of flux-pinning nanoparticles, twin boundaries, and other defects through holmium doping of YBCO, the critical current under perpendicular fields is substantially improved, reducing the amount of superconducting wire needed, and thus reducing both the size and the cost of the devices.

[Sponsored by NRL and ONR]

Reference

¹ R. Goswami, R.L. Holtz, M.W. Rupich, W. Zhang, and G. Spanos, "Effect of Holmium Additions on Microstructures in $\text{YBa}_2\text{Cu}_3\text{O}_{7-\delta}$," *Acta Materialia* **55**, 6746-6753 (2007) and references therein. ★

Molecular Memory Circuits Using a Virus as a Template

A.S. Blum, C.M. Soto, and B.R. Ratna
Center for Bio/Molecular Science and Engineering

Introduction: Significant challenges exist in constructing and manipulating the building blocks of a nanoscale device. After such a device is assembled, it is an additional challenge to electronically address or measure responses at the molecular level. We demonstrate the usefulness of individual virus particles as scaffolds to enable design, construction, and

measurement of nanoscale molecular electronics memory devices. Such devices are of great interest for their potential to enable lightweight, low-cost, and low-power technologies such as handheld electronic sensors and inexpensive disposable molecular memories. Taking advantage of molecular electronics requires developing novel techniques for organizing nanosized materials into usable devices. As biological interactions are better understood, there has been great interest in using the specificity and strong interactions present in biology for this purpose. By combining the structural specificity provided by biological systems with the material properties of synthetic systems it is possible to develop novel devices on the nanoscale. Using viruses as nanoscale scaffolds for devices offers the promise of exquisite control of positioning on the nanoscale, using a particle that can either interface with lithographically defined structures, or undergo further self-assembly into extended structures by itself. We use cowpea mosaic virus (CPMV) as a nanoscale scaffold for constructing molecular electronic circuits for use in memory applications.¹

Nanocircuit Assembly: Using genetically engineered CPMV allows the generation of specific patterns of functional amino acids, which provide a means to assemble complex structures with high spatial specificity on the nanometer scale. To construct nanoscale circuits, the amino acid cysteine was inserted in a specific predetermined pattern on the virus surface. Gold nanoparticles were bound to the inserted cysteine thiol groups. To make electronic circuits, the nanoparticles were then interconnected using conjugated conducting molecules, resulting in three-dimensional networks called viral nanoblocks (VNBs). Network properties were engineered by using molecular connectors with different properties. Networks consisting of just

molecular wires were compared with networks containing bipyridyl-dinitro oligophenylene ethynylene dithiol (BPDN), a molecule with two conductance states which has been shown to behave as a molecular switch.²

Measuring Molecular Circuits: The conductance of the molecular network self-assembled on isolated single VNBs was measured using scanning tunneling microscopy (STM). Although STM characterization is a well-established technique for determining the conductance of isolated molecules, our measurements are the first demonstration of a self-assembled molecular network on the nanometer scale. To carry out these measurements, a self-assembled monolayer of undecanethiol (C11) on a gold-on-mica substrate was used to isolate virus-based networks from each other. This substrate was exposed to virus-templated nanocircuits to produce isolated viruses bound to the underlying gold substrate via the inserted conducting molecules that

can be interrogated individually by the STM (Fig. 7(a)). Control samples exposed to unmodified viruses show dark areas that do not contain bright spots (Fig. 7(b)). These high contrast areas do not appear in films that have not been exposed to virus (not shown). Substrates exposed to viruses with attached gold nanoparticles show characteristic dark areas containing brighter spots (Fig. 7(c)). Within these darker areas are bright spots that are likely to be 5-nm gold nanoparticles attached to the virus. Substrates exposed to conductive VNBs show large bright features that are highly enhanced and prominent (Fig. 7(d)). The distinct change in VNB appearance after exposure to conductive molecules suggests that functionalization with molecular wires opens a pathway for charge transport across the molecular network templated on the viral scaffold.

Tunneling spectroscopy measurements were also made on VNBs after imaging to examine the conductance of the molecular networks. For tunnel-

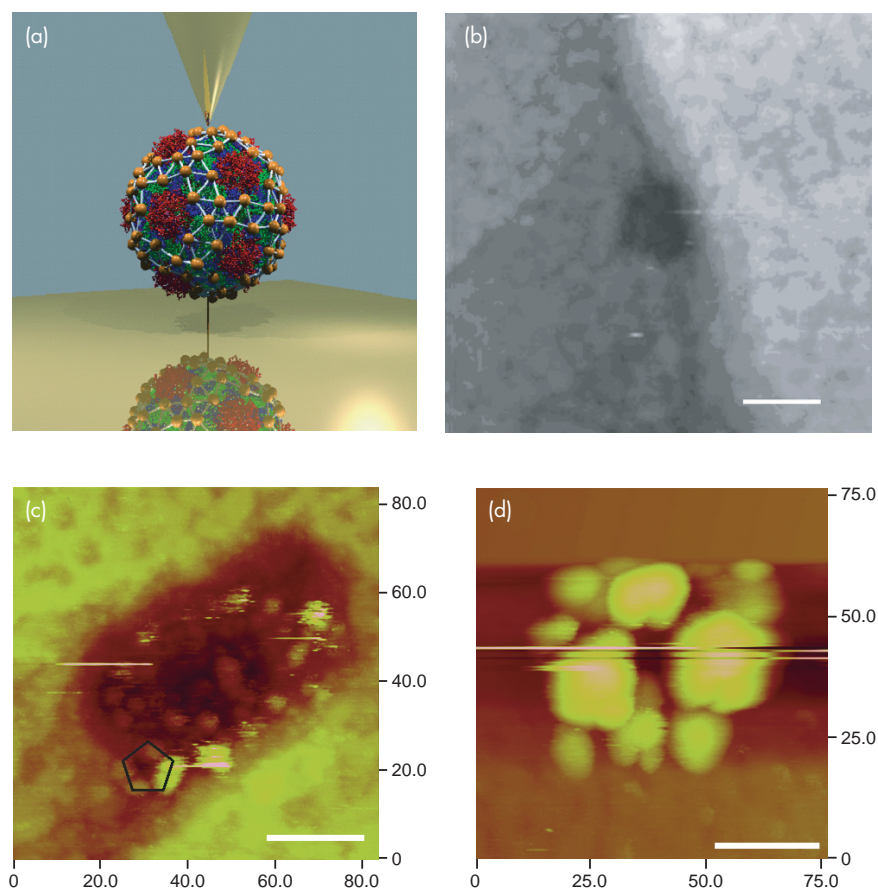


FIGURE 7

STM studies of viral nanoblocks. $I_t = 2.5$ pA, $V_{bias} = 1$ V. (a) Schematic of STM experiment, showing isolated conductive VNB attached to gold substrate through a conducting molecule inserted in an insulating C11 matrix. (b) STM image showing isolated CPMV virus (dark patch). Scale bar indicates 30 nm. (c) STM image of CPMV with 5-nm gold nanoparticles. The size and shape indicate that there are likely two viruses in this image. Pentagon indicates likely 5-fold axis. Scale bar indicates 20 nm. (d) STM image of conductive VNB in C11 alkane matrix. Scale bar indicates 20 nm.

ing spectroscopy, the STM tip was held over the VNB with the feedback turned off. The bias voltage was swept while recording the tunneling current (current vs voltage = I/V). Individual molecular wire networks show no discontinuities, hysteresis, or other non-linear behaviors over a voltage range of 0 to 2 V (Fig. 8(a)). In contrast to this linear I/V behavior measured for control molecular wire networks, STM measurements of isolated BPDN-containing networks (Fig. 8(b)) show pronounced hysteretic behavior.¹ BPDN-containing networks show a discontinuity in the measured I/V behavior that is similar to that observed in individual BPDN molecules.² Furthermore, the stepped features that appear at ~ 1.5 V and 2 V suggest that there are multiple conductance states accessible to the molecular network. These steps may occur when different molecules in the network change conductance state, and are in good agreement with calculated models of the molecular networks.

Discussion: We have produced conductive networks on the nanoscale using CPMV as a template for self-assembly and demonstrated that the network properties depend on the properties of the nanoscale components. Thus, we can engineer the behavior of nanoscale templated devices by selecting appropriate molecular components. Building such electronic cir-

cuits from molecular building blocks is an area of great interest. The CPMV scaffold uses the chemical specificity present in biological systems to organize inorganic components with great precision in three dimensions. In using molecules that can act as bistable molecular switches, we built switchable molecular networks with a 28 nm footprint. Such CPMV-based bit storage devices have a theoretical density of 1 petabit/cm², with the potential for increased storage density due to the availability of more than two conductance states on each virus. Future work in this area could produce additional functional templated devices such as biosensors or nanostructured light harvesters. By using bottom-up programmed self-assembly to produce a free-standing nanodevice, we showed that biological nanoparticles can be used in materials engineering.

Acknowledgments: The authors gratefully acknowledge A. Chatterji and J.E. Johnson of The Scripps Research Institute for providing the virus used in this work, and our many colleagues who contributed to the research discussed in this article, especially the synthetic expertise of M. Moore (NRL), T. Schull (NRL), S.K. Pollack (FDA), and J.M. Tour (Rice University).

[Sponsored by NRL]

References

- ¹A.S. Blum, C.M. Soto, C.D. Wilson, C. Amsinck, P. Franzon, and B.R. Ratna, "Electronic Properties of Molecular Memory Circuits on a Nanoscale Scaffold," *IEEE Trans. NanoBio.* **6**, 270-274 (2007).
- ²A.S. Blum, J.G. Kushmerick, D.P. Long, C.H. Patterson, J.C. Yang, J.C. Henderson, Y. Yao, J.M. Tour, R. Shashidhar, and B.R. Ratna, "Molecularly Inherent Voltage-controlled Conductance Switching," *Nature Materials* **4**, 167-172 (2005). ★

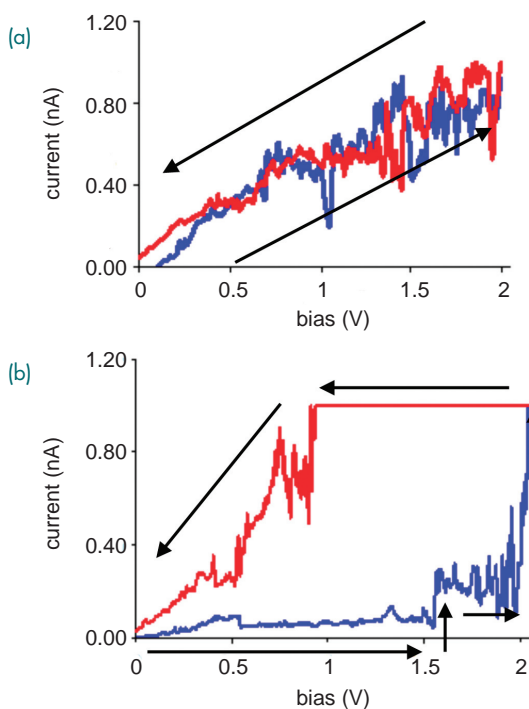


FIGURE 8
(a) Current vs voltage (I/V) for an isolated CPMV VNB network. This molecular wire network does not display non-linear behaviors. (b) Current vs voltage (I/V) measurement for isolated CPMV-BPDN network showing steps in conductance and multi-state behavior.

Single Crystal Diamond Nanomechanical Dome Resonator

M.K. Zalalutdinov,¹ J.W. Baldwin,² B.B. Pate,³ J. Yang,⁴ J.E. Butler,³ and B.H. Houston²

¹SFA, Inc.

²Acoustics Division

³Chemistry Division

⁴NOVA Research, Inc.

Introduction: Superior mechanical and optical properties of single crystal (SC) diamond in combination with a chemically inert and bio-compatible surface enable the design and fabrication of novel nanoscale devices for sensing and signal processing applications. In this letter, we present the first fabrication and operation of high-frequency nanomechanical resonators implemented in 100-nm-thick SC diamond films epitaxially grown on SC synthetic diamond.

The method of fabrication is based on introducing a pattern of localized mechanical stress in the epitaxial film and can be potentially extended below 10 nm film thickness. Reduction in film thickness and hence a reduction in the mass of the resonator is motivated by a straightforward gain in performance as a mass sensor. The corresponding increase in resonant frequency greatly facilitates operation in viscous media such as air and water. The exceptional mass sensitivity of nanomechanical resonators, combined with emerging methods of functionalization¹ that provide a diamond surface with the specificity toward analytes of interest, make SC diamond resonators a superb choice for chem/bio sensing applications.

Fabrication: Prior to epitaxial film growth, the substrate (Sumitomo Electric Type-Ib, high pressure high temperature (HPHT) synthetic single crystal) was polished and implanted with carbon (energy 180 keV, dose $1 \times 10^{16} \text{ cm}^{-2}$) to form a 230-nm-deep sacrificial layer. Implantation was followed by microwave plasma-assisted chemical vapor deposition of 100-nm-thick SC diamond film² and an electrolysis-based release process³ that partially undercuts the sacrificial layer. The optical micrograph in Fig. 9 and the atomic force microscope (AFM) image in Fig. 10 show examples of the resulting structures—domes with an outer diameter below 10 microns and elevation of $\sim 200 \text{ nm}$ at the apex. We attribute the dome formation to the presence of metallic (Fe, Co, Ni) inclusions on the surface of the substrate. According to our model, the high temperature of the CVD growth (900–1150 °C) and numerous defects created by the ion implantation facilitate the diffusion of the metal atoms along the sacrificial layer, possibly accompanied with local modification of the carbon-carbon bonds. Distortion of the substrate lattice contributes to stress in the CVD-grown film while the remaining particle at the center of the cloud is expected to generate a pinhole. During the electrolytic release step, the ionic transport removes the metal particle and preferentially etches the metal-enriched parts of the sacrificial layer creating a freely suspended circular membrane. Compressive stress accumulated in the CVD-grown film causes the membrane to buckle up, creating a dome-like structure. The resulting curvature of the domes provides us with an estimate for the pre-released stress in excess of 2 GPa. It should be noted that the ability to create a controlled pattern of such high stress (order of magnitude higher than in polysilicon, for example) can be exploited in numerous microelectromechanical system (MEMS) structures that require post-release self-assembly and/or shaping, with the domes being the simplest example.

Operation: The mechanical vibrational spectrum of the dome (thin shell clamped on periphery) exhibits

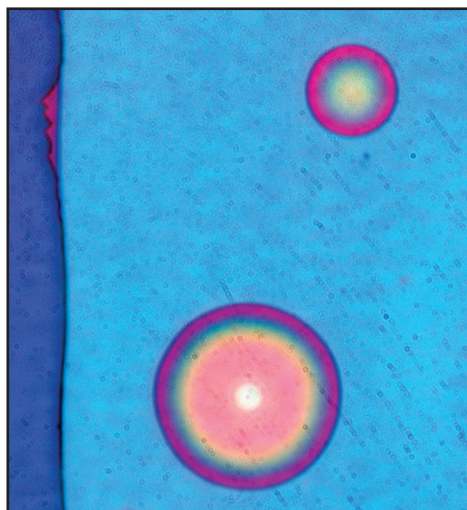


FIGURE 9
Optical micrograph of the SC diamond domes. The smaller dome is 9.2 microns in diameter.

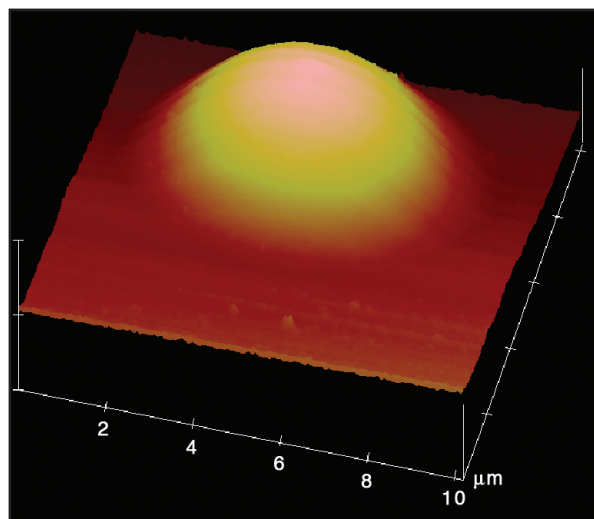


FIGURE 10
AFM image of the SC diamond dome resonator (diameter 8 microns, elevation at the apex 200 nm).

a series of sharp resonances corresponding to different configurations of standing flexural waves. Figure 11 shows the resonant peak at 130 MHz that corresponds to fundamental mode of vibration (γ_{00}) and demonstrates a quality factor $Q \sim 1000$ in vacuum ($P \sim 10^{-7}$ Torr). Extra rigidity added by the 3D nature of the shell is manifested by the upward shift of the resonance ($\delta f \sim 60 \text{ MHz}$ compared to a flat membrane of equal radius). Figure 12 shows a resonant peak at one of the overtones of the dome resonator at 630 MHz. These spectra were acquired using laser-based thermoelastic actuation and interferometric readout.⁴ A time-variable stress caused by modulated intensity of a laser beam (diode 412 nm) focused to a submicron spot within the dome was used to activate the dome vibrations.

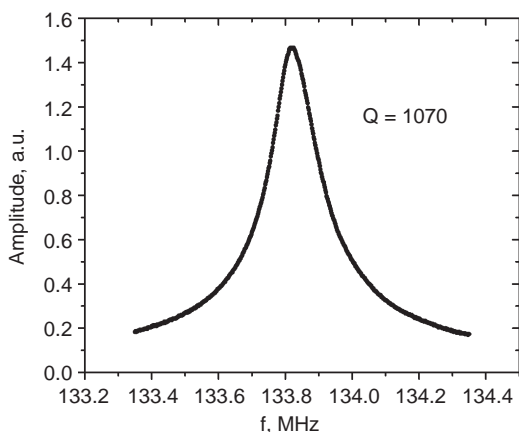


FIGURE 11
Frequency response of the SC diamond dome resonator (7.6 microns in diameter, fundamental mode of vibration).

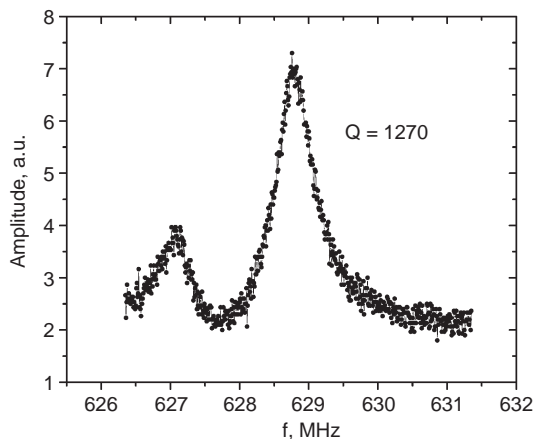


FIGURE 12
SC diamond dome resonator: overtone at 630 MHz.

The resulting motion was detected by monitoring the reflectivity of the second laser beam (HeNe 633 nm) focused on the dome. This optical method of interfacing nanomechanical resonators can be used to address structures enclosed in microchannels and/or exposed to a toxic environment. Further, it is implementable over a wide temperature range and most importantly, it provides the benefit of simplicity for the mechanical

structure itself, thus reducing the size and the mass of the resonator. A simple estimate for the sensitivity of the SC diamond dome resonator as a mass sensor can be extracted from Eq. (1):

$$\delta m \approx \frac{M_{\text{resonator}}}{Q}. \quad (1)$$

Summary: Our SC diamond dome resonators demonstrate a quality factor $Q \sim 500$ at ambient pressure, resulting in added mass sensitivity estimated as $\delta m \sim 10^{-15}$ g. We expect to reach atto-gram (10^{-18} g) sensitivity in air with the resonators fabricated from thinner (~ 10 nm) SC diamond films, which is a sensitivity range inaccessible with polycrystalline or nanocrystalline films. The superb ruggedness of the dome resonators, their ability to withstand submersion, sonication, etc., is an enabling factor for post-processing functionalization, where different chemical agents must be selectively placed on the surface of pre-fabricated and released nanoresonators. We are currently working on the design and fabrication of large arrays of SC diamond dome resonators grown on lithographically defined nanoscale metallic seed particles in order to demonstrate sensitivity and throughput efficiency largely exceeding the performance of existing thin-film and bulk resonator-based sensors.

[Sponsored by ONR]

References

- ¹ W. Yang, O. Auciello, J.E. Butler, W. Cai, J.A. Carlisle, J.E. Gerbi, D.M. Gruen, T. Knickerbocker, T.L. Lasseter, J.N. Russell, Jr., L.M. Smith, and R.J. Hamers, "DNA-modified Nanocrystalline Diamond Thin-films as Stable, Biologically Active Substrates," *Nature Materials* **1**, 253-257 (2002).
- ² J.E. Butler, M.W. Geis, K.E. Krohn, J. Lawless, Jr., S. Deneault, T.M. Lyszczarz, D. Flechtner, and R. Wright, "Exceptionally High Voltage Schottky Diamond Diodes and Low Boron Doping," *Semicond. Sci. Technol.* **18**, S67-S71 (2003).
- ³ M. Marchywka, P.E. Pehrsson, S.C. Binari, and D. Moses, "Electrochemical Patterning of Amorphous Carbon on Diamond," *J. Electrochem. Soc.* **140**, L19 (1993).
- ⁴ M. Zalalutdinov, J.W. Baldwin, M.H. Marcus, R.B. Reichenbach, J.M. Parpia, and B.H. Houston, "Two-dimensional Array of Coupled Nanomechanical Resonators," *App. Phys. Lett.* **88**, 143504 (2006). ★



Fiber-optic Interferometric Acoustic Sensors (1977-1990)

Fiber-optic sensor devices, which measure external fields and are found in diverse applications ranging from traffic control to medical care, are yet another NRL invention. Their origin is in the fiber-optic interferometric acoustic sensor first demonstrated and patented by NRL in 1977. However, it was envisioned from the outset as a generic device capable of responding to external perturbations, such as in electric fields, magnetic fields, or temperature, depending on the design of the fiber coating or mounting structure. The initial work sparked Navy, Department of Defense (DoD), and national interest and further research into both fiber-optic acoustic and nonacoustic sensors, and in 1978, NRL demonstrated the first Navy/DoD program in fiber-optic sensor systems (FOSS). In 1986, fiber-optic sensors were first tested at sea, leading to the development of the all-optical towed array with its full complement of fiber-optic acoustic sensors and, later, to the fiber-optic Lightweight Wide Aperture Array currently deployed on the Navy's new Virginia-class nuclear submarines.

195

Improving Underwater Imaging with Ocean Optics Research
W. Hou, A. Weidemann, and D. Gray

197

Large-Amplitude Internal Waves in the South China Sea
D.S. Ko, P.J. Martin, S.Y. Chao, P.T. Shaw, and R.C. Lien

200

Probabilistic Prediction for Improved Scientific Understanding and Improved Decision Making
J. Hansen, C. Bishop, J. Doyle, J.S. Goerss, T.R. Holt, J. McLay, and C. Reynolds

Improving Underwater Imaging with Ocean Optics Research

W. Hou, A. Weidemann, and D. Gray
Oceanography Division

Introduction: Underwater vision is vital to many Navy applications involving mine detection, diver visibility, and search and rescue. The ability to see better and farther has always been a central goal of underwater imaging projects. Unlike in the atmosphere, where visibility can be on the order of miles, the visual range in the underwater environment is rather limited, at best on the order of tens of meters, even in the clearest waters. This is the result of combined attenuation effects from both absorption, where photons disappear into water molecules, phytoplankton cells, and detritus, and scattering, where photons bounce away from the original path into different traveling directions. It is mostly the effects of scattering by water and particulates that make the water look dirty or less transparent, resulting in a blurred image recorded by cameras. Although traditional image enhancement techniques can be applied to imagery obtained from underwater environments, their effectiveness is considerably limited because they do not take into account any knowledge of the optical properties of the medium or the processes that lead to the degraded images. Our efforts aim to find ways to incorporate the knowledge of ocean optics to automatically enhance and restore such blurred images from underwater imaging systems, and in turn, to be able to estimate environmental optical properties via through-the-sensor techniques.

Reducing Image Blur using Knowledge of Ocean Optics: The most significant contributor to image blur is multiple scattering, where the path of a photon changes several times before reaching the camera. Associated with multiple scattering, the non-scattered direct beam that contributes to the sharp part of the image is correspondingly reduced, and the combined result is less contrast, which further lowers the quality of the image. The reduction in signal can be so great that the electronic noise of the system becomes a factor, further complicating the issue.

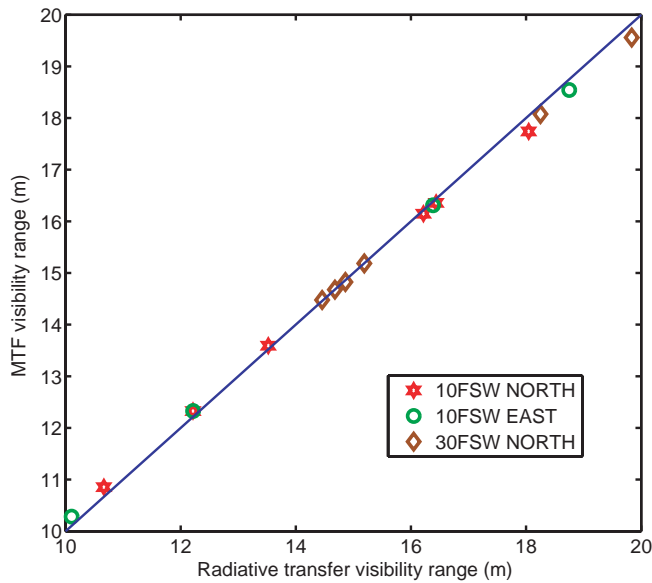
To reduce blur and improve imagery effectively, it is critical to incorporate knowledge of the optical properties of the water to better model the degradation process. The amount of blurring in an image can be described by how much blur a point-source will introduce over the imaging range. This property is the point-spread function (PSF) and its Fourier transformed form is the modulation transfer function (MTF), which describes how fast the details of an image degrade in a given environment. Little attention has been paid to associating these powerful imaging

descriptors to the controlling processes, namely, multiple scattering. We have developed a scattering-imaging model to link commonly measured optical properties of the water to the image degradation process. The effectiveness of this scattering-imaging model was successfully validated by comparing the visibility of the Secchi disk under this current model, to the visibility predicted by the classical radiative transfer model, shown in Fig. 1.¹ This scattering-imaging model enables us to automate the image restoration process using the framework discussed below.

NRL Image Restoration via Denoised Deconvolution (NIRDD): We have established a framework to automatically restore underwater imagery to the best level possible, working with both simulated and field measured data. Under this framework, the standard image restoration approach is extended by incorporating water optical properties into the system response function. The implementation of this automated restoration framework is termed NRL Image Restoration via Denoised Deconvolution (NIRDD),² shown in Fig. 2.

The key to automated processing is the ability to objectively determine underwater image quality, as small, incremental improvements in restored images cannot be measured by visual inspection due to time constraints and subjectivity. Therefore, a special, objective image quality metric (IQM) was developed for underwater imaging. This metric is based on weighted grayscale angle (WGSA), a sharpness metric constrained by a normalized high-frequency wavelet power spectrum. Due to the intensity variations involved in underwater sensing, denoising is carefully carried out by wavelet decompositions. This is necessary since in the underwater environment the effects of high-order scattering can be easily classified as either signal or noise.

The restoration framework first determines the quality of the subject image by IQM and arrives at a single value (WGSA), which serves as a reference to future improvements. The optimization process starts with a set of estimated optical properties of the water, which are converted to the PSF using our model. The modeled PSF is further used to deconvolve the subject image to a restored version and its quality is then assessed by the same IQM. The resulting WGSA is compared to the reference to determine if further optimization is needed. The final results yield the best restored images, as well as the best estimation of environmental optical properties such as absorption, scattering, and attenuation coefficients that are important in ocean optics, including remote sensing applications. The images used in the framework testing were from a 2006 NATO trial experiment in Panama City, Florida. In-water optical properties during the experiment were measured. These included the absorption and attenua-

**FIGURE 1**

Comparison of visibility ranges based on the classical radiative transfer method and the scattering property-derived imaging method (using the MTF). Data are from the GLOW experiment (Gauging Littoral Optics for the Warfighter, September 17–22, 2001, Pensacola, FL). Visibility measurements were taken at 10 ft (10 FSW) and 30 ft (30 FSW) water depths each day, facing different track directions as indicated. Solid blue line depicts 1:1 ratio.

tion coefficients, particle size distributions, and volume scattering functions. Using NIRDD, image restoration was achieved. In addition, the in-water optical properties were estimated as part of the final output via through-the-sensor techniques; results were in line with field measurements.

Summary: Using a systematic approach, we demonstrate the ability to apply ocean optics research results to achieve better underwater images. The framework is applicable to a wide array of imaging systems and platforms, complementing and enhancing hardware-based approaches in reducing effects of multiple scattering. Since it is based on a physical model, it has the benefit of scaling with new camera systems, such as high definition (HD) systems. It is also expandable

to include more complex imaging situations, such as those created by motion- and turbulence-induced phenomena, and under active illumination conditions. Applied inversely, our model also provides the means to generate accurate virtual environments for underwater scene simulations.

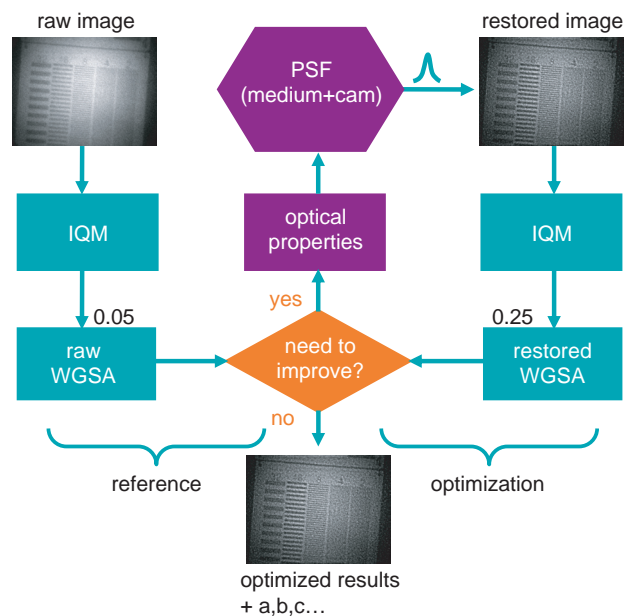
[Sponsored by NRL and ONR]

References

- ¹W. Hou, Z. Lee, and A. Weidemann, "Why Does the Secchi Disk Disappear? An Imaging Perspective," *Opt. Express* **15**, 2791-2802 (2007).
- ²W. Hou, D. Gray, A. Weidemann, G.R. Fournier, and J.L. Forand, "Automated Underwater Image Restoration and Retrieval of Related Optical Properties," *IEEE International Geoscience and Remote Sensing Symposium, IGARSS, Barcelona, Spain, 2007*, pp. 1889-1892 (2007). ★

FIGURE 2

Flow chart of NIRDD (NRL Image Restoration via Denoised Deconvolution). Images used are from a 2006 NATO field exercise in Panama City, FL. 0.05 and 0.25 are corresponding WGSA values of the images before and after restoration was applied. The total PSF consists of the effects of both the medium and the camera system ("cam"). When no further improvements can be made, the optimization loop exits with restored images and derived optical properties (a: absorption; b: scattering; c: attenuation).



Large-Amplitude Internal Waves in the South China Sea

D.S. Ko,¹ P.J. Martin,¹ S.Y. Chao,² P.T. Shaw,³
and R.C. Lien⁴

¹*Oceanography Division*

²*University of Maryland*

³*North Carolina State University*

⁴*University of Washington*

Prologue: One of the most spectacular phenomena recently discovered in the South China Sea is that of very large internal waves. Field observations and satellite images show that these internal waves are over 200 meters in amplitude and their crests extend more than 200 km (Fig. 3). These fast, transient, large-amplitude internal waves can push water up or down 200 meters in 10 minutes and seriously impact the safe operation of submerged vessels, particularly the less powerful unmanned undersea vessels, or UUVs. The large-amplitude internal waves can also have a strong effect on underwater sound propagation as reported by the Office of Naval Research (ONR) Asian Seas International Acoustics Experiment.¹ Several NRL scientists from the Acoustics and Oceanography Divisions participated in this experiment. In 2005, ONR launched the Nonlinear Internal Waves Initiative (NLIWI) to better understand the large-amplitude internal waves in the South China Sea. NRL teamed with university scientists to participate in the NLIWI to conduct internal wave studies using computer ocean models and observations.

Modeling Tools: We used a hydrostatic ocean model for the northern South China Sea and non-hydrostatic, process-oriented ocean models to study the large-amplitude internal waves. The hydrostatic model is the NRL Ocean Nowcast/Forecast System (ONFS).² The NRL ONFS was implemented using a nested grid system. The larger grid covers the East Asian Seas and provides boundary conditions for a higher-resolution grid that includes the Luzon Strait and northern South China Sea (Fig. 3). Tidal forcing is applied at the open boundary of the high-resolution grid. Temperature and salinity analyses generated from satellite altimeter and Multi-Channel Sea Surface Temperature (MCSST) data are assimilated into the model to produce a realistic stratification. Applying the NRL ONFS and non-hydrostatic models, numerical experiments were conducted and analyses were made to study the effects of bottom topography, tidal forcing, and stratification on the generation and propagation of the large-amplitude internal waves.

How Large-Amplitude Internal Waves are Generated: Figure 4 illustrates how the undersea ridges in

the Luzon Strait transform the ocean tide into large-amplitude internal waves. Large amounts of water rush through the Luzon Strait pushed by the tide. The ridges first convert the barotropic tides to internal tides. Propagating away from the ridges, the internal tidal wave steepens, and transforms the internal tide to an internal bore. The internal bore evolves into a large-amplitude, internal solitary wave as it propagates further away from the ridges. If the tide is strong, the solitary wave may develop into a packet of internal solitary waves.

Where is the Source? The east ridge in the middle reaches of the Luzon Strait is the major internal wave generation site where the internal tidal energy flux diverges (Fig. 4). There is a secondary generation site at the northern shallow reaches of the west ridge south of Taiwan. The internal tidal energy generated at these two locations propagates westward into the deep northern South China Sea and dissipates on the shallow shelf. The west ridge in the middle portion of the Luzon Strait blocks part of the incoming internal tidal energy from the east ridge.³

Which Tide Generates the Internal Waves? The barotropic tides are the major forcing that generates internal waves in the South China Sea. Without the tide, internal energy can be generated by the frontal instability of the Kuroshio current or by Kuroshio-topography interaction, but this energy is much weaker than the internal energy produced by the tides. The semidiurnal tide is more effective than the diurnal tide in generating the large-amplitude internal waves (Fig. 5). Although the strength of the semidiurnal and diurnal tides are about equal in the South China Sea, the internal tides generated by the semidiurnal tides have a shorter wave length and more easily evolve into large-amplitude internal waves. Concurrent satellite synthetic aperture radar (SAR) images and shipboard observations suggest that this is the case.

Can We Predict Large-Amplitude Internal Waves? The model predictability of the large-amplitude internal waves in the South China Sea was validated by field observations and satellite remote sensing data. NLIWI field observations taken during the 2005, 2006, and 2007 cruises and at three moorings during 2007 were used. The satellite SAR and Moderate Resolution Imaging Spectroradiometer (MODIS) images of 2005 were also used. The validation suggests that the timing and relative amplitude of the large-amplitude internal waves in the South China Sea can be predicted accurately (Fig. 5). The results of this study were presented to the Naval Oceanographic Office. NRL is now in the process of transitioning an internal wave prediction capability for operational application.

[Sponsored by ONR]

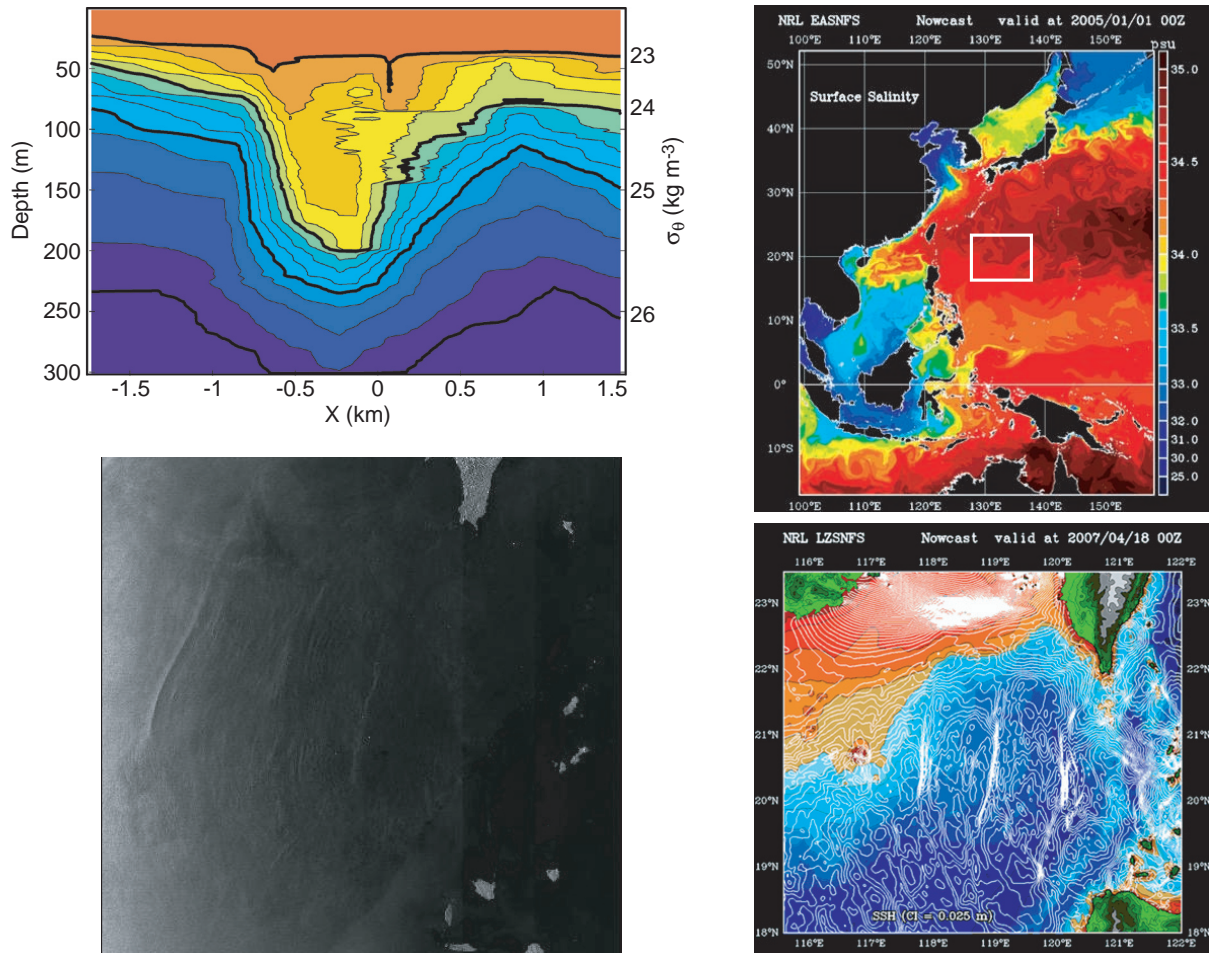
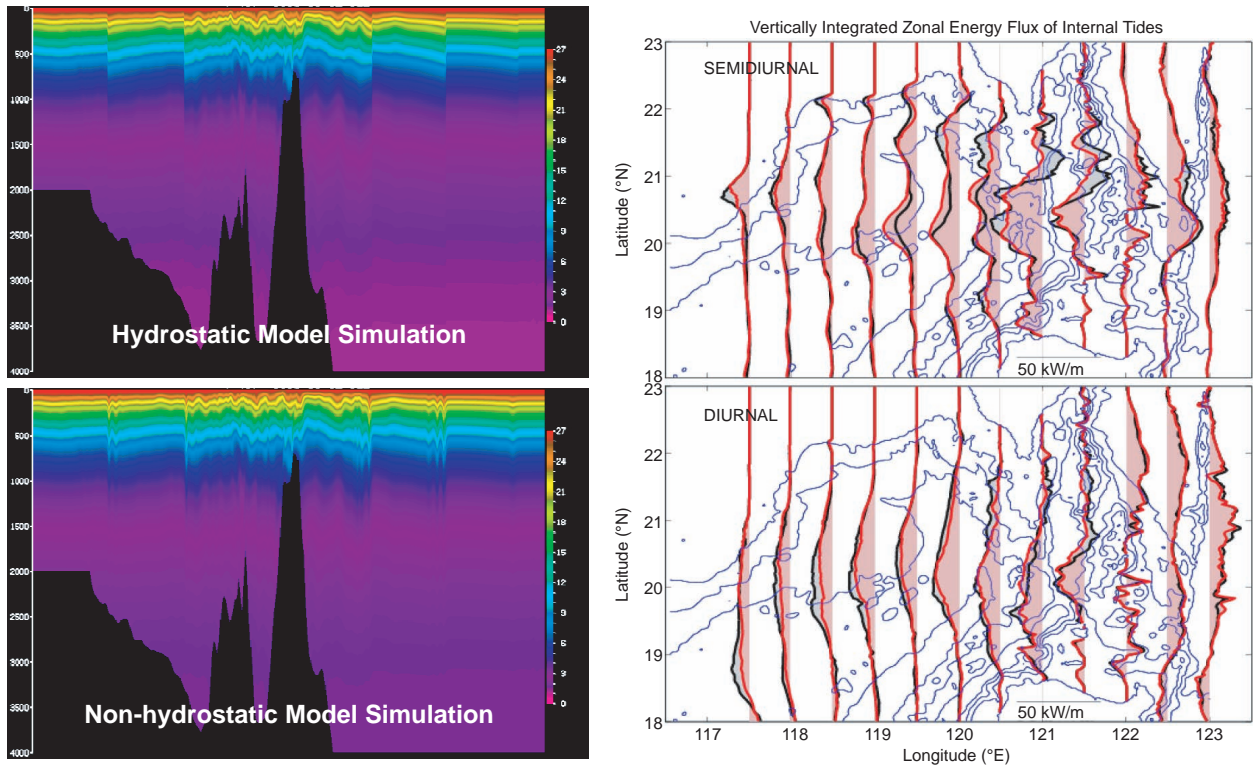
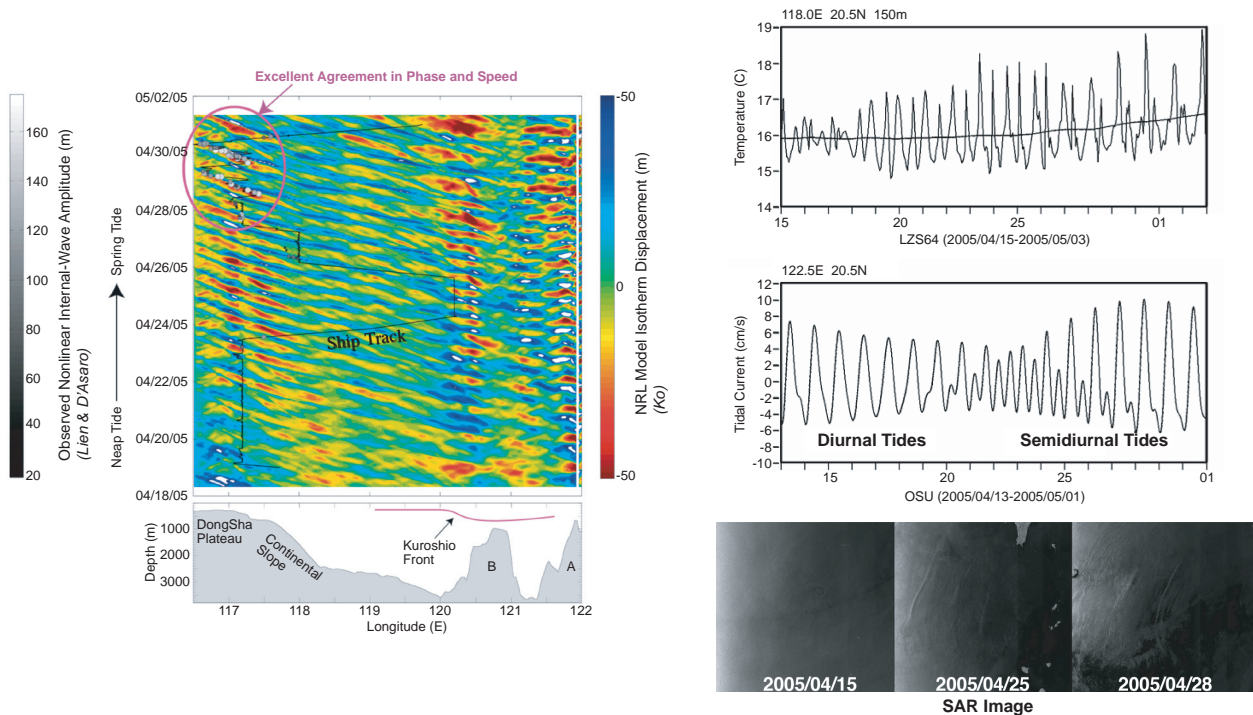


FIGURE 3 Internal waves in the South China Sea have amplitudes over 200 m (top left) and extend over 200 km (bottom left). A coupled NRL Ocean Nowcast/Forecast System with a nested grid (right) is used to study the internal waves.

**FIGURE 4**

Simulations of the internal-wave generation and propagation with hydrostatic and non-hydrostatic models (left). The energy flux of the internal tides (right); red and black correspond to results with and without west ridge blocking, respectively.

**FIGURE 5**

Comparison of predicted internal waves with shipboard observations (left). Comparison of model-predicted internal waves with corresponding tidal current and satellite synthetic aperture radar (SAR) images (right).

References

- ¹ J.F. Lynch, S.R. Ramp, C.-S. Chiu, T.Y. Tang, Y.J. Yang, and J.A. Simmen, "Research Highlights from the Asian Seas International Acoustics Experiment in the South China Sea," *IEEE J. Oceanic Eng.* **29**, 1067-1074 (2004).
- ² D.S. Ko, P.J. Martin, C.D. Rowley, and R.H. Preller, "A Real-Time Coastal Ocean Prediction Experiment for MREA04," *J. Marine Systems* **69**, 17-28 (2008). doi:10.1016/j.jmarsys.2007.02.022.
- ³ S.Y. Chao, D.S. Ko, R.C. Lien, and P.T. Shaw, "Assessing the West Ridge of Luzon Strait as an Internal Wave Mediator," in *J. Oceanogr.* **63**(6), 897-911 (2007). ★

Probabilistic Prediction for Improved Scientific Understanding and Improved Decision Making

J. Hansen, C. Bishop, J. Doyle, J.S. Goerss, T.R. Holt, J. McLay, and C. Reynolds
Marine Meteorology Division

Introduction: In recognition of the importance of quantifying uncertainty in atmosphere-ocean forecasting for the purpose of managing operational risk, NRL-Monterey (MRY) is involved in several related efforts in support of the design, utility, and evaluation of forecasts that utilize and quantify uncertainty. NRL-MRY recently stood up the Probabilistic Prediction Research Office (PRO) to help facilitate and coordinate these efforts. The PRO also reaches out to users, decision makers, and funding agencies to better understand the environment in which meteorology and oceanography (METOC)-related decisions are made and to identify situations in which probabilistic environmental information can be utilized.

NRL-MRY research efforts that attempt to exploit uncertainty information for improved understanding and decision making include the following: research on the design of the global atmospheric ensemble forecast system; research in the use of stochastic parameterizations to account for model uncertainty, which holds promise for improved ensemble forecasting of tropical cyclone track forecasts; the design of a new mesoscale atmospheric ensemble forecasting system, which accounts for model uncertainty through varying parameters in the physical parameterization schemes and perturbing sea surface and land surface forcing; use of ensemble-based covariances for data assimilation and adaptive observing applications; use of ensemble forecasts at the urban scale to quantify risk in the event of a toxic release; and the use of ensembles to learn about and improve model parameterizations. Some of these efforts are described below.

Global Modeling: Ensemble forecasting attempts to quantify forecast uncertainty by running many realizations of a numerical weather prediction (NWP) model, each from a different initial condition and/or

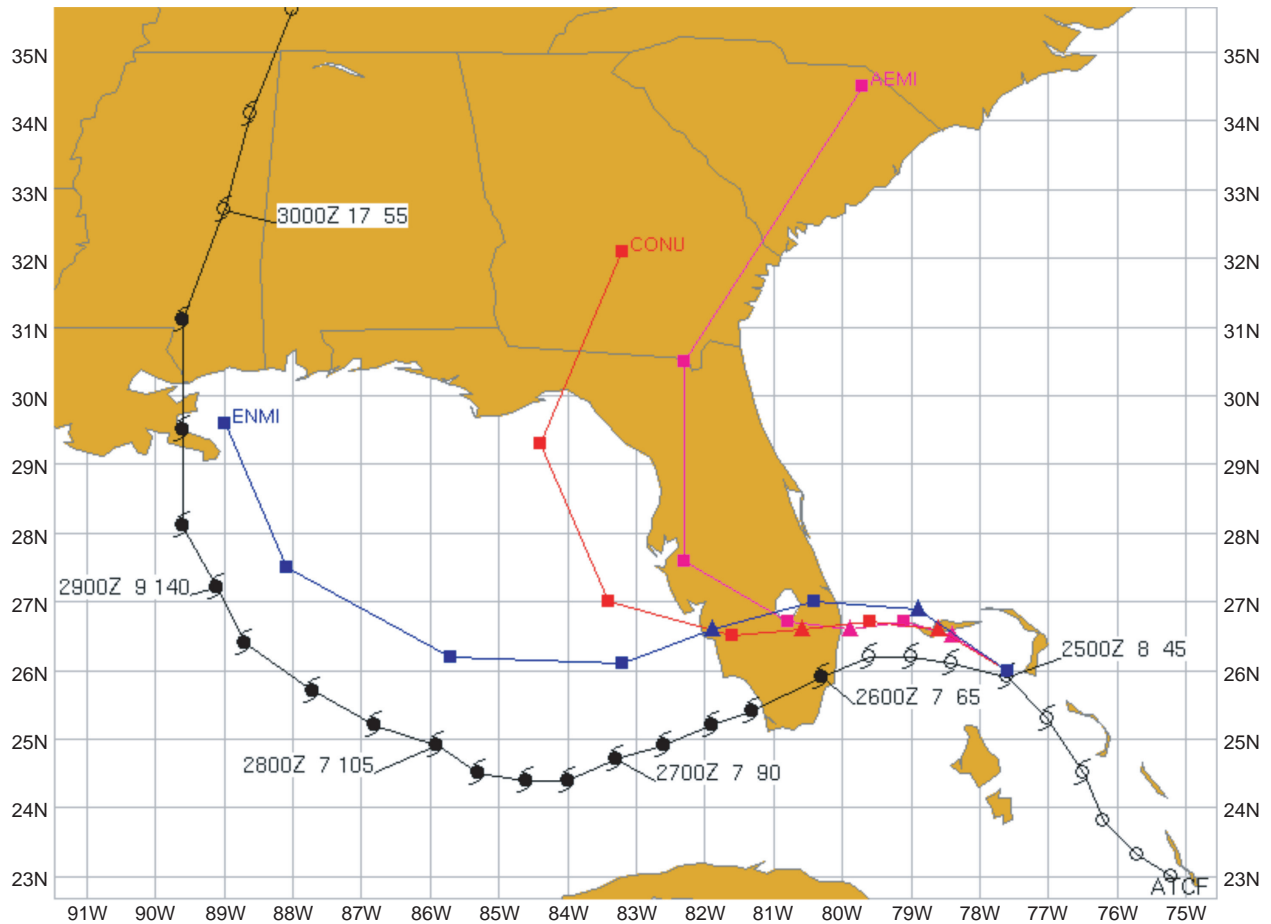
each being a different version of the forecast model. The research efforts on global atmospheric weather forecast model ensemble design have focused on both the initial uncertainty problem and the model uncertainty problem. The ensemble transform (ET) method combines flow-dependent information from short-term forecasts with error statistics from the data assimilation system to produce initial perturbations that are balanced and conditioned for growth. The ET scheme has been found superior to the current operational scheme under a variety of metrics, including lower ensemble mean rms errors and a stronger relationship between ensemble variance and forecast error variance.

In addition, a stochastic scheme has been developed to account for uncertainty in the physical parameterization of moist convection. Implementation of this scheme has led to improved ensemble performance in the tropics under a variety of measures. The stochastic convection ensemble also appears to provide useful information for 4- to 5-day tropical cyclone track forecasts, providing ensemble mean forecasts of comparable skill to the multi-model consensus forecast, averaged over the 2005 season (Fig. 6 shows one case).

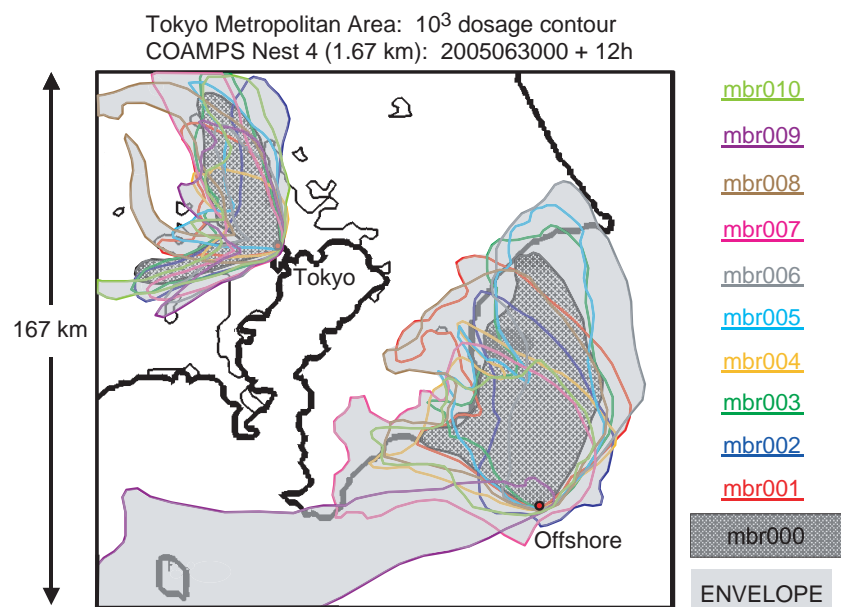
High-Resolution Regional Modeling: One of the attractive features of the ET ensemble generation technique is that it enables uncertainty information to be sampled at the scale of the simulation model. This is critically important for applications such as characterizing the uncertainty in forecasts of toxic plume dispersion in urban areas. Figure 7 depicts an ensemble of plume forecasts from two distinct release sites near Tokyo, Japan. If civil protection agencies had access to only a single forecast (mbr000), there would be a danger that they would not be cognizant of the many other areas that might be affected (indicated by the plumes mbr001 through mbr010). Apart from accounting for uncertainties in initial conditions, the ensemble simulations also accounted for uncertainties in the representations of urban and sea surface temperature effects on the plumes.

Physical parameterizations for processes such as surface heat and moisture exchange, boundary layer mixing, clouds, and precipitation also have inherent uncertainties in their formulations. For example, parameterization coefficients, which are often derived for a specific circumstance and then applied to all meteorological conditions, should be represented by a wider spectrum of values or, more accurately, by a probability density function if it is known. Preliminary research is under way to gain a better understanding of how to represent these uncertainties within the COAMPS®* suite of physical parameterizations appropriate for the mesoscale. Our current method involves

*COAMPS® is a registered trademark of the Naval Research Laboratory.

**FIGURE 6**

Tropical cyclone track forecasts for Hurricane Katrina, from 25 Aug. 2005, 00 UTC. The black track gives the observed storm track, the red track gives the multi-model consensus forecast, the pink track gives the NOAA Global Forecast System ensemble mean forecast, and the blue track gives the new ET-stochastic convection ensemble mean forecast.

**FIGURE 7**

An ensemble of plume forecasts from two distinct release sites near Tokyo, Japan. Different colors represent different ensemble members. The dark shaded plume, mbr000, is what would be available if only a deterministic forecast system were employed.

working with parameterization experts along with executing a series of model experiments to identify the most critical parameters and estimates of their uncertainties. A different parameter value is then chosen for each ensemble member. Ensemble verification statistics are used to diagnose which parameters are most sensitive. In the example shown in Fig. 8, model-predicted

clouds are shown to be sensitive to various parameters in boundary layer representation. None of the four boundary layer representations agree particularly well with the satellite image; however, the clouds derived from the ensemble mean are in the best agreement with the observations.

[Sponsored by NRL, ONR, and SPAWAR]

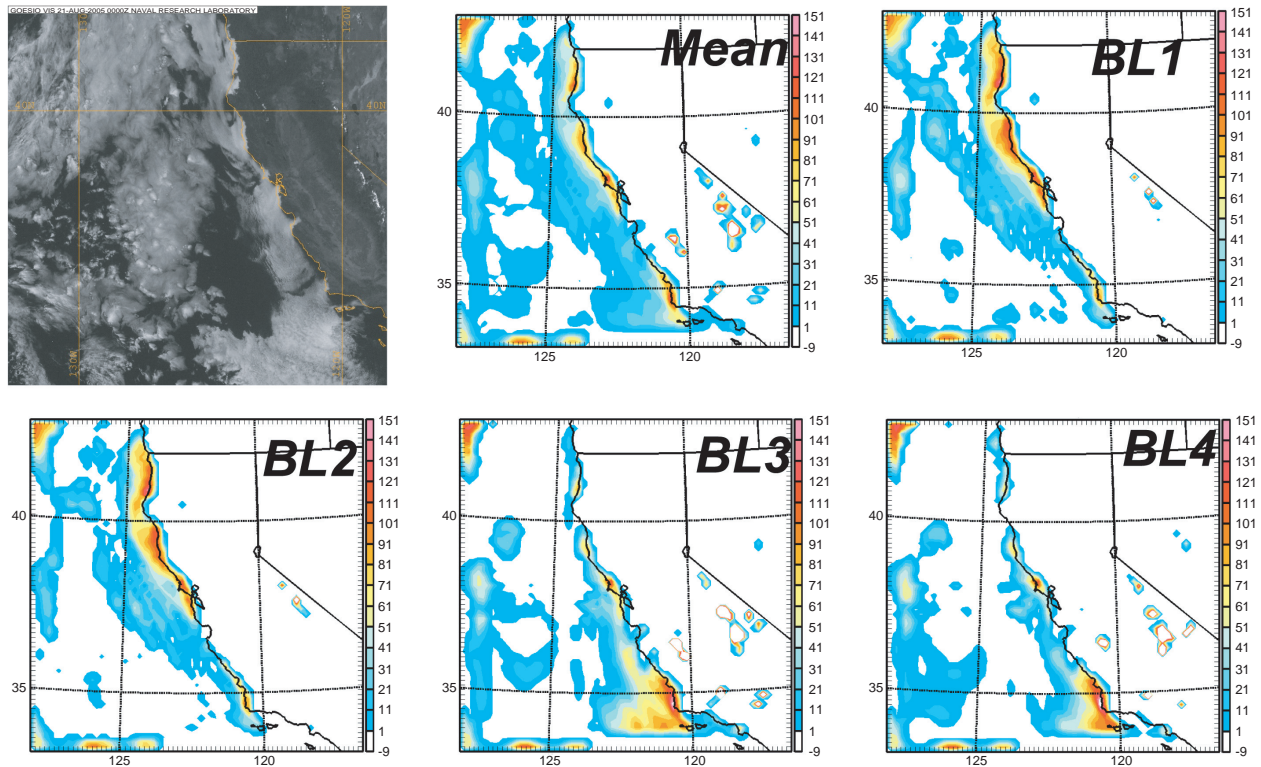


FIGURE 8
Example of the sensitivity of model-predicted clouds (vertically integrated clouds shown in color) to various formulations of the boundary layer parameterization (BL1 through BL4). Mean = ensemble mean.



N.C. Koon

Permanent Magnet Materials (1980-1985)

In 1980, NRL's N.C. Koon was the first scientist to examine the magnetic properties of the rare earth-iron-boron ($R_2-Fe_{14}B$) alloys, which showed promise for permanent magnet use. NRL scientists did the first work on these materials and hold the fundamental U.S. patents. The work was transferred to industry for development, and in the 25 years since first commercial production, permanent magnetic materials, especially neodymium-iron-boron, have been applied to a variety of products. They provide almost twice the magnetic energy density of the best materials previously available. Their higher power, cheaper cost, ability to operate at higher temperatures, better corrosion resistance, and ability to be easily formed into complex shapes have made them ubiquitous in both the military and commercial sectors. They are found in improved microwave tubes, sensors, powerful lightweight electric motors and generators, computer peripherals, and faster, more compact actuators. They also constitute important components of consumer products, from electronic devices to toys.

205

High-Fidelity Analog Fiber Optics and Photonics for Military Applications

V.J. Urick, P.S. Devgan, J.D. McKinney, F. Bucholtz, M.E. Godinez, A.S. Hastings, J.F. Diehl, C. Sunderman, K. Colladay, J.L. Dexter, and K.J. Williams

207

Tactical DIRCM Jamming Pod — Early Operational Assessment

K. Sarkady, H. Romero, G. Lynn, R. Mabe, R. Moore, V. Cassella, F. Barone, R. Cellucci, J.A. Schlupf, K. Strothers, K. Pick, B. Nichols, and D. Thonburg

210

Fiber-Optic Strain Monitoring on a Navy Cruiser

J.M. Nichols, M. Seaver, S.T. Trickey, K. Scandell, and L.W. Salvino

213

Infrared Ship Signature Model Validation from Measurements at Chesapeake Bay Detachment

R. Gignilliat and C. Miller

High-Fidelity Analog Fiber Optics and Photonics for Military Applications

V.J. Urick,¹ P.S. Devgan,¹ J.D. McKinney,¹
F. Bucholtz,¹ M.E. Godinez,² A.S. Hastings,¹
J.F. Diehl,² C. Sunderman,² K. Colladay,² J.L. Dexter,¹
and K.J. Williams¹

¹Optical Sciences Division

²SFA, Inc.

Introduction: Radio-frequency (RF) photonics provides increased or previously unavailable capabilities for many military platforms and applications. As compared to electronic approaches, photonics offers increased transmission distances in antenna-remoting applications, unrivaled bandwidth in signal-processing and other electromagnetic-warfare applications, and decreased size and weight in numerous military platforms. In addition, fiber optics as a transmission medium offers invulnerability to electromagnetic interference and near-complete electrical isolation.

We describe advances in the theoretical understanding of analog-photonic systems made at NRL in 2007, along with the accompanying record-setting performance demonstrated in our experiments. We have applied our expertise to the design and implementation of two state-of-the-art prototype systems for military antenna-remoting and electromagnetic-warfare applications. Each of these prototypes and their significance are described below.

Theoretical and Experimental Analysis: The three most important metrics for an analog-photonic system are RF gain, RF noise figure, and spurious-free dynamic range (SFDR). Understanding the relationship between these traditionally employed electronic metrics and the underlying optics in a RF photonic system is crucial to maximizing performance. We have

significantly advanced the understanding of these relationships using the two new concepts of generalized relative intensity noise and the optical amplifier noise penalty.^{1,2} The generalized relative intensity noise formalism allows for a convenient analytical description of RF photonic systems in terms of the experimentally determined parameters.¹ We have formulated all of the RF performance metrics for optically intensity- and phase-modulated analog photonic links, demonstrating unique and previously unrealized advantages afforded by an optical phase modulation format.¹ We conceived and employ the noise penalty metric to describe the effect that optical amplification has on the RF performance of a fiber-optic system.² Prior to the advent of the noise penalty metric, this relationship was not clearly understood by the community as a whole. We have also presented a novel graphical approach used to describe the design tradeoffs that exist between the RF performance metrics in an intensity-modulated analog-photonic link.³

We have applied our theories to demonstrate two record-setting experiments at NRL, the measured results of which are shown in Fig. 1. We have achieved the largest signal gain demonstrated to date in an analog-photonic link at any frequency and have recorded 44 dB of signal gain above 1 GHz. For the record-setting gain experiment, we used a suppressed-carrier modulation format with strong optical amplification. We have also demonstrated the first noise figure below 10 dB in the 1 to 10 GHz range using a balanced intensity-modulated link.⁴ Both of these experiments served to broaden the scope of RF photonic applications.

High Dynamic-Range Optical Links for Antenna Remoting: We have designed and demonstrated a novel fiber-optic link for high-frequency (HF, 2 to 30 MHz) antenna remoting with a SFDR = 117 dB·Hz^{2/3}

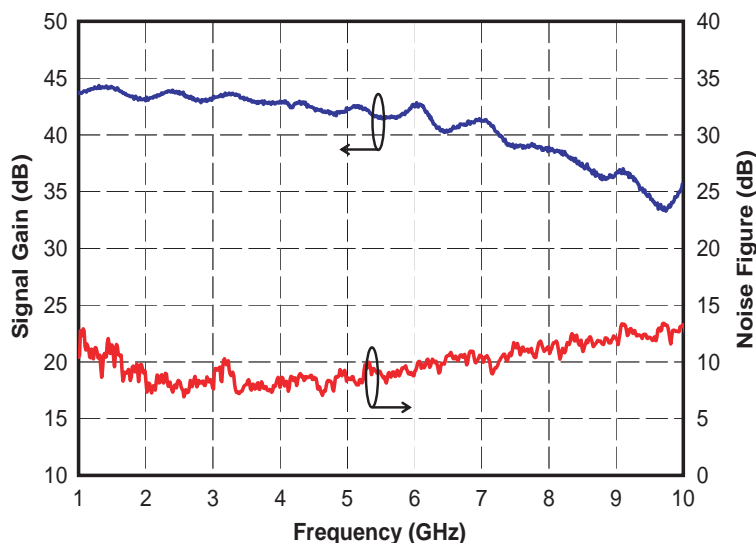


FIGURE 1

The measured results from two separate record-setting experiments. The highest signal gain for a photonic link reported to date is shown in blue and the first sub-10-dB noise figure in the 1 to 10 GHz range for a photonic link is shown in red.

at 30 MHz. Prior to our work this year, HF collection sites could be separated a maximum distance of 300 m from the signal-processing and storage facilities, limited by the loss in electronic cabling. This severely restricted placement of the collection sites because the signal-processing and storage facilities must be protected whereas the HF antenna themselves are relatively expendable. We have produced a prototype fiber-optic link for HF antenna remoting that maintains system performance and is capable of a 7-km transmission distance, a 23-fold increase in capability (Fig. 2). A

complete system employing this design is scheduled for deployment in February 2008 and will feed actionable intelligence directly to the U.S. Southern Combatant Command. This specific intelligence would not be available without the novel fiber-optic link, and no other fiber-optic link provides this capability.

Analog Optical Delay Lines for Electromagnetic Warfare: An analog optical delay line is employed to store an RF spectrum in the fiber itself for a time defined by the fiber length and speed of light in fiber.

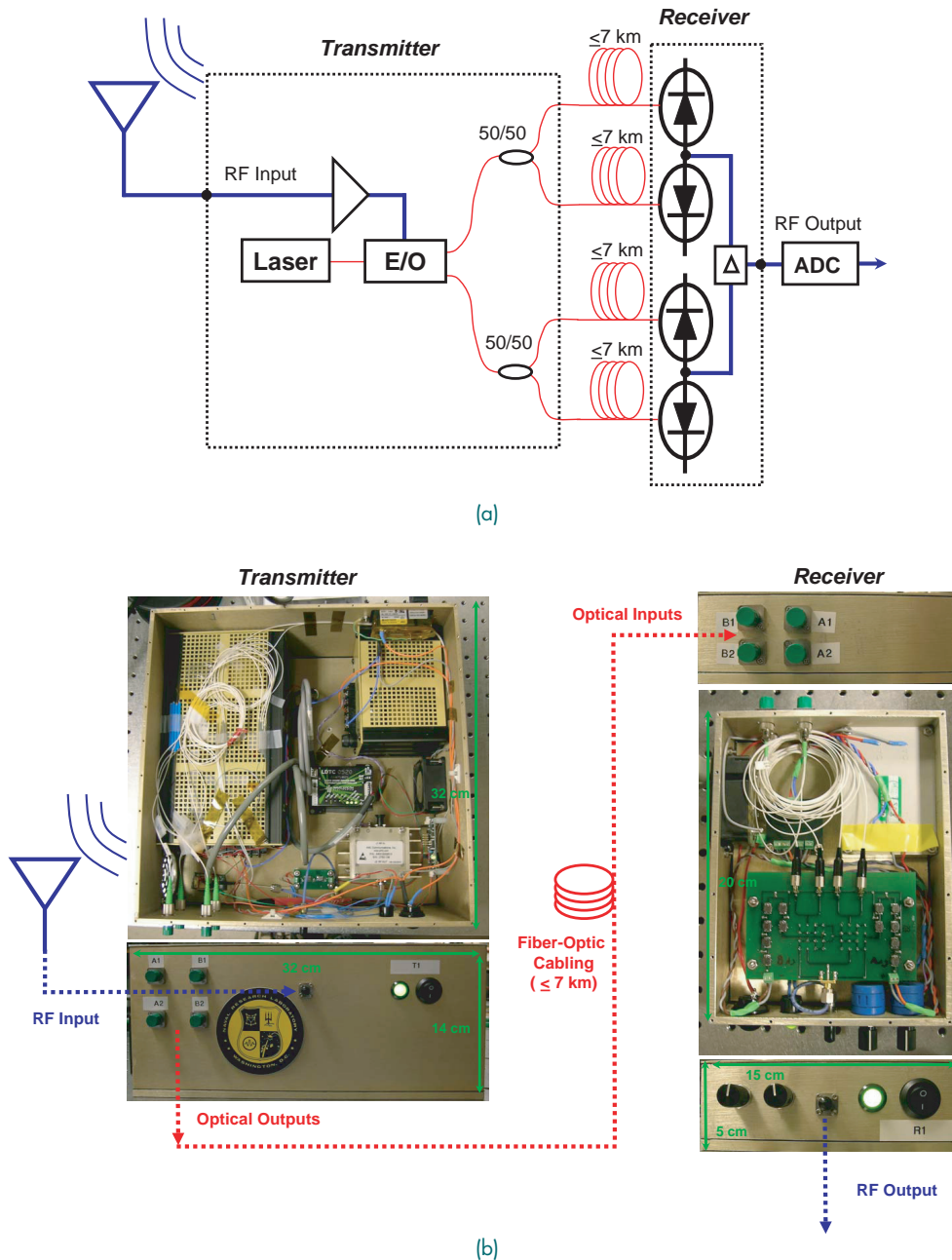


FIGURE 2

The (a) schematic and (b) photograph of a custom fiber-optic link for antenna-remoting applications. The electrical paths are shown in blue and the optical paths are shown in red. (E/O is electrical-to-optical conversion; ADC is analog-to-digital converter.)

We have demonstrated a state-of-the-art 60-km (300- μ s) optical delay line with a SFDR = 108 dB-Hz^{2/3} at 1 GHz. We have demonstrated and delivered hardware prototypes based on these optical delay lines in 2007 (Fig. 3). Electromagnetic-warfare systems that rely on these technologies are scheduled to be mass produced and deployed. These systems significantly enhance the signal-processing capabilities of the U.S. military, leveraging the bandwidth advantages of fiber optics over analog-to-digital converter technology.

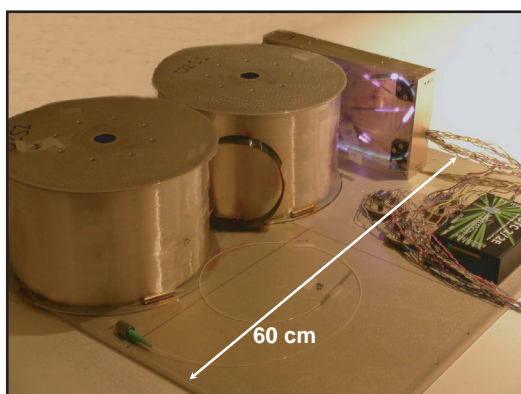


FIGURE 3

Photograph of a 60-km analog optical delay line with a custom optical amplifier for electromagnetic-warfare applications. Each spool contains 30-km (~19 miles) of optical fiber. The green emission shown in the optical amplifier box is due to an optical transition in the gain medium (the optical signal wavelength is 1550 nm). The purple is not visible to the naked eye and attributed to the camera's response to pump light at 980 nm.

Summary: We have demonstrated significant advancements in the theoretical understanding of RF photonic and fiber-optic systems, including the generalized relative intensity noise formalism, the noise penalty metric, the analytical analysis of phase-modulated and suppressed-carrier modulation formats, and a novel graphical description of performance tradeoffs. Our expertise has allowed for the experimental demonstrations of the highest signal gain reported to date and the first noise figure below 10 dB in the 1 to 10 GHz range. In addition, we have designed and implemented two RF photonic prototype systems for antenna-remoting and electromagnetic-warfare applications. Both of these systems provide new solutions to important military problems and ultimately increase the technological advantage of the U.S. military.

[Sponsored by ONR]

References

¹V.J. Urick, F. Bucholtz, P.S. Devgan, J.D. McKinney, and K.J. Williams, "Phase Modulation with Interferometric Detection as an Alternative to Intensity Modulation with Direct Detection for Analog-photonic Links," *IEEE Trans. Microwave Theory Tech.* 55(9), 1978-1985 (2007).

²P.S. Devgan, V.J. Urick, J.D. McKinney, and K.J. Williams, "Cascaded Noise Penalty for Amplified Long-haul Analog Fiber-optic Links," *IEEE Trans. Microwave Theory Tech.* 55(9), 1973-1977 (2007).

³F. Bucholtz, V.J. Urick, M. Godinez, and K.J. Williams, "Graphical Approach for Evaluating Performance Limitations in Externally-modulated Analog Photonic Links," *IEEE Trans. Microwave Theory Tech.* 56(1) 242-247 (2008).

⁴J.D. McKinney, M. Godinez, V.J. Urick, S. Thaniyavarn, W. Charczenko, and K.J. Williams, "Sub-10-dB Noise Figure in a Multiple-GHz Analog Optical Link," *IEEE Photon. Technol. Lett.* 19(7) 465-467 (2007). ★

Tactical DIRCM Jamming Pod — Early Operational Assessment

K. Sarkady,¹ H. Romero,¹ G. Lynn,¹ R. Mabe,¹ R. Moore,¹ V. Cassella,¹ F. Barone,¹ R. Cellucci,² J. A. Schlupf,² K. Strothers,² K. Pick,² B. Nichols,² and D. Thonburg³

¹Optical Sciences Division

²Orion, Inc.

³DCS, Inc.

Introduction: Infrared-guided surface-to-air missiles (SAM) and air-to-air missiles (AAM) continue to pose grave danger to U.S. Navy and Marine Corps aircraft. Current tactics against these threats include the execution of evasive maneuvers and the dispensing of flare countermeasures. Improved self-protection capabilities that are essential to enhance aircraft survivability include: 1) the deployment of passive missile warning technologies capable of providing the earliest detection of the threat missile plume ignition and 2) the development of more effective covert laser-based countermeasure techniques. We describe here the development, fabrication, and testing of an operational prototype pod designed to protect U.S. Navy tactical aircraft against the most advanced infrared (IR) guided missile threats.

The TADIRCM EOA Pod: NRL's Tactical Aircraft Directed Infrared Countermeasures (TADIRCM) system is comprised of a suite of wide field-of-view (FOV), passive, two-color, IR missile warning sensors, a computer processor (CP), and an active, all-band, IR jammer. As part of an Early Operational Assessment (EOA) program, these subsystems have been assembled into an autonomous pod to be used for determining the suitability of NRL's technologies for deployment in a tactical airborne environment. The TADIRCM EOA pod is populated with six sensors, built by DRS Infrared Technologies, which provide full spherical coverage except for the limited area blocked by the aircraft. The sensors are based on a 256 × 256 pixel mercury cadmium telluride focal plane array (FPA)

that is configured as a stacked detector to provide simultaneous and co-located two-color operation. The two-color IR imagery is transmitted to an NRL-built missile warning processor for autonomous detection of threat missile plume signatures. Following rapid declaration, the threat location is conveyed to the laser-based IR jammer (Agile Eye-II), built by BAE Systems. Agile Eye-II is a fast-steering gimbal capable of directing a beam of modulated infrared radiation toward the approaching missile. The infrared radiation, generated by the Tactical Multiband Infrared Laser, is modulated in a manner to create a series of one or more virtual targets within the missile seeker's FOV. These jamming codes force the missile seeker to track false targets and steer its tracking mirror away from the targeted platform. Optical break-lock (OBL) is achieved when the missile seeker's tracking mirror has been steered to a point where the targeted platform is no longer within the seeker FOV. During TADIRCM EOA testing, NRL-based jamming codes were used with great effectiveness. Figure 4 shows the hardware comprising the TADIRCM EOA pod and the pod on board station 2 of the test FA-18 aircraft.

EOA Tests: TADIRCM EOA tests were carried out both at the Atlantic Test Range (ATR), Naval Air Station, Patuxent River, MD, and at the China Lake Naval Air Station, China Lake, CA. The ATR tests established the airworthiness of the EOA pod during a captive carriage flight. Three additional flights were performed to obtain functional operational integration data for NRL's Missile Warning Set (MWS) and BAE's Agile Eye-II jammer subsystems.

EOA China Lake Flights: China Lake testing of the TADIRCM EOA pod was carried out in four flights. In the first three flights, the various timelines of the integrated system were established. To do this, the setup illustrated in Fig. 5 was adopted with five missile-launch stimulator sources. Repeated passes of the FA-18 aircraft over the China Lake airfield provide performance data of various scenarios likely to be encountered in close air support missions of this aircraft. Each of the sources in Fig. 5 is comprised of a set of propane burners designed to generate infrared signatures with spectral characteristics similar to those of a threat missile. The TADIRCM MWS algorithms track spectral and temporal features to discriminate fast ignition-like events from potential false alarm events. During China Lake tests, the ignition sequence of the threat simulators exhibited sporadic dropouts. In these instances, the simulated events were not declared by the MWS as valid threats and were not included in the determination of system performance metrics as they do not properly represent an attacking missile.

The five stimulator sources used in EOA tests were: 1) the OBE/WAAN instrument, which is capable of determining the centroid and spatial extent of the Agile Eye-II laser beam; 2) a set of burners at the NRL surrogate location, so designated because of the presence of a surrogate imaging threat seeker; 3) the Center for Counter Measures (CCM) seeker van, which included a number of foreign and domestic threat seekers used to evaluate the effectiveness of NRL's jamming codes; and 4) two IR Stimulator/Target Array System (ISTAR) sources.

Sample TADIRCM EOA Performance: A typical flight over the China Lake airfield is illustrated by the results shown in Fig. 6, which portrays pass 12 on March 16, 2007. Five sources were used in this engagement. Two of the sources were deployed twice, resulting in a total of seven engagements. In Fig. 6, light blue indicates the time over which the burner is active, i.e., it denotes truth for the particular event. Below this sequence, the performance of the MWS is illustrated. Specifically, green denotes the start of a track, and red denotes the declaration of that track as a missile threat. The status of the jammer is presented in the third bar sequence in dark blue. Note that the MWS starts tracks without failure at the same time as the missile plume stimulator is engaged. Also, note that each of these tracks is declared a threat in each of the engagements shortly after track initiation. This pattern of events (track initiation followed by a rapid track threat declaration) was observed in 96% of all valid engagements during EOA testing.

During single threat events, the IR jammer is cued into action at the time the track is declared a valid threat. The time at which laser energy is delivered to the attacking threat is given by the solid blue bar in Fig. 6. Thus, the interval between the onset of threat declaration and the onset of laser on target represents the time it takes for the Agile Eye-II to slew to the threat location, acquire the target, and establish a stable track.

We note that many of the events in EOA testing were designed to simulate simultaneous threat engagement scenarios. In particular, the events in Fig. 6 labeled 168401 and 168444 are simultaneous threat engagement events. During all these events, the TADIRCM EOA pod correctly jammed the first such declared event and then proceeded to engage the subsequently declared threat. In some of the longer burning instances, we observed the system re-visit an already jammed threat once all other pending threats had been properly engaged.

TADIRCM EOA IR Jammer Performance: The CCM seeker van test facility was used to test four seekers. The seekers available for this test correspond

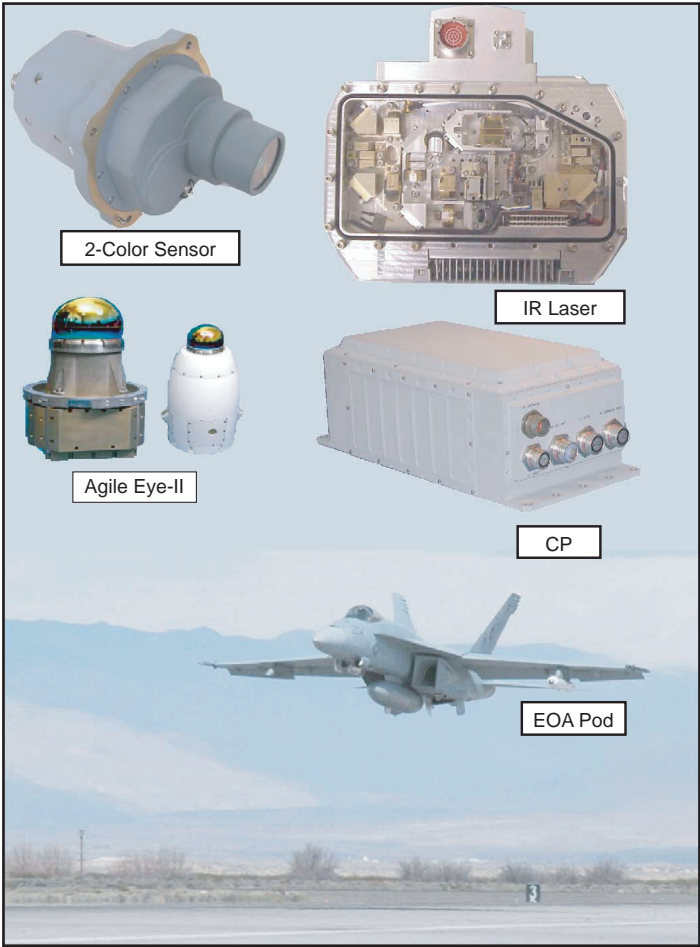


FIGURE 4
TADIRCM components and the EOA pod.

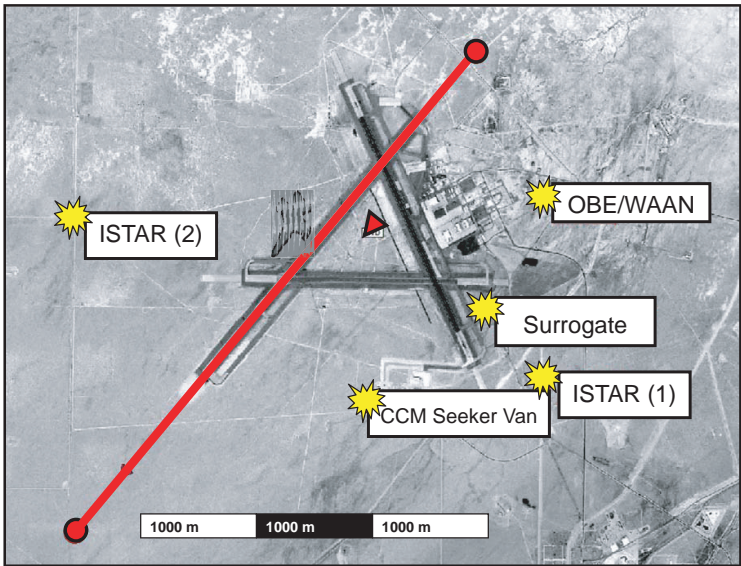


FIGURE 5
EOA testing configuration at the
China Lake Naval Air Station.

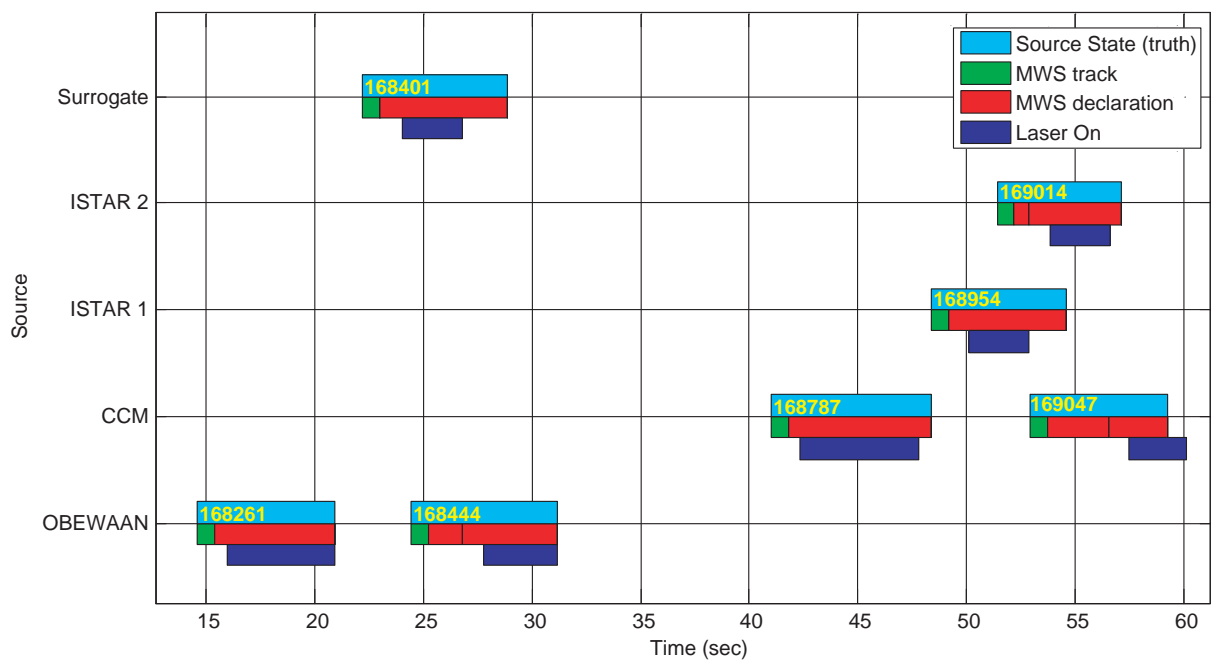


FIGURE 6
Sample TADIRCM performance timelines.

to a domestic threat, an air-to-air threat, and two commonly available SAM threats. Propane burners co-located with the CCM seeker van were used to stimulate the TADIRCM MWS. A variety of detectors at the CMM facility measured the time at which laser energy was delivered to the simulated threat as illustrated by the dark blue bars in Fig. 6. Of course, also measured was the time it took for a particular seeker to be defeated. This time depends on the order in which a given jamming code is delivered.

Summary TADIRCM EOA Performance: Table 1 provides the statistics for system performance. The MWS performance is expressed as the percent of valid threat events where the system rapidly declared the simulated threat event. The IR jammer performance is expressed as the percent of valid MWS declarations where all tested seekers were successfully defeated by the NRL jamming codes.

TABLE 1 — Summary TADIRCM EOA Performance Metrics.

MWS	96%
IR Jammer	99%

The performance of NRL’s TADIRCM system during EOA tests, as summarized by Table 1 above, is excellent. Based on these results, the Navy’s Operational Test and Evaluation Force is recommending the TADIRCM EOA pod for deployment in tactical platforms. In addition, the Naval Air Systems Command is

beginning an acquisition program for the deployment of NRL’s MWS technologies for the protection of Navy and Marine Corps rotary wing platforms. Continued work remains in this NRL project to provide indication of the presence of ballistic weapons and navigational visual aid to the pilots.

[Sponsored by the Naval Air Systems Command and ONR]



Fiber-Optic Strain Monitoring on a Navy Cruiser

J.M. Nichols,¹ M. Seaver,¹ S.T. Trickey,¹ K. Scandell,² and L.W. Salvino³

¹Optical Sciences Division

²NSWC Norfolk

³NSWC Carderock

Introduction: A number of CG class vessels in the U.S. Navy are experiencing cracking at various locations on the aluminum superstructure. The cracking has been observed on the 04 level deckplate, the overhead of one of the AN/SPG-62 Illuminator (radar) rooms, the intake bulkhead, and several other locations on one particular class of vessel.^{1,2} The cracking is, in many cases, persistent, recurrent (even after repairs), and has the potential to influence mission critical operations aboard ships.

Currently, the cause of this cracking has been investigated and is believed to be stress corrosion caused by sensitization of the aluminum alloy used in construc-

tion (5456 material). However, in order for this type of cracking to initiate and persist, the material must be sustaining large stresses. The origin of these stresses is still in question. The goal of this work was to instrument one of the affected areas, monitor the stresses over a 36-hour period during transit, and try to discern the types of ship maneuvers or ambient conditions that are leading to stress concentrations. The specific area under observation was the deckplate (overhead) of the #4 Radar room (05-316-0-C) onboard a ship from the affected class. This location was chosen because there has been repeated cracking of this deckplate and because this room provided the most convenient, unobstructed location for installation.

Sensing System and Installation: The sensing system used for this application was a fiber-optic strain-sensing system developed at the Naval Research Laboratory. This system is ideal for use in monitoring stresses in corrosive environments (in this case, a marine environment), is lightweight and unintrusive, and is capable of measuring slowly varying stresses (down to DC) with high accuracy.

The sensing system was installed during a single day on May 15, 2007. Four fiber Bragg grating (FBG) rosettes (referred to as A, B, C, and D in this article) were installed in the overhead of #4 Radar (05-316-0-C) where the ship had previously experienced cracking. This space houses mission-critical equipment (both communications and weapons) and was therefore deemed an ideal candidate for monitoring. Additionally, this particular location allowed for the simplest, most unintrusive installation of all potential areas surveyed. The FBG strain rosettes, each consisting of three FBG sensors, were used to monitor the principal strains experienced by the deck plate. Figure (7(a)) shows the inside of the radar room and the sensing equipment

used to record the strain data while Fig. (7(b)) shows the locations of the strain rosettes.

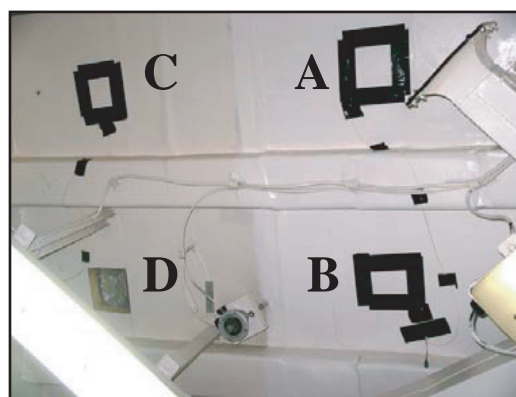
Strains on this deckplate were monitored over a two-day period during a variety of maneuvers at a sampling rate of 360 Hz. First, a series of tests was coordinated with the ship's Captain whereby the ship performed "hard turns" at a variety of increasing speeds. The goal here was to discern the effects of inertial loading on the deckplate resulting from simulated combat maneuvers. Next, the AN/SPG-62 Illuminator was rotated to determine its influence on the deck strains. The maximum rotational speed this particular AN/SPG-62 Illuminator can achieve is roughly 1/6 Hz (thus the sampling rate is more than sufficient).

Deck Plate Response to Ship Maneuvers: Figure 8 shows plots of the principal stresses vs time for rosettes C and D (see again Fig. 7 for rosette placement). In this figure, note that the measured stresses are all compressive, with the largest magnitudes beginning about 2000 hours and ending near 0600 the next morning. Also plotted is a measure of engine load (shaft rpm \times pitch). The data shows a strong correlation between engine load and deckplate compressive stress. As the ship picks up speed, the stress observed in the deckplate tends to increase. This may be due to thermal loading from the engine transferring to and stabilizing in the ship structure or perhaps direct structural loading resulting from drag created by speed increases. Engine load appears to be one of the primary mechanisms causing excessive stress in the deckplate. Also plotted in Fig. 8 is the yield stress for the deckplate material, σ_{yield} . The observed strain variations are 50% yield of the base metal.

A series of turns was performed at varying speeds to determine the influence of ship maneuvers on the deck strains. Beginning at approximately 19:24, the ship's speed was reduced to 8 knots. The speed was



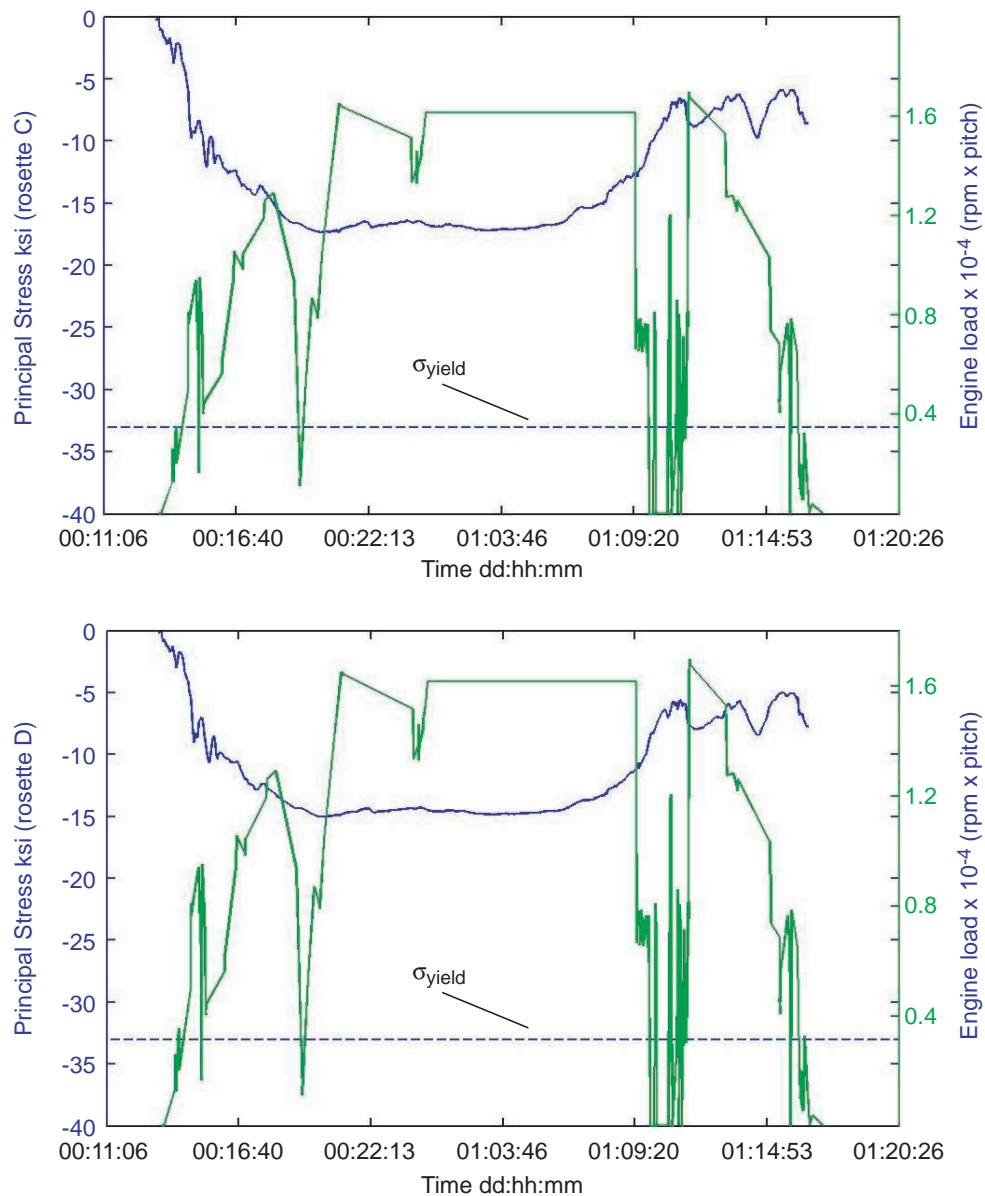
(a)



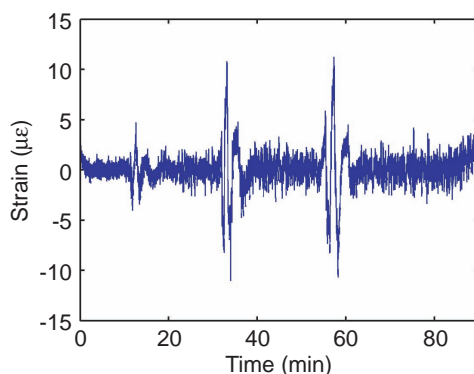
(b)

FIGURE 7

(a) The computer and demodulation hardware are located on the middle shelf in the back corner of the radar room. (b) The overhead directly above the shelves is where the gratings were located. The four FBG rosettes (A, B, C, and D) are shown with most of the insulation replaced.

**FIGURE 8**

Principal stresses recorded during the trip from rosettes C and D. Also shown is the yield stress for the deck material. Note that the largest stresses began near sunset on 6/7/07 and ended about sunrise on 6/8/07. Stress correlates well with engine load.

**FIGURE 9**

Sensor data recorded from sensor 3 of rosette C showing the strain values recorded during a series of hard turns at high speed.

then slowly increased to 20 knots over the course of the next 45 min. At 20:11, moving at 20 knots, the ship performed a sharp right turn (“hard rudder right”), followed by a hard left turn, followed by another hard right turn. The entire sequence lasted approximately 5 minutes. The ship’s speed was then increased to 27 knots and the same sequence of turns was conducted. Finally, the ship’s speed was set in excess of 27 knots and the sequence repeated once more. This final set of turns was completed at 21:00. Figure 9 displays the sequence of data recorded during maneuvers. The time axis shown in Fig. 9 is shown relative to the beginning of the maneuvers. Several observations can be made regarding the deckplate response to high speed turns. First and foremost, the maximum strains observed due to the ship maneuvers were roughly $\pm 10 \mu\epsilon$. These values are extremely small and are not likely to be the cause of any significant structural damage. Although the magnitude of the strain values do increase with speed, the ship will not likely see maximum knots for prolonged periods, thus hard turns at speed are not an issue in deckplate cracking.

As was previously mentioned, testing was also performed to see whether or not slewing of the AN/SPG-62 Illuminator mounted to the surface of the deckplate caused excessive strain. No such strain was observed throughout these tests. We could discern no difference from the ship’s ambient vibrations and therefore conclude that AN/SPG-62 Illuminator motion is not an issue with regard to the deck cracking.

Conclusions and Recommendations: The data collection from this particular ship was largely successful and resulted in some preliminary results that are useful in understanding the cause of the recurring deck cracking. First of all, the primary source of strain on the deckplate cannot be attributed to ship maneuvers or slewing of the AN/SPG-62 Illuminator. Neither action resulted in more than $10 \mu\epsilon$ of load. Secondly, the primary strain does not appear to be the result of thermal affects. Rather there exists a large compressive load, correlated with engine speed, that forms in the deckplate as the ship gets underway.

Future Enabling Technology Vision: Integrating this technology, with proper engineering design, into hull forms at new construction and capturing real-time hull load data could significantly expand Fleet operator’s envelope for ship performance by reporting actual forces acting on the hull at any given point in time. This could enable ships to operate in higher sea state at higher speeds; enable submarines to dive deeper and faster; and enable Commanding Officer’s power of informed decision, each of which is not enabled based on ship operational parameters being limited by modeling and safety factor alone.

Acknowledgments: The participants of this report extend their gratitude to Dr. Perez et al. at ONR, the Staff at Commander, Naval Surface Force Atlantic (CNSF), and especially to the Command and crew of the ship for ardently supporting this project.

[Sponsored by ONR]

References

- 1 J.P. Soisson and E. Murcko, “Trip Report: Visit with USS *Vella Gulf* (CG 72) to Inspect and Discuss Cracked Superstructure Deckplate,” NAVSEA: Ser 61/06-489, Aug. 11, 2006.
- 2 J.P. Soisson and E. Murcko, “Trip Report: Metallurgical Evaluation of Cracked Intake Bulkhead from USS *Vicksburg* (CG 69) and Corrective Measures for 5xxx Series Aluminum Alloy Material,” NAVSEA: Ser 61/61-500, Aug. 25, 2006. ★

Infrared Ship Signature Model Validation from Measurements at CBD

R. Gignilliat and C. Miller
Tactical Electronic Warfare Division

Introduction: Increasingly, U.S. Navy ships are operating in the littorals where they may be exposed to many threat weapons and sensors. NRL uses infrared (IR) propagation and signature models to predict ship vulnerability and to evaluate the effectiveness of current and proposed self-defense systems against IR threats that are more prevalent in the littorals. Ship signature models are also being heavily used during

the design phase for many of the Navy's new ship programs, such as DDG-1000, CVN-21, and CG(X). Reliance on the predictions of the models requires a validation of the model accuracy. With well-instrumented measurements of physical phenomena, a confirmation of the model predictions can be achieved. For this purpose, NRL organized and participated in the NATO SAPPHIRE (Ship and Atmospheric Propagation **P**henomenon **I**nfraRed **E**xperiment) trial.

NATO SAPPHIRE Field Trial: The NATO SAPPHIRE trial was conducted at the NRL Chesapeake Bay Detachment (CBD)/Tilghman Island test site in June 2006. After considering many test sites worldwide, NRL's CBD facility was selected specifically for its warm water, littoral features, and environmental conditions likely to produce super-refractive propagation conditions. These unique features satisfied a wide set of conditions missing from previous IR model validation data sets. Additionally, this area of the Chesapeake Bay possesses many buoys and meteorological stations that provide crucial supplemental data.

The SAPPHIRE trial included the research teams of 10 NATO partner nations (United States, Canada, Denmark, France, Germany, Italy, Netherlands, Norway, Poland, and the United Kingdom). NRL was chosen to host and organize the trial due to NRL's expertise in this field. The trial was the product of 2 years of coordination by NRL along with organizations from the nine other NATO countries. Unlike many other trials, SAPPHIRE was designed from the onset for collecting data to support validation efforts of both ship/background signature prediction models and atmospheric scintillation/refraction models. The trial represents "state-of-the-art" techniques in experimental design and execution possible only through the experience and combined resources of the multinational participants.

During the trial, radiometric IR measurements were made on many types of targets: a 77-m research ship, small craft (such as a speed boat and a jet ski), IR ship decoys, and a small calibrated source that simulated the signature of an antiship cruise missile (ASCM). In addition to these "target" measurements, second-order propagation effects were characterized, such as scintillation and refraction. All of the participating countries combined their results into a comprehensive database, which is available to all NATO countries.

Validation of ShipIR for Littoral Environments:

The data captured at the SAPPHIRE trial are being used to validate and improve the signature model ShipIR. ShipIR is a physics-based model that has been adopted by both NATO and the U.S. Navy as a common tool for predicting the IR signature of Navy ships in a maritime background. The model simulates the

steady-state IR radiance of both the ship targets and the maritime background by employing several major submodels: sky radiance, sea radiance, ship surface temperature, ship surface emission/reflection, and plume radiance. Thorough validation of the model is performed by comparing measured data to predicted data for each submodel component. This approach is necessary because the output of one submodel is often the input of another submodel. Validating at the submodel level allows for the identification and prioritization of specific portions of the code that demonstrate need for improvement. Validating the model as a single system will not provide the data necessary to isolate the specific source of any errors. Since the original version of ShipIR was released in 1992, NRL has applied this submodel validation methodology to iteratively refine the code.

Using the data collected during the SAPPHIRE trial, NRL has continued to validate ShipIR to assess model accuracy and to further improve the code. NRL began the validation in 2007 by analyzing the measured SAPPHIRE data to identify the runs suitable for model validation. This step ensures that the model receives reliable input data, mitigating one source of potential error between the IR ship signature measurements and the eventual ShipIR predictions. ShipIR models the IR environments for each of the selected SAPPHIRE runs based on inputs of geography, date, time, measured meteorological conditions, and aerosols. The prediction of solar irradiance and thermal contributions of the environment on the ship surfaces were verified to be accurate by comparing the data to values recorded by instruments designed to measure these types of physical phenomena. The accuracy of these solar and thermal irradiance predictions is critical to the ship surface temperature model accuracy. The 3D ship geometry was then processed within each environment and the ship surface temperatures were computed. The surface temperature predictions were also found to be sufficiently accurate by comparing ShipIR output to data measured from thermal measurement instruments, which were installed at several locations throughout the ship.

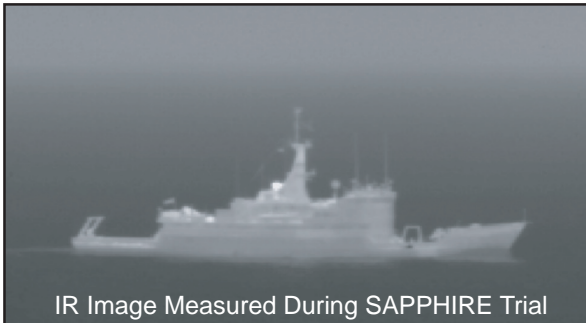
Ultimately, ShipIR produces a radiometric image of the ship within the environment for a defined IR spectral band and observer location. Figure 10 shows an example of corresponding measured and predicted IR images, along with a visual photograph of the test ship. Such predicted ShipIR images are frequently used to run other types of simulations, such as missile engagement scenarios and hit-point analyses.

Contribution to the New Capability for the Fleet:

The SAPPHIRE trial was a multinational IR phenomenology trial designed and executed with the sole purpose of capturing data to validate signature and propa-



Ship IR Predicted Image



IR Image Measured During SAPPHIRE Trial



Photo of Test Ship

FIGURE 10

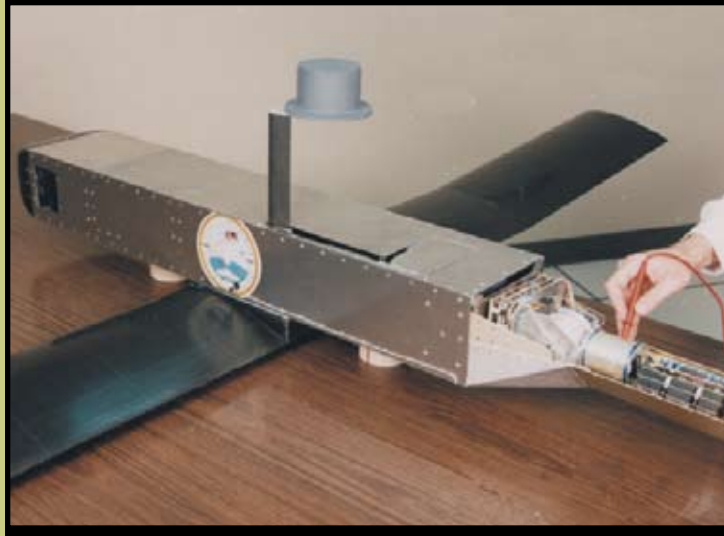
Images of the test ship used for validation.

gation models. High-fidelity data were collected to support a variety of Electronic Warfare (EW) programs, not just in the U.S. Navy but for our NATO partners as well. The data collected provided essential information that resulted in the enhanced credibility of the ShipIR

model. The 21st Century Navy now has the opportunity of applying very accurate IR models that can recreate many more “virtual field trials” over a wide range of environmental conditions in a cost-effective way.

[Sponsored by ONR]





Optical Fiber Gyroscope (1983-1986)

NRL's demonstration of long-term, inertial-quality performance in a fiber-optic gyroscope was a pivotal milestone in the device's development into a practical, precision navigation instrument. With a longer lifetime, higher reliability, and lower weight, size, and cost than spinning mass gyroscopes currently in use, the fiber-optic devices represented a revolution in rotation-sensing technology. These devices are impacting both military and commercial navigation and are being produced in the U.S., Europe, and Japan.

219

Vantage™ Unmanned Air Vehicle

J.R. Southwick

220

The Scintillation and Tomography Receiver in Space (CITRIS) Instrument for Ionospheric Research

P.A. Bernhardt, C.L. Sieftring, I.J. Galysh, and D.E. Koch

222

Carbon Fiber Reinforced Polymer (CFRP) Telescope Program at the Naval Research Laboratory

S.R. Restaino, J.R. Andrews, T. Martinez, C. Wilcox, F. Santiago, S.W. Teare, R.C. Romeo, and R.N. Martin

224

Monitoring Global Surface Soil Moisture with the WindSat Polarimetric Microwave Radiometer

L. Li and P. Gaiser

Vantage™ Unmanned Air Vehicle

J.R. Southwick

Tactical Electronic Warfare Division

Introduction: The Vehicle Research Section (VRS) at the Naval Research Laboratory (NRL) in Washington, DC, has been developing airborne unmanned air platforms to support electronic warfare (EW) and intelligence, surveillance, and reconnaissance (ISR) missions for over 30 years. The Vantage™ unmanned air vehicle (UAV) is one such platform. Here at NRL the goal is to push technology and develop concept vehicles that can be transitioned into industry to better meet the needs of the Armed Forces. NRL conceives and develops designs for the technologically advanced warfare needs of the future.

Vantage™ Evolution: The VRS often receives requests from a branch of the Armed Forces to develop vehicles with specific requirements to complete a specified mission. The Vantage™ vehicle (Fig. 1) evolved directly from the Dragon Warrior vehicle, originally developed at NRL for the Marine Corps Warfighting Laboratory (MCWL) specifically for reconnaissance and communications relay missions. During the Dragon Warrior program, the vehicle under development evolved into a three-bladed main rotor, ducted electric tail rotor helicopter vehicle with a Wankel rotary heavy-fuel engine. When the Dragon Warrior program ended, the vehicle continued development under the name of Vantage™.

The Dragon Warrior program had involved three research groups at NRL: the Vehicle Research Section, for the vehicle design and development; the Optical

Sciences Division, for development of the HMMWV (Humvee)-based Ground Control Station (GCS), along with the integration of the MCWL-selected electro-optic/infrared/laser range finding (EO/IR/LRF) camera gimbal, RF links, and all non-flight control system (FCS) avionics; and the Transmission Technology Branch, for integration of a communications relay as the secondary payload.

Vantage™ Vehicle Features: One of the key groundbreaking products developed during the Dragon Warrior program was a 44-hp heavy-fuel engine. No engine of this size was available before the development in this program. UEL Engines Ltd. from the UK modified their existing AR-801 water-cooled rotary engine to accept heavy fuel. In just under six months, UEL was able to deliver their heavy-fuel engine. NRL took on the task of further modifying the propulsion system and operation sequence to allow integration and use of the AR-801.

Another unique development was the ducted electronic tail rotor. An electric motor offers several advantages. First, it is an efficient and reliable system. It also allows for a much simpler transmission. The VRS estimates that use of the electronic tail rotor eliminated nearly 140 parts as compared to a standard tail rotor and linkage. There is also a weight savings in trading the complexity of a mechanically driven system with an electric motor. The directional stability is controlled by rpm, instead of a direct-drive pitch-controlled system.

The vehicle's three-bladed rigid main rotor is highly responsive. It would be impossible for a human to fly the vehicle without computer assistance, so even when the vehicle is under pilot control, it is augmented by a highly sophisticated control system. A linear



FIGURE 1
The Vantage™ vehicle in storage configuration.

Proportional Integral Derivative (PID) autopilot was developed for the Vantage™ by the VRS for slow-speed autonomous flight.

One of the original requirements of the Dragon Warrior program was that the entire system fit into the back of a HMMWV (Fig. 2). This was one of the reasons that the VRS decided to locate the payload bay in the nose of the UAV and to make the nose removable. This allows the payload to be changed with only four simple latches. It also shortened the body of the UAV to enable it to fit inside the HMMWV.

The Vantage™ program was considered complete on November 14, 2005, when an autonomous flight demonstration was performed for NRL's Commanding Officer, CAPT Daniel Gahagan, and Director of Research, Dr. John Montgomery (Fig. 3).



FIGURE 2

The original Dragon Warrior vehicle as it would be transported in a HMMWV along with the onboard Ground Control Station.



FIGURE 3

The Vantage™ vehicle during the November 14, 2005, flight demonstration.

Formation of the CRADA: The VRS participates in various shows every year to demonstrate its capabilities and to offer the technologies developed at the NRL to other entities. The Dragon Warrior/Vantage™ program has been exhibited at these various events since July 2002. At the Association for Unmanned Vehicle Systems International (AUVERSI) Symposium in August 2006, the president of CybAero LLC, Peter Muhlrud, stopped at the NRL display booth and pressed for more information on the Vantage™ vehicle. The vehicle and its capabilities nearly mirrored the capabilities that CybAero was seeking.

One month later, Mr. Muhlrud contacted the VRS and requested an on-site visit to discuss any developing opportunities with the Vantage™ vehicle. On November 14, 2006, the VRS hosted CybAero LLC, and a discussion of developing a Cooperative Research and Development Agreement (CRADA) commenced.

On July 12, 2007, a CRADA between NRL and CybAero LLC was fully executed. This CRADA is intended to demonstrate the overall design capabilities of the Vantage™ vehicle. CybAero LLC will fund NRL to perform modifications to the vehicle to allow for autonomous takeoff and landing and to perform high-speed flight tests of up to 100 knots. With guidance from the VRS, CybAero LLC will choose, or develop, an autopilot that will interface with the vehicle to perform fully autonomous high-speed flight.

If this research is successful, CybAero LLC intends to put this vehicle concept into production. Once in production, industry and the military can benefit from the use of this vehicle for activities such as pipeline monitoring, power line monitoring, border patrol, remote sensing, forest inspection, communication relay, reconnaissance, surveillance, and target acquisition.

This CRADA is one example of the capability of NRL to interface with industry to develop programs that take advantage of the Laboratory's multifaceted and multidisciplinary research.

[Sponsored by CybAero LLC]



The Scintillation and Tomography Receiver in Space (CITRIS) Instrument for Ionospheric Research

P.A. Bernhardt,¹ C.L. Siefring,¹ I.J. Galysh,² and D.E. Koch²

¹Plasma Physics Division

²Space Systems Development Department

Introduction: The ionosphere is a source of error and data loss for many communications, navigation, and radar systems. As satellite radio signals propagate from space through the ionosphere to the ground,

they can become distorted by a large number of effects including phase fluctuations, Faraday rotation, amplitude fluctuations, group delay, absorption, scattering, frequency shifts, and multipath. Ionospheric characterization is needed to identify these influences, to predict their occurrence, and if possible, to mitigate their effects.

Radio beacon measurements of ionospheric total electron content (TEC) can be used by data assimilation models to improve ionospheric density specifications. Current assimilation models have been developed to incorporate many sources of ionospheric data including ground GPS TEC, bottom-side ionospheric profiles from ionosondes, and TEC from low-Earth-orbit (LEO) beacon transmissions to ground receivers. Until now, there has not been any beacon receiver in low Earth orbit that can provide rapid TEC and radio scintillation measurements from ground beacons and from other beacons in LEO.

The CITRIS Instrument: A new beacon receiver system called the Scintillation and Tomography Receiver in Space (CITRIS) is currently in orbit sampling the ionosphere. CITRIS was developed at NRL to (a) permit ionospheric measurements over the ocean and other remote areas of the Earth and (b) use the unique geometry of LEO-to-LEO satellite paths to determine absolute TEC and locate ionospheric scintillation regions.¹ The CITRIS receiver uses the frequency dispersion of the ionospheric plasma to remove frequency-independent effects like beacon-to-receiver range and neutral refractive index fluctuations. The CITRIS receiver tracks the Doppler-shifted changes in the radio beacon transmissions. With the highest frequency reference, the relative changes at the lower frequencies are captured in the CITRIS data. The variations of amplitude and phase in this data are due only to the ionosphere.

Sample Results: The CITRIS operations are scheduled based on orbit predictions for both the CITRIS receiver and beacon satellites. The NRL Coherent Electromagnetic Radio Tomography (CERTO) beacons on the COSMIC satellites² operating at 150 and 400 MHz provided the radio wave source for this example. An orbit segment is illustrated in Fig. 4 for the CERTO beacon satellite and for the STPSAT1 satellite with the CITRIS receiver. On 19 May 2007, the CITRIS receiver picked up the CERTO beacon signal along a 5000 km horizontal path when the tangent point was 270 km above the Earth's surface. At closest approach, the radio measurement was along a nearly vertical path of 232 km between COSMIC FM5 at 767 km altitude and STPSAT1 at 560 km altitude. After this, the satellite orbits diverged until the path was tangent to the orbit of the lower altitude STPSAT1 satellite with the CITRIS receiver. Further separation of the orbits caused the tangent altitude to drop below the CITRIS altitude until the signal was lost when the path intersected the Earth. No measurements were made when the tangent altitude was below the Earth's surface.

The minimum total electron current along the straight line between the satellites is found where the satellites are closest together (Fig. 5). The asymmetry in the curve of TEC versus intra-satellite distance demonstrates that the ionosphere is denser to the west of the satellite orbit crossing point. Geometric analysis is needed to convert the relative TEC provided by CITRIS to absolute values. The plot in Fig. 5 of TEC versus intra-satellite distance shows a linear variation near the point of closest approach (PCA). Extrapolation with the TEC curve to zero satellite separation sets the zero calibration point for the TEC values of the whole curve. This procedure is critical to providing absolute ionospheric measurements with an accuracy of 0.01 to 0.1 TECU where one TECU = 10^{16} electrons per m^2 . This method of calibration is much better than other

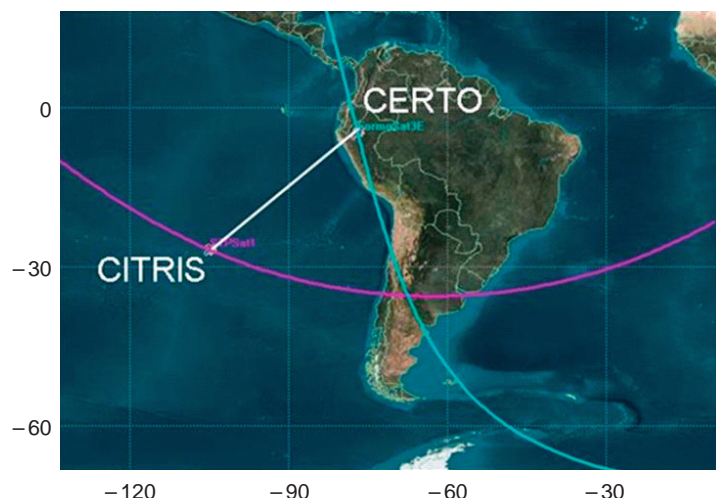
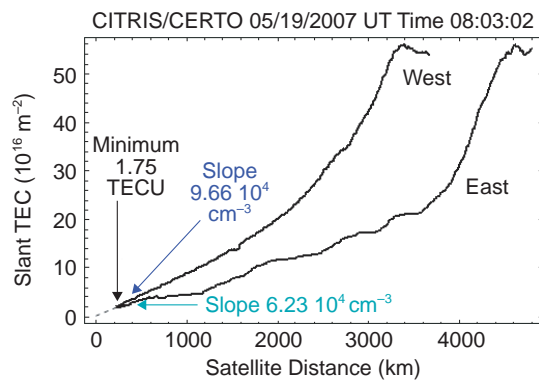


FIGURE 4

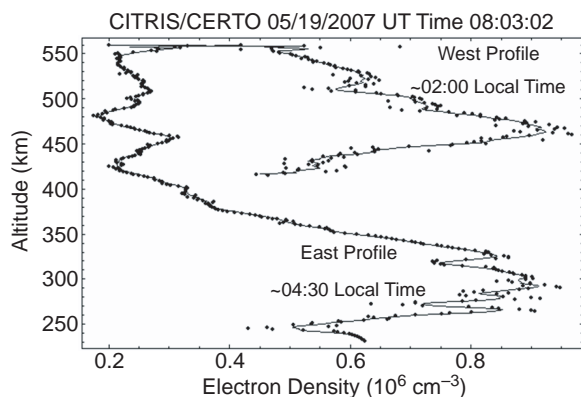
Orbit of CITRIS relative to the CERTO radio beacon transmitter on the COSMIC FM5 satellite. The orbits cross at a latitude of -35.5° N and a longitude of -68.0° E where the distance between the satellites is only 232 km.


FIGURE 5

Measurements of total electron content (TEC) on the west and east side of the point of closest approach. Determination of absolute TEC uses extrapolation to zero separation between beacon and receiver satellites. The electron density is estimated from the derivative of the TEC with intra-satellite distance.

measurements of TEC such as GPS that rely on system calibrations that can only provide TEC with an accuracy of 1 to 3 TECU. The slopes of the lines near the PCA give the average electron density on each side.

With the assumption that the ionosphere is spherically symmetric, the Abel inversion technique can be used to estimate layer profiles. The CITRIS-CERTO geometry provides two occultation opportunities with two LEO satellite orbits. The TEC profiles from the occultation portion of the CITRIS observations show that the layer on the west side of the PCA is higher in altitude than the layer on the east side. Applying the Abel inversion to the TEC profile data yields the electron density profiles (Fig. 6). The primary reason for the layer differences is the latitude of the layers. The east layer region is near the equator at -8° geomagnetic latitude where the layer tends to be higher than at mid-latitudes. The west layer is near a mid-latitude region at -35° geomagnetic latitude.


FIGURE 6

CERTO/CITRIS profiles of electron density. The dots are results of the Abel inversion with 1-km altitude separation in measured horizontal TEC. The solid line is the profile estimation using a 7-point running mean of the 1-km TEC samples.

Summary: The CITRIS receiver in low Earth orbit is acquiring high-accuracy TEC data to provide specifications of ionospheric TEC and derived electron density.

[Sponsored by ONR]

References

- ¹P.A. Bernhardt, C.L. Siefring, I.J. Galysh, T.F. Rodilosso, D.E. Koch, T.L. MacDonald, M.R. Wilkens, and G.P. Landis, "Ionospheric Applications of the Scintillation and Tomography Receiver in Space (CITRIS) Mission when used with the DORIS Radio Beacon Network," in *J. Geodesy* **80**, 473-485 (2006).
- ²P.A. Bernhardt, C.A. Selcher, S. Basu, G. Bust, and S.C. Reising, "Atmospheric Studies with the Tri-Band Beacon Instrument on the COSMIC Constellation," Ch. 10 in L.-C. Lee, R. Kursinski, and C. Rocken, eds., *Applications of Constellation Observing System for Meteorology, Ionosphere & Climate*, p. 291-312 (Springer, Hong Kong, 2001).



Carbon Fiber Reinforced Polymer (CFRP) Telescope Program at the Naval Research Laboratory

S.R. Restaino,¹ J.R. Andrews,¹ T. Martinez,¹ C. Wilcox,¹ F. Santiago,¹ S.W. Teare,² R.C. Romeo,³ and R.N. Martin³

¹Remote Sensing Division

²New Mexico Institute of Mining and Technology

³Composite Mirror Applications, Inc.

Introduction: The Navy Prototype Optical Interferometer (NPOI) is actively involved in a program to upgrade its collection apertures from a few tens of centimeters to 1.4 meters. This will dramatically increase its light collection capabilities and thus improve the sensitivity from 6th to nearly 12th magnitude, opening up a much larger selection of observable stars. This program leverages the use of lightweight carbon fiber reinforced polymer (CFRP) for telescope construction, allowing each telescope to be moved from one location to another, providing a reconfigurable array of telescopes¹ rather than a large number of fixed telescopes.

There are several advantages to using CFRP as the construction material for telescopes, including an order of magnitude decrease in weight, which supports easier transportation from station to station on the array. As all components of the telescope, including optics, are constructed from composite materials having a low coefficient of thermal expansion, dimensional changes due to temperature variations can be minimized. A major benefit to this approach, which requires multiple, identical optical components, is that they are made from a single, high-precision tool, allowing a much shorter production cycle than traditional steel and glass telescopes² and keeping all replicated components

identical and interchangeable. Composite materials provide a structurally stiff and very durable telescope that has superior performance to glass in harsh environments such as space.

Lightweight Telescope: Construction of optical quality surfaces from composite material required an iterative process to meet the near-diffraction-limited performance required in the design. The first step was to construct a prototype 0.4-meter telescope (Fig. 7). This provided a fully functional telescope available for testing and troubleshooting while the 1.4-meter telescope was under development.

The development of the 1.4-meter telescope will require adaptive optics (AO) to correct for the effects of the atmosphere in degrading the optical wavefront quality. Novel AO systems have been developed and tested that make use of technological advancements in computer controls and microelectromechanical systems (MEMS) hardware that have reduced the size and cost of an AO system.

Prototype 0.4-meter CFRP Telescope and Mount with Integrated AO: The prototype 0.4-meter CFRP telescope has been under development since 2004. The final weight of each component is given in Table 1. This system could be reconfigured with the electronics box setup in a fixed location to maintain lower weight of the optical telescope assembly (OTA), mount, drive motors, and AO. As a comparison, the 0.4-meter Meade telescope weighs 104 kg without an AO system, mount, or counterweights.

A direct drive system was chosen for maximum stiffness and pointing precision. This drive system is realized with ultrasonic piezoelectric motors driving a static ceramic ring. This unique drive configuration is possible because of the low mass (and low rotational

TABLE 1 — Mass of 0.4-meter Telescope Components

OTA with CFRP optics	10 kg
Mount, electronics box (no electronics)	80 kg
White AO box	16 kg
Breadboard	7 kg
AO optics	<10 kg
Counterweights	8–10 kg

inertia) of the system. This system has realized a maximum slew speed in excess of 15 deg/s with tracking speed exceeding 1 deg/sec. The encoders and feedback system have so far produced a pointing accuracy of 1.5 arcseconds, but ongoing work on mount characterization should realize a further reduction in error.

The 1.4-meter CFRP Telescope: The 1.4-meter telescope, currently under development at Composite Mirror Applications Inc., is anticipated to have a weight of 120 kg, including all optics (Fig. 8). A traditional steel and glass telescope of comparable size can easily weigh more than a ton. The current telescope design, when used to populate the NPOI array, will track at sidereal rate; however, the drive system is capable of dramatically exceeding sidereal rate.

A hexapod structure is used to adjust the secondary mirror for alignment with six degrees of freedom. In order to keep the weight near the center of gravity as much as possible, piezoelectric screw-drive motors were designed into the telescope base as shown in Fig. 9. Computer control will allow adjustment of the secondary mirror in x, y, and z translation, as well as tip, tilt, and piston. Additionally, temperature sensors and accelerometers will be fitted into the support structure of the 1.4-meter telescope. This will allow real-time measurement of critical performance parameters.

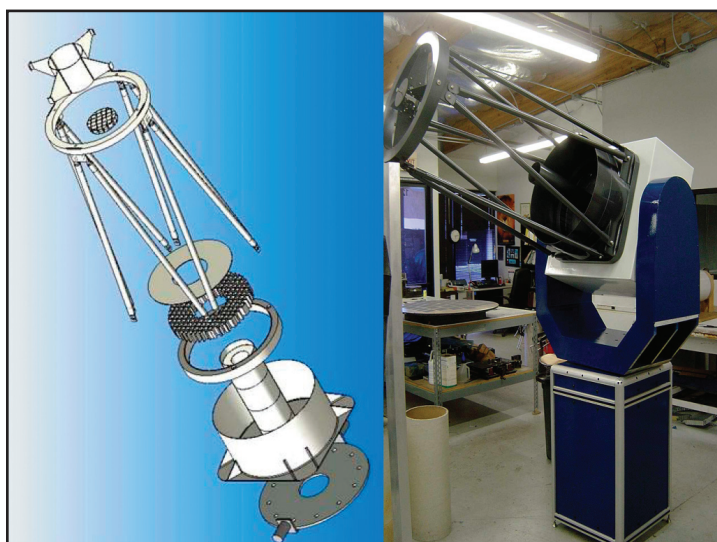


FIGURE 7
Exploded view of the 0.4-meter telescope's optical telescope assembly (OTA) with all CFRP components, and the fully constructed 0.4-meter telescope with mount and integrated adaptive optics (AO) box.

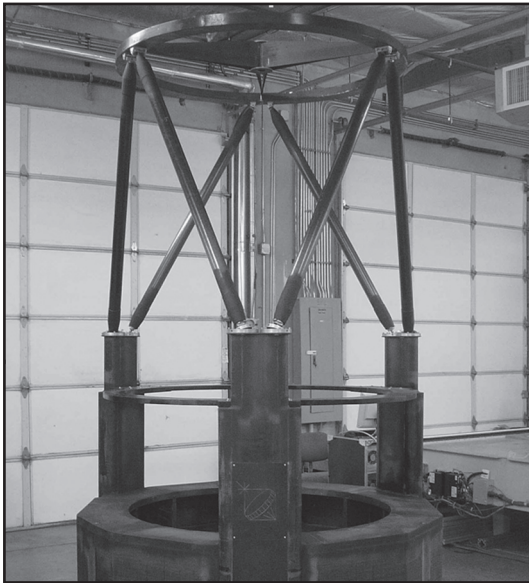


FIGURE 8
Fully constructed 1.4-meter CFRP telescope with hexapod controlled secondary ring.

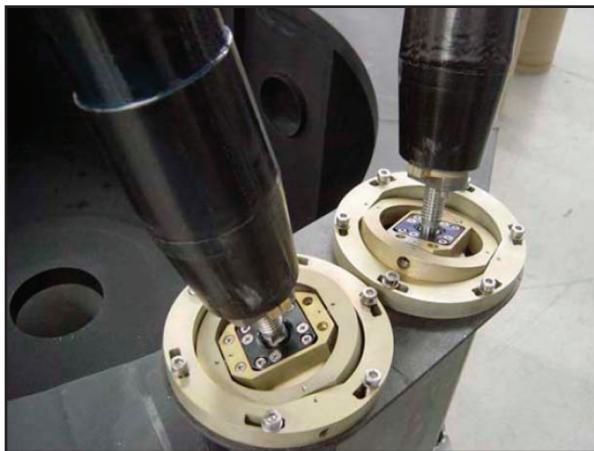


FIGURE 9
Piezoelectric screw-drive actuators for control of hexapod secondary ring.

Conclusions: The CFRP optics and telescope program at NRL will provide a significant improvement to the sensitivity of the NPOI measurements. The need for enhancing the performance of the NPOI has driven many of the advances and improvements in CFRP optics and telescope assemblies. These improvements have already generated the 0.4-meter telescope with integrated AO and a 1.4-meter telescope for use on the array. The advances in CFRP technology have spawned the development of CFRP deformable mirrors, and current efforts include analysis of the performance and long-term stability of these devices.
[Sponsored by ONR]

References

- ¹ S.R. Restaino, T. Martinez, J.R. Andrews, C.C. Wilcox, F. Santiago, R. Romeo, and R. Martin, "Ultra-light Weight Telescope Coupled with Portable AO System for Laser Communications Applications," *Proc. SPIE* **6105**, 61050M (2006).
- ² J.R. Andrews, F.E. Penado, S.T. Broome, C.C. Wilcox, S.R. Restaino, T. Martinez, S.W. Teare, and F. Santiago, "Characterization of the Lightweight Telescope Developed for the NPOI," *Proc. SPIE* **6267**, 6267EQ (2006). ★

Monitoring Global Surface Soil Moisture with the WindSat Polarimetric Microwave Radiometer

L. Li and P. Gaiser
Remote Sensing Division

Introduction: Soil moisture monitoring from space has been designated a very high science and operational priority by the DoD, NOAA, NASA, and the National Research Council Earth Science Decadal Survey. Soil moisture is also a linchpin environmental variable supporting Battlespace Environment assessment/prediction and C4ISR (command, control, communications, computers, intelligence, surveillance, and reconnaissance). Despite the importance of soil moisture applications, current sensors and algorithms do not satisfy measurement requirements. Using data from the NRL WindSat sensor,¹ we have developed a passive microwave land algorithm to retrieve soil moisture and vegetation water content globally from space. The validation results suggest that the algorithm can meet the requirements of 50 km resolution soil moisture mapping under low to moderate vegetation conditions.

Methodology: The WindSat land algorithm is a physically based, multi-channel, maximum-likelihood estimator using 10, 18, and 37 GHz data. The surface parameters considered by the algorithm include soil moisture, vegetation water content, land surface temperature, surface type, precipitation, and snow cover. The solution is found by iteratively minimizing the difference between WindSat measured brightness temperatures and those obtained from radiative transfer simulations. In this way, we can provide retrievals that not only are consistent with our radiative transfer model, but also handle directly the nonlinearity of the vegetation effects and non-uniqueness of the solution.

Results: The retrievals have been validated against multi-scale data including soil moisture climatology, ground in situ network data, precipitation patterns, and vegetation data from AVHRR sensors. Figure 10 shows composite WindSat global surface soil moisture retrieval-

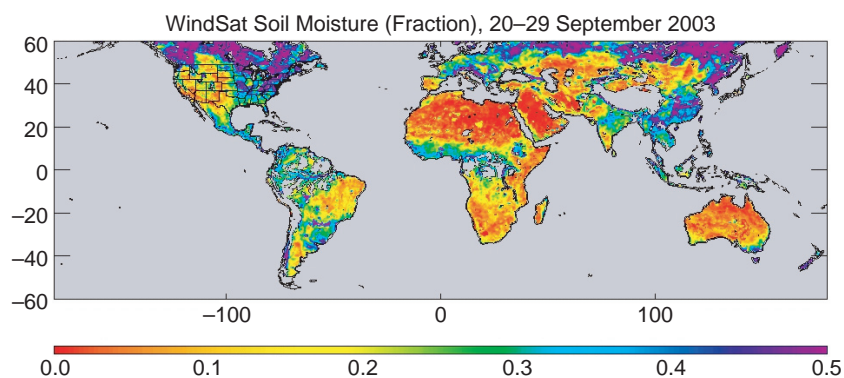


FIGURE 10
Global soil moisture retrievals for 20–29 September 2003.

als for the period 20–29 September 2003. Overall, the soil moisture retrievals are very consistent with global dry/wet patterns of climate regimes. All the deserts and arid regions were captured well by the retrievals. In the United States, there are two distinct patterns of continental climate: the humid East and the arid West. The climate transition zone is around the 100° west longitude line, extending through the Great Plains from North Dakota to Texas. Such a pattern of dry in the west and wet in the east is clearly depicted by the WindSat soil moisture retrievals. They exhibit a distinct and sharp boundary, which agrees well with the strong west-to-east soil moisture gradient near this boundary that is predicted by the NASA Catchment Land Surface Model.²

The quantitative algorithm validation is based on soil moisture data from the top 5 cm soil layer acquired using a dense in situ soil moisture measurement network during the Soil Moisture Experiment (SMEX) over the United States by the U.S. Department of Agriculture.³ The available SMEX data cover the summer months in three years: 2003 in Oklahoma, 2004 in Arizona, and 2005 in Iowa. These three experiment sites provide diverse vegetation covers (rangeland, winter wheat, sparse shrubland, agricultural domain with corn and soybean) and extreme wet and dry soil

conditions. Figure 11 plots the area-averaged in situ soil moisture data against the WindSat retrievals for all three SMEX field experiments. In general, the WindSat retrievals agree very well with the in situ data from all the SMEX sites, with an uncertainty of about 4% and bias of 0.4%. The retrieved soil moisture is also highly correlated with in situ data with a correlation coefficient of 0.89.

The comparison of soil moisture retrievals and precipitation patterns offers an indirect, qualitative, but multi-scale way to validate soil moisture retrievals.⁴ As an example, at the synoptic scale, the hot and dry period in July and August 2003 resulted in extreme short-term drought conditions from the western Great Lakes to the northern Rockies and Great Plains, including Nebraska, Kansas, and Oklahoma.⁵ On 11 September 2003, a very heavy rain band developed across the northern and central plains (Minnesota, Nebraska, and Kansas), which lasted for many hours and created ground saturation conditions. Figure 12(a) shows the 24-hour rainfall total for 11 September. The rain band location is illustrated well in the image. By the morning of 12 September, the rain started to move to the east of the Mississippi River and then diminished, as shown in Fig. 12(b). Soil moisture retrievals from the WindSat morning pass on 12 September exhibit a swath lined

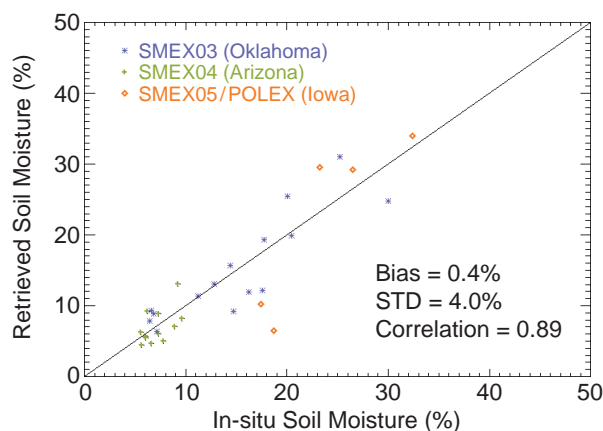


FIGURE 11
WindSat solid moisture validation against SMEX data.

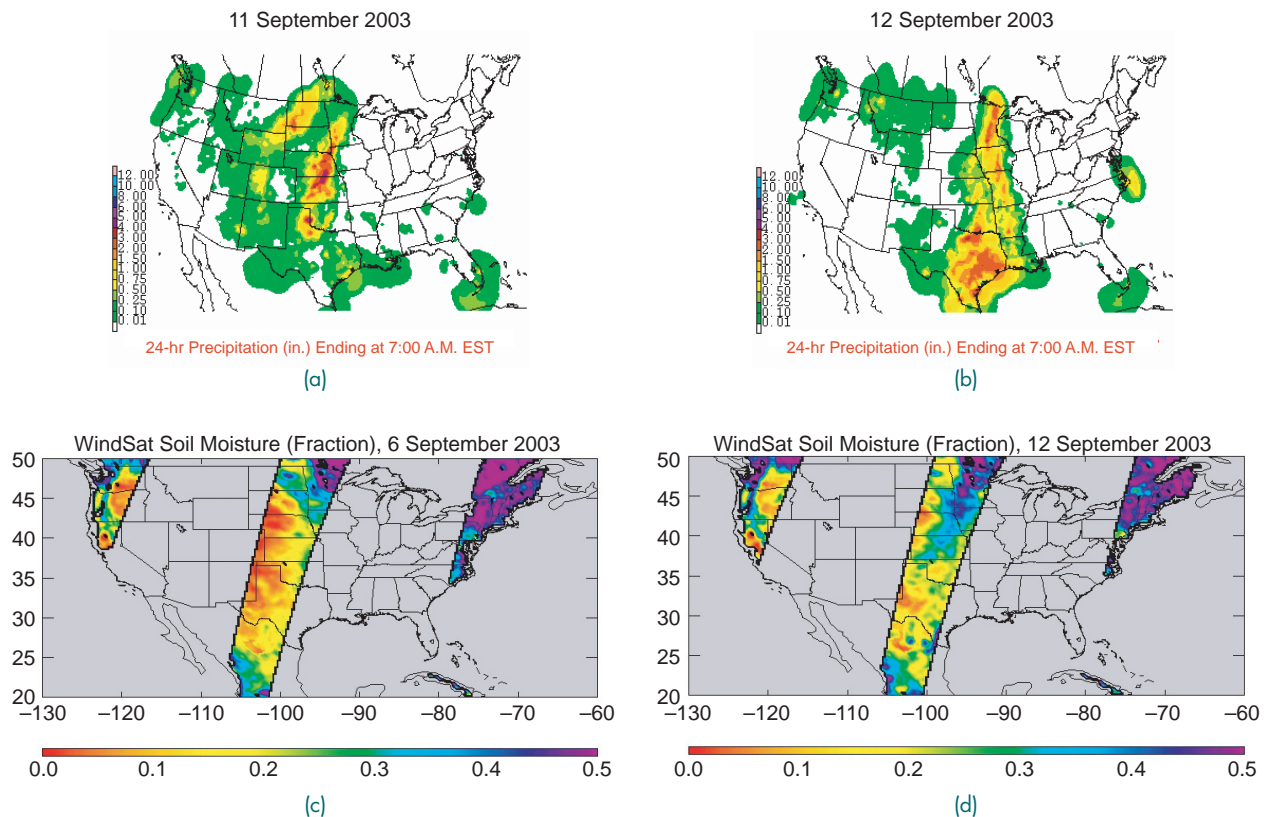


FIGURE 12

Comparisons of precipitation with soil moisture retrievals before and after the rain event. The precipitation images are provided by Dr. Andy Jones, CIRA, Colorado State University.

up well with the rain band on the previous day, and capture the wet event under rain-free conditions. Figure 12(c) and (d) depict the Windsat soil moisture retrievals over the similar region on September 6 and 12, respectively. Figure 12(c) shows mostly very dry conditions prior to the rain event, and Fig. 12(d) the very wet conditions after the rain. Not only are the WindSat soil moisture data able to capture these two extreme dry and wet conditions well, demonstrating sufficient retrieval sensitivity, but the spatial patterns of rainfall and soil moisture also show strong correlations. The locations of the patterns correspond well with each other, which suggests that WindSat soil moisture data can capture the hydrological processes at the synoptic scale.

Impact: Soil moisture is a desired input to NWP models, including the Navy's NOGAPS and COAMPS® models, because it controls the land-atmosphere interaction, dust emission, and heating/moistening of the lower atmosphere. It also has great importance across the full spectrum of the DoD mission from anti-terrorism operations to major conflicts. Knowledge of the spatial distributions of soil moisture is necessary to support the employment of electro-optical weapon systems; to evaluate mesoscale weather effects; to

understand the state of the ground; and, therefore, for trafficability assessment, deployment of ground and amphibious forces, and mine placement and detection. The information is also required for the Future Combat Systems to plan maneuvers on the battlefield in adverse weather conditions.

[Sponsored by NRL and ONR]

References

- ¹ P.W. Gaiser et al., "The WindSat Spaceborne Polarimetric Microwave Radiometer: Sensor Description and Early Orbit Performance," *IEEE Trans. Geosci. Rem. Sens.* **42**, 2347-2361 (2004).
- ² R.D. Koster, M.J. Suarez, A. Ducharme, M. Stieglitz, and P. Kumar, "A Catchment-based Approach to Modeling Land Surface Processes in a General Circulation Model: 2. Parameter Estimation and Model Demonstration," *J. Geophys. Res.* **105** (D20), 24823-24838 (2000).
- ³ T.J. Jackson, R. Bindlish, A.J. Gasiewski, B. Stankov, M. Klein, E.G. Njoku, D. Bosch, T.L. Coleman, C.A. Laymon, and P. Starks, "Polarimetric Scanning Radiometer C- and X-Band Microwave Observations during SMEX03," *IEEE Trans. Geosci. Rem. Sens.* **43**, 2418-2430 (2005).
- ⁴ M.F. McCabe, H. Gao, and E.F. Wood, "Initial Soil Moisture Retrievals from AMSR-E: Multiscale Comparison using In Situ Data and Rainfall Patterns over Iowa," *Geophysical Research Letters* **32**, L06403 (2005). doi:10.1029/2004GL021222.
- ⁵ <http://www.ncdc.noaa.gov/oa/climate/research/monitoring.html>





Decadal Impact of El Niño (1994)

NRL's researchers were the first to show that the oceanic effects of El Niño events can be extremely long-lived. Using evidence from modeling and observations, NRL explained that planetary-scale oceanic waves, generated by reflection of equatorial shallow-water waves from the American coasts during the 1982–1983 El Niño, had crossed the North Pacific and a decade later caused a northward rerouting of the Kurishio Extension (a strong current that normally advects large amounts of heat from the southern coast of Japan eastward into the mid-latitude Pacific). This resulted in significant increases in sea-surface temperature at high latitudes in the northwestern Pacific, of the same amplitude and with the same spatial extent as those seen in the tropics during important El Niño events. These changes may have influenced weather patterns over the North American continent during the past decade. This discovery was recognized by *Discover* magazine as one of the top 75 science stories in 1994.

229

CREW Modeling of Effectiveness and Compatibility for Operational Test and Evaluation

B. Sjoberg, A. Szymanski, J. Walters, J. Durbin, D. Malloy, I. Will, E. Phillippi, C. Mamaril, K. Lilley, H. Dettmar, A. Bowen, Z. Mistry, and V. Ortiz

231

Dynamics of Coronal Mass Ejections (CMEs)

J. Chen, P.W. Schuck, and V. Kunkel

234

Enabling Coordination During Security, Stabilization, Transition, and Reconstruction Operations

R. Mittu and S. Guleyupoglu

CREW Modeling of Effectiveness and Compatibility for Operational Test and Evaluation

B. Sjoberg,¹ A. Szymanski,¹ J. Walters,¹ J. Durbin,¹ D. Malloy,¹ I. Will,¹ E. Phillippi,² C. Mamaril,² K. Lilley,³ H. Dettmar,³ A. Bowen,³ Z. Mistry,⁴ and V. Ortiz⁵

¹Tactical Electronic Warfare Division

²SFA, Inc.

³ITT Corporation

⁴Vangent, Inc.

⁵AVW Technologies, Inc.

Background and Problem Area: There is an ongoing threat of radio-controlled improvised explosive devices (RCIED) being used against coalition troops in Iraq and Afghanistan, and countering these devices is a top priority for the Department of Defense. The Joint Improvised Explosive Device Defeat Organization (JIEDDO) initiated the Counter RCIED Electronic Warfare (CREW) program for this purpose. Builder CREW Modeling and Simulation Tool (CMAST), a modification of the Interactive Scenario Builder software program developed by the Advanced Tactical Environmental Simulation Team (ATEST), has been designated as the primary modeling and simulation tool for the CREW effort. Builder CMAST provides a user-friendly graphical interface to simulate the radio frequency (RF) capabilities of a number of different CREW systems. The software uses physics-based models to accurately compute signal levels in the presence of varying terrain, objects, soil conditions, atmospheric conditions, and other situations. The results of simulations are used to determine a CREW system's effectiveness at suppressing the operation of various enemy communication links.

Overview of Builder Capability: Interactive Scenario Builder (commonly referred to as Builder) is a computer simulation tool that provides insight into and visualization of the RF capabilities of various transmitters and receivers interacting in communications links. In addition, it provides geospatial and temporal situation awareness. Builder models communication and radar systems by calculating one-way and two-way RF propagation loss. It incorporates complex antenna pattern data as well as the effects of meteorology, terrain, environmental factors, and electronic countermeasures when predicting performance of these systems. It visualizes many National Geospatial-Intelligence Agency (NGA) map products, including CADRG and CIB. Builder can be used for pre-mission planning, real-time situational awareness, and after-action debriefing.

CMAST Enhancements for CREW Effectiveness

Analysis: CMAST accurately models various CREW effectiveness scenarios. A CREW system mounted on a convoy vehicle can be modeled as a transceiver connected to an antenna mounted on the vehicle. An accurate antenna model is used to show the overall antenna pattern created by the antenna and the conducting surface of the vehicle itself. An example of a representative antenna pattern is shown in Fig. 1. RF propagation is calculated at regular points along the vehicle's path of motion. For active operation of a CREW system, this process consists of modeling the transmission to the threat receiver attached to the explosive device. In the case of a reactive CREW system, this additionally includes modeling the transmission of the signal from the threat transmitter (triggerman) to the CREW system's receiver, which initiates the countermeasure signal to the threat receiver. CMAST compares the signals from the threat transmitter and the CREW device transmitter at the threat receiver to calculate the effectiveness of the countermeasure. The CMAST graphical representation is shown in Fig. 2. CMAST can analyze scenarios involving multiple threats at various specific and variable positions along the vehicle route. Enhancements have been made to the propagation engine to accommodate various near-Earth phenomena such as urban environments and soil dielectric variability. A Threat Receiver and Countermeasure (TRAC) Database has been created to store defeat parameter data that have been obtained by laboratory analysis of different CREW systems interacting with threat devices using various techniques for signal generation and transmission.

CMAST Enhancements for CREW Compatibility

Analysis: Because the CREW systems emit RF radiation over a wide range of frequencies in order to suppress the RCIED threats, it is necessary to evaluate their compatibility with other communications and navigational RF devices in the geographical area of operation. This includes friendly force communications, other CREW systems, both U.S. and coalition, and civil communications systems. In particular, CMAST has been used by the Federal Aviation Administration (FAA) to analyze interference with commercial aviation communication and navigation transmissions while CREW systems are under test on U.S. test ranges.

Validation Testing: The CREW systems are configured to emit a set of frequencies and power levels suited to specific collections of threat devices. These configurations are tested on an open-air test range to judge effectiveness of the systems. CMAST has been programmed with parameters obtained from such tests and has been shown to produce good correlation with

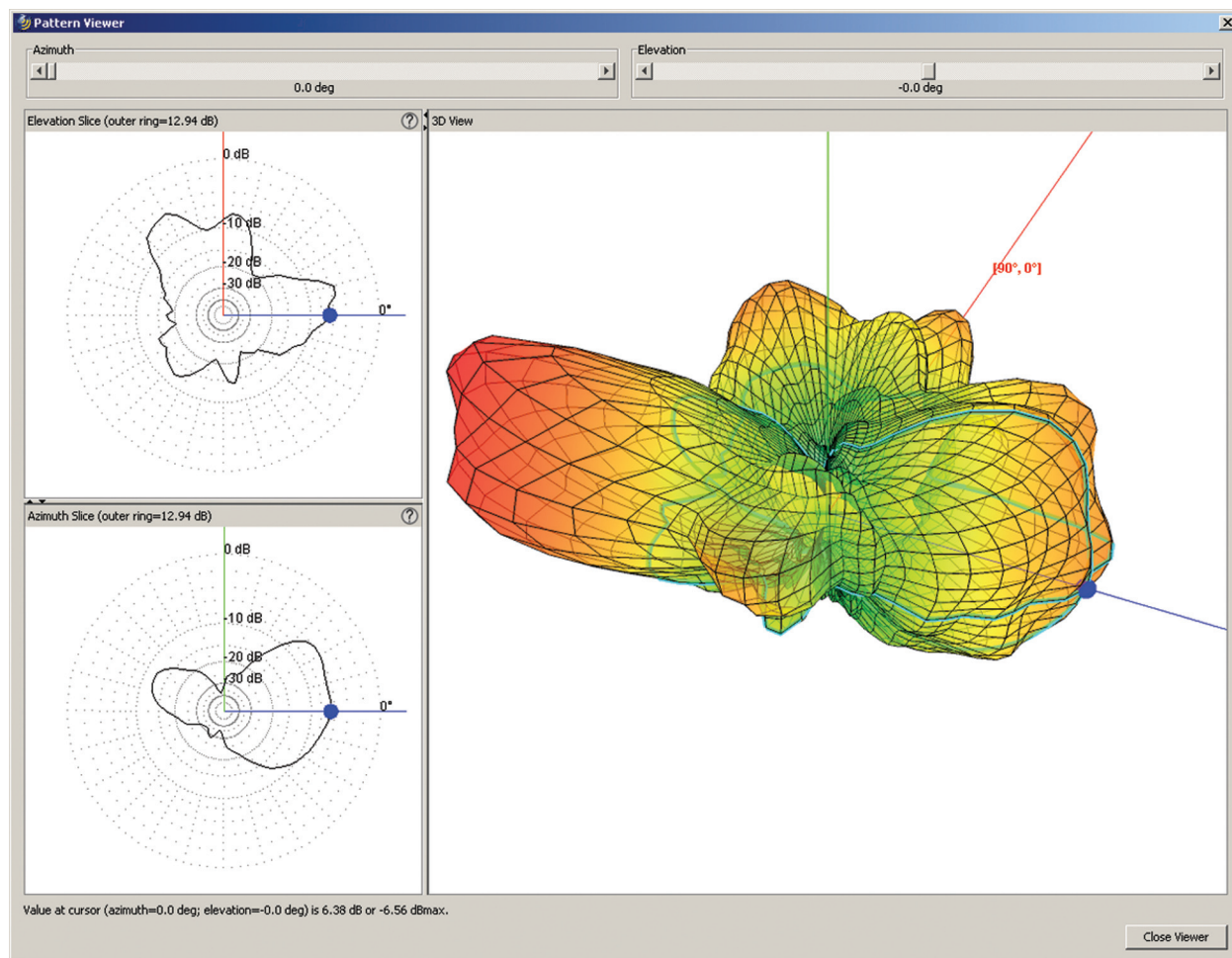


FIGURE 1
Representative display of a CMAST antenna pattern that includes the effect of the surrounding platform.

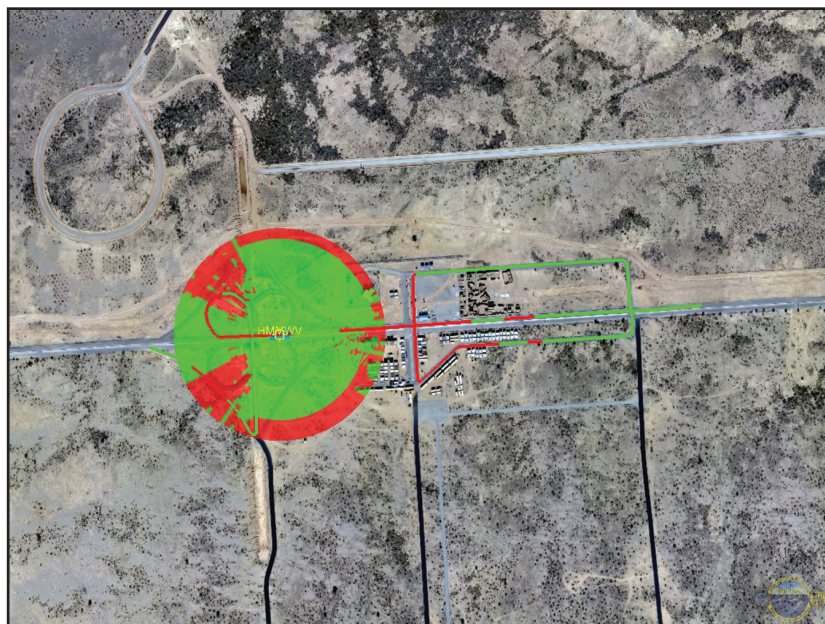


FIGURE 2
CMAST display of the effectiveness of a CREW device mounted on a military vehicle traveling a convoy route through an urban area against a threat at an unknown location. A circular region around the vehicle at any point on the route shows where a threat device would be defeated (green) or not defeated (red). Additionally, each point of the path is colored green or red according to the effectiveness criterion for the ratio of green to red in the circle centered at that point.

the measured test results. CMAST provides modeling and simulation capability as a substitute for certain aspects of open air testing, such as allowing tests for many permutations of parameter sets in a short period of time and under identical conditions. This will permit new and reconfigured CREW systems to be fielded in less time and with greater confidence. It also allows new threats discovered in theater to be analyzed more quickly than by use of field testing alone. CMAST is being enhanced to model not only the propagation of the signals between antennas, but also to model actual waveforms so that it can drive a coaxial test network in order to predict the effectiveness of new systems in development, decreasing the need for costly range time.

Summary: The IED threat has a worldwide presence, and exists in a multitude of environmental, social, and geographical settings. Therefore, Builder CMAST is continually undergoing modifications and improvements to handle as many of these scenarios as possible. NRL works closely with other organizations to develop modeling and simulation programs to faithfully model antenna patterns, threat protocols, and various geographical and environmental configurations. The Builder CMAST program will be transitioned to JIEDDO and all branches of the military for use in modeling and simulation of CREW systems. The tool will be utilized to refine operating parameters of the CREW devices and to provide the operational community with a tool for mission rehearsal and route planning.

[Sponsored by ONR, NAVSEA, and JIEDDO] ★

Dynamics of Coronal Mass Ejections (CMEs)

J. Chen,¹ P.W. Schuck,¹ and V. Kunkel²

¹*Plasma Physics Division*

²*George Mason University*

Introduction: Strong geomagnetic storms cause disturbances in the ionosphere that can modify conditions in the operational environment of the Navy around the globe. If severe enough, they can degrade or cause outages in SATCOM and GPS operations, impairing the Navy's ability to maintain environmental awareness and continuous connectivity of the widely dispersed fleet. The ultimate cause of strong storms is the eruption of Earth-directed coronal mass ejections (CMEs) at the Sun. CMEs, which are strongly magnetized plasma structures, represent ejection of 10^{16} g of material at up to 2000 km/s from the Sun.

The magnetic geometry and the driving mechanism of CMEs have been two major questions of modern solar physics. These questions are closely

related: the driving forces acting on a magnetized plasma structure critically depend on its magnetic geometry in three dimensions. Unfortunately, neither the magnetic field of the eruptive structure nor the forces acting on it can be directly measured. Under an NRL basic research program supplemented by NASA grants, we have developed a first-principles theory to understand the 3D magnetic geometry and the nature of the force from directly observable quantities.

What is the 3D Magnetic Geometry of CMEs?

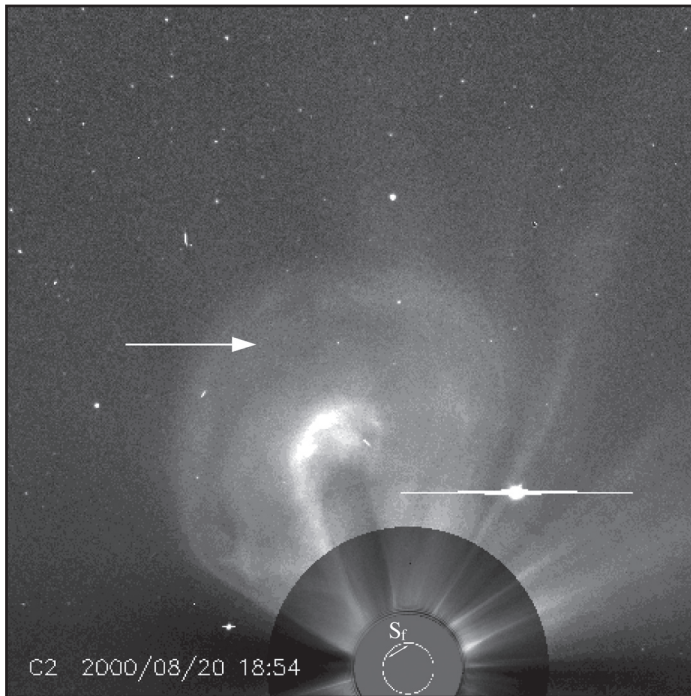
With the launch of NRL's Large Angle and Spectrometric Coronagraph (LASCO) instruments on the Solar and Heliospheric Observatory (SOHO) satellite in 1995, CME acceleration—the net accelerating force per unit mass—has been extensively documented in the region 2–30 solar radii (R_{\odot}). Our work with LASCO data has shown that the underlying magnetic field of a CME is that of a “flux rope”: pictorially speaking, a bent coil of magnetic field lines, whose two ends are connected to the Sun. Figure 3 shows a composite image of a CME (arrow) observed by the LASCO C2 and C3 telescopes on 20 August 2000. In this figure, the small white circle at the bottom indicates the limb of the Sun. The circular disk of radius $2R_{\odot}$ corresponds to the occulter of the C2 telescope. The two legs of the CME connected to the Sun are separated by distance S_f , as illustrated in the figure.

Using a theoretical model previously developed at NRL, we demonstrated that the height Z_{\max} above the photosphere at which the acceleration of the leading edge attains its maximum value scales with the distance S_f between the photospheric footpoints of the CME's legs in such a way that the following inequality is satisfied:¹

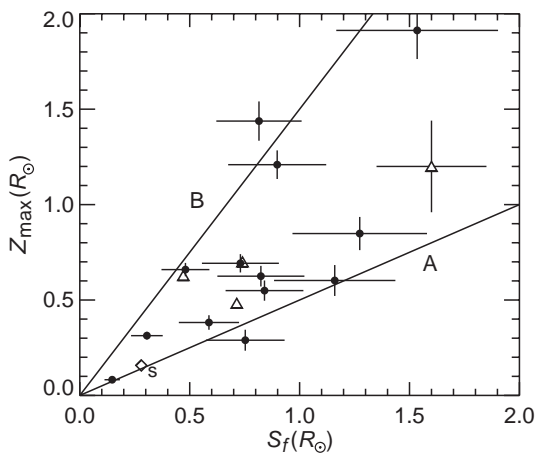
$$\frac{S_f}{2} \leq Z_{\max} \leq \frac{3}{2} S_f. \quad (1)$$

This relationship was directly tested against 17 well-observed CMEs and eruptive prominences (EPs), where (i) the source regions were visible so that we could determine the approximate distance (S_f) between the footpoints and (ii) the data contained sufficient numbers of height measurement to allow us to determine the maximum-acceleration height (Z_{\max}). Radio data and data from the Extreme Ultraviolet Imaging Telescope (EIT) on SOHO were used to estimate S_f .

Each event was analyzed to determine a pair of numbers, Z_{\max} and S_f . Figure 4, adapted from Ref. 1, shows the data points for the 17 events. The lines A and B are defined by $Z_{\max} = S_f/2$ and $Z_{\max} = 1.5 S_f$, respectively, corresponding to the lower and upper limits of the inequality above. The plot shows that inequality (1) is satisfied by all the events in this sample consistent with the uncertainties in the data.

**FIGURE 3**

A LASCO C2-C3 composite image of a CME, indicated by an arrow, observed on 20 August 2000. The white circle at the bottom indicates the Sun. The bright object on the right is a planet, with the horizontal rays caused by the saturated instrument.

**FIGURE 4**

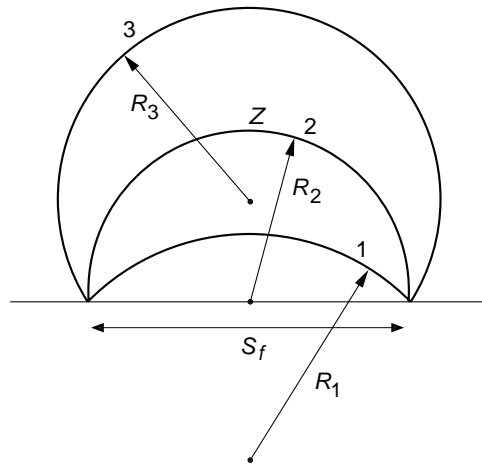
Comparison of theory and data. Z_{\max} and S_f are determined from data. The point marked by "S" denotes a numerical simulation result. Data points lying between lines A and B satisfy the flux-rope scaling law, inequality (1).

What is the Force that Drives CMEs? What can we deduce from the excellent agreement between the theoretical prediction and observational data? The flux-rope scaling law, inequality (1), is based on two assumptions: (i) the magnetic structure is that of a flux rope with footpoints separated by S_f and (ii) the structure is driven by the "hoop force," a particular form of Lorentz force acting on curved, current-carrying plasmas, including tokamaks in laboratories for magnetic fusion. This force has the unique property that

$$\frac{d^2 Z}{dt^2} \propto \left(\frac{1}{R}\right)^2 \left(\frac{1}{\ln R}\right)^2 \quad (2)$$

where R is the major radius of the flux rope. The right-hand side is maximum where curvature ($1/R$) is maximum.

The physics of this process is schematically illustrated in Fig. 5. Imagine that the lowest arc corresponds to the initial flux rope characterized by radius R_1 or curvature $1/R_1$ and footpoint separation S_f . As the flux rope rises with the footpoints held stationary, the curvature increases. Curvature reaches its maximum value when the arc is a semi-circle with $Z = R = S_f/2$, where Z is the height of the apex. Thereafter, the curvature monotonically decreases. Thus, if the flux rope is driven by the hoop force, the acceleration, i.e., the force per unit mass, necessarily peaks when the flux rope

**FIGURE 5**

Flux-rope scaling law. The arcs schematically represent a rising flux rope.

reaches the semi-circular position. The good agreement shown in Fig. 4 implies that CMEs are consistent with magnetic flux ropes and expand under the Lorentz force. Physically, the result shows that CME acceleration is governed by the footpoint separation distance S_f .

How Does a CME Propagate? After the initial acceleration, a CME continually expands away from the Sun. The propagation through the interplanetary medium, however, could not be observed until recently. With the launch of a pair of Solar Terrestrial Relations Observatory (STEREO) satellites with the NRL suite of instruments called Sun-Earth Connection Coronal and Heliospheric Investigation (SECCHI)² on board, it has now become possible to quantitatively study the dynamics of CMEs in interplanetary space.

Figure 6 shows the trajectory of a CME observed by SECCHI (COR2, HI 1, and HI 2) and LASCO (C2 and C3) in May 2007. The height of the leading edge of the CME measured from the solar surface is shown

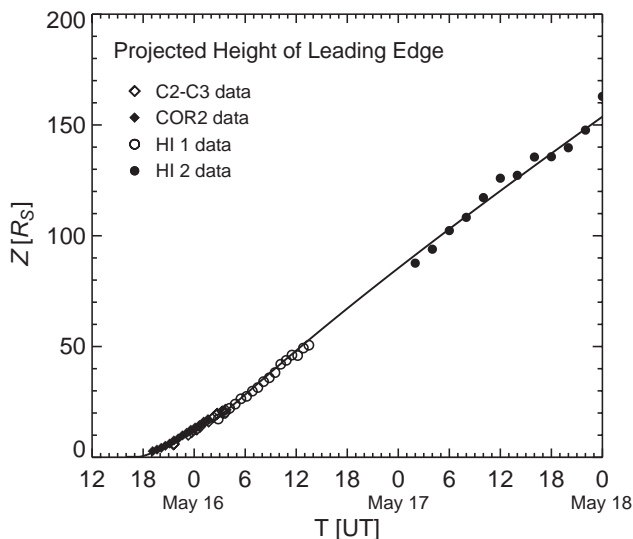
by various symbols corresponding to different instruments. The curve is the initial-value solution of the theoretical model. The figure shows that the model is capable of producing a solution that accurately reproduces the observed dynamics throughout the field of view, from R_\odot to about $3/4$ AU.

We have established with strong quantitative evidence that CMEs are magnetic flux ropes accelerated by the Lorentz hoop force. Figure 6 represents the first successful theoretical modeling of CME acceleration in the inner corona and the subsequent propagation in interplanetary space.

[Sponsored by ONR and NASA]

References

- ¹ J. Chen, C. Marque, A. Vourlidis, J. Krall, and P.W. Schuck, "The Flux-Rope Scaling of the Acceleration of Coronal Mass Ejections and Eruptive Prominences," *Astrophys. J. Lett.* **649**, 452 (2006).
- ² R.A. Howard et al., "Sun Earth Connection Coronal and Heliospheric Investigation (SECCHI)," in *Space Sci. Rev.* **136**, 67-115 (2008). ★

**FIGURE 6**

Theoretical solution directly compared with SECCHI data. Measured height-time data are represented by various symbols corresponding to different telescopes. The curve is the "best-fit" theoretical solution.

Enabling Coordination during Security, Stabilization, Transition, and Reconstruction Operations

R. Mittu¹ and S. Guleyupoglu²

¹*Information Technology Division*

²*ITT Advanced Engineering Sciences*

Introduction: The emergence of Department of Defense Directive 3000.05¹ is enabling Security, Stabilization, Transition, and Reconstruction (SSTR) operations to become a core U.S. military mission. These operations are now given equal priority to combat operations. The immediate goal in SSTR is to provide the local populace with security, restore essential services, and meet humanitarian needs. The long-term goal is to help develop indigenous capacity for securing and maintaining essential services. Therefore, many SSTR operations are best performed by indigenous groups, with support from foreign agencies and professionals. However, SSTR operations in response to large-scale disasters may benefit from military involvement. This article describes a conceptual portal, Share-InfoForPeople, that incorporates advanced Information and Communication Technology (ICT) to enable collaboration, coordination, and information sharing across the civil-military boundary during SSTR operations.

Security, Stabilization, Transition, and Reconstruction: SSTR operations are conducted outside the boundaries of U.S. lands and territories, and are best performed by indigenous groups, with support from foreign or U.S. civilian professionals. Complex and large-scale disasters are an example where military support to SSTR operations will undoubtedly provide significant value to foreign governments and non-governmental organizations, which may already be under great stress to respond in a timely manner. The command and control structure, resources, and assets the military can offer in such situations can shorten the response timeline. However, without the means to properly coordinate the efforts of such a large and diverse group spanning the civil-military boundary, basic assistance and relief operations may be severely impacted, leading to delays or waste in the overall response cycle.

A key element in the success of SSTR operations is the ability of the U.S. (or other lead activity) to obtain and process information about the situation and status of participating partners, while disseminating (or making accessible) the widest amount of relevant information to the partners in the ad hoc coalition. Through the sharing of unclassified information via an appropriate ICT framework and supporting analytical tools,

the goal is to increase the overall level of coordinated activity among the participants.

Information and Communication Technologies:

The Internet is driving emergent behavior in personal and group communications and is leading to new forms of interaction, as witnessed through the growing popularity of social networking web sites. The DoD is also experimenting with social networking as a mechanism for improving SSTR operations. The ShareInfoForPeople portal (Fig. 7), being developed by NRL, provides a set of social networking tools through a web browser interface to enable coordination and information sharing. The key features and capabilities of the portal include the following:

- Fully Indexed Site, based on user-defined keyword tags to facilitate efficient search.
- Real Simple Syndication (RSS) and Geospatial RSS Feeds, to incorporate real-time content from external sites, which can be visualized on various maps.
- Collaborative Authoring, via a wiki capability to promote shared knowledge. A community wiki should enable convergence toward accurate information being shared.
- Upload or Create Content, such as video, audio, and pictures within a group-based structure. Additional content such as weblogs (a.k.a. blogs), events, and disaster assessment reports can also be created. The various forms of content are indexed to support search, and can be geo-referenced for visualization on various maps.
- Picture Annotation Capability, which enables a bounding box to be overlaid on the stored picture, including an area for free-form comments to describe the image under the bounding box. User-defined keyword tags facilitate searching through the image gallery, and the images are geo-referenced for display on various maps.
- Subscription-based Email Notifications, to permit users to receive email notification when new or relevant content has been posted to a group.
- Subject Matter Expert (SME) Registry, to enable users to find individuals who are able to offer specific services, support, or other assistance during a crisis situation.
- Multilingual Chat, to enable real-time language translation, allowing communication between those who do not share a common language.

The baseline implementation of ShareInfoForPeople is providing the foundation on which more sophisticated capabilities are being developed, such as social network analysis and task management tools. Furthermore, the design philosophy embraces free and open software and standards to enable interoperability

235

with other systems. We believe this philosophy offers an increased opportunity to instantiate an enterprise-wide capability composed of loosely coupled, agile systems that provide synergistic capabilities.

Experimentation in Trident Warrior: The ShareInfoForPeople portal underwent user assessment during the Trident Warrior experimentation exercise in March 2007. Trident Warrior is a yearly exercise that provides a venue for technology experimentation in support of the Navy's FORCEnet² vision. The portal was used by various civil and military groups in response to a hypothetical scenario consisting of a bird flu outbreak on the Cape Verde Islands off the coast of West Africa.

Through participation in Trident Warrior, valuable feedback was collected in order to improve the future capabilities of the portal. The portal underwent similar user assessment during the U.S. Joint Forces Command's Noble Resolve experiment in 2007.

Summary: The ShareInfoForPeople portal enables coordination and information sharing between the civil and military communities during SSTR operations.

The architecture is based on the Drupal³ framework, an open source content management system. Furthermore, the design philosophy embraces open source software and standards to enable future interoperability with other portals that provide complementary capabilities. The portal was used at the Trident Warrior 2007 experiment in order to gather user feedback to support near-term improvements. The portal is expected to be included in future experiments in order to collect additional user requirements, which will enable the portal's capabilities to be refined for eventual transition into operational usage.

[Sponsored by OSD/Network and Information Integration]

References

¹U.S. Department of Defense, DoD Directive 3000.05, "Military Support for Stability, Security, Transition, and Reconstruction (SSTR) Operations," November 28, 2005. <http://www.dtic.mil/whs/directives/corres/html/300005.htm>, last accessed July 23, 2007.

²FORCEnet, <http://www.globalsecurity.org/military/systems/ship/systems/forcenet.htm>, last accessed February 8, 2008.

³Drupal, <http://www.drupal.org>, last accessed July 23, 2007. ★



Project Rampant Lion (2006)

A one-of-a-kind multisensor airborne study of most of Afghanistan, Project Rampant Lion collected remote sensing data to support economic and civil infrastructure development and has thus enhanced the stability of that nation and of its democratic government. The project simultaneously provided valuable data to support current and future military operations. Investigators from NRL and the U.S. Geological Survey flew aboard an NP-3D Orion aircraft operated by VXS-1, operating dual gravimeters, scalar and vector magnetometers, a digital photogrammetric camera, a hyperspectral imager, and an L-band polarimetric synthetic aperture radar. Data from all sources was precisely co-registered to the ground by a combination of interferometric-mode Global Positioning System and inertial measurements. The data from this integrated mapping mission supports numerous efforts in Afghanistan: combat operations; economic exploration for oil, gas, and minerals; humanitarian missions; development of civil infrastructure; and agricultural resource management.

239

FREND: Pushing the Envelope of Space Robotics

B.E. Kelm, J.A. Angielski, S.T. Butcher, N.G. Creamer, K.A. Harris, C.G. Henshaw, J.A. Lennon, W.E. Purdy, F.A. Tasker, W.S. Vincent, and B.P. Whalen

241

Wide Field of View Imaging with a VHF Phased Array

J. Lazio, T. Clarke, W. Lane, D. Wood, P. Ray, and N. Kassim

243

The Target Indicator Experiment on TacSat-2

T.M. Duffey, C.M. Huffine, S.B. Nicholson, and M.L. Steininger

245

Development of a Bearingless Ammonia Pump for Spacecraft Thermal Control

R.W. Baldauff, T. Kawecki, W. Purdy, and T.T. Hoang

FREND: Pushing the Envelope of Space Robotics

B.E. Kelm,¹ J.A. Angielski,² S.T. Butcher,¹ N.G. Creamer,¹ K.A. Harris,¹ C.G. Henshaw,¹ J.A. Lennon,¹ W.E. Purdy,³ F.A. Tasker,¹ W.S. Vincent,¹ and B.P. Whalen¹

¹Spacecraft Engineering Department

²The PTR Group, Inc.

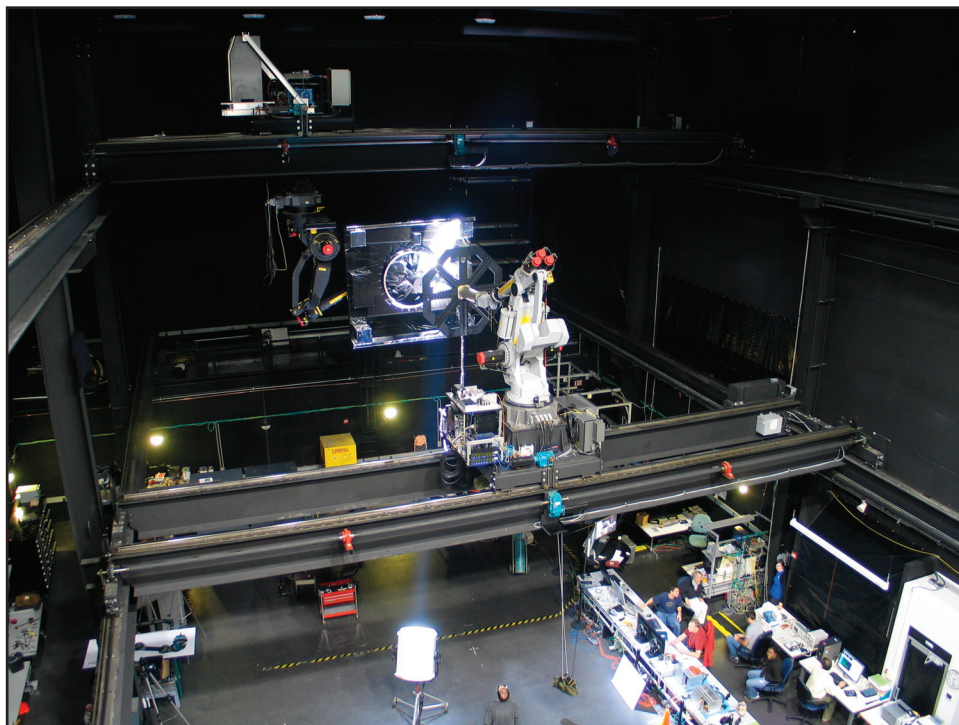
³Purdy Engineering, Inc.

Introduction: The Front-end Robotics Enabling Near-term Demonstration (FREND) project is a DARPA-sponsored effort that is developing the state of the art in autonomous rendezvous and docking with satellites not pre-designed for servicing. This capability allows nearly any satellite to be repositioned on-orbit and provides a number of national benefits including better ground coverage in time of crisis, satellite life extension by eliminating the requirement imposed on fully functional satellites to expend their fuel to move to a safe disposal orbit, and disposal of derelict spacecraft which present navigation hazards to active satellites. FREND has successfully demonstrated autonomous rendezvous and docking in a ground test environment using research grade robotics and spaceflight traceable control software under simulated orbital conditions. NRL will soon perform these same demonstrations with the prototype and flight robotic arms to prove that this capability is ready for space-flight operations.

Demonstrations: The FREND mission concept uses robotic arms to position a grappling tool at a customer spacecraft structural hardpoint, and docks the two spacecraft together by first rigidizing this tool, then rigidizing the positioning robotics. NRL performed two demonstrations of this technology in FY2007. In both, FREND docked with a geosynchronous satellite mock-up using only the pre-existing satellite-to-launch-vehicle interfaces that are common to most satellites. The first demonstration used hardware from an FY2005 proof-of-concept demonstration with improved, more flight-like software. Five times out of five, FREND successfully rendezvoused with the satellite mock-up and docked with a bolt hole interface. The second demonstration consisted of an upgraded satellite mock-up with flight-like blanketing, a Marman band interface, and a navigation sensor simulator. A new end effector tool was designed by NRL to dock with the Marman band interface. Furthermore, orbital lighting conditions were simulated to demonstrate the increased robustness of the NRL system. FREND again performed successfully, this time ten out of ten times. FREND has consistently shown the ability to dock with both of the hardpoint launch vehicle interfaces commonly found on existing satellites.

Simulation Facilities: NRL's Proximity Operations Testbed (Fig. 1) was used for both demonstrations. This unique facility allows the full-scale simulation of two satellites operating with six degrees of freedom in close proximity to each other and accurately simulates orbital dynamics and thruster effects during rendezvous and docking. A commercial robot arm was used for both demonstrations, in advance of the prototype spaceflight robot arm (Fig. 2). This prototype arm was designed and built by Alliance Spacesystems during FY2007 for future FREND testing. An optical testbed is used to test machine vision algorithms against a variety of simulated on-orbit lighting conditions, satellite thermal blanket configurations, and camera placements. The Gravity Offset Table is a granite table supporting a test frame fitted with air bearings that allow the test frame to hover above the table surface. Different weight configurations on the test frame simulate different classes of satellites, and an optical measurement system precisely tracks the positions of the robot arm and the test frame. This testbed allows simulation of zero gravity contact dynamics between the robot arm and the customer satellite and investigates issues such as angle of approach, end effector finger configuration, and time needed to dock.

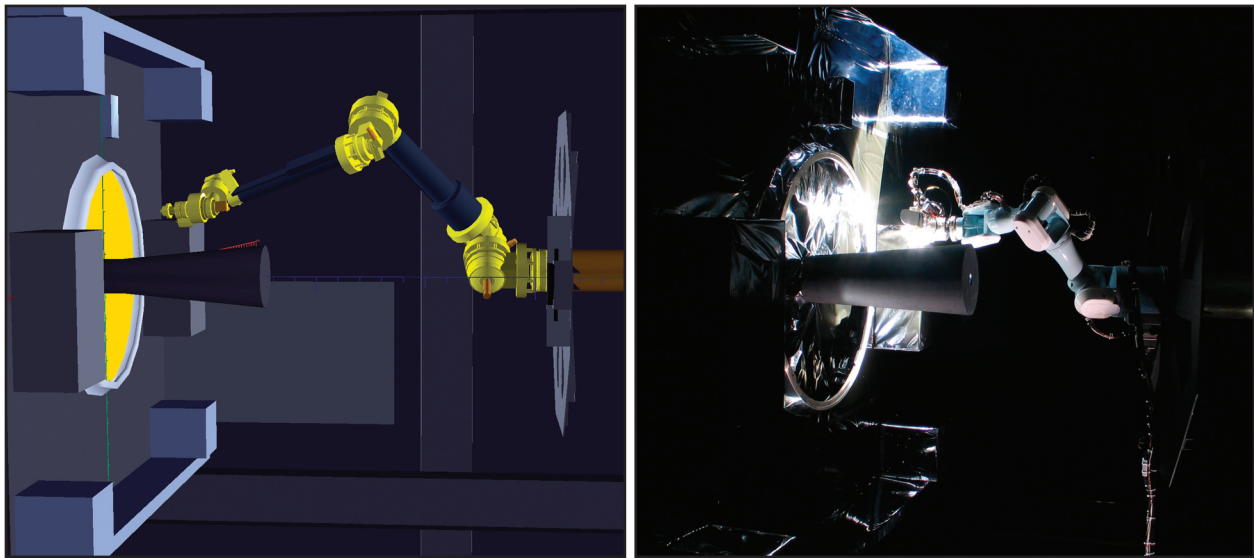
Algorithms Development: FREND is fully autonomous from test start to stop, demonstrating the robustness that will be needed for spaceflight operations. A simulated satellite bus thruster system controls the approach and position hold near the customer satellite. A novel trajectory planner develops the commands that will move the robot arm from its stored position to the docking interface feature, using laser-based time-of-flight and triangulation data to estimate the customer's location and orientation, and machine vision data to home in on the docking interface. The machine vision algorithms locate the docking feature out of the images provided by cameras mounted at the end of the robot arms. They must be robust to the extreme lighting conditions found in space and to the reflective nature of many blanketing materials. A compliance controller moderates the robot arm's contact with the docking feature, emulating a soft spring-mass-damper system rather than a rigid contact that pushes the customer away. Fault detection routines monitor sensor inputs to ensure safe operations. A mission sequencer organizes the interactions between these algorithms and the hardware and controls progress through the test. Engineers monitor telemetry and issue emergency commands if necessary using the NRL-developed Comet ground system. Mathematical simulations and visualization software (Fig. 3) are used for planning, verification, and test planning, allowing us to safely test trajectories and parameter tunings in simulation before applying them to full hardware test environment.

**FIGURE 1**

Proximity Operations Testbed. Full-scale rendezvous and docking testing for FRENED includes a servicing satellite simulator, shown here as an octagon in the center of the image, and a mock-up of a customer satellite, shown here as one face of a rectangular satellite in the distant center. Unique track and trolley system provides two degrees of positional freedom, while industrial robot arms on the upper and lower trolleys provide a third degree of positional freedom and all three degrees of rotational freedom for a simulated spacecraft.

**FIGURE 2**

FRENED flight prototype robotic arm. The engineering development unit (EDU) arm is the ground test unit to the spaceflight arm under development. The EDU has the full form, fit, and function of the flight arm, but has cost-saving material substitutions that are not qualified for the space environment.

**FIGURE 3**

FREN simulation environment. FREN's software test environment allows algorithm development and testing to simulate all hardware components virtually before proceeding to full system testing with hardware-in-the-loop demonstrations. Images depict the grapple of a satellite Marman band interface, the structural "hardpoint" which attached the satellite to its rocket booster during launch.

Summary: The DARPA/NRL team working on FREN is currently leading the world in research and development necessary to autonomously rendezvous and dock with satellites not pre-designed for servicing. NRL continues to advance the technology readiness to be spaceflight ready in terms of both hardware and software. Once ground development and testing are complete, DARPA and NRL will be ready to perform an on-orbit demonstration of revolutionary new spacecraft operations.

[Sponsored by DARPA]



Wide Field of View Imaging with a VHF Phased Array

J. Lazio,¹ T. Clarke,² W. Lane,¹ D. Wood,³
P. Ray,⁴ and N. Kassim¹

¹*Remote Sensing Division*

²*Interferometrics, Inc.*

³*Praxis, Inc.*

⁴*Space Science Division*

Introduction: The Long Wavelength Array (LWA; <http://lwa.unm.edu/>) is an ONR-funded project to design and construct a large, next-generation facility focusing on both ionospheric and astronomical research and operating in the high frequency (HF) and very high frequency (VHF) bands (20–80 MHz). The baseline design for the LWA consists of approximately 50 dipole-based phased-array stations, with each

station consisting of 256 dual-polarization dipoles, distributed over approximately 400 km in the state of New Mexico. In operation, the stations themselves would be phased together to form a radio interferometer.

The Long Wavelength Demonstrator Array (LWDA) was funded by NRL and developed jointly by NRL and the Applied Research Laboratories of the University of Texas at Austin (ARL:UT), with assistance from the University of New Mexico. The LWDA serves as a technology and scientific testbed for the LWA project by fielding prototype hardware and by providing experience with site preparation, radio frequency interference monitoring and mitigation, software development, environmental concerns, and initial science capability. The LWDA consists of 16 dual linear polarization dipoles, tunable in the frequency range of 60 to 80 MHz with an instantaneous received bandwidth of 1.6 MHz. The dipoles have an intrinsically large field of view (field of regard) and images of the entire sky are now being produced routinely. As part of the scientific prototyping work with the LWDA, these images are being used to search for transient celestial radio emitters at higher sensitivity levels than previously accessible. The LWDA also has obtained data, currently under study, containing passive radar observations of meteor scatter, anomalous propagation phenomena, and aircraft.

Technical Approach: Figure 4 shows the LWDA, which is located on the Plains of San Agustin in central New Mexico. The locations for the 16 LWDA antennas were chosen as a subset of those planned for a

**FIGURE 4**

The 16 antennas of the LWDA on the Plains of San Agustin in central New Mexico. In the background is the shielded electronics hut and 25-m-diameter antennas that are part of the National Radio Astronomy Observatory's Very Large Array.

much larger LWA station. The baseline LWA station consists of 256 dual-polarization dipoles distributed in a pseudo-random array over a circular area 50 m in radius and optimized for reduction of sidelobes from its phased-array operation mode. The 16 antennas of the LWDA are located in what would be the northeast quadrant of a full LWA station.

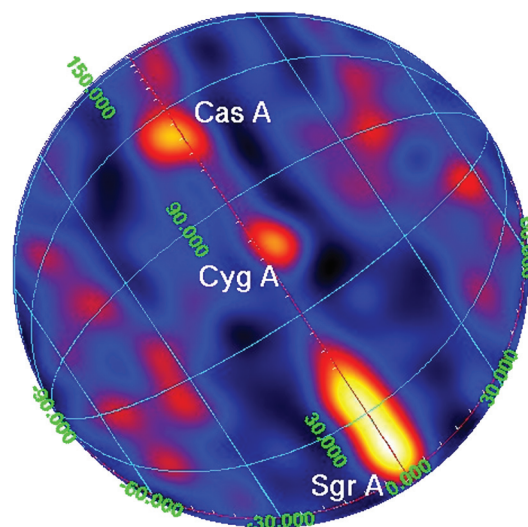
An LWDA antenna is a “droopy dipole,” standing approximately 1.5 meters tall and with the dipole arms inclined at 45° to the horizontal. Each polarization of a dipole is mated with an NRL-developed, low-noise “balun” for impedance matching and improved frequency dynamic range. Signals from the antennas are transmitted to a shelter, heavily shielded against electromagnetic interference (EMI), where FPGA-based digital receivers and signal combiners are located. Significant EMI shielding (100 dB) is required both to prevent the LWDA electronics from corrupting the extremely faint celestial signals of interest and to avoid producing interference in the operation of the nearby astronomical radio interferometer, the National Radio Astronomy Observatory's Very Large Array.

Two operational modes of the LWDA are possible. In the first, digital delay beamforming of the signals from the dipoles generates two fully independent beams of 1.6 MHz bandwidth. In the second, signals from the 120 unique pairs of dipoles are cross-correlated (multiplied and integrated) producing estimates of the visibility function, which is the Fourier transform of the sky brightness under the van Cittert-Zernike theorem. The field of view of the individual dipoles effectively encompasses the entire sky, so an inverse Fourier transform of the measured visibility function produces an image of the entire sky.

In the second data acquisition mode, the estimated visibility function from successive pairs of dipoles is acquired cyclically. The measurement of the visibility function for a pair of dipoles requires 50 ms, so that

the measurement of the visibility function from the full array (120 unique pairs = $16 \times 15/2$) requires a total of 6 s. In addition, relatively constant phase and gain calibrations, as determined during the array installation, are applied to each of the visibilities.

Results: Figure 5 shows an LWDA all-sky image. Clearly visible are a number of strong astronomical

**FIGURE 5**

An all-sky image from the LWDA. Three of the strongest (temporally constant) celestial sources are indicated: Cas A, the remnant of a massive stellar explosion in the constellation Cassiopeia; Cyg A, an active galaxy in the constellation Cygnus; and Sgr A, the nuclear region of the Milky Way Galaxy in the constellation Sagittarius. Grid lines indicate the Galactic coordinate system, defined by the spiral disk of the Milky Way Galaxy. Approximately 80 hr of data have been acquired, allowing movies to be constructed, and the images are being used to search for transient celestial radio emitters. (See http://www.phys.unm.edu/~lwa/progress_photos.shtml for examples of movies.)

radio emitters. To date, approximately 80 hr of data have been acquired in late 2006 and early 2007, allowing dynamic all-sky movies to be constructed.

One of the key scientific drivers for the LWA is to search for transient radio emitters, particularly celestial emitters. Traditional radio astronomical imaging assumes that the sky is constant in time, but a variety of recent results is beginning to suggest that numerous celestial emitters can have significant variability in time. In extreme cases, these transient events can have quite low duty cycles and limited emission durations (< 1 s). We are using the LWDA movies to develop the software to search for transient celestial emitters, a precursor to the studies eventually possible with the full LWA.

While the initial data analysis is ongoing, we already can begin to place limits on the event rate of celestial transients. Our current limit is that we find no celestial transients above a rate of 0.01 events/year/deg² for pulses stronger than -136 dB(J/m²) at 74 MHz over the 1.6 MHz bandwidth. Even this initial limit is comparable to results obtained at higher frequencies and is significantly better than what has been obtained previously for celestial transients in the low VHF band. As more observations are analyzed, we expect to be able to improve these results significantly, either by finding celestial transients or by improving the upper limits on the pulse strength and event rate.

[Sponsored by NRL]



The Target Indicator Experiment on TacSat-2

T.M. Duffey,¹ C.M. Huffine,² S.B. Nicholson,³ and M.L. Steininger⁴

¹*Spacecraft Engineering Department*

²*Space Systems Development Department*

³*S. Nicholson Consulting*

⁴*Space/Ground Systems Solutions*

Introduction: The Navy's Target Indicator Experiment (TIE) payload is part of the Air Force Research Laboratory (AFRL)-developed TacSat-2 spacecraft, which is the second in a series of Operationally Responsive Space (ORS) satellites built to experiment with making space-based assets more responsive to the needs of tactical forces. TacSat-2 was launched on 16 December 2006 from NASA's Wallops Flight Facility on a Minotaur 1 launch vehicle. The spacecraft was placed into a 420 km orbit at an inclination of 40 degrees. The NRL TIE payload is designed to perform real-time collection of RF signals from 0.5 to 18.0 GHz using an adaptation of an unmanned air vehicle payload. The TIE payload is also capable of collecting the Automatic Identification System (AIS) signal now required on large ships for maritime safety and security.

Payload Development: Our sponsors at the Office of Naval Research, DoD Office of Force Transformation, the DoD Advanced Concept Technology Demonstration (ACTD) process, and the Air Force Space Test Program accepted a higher level of risk than is found in the typical spacecraft payload development program, and encouraged the use of novel approaches to hardware and software development. On the hardware side, this allowed the NRL team to use non-radiation-hardened commercial off-the-shelf (COTS) and government off-the-shelf (GOTS) hardware. The TIE payload contains numerous field programmable gate arrays, random access memory, and processors that are considered soft and subject to single event upset. While TacSat-2 is in a relatively benign orbit from a radiation standpoint, the TIE payload has not experienced any reboots or data corruptions that were radiation induced. On the software side, our sponsor's approach allowed us to use the network-connected, LINUX-based computers that are at the heart of the TIE payload. Because of this LINUX implementation, considerable capability exists for both adapting and reprogramming the payload to accommodate on-orbit anomalies, new experimentation possibilities, and evolving requirements. In addition, the AIS receiver system was implemented as a software-reconfigurable radio to optimize its performance and flexibility. This makes it possible to upload new software to the radio to improve its performance.

Development of the TIE payload was conducted in parallel with that of the TacSat-2 spacecraft. In order to minimize integration issues late in the program, simulators were used to emulate the spacecraft, ensuring the payload's compliance with established Interface Control Documents. This resulted in a very efficient test and integration campaign when the TIE flight hardware was delivered to AFRL. The use of software industry standards, including TCP/IP and Ethernet, and space standards such as those of the Consultative Committee for Space Data Systems (CCSDS) reduced the need for custom software, and were critical to meeting the aggressive schedule and integration challenges.

AIS Background: AIS messages provide situational awareness for ships as they transit the oceans and move through busy harbors. These messages include information about the ship such as its name, heading and speed, size, and cargo. AIS transponders are required on many commercial vessels by international treaty, insurance requirements, and U.S. law. AIS signals are broadcast in the VHF marine band, and are primarily line-of-sight. From the mast of a ship, a radius of about 25 kilometers is a typical AIS reception area. From a low Earth orbiting spacecraft, AIS messages can be received over very significant footprints, almost 13.9 million

square kilometers for the TIE payload. AIS messages are self-organizing time division multiple access (STDMA) messages. This critical design feature allows ground-based systems to self-deconflict messages. However, collection platforms that see beyond line-of-sight, such as a spacecraft, will see many self-organized networks of transponders, making this feature one source of interference. Additional sources of interference include other in-band and near-band licensed spectrum users. One method the TIE payload uses to mitigate these interference issues is to use a phased array antenna. The physical size of the array is important since at VHF frequencies it allows the beamforming electronics to create a beam with some amount of directivity and about 10 dB of gain.

On-Orbit Results: From the data that TIE has collected, it is apparent that the interference concerns are valid. We experience both co-channel interference caused by AIS transmitter density issues, and near-band interference caused by high-power radiations in adjacent bands of the receiver. The most disabling

interference appears to be the near-band interference that is primarily continuous-wave in nature. When this high duty-cycle interference is present, the TIE AIS receiver performance drops to zero. This interference is the most likely source of our performance degradation over the United States, particularly the East coast, as shown in Fig. 6. Where many ships should be present, none are detected. Other regions of the Earth where ship density is known to be very high, such as the South China Sea and Malacca Straits, do not experience a drop-off in performance, as shown in Fig. 7. In these figures, each ship icon represents a unique AIS message detected by the TIE payload.

Summary: With careful consideration of the orbital environment and the appropriate use of screening and testing, COTS and GOTS electronic components can be used successfully for higher-risk, short-duration space missions. Industry standard operating systems, scripting languages, and software protocols can be used to leverage commercial software developments to save time and money while produc-

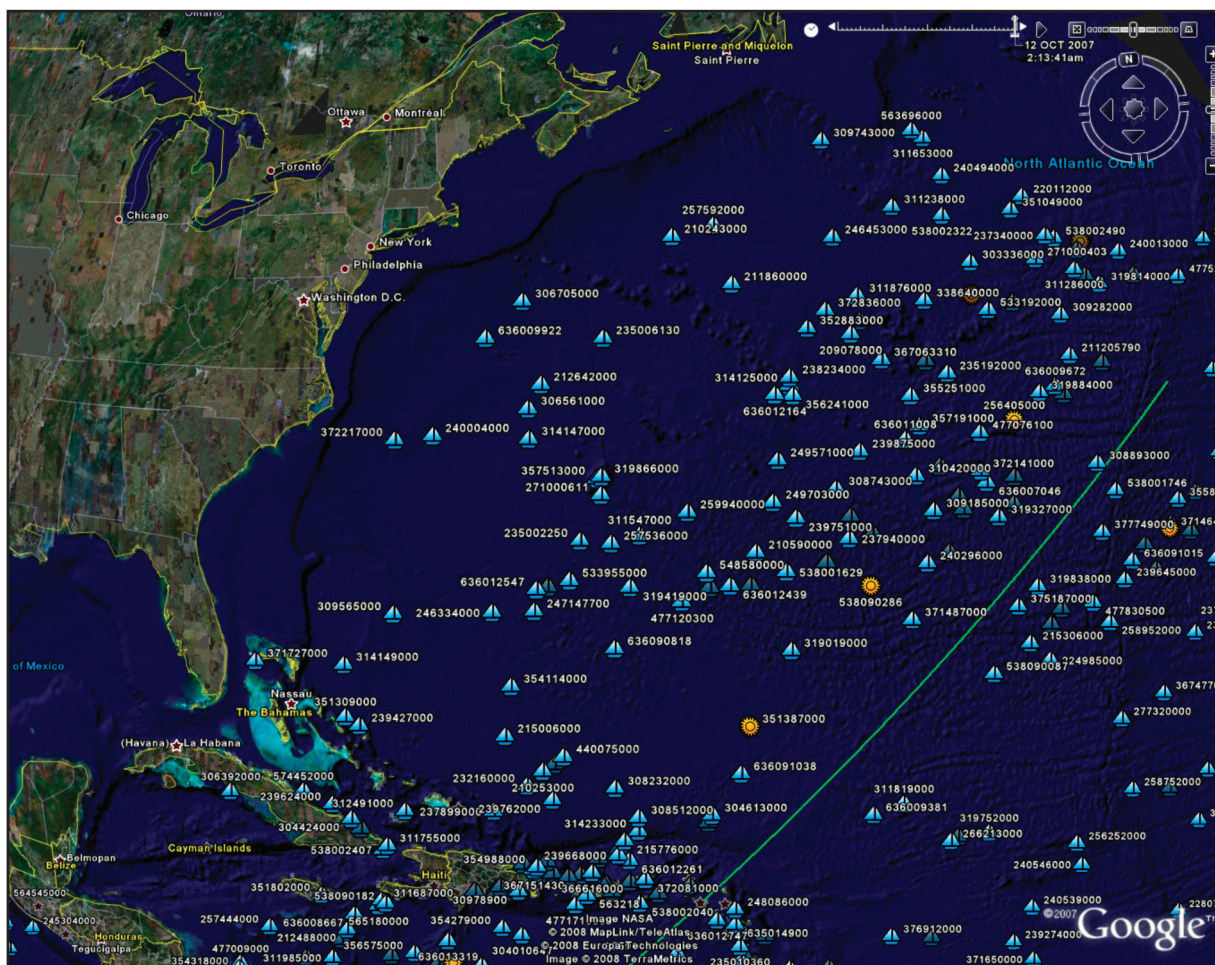


FIGURE 6
TIE AIS receiver performance degradation along the U.S. Eastern and Gulf coasts.



FIGURE 7
TIE AIS receiver performance in an area of high ship traffic density—South China Sea and Malacca Straits.

ing a flexible spaceflight payload system that meets design requirements. The TIE payload successfully collects AIS messages from space, even in areas of high traffic density, supporting maritime safety and security. However, certain near-band transmissions present challenges to the collection of AIS messages from space.

[Sponsored by ONR and DoD/AS&C] ★

Development of a Bearingless Ammonia Pump for Spacecraft Thermal Control

R.W. Baldauff, T. Kawecki, W. Purdy, and T.T. Hoang
Spacecraft Engineering Department

Advanced Thermal Control Technology for Navy's Future Needs: The potential increase in payload capability of Navy/DoD spacecraft resulting from advances in electronics miniaturization cannot be realized without concurrent advances in thermal management. More and more heat-dissipating electron-

ics have to be packaged tightly in a smaller volume to compete with the other subsystems for limited spacecraft "real estate." In a recent study, projection for the thermal requirement of future Navy spacecraft is about ten times that of today. Current state-of-the-art technologies simply will not meet this demand. Accordingly, NRL's Spacecraft Engineering Department (SED) acquired external sponsorship to initiate a research and development effort in FY2007 in pursuit of an ammonia bearingless pump that enables the Thermal Control Subsystem (TCS) to enhance its heat transport capacity at least tenfold while retaining other operational attributes (e.g., reliability and long life).

Technical Overview: The ammonia bearingless pump belongs to a new class of magnetically driven pumps that exploits the "buoyancy" force to self-center its impeller inside a hermetically sealed housing. The novel pump concept was patented by Advanced Bionics Inc. (ABI) of Minnesota. A cross-sectional view of the bearingless pump is shown in Fig. 8. It consists of two physically separate parts: an impeller housing assem-

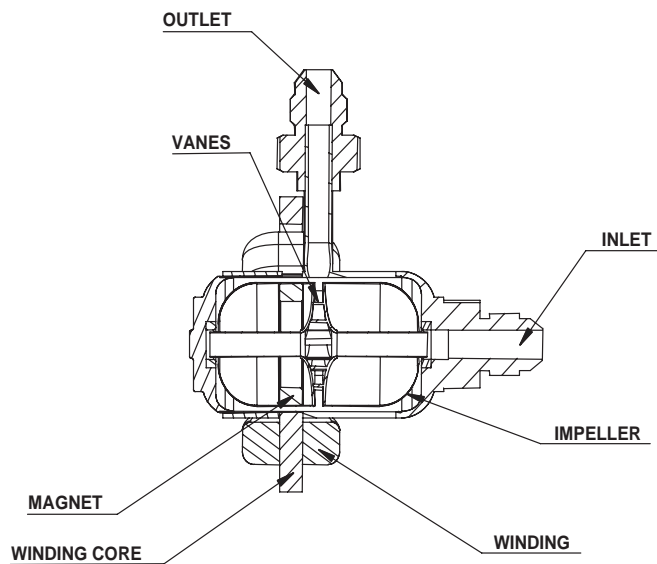
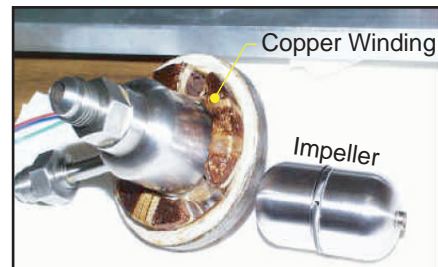


FIGURE 8
ABI bearingless pump.

bly and an external motor drive. Permanent magnets embedded in the impeller are magnetically coupled to the motor drive (located on the outer surface of the pump housing), which in turn rotates the impeller. Hence, like other magnetically driven pumps, the ABI pump does not need a driving shaft between the motor and the impeller. This allows the fluid system to be hermetically sealed from the surrounding to mitigate fluid leakage.

Central to the ABI impeller design (Fig. 9) is that the effective density of the impeller, including the embedded magnets, needs to be approximately 70% of the fluid density. When the impeller spins, the induced centrifugal gravity field in the fluid compels the lighter-than-the-fluid impeller to float to the center of the pump housing. In other words, the impeller naturally maintains a small clearance between itself and the pump housing. There is no need for bearings to restrain the impeller in any way, resulting in a lubrication-free fluid system. The external motor drive itself is



simply a copper winding (solid-state) whose magnetic field is regulated by an electronic controller to maintain the impeller rotational speed to any desired level. In short, the ABI bearingless pump has only one moving part, requiring no shaft, seal, or bearing. Its operational reliability and long life are therefore suitable for unmanned space applications.

Potential Navy Applications: Next-generation Navy/DoD spacecraft will increase the payload capability substantially as the direct result of advances in optics, sensors, and electronics. Forecasts of Navy/DoD spacecraft five to ten years from now indicate that heat transport will increase at least tenfold, rendering today's state-of-the-art devices obsolete. The SED identified several potential applications of the ABI bearingless pump for space-based TCS, as depicted in Fig. 10: (i) high-capacity hybrid ammonia heat transport loop, (ii) steerable radiators, and (iii) spray cooling for ultra high heat flux sources. The hybrid loop combines

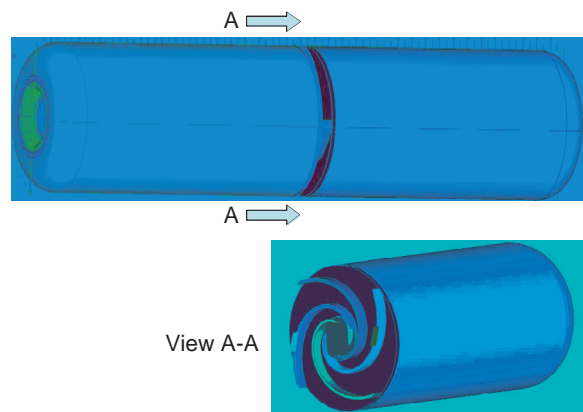


FIGURE 9
Bearingless pump impeller design.

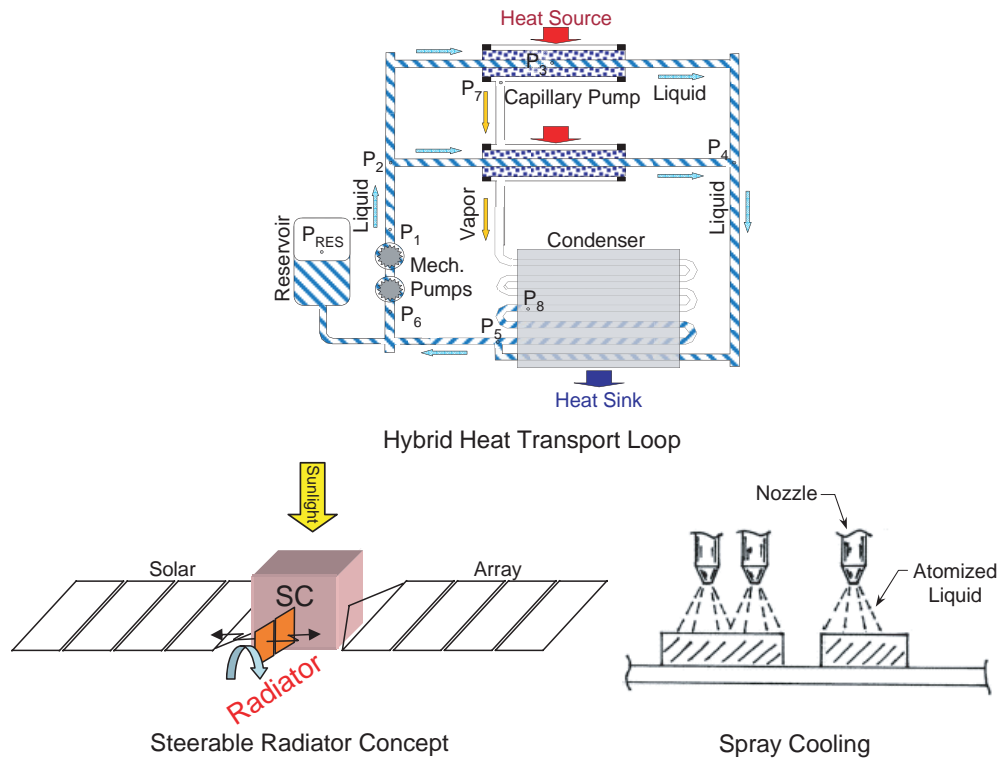


FIGURE 10
Potential applications for the bearingless pump.

state-of-the-art technology (capillary-pumped heat transport devices) and the bearingless pump into one system. It retains all beneficial attributes of the capillary loop while the bearingless pump provides a significant increase in the pumping capacity (at least one order of magnitude). The steerable radiator concept is proposed to reduce the overall TCS weight (>50%). The large pressure head provided by the bearingless pump

enables ammonia to flow in small-diameter stainless steel tubing flexible enough to allow the steerable radiator to point to any attitude for optimal heat rejection. The bearingless pump can also be utilized in a spray cooling system that atomizes liquid through a nozzle and impinges the liquid droplets onto a high heat flux source (laser diodes).

[Sponsored by USAF]



PROGRAMS FOR NRL EMPLOYEES

The Human Resources Office continues to support and provide traditional and alternative methods of training for employees. NRL employees are encouraged to develop their skills and enhance their job performance so they can meet the future needs of NRL and achieve their own goals for growth.

One common study procedure is for employees to work full time at the Laboratory while taking job-related scientific courses at universities and schools local to their job site. The training ranges from a single course to full graduate and postgraduate programs. Tuition for training is paid by NRL. The formal programs offered by NRL are described here.

GRADUATE PROGRAMS

- The **Advanced Graduate Research Program** (formerly the Sabbatical Study Program, which began in 1964) enables selected professional employees to devote full time to research or pursue work in their own or a related field for one year at an institution or research facility of their choice without the loss of regular salary, leave, or fringe benefits. NRL pays all travel and moving expenses for the employee. Criteria for eligibility include professional stature consistent with the applicant's opportunities and experience, a satisfactory program of study, and acceptance by the facility selected by the applicant. The program is open to employees who have completed six years of Federal Service, four of which have been at NRL.

- The **Edison Memorial Graduate Training Program** enables employees to pursue advanced studies in their fields at local universities. Participants in this program work 24 hours each workweek and pursue their studies during the other 16 hours. The criteria for eligibility include a minimum of one year of service at NRL, a bachelor's or master's degree in an appropriate field, and professional standing in keeping with the candidate's opportunities and experience.

- To be eligible for the **Select Graduate Training Program**, employees must have a college degree in an appropriate field and must have demonstrated ability and aptitude for advanced training. Students accepted into this program devote three academic semesters to graduate study. While attending school, they receive one-half of their salary, and NRL pays for tuition and laboratory expenses.

- The **Naval Postgraduate School (NPS)**, located in Monterey, California, provides graduate programs to enhance the technical preparation of Naval officers and civilian employees who serve the Navy in the fields of science, engineering, operations analysis, and management. It awards a master of arts degree in national security affairs and a master of science degree in many technical disciplines. NRL employees desiring to pursue graduate studies at NPS may apply for a maximum of six quarters away from NRL, with thesis work accomplished at NRL. Participants continue to receive full pay and benefits during the period of study.

- In addition to NRL and university offerings, application may be made to a number of noteworthy programs and fellowships. Examples of such opportunities are the **Capitol Hill Workshops**, the **Legislative Fellowship (LEGIS) program**, the **Federal Executive Institute (FEI)**, the **Fellowship in Congressional Operations**, and the **Executive Leadership Program for Mid-Level Employees**. These and other programs are announced from time to time, as schedules are published.

- Research conducted at NRL may be used as **thesis material for an advanced degree**. This original research is supervised by a qualified employee of NRL who is approved by the graduate school. The candidate should have completed the required course work and should have satisfied the language, residence, and other requirements of the graduate school from which the degree is sought. NRL provides space, research facilities, and supervision but leaves decisions on academic policy to the cooperating schools.

CONTINUING EDUCATION

- **Undergraduate and graduate courses** offered at local colleges and universities are subsidized by NRL for employees interested in improving their skills and keeping abreast of current developments in their fields.

- NRL offers **short courses** to all employees in a number of fields of interest including technical and administrative subjects, and supervisory and management techniques. Laboratory employees may also attend these courses at nongovernment facilities.

For further information on any of the above Graduate and Continuing Education programs, contact the Employee Relations and Development Branch (Code 1850) at (202) 767-6737 or via email at Training@hro.nrl.navy.mil.

- The **Scientist-to-Sea Program (STSP)** provides opportunities for Navy R&D laboratory/center personnel to go to sea to gain first-hand insight into operational factors affecting system design, performance, and operations on a variety of ships. NRL is a participant of this Office of Naval Research (ONR) program. Contact: Mr. Mike McCord (Code 7120) at (202) 767-2945.

PROFESSIONAL DEVELOPMENT

NRL has several programs, professional society chapters, and informal clubs that enhance the professional growth of employees. Some of these are listed below.

- The **Counseling Referral Service (C/RS)** helps employees to achieve optimal job performance through counseling and to resolve problems such as family and work-related stress and relationship difficulties, and behavioral, emotional, and substance use problems that may adversely impact job performance. C/RS provides confidential assessments and short-term counseling, training workshops, and referrals to additional resources in the community. Contact: Ms. Lois Burleigh, MSW, LGSW, at (202) 767-6857.

- The **NRL Women in Science and Engineering (WISE) Network** was formed in 1997 through the merger of the NRL chapter of WISE and the Women in Science and Technology Network. Luncheon meetings and seminars are held to discuss scientific research areas, career opportunities, and career-building strategies. The group also sponsors projects to promote the professional success of the NRL S&T community and improve the NRL working environment. Membership is open to all S&T professionals. Contact: Dr. Kathy Wahl at (202) 767-5419 or Ms. Jennifer Stepnowski at (202) 767-8533.

- **Sigma Xi**, The Scientific Research Society, encourages and acknowledges original investigation in pure and applied science. It is an honor society for research scientists. Individuals who have demonstrated the ability to perform original research are elected to membership in local chapters. The NRL Edison Chapter, comprising approximately 400 members, recognizes original research by presenting awards annually in pure and applied science to outstanding NRL staff

members. The chapter also sponsors lectures at NRL on a wide range of scientific topics for the entire NRL community. These lectures are delivered by scientists from all over the nation and the world. The highlight of the Sigma Xi lecture series is the Edison Memorial Lecture, traditionally featuring a distinguished scientist. Contact: Mr. Jeff Long at (202) 404-8697.

- The **NRL Mentor Program** was established to provide an innovative approach to professional and career training and an environment for personal and professional growth. It is open to permanent NRL employees in all job series and at all sites. Mentorees are matched with successful, experienced colleagues having more technical and/or managerial experience who can provide them with the knowledge and skills needed to maximize their contribution to the success of their immediate organization, to NRL, to the Navy, and to their chosen career fields. The ultimate goal of the program is to increase job productivity, creativity, and satisfaction through better communication, understanding, and training. NRL Instruction 12400.1A provides policy and procedures for the program. Contact: Ms. Rimentha Thomas at (202) 767-2957.

- Employees interested in developing effective self-expression, listening, thinking, and leadership potential are invited to join the Forum Club, a chapter of **Toastmasters International**. Members of this club possess diverse career backgrounds and talents and to learn to communicate not by rules but by practice in an atmosphere of understanding and helpful fellowship. NRL's Commanding Officer and Director of Research endorse Toastmasters. Contact: Dr. David Fromm at (202) 404-4670.

EQUAL EMPLOYMENT OPPORTUNITY (EEO) PROGRAMS

Equal employment opportunity (EEO) is a fundamental NRL policy for all employees regardless of race, color, national origin, sex, religion, age, or disability. The NRL EEO Office is a service organization whose major functions include counseling employees in an effort to resolve employee/management conflicts, processing formal discrimination complaints, providing EEO training, and managing NRL's affirmative employment recruitment program. The NRL EEO Office is also responsible for sponsoring special-emphasis programs to promote awareness and increase sensitivity and appreciation of the issues or the history relating to females, individuals with disabilities, and minorities. Contact the NRL Deputy EEO Officer at (202) 767-2486 for additional information on any of their programs or services.

OTHER ACTIVITIES

- The award-winning **Community Outreach Program** directed by the NRL Public Affairs Office fosters programs that benefit students and other community citizens. Volunteer employees assist with and judge science fairs, give lectures, and serve as tutors, mentors, coaches, and classroom resource teachers. The program sponsors African American History Month art and essay contests for local schools, student tours of NRL, and an annual holiday party for neighborhood children in December. Through the Community Outreach Program, NRL has active partnerships with four District of Columbia public schools. Contact: Mr. Dom Panciarelli at (202) 767-2541.

- Other programs that enhance the development of NRL employees include sports and theater groups and the **Amateur Radio Club**. The **NRL Recreation Club** encourages wide interest in sports for employees with its many facilities and programs, such as a heated indoor pool, hot tub, table tennis, basketball courts, recreation room, free weight room, new selectorized weight equipment, and volleyball courts. Sportswear and NRL and seasonal paraphernalia are available at the Recreation Club. The NRL Showboaters Theatre, organized in 1974, is in the dark. Visit www.nrl.navy.mil/showboaters/Past_Productions.php for pictures from past productions such as *Annie Get Your Gun*, *Gigi*, and *Hello Dolly*. Contact: Ms. Barbarajo Cox at (202) 404-4998 for Play Reader's meetings at NRL.

PROGRAMS FOR NON-NRL EMPLOYEES

Several programs have been established for non-NRL professionals. These programs encourage and support the participation of visiting scientists and engineers in research of interest to the Laboratory. Some of the programs may serve as stepping-stones to federal careers in science and technology. Their objective is to enhance the quality of the Laboratory's research activities through working associations and interchanges with highly capable scientists and engineers and to provide opportunities for outside scientists and engineers to work in the Navy laboratory environment. Along with enhancing the Laboratory's research, these programs acquaint participants with Navy capabilities and concerns and provide a path to full-time employment.

RECENT PH.D., FACULTY MEMBER, AND COLLEGE GRADUATE PROGRAMS

- The **National Research Council (NRC) Cooperative Research Associateship Program** selects associates who conduct research at NRL in their chosen fields in collaboration with NRL scientists and engineers. The tenure period is two years (renewable for a possible third year).

- The **NRL/ASEE Postdoctoral Fellowship Program**, administered by the American Society for Engineering Education (ASEE), aims to increase the involvement of highly trained scientists and engineers in disciplines necessary to meet the evolving needs of naval technology. Appointments are for one year (renewable for a second and possible third year).

- The **Naval Research Enterprise Intern Program (NREIP)** is a ten-week program involving NROTC

colleges/universities and their affiliates. The Office of Naval Research (ONR) offers summer appointments at Navy laboratories to current sophomores, juniors, seniors, and graduate students from participating schools. Application is online at www.asee.org/nreip through the American Society for Engineering Education. Electronic applications are sent for evaluation to the point of contact at the Navy laboratory identified by the applicant. Students are provided a stipend of \$5,500 (undergraduates) or \$6,500 (graduate students).

- The American Society for Engineering Education also administers the **Navy/ASEE Summer Faculty Research and Sabbatical Leave Program** for university faculty members to work for ten weeks (or longer, for those eligible for sabbatical leave) with professional peers in participating Navy laboratories on research of mutual interest.

- The **NRL/United States Naval Academy (USNA) Cooperative Program for Scientific Interchange** allows faculty members of the U.S. Naval Academy to participate in NRL research. This collaboration benefits the Academy by providing the opportunity for USNA faculty members to work on research of a more practical or applied nature. In turn, NRL's research program is strengthened by the available scientific and engineering expertise of the USNA faculty.

- The **National Defense Science and Engineering Graduate Fellowship Program** helps U.S. citizens obtain advanced training in disciplines of science and engineering critical to the U.S. Navy. The three-year program awards fellowships to recent outstanding graduates to support their study and research lead-

ing to doctoral degrees in specified disciplines such as electrical engineering, computer sciences, material sciences, applied physics, and ocean engineering. Award recipients are encouraged to continue their study and research in a Navy laboratory during the summer.

For further information about the above six programs, contact Ms. Lesley Renfro at (202) 404-7450.

PROFESSIONAL APPOINTMENTS

- **Faculty Member Appointments** use the special skills and abilities of faculty members for short periods to fill positions of a scientific, engineering, professional, or analytical nature at NRL.

- **Consultants and experts** are employed because they are outstanding in their fields of specialization or because they possess ability of a rare nature and could not normally be employed as regular civil servants.

- **Intergovernmental Personnel Act Appointments** temporarily assign personnel from state or local governments or educational institutions to the Federal Government (or vice versa) to improve public services rendered by all levels of government.

COLLEGE AND HIGH SCHOOL STUDENT PROGRAMS

The student programs are tailored to high school, undergraduate, and graduate students to provide employment opportunities and work experience in naval research. These programs are designed to attract applicants for student and full professional employment in fields such as engineering, physics, mathematics, and computer sciences. The student employment programs are designed to help students and educational institutions gain a better understanding of NRL's research, its challenges, and its opportunities.

Employment programs for college students include the following:

- The **Student Career Experience Program** (formerly known as the Cooperative Education Program) employs students in study-related occupations. The program is conducted in accordance with a planned schedule and a working agreement among NRL, the educational institution, and the student. Primary focus is on the pursuit of bachelor's degrees in engineering, computer science, or the physical sciences.

- The **Student Temporary Employment Program (STEP)** enables students to earn a salary while continuing their studies and offers them valuable work experience.

- The **Summer Employment Program** employs students for the summer in paraprofessional and technician positions in engineering, physical sciences, computer sciences, and mathematics.

- The **Student Volunteer Program** helps students gain valuable experience by allowing them to voluntarily perform educationally related work at NRL.

For additional information on these student programs, contact Code 1810 at (202) 767-8313.

For high school students, the **DoD Science & Engineering Apprentices Program (SEAP)** offers students grades 9 to 12 the opportunity to serve for eight weeks as junior research associates in a DoD laboratory. Under the direction of a mentor, students gain a better understanding of the challenges and opportunities of research through participation in scientific programs. Criteria for eligibility are based on science and mathematics courses completed and grades achieved; scientific motivation, curiosity, and capacity for sustained hard work; a desire for a technical career; teacher recommendations; and achievement test scores. The NRL program is the lead program and the largest in DoD. For additional information, contact Ms. Kimentha Thomas (Code 1850) at (202) 767-2957.

general information

277

Technical Output

278

Key Personnel

279

Contributions by Divisions, Laboratories, and Departments

282

Subject Index

286

Author Index

287

Employment Opportunities

TECHNICAL OUTPUT

The Navy continues to be a pioneer in initiating new developments and a leader in applying these advancements to military requirements. The primary method of informing the scientific and engineering community of the advances made at NRL is through the Laboratory's technical output—reports, articles in scientific journals, contributions to books, papers presented to scientific societies and topical conferences, patents, and inventions.

The figures for calendar year 2007 presented below represent the output of NRL facilities in Washington, D.C.; Bay St. Louis, Mississippi; and Monterey, California.

In addition to the output listed, NRL scientists made more than 1316 oral presentations during 2007.

Type of Contribution	Unclassified	Classified	Total
Articles in periodicals, chapters in books, and papers in published proceedings	1027*	0	1027*
NRL Formal Reports	12	2	14
NRL Memorandum Reports	56	3	59
Books	0	0	0
Patents granted	56		56
Statutory Invention Registrations (SIRs)	1		1

*This is a provisional total based on information available to the Ruth H. Hooker Research Library on April 14, 2008. Additional publications carrying a 2007 publication date are anticipated. Total includes non-refereed SPIE (International Society for Optical Engineering) and MRS (Materials Research Society) proceedings.

KEY PERSONNEL

Area Code (202) unless otherwise listed
Personnel Locator - 767-3200
DSN-297 or 754

Code	Office	Phone Number
EXECUTIVE DIRECTORATE		
1000	Commanding Officer	767-3403
1000.1	Inspector General	767-3621
1001	Director of Research	767-3301
1001.1	Executive Assistant	767-2445
1002	Chief Staff Officer	767-3621
1004	Head, Technology Transfer	767-3083
1006	Head, Office of Program Administration and Policy Development	767-3091
1008	Office of Counsel	767-2244
1030	Public Affairs Officer	767-2541
1100	Director, Institute for Nanoscience	767-3261
1200	Head, Command Support Division	767-3621
1220	Head, Security	767-0793
1400	Head, Military Support Division	767-2273
1600	Commanding Officer, Scientific Development Squadron One	301-342-3751
1800	Director, Human Resources Office	767-3421
1830	Deputy EEO Officer	767-5264
3005	Deputy for Small Business	767-6263
3540	Head, Safety Branch	767-2232
BUSINESS OPERATIONS DIRECTORATE		
3000	Comptroller/Associate Director of Research	767-2371
3200	Head, Contracting Division	767-5227
3300	Head, Financial Management Division	767-3405
3400	Head, Supply and Information Services Division	767-3446
3500	Director, Research and Development Services Division	404-4054
SYSTEMS DIRECTORATE		
5000	Associate Director of Research	767-3425
5300	Superintendent, Radar Division	404-2700
5500	Superintendent, Information Technology Division/ NRL Chief Information Officer*	767-2903
5600	Superintendent, Optical Sciences Division	767-7375
5700	Superintendent, Tactical Electronic Warfare Division	767-6278
MATERIALS SCIENCE AND COMPONENT TECHNOLOGY DIRECTORATE		
6000	Associate Director of Research	767-3566
6030	Head, Laboratory for Structure of Matter	767-2665
6100	Superintendent, Chemistry Division	767-3026
6300	Superintendent, Materials Science and Technology Division	767-2926
6400	Director, Laboratory for Computational Physics and Fluid Dynamics	767-3055
6700	Superintendent, Plasma Physics Division	767-2723
6800	Superintendent, Electronics Science and Technology Division	767-3693
6900	Director, Center for Bio/Molecular Science and Engineering	404-6000
OCEAN AND ATMOSPHERIC SCIENCE AND TECHNOLOGY DIRECTORATE		
7000	Associate Director of Research	404-8690
7100	Superintendent, Acoustics Division	767-3482
7200	Superintendent, Remote Sensing Division	767-3391
7300	Superintendent, Oceanography Division	228-688-4670
7400	Superintendent, Marine Geosciences Division	228-688-4650
7500	Superintendent, Marine Meteorology Division	831-656-4721
7600	Superintendent, Space Science Division	767-6343
NAVAL CENTER FOR SPACE TECHNOLOGY		
8000	Director	767-6547
8100	Superintendent, Space Systems Development Department	767-0410
8200	Superintendent, Spacecraft Engineering Department	404-3727

*Additional Duty

CONTRIBUTIONS BY DIVISIONS, LABORATORIES, AND DEPARTMENTS

Radar Division

- 149 Generalized FFT Beamsteering
J.O. Coleman

Information Technology Division

- 131 Environmental Mission Impact Assessment
J. Ballas, J. Cook, and D. Jones
- 159 Mitigating Motion Sickness in Ground Vehicles
*J.T. Coyne, R. Stripling, E. Rovira, D. Hunter,
J.V. Cohn, K. Brendley, G. Zwick, and G. Carter*
- 163 Measurement and Analysis of Clutter in Elec-
tronic Displays
*M.C. Lohrenz, M.R. Beck, J.G. Trafton, and
M.L. Gendron*
- 234 Enabling Coordination During Security,
Stabilization, Transition, and Reconstruction
Operations
R. Mittu and S. Guleyupoglu

Optical Sciences Division

- 101 Plant Proanthocyanidins Bind To and Neutralize
Bacterial Lipopolysaccharides
*J.B. Delehanty, B.J. Johnson, T.E. Hickey,
T. Pons, and F.S. Ligler*
- 151 Graded Bandgap Type-II Superlattice
Photodiodes
*E.H. Aifer, I. Vurgaftman, C.L. Canedy,
E.M. Jackson, J.G. Tischler, J.H. Warner,
R. Stine, J.R. Meyer, and L.J. Whitman*
- 205 High-Fidelity Analog Fiber Optics and Photon-
ics for Military Applications
*V.J. Urick, P.S. Devgan, J.D. McKinney,
F. Bucholtz, M.E. Godinez, A.S. Hastings,
J.F. Diehl, C. Sunderman, K. Colladay,
J.L. Dexter, and K.J. Williams*
- 207 Tactical DIRCM Jamming Pod – Early Opera-
tional Assessment
K. Sarkady, H. Romero, G. Lynn, R. Mabe,

*R. Moore, V. Cassella, F. Barone, R. Cellucci,
J.A. Schlupf, K. Strothers, K. Pick, B. Nichols,
and D. Thonburg*

- 210 Fiber-Optic Strain Monitoring on a Navy
Cruiser
*J.M. Nichols, M. Seaver, S.T. Trickey,
K. Scandell, and L.W. Salvino*

Tactical Electronic Warfare Division

- 213 Infrared Ship Signature Model Validation
from Measurements at Chesapeake Bay Detach-
ment
R. Gignilliat and C. Miller
- 219 Vantage™ Unmanned Air Vehicle
J.R. Southwick
- 229 CREW Modeling of Effectiveness and Compat-
ibility for Operational Test and Evaluation
*B. Sjoberg, A. Szymanski, J. Walters, J. Durbin,
D. Malloy, I. Will, E. Phillippi, C. Mamaril,
K. Lilley, H. Dettmar, A. Bowen, Z. Mistry, and
V. Ortiz*

Laboratory for Structure of Matter

- 71 Polymorphism in Energetic Materials
J.R. Deschamps, D.A. Parrish, and R.J. Butcher

Chemistry Division

- 141 Aerobic Miniature Microbial Fuel Cells
*B.R. Ringeisen, J.C. Biffinger, J. Pietron, R. Ray,
and B. Little*
- 151 Graded Bandgap Type-II Superlattice
Photodiodes
*E.H. Aifer, I. Vurgaftman, C.L. Canedy,
E.M. Jackson, J.G. Tischler, J.H. Warner,
R. Stine, J.R. Meyer, and L.J. Whitman*
- 171 Carbon Surface Modification for Enhanced Cor-
rosion Resistance
*P.M. Natishan, F.J. Martin, E.J. Lemieux,
T.M. Newbauer, R. Rayne, and R.A. Bayles*

- 183 Multifunctional Electrode Nanoarchitectures for Electrochemical Capacitors
J.W. Long and D.R. Rolison

- 189 Single Crystal Diamond Nanomechanical Dome Resonator
M.K. Zalalutdinov, J.W. Baldwin, B.B. Pate, J. Yang, J.E. Butler, and B.H. Houston

Materials Science and Technology Division

- 143 Innovative Ionic Liquids: Electrolytes for Ion Power Sources
T.E. Sutto, H.-S. Kim, and A. Piqué
- 177 Creating Spin Currents in Silicon
B.T. Jonker, G. Kioseoglou, A.T. Hanbicki, C.H. Li, and P.E. Thompson
- 185 Enhancement of Electrical Properties by Tailoring Nanoparticles in Holmium-doped $\text{YBa}_2\text{Cu}_3\text{O}_{7-\delta}$ Superconductors
R.L. Holtz, R. Goswami, and G. Spanos

Laboratory for Computational Physics and Fluid Dynamics

- 79 First-Principles Simulations of Violent Space-Weather Events
C.R. DeVore and S.K. Antiochos

Plasma Physics Division

- 89 High-Power Fiber Lasers for Directed-Energy Applications
P. Sprangle, A. Ting, J. Peñano, R. Fischer, and B. Hafizi
- 220 The Scintillation and Tomography Receiver in Space (CITRIS) Instrument for Ionospheric Research
P.A. Bernhardt, C.L. Siefring, I.J. Galysh, and D.E. Koch
- 231 Dynamics of Coronal Mass Ejections (CMEs)
J. Chen, P.W. Schuck, and V. Kunkel

Electronics Science and Technology Division

- 151 Graded Bandgap Type-II Superlattice Photodiodes
E.H. Aifer, I. Vurgaftman, C.L. Canedy, E.M. Jackson, J.G. Tischler, J.H. Warner, R. Stine, J.R. Meyer, and L.J. Whitman

- 153 Dynamics of Forward Voltage Drift in 4H-SiC PiN Diodes
J.D. Caldwell, R.E. Stahlbush, K.D. Hobart, and O.J. Glembocki

- 173 Lifetime Limiting Defects in 4H-SiC
P.B. Klein, B.V. Shanabrook, S.W. Huh, A.Y. Polyakov, M. Skowronski, J.J. Sumakeris, and M.J. O'Loughlin

- 174 Mobility Enhancement in Strained Antimonide Quantum Wells
B.R. Bennett, J.B. Boos, M.G. Ancona, N. Papanicolaou, J.G. Champlain, R. Bass, and B.V. Shanabrook

- 177 Creating Spin Currents in Silicon
B.T. Jonker, G. Kioseoglou, A.T. Hanbicki, C.H. Li, and P.E. Thompson

Center for Bio/Molecular Science and Engineering

- 101 Plant Proanthocyanidins Bind To and Neutralize Bacterial Lipopolysaccharides
J.B. Delehanty, B.J. Johnson, T.E. Hickey, T. Pons, and F.S. Ligler
- 187 Molecular Memory Circuits Using a Virus as a Template
A.S. Blum, C.M. Soto, and B.R. Ratna

Acoustics Division

- 123 Underwater Acoustic Communications for Bottom-Mounted Sensor Networks
P.J. Gendron
- 125 Environmental Acoustic Variability Characterization for Adaptive Sampling
J.P. Fabre, C. Rowley, G. Jacobs, E. Coelho, C. Bishop, X. Hong, and J. Cummings
- 189 Single Crystal Diamond Nanomechanical Dome Resonator
M.K. Zalalutdinov, J.W. Baldwin, B.B. Pate, J. Yang, J.E. Butler, and B.H. Houston

Remote Sensing Division

- 222 Carbon Fiber Reinforced Polymer (CFRP) Telescope Program at the Naval Research Laboratory
S.R. Restaino, J.R. Andrews, T. Martinez, C. Wilcox, F. Santiago, S.W. Teare, R.C. Romeo, and R.N. Martin

- 224 Monitoring Global Surface Soil Moisture with the WindSat Polarimetric Microwave Radiometer
L. Li and P. Gaiser

- 241 Wide Field of View Imaging with a VHF Phased Array
J. Lazio, T. Clarke, W. Lane, D. Wood, P. Ray, and N. Kassim

Oceanography Division

- 125 Environmental Acoustic Variability Characterization for Adaptive Sampling
J.P. Fabre, C. Rowley, G. Jacobs, E. Coelho, C. Bishop, X. Hong, and J. Cummings
- 141 Aerobic Miniature Microbial Fuel Cells
B.R. Ringeisen, J.C. Biffinger, J. Pietron, R. Ray, and B. Little
- 195 Improving Underwater Imaging with Ocean Optics Research
W. Hou, A. Weidemann, and D. Gray
- 197 Large-Amplitude Internal Waves in the South China Sea
D.S. Ko, P.J. Martin, S.Y. Chao, P.T. Shaw, and R.C. Lien

Marine Geosciences Division

- 160 Unmanned Vehicle Mission Planning Using 4D Forecasts
B.S. Bourgeois and H.A. Morris
- 163 Measurement and Analysis of Clutter in Electronic Displays
M.C. Lohrenz, M.R. Beck, J.G. Trafton, and M.L. Gendron

Marine Meteorology Division

- 125 Environmental Acoustic Variability Characterization for Adaptive Sampling
J.P. Fabre, C. Rowley, G. Jacobs, E. Coelho, C. Bishop, X. Hong, and J. Cummings
- 131 Environmental Mission Impact Assessment
J. Ballas, J. Cook, and D. Jones
- 134 On Tropical Cyclone Formation
M.S. Peng, B. Fu, and T. Li

- 200 Probabilistic Prediction for Improved Scientific Understanding and Improved Decision Making
J. Hansen, C. Bishop, J. Doyle, J.S. Goerss, T.R. Holt, J. McLay, and C. Reynolds

Space Science Division

- 109 Exploring Solar Flares with Gamma Rays and Neutrons
R. Murphy
- 136 SHIMMER: Innovative Technology Enabling Unprecedented Science
C.R. Englert, M.H. Stevens, D.E. Siskind, S.D. Eckermann, J.M. Harlander, K. Nielsen, and F.L. Roesler
- 166 NRL Global Vessel Tracking Project (VTP)
D.J. Bielecki
- 241 Wide Field of View Imaging with a VHF Phased Array
J. Lazio, T. Clarke, W. Lane, D. Wood, P. Ray, and N. Kassim

Space Systems Development Department

- 220 The Scintillation and Tomography Receiver in Space (CITRIS) Instrument for Ionospheric Research
P.A. Bernhardt, C.L. Siefring, I.J. Galysh, and D.E. Koch
- 243 The Target Indicator Experiment on TacSat-2
T.M. Duffey, C.M. Huffine, S.B. Nicholson, and M.L. Steininger

Spacecraft Engineering Department

- 239 FRENDO: Pushing the Envelope of Space Robotics
B.E. Kelm, J.A. Angielski, S.T. Butcher, N.G. Creamer, K.A. Harris, C.G. Henshaw, J.A. Lennon, W.E. Purdy, F.A. Tasker, W.S. Vincent, and B.P. Whalen
- 243 The Target Indicator Experiment on TacSat-2
T.M. Duffey, C.M. Huffine, S.B. Nicholson, and M.L. Steininger
- 245 Development of a Bearingless Ammonia Pump for Spacecraft Thermal Control
R.W. Baldauff, T. Kawecki, W. Purdy, and T.T. Hoang

SUBJECT INDEX

- 3D Virtual and Mixed Environments Laboratory, 45
- 3-MV Tandem Pelletron Accelerator Facility, 48
- Acoustic adaptive sampling capabilities, 38
- Acoustic Doppler current profilers (ADCPs), 59
- Acoustic Seafloor Characterization System (ASCS), 60
- Acoustic simulation, 125
- Acoustics Division, 52
- Adaptive sampling, 125
- Administrative Services Branch, 64
- Advanced Graduate Research Program, 271
- Advanced Multifunction Radio Frequency Concept (AMRFC), 42
- Advanced Silicon Carbide Epitaxial Research Laboratory (ASCERL), 50
- Airborne Polarimetric Microwave Imaging Radiometer (APMIR), 58, 66
- Amateur Radio Club, 273
- Ammonia system, 245
- Antimonides, 174
- Aqua, 60
- ATDnet, 43
- Atmosphere, 136
- Atmospheric Science and Technology, 224
- Atomic resolution transmission electron microscopy (ARTEM), 48
- Audio Laboratory, 44
- Automatic identification system, 243
- Autonomous satellite servicing, 239
- Autonomous Systems Research Lab, 67
- Bacteria, 101
- Battery, 183
- Bearingless pump, 245
- Bergen Data Center, 61, 65
- Biotechnology, 141
- BoSSNET, 43
- Capacitor, 183
- Cape Canaveral Air Force Station (CCAFS), 62
- Capitol Hill Workshops, 271
- Carbon fiber, 222
- Carrier lifetime, 173
- Center for Bio/Molecular Science and Engineering, 51
- Center for Computational Science (CCS), 44
- Center for Higher Learning, 65
- Charge-coupled device (CCD), 55
- Chemical analysis facilities, 47
- Chemistry Division, 46
- Chesapeake Bay Detachment (CBD), 42, 45, 66, 213
- Chlorofluorocarbon (CFC), 57
- Class 100 clean room facility, 51
- Class 1000 clean room, 52
- Classified Satellite/Radar Data Processing Facility, 61
- Clutter, 163
- CMES, 231
- Coastal Ocean Imaging Spectrometer (COIS), 55
- COBALT, 66
- Coherent Stand-In Jammer (CSIJ), 37
- Collaborative work system, 234
- College and high school student programs, 274
- Combat Development Command, 66
- Combat Surface Ship Qualifications Trials (CSSQT), 66
- Common distributed virtual database, 166
- Communications Security (COMSEC)/Information Security (INFOSEC), 44
- Community Outreach Program, 41, 273
- Compact Antenna Range, 42
- Compact power sources, 141
- Complementary circuits, 174
- Compound Semiconductor Processing Facility (CSPF), 50
- Comprehensive Maritime Awareness Joint Capability Technology Demonstration (CMA JCTD), 40
- Computational Electromagnetics (CEM) Facility, 42
- Computer numerically controlled (CNC) milling machine, 51
- Computing and modeling, 125
- Computing and space weather, 79
- Conical-scanning Microwave Imager/Sounder (CMIS), 58
- Connection Machine, 57
- Continuing education, 271
- Cooperative Aircraft Identification system, 43
- Cooperative Engagement Capability (CEC), 66
- Cooperative Research and Development Agreements (CRADAs), 63, 219
- Coronal mass ejections, 231
- Corporate Facilities Investment Plan (CFIP), 67
- Corrosion, 171
- Cosmic Ray Effects on Micro Electronics (CRÈME), 63
- Counseling Referral Service (C/RS), 272
- Coupled Ocean/Atmosphere Mesoscale Prediction System—On Scene (COAMPS-OS®), 65
- Crystallography, 71
- Cyber Defense Development Lab, 44
- Deck cracking, 210
- Deep-Towed Acoustics/Geophysics System (DTAGS), 60
- Defects, 173
- Defense Meteorological Satellite Program, 60
- Defense Research and Engineering Network (DREN), 43, 60
- Diamond, 189
- Digital acquisition buoy systems (DABS), 55
- Digital Library, 64
- Digital publishing technology, 63
- Directed energy (DE), 38, 89
- DoD Science & Engineering Apprentice Program (SEAP), 274
- Dragon Warrior, 43
- Dual Band Radar (DBR) Engineering Development Model, 36
- Early operational assessment of pod-mounted directional infrared counter-measures system, 36
- Edison Memorial Graduate Training Program, 271
- Efficient electrical spin injection, 37
- Electra, 49
- Electrical, Magnetic, and Optical Measurement Facility, 47
- Electromagnetic Gun Laboratory, 50
- Electron density, 220
- Electron energy loss spectroscopy (EELS), 48
- Electron microscopy, 185
- Electronic displays, 163
- Electronic Key Management System (EKMS), 44
- Electronics Research Lab, 67
- Electronics Science and Technology Division, 50
- EMI test chamber, 44
- Empire Challenge 07, 66
- Empirical orthogonal function (EOF), 39
- Energetic materials, 71
- Energy harvesting, 141
- Ensemble, 200
- Environmental Chemistry Laboratory, 65
- Environmental impacts, 131
- Environmental Protection Agency's Gulf of Mexico Program, 65
- Epicer, 50
- EPIGRESS reactor, 51
- Equal Employment Opportunity (EEO) programs, 272
- Executive Leadership Program for Mid-Level Employees, 271

- Exhibits Program, 63
- Extreme Ultraviolet Imaging Telescope (EIT), 62
- ex-USS *Shadwell* (LSD 15), 47, 67
- Federal Executive and Professional Association, 41
- Federal Executive Institute (FEI), 271
- Federal Technology Transfer Act, 63
- Fellowship in Congressional Operations, 271
- Fiber optics, 205, 210
- Fight Support Detachment, 41
- Fleet Battle Experiments, 43
- Fleet Numerical Meteorology and Oceanography Center (FNMOC), 58, 60, 65
- Focal Plane Array Evaluation Facility, 46
- Force protection/homeland defense (FP/HD), 47
- Formation genesis, 134
- Forms and Reports Management Programs, 64
- Freespace Laser Communications Laboratory, 45
- Free-Surface Hydrodynamics Laboratory, 57
- Front End Robotics Enabling Near-term Demonstration (FREND), 40
- Gamble II, 49
- Gamma Ray Large Area Space Telescope (GLAST), 62
- Gamma rays, 109
- General Electronics Environmental Test Facility, 43
- Geoacoustic Model Fabrication Laboratory, 54
- Geochemistry Laboratory, 60
- Geospatial Information Data Base (GIDB), 60
- Global Assimilation of Ionospheric Measurement (GAIM), 63
- Global Information Grid Evaluation Facility (GIG-EF), 43
- Global operational 4D-variational data assimilation system, 39
- GOES-E, 60
- GOES-W, 60
- Government Purpose Licenses, 63
- Graduate programs, 271
- Graphics support, 63
- Helium Resonance Scatter in the Corona and Heliosphere (HERSCHEL) experiment, 62
- Helmet-mounted environmental sensors, 37
- High Energy Laser Laboratory, 50
- High Frequency Active Auroral Research Program (HAARP), 45
- High-power fiber lasers, 89
- Human factors, 131
- Human performance, 159, 163
- Human Resources Office, 271
- Hybrid Coordinate Ocean Model (HYCOM), 39
- Hydroxyl, 136
- Hyperspectral Imager for the Coastal Ocean (HICO), 55
- IED, 229
- Immersive Simulation Laboratory, 44
- In Situ Sediment Acoustic Measurement System (ISSAMS), 60
- Incoherent combining, 89
- Inertial confinement fusion (ICF), 49
- Information architecture, 234
- Information Technology Division (ITD), 43
- Information technology, 159
- Infrared detector, 151
- Infrared ship signature, 213
- Infrastructure protection, 166
- Institute for Nanoscience, 42
- Integrated Communications Technology (ICT) Test Lab, 43
- Intent/Deception (ID) Laboratory, 45
- Interferometry, 241
- Inverse synthetic aperture radar (ISAR), 42
- Ionic liquid, 143
- Ionosphere, 220
- IR Missile-Seeker Evaluation Facility, 46
- JEOL 2010F transmission electron microscope, 48
- Joint Experimentation, 43
- Joint Forces Command Modeling & Simulation, 43
- Joint Tactical Radio System, 43
- Joint Typhoon Warning Center, 60
- JTF WARNET, 43
- Key Management Infrastructure (KMI), 44
- Knowledge management, 234
- Knowledge sharing, 234
- Laboratory for Advanced Materials Synthesis (LAMS), 50
- Laboratory for Computational Physics and Fluid Dynamics, 49
- Laboratory for Structure of Matter, 46
- Large Angle Spectrometric Coronagraph (LASCO), 61
- Large Area Plasma Processing System (LAPPS) facility, 49
- Large Data (LD) Joint Capability Technology Demonstration (JCTD), 36
- Large Data lab, 44
- Large-amplitude internal wave, 197
- Laser Communications Test Facility, 45
- Laser Doppler vibrometry (LDV), 52
- Legislative Fellowship (LEGIS) program, 271
- Leo scanning electron microscope, 49
- Lidar system, 58
- Lipopolysaccharide, 101
- Lithium, 143
- Long Wavelength Array (LWA), 38, 57
- Long Wavelength Demonstrator Array (LWDA), 39, 57
- Low-power electronics, 174
- Machine vision, 239
- Magnetoelectronics Fabrication Facility, 47
- Major Shared Resource Center (MSRC), 65
- Marine Corrosion Test Facility, 47, 67
- Marine Geosciences Division, 59
- Marine Meteorology Center, 67
- Marine Meteorology Division (NRL-MRY), 60, 65
- Maritime domain awareness, 166
- Maritime Hyperspectral Imaging, 55
- Mass Spectrometer and Incoherent Scatter Radar (MSIS), 62
- Master Environmental Library, 65
- Materials Processing Facility, 48
- Materials Science and Technology Division, 47
- Materials Synthesis/Property Measurement Facility, 47
- Mechanical Characterization Facility, 48
- Mercury, 49
- Mesospheric clouds, 136
- Micro/Nanostructure Characterization Facility, 48
- Microbial fuel cells (MFCs), 37
- Microstructure, 185
- Microwave Microscope (MWM), 43
- Midway Research Center (MRC), 66
- Millimeter-Wave Vacuum Electronics Synthesis Facility (MWVESF), 50
- Missile Defense Agency, 66
- Mission planning, 160
- Mobile and Dynamic Network Laboratory, 43
- Mobile Atmospheric Aerosol and Radiation Characterization Observatory (MAARCO), 61
- Moderate Resolution Imaging Spectroradiometer (MODIS), 59
- Molecular beam epitaxy (MBE), 51, 174
- Molecular electronics, 187
- Monterey Bay Crescent Ocean Research Consortium, 66
- Moore's Law, 177
- Motion Imagery Laboratory, 44
- Motion sickness, 159
- Moving Map Composer Facility, 60
- Multi-criteria decision making, 160
- Nanomechanical resonator, 189
- Nanometer Characterization/Manipulation Facility, 47
- Nanotechnology, 28, 187
- National Coastal Data Development Center, 65
- National Data Buoy Center, 65
- National Defense Science and Engineering Graduate Fellowship Program, 273
- National Geospatial-Intelligence Agency (NGA), 66
- National Polar-orbiting Operational Environmental Satellite System (NPOESS), 58
- National Radio Astronomy Observatory's (NRAO) Very Large Array (VLA), 57
- National Research Council (NRC) Cooperative Research Associateship Program, 273
- National Weather Service Forecast Office (NWSFO), 65
- NATO Undersea Research Center (NURC), 59

- Naval Center for Space Technology (NCST), 63
- Naval Cryptographic Technology Laboratory, 44
- Naval Key Management Laboratory, 44
- Naval Meteorology and Oceanography Command, 65
- Naval Oceanographic Office, 65
- Naval Postgraduate School (NPS), 65, 271
- Naval Research Enterprise Intern Program (NREIP), 273
- Navy cruiser, 210
- Navy Cyber Defense Operations Command (NCDOC), 44
- Navy Operational Global Atmospheric Prediction System (NOGAPS), 39
- Navy Operational Global Atmospheric Prediction System–Advanced Level Physics High Altitude (NOGAPS-ALPHA), 62
- Navy Prototype Optical Interferometer (NPOI), 57
- Navy Small Craft Instruction and Training Center, 65
- Navy Technology Center for Safety and Survivability, 66
- Navy/ASEE Summer Faculty Research and Sabbatical Leave Program, 273
- Nearfield scanning optical microscope (NSOM), 54
- Neutrons, 109
- Nike 3-kJ KrF laser facility, 49
- NLIWI, 197
- NOWCAST, 61
- NP-3D EW flying laboratory, 46
- NP-3D Orion aircraft, 66
- NRL Federal Credit Union (NRLFCU), 41
- NRL Mentor Program, 272
- NRL Recreation Club, 273
- NRL Technology Transfer Office (TTO), 63
- NRL/ASEE Postdoctoral Fellowship Program, 273
- NRL/United States Naval Academy (USNA) Cooperative Program for Scientific Interchange, 273
- Nuclear-enhanced radiation belt remediation, 38
- Numerical weather prediction (NWP), 60
- Ocean Dynamics and Prediction Computational Network Facility, 59
- Ocean optics, 195
- Oceanography Division, 58
- Online Bibliography service, 65
- Optical Calibration Facility, 55
- Optical Sciences Division, 45
- Optics, 205
- P-3 aircraft, 42
- Perception, 163
- Persistent surveillance, 141
- Pharos III, 49
- Phase array, 149, 241
- Phillips CM30 transmission electron microscope, 49
- Photographic services, 64
- Photonics, 205
- Plasma Physics Division, 49
- Polar mesospheric clouds (PMCs), 40
- Polar Ozone and Aerosol Measurement (POAM) instrument, 57
- Polymorphism, 71
- Portable Hyperspectral Imager for Low-Light Spectroscopy (PHILLS) system, 55
- Power Device Characterization Facility, 50, 51
- Power sources, 143, 183
- Probability, 200
- Professional appointments, 274
- Profiling Optics Package, 55
- Publication services, 63
- Pulsed laser deposition (PLD), 48
- QuikSCAT, 60
- Radar Division, 42
- Radar Imaging Facility, 42
- Radar Signature Calculation Facility, 42
- Radar Testbed Facility, 42
- Radio astronomy, 241
- Radio-frequency photonics, 205
- RC-12 Beech King Air research aircraft, 66
- Real-time eddy-resolving ($1/12^\circ$) global ocean prediction system, 39
- Records management services, 64
- Recreation Club, 41
- Remote Sensing Division, 55
- Remote sensing, 224
- Robot trajectory planning, 239
- Robotics and Autonomous Systems Laboratory, 44
- Ruth H. Hooker Research Library, 64
- Salt Water Tank Facility, 54
- Satellite Data Processing Laboratory, 60
- Satellite remote sensing, 220
- Satellite rendezvous and docking, 239
- Satellite/Radar Processing Facility, 65
- Scanfish, 59
- Scanning transmission electron microscopy (STEM), 48
- Scientific Development Squadron One (VXS-1), 66
- Scientist-to-Sea Program (STSP), 272
- SEAWifs, 60
- SECCHI Payload Operations Center (POC), 62
- Sediment Core Laboratory, 60
- Sediment Physical and Geotechnical Properties Laboratory, 60
- Select Graduate Training Program, 271
- Self-assembly, 187
- Sensor, 189
- Sepsis, 101
- Septic shock, 101
- Service oriented architecture, 131
- Session Initiation Protocol (SIP), 44
- Ship signature model, 213
- Ship tracking, 166
- Ship-motion simulator (SMS), 66
- SiC, 173
- Sigma Xi, 41, 272
- Silicon Carbide Processing Facility (SCPF), 50
- Silicon, 177
- Simulation, 79, 229
- Single crystal, 189
- Single-domain antibodies for biothreat detection, 38
- SIPRNET, 61
- Slocum Gliders, 59
- Slope to Shelf Energetics and Exchange Dynamics project, 39
- Solar and Heliospheric Observatory (SOHO), 61
- Solar Coronagraph Optical Test Chamber (SCOTCH), 61
- Solar eruptions, 231
- Solar flares, 109, 231
- Solar physics, 231
- Solar Terrestrial Relations Observatory (STEREO), 40, 62
- SONoMAGnetic LABoratory (SOMALAB), 54
- South China Sea, 197
- Space Physics Simulation Chamber (SPSC), 50
- Space robotics, 239
- Space Science Division, 61
- Space Solar Cell Characterization Facility (SSCCF), 50
- Space Systems Technology Lab, 67
- Spacecraft thermal control, 245
- Spatial Heterodyne Imager for Mesospheric Radicals (SHIMMER), 40, 62
- Spatial heterodyne spectroscopy (SHS), 40
- Special Boat Team-Twenty-two, 65
- Special Sensor Microwave Imager/Sounder (SSMIS), 58
- Spectroscopy, 136
- Spin injection, 177
- Spin-polarized, 177
- Spintronics, 177
- SPY-3 multi-function radar, 36
- Stainless steel, 171
- Stennis Space Center (NRL-SSC), 65
- Structural health monitoring, 210
- Student Career Experience Program, 41, 274
- Student Temporary Employment Program (STEP), 274
- Student Volunteer Program, 274
- Summer Employment Program, 274
- Sun Earth Connection Coronal and Heliospheric Investigation (SECCHI), 40, 61
- Supercomputing Resource Center, 65
- Superconducting quantum interference device (SQUID), 47
- Superconductivity, 185
- Surface modification wear resistance, 171
- Synchrotron Radiation Facility, 47
- Table-Top Terawatt (T^3) laser, 49
- Tactical aircraft directed infrared countermeasures suite, 207
- Tactical Electronic Warfare (TEW) Division, 46
- Technical Information Services (TIS) Branch, 63
- Telescopes, 222
- Tera, 60

Tether Physics and Survivability Experiment (TiPS), 62
 Theatre High Altitude Area Defense and Aegis Missile Defense, 66
 Thin-Film Materials Synthesis and Processing Facility, 48
 Through-the-sensor sediment data collection, 39
 Ti:Sapphire Femtosecond Laser (TFL), 49
 Toastmasters International, 41, 272
 TORPEDO Ultra, 65
 Transistor, 174
 Transmission electron microscopy (TEM), 48
 Transmission Electron Microscopy Facility, 60
 Traumatic brain injury (TBI), 37
 TRMM, 60
 Tropical cyclone, 134
 Two-phase heat transport, 245
 Type-II superlattice, 151
 U.S. Geological Survey, 65
 UAV, 219
 Ultrafast Laser Facility (ULF), 50
 Ultralow-loss Infrared (IR) Fiber-Optic Waveguide Facility, 46
 Uncertainty, 200
 Underwater imaging, 195
 United Arab Emirates United Aerosol Experiment (UAE²), 61
 Unmanned, 219
 Vacuum Ultraviolet Space Instrument Test Facility, 61
 Vantage, 219
 Vertical Microstructure Profiler (VMP), 59
 Video services, 64
 Volume Search Radar (VSR), 36
 Wafer Bonding Facility (WBF), 50
 Warfighter Human-Systems Integration Laboratory (WHSIL), 44
 W-band Advanced Radar for Low Observable Control (WARLOC), 42
 Web services, 131
 WESTPAC Airborne Geophysical Sensor Suite (WAGSS), 66
 WindSat, 57
 Women in Science and Engineering (WISE) Network, 41, 272
 Z-contrast imaging, 48

AUTHOR INDEX

- Aifer, E.H., 151
 Ancona, M.G., 174
 Andrews, J.R., 222
 Angielski, J.A., 239
 Antiochos, S.K., 79
 Baldauff, R.W., 245
 Baldwin, J.W., 189
 Ballas, J., 131
 Barone, F., 207
 Bass, R., 174
 Bayles, R.A., 171
 Beck, M.R., 163
 Bennett, B.R., 174
 Bernhardt, P.A., 220
 Bielecki, D.J., 166
 Biffinger, J.C., 141
 Bishop, C., 125, 200
 Blum, A.S., 187
 Boos, J.B., 174
 Bourgeois, B.S., 160
 Bowen, A., 229
 Brendley, K., 159
 Bucholtz, F., 205
 Butcher, R.J., 71
 Butcher, S.T., 239
 Butler, J.E., 189
 Caldwell, J.D., 153
 Canedy, C.L., 151
 Carter, G., 159
 Cassella, V., 207
 Cellucci, R., 207
 Champlain, J.G., 174
 Chao, S.Y., 197
 Chen, J., 231
 Clarke, T., 241
 Coelho, E., 125
 Cohn, J.V., 159
 Coleman, J.O., 149
 Colladay, K., 205
 Cook, J., 131
 Coyne, J.T., 159
 Creamer, N.G., 239
 Cummings, J., 125
 Delehanty, J.B., 101
 Deschamps, J.R., 71
 Dettmar, H., 229
 Devgan, P.S., 205
 DeVore, C.R., 79
 Dexter, J.L., 205
 Diehl, J.F., 205
 Doyle, J., 200
 Duffey, T.M., 243
 Durbin, J., 229
 Eckermann, S.D., 136
 Englert, C.R., 136
 Fabre, J.P., 125
 Fischer, R., 89
 Fu, B., 134
 Gaiser, P., 224
 Galysh, I.J., 220
 Gendron, M.L., 163
 Gendron, P.J., 123
 Gignilliat, R., 213
 Glembocki, O.J., 153
 Godinez, M.E., 205
 Goerss, J.S., 200
 Goswami, R., 185
 Gray, D., 195
 Guleyupoglu, S., 234
 Hafizi, B., 89
 Hanbicki, A.T., 177
 Hansen, J., 200
 Harlander, J.M., 136
 Harris, K.A., 239
 Hastings, A.S., 205
 Henshaw, C.G., 239
 Hickey, T.E., 101
 Hoang, T.T., 245
 Hobart, K.D., 153
 Holt, T.R., 200
 Holtz, R.L., 185
 Hong, X., 125
 Hou, W., 195
 Houston, B.H., 189
 Huffine, C.M., 243
 Huh, S.W., 173
 Hunter, D., 159
 Jackson, E.M., 151
 Jacobs, G., 125
 Johnson, B.J., 101
 Jones, D., 131
 Jonker, B.T., 177
 Kassim, N., 241
 Kawecki, T., 245
 Kelm, B.E., 239
 Kim, H.-S., 143
 Kioseoglou, G., 177
 Klein, P.B., 173
 Ko, D.S., 197
 Koch, D.E., 220
 Kunkel, V., 231
 Lane, W., 241
 Lazio, J., 241
 Lemieux, E.J., 171
 Lennon, J.A., 239
 Li, C.H., 177
 Li, L., 224
 Li, T., 134
 Lien, R.C., 197
 Ligler, F.S., 101
 Lilley, K., 229
 Little, B., 141
 Lohrenz, M.C., 163
 Long, J.W., 183
 Lynn, G., 207
 Mabe, R., 207
 Malloy, D., 229
 Mamaril, C., 229
 Martin, F.J., 171
 Martin, P.J., 197
 Martin, R.N., 222
 Martinez, T., 222
 McKinney, J.D., 205
 McLay, J., 200
 Meyer, J.R., 151
 Miller, C., 213
 Mistry, Z., 229
 Mittu, R., 234
 Moore, R., 207
 Morris, H.A., 160
 Murphy, R., 109
 Natishan, P.M., 171
 Newbauer, T.M., 171
 Nichols, B., 207
 Nichols, J.M., 210
 Nicholson, S.B., 243
 Nielsen, K., 136
 O'Loughlin, M.J., 173
 Ortiz, V., 229
 Papanicolaou, N., 174
 Parrish, D.A., 71
 Pate, B.B., 189
 Peñano, J., 89
 Peng, M.S., 134
 Phillippi, E., 229
 Pick, K., 207
 Pietron, J., 141
 Piqué, A., 143
 Polyakov, A.Y., 173
 Pons, T., 101
 Purdy, W.E., 239, 245
 Ratna, B.R., 187
 Ray, P., 241
 Ray, R., 141
 Rayne, R., 171
 Restaino, S.R., 222
 Reynold, C., 200
 Ringeisen, B.R., 141
 Roesler, F.L., 136
 Rolison, D.R., 183
 Romeo, R.C., 222
 Romero, H., 207
 Rovira, E., 159
 Rowley, C., 125
 Salvino, L.W., 210
 Santiago, F., 222
 Sarkady, K., 207
 Scandell, K., 210
 Schlupf, J.A., 207
 Schuck, P.W., 231
 Seaver, M., 210
 Shanabrook, B.V., 173, 174
 Shaw, P.T., 197
 Siefiring, C.L., 220
 Siskind, D.E., 136
 Sjoberg, B., 229
 Skowronski, M., 173
 Soto, C.M., 187
 Southwick, J.R., 219
 Spanos, G., 185
 Sprangle, P., 89
 Stahlbush, R.E., 153
 Steininger, M.L., 243
 Stevens, M.H., 136
 Stine, R., 151
 Stripling, R., 159
 Strothers, K., 207
 Sumakeris, J.J., 173
 Sunderman, C., 205
 Sutto, T.E., 143
 Szymanski, A., 229
 Tasker, F.A., 239
 Teare, S.W., 222
 Thompson, P.E., 177
 Thonburg, D., 207
 Ting, A., 89
 Tischler, J.G., 151
 Trafton, J.G., 163
 Trickey, S.T., 210
 Urick, V.J., 205
 Vincent, W.S., 239
 Vurgaftman, I., 151
 Walters, J., 229
 Warner, J.H., 151
 Weidemann, A., 195
 Whalen, B.P., 239
 Whitman, L.J., 151
 Wilcox, C., 222
 Will, I., 229
 Williams, K.J., 205
 Wood, D., 241
 Yang, J., 189
 Zabalutdinov, M.K., 189
 Zwick, G., 159

EMPLOYMENT OPPORTUNITIES

for Highly Innovative, Motivated, and Creative Professionals

NRL offers a wide variety of challenging S&T positions that involve skills from basic and applied research to equipment development. The nature of the research and development conducted at NRL requires professionals with experience. Typically there is a continuing need for electronics, mechanical, aerospace, and materials engineers, metallurgists, computer scientists, and oceanographers with bachelor's and/or advanced degrees and physical and computer scientists with Ph.D. degrees.



■ **Biologists.** Biologists conduct research in areas that include biosensor development, tissue engineering, molecular biology, genetic engineering, proteomics, and environmental monitoring.

■ **Chemists.** Chemists are recruited to work in the areas of combustion, polymer science, bioengineering and molecular engineering, surface science, materials, synthesis, nanostructures, corrosion, fiber optics, electro-optics, microelectronics, electron-device technology, and laser physics.

■ **Electronics Engineers and Computer Scientists.** These employees may work in the areas of communications systems, electromagnetic scattering, electronics instrumentation, electronic warfare systems, radio frequency/microwave/millimeter-wave/infrared technology, radar systems, laser physics technology, radio-wave propagation, electron device technology, spacecraft design, artificial intelligence, information processing, signal processing, plasma physics, vacuum science, microelectronics, electro-optics, fiber optics, solid state, software engineering, computer design/architecture, ocean acoustics, stress analysis, and expert systems.

■ **Materials Scientists/Engineers.** These employees are recruited to work on materials, microstructure characterization, electronic ceramics, solid-state physics, fiber optics, electro-optics, microelectronics, fracture mechanics, vacuum science, laser physics and joining technology, and radio frequency/microwave/millimeter wave/infrared technology.

■ **Mechanical and Aerospace Engineers.** These employees may work in areas of spacecraft design, remote sensing, propulsion, experimental and computational fluid mechanics, experimental structural mechanics, solid mechanics, elastic/plastic fracture mechanics, materials, finite-element methods, nondestructive evaluation, characterization of fracture resistance of structural alloys, combustion, CAD/CAM, and multi-functional material response.

■ **Oceanographers, Meteorologists, and Marine Geophysicists.** These employees work in the areas of ocean and atmospheric dynamics, air-sea interaction, upper-ocean dynamics, oceanographic bio-optical modeling, oceanic and atmospheric numerical modeling and prediction, data assimilation and data fusion, retrieval and application of remote sensing data, benthic processes, aerogeophysics, marine sedimentary processes, advanced mapping techniques, atmospheric physics, and remote sensing. Oceanographers and marine geophysicists are located in Washington, DC, and at the Stennis Space Center, Bay St. Louis, Mississippi. Meteorologists are located in Washington, DC, and Monterey, California.

■ **Physicists.** Physics graduates may concentrate on such fields as materials, solid-state physics, fiber optics, electro-optics, microelectronics, vacuum science, plasma physics, fluid mechanics, signal processing, ocean acoustics, information processing, artificial intelligence, electron-device technology, radio-wave propagation, laser physics, ultraviolet/X-ray/gamma-ray technology, electronic warfare, electromagnetic interaction, communications systems, radio frequency/microwave/millimeter-wave/infrared technology, computational physics, radio and high-energy astronomy, solar physics, and space physics.

**For more information and current vacancy listings,
visit <http://hroffice.nrl.navy.mil/>**

NAVAL RESEARCH LABORATORY

4555 Overlook Ave., SW • Washington, DC 20375-5320

LOCATION OF NRL IN THE CAPITAL AREA



Quick Reference Telephone Numbers

	NRL Washington	NRL- SSC	NRL- Monterey	NRL CBD	NRL VXS-1 Patuxent River
Hotline	(202) 767-6543	(202) 767-6543	(202) 767-6543	(202) 767-6543	(202) 767-6543
Personnel Locator	(202) 767-3200	(228) 688-3390	(831) 656-4763	(410) 257-4000	(301) 342-3751
DSN	297- or 754-	828	878	—	342
Direct-in-Dialing	767- or 404-	688	656	257	342
Public Affairs	(202) 767-2541	(228) 688-5328	(202) 767-2541	—	(202) 767-2541

Additional telephone numbers are listed on page 278.

www.nrl.navy.mil

